



buildings

Special Issue Reprint

Building Energy-Saving Technology

Edited by
Yaolin Lin and Wei Yang

mdpi.com/journal/buildings



Building Energy-Saving Technology

Building Energy-Saving Technology

Editors

Yaolin Lin

Wei Yang



Basel • Beijing • Wuhan • Barcelona • Belgrade • Novi Sad • Cluj • Manchester

Editors

Yaolin Lin
University of Shanghai for
Science and Technology
Shanghai, China

Wei Yang
The University of Melbourne
Melbourne, Australia

Editorial Office

MDPI
St. Alban-Anlage 66
4052 Basel, Switzerland

This is a reprint of articles from the Special Issue published online in the open access journal *Buildings* (ISSN 2075-5309) (available at: https://www.mdpi.com/journal/buildings/special_issues/Building_Energy_Saving_Technology).

For citation purposes, cite each article independently as indicated on the article page online and as indicated below:

Lastname, A.A.; Lastname, B.B. Article Title. <i>Journal Name</i> Year , <i>Volume Number</i> , Page Range.
--

ISBN 978-3-0365-9302-9 (Hbk)

ISBN 978-3-0365-9303-6 (PDF)

doi.org/10.3390/books978-3-0365-9303-6

© 2023 by the authors. Articles in this book are Open Access and distributed under the Creative Commons Attribution (CC BY) license. The book as a whole is distributed by MDPI under the terms and conditions of the Creative Commons Attribution-NonCommercial-NoDerivs (CC BY-NC-ND) license.

Contents

About the Editors	vii
Yaolin Lin and Wei Yang Building Energy-Saving Technology Reprinted from: <i>Buildings</i> 2023 , <i>13</i> , 2161, doi:10.3390/buildings13092161	1
Abdalrahman A. Alghamdi, Ali M. Alqarni and Abdullah A. AlZahrani Numerical Investigation of Effects of Camlock System on Thermal Conductivity of Structural Insulated Panels Reprinted from: <i>Buildings</i> 2023 , <i>13</i> , 413, doi:10.3390/buildings13020413	5
Abdullah A. AlZahrani, Abdulrahman A. Alghamdi and Ahmad A. Basalah Computational Optimization of 3D-Printed Concrete Walls for Improved Building Thermal Performance Reprinted from: <i>Buildings</i> 2022 , <i>12</i> , 2267, doi:10.3390/buildings12122267	19
Jolanta Šadauskienė, Juozas Ramanaukas, Dorota Anna Krawczyk, Eglė Klumbytė and Paris A. Fokaides Investigation of Thermal Bridges of a New High-Performance Window Installation Using 2-D and 3-D Methodology Reprinted from: <i>Buildings</i> 2022 , <i>12</i> , 572, doi:10.3390/buildings12050572	35
Yonghan Li, Wei Yin, Yawen Zhong, Mingqiao Zhu, Xiaoli Hao, Yongcun Li, et al. Energy Consumption of Apartment Conversion into Passive Houses in Hot-Summer and Cold-Winter Regions of China Reprinted from: <i>Buildings</i> 2023 , <i>13</i> , 168, doi:10.3390/buildings13010168	55
Nuonan Zhang, Yun Guo, Weijian Yuan and Yaolin Lin Energy-Saving Design and Energy Consumption Analysis of a New Vacuum Refrigerator Reprinted from: <i>Buildings</i> 2022 , <i>12</i> , 203, doi:10.3390/buildings12020203	77
Qian-Cheng Wang, Ke-Xin Xie, Xuan Liu, Geoffrey Qi Ping Shen, Hsi-Hsien Wei and Tian-Yi Liu Psychological Drivers of Hotel Guests' Energy-Saving Behaviours—Empirical Research Based on the Extended Theory of Planned Behaviour Reprinted from: <i>Buildings</i> 2021 , <i>11</i> , 401, doi:10.3390/buildings11090401	95
Yaolin Lin, Zhenyan Bu, Wei Yang, Haisong Zhang, Valerie Francis and Chun-Qing Li A Review on the Research and Development of Solar-Assisted Heat Pump for Buildings in China Reprinted from: <i>Buildings</i> 2022 , <i>12</i> , 1435, doi:10.3390/buildings12091435	113
Mohammad Khairul Basher, Mohammad Nur-E-Alam, Md Momtazur Rahman, Kamal Alameh and Steven Hinckley Aesthetically Appealing Building Integrated Photovoltaic Systems for Net-Zero Energy Buildings. Current Status, Challenges, and Future Developments—A Review Reprinted from: <i>Buildings</i> 2023 , <i>13</i> , 863, doi:10.3390/buildings13040863	147
Yaolin Lin, Jingye Liu, Kamiel Gabriel, Wei Yang and Chun-Qing Li Data-Driven Based Prediction of the Energy Consumption of Residential Buildings in Oshawa Reprinted from: <i>Buildings</i> 2022 , <i>12</i> , 2039, doi:10.3390/buildings12112039	173

Qunfeng Ji, Yangbo Bi, Mehdi Makvandi, Qinli Deng, Xilin Zhou and Chuancheng Li Modelling Building Stock Energy Consumption at the Urban Level from an Empirical Study Reprinted from: <i>Buildings</i> 2022 , <i>12</i> , 385, doi:10.3390/buildings12030385	199
Bundit Buddhahai, Suratsavadee Koonlaboon Korkua, Pattana Rakkwamsuk and Stephen Makonin A Design and Comparative Analysis of a Home Energy Disaggregation System Based on a Multi-Target Learning Framework Reprinted from: <i>Buildings</i> 2023 , <i>13</i> , 911, doi:10.3390/buildings13040911	215
Guang Yang, Yingli Xuan and Zeng Zhou Influence of Building Density on Outdoor Thermal Environment of Residential Area in Cities with Different Climatic Zones in China—Taking Guangzhou, Wuhan, Beijing, and Harbin as Examples Reprinted from: <i>Buildings</i> 2022 , <i>12</i> , 370, doi:10.3390/buildings12030370	231
Germán Ramos Ruiz, Alba Olloqui del Olmo Climate Change Performance of nZEB Buildings Reprinted from: <i>Buildings</i> 2022 , <i>12</i> , 1755, doi:10.3390/buildings12101755	247
Yuan Chang, Geng Geng, Chongjie Wang, Yibing Xue and Tian Mu Design of Rural Human Settlement Unit with the Integration of Production-Living-Ecology of China Based on Dynamic Emergy Analysis Reprinted from: <i>Buildings</i> 2023 , <i>13</i> , 618, doi:10.3390/buildings13030618	267

About the Editors

Yaolin Lin

Dr. Yaolin Lin is an associate professor at Shanghai University of Science and Technology. Before that, he worked as an associate professor at Wuhan University of Technology, and as a principle engineer at a leading building energy efficiency consulting company in California, USA. He received his PhD degree in building engineering from Concordia University in Canada. He has over 7 years of industrial experience on building HVAC controls, building energy management, retro-commissioning of building systems, and advanced controller development, and over 10 years of research experience on green and sustainable buildings, HVAC system control optimization, and building energy system modeling and simulation, leading over 50 industrial projects across five different countries, including the USA, Canada, France, Singapore, and China. He has published over 90 journal papers, book chapters, and peer-reviewed conference papers on building energy efficiency and simulation. Dr. Lin is an associate editor of the international journal of *Frontiers in Built Environment*, a topic editor for the international journal of *Energies*, a leading guest editor for the international journal of *Energy Exploration & Exploitation*, and a guest editor for the international journal of *Sustainability*. He serves as an editorial member for the SCI journals *Buildings* and *Advances in Meteorology* and for the EI journal *Energy Engineering*. He is a reviewer for over 40 renowned international journals, such as *Energy*, *Applied Energy*, *Energy and Buildings*, *Building and Environment*, and *Renewable Energy*.

Wei Yang

Dr. Wei Yang is a senior lecturer in the Faculty of Architecture, Building and Planning at The University of Melbourne. She holds a PhD in building science awarded by the National University of Singapore (NUS). She has broad research expertise and interest in building energy efficiency, sustainable building design, building performance evaluation, and life cycle assessment. She has over 80 peer-reviewed journal publications, and her google scholar h-index is 26. Currently, she serves as the associate editor for *Frontiers in Built Environment*. She is also on the topical advisory panel for the journal of *Atmosphere*.

Building Energy-Saving Technology

Yaolin Lin ^{1,*} and Wei Yang ²

¹ School of Environment and Architecture, University of Shanghai for Science and Technology, Shanghai 200093, China

² Faculty of Architecture, Building and Planning, The University of Melbourne, Melbourne 3010, Australia; wei.yang@unimelb.edu.au

* Correspondence: ylin@usst.edu.cn

Abstract: Buildings consume about 40% of the global energy. Therefore, the building sector plays a key role in achieving the goals of carbon peak and carbon neutrality. Various energy-saving technologies for buildings, such as building envelopes, mechanical systems, and energy resources, have been developed to help to achieve zero- or even net-energy buildings while maintaining comfort and a healthy indoor environment. This Special Issue on building energy-saving technology was open to all contributors in the field of building engineering. The original experimental studies, numerical simulations, and reviews in all aspects of building energy utilization, management, and optimization have been considered. For this event, all of these topics were covered in the extensive submissions which were accepted, but interesting papers on other aspects of building energy efficiency were also received. The purpose of this editorial is to summarize the main research findings of the accepted papers in this Special Issue, including the energy-saving technologies involved in building envelopes, mechanical systems, and occupant behaviors, and to identify a number of research questions and research directions.

1. Research Topics Investigated

The accepted papers cover the energy-saving technologies related to the improvement of building envelopes, mechanical systems, occupants' behavior, renewable energy utilization, energy prediction and disaggregation, building planning, and climate-adaptive design. All of the technologies can be used for low-carbon building design.

1.1. Energy Saving through Building Envelop

The thermal performance of the building envelop determines the amount of heat gain/loss that needs to be addressed by the heating, ventilation, and air-conditioning (HVAC) systems. Alghamdi et al. [1] proposed structural insulated panels (SIPs) joined with embedded camlock systems to solve the thermal bridge problem due to using framing members and nails to join SIPs. They found that SIP thickness is the dominant factor that affects its thermal performance, and the reduction in the R-value of the SIP caused by the embedded camlock systems is less than 13.8%. AlZahrani et al. [2] performed optimization on concrete walls using 3D-printed technology. They found that the infill structure of the walls affects their thermal conductivities and, thus, their thermal performance. Compared to conventional walls, the energy cost savings of the 3D-printed concrete (3DPC) walls were about USD 1/m². Šadauskienė et al. [3] investigated the effect of installation methods on the thermal performance of a new, high-performance window and found that the difference in the calculation results using the 2D method and the 3D method could be up to 68%. They insulated the window frame with SWB, not evaluating that the mental fastener could reduce the thermal bridge at the junction and frame by 80% (up to 37% when evaluating the mental fastener) compared to the traditional choice without insulation. Li et al. [4] evaluated the energy-saving potential of improving the insulation and air-tightness level of windows and doors for a passive house in regions with hot summers and cold winters

Citation: Lin, Y.; Yang, W. Building Energy-Saving Technology. *Buildings* **2023**, *13*, 2161. <https://doi.org/10.3390/buildings13092161>

Received: 3 August 2023

Accepted: 23 August 2023

Published: 25 August 2023



Copyright: © 2023 by the authors. Licensee MDPI, Basel, Switzerland. This article is an open access article distributed under the terms and conditions of the Creative Commons Attribution (CC BY) license (<https://creativecommons.org/licenses/by/4.0/>).

in China. A reduction in heating energy consumption of up to 62% was found. However, overheating during the transition and summer seasons also occurred, which need to be resolved using natural and hybrid ventilation.

1.2. Energy Savings through Mechanical System

Mechanical systems account for a large proportion of building energy consumption. Determining how to improve their energy efficiency is crucial for improving the building performance. Zhang et al. [5] proposed a vacuum refrigeration energy-saving device with a new sealing door structure to reduce the number of vacuum refrigeration pumps and reduce the energy loss during operation.

1.3. Energy Savings through Occupants' Behavior Regulation

As people spend most of their time indoors, their energy usage behavior plays an important role in determining the building's energy consumption. Wang et al. [6] used the theory of planned behavior (TPB) and two extension models to evaluate the factors affecting the energy-efficient intentions and behaviors of the hotel guests. They found that past behaviors and self-determined motivation have strong correlations with hotel energy savings, and they suggest encouraging hotel guests to engage in pro-environmental behaviors.

1.4. Energy Savings through Renewable Energy Usage

The usage of renewable energy resources helps to reduce building energy consumption. Lin et al. [7] performed a review on the research and development of solar-assisted heat pumps for buildings in China. They found that the current research focuses on the theoretical and experimental investigation of the energy performance of the main components of the heat pump system, but less attention was paid to intelligent control, operation optimization, and integration with buildings. Building-integrated photovoltaic (BIPV) modules can be adopted to achieve net-zero energy buildings (NZEBs); however, this is not widely accepted by the architects and builders [8]. Basher et al. [8] performed a review on aesthetically appealing BIPV systems and recommended the development of high-definition colored PV (HDPV) modules with adequate image contrast in order to boost the productions and expand the BIPV market. The power conversion efficiency (PCE) of this product outperformed 85% of a bare panel.

1.5. Energy Savings through Energy Modeling, Prediction and Disaggregation, Building Planning, and Climate-Adaptive Design

It is crucial to know the importance of the factors that affect building energy consumption in order to determine the energy consumption of the buildings. Big data analysis based on field data collection can be employed to find the variable importance (VI) of each variable during the prediction of building energy consumption. Lin et al. [9] developed and compared the performance of eight data-driven energy prediction models for residential buildings in Oshawa, Canada. They found that back propagation neural network (BPNN) models had the best performance in terms of predicting both annual building electricity consumption and gas consumption, with mean absolute percentage errors (MAPEs) of less than 2.63%. The heating system type, fuel type for domestic water heaters, floor area, heating system efficiency, age of the heating system, and fuel type for the heating system are the most influential factors on electricity consumption, while the fuel type for the heating system, air change rate per hour (ACH), heating system efficiency, number of fluorescent bulbs used outdoors, and fuel type for domestic water heaters are the most important factors for gas consumption.

Despite knowing the individual building's energy performance, it is also very important to determine the whole building's energy consumption at a larger scale, as buildings interact with each other as well as the local environment. Ji et al. [10] developed a physical-based bottom-up method to predict the building operation energy consumption at the

urban scale, and used imported topography to consider the shading effects on buildings. The outcomes of the results were found to agree with the benchmark. Commercial and transport buildings were found to have large energy use intensity (EUI), where the cooling energy demand is far greater than the heating energy demand.

It is equally important to determine the contribution of each electrical power appliance to a building's energy consumption. Buddhahai et al. [11] proposed an experimental design to disaggregate home energy consumption under a multi-target learning framework. They found that the performance of a prediction mode using the F-score (micro-averaged) and the power estimation accuracy index was better than that of a deep-learning-based denoising auto-encoder network approach, and was able to be used for home energy monitoring.

Building planning has an impact on the local micro-climate, which indirectly affects the energy consumption of the buildings in the community. Yang et al. [12] carried out a study on the influence of building density on the outdoor environmental thermal comfort of residential buildings in different climatic regions in China. They found that, when the building distance was in the range of 20–50 m, the mean radiant temperature (MRT) of the outdoor environment increased by 1.25 °C for every increase of 10 m in the distance.

Due to the global warming effect, there is a need to know the adaptivity of the buildings against climate change. Ruiz et al. [13] examined the performance of a semi-detached house with different Spanish energy regulations in different future climate change scenarios. They found that the buildings with nearly zero energy building (nZEB) criteria outperformed buildings with the other two energy regulations by an average of 84.36% in energy consumption reduction, while, at the same time, the “slightly cool” hours were reduced by 57% and there was an improvement by up to eight times in the “slight warm” category.

As difference sources of energy vary in qualities, energy is used to overcome this barrier. Chang et al. [14] employed a dynamic energy analysis method for the design of a rural human settlement unit integrated with product-living-ecology. They found that the energy self-sufficiency ratio and sustainable indices decreased over time, from 0.34 to 0.15 and from 0.76 to 0.57, respectively. At the same time, the values of the energy investment ratio, net energy yield ratio, and environmental load ratio increased.

2. Conclusions

The papers in this Special Issue generate new insights into energy-saving technologies for buildings from various aspects (i.e., building envelop systems, building mechanical systems, occupants' behaviors, building density, solar energy utilization, etc.). The following sets of research questions and research directions are compiled:

- (1) Low-carbon buildings require the integration of building energy-saving technologies in building envelops and mechanical systems, as well as regulation of the building occupants' behavior.
- (2) Integration of buildings with renewable energy sources is the key to achieving carbon peak and carbon neutrality, and ways to improve building energy efficiency with the integration of renewable energy technology will continue to be a hot topic.
- (3) A big-data-driven approach is very important in building energy prediction and energy-efficient operation of a building's mechanical system, and will be an interest of many researchers in building energy-saving and mechanical system control.

Author Contributions: Conceptualization, Y.L. and W.Y.; writing—original draft preparation, Y.L.; writing—review and editing, Y.L. and W.Y. All authors have read and agreed to the published version of the manuscript.

Funding: This research received no external funding.

Acknowledgments: We would like to thank the authors for their contribution to the Special Issue and the reviewers for their thorough and timely reviews. We believe that this Special Issue provides a valuable contribution to building energy-saving technology, which will generate insights for achieving low-carbon buildings.

Conflicts of Interest: The authors declare no conflict of interest.

References

1. Alghamdi, A.; Alqarni, A.; AlZahrani, A. Numerical Investigation of Effects of Camlock System on Thermal Conductivity of Structural Insulated Panels. *Buildings* **2023**, *13*, 413. [[CrossRef](#)]
2. AlZahrani, A.; Alghamdi, A.; Basalah, A. Computational Optimization of 3D-Printed Concrete Walls for Improved Building Thermal Performance. *Buildings* **2022**, *12*, 2267. [[CrossRef](#)]
3. Šadauskienė, J.; Ramanauskas, J.; Krawczyk, D.; Klumbytė, E.; Fokaides, P. Investigation of Thermal Bridges of a New High-Performance Window Installation Using 2-D and 3-D Methodology. *Buildings* **2022**, *12*, 572. [[CrossRef](#)]
4. Li, Y.; Yin, W.; Zhong, Y.; Zhu, M.; Hao, X.; Li, Y.; Ouyang, Y.; Han, J. Energy Consumption of Apartment Conversion into Passive Houses in Hot-Summer and Cold-Winter Regions of China. *Buildings* **2023**, *13*, 168. [[CrossRef](#)]
5. Zhang, N.; Guo, Y.; Yuan, W.; Lin, Y. Energy-Saving Design and Energy Consumption Analysis of a New Vacuum Refrigerator. *Buildings* **2022**, *12*, 203. [[CrossRef](#)]
6. Wang, Q.; Xie, K.; Liu, X.; Shen, G.; Wei, H.; Liu, T. Psychological Drivers of Hotel Guests' Energy-Saving Behaviours—Empirical Research Based on the Extended Theory of Planned Behaviour. *Buildings* **2021**, *11*, 401. [[CrossRef](#)]
7. Lin, Y.; Bu, Z.; Yang, W.; Zhang, H.; Francis, V.; Li, C. A Review on the Research and Development of Solar-Assisted Heat Pump for Buildings in China. *Buildings* **2022**, *12*, 1435. [[CrossRef](#)]
8. Basher, M.; Nur-E-Alam, M.; Rahman, M.; Alameh, K.; Hinckley, S. Aesthetically Appealing Building Integrated Photovoltaic Systems for Net-Zero Energy Buildings. Current Status, Challenges, and Future Developments—A Review. *Buildings* **2023**, *13*, 863.
9. Lin, Y.; Liu, J.; Gabriel, K.; Yang, W.; Li, C. Data-Driven Based Prediction of the Energy Consumption of Residential Buildings in Oshawa. *Buildings* **2022**, *12*, 2039. [[CrossRef](#)]
10. Ji, Q.; Bi, Y.; Makvandi, M.; Deng, Q.; Zhou, X.; Li, C. Modelling Building Stock Energy Consumption at the Urban Level from an Empirical Study. *Buildings* **2022**, *12*, 385. [[CrossRef](#)]
11. Buddhahai, B.; Korkua, S.; Rakkwamsuk, P.; Makonin, S. A Design and Comparative Analysis of a Home Energy Disaggregation System Based on a Multi-Target Learning Framework. *Buildings* **2023**, *13*, 911. [[CrossRef](#)]
12. Yang, G.; Xuan, Y.; Zhou, Z. Influence of Building Density on Outdoor Thermal Environment of Residential Area in Cities with Different Climatic Zones in China—Taking Guangzhou, Wuhan, Beijing, and Harbin as Examples. *Buildings* **2022**, *12*, 370. [[CrossRef](#)]
13. Ramos Ruiz, G.; Olloqui del Olmo, A. Climate Change Performance of nZEB Buildings. *Buildings* **2022**, *12*, 1755. [[CrossRef](#)]
14. Chang, Y.; Geng, G.; Wang, C.; Xue, Y.; Mu, T. Design of Rural Human Settlement Unit with the Integration of Production-Living-Ecology of China Based on Dynamic Energy Analysis. *Buildings* **2023**, *13*, 618. [[CrossRef](#)]

Disclaimer/Publisher's Note: The statements, opinions and data contained in all publications are solely those of the individual author(s) and contributor(s) and not of MDPI and/or the editor(s). MDPI and/or the editor(s) disclaim responsibility for any injury to people or property resulting from any ideas, methods, instructions or products referred to in the content.

Article

Numerical Investigation of Effects of Camlock System on Thermal Conductivity of Structural Insulated Panels

Abdallah A. Alghamdi *, Ali M. Alqarni and Abdullah A. AlZahrani

Mechanical Engineering Department, Umm Al-Qura University, Makkah 21955, Saudi Arabia

* Correspondence: aasghamdi@uqu.edu.sa

Abstract: Structural insulated panels (SIPs) are widely used in residential and commercial buildings due to their reliable mechanical and thermal performance. However, using framing members and nails to join SIPs causes thermal bridging across the insulation and thus increases heat losses from the building envelope. Alternatively, SIPs joined with embedded camlock systems can overcome this issue. In this paper, a parametric study of the effects of the camlock system material and SIP geometric design on the thermal performance of SIP walls was investigated using a multi-scale finite element modeling approach. The model considers the structural design details of the camlock system. In addition, the effects of the SIP materials, SIP thickness, and the number of camlock systems per unit area on the through-thickness thermal conductivity of the SIP walls are examined. It was found that the SIP thickness is a dominating factor influencing the thermal performance of the SIP. The through-thickness (overall) thermal conductivity of the SIP wall increases linearly with the increase in the number of camlock systems used per unit area. However, it rises exponentially with the increasing SIP thickness. The reduction in the overall R-value of the SIP caused by the camlock system embedded in the SIP did not exceed 13.8%.

Keywords: structural insulated panels (SIPs); thermal analyses; multi-scale finite element modeling; parametric analysis

Citation: Alghamdi, A.A.; Alqarni, A.M.; AlZahrani, A.A. Numerical Investigation of Effects of Camlock System on Thermal Conductivity of Structural Insulated Panels. *Buildings* **2023**, *13*, 413. <https://doi.org/10.3390/buildings13020413>

Academic Editors: Yaolin Lin and Wei Yang

Received: 29 December 2022

Revised: 16 January 2023

Accepted: 31 January 2023

Published: 2 February 2023



Copyright: © 2023 by the authors. Licensee MDPI, Basel, Switzerland. This article is an open access article distributed under the terms and conditions of the Creative Commons Attribution (CC BY) license (<https://creativecommons.org/licenses/by/4.0/>).

1. Introduction

Residential energy consumption accounts for more than one-third of global electrical energy consumption [1–3]. Consequently, interest in green construction materials has grown, particularly for the exterior walls of buildings, which separate and protect structures from the climate. Reducing heat transfer via outside walls is critical without sacrificing structural integrity. These factors should be considered early on during the design process, and they have been the focus of much of the research on advanced construction technologies [4].

Structural insulated panels (SIPs) are energy-efficient building systems composed of a rigid, lightweight insulating material sandwiched between two outer structural skins. The insulation core is typically composed of insulating foams such as polyurethane (PUR), expanded polystyrene (EPS), or extruded polystyrene (XPS). The outer skin is usually composed of sheet metal, magnesium-oxide boards, cement-fiber boards, plywood, or oriented strand boards (OSBs). Owing to their high thermal insulation performance, SIPs are extensively used as building envelope materials in extreme climate regions, such as the Arctic [5–7]. According to Harries et al. [8], SIP walls have nearly a 42% higher R-value than typical timber-framed walls. SIP-built houses save about 14% energy use compared to stud-framed houses [9] and 60% compared to brick–concrete structure houses [10]. According to Lu and Memari [11], the thermal performance of SIP walls depends mainly on the insulation thickness and panel size. They estimated the annual energy savings from implementing 3.5 in and 5.5 in SIP walls compared to standard framing walls to be 3.08% and 7.62%, respectively. Another advantage of SIPs is the panels' easy and quick installation process, which, in turn, reduces installation costs [12]. According to Mullens and Arif, installing SIPs on walls and roofs saves up to two-thirds of the on-site framing labor [13].

However, the thermal insulation performance of any SIP envelope is vulnerable to the panel's joints, where air and moisture infiltration and thermal bridging may occur [14]. Abdou [15] examined the influence of a joint sealant on the thermal performance of an interlocking SIP envelope composed of fiber-reinforced plastic. The absence of a joint sealant reduced the SIP wall's overall thermal resistance (R) due to the air leakage. This reduction ranged from 5% to 46%, depending on different factors. Wyss et al. [16] and Kayello et al. [17] published similar findings. They conducted experimental studies to determine the airtightness and thermal performance of SIP joints subjected to pressure differences that may cause joint openings. They used oriented strand boards and expanded polystyrene for the SIPs and wood for the joints.

Qiang Du et al. [18] conducted an experimental study on the thermal transmittance of different types of spline joints commonly used in SIP walls. They also performed a FE numerical parametric study to examine the influence of insulation thickness, nail dimensions, and spacing on the thermal performance of SIP walls. They reported that the thermal transmittance increases significantly with the increase in the size of the spline.

A SIP joint has less thermal resistance than the SIP center owing to thermal bridging at the framing members. Therefore, the overall R-value of the SIP wall is reduced; this reduction is estimated to be 10–20% depending on the size and geometry of the joining mechanism [19]. As a solution, the camlock system enhances the thermal performance of SIP walls by providing outstanding tight connections to the SIPs. A cam locks system is a fastening mechanism used to connect two SIPs. It comprises two halves, one containing a pin and the other having a cam, which rotates by using a key to connect or disconnect the SIPs. The use of the camlock system eliminates the need for frame members and nails, which are responsible for thermal bridging. However, there exists a significant gap in the literature on the thermal performance of SIPs with embedded camlock systems.

Therefore, the objective of this paper is to investigate the thermal performance of the SIP walls joint by a camlock system which has never been considered in the previous literature. Furthermore, the thermal performance of the alternative joining method is considered, namely the surface spline; thus, the thermal performance—through-thickness thermal conductivity—of both options can be compared and discussed. In order to achieve the objective of this study, a multi-scale finite element (FE) model was developed and validated to predict the through-thickness thermal conductivity of SIP walls. The model results were firstly verified by experimental results obtained by other researchers [18] where they used a hot box apparatus. Then, utilizing the powerful commotional capabilities of the model, the effects of different measures on the thermal insulation performance of the SIP walls joined by camlock systems were investigated. Specifically, the thermal conductivity of the camlock system, the thermal conductivity of the SIPs, the thickness of the SIPs, and the number of camlock systems per unit area were all examined. The results provide comprehensive data on these various design options that can guide future research and development.

2. Experimental Measurement

2.1. Test Setup

The experimental work of Qiang Du and his colleagues [18]—who used a hot box apparatus according to ASTM C1363-11 [20] in order to measure the thermal transmittance of SIP wall samples of size $1.5 \times 1.5 \times 0.165 \text{ m}^3$ —was used in this study for validation. This apparatus consists of two boxes, one chilled to sub-zero temperature (called the cold box) and one kept near room temperature (called the hot box). The wall sample is positioned in an insulated test frame which is placed between the hot and cold boxes. Two heat flow meters are glued to the SIP wall sample from the side of the hot box. The thermal resistance (R-value) of the SIP wall sample is then determined as follows:

$$R = \frac{A \times (T_{hot} - T_{cold})}{Q} \quad (1)$$

where R is the thermal resistance of the SIP wall sample ($\text{m}^2 \text{K/W}$), Q is the quantity of heat received by the SIP wall surface in the hot box (W), A is the surface area of the SIP wall (m^2), and T_{hot} and T_{cold} are the surface temperatures facing the hot and cold boxes, respectively.

The heat received by the SIP wall surface in the hot box was measured in the thermal bridge areas of the SIP wall using two heat flow meters. The hot and cold surface temperatures were measured using four thermocouples, two for each side.

The thermal transmittance U , in ($\text{W/m}^2\text{-K}$), can be calculated from the R -value as follows:

$$U = \frac{1}{R} \quad (2)$$

Thermal conductivity is then determined as follows:

$$k = U \times L \quad (3)$$

where k is the thermal conductivity of the SIP wall sample (W/m-K) and L is the thickness of the SIP wall sample in meters.

2.2. SIP Wall Samples

The SIP used in the experimental work of Qiang Du and his colleagues [18] was made of 143 mm of an EPS sandwich between two layers of OSB with a thickness of 11 mm. The total thickness of the SIP wall samples was 165 mm. They first examined a single SIP without any joints. The second sample was a SIP wall with a joint in the middle of the SIP wall. The SIPs were connected by a surface spline joint. The dimensions of the nails used in the surface spline joints were 3.2 mm in diameter and 60 mm in length, with a constant spacing of 150 mm as outlined in the international building code [21].

3. Finite Element Modeling

3.1. Geometrical Modeling

Figure 1 illustrates a schematic of the SIP wall connected by surface spline and embedded camlock systems and shows the unit cells of each wall. The unit cell can be defined as a regular and repetitive pattern that forms the structure of the wall by repeating itself along the X and Y spatial planes. Figure 2 shows the top view schematics of the unit cell of the SIP wall connected by surface spline and embedded camlock systems. Figure 3 shows a transparent model of the camlock system revealing the interior structure.

Creating a single SIP wall model containing the minute details of the camlock system will result in a complex model with a huge number of nodes and consequently a very long computational time. Therefore, to enhance the accuracy of the model and to reduce the computational time, a two-scale finite element homogenization methodology (Figure 4) was employed in this study. This technique was used to predict the equivalent thermal conductivity of a SIP wall connected by embedded camlock systems. At the first scale, the thermal conductivities of a camlock system were determined along the X -, Y -, and Z -directions using a camlock model. In the second scale, the SIP wall was modeled using the SIP wall unit cell. The camlock system in the SIP wall unit cell was replaced with a homogenous solid cuboid. The conductivities obtained from the first scale (the camlock model) were assigned to this solid homogenous cuboid. The through-thickness thermal conductivity of the SIP wall and the effect of various factors that may reduce the thermal insulation of the wall were predicted. All of the finite element modeling was performed using the 6.14 ABAQUS software package [22].

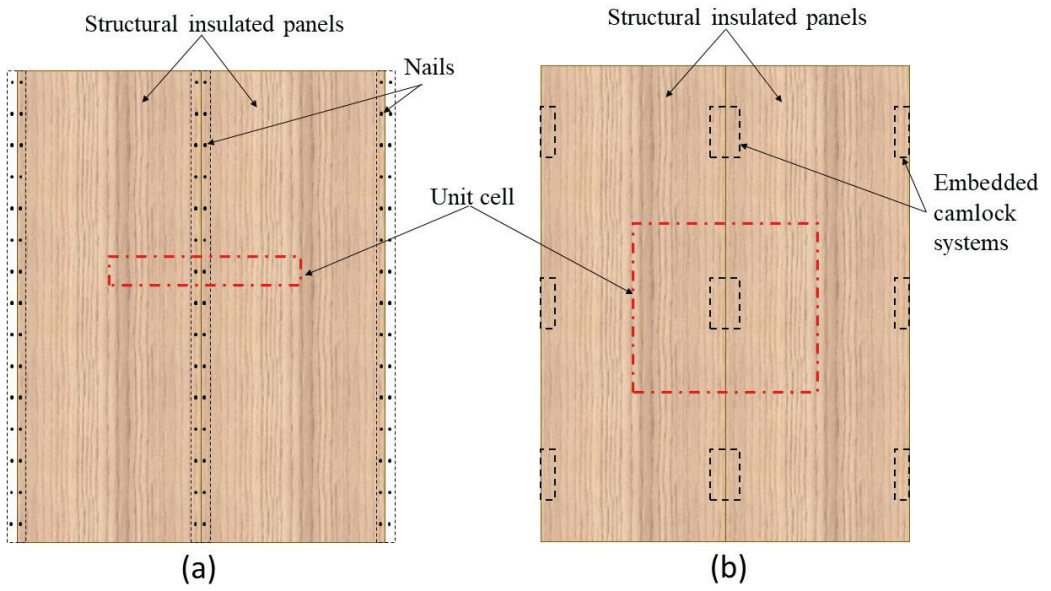


Figure 1. Schematic of SIPs connected by (a) surface spline and (b) embedded camlock systems.

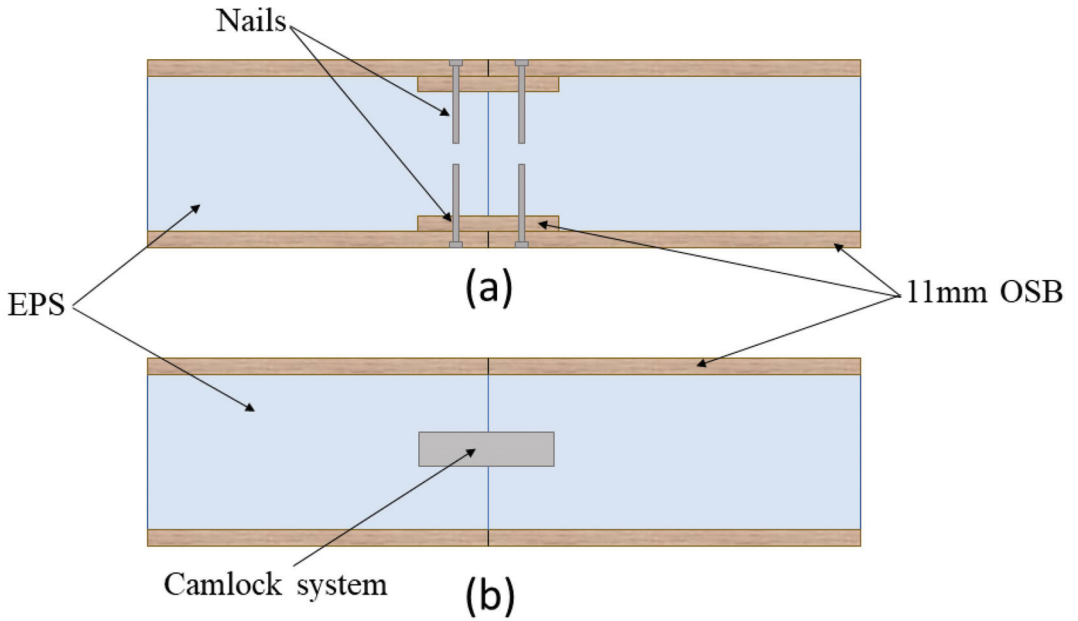


Figure 2. Top view schematics of the unit cell of the SIP wall connected by (a) surface spline and (b) embedded camlock systems.

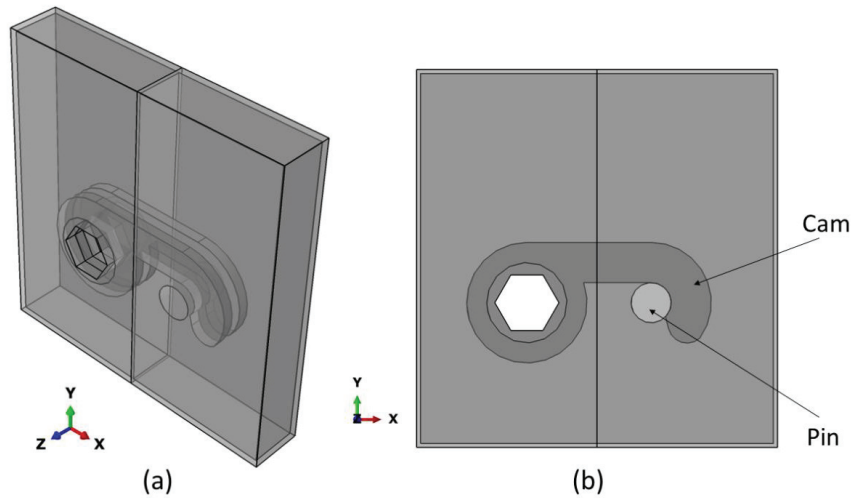


Figure 3. Three-dimensional transparent model of (a) the camlock system and (b) the transparent front view of the camlock system.

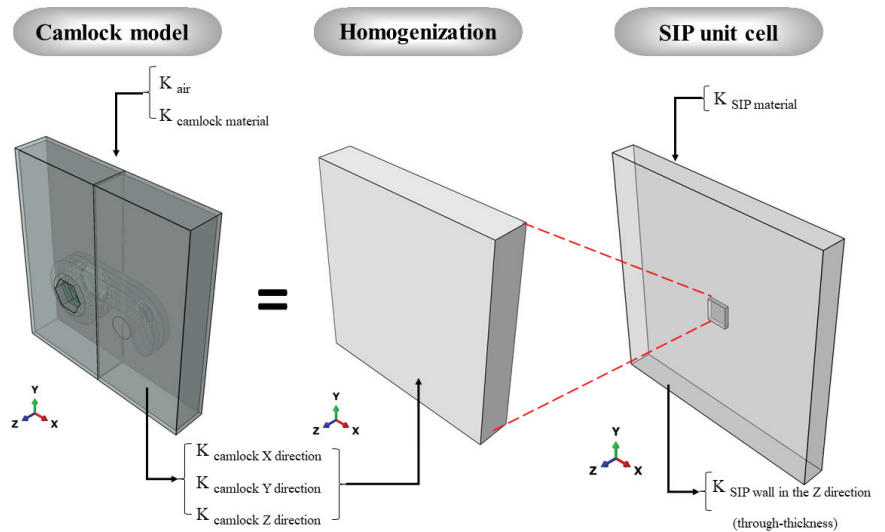


Figure 4. Two-scale finite element homogenization methodology.

3.2. Camlock Model

The camlock model was a $90 \times 94 \times 16$ mm hollow cuboid with 1 mm-thick walls. It featured two cams on the left half and one pin on the right half, as shown in Figure 3. A hexagonal wrench hole was used to rotate the cams to lock them with the pin. Additional details regarding the dimensions of the camlock system can be found on the manufacturer's sheet [23]. The properties of air are assigned to the interior cavities of the camlock finite element model. The finite element mesh of the camlock model comprised 324,918 nodes and 1,835,261 tetrahedral elements of type DC3D4.

3.3. SIP Unit Cell

A SIP wall unit cell was built based on the periodic features of the camlock system in the SIP wall. The SIP unit cell consisted of a small cuboid embedded inside a larger cuboid,

as shown in Figure 3. The larger cuboid represents the SIP, whereas the smaller cuboid represents the camlock system. The orthotropic thermal conductivities derived from the camlock model were assigned to the small cuboid that represented the camlock system. Multiple SIP unit cells were constructed with various dimensions to investigate different parameters: the wall thickness, number of camlock systems per square meter, thermal conductivity of the camlock system, and thermal conductivity of the SIP. The examined thermal conductivities of the SIP were 0.05, 0.1, 0.15, 0.2, 0.25, and 0.3 W/m-K.

3.4. Boundary Conditions

The hot box experimental setup was used to measure the thermal conductivity (k) of the specimen, with Fourier's law:

$$k = -\frac{Q}{A} \times \frac{L}{T_{Hot} - T_{Cold}} \quad (4)$$

where Q is the total heat flux from the higher to the lower temperature. A and L are the cross-sectional area and thickness of the sample, respectively. T_{Hot} and T_{Cold} represent the surface temperatures on the hot and cold boxes, respectively.

This setup can be simulated using finite element software through steady-state thermal analysis. The boundary conditions of this steady-state thermal analysis involve setting two different temperatures (T_{Hot} and T_{Cold}) on two opposite faces perpendicular to any spatial direction, while the remaining faces are insulated. These boundary conditions result in a constant unidirectional heat flow (Q) toward the surface at a lower temperature (T_{Cold}). The value of Q can be extracted from the model and inserted in Equation (4) to determine the thermal conductivity.

3.5. Material Properties of the Constituents

Table 1 lists the input thermal properties of EPS, OSB, air, and galvanized steel for the nails and camlock systems. Six different materials were examined as material options for the camlock systems. These materials are polypropylene, stainless steel, steel, galvanized steel, brass, and aluminum. The thermal conductivities of these materials are also listed in Table 1.

Table 1. Thermal conductivities of constituent materials of the SIP wall.

Material	Thermal Conductivity	Source
	(W/m-K)	
EPS	0.038	[18]
OSB	0.13	[18]
Galvanized steel	61.98	[24]
Air	0.026	[25]
Polypropylene	0.22	[26]
Steel	53	[27]
Stainless steel	25	[28]
Brass	146.87	[29]
Aluminum	239	[28]

4. Results

4.1. Validation of the FE Model

The steady-state FE thermal analyses of the single SIP without any joint along the Z-direction yielded a through-thickness thermal conductivity of 0.0419 W/m-K, with a marginal error of 2.3% lower than that experimentally obtained by a hot box apparatus, i.e., 0.0429 W/m-K [18]. The experimental and simulated through-thickness thermal conductivities of the affected area unit of the surface spline were 0.048 W/m-K [18] and 0.0473 W/m-K, respectively. Note that the experimental measurements were conducted twice for each type, and the comparison here was carried out with the mean values. The

negligible difference between the experimental and simulated results may be due to heat transfer effects by convection inside the experimental hot and cold boxes, which were not considered in the FE model. However, the FE model results are in excellent agreement with the experimental results; accordingly, the used FE model is deemed satisfactorily validated.

4.2. Camlock Model

The orthotropic thermal conductivity values of the camlock model were predicted by repeating the steady-state thermal analysis along all three directions (X, Y, and Z). Similar thermal conductivities are expected in the X- and Y-directions as the structure of the camlock model is similar along both these directions. Table 2 summarizes all the resulting thermal conductivities derived from the camlock model for the six different materials with varying thermal conductivities. Polypropylene has the lowest thermal conductivity, three orders of magnitude lower than aluminum, with the highest thermal conductivity. Figures 5–7 present the heat flux contour maps of the camlock model with polypropylene and aluminum in the X-, Y-, and Z-directions, respectively. Similar to thermal conductivity, the heat flux flowing in the polypropylene camlock model is three orders of magnitude lower than aluminum.

Table 2. Orthotropic thermal conductivities derived from the camlock model.

Material	Camlock Model Thermal Conductivity (W/m-K)		
	X-Direction	Y-Direction	Z-Direction
Polypropylene	0.061	0.060	0.045
Stainless steel	3.975	3.800	1.891
Steel	8.382	8.017	3.975
Galvanized steel	9.795	9.369	4.644
Brass	23.153	22.152	10.963
Aluminum	37.651	36.025	17.821

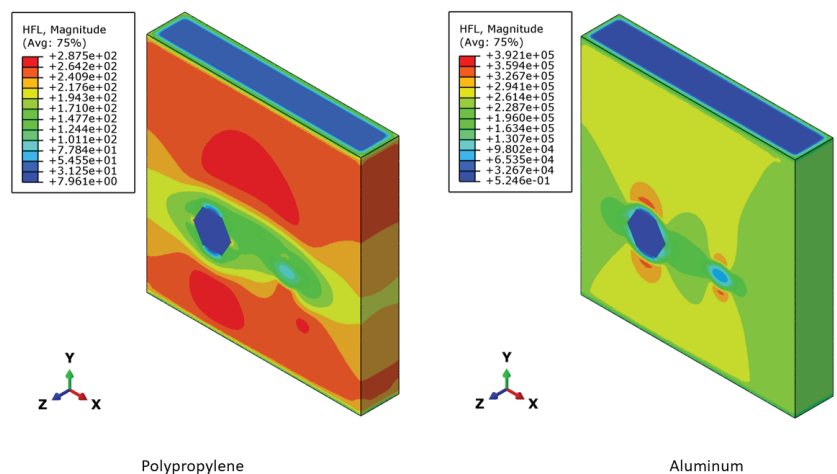


Figure 5. Heat flux in the X-direction of the camlock model with different materials.

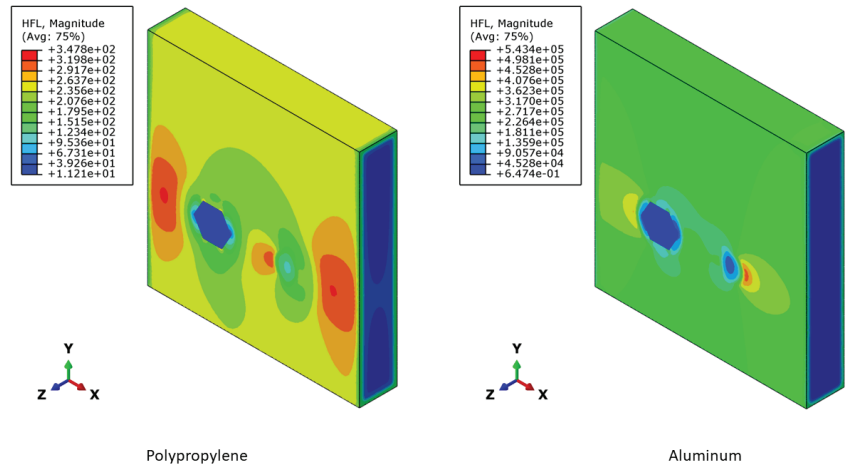


Figure 6. Heat flux in the Y-direction of the camlock model with different materials.

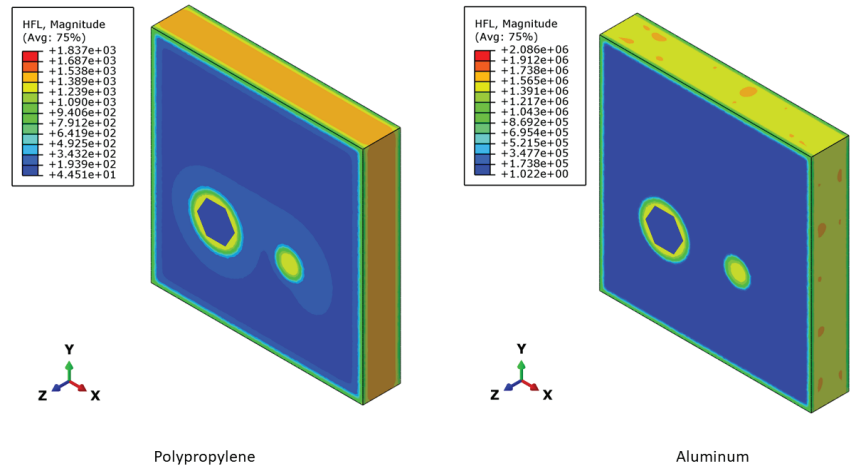


Figure 7. Heat flux in the Z-direction of the camlock model with different materials.

4.3. SIP Unit Cell

A steady-state thermal analysis was carried out on the SIP unit cell in the Z-direction to predict the through-thickness thermal conductivity of the SIP walls, one containing a surface spline joint and the other one containing camlock systems. In both models, galvanized steel properties were assigned to the nails and camlock systems. The resulting thermal conductivities were 0.04201 and 0.0427 W/m-K for the SIP walls containing a camlock system and surface spline joint, respectively.

In the parametric study, four main parameters were examined. Two of these parameters are related to the camlock system: the camlock materials and density (quantity per unit area). The other two parameters, that is, the thickness and thermal conductivity, are related to the SIP. More than 300 simulations were conducted. The corresponding results are presented in Tables 3–5.

Table 3. Thermal conductivity of the SIP wall with different camlock materials, SIP thermal conductivities, and wall thicknesses.

SIP Wall Thickness = 20 mm							
	Without Camlock	Camlock Material					
		Polypropylene	Stainless Steel	Steel	Galvanized Steel	Brass	Aluminum
SIP wall thermal conductivity (W/m-K) $\times 10^{-1}$	0.500	0.500	0.517	0.519	0.519	0.520	0.520
	1.000	0.996	1.030	1.035	1.036	1.039	1.039
	1.500	1.492	1.540	1.549	1.551	1.556	1.558
	2.000	1.988	2.047	2.061	2.063	2.073	2.076
	2.500	2.484	2.552	2.572	2.575	2.589	2.594
	3.000	2.980	3.057	3.081	3.086	3.104	3.111
SIP wall thickness = 40 mm							
	Without camlock	Camlock material					
		Polypropylene	Stainless steel	Steel	Galvanized steel	Brass	Aluminum
SIP wall thermal conductivity (W/m-K) $\times 10^{-1}$	0.500	0.500	0.504	0.504	0.504	0.504	0.504
	1.000	0.997	1.007	1.007	1.007	1.007	1.008
	1.500	1.495	1.510	1.511	1.511	1.511	1.511
	2.000	1.991	2.012	2.013	2.014	2.014	2.015
	2.500	2.488	2.514	2.516	2.517	2.518	2.519
	3.000	2.985	3.016	3.019	3.020	3.022	3.022
SIP wall thickness = 60 mm							
	Without camlock	Camlock material					
		Polypropylene	Stainless steel	Steel	Galvanized steel	Brass	Aluminum
SIP wall thermal conductivity (W/m-K) $\times 10^{-1}$	0.500	0.500	0.502	0.502	0.502	0.502	0.502
	1.000	0.998	1.004	1.004	1.004	1.004	1.004
	1.500	1.496	1.505	1.506	1.506	1.506	1.506
	2.000	1.993	2.007	2.008	2.008	2.008	2.009
	2.500	2.490	2.508	2.509	2.510	2.510	2.510
	3.000	2.987	3.009	3.011	3.011	3.012	3.012
SIP wall thickness = 80 mm							
	Without camlock	Camlock material					
		Polypropylene	Stainless steel	Steel	Galvanized steel	Brass	Aluminum
SIP wall thermal conductivity (W/m-K) $\times 10^{-1}$	0.500	0.500	0.501	0.501	0.501	0.502	0.502
	1.000	0.999	1.003	1.003	1.003	1.003	1.003
	1.500	1.497	1.504	1.504	1.504	1.505	1.505
	2.000	1.994	2.005	2.005	2.005	2.006	2.006
	2.500	2.492	2.506	2.507	2.507	2.507	2.507
	3.000	2.990	3.007	3.008	3.008	3.009	3.009
SIP wall thickness = 100 mm							
	Without camlock	Camlock material					
		Polypropylene	Stainless steel	Steel	Galvanized steel	Brass	Aluminum
SIP wall thermal conductivity (W/m-K) $\times 10^{-1}$	0.500	0.500	0.501	0.501	0.501	0.501	0.501
	1.000	0.999	1.002	1.002	1.002	1.002	1.002
	1.500	1.497	1.503	1.503	1.503	1.503	1.503
	2.000	1.996	2.004	2.004	2.004	2.005	2.005
	2.500	2.493	2.504	2.505	2.505	2.505	2.506
	3.000	2.992	3.005	3.006	3.006	3.007	3.007

Table 4. Percentage change in the thermal conductivity of the SIP wall with different camlock materials, SIP thermal conductivities, and wall thicknesses.

SIP Wall Thickness = 20 mm							
	Without Camlock	Camlock Material					
		Polypropylene	Stainless Steel	Steel	Galvanized Steel	Brass	Aluminum
Increase in SIP wall thermal conductivity (%)	0.00	−0.08	3.47	3.77	3.81	3.96	4.00
	0.00	−0.42	3.00	3.49	3.57	3.85	3.93
	0.00	−0.53	2.65	3.28	3.38	3.76	3.88
	0.00	−0.62	2.33	3.04	3.16	3.64	3.80
	0.00	−0.65	2.09	2.86	3.00	3.55	3.74
	0.00	−0.67	1.88	2.70	2.85	3.47	3.69
SIP wall thickness = 40 mm							
	Without camlock	Camlock material					
		Polypropylene	Stainless steel	Steel	Galvanized steel	Brass	Aluminum
Increase in SIP wall thermal conductivity (%)	0.00	−0.05	0.70	0.73	0.73	0.75	0.75
	0.00	−0.27	0.66	0.71	0.71	0.74	0.75
	0.00	−0.36	0.64	0.70	0.71	0.75	0.76
	0.00	−0.45	0.58	0.66	0.68	0.72	0.74
	0.00	−0.49	0.55	0.65	0.67	0.72	0.74
	0.00	−0.51	0.53	0.64	0.66	0.72	0.74
SIP wall thickness = 60 mm							
	Without camlock	Camlock material					
		Polypropylene	Stainless steel	Steel	Galvanized steel	Brass	Aluminum
Increase in SIP wall thermal conductivity (%)	0.00	−0.02	0.41	0.42	0.42	0.43	0.43
	0.00	−0.19	0.39	0.41	0.41	0.43	0.43
	0.00	−0.29	0.36	0.39	0.40	0.41	0.42
	0.00	−0.34	0.35	0.39	0.40	0.42	0.42
	0.00	−0.39	0.32	0.37	0.38	0.41	0.41
	0.00	−0.42	0.30	0.36	0.37	0.40	0.41
SIP wall thickness = 80 mm							
	Without camlock	Camlock material					
		Polypropylene	Stainless steel	Steel	Galvanized steel	Brass	Aluminum
Increase in SIP wall thermal conductivity (%)	0.00	−0.03	0.28	0.29	0.29	0.29	0.29
	0.00	−0.15	0.26	0.28	0.28	0.29	0.29
	0.00	−0.21	0.27	0.29	0.29	0.31	0.31
	0.00	−0.28	0.24	0.27	0.27	0.28	0.29
	0.00	−0.31	0.23	0.27	0.27	0.29	0.30
	0.00	−0.33	0.23	0.27	0.28	0.30	0.30
SIP wall thickness = 100 mm							
	Without camlock	Camlock material					
		Polypropylene	Stainless steel	Steel	Galvanized steel	Brass	Aluminum
Increase in SIP wall thermal conductivity (%)	0.00	−0.01	0.23	0.24	0.24	0.24	0.24
	0.00	−0.11	0.22	0.23	0.23	0.24	0.24
	0.00	−0.18	0.20	0.22	0.22	0.23	0.23
	0.00	−0.22	0.20	0.22	0.22	0.23	0.24
	0.00	−0.26	0.17	0.20	0.20	0.22	0.22
	0.00	−0.28	0.17	0.20	0.20	0.22	0.23

Table 5. Percentage change in the thermal conductivity of the SIP wall with different densities of camlock systems, SIP thermal conductivities, and wall thicknesses.

SIP Wall Thickness = 20 mm											
	Number of Camlock Systems per Square Meter					Increase in SIP wall thermal conductivity (%)	Number of Camlock Systems per Square Meter				
	0	1	2	3	4		0	1	2	3	4
	SIP wall thermal conductivity (W/m-K) $\times 10^{-1}$	0.5	0.52	0.54	0.56		0.58	0.00	4.00	8.17	12.80
	1	1.04	1.08	1.13	1.16	0.00	3.93	8.03	12.56	15.70	
	1.5	1.56	1.62	1.68	1.73	0.00	3.88	7.89	12.32	15.43	
	2	2.08	2.16	2.24	2.3	0.00	3.80	7.76	12.10	15.17	
	2.5	2.59	2.69	2.8	2.87	0.00	3.74	7.62	11.88	14.91	
	3	3.11	3.23	3.35	3.44	0.00	3.69	7.50	11.67	14.66	
SIP wall thickness = 40 mm											
	Number of camlock systems per square meter					Increase in SIP wall thermal conductivity (%)	Number of camlock systems per square meter				
	0	1	2	3	4		0	1	2	3	4
	SIP wall thermal conductivity (W/m-K) $\times 10^{-1}$	0.5	0.5	0.51	0.51		0.52	0.00	0.75	1.55	2.34
	1	1.01	1.02	1.02	1.03	0.00	0.75	1.54	2.32	3.02	
	1.5	1.51	1.52	1.53	1.54	0.00	0.76	1.53	2.30	2.99	
	2	2.01	2.03	2.05	2.06	0.00	0.74	1.52	2.29	2.98	
	2.5	2.52	2.54	2.56	2.57	0.00	0.74	1.50	2.27	2.95	
	3	3.02	3.04	3.07	3.09	0.00	0.74	1.50	2.25	2.93	
SIP wall thickness = 60 mm											
	Number of camlock systems per square meter					Increase in SIP wall thermal conductivity (%)	Number of camlock systems per square meter				
	0	1	2	3	4		0	1	2	3	4
	SIP wall thermal conductivity (W/m-K) $\times 10^{-1}$	0.5	0.5	0.5	0.51		0.51	0.00	0.43	0.89	1.32
	1	1	1.01	1.01	1.02	0.00	0.43	0.88	1.31	1.72	
	1.5	1.51	1.51	1.52	1.53	0.00	0.42	0.88	1.31	1.71	
	2	2.01	2.02	2.03	2.03	0.00	0.42	0.87	1.30	1.69	
	2.5	2.51	2.52	2.53	2.54	0.00	0.41	0.86	1.29	1.68	
	3	3.01	3.03	3.04	3.05	0.00	0.41	0.86	1.28	1.68	
SIP wall thickness = 80 mm											
	Number of camlock systems per square meter					Increase in SIP wall thermal conductivity (%)	Number of camlock systems per square meter				
	0	1	2	3	4		0	1	2	3	4
	SIP wall thermal conductivity (W/m-K) $\times 10^{-1}$	0.5	0.5	0.5	0.5		0.51	0.00	0.29	0.62	0.94
	1	1	1.01	1.01	1.01	0.00	0.29	0.62	0.94	1.22	
	1.5	1.5	1.51	1.51	1.52	0.00	0.31	0.62	0.93	1.21	
	2	2.01	2.01	2.02	2.02	0.00	0.29	0.61	0.92	1.20	
	2.5	2.51	2.52	2.52	2.53	0.00	0.30	0.60	0.92	1.19	
	3	3.01	3.02	3.03	3.04	0.00	0.30	0.60	0.91	1.18	
SIP wall thickness = 100 mm											
	Number of camlock systems per square meter					Increase in SIP wall thermal conductivity (%)	Number of camlock systems per square meter				
	0	1	2	3	4		0	1	2	3	4
	SIP wall thermal conductivity (W/m-K) $\times 10^{-1}$	0.5	0.5	0.5	0.5		0.5	0.00	0.24	0.48	0.73
	1	1	1	1.01	1.01	0.00	0.24	0.47	0.72	0.94	
	1.5	1.5	1.51	1.51	1.51	0.00	0.23	0.47	0.72	0.93	
	2	2	2.01	2.01	2.02	0.00	0.24	0.47	0.71	0.93	
	2.5	2.51	2.51	2.52	2.52	0.00	0.22	0.47	0.71	0.92	
	3	3.01	3.01	3.02	3.03	0.00	0.23	0.47	0.70	0.91	

5. Discussion

The use of the camlock system in joining SIPs reduces the thermal bridges compared to the spline surface. The camlock system has the advantage of not being exposed to the environment.

The camlock thermal conductivity of each material was derived from the camlock model, as listed in Table 2. The through-thickness (Z-direction) thermal conductivity of the polypropylene camlock system was 0.045 W/m-K, which is lower than the previously recorded values of SIP thermal conductivity. Therefore, the through-thickness thermal conductivities of the SIP wall were reduced in all the SIP unit cell models containing a polypropylene camlock system. These results vary between -0.01 to -0.67% . All of the camlock materials, except for polypropylene, increased the through-thickness thermal conductivity of the SIP wall. This increase depended primarily on the thickness of the SIP; it varied by approximately 2–4% in the SIP wall with a thickness of 20 mm contained on the camlock system, as shown in Figure 6. However, the effect of the camlock system on the wall thermal conductivity was reduced with an increase in the thickness of the SIP wall. For instance, the increase in the SIP wall with a thickness of 100 mm did not exceed 0.24%. Similar to the camlock material, the effect of the SIP thermal conductivity was evident for the SIP thickness of 20 mm. However, it was minimal in the thicker SIPs. Unexpectedly, the lower the SIP thermal conductivity, the stronger the effect of the camlock system. For example, the thermal conductivity of the SIP wall increased by 4 and 3.69 percent when an aluminum camlock system was installed in a 20 mm-thick SIP with thermal conductivities of 0.05 and 0.3 W/m-K, respectively.

Furthermore, the effect of the density of camlock systems (the number of camlock systems per square meter) was investigated with an aluminum camlock and variable SIP thicknesses and thermal conductivities. The thermal conductivity of the SIP wall increases with the camlock density. This increase was linear with respect to the density of the camlock system. For instance, a constant increase of 0.24% per camlock was noted under the SIP thickness of 100 mm and thermal conductivity of 0.05 W/m-K. Similar to the results in Table 3, as the SIP thermal conductivity decreased, the effect of the density of the camlock system on the overall SIP wall thermal conductivity increased. Moreover, the effect of the camlock system density on the overall SIP wall thermal conductivity decreased exponentially as the SIP thickness increased. Therefore, it is essential to reduce the number of camlock systems in the SIPs wall, but without jeopardizing the airtightness performance of the wall, especially with reduced thickness SIPs.

The highest reduction in the overall R-value of the SIPs with camlock connections was 3.85% when the thickness of the SIP was 20 mm and the camlock material was aluminum. This reduction goes up to 13.8% in the same condition with four camlock systems per square meter. McIntosh and Guthrie [19] reported that the thermal bridging at the framing members of SIPs joint causes a 10–20% reduction in the overall R-value of the SIP wall. Therefore, from the thermal point of view, it is better to use camlock systems to connect the SIPs.

6. Conclusions

In this study, steady-state thermal analyses were performed on two-scale finite element models to determine the effects of camlock systems on the thermal conductivity of SIP walls. The main findings of this study can be summarized as follows:

- The use of the camlock system in joining SIPs reduces the thermal bridges compared to the spline surface.
- The lower the SIP thermal conductivity, the stronger the effect of the camlock system.
- The thicker the SIP, the lower the effect of the camlock system.
- Variations in the SIP wall through-thickness thermal conductivity were linear with respect to the camlock density and the thermal conductivity of both the SIPs and the camlock system.
- Changes in the through-thickness thermal conductivity of the SIP wall were exponential with respect to the SIP thickness.
- Optimizing the embedded camlock systems density (the number of embedded camlock systems per unit area) is critical to reduce the thermal conductivity of the SIP wall

without jeopardizing the airtightness performance of the wall, especially with reduced thickness SIPs.

- The reduction of the overall R-value of the SIP caused by the camlock system embedded in the SIP did not exceed 13.8%.
- Extensive experimental work is needed to evaluate the thermal and mechanical behavior of SIPs with embedded camlock systems.

Author Contributions: A.A.A. (Abdulrahman A. Alghamdi): Conceptualization, Methodology, Modeling, Validation, Formal analysis. A.A.A. (Abdullah A. AlZahrani): Project administration, Investigation, Formal analysis, Writing—original draft. A.M.A.: Modeling, Writing—review and editing, Resources. All authors have read and agreed to the published version of the manuscript.

Funding: This research did not receive any specific grant from funding agencies in the public, commercial, or not-for-profit sectors.

Data Availability Statement: Not applicable.

Conflicts of Interest: The authors declare that there is no conflict of interest.

References

1. IEA. *World Energy Balances 2019*; OECD Publishing: Paris, France, 2019.
2. Bosseboeuf, D. *Energy Efficiency Trends and Policies in the Household and Tertiary Sectors An Analysis Based on the ODYSSEE and MURE Databases*; Thailand Greenhouse Gas Management Organization (TGO): Bangkok, Thailand, 2015.
3. Bassiouny, R.; Ali, M.R.O.; NourEldeen, E.-S.H. Modeling the Thermal Behavior of Egyptian Perforated Masonry Red Brick Filled with Material of Low Thermal Conductivity. *J. Build. Eng.* **2016**, *5*, 158–164. [[CrossRef](#)]
4. AlZahrani, A.A.; Alghamdi, A.A.; Basalah, A.A. Computational Optimization of 3D-Printed Concrete Walls for Improved Building Thermal Performance. *Buildings* **2022**, *12*, 2267. [[CrossRef](#)]
5. Adams, W.A.; McMahan, D.; Russell, P. Sustainable Housing, Transportation and Energy for Remote Communities in the Canadian Arctic. In Proceedings of the EIC Climate Change Technology Conference 2013, Montreal, QC, Canada, 27–29 May 2013; pp. 1–16.
6. Cornick, S.M.; Rousseau, M.Z.; Parekh, A.; Maref, W. An Energy Simulation Study of Wall Systems for Canadian Arctic Homes. In Proceedings of the 4th International Building Physics Conference, Istanbul, Turkey, 15 June 2009.
7. Said, M.N.A. *Task 2: Literature Review: Building Envelope, Heating, and Ventilating Practices and Technologies for Extreme Climates*; Institute for Research in Construction National Research Council Canada: Ottawa, ON, Canada, 2006.
8. Harris, J.; Durdyev, S.; Tokbolat, S.; Ismail, S.; Kandymov, N.; Mohandes, S.R. Understanding Construction Stakeholders' Experience and Attitudes toward Use of the Structurally Insulated Panels (SIPs) in New Zealand. *Sustainability* **2019**, *11*, 5458. [[CrossRef](#)]
9. Dhaif, M.; Stephan, A. A Life Cycle Cost Analysis of Structural Insulated Panels for Residential Buildings in a Hot and Arid Climate. *Buildings* **2021**, *11*, 255. [[CrossRef](#)]
10. Geng, Y.; Han, X.; Zhang, H.; Shi, L. Optimization and Cost Analysis of Thickness of Vacuum Insulation Panel for Structural Insulating Panel Buildings in Cold Climates. *J. Build. Eng.* **2021**, *33*, 101853. [[CrossRef](#)]
11. Lu, X.; Memari, A. Comparative Energy Analysis and Life-Cycle Assessment of Innovative Residential Wall Systems in Cold Regions. *Pract. Period. Struct. Des. Constr.* **2019**, *24*, 04019015. [[CrossRef](#)]
12. Mugahed Amran, Y.H.; El-Zeadani, M.; Huei Lee, Y.; Yong Lee, Y.; Murali, G.; Feduik, R. Design Innovation, Efficiency and Applications of Structural Insulated Panels: A Review. *Structures* **2020**, *27*, 1358–1379. [[CrossRef](#)]
13. Mullens, M.A.; Arif, M. Structural Insulated Panels: Impact on the Residential Construction Process. *J. Constr. Eng. Manag.* **2006**, *132*, 786–794. [[CrossRef](#)]
14. Panjehpour, M.; Abang Ali, A.A.; Voo, Y.L. Structural Insulated Panels: Past, Present, and Future. *J. Eng. Proj. Prod. Manag.* **2013**, *3*, 2–8. [[CrossRef](#)]
15. Abdou, O.A. Thermal Performance of an Interlocking Fiber-Reinforced Plastic Building Envelope System. *J. Archit. Eng.* **1997**, *3*, 9–14. [[CrossRef](#)]
16. Wyss, S.; Fazio, P.; Rao, J.; Kayello, A. Investigation of Thermal Performance of Structural Insulated Panels for Northern Canada. *J. Archit. Eng.* **2015**, *21*, 04015006. [[CrossRef](#)]
17. Kayello, A.; Ge, H.; Athienitis, A.; Rao, J. Experimental Study of Thermal and Airtightness Performance of Structural Insulated Panel Joints in Cold Climates. *Build. Environ.* **2017**, *115*, 345–357. [[CrossRef](#)]
18. Du, Q.; Jin, L.; Lv, J.; Cai, C.; Zhang, R. Experimental and Numerical Studies on the Thermal Performance of Structural Insulated Panel Splines. *J. Build. Eng.* **2021**, *44*, 103334. [[CrossRef](#)]
19. McIntosh, J.; Guthrie, C. Structural insulated panels: A sustainable option for house construction in New Zealand. *Int. J. Hous. Sci. Its Appl.* **2010**, *34*.

20. ASTM C1363-11—Standard Test Method for Thermal Performance of Building Materials and Envelope Assemblies by Means of a Hot Box Apparatus. Available online: <https://webstore.ansi.org/standards/astm/astmc136311> (accessed on 23 December 2022).
21. *International Building Code*; International Code Council: Washington, DC, USA, 2006.
22. *Abaqus 6.14*; Dassault Systemes Simulia Corp.: Johnston, IL, USA, 2015.
23. Kunlong SK1-R5-007 Sliding Hook Lock Cam Lock Accessories Zipper—Buy Handle Lock, Truck Lock, Panel Door Lock Product on ShangKun Industrial Technology Co., Ltd. Available online: <http://www.chinalatch.com/sk1-r5-007-kunlong-concealed-heavy-duty-draw-latch.html> (accessed on 23 December 2022).
24. Singh, M.; Gulati, R.; Srinivasan, R.S.; Bhandari, M. Three-Dimensional Heat Transfer Analysis of Metal Fasteners in Roofing Assemblies. *Buildings* **2016**, *6*, 49. [[CrossRef](#)]
25. Lemmon, E.W.; Jacobsen, R.T. Viscosity and Thermal Conductivity Equations for Nitrogen, Oxygen, Argon, and Air. *Int. J. Thermophys.* **2004**, *25*, 21–69. [[CrossRef](#)]
26. Patti, A.; Acierno, D. Thermal Conductivity of Polypropylene-Based Materials. In *Polypropylene—Polymerization And Characterization Of Mechanical And Thermal Properties*; Books on Demand: Élysées, Paris, 2020.
27. Eurocode 3: Design of Steel Structures | Eurocodes: Building the Future. Available online: <https://eurocodes.jrc.ec.europa.eu/EN-Eurocodes/eurocode-3-design-steel-structures> (accessed on 23 December 2022).
28. Carvill, J. *Mechanical Engineer's Data Handbook*; Butterworth-Heinemann: Oxford, UK, 1994; ISBN 978-0-7506-1960-8.
29. Muldiani, R.F.; Hadiningrum, K.; Pratama, D. Experiments for Determining the Thermal Conductivity of Brass and 304 Stainless Steel with Direct Temperature Measurement Techniques Using Lorenz Number as Validation. In Proceedings of the 2nd International Seminar of Science and Applied Technology (ISSAT 2021), Video Conference. 12 October 2021; pp. 123–129.

Disclaimer/Publisher's Note: The statements, opinions and data contained in all publications are solely those of the individual author(s) and contributor(s) and not of MDPI and/or the editor(s). MDPI and/or the editor(s) disclaim responsibility for any injury to people or property resulting from any ideas, methods, instructions or products referred to in the content.

Article

Computational Optimization of 3D-Printed Concrete Walls for Improved Building Thermal Performance

Abdullah A. AlZahrani *, Abdulrahman A. Alghamdi and Ahmad A. Basalah

Department of Mechanical Engineering, Umm Al-Qura University, Makkah 21955, Saudi Arabia

* Correspondence: aarzahrani@uqu.edu.sa

Abstract: Three-dimensional printing technologies are transforming various sectors with promising technological abilities and economic outcomes. For instance, 3D-printed concrete (3DPC) is revolutionizing the construction sector with a promise to cut projects' costs and time. Therefore, 3DPC has been subjected to extensive research and development to optimize the mechanical and thermal performance of concrete walls produced by 3D printing. In this paper, we conduct a comparative investigation of the thermal performance of various infill structures of 3DPC walls. The targeted outcome is to produce an infill structure with optimized thermal performance to reduce building energy consumption without incurring additional material costs. Accordingly, a computational model is developed to simulate the thermal behavior of various infill structures that can be used for 3DPC walls. The concrete composition and the concrete-to-void fraction are maintained constant to focus on the impact of the infill structure (geometric variations). The thermal performance and energy-saving potential of the 3DPC walls are compared with conventional construction materials, including clay and concrete bricks. The results show that changing the infill structure of the 3DPC walls influences the walls' thermal conductivity and, thereby, the building's thermal performance. The thermal conductivity of the examined infill structures is found to vary between 0.122 to 0.17 W/m.K, while if these structures are successful in replacing conventional building materials, the minimum annual saving in energy cost will be about \$1/m². Therefore, selecting an infill structure can be essential for reducing building energy consumption.

Keywords: building efficiency; energy saving; sustainable building; thermal conductivity; 3D printing; 3D-printed concrete walls

Citation: AlZahrani, A.A.; Alghamdi, A.A.; Basalah, A.A. Computational Optimization of 3D-Printed Concrete Walls for Improved Building Thermal Performance. *Buildings* **2022**, *12*, 2267. <https://doi.org/10.3390/buildings12122267>

Academic Editors: Yaolin Lin, Paulo Santos and Wei Yang

Received: 14 November 2022

Accepted: 15 December 2022

Published: 19 December 2022

Publisher's Note: MDPI stays neutral with regard to jurisdictional claims in published maps and institutional affiliations.



Copyright: © 2022 by the authors. Licensee MDPI, Basel, Switzerland. This article is an open access article distributed under the terms and conditions of the Creative Commons Attribution (CC BY) license (<https://creativecommons.org/licenses/by/4.0/>).

1. Introduction

Three-dimensional (3D) printing technologies are transforming various sectors with vast technical and economic advantages. For instance, three-dimensional-printed concrete (3DPC) walls revolutionized the construction sector with promising potential to produce energy-efficient buildings at reduced cost and construction time. These gains are not limited to the building owners or end-users, but they positively impact the environment and the global community at large. The reduction of energy consumption in the residential sector will help reduce energy-related emissions, achieve the global objective of net-zero emissions by 2050, and limit climate change. The construction industry is responsible for about 38% of greenhouse gas emissions [1–3]. Therefore, reducing the construction time will directly reduce the emissions produced by the construction equipment and the labor cost; 3D printing has been demonstrated to save up to 60% of construction waste, 70% of production time, and 80% of labor expenses when compared to conventional concrete building methods [4]. However, 3DPC technologies are still in the early stages and undergoing extensive research and development to utilize their full potential and realize environmentally friendly materials that can make the future building more sustainable and environmentally benign [5].

The technology of 3D printing, scientifically named additive manufacturing technology, is defined based on ASTM (F2792-12a) as a process of joining materials to make objects from 3D model data, usually layer upon layer, as opposed to subtractive manufacturing methodologies [6]. Along with the assistance of computer-aided designing (CAD) to generate the model, this process involves three primary steps: (1) the CAD design of the product, (2) slicing software to convert the CAD model into layers, and (3) the G-code describing the path for printing these layers. Thus, the 3D printing machine includes a computer or a processor responsible for executing the printing assignments in an optimized sequence. However, to achieve the optimum concrete printing results, the combination of the concrete mixture properties and the printing parameters must be simultaneously optimized. These cutting-edge machines can manufacture significantly more complicated structures with excellent precision when used in building rather than conventional formwork. In addition to printing concrete, this technique can also be used for printing polymers, metals, and ceramics for building [7]. Further details on the recent advances in 3DPC and concrete materials can be found elsewhere [8–10].

The contemporary built environment relies on concrete as an essential element for construction, which comprises the most significant share by volume due to its numerous favorable characteristics, including its strength, high durability and design flexibility, fire resistance, and availability at low cost [11]. Concrete is commonly prepared by mixing portions of cement, fine and coarse aggregates, mineral admixtures, and water. Conventional concrete casting methods utilize wooden or metal formwork to cast the concrete into the desired shape. One of the major drawbacks of traditional concrete casting is the need for wooden and metal formwork, which costs 50% of the overall concrete cost [12]. Moreover, when it comes to building complicated geometries, conventional construction techniques cannot do so without structural support and formwork [13], which limits the concrete structure design [9]. However, 3DPC technology has vast potential in multiple aspects, including enhancing material and design flexibility, reducing material and labor costs, and improving construction agility [9]. Furthermore, the 3DPC technique enables air cavities to be created in the wall while optimizing the structure for maximum mechanical and thermal performances [13]. For extrusion-based 3D printing innovations, contour crafting and solid printing have become the primary building method in the construction sector.

The numerous advantages of 3DPC has motivated many companies to invest in and capitalize on these technologies. Accordingly, the industrial sector has witnessed a successful demonstration with promising potential to be explored in the near future. For example, CyBe, Apis Cor, and Winsun are examples of many companies that develop and provide 3DPC solutions and are already in the construction market employing 3DPC in different construction projects around the world [14]. For instance, the WinSun firm used the contour crafting technique to build a five-story residence in China in 2015. The Acciona Company 3D printed a pedestrian bridge using D-shape technology in 2016. Another demonstration project is that constructed by Apis Cor, through 3D printing. It was marked as the largest 3D-printed building with a 640 m² area and a height of 9.5 m. During this project, it was reported that the number of workers was reduced to only three while the 3D concrete printing machine executed most of the work [15]. Thus, the future of 3D printing in the building of homes, bridges, and skyscrapers seems more promising in light of the rising construction sector throughout the world.

The mechanical performance and sustainability of 3DPC are of great importance and relevance to the development of 3DPC technologies, which were the focus of numerous articles. For example, Han et al. [16] measured the axial loading on large-scale 3DPC walls. Their research outcomes will contribute to the development of the Code for Design of Concrete Structure. Additional studies considering mechanical and sustainability performance include [17–19]. The published literature shows systematic progress in investigating the mechanical performance of 3DPC to establish standardized codes and regulations for construction [20]. However, a limited number of studies have been dedicated to examining

and standardizing the thermal performance of 3DPC. Thus, the optimization of the 3DPC wall infill structure for enhanced thermal performance is the scope of this study.

The thermal performance of the built environment is an essential parameter for improving the building's energy efficiency. It was reported that the exterior walls are responsible for a substantial share of heat loss that can reach as much as 25% of the total thermal energy loss [13]. Al-Tamimi et al. [21] investigated the optimum geometry of holes within concrete bricks to reduce the thermal conductivity of walls and thereby reduce energy consumption in buildings for air conditioning in hot climate conditions such as in Saudi Arabia. They considered 23 different models and used FEM to evaluate heat transfer through these brick configurations and determine the impact on the building's internal wall temperature. Interestingly, their results showed that the inner temperature could be reduced by as much as 7.18 °C when a 51% hallow ratio is utilized.

The thermal performance of conventional concrete has been widely studied and included in many building guidelines and standards to achieve desired human comfort and energy saving. However, 3DPC is still relatively new in the construction market, with novel design parameters that significantly influence the thermal behavior of these walls [22]. For example, the inclusion of air cavities or filling materials, the variation in thicknesses, and cross-sectional structures are some techniques proposed for controlling the thermal performance of 3DPC walls. In this regard, some researchers constructed a 3DPC wall for testing thermal performance and energy savings [23]. Yawen He et al. [24] studied the energy-saving potential of a large-scale 3DPC building with an integrated green wall system. They utilized 3D-printed multifunctional wall modular units to serve as building enclosures and supports for the green wall. The results, based on a prototype of this wall design developed in China, showed improved thermal comfort and energy-saving potential. Sun et al. [25] experimentally tested the thermal performance of a 3DPC wall. They reported high non-uniformity in temperature distribution, which was attributed to the variations in the printing path and the cross-section design. They highly recommend further studies of 3DPC walls to ensure that printed wall designs achieve the required thermal insulation.

A limited number of studies has evaluated the effect of the cavity configurations of 3DPC walls on the overall thermal performance of the wall. Alkhalidi and Hatuqay [26] investigated the energy performance of 3DPC walls with triangular cavities. They predicted the effect of wall thickness and the number of rows on the thermal performance of the printed wall. Marais et al. [27] conducted a similar study on 3DPC walls with rectangular cavities. The main drawback of both studies is that they limited the number of cavity shapes investigated. Suntharalingam et al. [13,28,29] have since overcome this drawback by creating FEMs of the printed wall with four different cavity shapes at different configurations, wall thicknesses, and number of rows. Unfortunately, the concrete volume fractions in their models were not the same. Thus, their assessment of the effect of the cavity shape is not accurate. The current study overcomes this point by constructing finite element models of the 3DPC wall with different infill shapes with equal volume fractions. Furthermore, it provides a comparative performance analysis between the examined shapes and the conventional building materials.

Therefore, the contribution of this study can be highlighted in the following outcomes, which have not been considered in previous research works:

1. Several infill structures are modeled for optimizing their geometry based on printable shapes, while the void-to-concrete ratio of these structures is maintained constant.
2. The thermal performance of each infill structure is evaluated after determining the effective thermal conductivity of that infill structure.
3. The thermal performance of 3DPC walls based on the studied infill geometry is compared with conventional building materials, including concrete brick walls, red clay brick walls, and insulated red brick walls.
4. The study also considered two cases in which steel wire joints are used in different arrangements to reinforce 3DPC walls, which have not been considered in the litera-

ture. Moreover, the impact of implementing these 3DPC walls in building on energy consumption is evaluated, and the potential economic advantage is estimated and discussed in comparison with conventional building materials.

2. Methodology and Analysis

In order to investigate the impact of the variation of the internal structure (infill structure) of 3DPC walls on the thermal performance of these walls, several 3D drawings of wall-sections were developed with various infill structures that should be 3D printable. These 3DPC wall-sections were selected based on the geometries commonly reported in the literature. For each type of infill section, a representative unit with fixed concrete to void fraction was selected, meshed, and introduced for heat transfer modeling. In the FEM, the model was solved subject to the boundary conditions, which will be explained in the following section. The results determine the effective thermal conductivity of each infill structure and to compare its thermal performance with other infill structures as well as conventional materials. Further details and description of the approach of this investigation are provided in the following sections.

2.1. Geometries of 3DPC Walls

One of the advantages of 3D concrete printing is the vast flexibility this technology offers for infill structure geometry. Therefore, infill geometry can be an additional factor that can be optimized for building energy efficiency. Thus, for example, the infill structure of the exterior walls—which is responsible for heat losses into or out of the building envelope—can be redesigned to minimize heat transfer for better building energy efficiency. This can be achieved by creating interior air cavities within the wall. However, these cavities must not compromise the walls' strength and mechanical properties.

Furthermore, since 3D printing technology executes the printing project in a layer-by-layer approach, repeated unit design is preferred for the current study. Therefore, in this study, five different 3D-printed wall-sections were selected. These geometries were selected subject to one constraint: they all must have the exact void-to-concrete fraction (volume of concrete to volume of air per unit). Figure 1 presents the selected geometries that were considered.

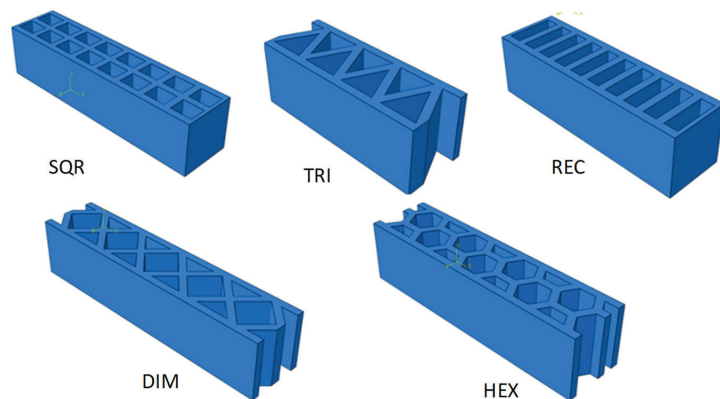


Figure 1. Isometric view of selected sections of 3DPC walls with different infill structures.

Figure 2 presents the case of 3DPC walls reinforced with steel wire joints in two arrangements, i.e., truss type (TRS-TR) and ladder type (LDR-TR). These steel joints are expected to enhance the strength of 3DPC walls, but they may also influence the thermal performance of these walls. Therefore, the thermal performance of these reinforced designs was examined and compared with that of the designs presented in Figure 1.

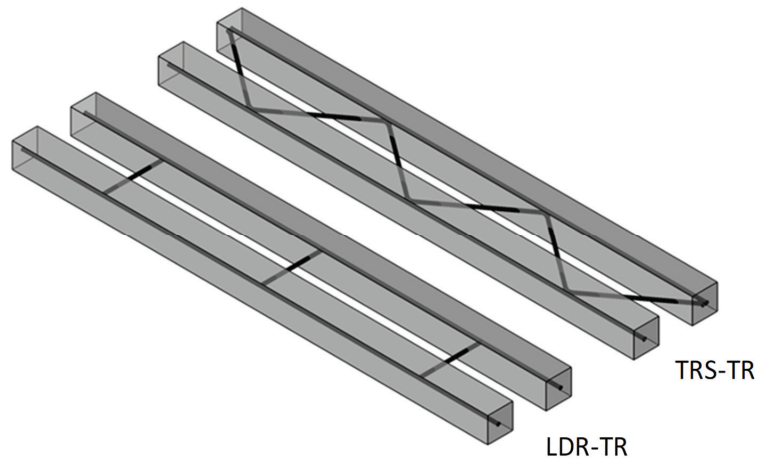


Figure 2. Two types of reinforced 3DPC wall sections.

Hence, both infill groups have periodic structures, and it is sufficient to create a representative unit cell for each type. This unit cell creates the structure of the printed wall by repeating itself in the three orthogonal directions X, Y, and Z. Figure 3 shows the different unit cells for the different types of infill structures. Figure 4 shows the unit cells of the 3DPC wall, which are reinforced with joint reinforcement. To display the inner details, the concrete and void were given transparent colors. The width of the wall in both groups is 0.2 m.

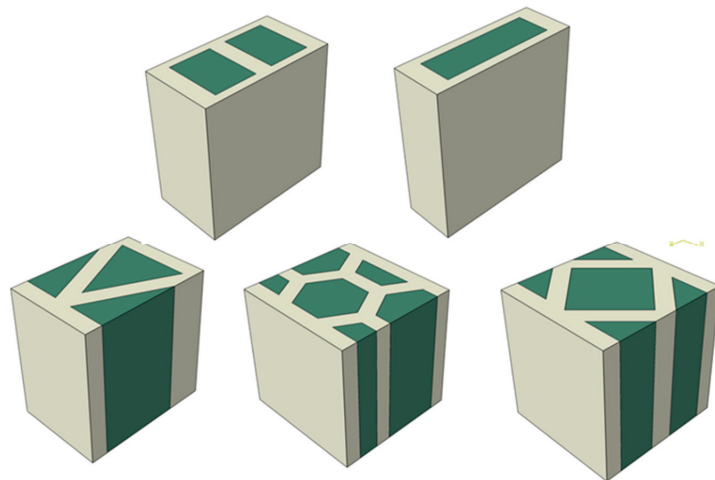


Figure 3. The unit cells of the 3DP concrete wall for the different shapes considered.

The concrete walls were modeled based on a repeated unit that represents the wall structure for the shapes presented in Figure 1; a repeating unit was constructed as per Figure 4.

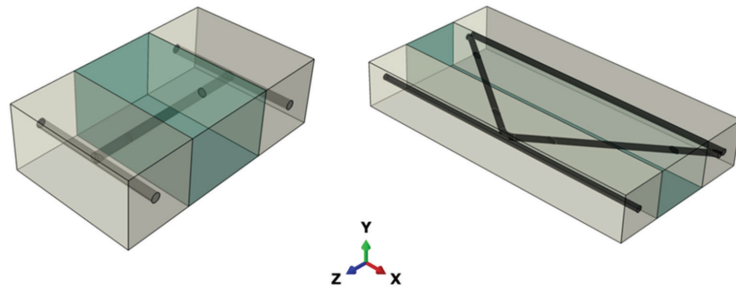


Figure 4. Isometric view of two unit cells for reinforced 3DPC wall.

2.2. Heat Transfer Analysis

In the heat transfer process between the two sides of the 3DPC walls, the three processes of conduction, convection, and radiation are involved; however, conduction dominates the heat transfer, considering the stagnant air within the infill and the relatively low temperatures of the surfaces. The heat transfer by convection and radiation dominates between the ambient air and the outer and inner wall surfaces. Accordingly, the temperature distribution within the 3DPC wall for steady state, three-dimensional heat conduction in a homogenous medium with constant thermal conductivity considering no heat source is governed by the following partial differential equation [21].

$$\frac{\partial^2 T}{\partial x^2} + \frac{\partial^2 T}{\partial y^2} + \frac{\partial^2 T}{\partial z^2} = 0, \quad (1)$$

where the heat flux q'' along x direction is in (W/m^2),

$$q'' = -k \partial T / \partial x \quad (2)$$

and the thermal conductivity k is in ($W/m.K$) and are given as

$$k = \rho a c_p \quad (3)$$

2.3. Finite Element Modeling

The finite element models of the different types of 3D-printed concrete walls were divided into two groups depending on the reinforcement strategy. The first group was entirely made from printed concrete and reinforced with internal infill with different cavity shapes. These cavity shapes were triangular (TRI), square (SQR), hexagonal (HEX), rectangular (REC), and diamond (DIM). These models were designed carefully to have an equal void fraction, which was 0.48. Figure 1 shows the different types of investigated infills. The second group was reinforced with steel wire joint reinforcements, which are used extensively to reinforce traditional brick walls. In 3D-printed walls, joint reinforcements were placed manually between layers during the printing process. The most common types of steel wire joint reinforcements are LDR-TR and TRS-TR. Figure 2 illustrates a printed layer reinforced with joint reinforcements. The void and steel fractions were 0.397 and 0.014, respectively, and the steel wire diameter was 8 mm. Table 1 lists the input thermal conductivities of all materials used in this study.

Table 1. Thermal conductivities of the materials considered in this study.

Phase	Thermal Conductivity k (W/m.K)	Source
Concrete mixture	0.371	[27,30]
Steel	53	[31]
Air	0.026	[32]

2.4. Boundary Conditions

The thermal conductivity of construction materials was measured by using the guarded hot-plate (GHP) technique, which works on the principle proposed in the early 1900s by Dickinson and Van Dusen [33]. In this technique, a temperature gradient is applied on two opposing faces of the test sample, while the remaining faces are insulated. These conditions generate a constant heat flux going towards the front with low temperature. By measuring the total heat flux (q''), the thermal conductivity of the sample can be calculated as follows:

$$k = -q'' \frac{L}{(T_{hot} - T_{cold})} \quad (4)$$

where k and L are the thermal conductivity and the thickness of the sample in the same direction as the temperature gradient is applied, respectively. T is the temperature, whereas the subscript hot and cold represent the hot and cold faces of the sample, respectively.

The thermal conductivity of any material can be predicted numerically by applying the same boundary conditions as the hot guarded-plate method, where hot and cold temperatures are applied across two opposite faces of a finite element model.

These hot and cold temperatures generate heat flux flowing towards the cold surface. The total heat flux q'' is calculated at the cold surface by the simulation FEM software package ABAQUS [34]. Finally, by knowing the dimensions of the FEM of the material, the thermal conductivity is calculated by using Equation (2). The ABAQUS software is part of the multiphysics modeling and simulation package, one of the widely used commercial software for solving various engineering problems, including dynamic, material behavior, and optimization problems. The software can generate the mesh, discretize the solution model, and solve the model based on user-defined conditions [34].

2.5. Energy Savings and Economic Outcomes

Furthermore, the economic performance of the 3DPC wall was compared with conventional brick walls considering the city of Makkah, in Saudi Arabia, as it was reported to have the highest cooling degree-days (CDDs) value in Saudi Arabia [35]. It must be emphasized that the CDD varies from one location to another according to the climate zone, and a larger CDD number indicates more cooling hours required to maintain the building interior within human comfort. The current economic analysis considered a location where the building cooling load dominates, but this analysis is still valid for locations where the heating load dominates. In such a case, heating degree-days (HDDs) accounts for the number of hours when heating is required.

This implies that using the proposed 3DPC walls, characterized by low thermal conductivity, would have a high economic advantage in territories with climate types such as Desert, Oceanic, and Humid Continental. It would also have a moderate economic advantage in territories with Equatorial, Mediterranean, and Humid Subtropical climate zones. This is due to the annual variations in the temperature difference, or the CDDs, as will be shown by the following equation.

The amount of heat transferred through the wall Q can be calculated as follows:

$$Q = UA(T_{out} - T_{in}) \quad (5)$$

where U is the thermal transmittance of the wall, A is the wall's surface area, and T_{in} and T_{out} are the indoor and outdoor temperatures set as 21 °C and 30 °C, respectively. The outdoor temperature is the daily mean outdoor temperature of Makkah, Saudi Arabia. Wall conductance U is the reciprocal of the total thermal resistance of the wall R and can be determined based on the following relations:

$$U = \frac{1}{R} = \frac{AK}{\Delta x} \quad (6)$$

where K is the overall thermal conductivity of the wall, Δx is the thickness of the wall, and A is the surface area, which is assumed to be one square meter. The calculations for the 3DPC wall reinforced with LDR-TR and TRS-TR steel wire joint were examined at 12 cm vertical spacing between joint reinforcement.

In order to calculate the energy saved for each case, the heat transferred through the conventional wall, Q_C , was incorporated into the following equation:

$$E_{sav} = \frac{(Q_C - Q_P)\Delta t}{COP} \quad (7)$$

Here, E_{sav} is the energy saved, Q_P is the heat transferred through the 3DPC wall, COP is the coefficient of performance of the cooling system (assuming that the air conditioner is positioned in a window), and Δt is the annual equivalent of full-load cooling operation hours, which can be calculated by using the following equation:

$$\Delta t = O_h \frac{T_{out} - T_{in}}{T_{design} - T_{in}} \quad (8)$$

where T_{design} is the design temperature of the outdoor air, which is 37 °C, and O_h is the annual operation hours of the air conditioner, which is assumed to be 8760 h/y (i.e., 24 h per day).

Finally, the annual saved energy cost C_{ES} can be calculated as follows:

$$C_{ES} = E_s C_E \quad (9)$$

where C_E is the electricity cost, which is 0.08 USD/kWh. The electricity prices for the residential sector in Saudi Arabia depend on the monthly consumption, which is 0.05 USD/kWh for consumption below 6000 kWh/month, and 0.08 USD/kWh for consumption above 6000 kWh/month.

3. Results and Discussion

3.1. Mesh Independence of Developed Model

Mesh sensitivity analysis was carried out for one of the constructed models, i.e., TRI, to determine the optimal element size that gives accurate results with minimum computational time. Therefore, eight different mesh sizes were examined, varying from 75 mm to 2.5 mm. Figure 5 shows the TRI infill unit cell after applying the finite element model mesh at three different mesh sizes.

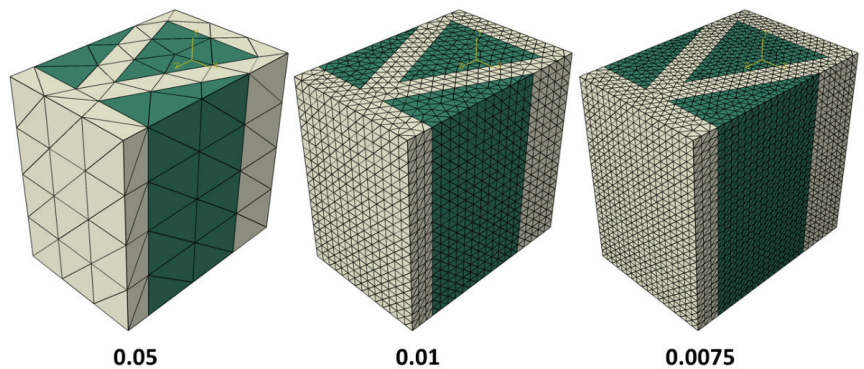


Figure 5. Three different mesh sizes of the triangular infill unit cell.

The results of the mesh sensitivity analysis are shown in Figure 6. The thermal conductivity decreased as the mesh sizes decreased. This decrease was significant when the mesh size was larger than 0.01 m and very minimal when the mesh size was smaller

than 0.01 m. The computational time, on the other hand, increased with decreases in the mesh size. However, the computational time increase was insignificant when the mesh size was refined to 0.0075 m. At smaller mesh sizes, i.e., 0.005 and 0.0025 m, the increase in computational time was quite significant. Therefore, a mesh size of 0.0075 m was considered for this study.

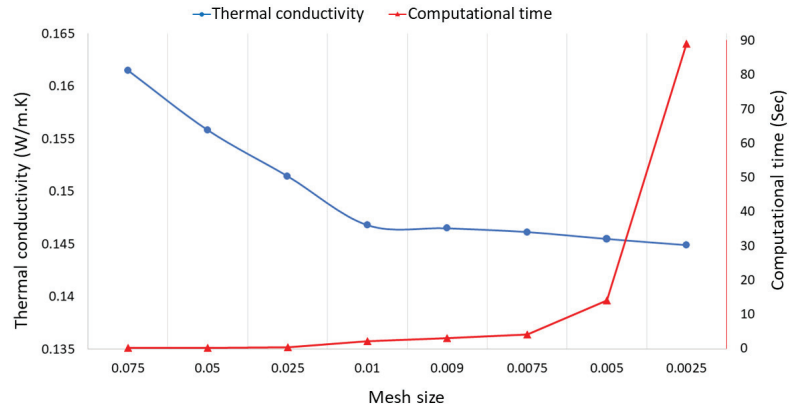


Figure 6. Mesh sensitivity analysis showing variation in the thermal conductivity and computational time versus mesh size.

3.2. Effect of Infill Shapes

Steady-state boundary conditions were applied to all the constructed models in the Z directions to predict the thermal conductivity of each 3DPC wall unit cell in the through-thickness direction. As evident from the results (Table 2), the infill shape influenced the through-thickness thermal conductivity of the 3DPC walls. The lowest thermal conductivity of 0.122 W/m.K was found in the 3DPC wall with the DIM shape infill. HEX and SQU infills came next, with almost equal thermal conductivity values of 0.130 and 0.131 W/m.K. The TRI infill shape had a higher thermal conductivity value of 0.146 W/m.K. The 3DPC model with the rectangular infill exhibited the highest thermal conductivity of 0.170 W/m.K.

Table 2. Thermal conductivities of the 3DPC wall unit cell models with different infill shapes.

Infill Shape	Abbreviation	Thermal Conductivity (W/m.K)
Square	SQR	0.131
Triangular	TRI	0.146
Rectangular	REC	0.170
Hexagonal	HEX	0.130
Diamond	DIM	0.122

Figure 7 shows the heat flux within the unit cells of different infill structures of 3DPC walls. From Table 2 and Figure 7, it is clear that two main factors controlled the thermal conductivity of these models, firstly, the distance needed for the heat to transfer from the hot surface to the cold one. The 3DPC wall with DIM infill had the longest distance and the lowest thermal conductivity. In contrast, the 3DPC wall with a rectangular infill had the shortest distance and the highest thermal conductivity. The second factor was the existence of branches that reduced heat transfer to the other side. This could be seen by comparing the 3DPC wall with REC and SQR infills.

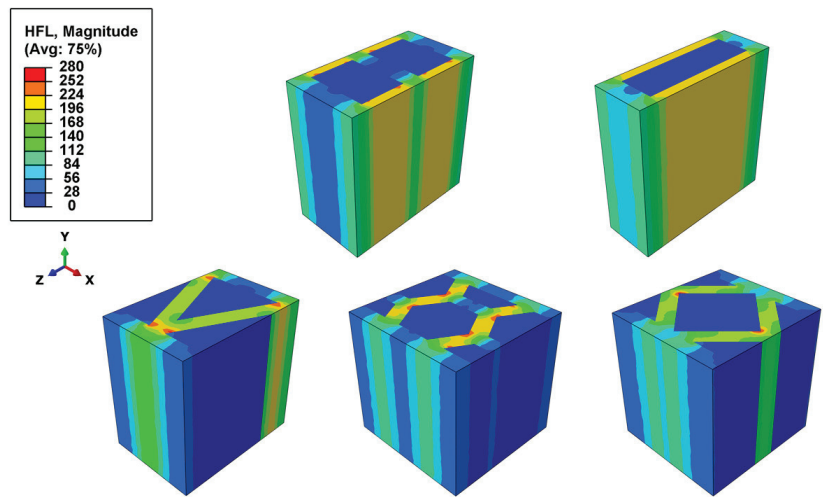


Figure 7. Heat flux within the 3DPC walls for the various infill shapes.

3.3. Effect of Wire Joint Reinforcements

The through-thickness thermal conductivity of the 3DPC wall reinforced with LDR-TR and TRS-TR steel wire joints were examined at various vertical spacing values between joint reinforcements. As shown in Table 3, the 3DPC wall reinforced with a TRS-TR steel wire joint had lower thermal conductivity than that reinforced with an LDR-TR steel wire joint. The thermal conductivity of the 3DPC wall reinforced with the TRS-TR steel wire joint was almost half that of the 3DPC wall reinforced with the LDR-TR steel wire joint when the vertical spacing between the reinforcement was 6 cm. However, this difference in thermal conductivity decreased with the increase in the vertical spacing between the reinforcement.

Table 3. Thermal conductivity of 3DPC wall reinforced with LDR-TR and TRS-TR steel wire joints at various vertical spacings between joint reinforcements.

Type of Joint Reinforcement	Vertical Spacing between Joint Reinforcement (cm)	Thermal Conductivity (W/m.K)
TRS-TR	6	0.203
TRS-TR	12	0.152
TRS-TR	18	0.132
LDR-TR	6	0.39
LDR-TR	12	0.252
LDR-TR	18	0.204

3.4. Comparison with Conventional Brick

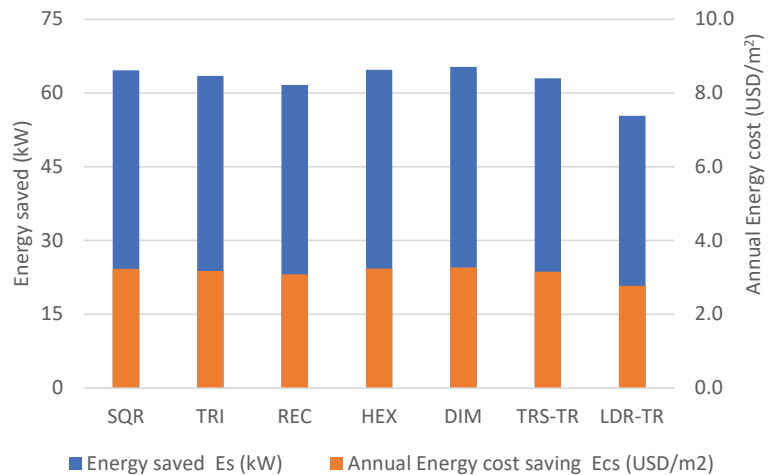
The through-thickness thermal conductivity of conventional brick walls constructed with different types of bricks was obtained experimentally by Ahmad and Al-Hadrami [36,37]. The thermal conductivity values of brick wall samples constructed from fired-red clay and concrete bricks were reported to be 0.495 and 0.976 W/m.K, respectively. The 3DPC wall exhibited much lower thermal conductivity than conventional brick walls.

Table 4 shows the values of wall conductance and heat transferred through the different types of conventional and 3DPC walls. The various infill structures used for 3DPC exhibited variation in their thermophysical properties include thermal conductivity, thickness, wall conductance, and the corresponding heat transfer rate through the wall. These variations are due to structure variation.

Table 4. Thermal characteristics of conventional and 3DPC walls.

Case	Thermal Conductivity k (W/m.K)	Thickness Δx (m)	Wall Conductance U (W/m ² .K)	Heat Transferred through the Wall Q (W)
Red clay brick (Conventional wall)	0.495	0.2	2.475	22.3
Concrete brick (Conventional wall)	0.976	0.2	4.88	43.9
Insulated red clay brick (Conventional wall)	0.262	0.2	1.31	11.8
3DPC wall (SQR infill)	0.131	0.2	0.655	5.90
3DPC wall (TRI infill)	0.146	0.2	0.73	6.57
3DPC wall (REC infill)	0.17	0.2	0.85	7.65
3DPC wall (HEX infill)	0.13	0.2	0.65	5.85
3DPC wall (DIM infill)	0.122	0.2	0.61	5.49
3DPC wall (TRS-TR)	0.152	0.2	0.76	6.84
3DPC wall (LDR-TR)	0.252	0.2	1.26	11.3

In Figures 8–13, the energy and economic performance of the 3DPC infill structures are presented and compared with the conventional wall materials that are commonly used in contemporary buildings, such as concrete brick walls, red clay brick walls, and insulated red brick walls. The electricity rate for the residential sector in Saudi Arabia changes according to the monthly consumption category, whether it falls below or above 6000 kWh per month. Thus, the electricity rate is 0.05 USD/kWh for consumption below 6000 kWh and 0.08 USD/kWh for consumption above 6000 kWh.

**Figure 8.** Energy saved and associated electricity cost (\$0.05/kWh) using different 3DPC infill structures versus a concrete brick wall.

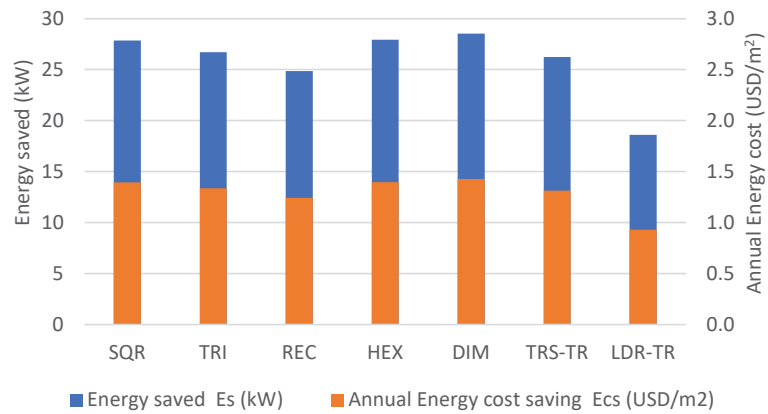


Figure 9. Energy saved and associated electricity cost reduction ($\$0.05/\text{kWh}$) using different 3DPC infill structures versus a red clay brick wall.

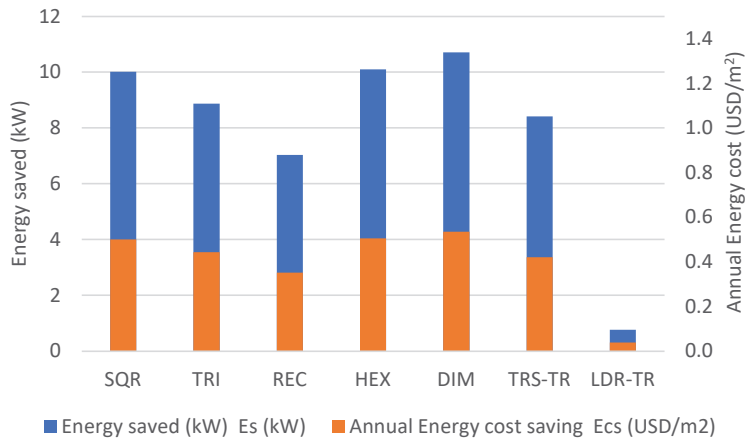


Figure 10. Energy saved and associated electricity cost reduction ($\$0.05/\text{kWh}$) using different 3DPC infill structures versus an insulated red brick wall.

The potential energy savings and electricity bill reductions in the case of utilizing the various 3DPC infill structures compared with the concrete brick wall are presented in Figure 8 based on the electricity rate of $0.05 \text{ USD}/\text{kWh}$. The saved energy rates were over 60 kW , except for the case of LDR-TR, which fell just below 60 kW . At the same time, the potential annual energy cost reduction was around $3 \text{ USD}/\text{m}^2$. It could be noticed that the size of the building and the type of the building in terms of energy consumption have a significant impact on the overall energy savings and potential electricity bill reduction.

In Figure 9, the energy and economic performance of these 3DPC infill structures are compared with another building material that is widely used, especially in exterior walls, i.e., the red clay brick wall, which is considered an excellent thermal insulator. Though red clay brick walls appeared to perform better than concrete brick walls, the 3DPC infill structures outperformed the red clay brick, as clearly shown in Figure 9. The various infill structures considered achieved an energy saving rate of about 25 kW except for the LDR-TR, which achieved over 15 kW . Nevertheless, a minimum annual energy cost reduction of about $1 \text{ USD}/\text{m}^2$ was expected.

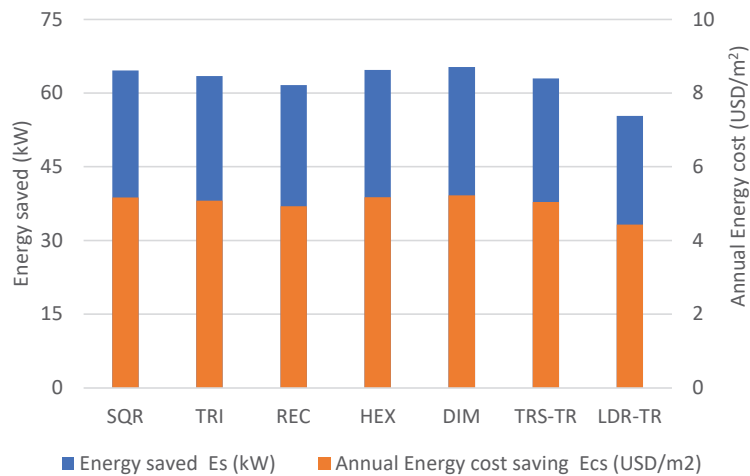


Figure 11. Energy saved and associated electricity cost (\$0.08/kWh) using different 3DPC infill structures versus a concrete brick wall.

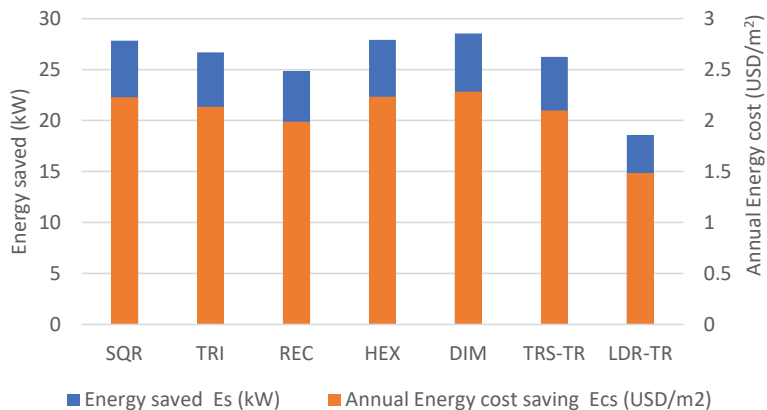


Figure 12. Energy saved and associated electricity cost reduction (\$0.08/kWh) using different 3DPC infill structures versus red clay brick wall.

In Figure 10, the energy and economic performance of the 3DPC infill structures is compared against the case of insulated red brick. The figure shows relative variation in the performance of the various 3DPC infill structures. For example, the LDR-TR shows a minimum advantage with comparable thermal performance. However, the various other structures achieved an average of about 9 kW energy saving with an average cost reduction of less than 0.5 USD/m².

Figure 11 shows an average annual energy cost reduction of over 4 USD/m², which is achievable if 3DPC walls utilizing the proposed structures are used to replace the concrete brick walls. However, this figure decreases to about 2 USD/m² for the case of red clay brick, as shown in Figure 12, while in Figure 13, these 3DPC infill structures present an average annual energy cost of about 0.08 USD/m². In addition to the economic advantage, the presented potential energy saving will contribute significantly to reducing carbon emissions due to residential energy consumption and help mitigate the global challenge of climate change.

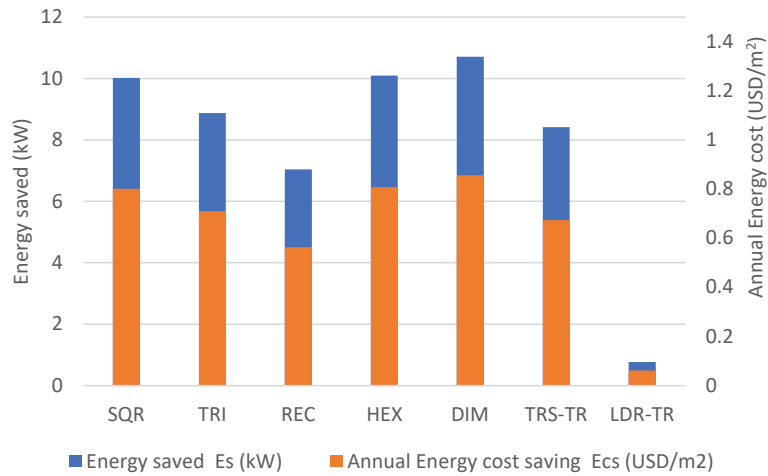


Figure 13. Energy saved and associated electricity cost reduction (\$0.08/kWh) using different 3DPC infill structures versus an insulated red brick wall.

Table 5 summarizes the amount of energy saved and the annual energy cost savings for the different 3DPC infill structures compared with the three conventional walls, i.e., concrete brick walls, red clay brick walls, and insulated red clay brick walls. In this table, the electricity rating considered for electricity cost reduction is 0.08 USD/kWh. The table shows as high as 5 USD/m² in annual electricity bill savings. However, further detailed studies are required to include the initial cost and provide clarification on overall building life cycle costing. Nevertheless, the current economic evaluation reveals that the future of 3DPC is promising to reduce building construction and energy consumption costs, as thoroughly discussed in the preceding sections.

Table 5. Energy-saving for each 3DPC wall compared with three different types of conventional walls.

3DPC Wall	Compared with Conventional Wall					
	Concrete Brick Wall		Red Clay Brick Wall		Insulated Red Clay Brick Wall	
	Energy Saved	Annual Energy Cost Saving	Energy Saved	Annual Energy Cost Saving	Energy Saved	Annual Energy Cost Saving
	Es (kW)	Es (USD/m ²)	Es (kW)	Es (USD/m ²)	Es (kW)	Es (USD/m ²)
SQR infill	64.610	5.169	27.832	2.227	10.016	0.801
TRI infill	63.463	5.077	26.685	2.135	8.870	0.710
REC infill	61.628	4.930	24.850	1.988	7.034	0.563
HEX infill	64.686	5.175	27.908	2.233	10.093	0.807
DIM infill	65.298	5.224	28.520	2.282	10.705	0.856
TRS-TR	63.004	5.040	26.226	2.098	8.411	0.673
LDR-TR	55.358	4.429	18.580	1.486	0.765	0.061

4. Conclusions

The thermal performance of various 3DPC wall infill structures was numerically modeled to investigate the optimization of the infill shape for maximum thermal performance with minimum variation in the added materials. The infill structure was found to influence the thermal conductivity of the examined 3DPC walls. For example, among the tested infill structure geometries, the DIM shape achieved the lowest thermal conductivity of 0.122 W/m.K, while the HEX, SQR, and TRI shapes achieved 0.130, 0.131, and 0.146 W/m.K, respectively. The highest thermal conductivity of 0.17 W/m.K was achieved by the REC infill shape. Buswell et al. [38] reported testing two 3DPC wall designs with

structures comparable to that presented in Figure 1. The thermal conductivities of the tested structures ranged from 0.122 to 0.244 W/m.K. These values were produced based on a UKAS-accredited EN 12667 guarded hot plate apparatus [38]. The calculated thermal conductivities of the various infill designs considered in the current study are within this range, i.e., 0.122–0.170 W/m.K. This serves as an experimental validation of the current numerical work.

In addition, the study examined the impact of using TRS-TR and LDR-TR steel wire joints to reinforce the 3DPC walls on thermal performance. The results revealed that the thermal conductivity of the 3DPC wall with TRS-TR is almost half that of the LDR-TR. However, the conductivities were found to decrease with increased vertical spacing between the joint reinforcements. These results provide the construction designer with informative options to make the choice that serves the building's needs. However, a few limitations should also be highlighted, including the interlayer variation in the 3DPC walls, which may result in variation in the thermal conductivity of the concrete structure. This point, in addition to the possibility of variation in the concrete compositions, should be further investigated in future studies.

Author Contributions: A.A.A. (Abdullah A. AlZahrani): Project administration, Funding acquisition, Investigation, Formal analysis, Writing—original draft. A.A.A. (Abdulrahman A. Alghamdi): Conceptualization, Methodology, Modeling, Validation, Formal analysis. A.A.B.: Modeling, Writing—review and editing, Resources. All authors have read and agreed to the published version of the manuscript.

Funding: This research received no external funding.

Data Availability Statement: Not applicable.

Acknowledgments: The authors acknowledge the support provided by Umm Al-Qura University (UQU) and the Ministry of Education.

Conflicts of Interest: The authors declare no conflict of interest.

References

1. Cao, X.; Dai, X.; Liu, J. Building Energy-Consumption Status Worldwide and the State-of-the-Art Technologies for Zero-Energy Buildings during the Past Decade. *Energy Build.* **2016**, *128*, 198–213. [\[CrossRef\]](#)
2. Gengnagel, C.; Baverel, O.; Burry, J.; Ramsgaard Thomsen, M.; Weinzierl, S. Correction to: Impact: Design with All Senses. In *Proceedings of the Design Modelling Symposium Berlin*; Springer: Berlin/Heidelberg, Germany, 2019; p. C1.
3. Divyah, N.; Prakash, R.; Srividhya, S.; Sivakumar, A. Parametric Study on Lightweight Concrete-Encased Short Columns under Axial Compression-Comparison of Design Codes. *Struct. Eng. Mech.* **2022**, *83*, 387–400. [\[CrossRef\]](#)
4. El Sakka, F.; Hamzeh, F. 3D Concrete Printing in the Service of Lean Construction. In Proceedings of the 25th Annual Conference of the International Group for Lean Construction (IGLC), Heraklion, Greece, 9–12 July 2017.
5. Barbosa, M.S.; dos Anjos, M.A.S.; Cabral, K.C.; Dias, L.S. Development of Composites for 3D Printing with Reduced Cement Consumption. *Constr. Build. Mater.* **2022**, *341*, 127775. [\[CrossRef\]](#)
6. ASTM. International Standard Terminology for Additive Manufacturing Technologies. Available online: <https://www.astm.org/f2792-12.html> (accessed on 16 July 2022).
7. Laubier, R.; Wunder, M.; Witthöft, S.; Rothballer, C. The Boston Consulting Group (BCG) Global. 23 January 2018. Available online: <https://www.bcg.com/publications/2018/will-3d-printing-remodel-construction-industry> (accessed on 5 August 2022).
8. Al Rashid, A.; Khan, S.A.; Al-Ghamdi, S.G.; Koç, M. Additive Manufacturing: Technology, Applications, Markets, and Opportunities for the Built Environment. *Autom. Constr.* **2020**, *118*, 103268. [\[CrossRef\]](#)
9. Khan, S.A.; Koç, M.; Al-Ghamdi, S.G. Sustainability Assessment, Potentials and Challenges of 3D Printed Concrete Structures: A Systematic Review for Built Environmental Applications. *J. Clean. Prod.* **2021**, *303*, 127027. [\[CrossRef\]](#)
10. Liu, J.; Setunge, S.; Tran, P. 3D Concrete Printing with Cement-Coated Recycled Crumb Rubber: Compressive and Microstructural Properties. *Constr. Build. Mater.* **2022**, *347*, 128507. [\[CrossRef\]](#)
11. Valipour, M.; Yekkalar, M.; Shekarchi, M.; Panahi, S. Environmental Assessment of Green Concrete Containing Natural Zeolite on the Global Warming Index in Marine Environments. *J. Clean. Prod.* **2014**, *65*, 418–423. [\[CrossRef\]](#)
12. Agustí-Juan, I.; Habert, G. Environmental Implications and Opportunities of Digital Fabrication. In *Expanding Boundaries: Systems Thinking in the Built Environment*; vdf Hochschulverlag AG an der ETH Zürich: Zürich, Switzerland, 2016; pp. 304–308.
13. Suntharalingam, T.; Upasiri, I.; Gatheeshgar, P.; Poologanathan, K.; Nagaratnam, B.; Santos, P.; Rajanayagam, H. Energy Performance of 3D-Printed Concrete Walls: A Numerical Study. *Buildings* **2021**, *11*, 432. [\[CrossRef\]](#)

14. Alhumayani, H.; Gomaa, M.; Soebarto, V.; Jabi, W. Environmental Assessment of Large-Scale 3D Printing in Construction: A Comparative Study between Cob and Concrete. *J. Clean. Prod.* **2020**, *270*, 122463. [CrossRef]
15. World's Largest 3D Printed Building. Available online: <https://www.apis-cor.com/dubai-project> (accessed on 9 April 2022).
16. Han, X.; Yan, J.; Liu, M.; Huo, L.; Li, J. Experimental Study on Large-Scale 3D Printed Concrete Walls under Axial Compression. *Autom. Constr.* **2022**, *133*, 103993. [CrossRef]
17. Daungwilailuk, T.; Pheinsusom, P.; Pansuk, W. Uniaxial Load Testing of Large-Scale 3D-Printed Concrete Wall and Finite-Element Model Analysis. *Constr. Build. Mater.* **2021**, *275*, 122039. [CrossRef]
18. Rahul, A.V.; Santhanam, M.; Meena, H.; Ghani, Z. Mechanical Characterization of 3D Printable Concrete. *Constr. Build. Mater.* **2019**, *227*, 116710. [CrossRef]
19. Mahadevan, M.; Francis, A.; Thomas, A. A Simulation-Based Investigation of Sustainability Aspects of 3D Printed Structures. *J. Build. Eng.* **2020**, *32*, 101735. [CrossRef]
20. Aramburu, A.; Calderon-Uriszar-Aldaca, I.; Puente, I. 3D Printing Effect on the Compressive Strength of Concrete Structures. *Constr. Build. Mater.* **2022**, *354*, 129108. [CrossRef]
21. Al-Tamimi, A.S.; Al-Osta, M.A.; Al-Amoudi, O.S.B.; Ben-Mansour, R. Effect of Geometry of Holes on Heat Transfer of Concrete Masonry Bricks Using Numerical Analysis. *Arab. J. Sci. Eng.* **2017**, *42*, 3733–3749. [CrossRef]
22. Pessoa, S.; Guimarães, A.S.; Lucas, S.S.; Simões, N. 3D Printing in the Construction Industry—A Systematic Review of the Thermal Performance in Buildings. *Renew. Sustain. Energy Rev.* **2021**, *141*, 110794. [CrossRef]
23. Araújo, R.A.; Martinelli, A.E.; Cabral, K.C.; Dantas, A.F.; Silva, I.F.; Xavier, A.A.; Santos, A.L. Thermal Performance of Cement-Leca Composites for 3D Printing. *Constr. Build. Mater.* **2022**, *349*, 128771. [CrossRef]
24. He, Y.; Zhang, Y.; Zhang, C.; Zhou, H. Energy-Saving Potential of 3D Printed Concrete Building with Integrated Living Wall. *Energy Build.* **2020**, *222*, 110110. [CrossRef]
25. Sun, J.; Xiao, J.; Li, Z.; Feng, X. Experimental Study on the Thermal Performance of a 3D Printed Concrete Prototype Building. *Energy Build.* **2021**, *241*, 110965. [CrossRef]
26. Alkhalidi, A.; Hatuqay, D. Energy Efficient 3D Printed Buildings: Material and Techniques Selection Worldwide Study. *J. Build. Eng.* **2020**, *30*, 101286. [CrossRef]
27. Marais, H.; Christen, H.; Cho, S.; De Villiers, W.; Van Zijl, G. Computational Assessment of Thermal Performance of 3D Printed Concrete Wall Structures with Cavities. *J. Build. Eng.* **2021**, *41*, 102431. [CrossRef]
28. Suntharalingam, T.; Gatheeshgar, P.; Upasiri, I.; Poologanathan, K.; Nagaratnam, B.; Rajanayagam, H.; Navaratnam, S. Numerical Study of Fire and Energy Performance of Innovative Light-Weight 3D Printed Concrete Wall Configurations in Modular Building System. *Sustainability* **2021**, *13*, 2314. [CrossRef]
29. Suntharalingam, T.; Gatheeshgar, P.; Upasiri, I.; Poologanathan, K.; Nagaratnam, B.; Corradi, M.; Nuwanthika, D. Fire Performance of Innovative 3D Printed Concrete Composite Wall Panels—A Numerical Study. *Case Stud. Constr. Mater.* **2021**, *15*, e00586. [CrossRef]
30. American Society for Testing and Materials. *Committee D16 on Thermal Insulation. Standard Test Method for Thermal Performance of Building Materials and Envelope Assemblies by Means of a Hot Box Apparatus*; ASTM International: West Conshohocken, PA, USA, 2011.
31. *ISO E. 6946: 2017*; Building Components and Building Elements—Thermal Resistance and Thermal Transmittance—Calculation Methods. International Organization for Standardization: Geneva, Switzerland, 2017.
32. Lemmon, E.W.; Jacobsen, R.T. Viscosity and Thermal Conductivity Equations for Nitrogen, Oxygen, Argon, and Air. *Int. J. Thermophys.* **2004**, *25*, 21–69. [CrossRef]
33. Zarr, R.R. A History of Testing Heat Insulators at the National Institute of Standards and Technology. *Ashrae Trans.* **2001**, *107*, 661.
34. Abaqus Unified FEA—SIMULIATM by Dassault Systèmes®. Available online: <https://www.3ds.com/products-services/simulia/products/abaqus/> (accessed on 28 February 2022).
35. Al-Hadhrami, L.M. Comprehensive Review of Cooling and Heating Degree Days Characteristics over Kingdom of Saudi Arabia. *Renew. Sustain. Energy Rev.* **2013**, *27*, 305–314. [CrossRef]
36. Al-Hadhrami, L.; Ahmad, A. Assessment of Thermal Performance of Different Types of Masonry Bricks Used in Saudi Arabia. *Appl. Therm. Eng.* **2009**, *29*, 1123–1130. [CrossRef]
37. Ahmad, A.; Al-Hadhrami, L.M. Thermal Performance and Economic Assessment of Masonry Bricks. *Therm. Sci.* **2009**, *13*, 221–232. [CrossRef]
38. Freeform Construction: Mega-Scale Rapid Manufacturing for Construction. *Autom. Constr.* **2007**, *16*, 224–231. [CrossRef]

Article

Investigation of Thermal Bridges of a New High-Performance Window Installation Using 2-D and 3-D Methodology

Jolanta Šadauskienė^{1,*}, Juozas Ramanauskas^{1,2}, Dorota Anna Krawczyk³, Eglė Klumbytė^{1,*} and Paris A. Fokaides^{1,4}

¹ Faculty of Civil Engineering and Architecture, Kaunas University of Technology, Studentų Str. 48, LT-51367 Kaunas, Lithuania; juozas.ramanauskas@ktu.lt (J.R.); eng.fp@frederick.ac.cy (P.A.F.)

² Building Physics Laboratory of Institute of Architecture and Construction, Kaunas University of Technology, Tunelio Str. 60, LT-44405 Kaunas, Lithuania

³ Faculty of Civil Engineering and Environmental Sciences, Bialystok University of Technology, Wiejska 45 E, 15-351 Bialystok, Poland; d.krawczyk@pb.edu.pl

⁴ School of Engineering, Frederick University, Frederickou Str., Nicosia 1036, Cyprus

* Correspondence: jolanta.sadauskiene@ktu.lt (J.S.); egle.klumbyte@ktu.lt (E.K.)

Abstract: The investigation of building elements regarding energy saving is a paramount issue, with EU Directives driving achievement goals, focusing on buildings' energy performance and energy efficiency. This work focuses on investigating thermal bridges in a new high-performance window installation. This work aims to investigate the thermal properties of windows installed in the thermal insulation layer and to compare different installation methods and thermal bridge evaluation methodologies from the point of view of thermal physics. The results show that comparing the obtained values of the thermal bridge according to two- and three-dimensional domain (2-D and 3-D) calculation methods, the values show a difference of 68%. After examining the method of installing a new high-performance window in the thermal insulation layer, the effect of installing a window on the wall of a building is highlighted in this work. Given that windows are the most thermally conductive elements in a building, this paper provides guidance for both the scientific community and practitioners regarding trends in thermal bridges that change completely when using different assessment methods.

Keywords: thermal bridges; thermal transmittance; thermal insulation; passive energy buildings; window; building envelop

Citation: Šadauskienė, J.; Ramanauskas, J.; Krawczyk, D.A.; Klumbytė, E.; Fokaides, P.A. Investigation of Thermal Bridges of a New High-Performance Window Installation Using 2-D and 3-D Methodology. *Buildings* **2022**, *12*, 572. <https://doi.org/10.3390/buildings12050572>

Academic Editors: Yaolin Lin and Wei Yang

Received: 23 March 2022

Accepted: 26 April 2022

Published: 29 April 2022

Publisher's Note: MDPI stays neutral with regard to jurisdictional claims in published maps and institutional affiliations.



Copyright: © 2022 by the authors. Licensee MDPI, Basel, Switzerland. This article is an open access article distributed under the terms and conditions of the Creative Commons Attribution (CC BY) license (<https://creativecommons.org/licenses/by/4.0/>).

1. Introduction

The universal climate change problem has made it crucial for the European Union to invest in energy-saving methods. For this reason, members of the European Union have created an integrated national energy and climate plan from 2021 to 2030 [1]. The Energy Union and the Energy and Climate Policy Framework for 2030 pledge to reduce the amount of emitted gas, which is known to cause the greenhouse effect, by at least 40% compared to the amount emitted in 1990. According to the data of 2014, buildings used approximately 40% of all the energy generated in the EU countries. They emitted more than a third of the universally emitted amount of CO₂ gas [2]. Hence, it was concluded that the buildings sector has much potential to save energy.

Legal requirements for the new generation of buildings are stated in the renewed Directive (EU) 2018/844 [3], which focuses on the energy performance of buildings and energy efficiency. The Union's goal to develop an effective energy system by 2050 is difficult, since breakthroughs in energy efficiency move slowly. In 2014, about 3% of European buildings were Nearly Zero Energy Buildings (NZEB). That means 97% of the buildings were of low energy efficiency [4]. Currently, about 75% of buildings in the European Union are not energy efficient, but in 2050, 85–95% of them will still be in use.

Much effort is being put into renewing and supplementing the buildings' funds, because countless buildings were previously built following low energy usage efficiency standards. Nevertheless, only 1% of buildings are being efficiently renovated each year. For this reason, decisive action is required in order to achieve Europe's climate-neutral (net zero emissions) goals by 2050. According to the European Commission's 17 September Communication, due to Europe's 2030 climate ambitions [5], this norm must increase twice in order to achieve a more ambitious 2030 climate target of at least 55%. The Commission determined that renovation would be needed at an average rate of 3% annually in order to cost-effectively implement the Union's energy efficiency ambitions. For this reason, on 14 October 2020, the Commission presented a new renovation strategy called "A Renovation Wave for Europe—Greening our buildings, creating jobs, improving lives" [6].

In most European cities, buildings appeared during the past few decades and have not been properly taken care of for a long time. In most cases, buildings cannot satisfy modern requirements related to the quality of accommodation, energy usage efficiency, economy, and environmental protection. Doubtlessly, to achieve sustainability, one must emphasize the modern integrated renovation of already-built buildings and take notice of the usage of renewable energy and building insulation, heating, ventilation, and air conditioning (HVAC).

1.1. Thermal Bridge

One of the ways to effectively renovate buildings is to apply new high-performance windows. However, judging from experience, the low energy efficiency is often related to low quality of construction. Correct window installation is still one of the most difficult hurdles that must be overcome to achieve a higher energy efficiency in buildings [7]. Thermal imaging performed by professionals clearly shows thermal bridges at window openings (Figure 1) [8].

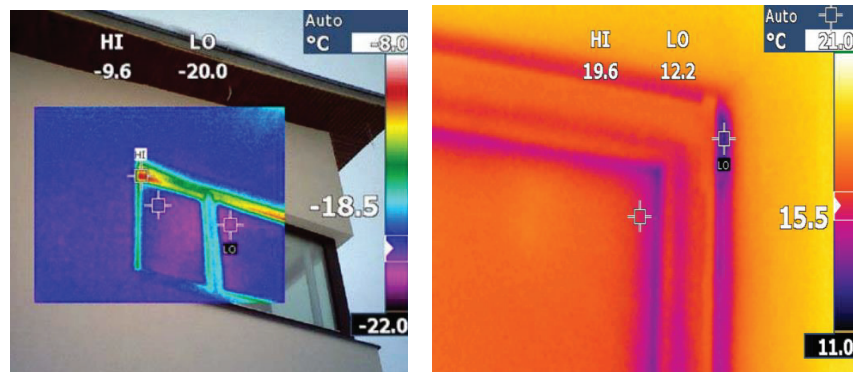


Figure 1. Thermal images of thermal bridges at window openings.

Thermal bridges are caused by full or partial penetration of the building envelope by materials with different thermal conductivities, changes in fabric thickness, and/or differences between internal and external areas, such as those found at wall/floor/ceiling junctions) [9]. According to a literature review, the total impact of thermal bridges on heating energy demand is generally significant, ranging from 5% to 39% [10–13]. The factors mentioned above are determined by weather conditions, insulation level, thermal bridge constructive solution, building type (use and geometry), and the method used to implement its effect within the calculation of the building energy demand [14].

Thermal bridges can impact a single point, a linear area, or an entire spatial configuration. Typically, the linear thermal bridges (LTB) that occur at the junction of two or more building envelope elements are evaluated in the calculations of the building's

energy demand. Several scientific studies have been conducted in which LTB was investigated using various calculation and simulation methodologies, such as static/dynamic and 1D/2D/3D [15–18].

The majority of studies present empirical LTB dependences, which determine the linear thermal transmittance value of a specific construction element [19]. On these foundations, numerical calculation software and catalogues have been developed. The European Standard EN ISO 14683 contains seventy-six cases referring to eight thermal bridge typologies (roofs, corners, intermediate floors, internal walls, slab-on-ground floors, suspended ground floors, pillars, window and door openings), and is one of the most widely used atlases. On the other hand, these atlases provide thermal bridge values calculated using the 2-D method. These calculations exclude point thermal bridges (PTB), which are formed by thermally conductive fasteners such as waxes, varnishes, etc. In terms of PTB, the effect of PTB is often neglected in analyses aimed at defining a building's energy performance. This study also addresses the significance of PTB in the calculation of thermal losses from thermal bridges in window installations.

1.2. A New High-Performance Window Installation

To partly resolve this problem, a new requirement was included in the Lithuanian national document [20], which stated that the thermal transmittance of a linear thermal bridge (LTB) of an NZEB or passive house must be a maximum of $0.05 \text{ W}/(\text{m}\cdot\text{K})$. However, attaining this value presents a severe difficulty for project designers and builders [21]. However, a new method of installing window frames directly onto thermal insulation layers has been found to reduce the effect of LTB [22].

Nowadays, a few alternative installation solutions are applied in the practical area of construction. Most window frameworks are pendent on reinforced anchor brackets (Figure 2a) or on rectangular wooden frames (chipboard) (Figure 2b) that are installed on a wall. However, these different cases of window mounting do not ensure that thermal bridges at the junction of wall and window will be avoided. Insufficiently isolated joints of window frames and facade walls increase the impact of building thermal leaks, and it does not ensure the required value of the airtightness of passive house, which must be equal to 0.6 air change rate at 50 Pa per hour. Furthermore, it is important to mention that the possibility of condensation and humidity increases when using the mentioned window mounting methods [23,24]. In this way, the building may lose its passive house status because of window installation defects [25,26].



Figure 2. System of window installation in the insulation layer: (a) on anchor brackets [27]; (b) on chipboard frame [28].

It is often incorrectly thought that by installing a window in the isolation layer, the thermal bridge will have no impact on the building's energy consumption. The value of

the thermal bridge of the openings depends on the length from the load-bearing layer and the mounting place of the window, and on the materials used to mount the window, such as installing foam, framework, fasteners and finishing elements. The longer the length between the wall and the window, the higher the required number of anchor brackets attached directly to the window frame and the outer wall retaining layer. However, point thermal bridges (PTB) appear at the points where the anchor brackets are attached. Thus, using a lot of them is not efficient.

Anchor holders are often made of plastic, which has a much lower thermal conductivity value than metal, to reduce energy loss due to point thermal bridges. However, the support force of this type of bracket has drawbacks: plastic is flexible. It may not withstand heavy high-performance windows in the thermal insulation layer that have a greater length than the load-bearing layer. The weight of the opening parts of such glass systems is a minimum of 130 kg. Therefore, only steel brackets, whose thermal transmittance value is 50 ($W/(m \cdot K)$), are suitable for installing windows in passive houses. This means the material of anchor brackets has a huge impact on the efficiency of high-energy-performance buildings. To assess the real energy consumption, buildings must evaluate the additional heat losses due to PTB. Otherwise, the energy efficiency calculations for the building might be incorrect.

Designers and builders are looking for new ways to reduce the impact of PTB on a building's energy costs [29]. A new method for installing windows in a thermal insulation layer is currently being applied in practice. A prefabricated frame, made of higher-density stone wool boards (SWB) and auxiliary elements, is being used for the installation of window frames (Figure 3). Practice shows that such window installation is not complicated due to the lightness of the thermal insulation board and the simplicity of the fastening elements. Moreover, it is suitable for installation on any retaining wall, and the thermal conductivity of the frame made of thermal insulation material is low. Such a frame's static properties are sufficient for installing a high-performance window up to 350 mm away from the retaining wall layer. Since metal fasteners do not connect, it is unlikely to create a PTB effect. However, installing windows in this way is little studied compared to the general thermal research context. Therefore, this work aims to investigate the thermal properties of windows installed in the thermal insulation layer in detail and to compare different installation methods and thermal bridge evaluation methodologies from the point of view of thermal physics.

A major concern regarding the design and manufacturing of advanced windows is related to their sound insulation performance. Recent studies have demonstrated the effectiveness of porous absorbent materials in the cavity perimeter of windows [30], as well as the effect of ventilation-enabling façade noise control devices for congested high-rise cities [31]. Active noise control, which uses a secondary sound to cancel unwanted noise, has been successfully implemented and is considered to be an established technique for enhancing the sound insulation of windows [32].

2. Methodology

2.1. Research Object

The schemes of the investigated wall structure and the window frame are given in Figure 3. Additionally, the values of the layer's thickness and thermal conductivity coefficient are shown in the same figure. Accordingly, the heat transfer coefficient of the wall structure is $U = 0.12 W/(m^2 \cdot K)$.

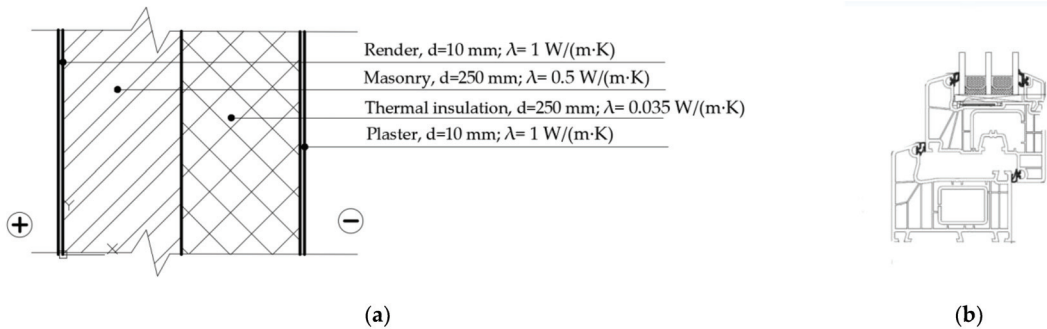


Figure 3. The scheme of the investigated wall structure (a) and of the investigated window frame (b).

The wooden frame of the analyzed window consists of 6 chambers, and its thickness is 100 mm. The value of the thermal conductivity coefficient $\lambda = 0.13 \text{ W}/(\text{m}\cdot\text{K})$. The calculations were simplified and the heat exchange over the glass area was not detailed.

The installation of a window on the wall's opening using stone wool boards (SWB) was chosen for the study (Figure 4). The thermal conductivity coefficient of the special rigid SWB is $\lambda = 0.059 \text{ W}/(\text{m}\cdot\text{K})$. The window frame fastener W length is 192 mm; width—50 mm; wall thickness—2 mm; thermal insulation thickness—48 mm. The length of the corner fastener CL of the thermal insulation panels (when the thickness of the thermal insulation layer was $> 200 \text{ mm}$) is 192 mm; width—192 mm (respectively 96 mm on one side of the corner); wall thickness—2 mm. The thermal insulation board interconnect EL length was 192 mm; width—192 mm; wall thickness—2 mm. The investigation evaluated two wall installation fasteners measuring $80 \times 100 \text{ mm}$. The calculations estimated one wall installation fastener measuring $80 \times 100 \text{ mm}$. This method of installation does not require gaskets, as the thermal insulation material is flexible and allows the window frame to be installed tightly.

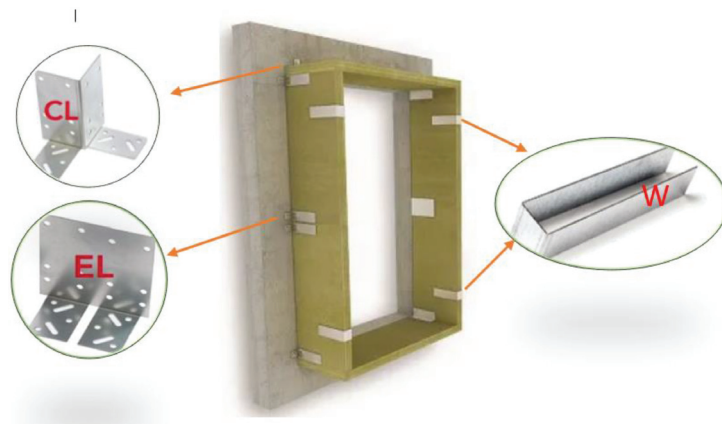


Figure 4. System of window installation in the insulation layer using the stone wool boards (SWB) REDAir TM LINK [33].

2.2. Thermal Bridge Evaluation Methodology

Regarding the evaluation of the thermal bridges, the standard EN ISO 14683:2017 [34] presents three different methodologies:

- Numerical simulation (3-D);
- Choosing from catalogues and atlases;

- Calculation under steady-state conditions (2-D).

This study was guided by methodologies 1 and 3, as this work investigated a new way of connecting windows using SWB. The thermal bridge values of such a connection between a window and the walls have not been studied so far. Therefore, these values are not given in catalogues.

Thermal bridges may be defined according to EN ISO 10211: 2017 [9]. The calculation scheme is given in Figure 5.

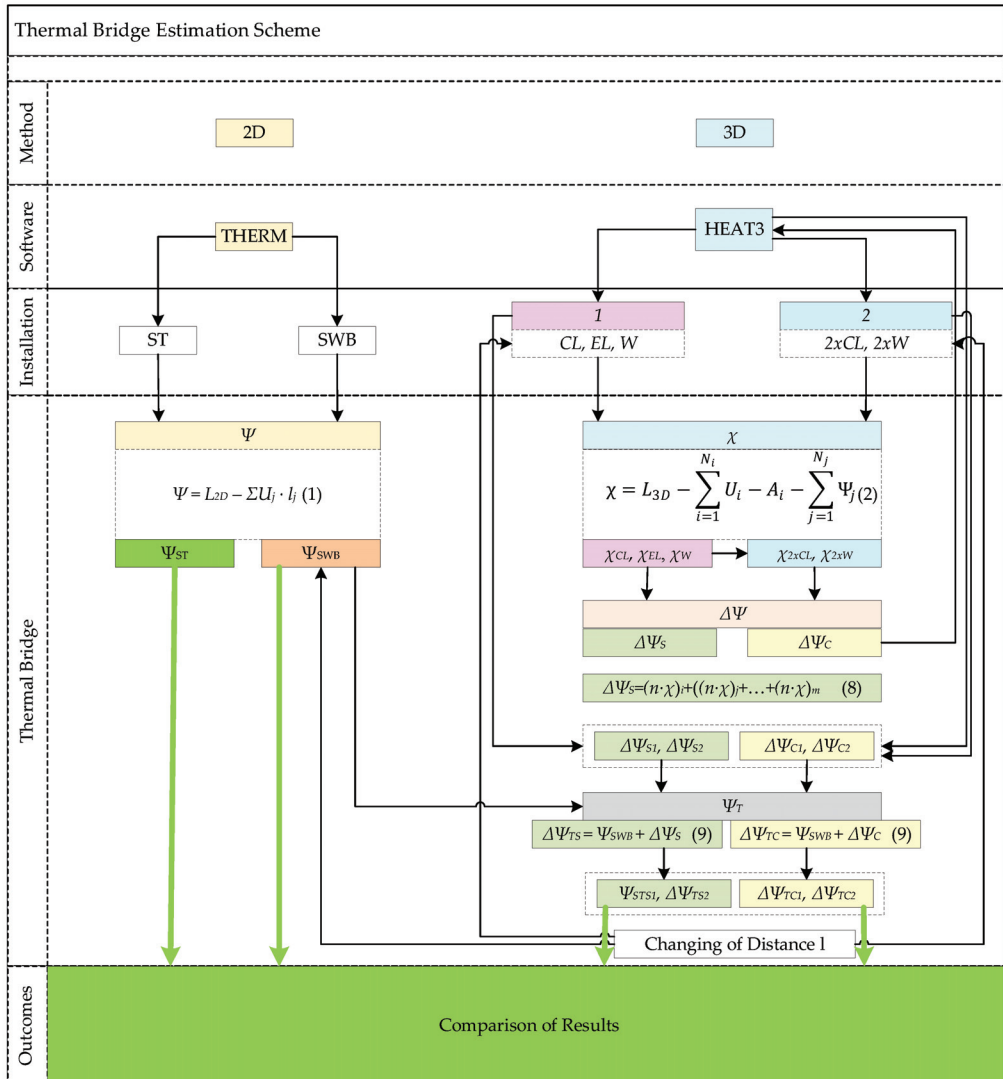


Figure 5. Thermal bridge estimation scheme (prepared by the authors based on [35]).

The LTB around the openings was calculated using the 2-D software THERM [36]. This method is based on the 2-D dimensions. The heat flow moves horizontally in the x-

and y -axis directions. The linear thermal transmittance of the thermal bridges (Ψ) was calculated according to Equation (1):

$$\Psi = L_{2D} - \sum U_j \cdot l_j \quad (1)$$

where L_{2D} is the linear thermal coefficient obtained by calculating the 2-D component for the two environments considered; U_j is the thermal transmittance of the 1-D component j separating the two environments being considered; l_j is the length within the 2-D model applied in the value of U_j .

At the beginning of the study, the LTB was calculated for installation of the window in a load-bearing layer without innovative installation elements and additional insulation; thus, standard Ψ_{ST} . The Ψ_{SWB} of the window opening with an SWB was determined in parallel using the same calculation method. Metal fasteners were not considered at this stage of the calculation.

To evaluate the influence of fasteners on heat loss through the window opening edge, the software HEAT3 [37], with a 3-D temperature field calculation, was used in this study.

For installing windows in the cross-section of thermal insulation material, various fasteners are used, and their influence on heat loss can be assessed by point thermal transmittance χ , $W/(m \cdot K)$. The point thermal transmittance (value— χ) was calculated as in Equation (2):

$$\chi = L_{3D} - \sum_{i=1}^{N_i} U_i - A_i - \sum_{j=1}^{N_j} \Psi_j \quad (2)$$

where L_{3D} is the linear thermal coefficient obtained by calculating the 3-D component for the two environments considered; U_i is the thermal transmittance of the 1-D component i separating the two environments considered; A_i is the area applied in the value U_i ; Ψ_j is linear thermal transmittance; l_j is the length which the value of Ψ_j applies; N_j is the number of 2-D components; N_i is the number of 1-D components.

The partial differential equation is replaced by a discrete approximation in the numerical formulation. Values at discrete points are used to approximate the temperature field. A computational mesh is created because of this. Δx_i , Δy_j , and Δz_k , are the increments in the x -, y -, and z -directions, respectively [38].

A cell (i, j, k) with the side lengths Δx_i , Δy_j , and Δz_k is shown in Figure 6. Figure 6 also indicates $(i, j, k+1)$ directly above the cell. There are six cells next to each other.

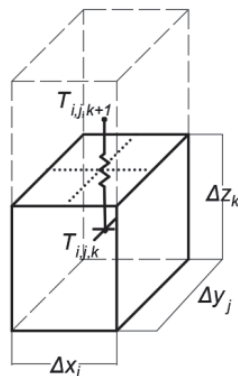


Figure 6. Computational cells (i, j, k) and $(i, j, k+1)$ [38].

The heat flow $Q_{i,j,k+1/2}$ (W), from cell (i,j,k) to cell $(i,j,k+1)$ is given by the thermal conductance multiplied by the temperature difference between these two cells (Equation (3)):

$$Q_{i,j,k+1/2} = K_{i,j,k+1/2} \cdot (T_{i,j,k} - T_{i,j,k+1}) \quad (3)$$

where $K_{i,j,k+1/2}$ is the conductance between the two cells (i,j,k) and $(i,j,k+1)$, W/K; $(T_{i,j,k} - T_{i,j,k+1})$ is the temperature difference between the two cells.

The other five heat flows pertaining to cell (i,j,k) are calculated correspondingly.

Figure 7 shows the six-thermal conductance of cell (i,j,k) . The conductance $K_{i,j,k+1/2}$, (W/K), between the two cells (i,j,k) and $(i,j,k+1)$ is calculated as [38]:

$$K_{i,j,k+1/2} = \frac{\Delta x_j \cdot \Delta y_i}{\frac{\Delta z_k}{(2 \cdot \lambda_{i,j,k})} + \frac{\Delta z_{k+1}}{(2 \cdot \lambda_{i,j,k+1})} + R_{i,j,k+1/2}} \quad (4)$$

where $\lambda_{i,j,k}$ is the thermal conductivity in cell (i,j,k) , W/(m·K); $(\Delta x_j \cdot \Delta y_i)$ is the conductance refers to the total heat flow through the area, m; Δz_k is the z-direction for half of the cell (i,j,k) ; $R_{i,j,k+1/2}$ is an optional additional thermal resistance at the interface between the two cells (i,j,k) and $(i,j,k+1)$, (m²·K/W).

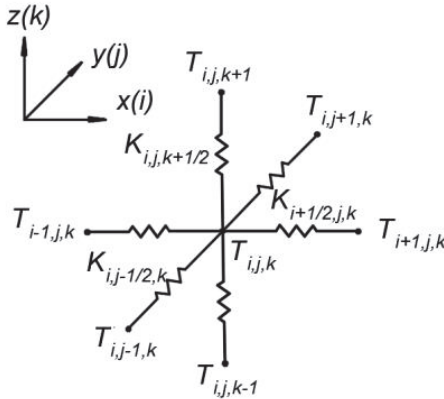


Figure 7. Thermal conductance connected to cell (i, j, k) [38].

The thermal resistance in the z-direction for half of the cell (i,j,k) is the first term in the denominator, and the resistance for half of the cell $(i,j,k+1)$ is the second term. $R_{i,j,k+1/2}$ is an optional extra thermal resistance at the interface between the two cells (i,j,k) and $(i,j,k+1)$.

Equation (4) is valid for all internal cells (an internal cell has at least one cell on each side). For boundary cells, the Equation (4) was modified in the following way. Consider cell $(1,j,k)$, which lies at a boundary. The conductance that couples the temperature $T_{1,j,k}$ with a boundary temperature is as shown in Equation (5):

$$K_{\frac{1}{2},j,k} = \frac{\Delta y_j \cdot \Delta z_k}{\frac{\Delta x_1}{(2 \cdot \lambda_{1,j,k})} + R_{\frac{1}{2},j,k}} \quad (5)$$

where $R_{1/2,j,k}$ is the boundary surface resistance, (m²·K/W).

An energy balance is made for each cell. The total heat flow to cell (i, j, k) from the six adjacent cells is put in the variable $H_{i,j,k}$, (W) (Equation (6)):

$$H_{i,j,k} = K_{i-\frac{1}{2},j,k} \cdot (T_{i-1,j,k} - T_{i,j,k}) + K_{i+\frac{1}{2},j,k} \cdot (T_{i+1,j,k} - T_{i,j,k}) + K_{i,j-\frac{1}{2},k} \cdot (T_{i,j-1,k} - T_{i,j,k}) + K_{i,j+\frac{1}{2},k} \cdot (T_{i,j+1,k} - T_{i,j,k}) + K_{i,j,k-\frac{1}{2}} \cdot (T_{i,j,k-1} - T_{i,j,k}) + K_{i,j,k+\frac{1}{2}} \cdot (T_{i,j,k+1} - T_{i,j,k}) \quad (6)$$

For a more quantitative comparison later, the average point thermal transmittance $\bar{\chi}$, $W/(m \cdot K)$, was calculating using Equation (7):

$$\bar{\chi} = \frac{\int_a^b \chi \, dl}{b - a} \quad (7)$$

where a —starting position; b —end position; χ —point thermal transmittance as a function of length from the masonry layer. In practice, the latter is determined by fitting a function over the graph.

At this stage of the calculation, two cases of window frame installation in SWB were analyzed (Figure 5):

1. A part of the wall 1 m high and with three fasteners: corner fastener CL, interconnect fastener EL, and window fastener W (Figure 4). The values χ_{CL} , χ_{EL} , χ_{W4} were determined;
2. A part of the wall 1 m high and with two corner fasteners CL and two window fasteners W (Figure 4). The values χ_{2xCL} , χ_{2xW} were determined.

The supplement $\Delta\Psi$ to the value of the LTB was evaluated in two ways:

The supplement of the total linear thermal bridge $\Delta\Psi_S$ of the separate fasteners was calculated according to Equation (8):

$$\Delta\Psi_S = (n \cdot \chi)_i + ((n \cdot \chi)_j) + \dots + (n \cdot \chi)_m \quad (8)$$

where n —average number of fasteners per meter of opening; i, j, \dots, m —different types of metal fasteners.

The supplement $\Delta\Psi_C$ of the LTB was calculated comprehensively for all fasteners used in the calculation. These results were provided by the HEAT3 computer program.

Thus, the total Ψ_T of the thermal bridges using SWB and metal fasteners was calculated from Equation (9):

$$\Psi_T = \Psi_{SWB} + \Delta\Psi \quad (9)$$

An analysis was also performed showing how the values of thermal bridges were distributed by changing the installation place of the window in the thermal insulation layer. Changing the place of the window installation was evaluated in the calculation. A value of 0 mm means that the window is mounted next to the edge of the load-bearing layer, and a value of 150 mm means that the window is installed right outside the wall (thermal insulation layer). Therefore, 75 mm denotes the middle of the thermal insulation layer (Figure 8). The values of the longitudinal thermal bridge in the thermal insulation layer were calculated starting from a value of 0 by adding 10 mm towards the outer side of the barrier, i , from $0 + 10_i + 10_j \dots + 10_n = 150$ mm.

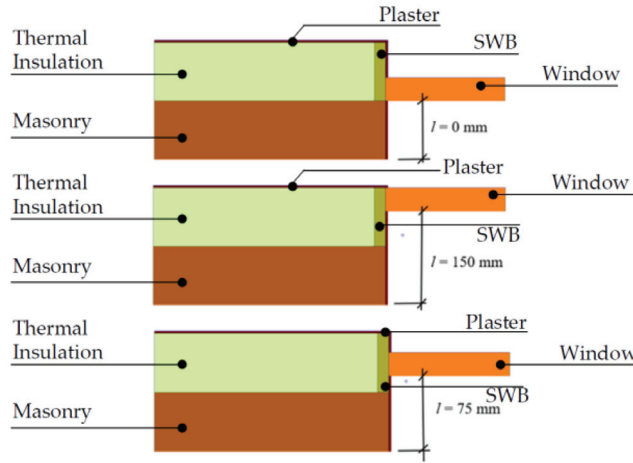


Figure 8. Schema of basic positions of the window frame in the section of the thermal insulation layer using SWB.

3. Results

3.1. Linear Thermal Bridges at Window Openings without Considering the Influence of Metal Fasteners

The results of the study show that the thermal bridge through the standard installation site (old building, without insulating the window frame with SWB) gives a transmittance of $\Psi_{ST} = 0.13 \text{ W}/(\text{m}\cdot\text{K})$, while using SWB for window framework insulation, the value of the thermal bridge transmittance is $\Psi_{SWB} = 0.026 \text{ W}/(\text{m}\cdot\text{K})$. The difference between these values is 80%.

By analyzing the dependence of the LTB on the window installation length in the thermal insulation material, the obtained results show (Figure 9) that the lowest value Ψ_{SWB} is obtained when the window-mounted place is at a distance of 70–80 mm from the load-bearing layer. The thermal transmittance average slowly increases, moving along the thermal insulation layer to the edge of the load-bearing layer.

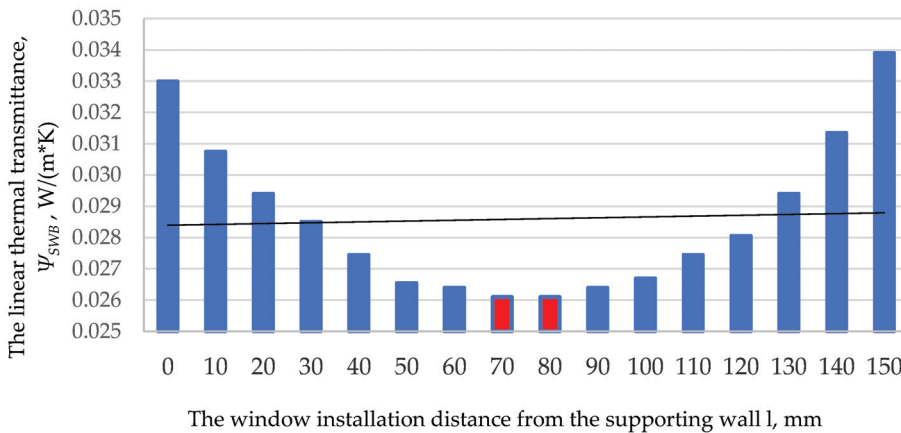


Figure 9. Dependence of the value of thermal transmittance on the installation length in SWB from the place of window to the load-bearing layer.

3.2. Thermal Bridges by Assessing the Influence of Metal Fasteners

3.2.1. Point Thermal Bridges

A computer simulation was performed to evaluate the influence of metal fasteners on the heat loss of the building. The results (Figure 10) show that $\chi_{CL} = 0.0114 \text{ W}/(\text{m}\cdot\text{K})$; $\chi_{EL} = 0.0225 \text{ W}/(\text{m}\cdot\text{K})$ and $\chi_{W} = 0.0181 \text{ W}/(\text{m}\cdot\text{K})$ when the mounting place of the window is 100 mm from the supported wall.

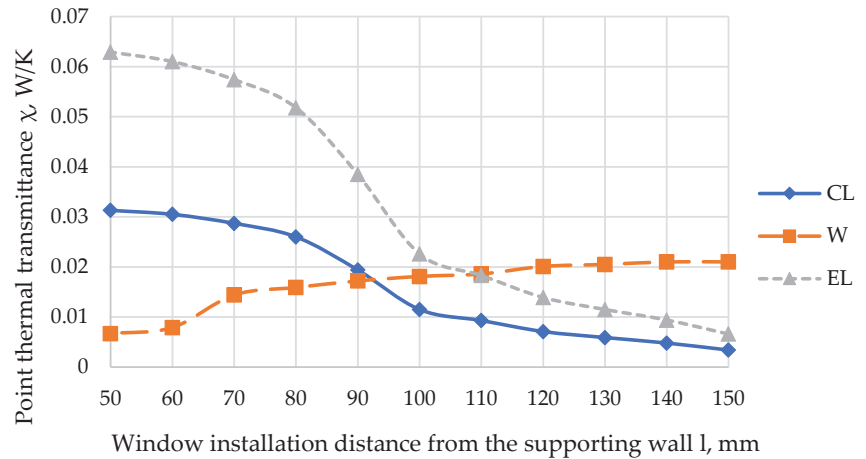


Figure 10. Dependence of the values of PTB on the window installation distance from the load-bearing layer edge for individual window mounting elements CL, EL, W.

By assessing how the values of the χ_{CL} , χ_{EL} , χ_{W48} depend on the distance between the window installation and the edge of the load-bearing layer wall for separate window mounting elements CL, EL, W, the research results (Figure 10) show that using corner fastener CL and interconnect fastener EL, the PTB is the highest at a distance of 50–100 mm from the load-bearing layer ($\chi_{CL} = 0.0313 \text{ W}/(\text{m}\cdot\text{K})$ and $\chi_{EL} = 0.0629 \text{ W}/(\text{m}\cdot\text{K})$). Meanwhile, the lowest values are obtained when $l = 150 \text{ mm}$ ($\chi_{CL} = 0.0034 \text{ W}/(\text{m}\cdot\text{K})$ and $\chi_{EL} = 0.00606 \text{ W}/(\text{m}\cdot\text{K})$). However, analyzing the PTB of fastener W, the results are the opposite. As the length l (length between the installed window framework and the load-bearing layer) decreases, the value of the PTB decreases, with a maximum value $\chi_W = 0.021 \text{ W}/(\text{m}\cdot\text{K})$ and minimum $\chi_W = 0.0067 \text{ W}/(\text{m}\cdot\text{K})$ at $l = 150 \text{ mm}$ and $l = 50 \text{ mm}$, respectively.

In addition, the average value of χ was calculated for each fastener. The results were $\chi_W = 0.0168 \text{ W}/(\text{m}\cdot\text{K})$, $\chi_{CL} = 0.0161 \text{ W}/(\text{m}\cdot\text{K})$ and $\chi_{EL} = 0.0319 \text{ W}/(\text{m}\cdot\text{K})$. Thus, on average, the interconnect fastener EL has twice the thermal transmittance as the corner fastener CL.

3.2.2. The Supplement of the Linear Thermal Bridges

The calculation of LTB's supplement was performed in two ways: 1 case summing the χ of separate fasteners (Figure 11b,c) (in this case, the value of LTB's supplement was found to be $\Delta\Psi_{s1} = 0.0521 \text{ W}/(\text{K}\cdot\text{m})$), and 2 case HEAT3 software provided the value of all three investigated fasteners in combination (Figure 11a). The described value of LTB's supplement was determined for separate fasteners (the 1 case in Figure 5). In this case, LTB's supplement's value was lower, and was equal to $\Delta\Psi_{c1} = 0.0515 \text{ W}/(\text{K}\cdot\text{m})$.

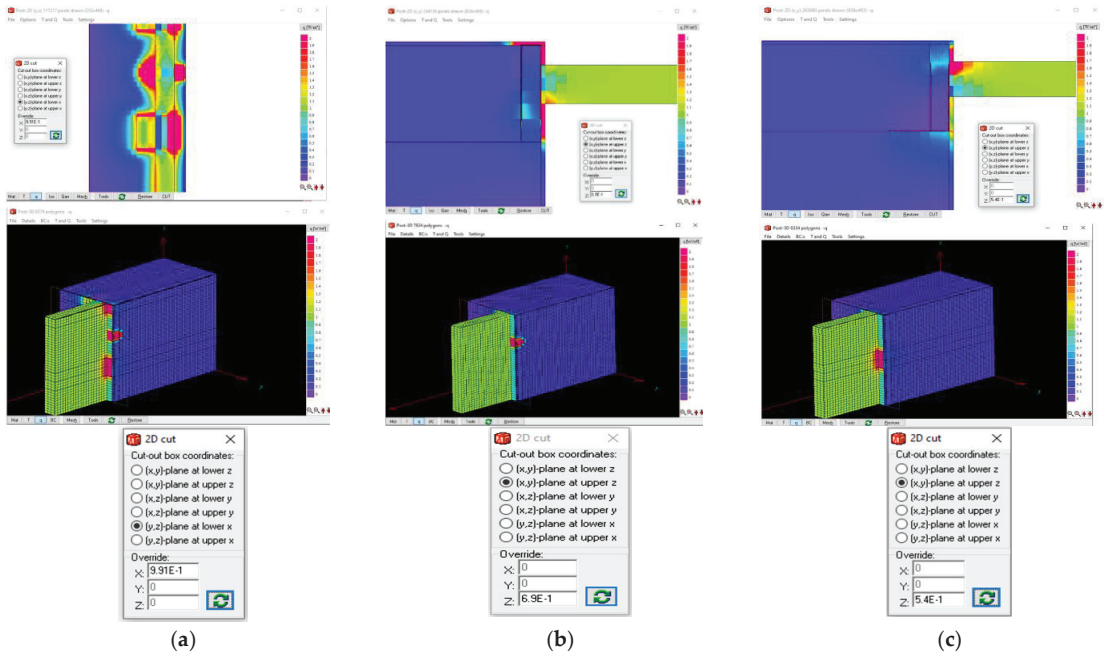


Figure 11. Intensity of heat flows in the cross-section of fasteners: (a) set of fasteners: corner fastener CL, interconnect fastener EL, and window frame fastener W; (b) separate W fastener; (c) separate EL fastener.

Analyzing the 2 case (Figure 5), involving an opening edge 1 m long with $2 \times CL$ and $2 \times W$, it was found that when evaluating the influence of four metal elements in a combination (calculation option 2), supplement heat loss through this element was $\Delta\psi_{c2} = 0.0591 \text{ W}/(\text{K}\cdot\text{m})$. After summing (calculation option 1) the point thermal bridges of separate fasteners ($2 \times CL$ and $2 \times W$), the supplement of the linear thermal bridges was $\Delta\psi_{s2} = 0.0592 \text{ W}/(\text{K}\cdot\text{m})$.

3.2.3. Total Linear Thermal Bridge

The results reveal that the sum of the separate fasteners' total linear thermal transmittance value is $\psi_{TS1} = 0.0781 \text{ W}/(\text{K}\cdot\text{m})$. A similar result $\psi_{TC1} = 0.0775 \text{ W}/(\text{K}\cdot\text{m})$ was obtained using the HEAT3 software, where the influence of the combination of metal fasteners was assessed.

In the case using $2 \times CL$ and $2 \times W$, the total thermal transmittance was found to be $\psi_{TS2} = 0.0852 \text{ W}/(\text{K}\cdot\text{m})$ (considering metal fasteners separately) and $\psi_{TC2} = 0.0852 \text{ W}/(\text{K}\cdot\text{m})$ (assessing the influence of the combined metal fasteners).

3.3. Comparison of the Values of Thermal Bridges Analyzed by Different Calculation Methods

A comparison of the values of all LTB analyzed in this study is presented in Figure 12. The study results show that the thermal bridge through the standard installation site (old building, without insulating the window frame with SWB) gives a transmittance of $\psi_{ST} = 0.13 \text{ W}/(\text{m}\cdot\text{K})$. Meanwhile, using SWB for window framework insulation, the value of the thermal bridge transmittance is $\psi_{SWB} = 0.026 \text{ W}/(\text{m}\cdot\text{K})$. The difference between these values is 80%. However, after estimating the metal fasteners, the difference is 37%.

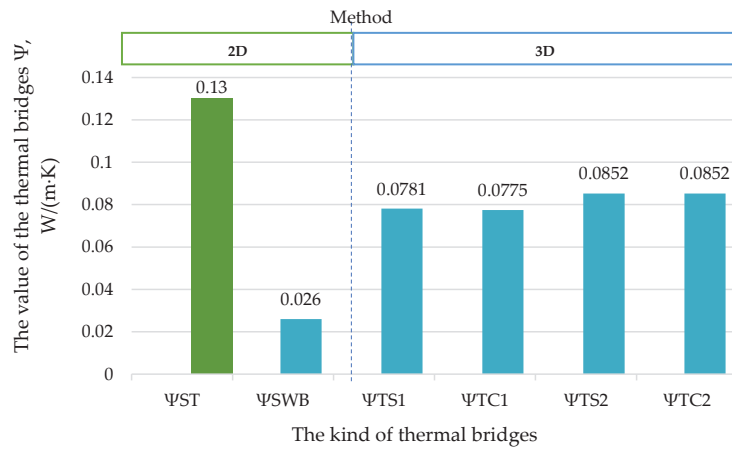


Figure 12. Comparison of the values of thermal bridges analyzed using different calculation methods.

If we compare the calculation results according to different methodologies, it can be seen that when the window is mounted into the load-bearing layer ($l = 0$ mm), the results of the total thermal bridge ($\Psi_{TS1} = 0.0781$ W/(m·K); $\Psi_{TS2} = 0.0852$ W/(m·K)) are almost the same (difference 0.8% and 0%) as those for the complex thermal bridge ($\Psi_{TC1} = 0.0775$ W/(m·K); $\Psi_{TC2} = 0.0852$ W/(m·K)); therefore, the calculation results according EN ISO 10211: 2008 [9] differ fractionally from the results provided by the HEAT3 program.

However, when assessing changes in the mounting place of the window in the thermal insulation layer, a discrepancy appears between the results of the different methodologies used. In this study, the distribution of the value of Ψ_T was analyzed by changing the window installation location in the thermal insulation layer and using different calculation methods to determine the supplement thermal bridge values: complex $\Delta\Psi_C$ (calculation option (2)) and summed $\Delta\Psi_S$ (calculation option (1)). The results (Figure 13) reveal that the summing values of the supplement thermal bridge ($\Delta\Psi_{S2}$) of $2 \times CL$ and $2 \times W$ may vary from 26.2% to 40.9% compared to the complex values $\Delta\Psi_{C2}$ used in the same calculations performed by the HEAT3 program. The thermal bridge values depend on the mounting location in the opening in terms of distance from the load-bearing layer. The trends indicate that the further away from the load-bearing layer, the bigger the difference between the thermal bridge values determined by different methods.

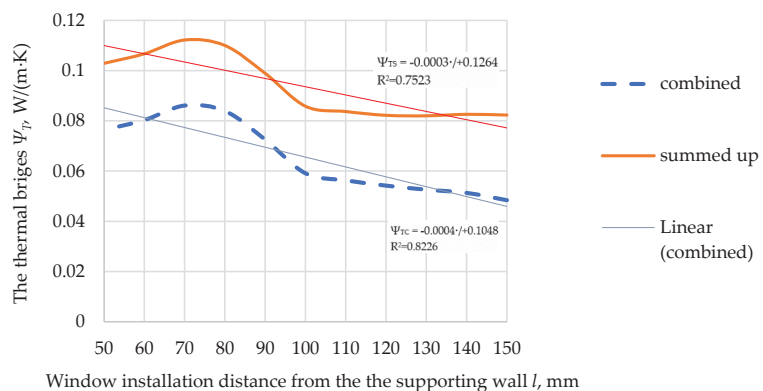


Figure 13. Dependence of the Ψ_T value of the thermal bridge on the distance of the window installation from the load-bearing layer edge and calculation method.

The results (Figure 13) also show that in the calculations, applying the summing (calculation option (1)) of thermal bridge values ($\Delta\Psi_{S2}$) and the value of thermal bridges of the window mounted in the thermal insulation layer at a length of 50–100 mm from the load-bearing layer was 28% greater than the window mounted in the span of 100–150 mm. The highest value of the thermal bridge ($\Psi_{TS2} = 0.1122$, W/(m·K)) was at a length of 70 mm from the load-bearing layer, and the lowest value of Ψ_{TS2} (0.0820, W/(m·K)) was at a length of 130 mm from the load-bearing layer.

The results (Figure 13) show that by applying $\Delta\Psi_{C2}$ (calculation option (2)) and mounting the window at a length of 50–100 mm from the load-bearing layer, the values of thermal bridges increased by 30% compared to the values of thermal bridges at a distance of 100–150 mm from the load-bearing layer. The highest value of the thermal bridge ($\Psi_{TC2} = 0.0861$, W/(m·K)) was at 70 mm from the load-bearing layer, and the lowest value of Ψ_{TC2} (0.0484, W/(m·K)) was at a length of 150 mm from the load-bearing layer.

4. Discussion

To meet the EU's goals of creating a sustainable, competitive, secure, and decarbonized energy system by 2050, the EU is stepping up the renovation process to turn old buildings into NZEB. Following Directive (EU) 2018/844 [3], the renovation of old buildings will mainly focus on renewable sources. However, important issues remain, namely, the insulation of the building envelope, the modernization of HVAC, and similar [22,39,40]. This work focused on the subtleties of installing new high-performance windows, which will ensure high energy efficiency, sufficient air thickness, and a comfortable indoor microclimate. Several assumptions have been made in analyzing this problem, such as that installing a window in a thermal insulation layer results in a zero thermal bridge or those metal fasteners have a negligible effect on thermal transmittance. However, the investigation has shown that these two assumptions were incorrect. A certain value of the thermal bridge of the opening edge is usually obtained due to the difference in the thickness of the window and wall structures and the different materials used at the window installation site.

The authors of this study analyzed the installation of windows using SWB. The study results revealed that the insulation of the window frame was a very important issue related to the energy consumption of the building. By insulating the window frame with SWB, it was possible to reduce the value of the thermal bridge at the junction of the wall and the window framework by 80% (but not 100%). Meanwhile, other researchers who have examined the issue of the thermal bridge of the window opening have stated that for some cases, placing the window in the most energy-efficient position reduces the linear thermal transmittance by more than 50% [41].

This excellent 80% result due to the heat saving of the building is given by the 2-D calculation method when neglecting the fasteners used in the installation scheme that are used for fastening a special thermal insulation board to the masonry and the window. It is always an important question what influence the attachment of metal elements (various bolts, etc.) to the load-bearing structure and each other has on the evaluation of thermal bridges. The study showed that using SWB and considering the metal reinforcement details reduces the value of the thermal bridge by up to 37% compared to the standard without the insulation option. In this case, the metal elements closer to the warm and cold partition sides do not come into contact, so there is no continuous heat flow through the metal elements.

The maximum value of χ was achieved for the fastener W. In practice, the middle fastener W, which is used to join the insulation boards, may be missing if the window is not large, because the length of the insulation boards is 1500 mm. Therefore, if the window dimension is less than 1400 mm, no joining of the panels will be required, which means that the parts will need W either. Therefore, the total value of the thermal bridge will change significantly.

Analysis of the different calculation methods revealed a 0.8% difference between 2-D (calculation according to EN ISO 10211: 2017) and 3-D (numerical simulation with HEAT3).

Comparing calculation options of the composite (2) and summing (1) models of evaluation of the thermal bridge with the fasteners 2xCL and 2xW at a length of 1 m, the opening edge showed no difference between the results. However, the study results showed that different calculation methodologies could significantly skew the results if the length from the load-bearing layer assesses. As the window mount further away from the load-bearing layer, the thermal bridge values difference due to using the different methods is bigger. Calculating the total thermal bridge regarding summing model of separate fasteners ($\Delta\Psi_{S2}$) might change the results by 26% to 41% compared to the same calculations using composite model ($\Delta\Psi_{C2}$), calculated by the HEAT3 program. The above-mentioned appears because the heat flows of these fasteners interact with each other, even though a large thermal insulation layer allocates these fasteners. Therefore, it would be appropriate to evaluate the PTB of each fastener separately. It would also be easy to estimate the additional heat loss through the opening edge of any particular window by having PTB for the individual elements and a mounting scheme for any window. However, it is very difficult to assess these small fasteners properly, as they can vary greatly in dimensions (length, cross-section), numbers (depending on loads, base, technological requirements) and the materials to which they are attached (different bases). Therefore, the calculations may differ from case to case.

3-D thermal numerical simulation is required to estimate the influence of metal fasteners on heat loss accurately. This study shows that evaluating the composite model of these fasteners (using HEAT3) results in a lower additional heat flux compared to the total heat fluxes of the summing of separate fasteners. However, to properly assess the influence of metal fasteners, the composite thermal bridge model should be calculated using the 3-D calculation method for each window according to a separate installation scheme. For designers, such a calculation method would become a serious challenge because, without special software, it is impossible to do so. Therefore, in the frequent case of assessing the energy performance of a building, the second assumption is made not to evaluate metal fasteners and to limit oneself to the 2-D calculation method.

The authors compared the obtained values of the thermal bridge by using the 2-D and 3-D calculation methods, and the calculation results using a 2-D environment showed that $\Psi_{SWB} = 0.026 \text{ W}/(\text{m}\cdot\text{K})$, while in the 3-D environment, this value was accordingly, $\Psi_T = 0.0815 \text{ W}/(\text{m}\cdot\text{K})$. The difference was 68%. From the results of this study, one can conclude that by ignoring PTB and using metal elements for window mounting, a significant difference can be obtained between the calculated (2-D method) and the expected real heat loss (3-D method). This fact is confirmed by other scientists [42].

Additionally, comparing 2-D and 3-D calculation methodologies, the arrangement of thermal bridge values by length l took the opposite trend (Figure 7). In the 2-D temperature field, the thermal bridge values were lowest when the window was installed in a layer of thermal insulation material at a distance of 70–80 mm from the load-bearing layer $\Psi_{SWB} \approx 0.026 \text{ W}/(\text{K}\cdot\text{m})$. The results presented in Figure 9 show that with increasing length l , the value of the thermal bridge also increased. Similar results have been obtained by other researchers [11,17,43]. Ilomets et al. [44] state that insulating the walls of an existing building with a > 200-mm-thick layer of thermal insulation increases the value of the thermal bridge at the window opening by 34%. The authors mentioned above investigated cases where metal parts were fixed directly to the load-bearing layer or brackets. Meanwhile, the values of thermal bridges calculated by the 3-D method were distributed with the opposite trend: as the length l increased, the thermal bridge values decreased. This can be explained by the fact that when using SWB, metal fasteners do not cross the layer of thermal insulation material directly and do not come into contact with each other—they do not act as direct heat conductors. Therefore, it is risky to evaluate thermal bridges only using the 2-D methodology when designing energy-efficient buildings.

In addition, looking at the results shown in Figure 14, an interpolation of the curves can be performed to deduce the crossing point of both graphs. In this case, both curves cross at around 180 mm with $0.0408 \text{ W}/(\text{K}\cdot\text{m})$. It follows that there is no difference between

2-D and 3-D methodologies around that point. Thus, metal fasteners do not affect the window's overall thermal performance.

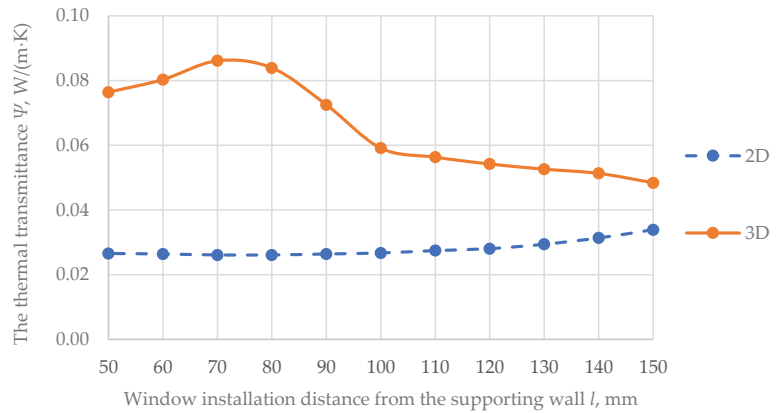


Figure 14. Trends in the values of thermal bridges due to the change of the installation location in the layer of thermal insulation material, applying different calculation methodologies.

The linear thermal transmittance of the NZEB must be a maximum of $0.05 \text{ W}/(\text{K}\cdot\text{m})$ according to the Lithuanian national document STR 2.01.02: 2016 [20]. The results (Figure 15) show that if thermal bridges are evaluated using the 2-D method, i.e., without considering metal fasteners, then the solution for window mounting using SWB always complies with the requirements of STR. If one considers metal fasteners, the window must be installed no closer than 100 mm from the retaining wall for the value of the thermal bridge at the window opening to meet the requirements of STR (Figure 15). The study results show that the installation position of the window in the layer of thermal insulation material is a very important issue. The results show that in NZEB buildings where the wall insulation layer is greater than 200 mm, the windows need to be mounted using SWB. This installation method ensures the lowest thermal bridges and sufficient static loads by extending the window frame into the thermal insulation layer at a length of more than 100 mm from the retaining wall. The farther from the retaining wall, the smaller the thermal bridge. It has been mentioned earlier that other methods of installing windows show the opposite results, which makes it difficult to ensure the status of an NZEB when using such mounting methods.

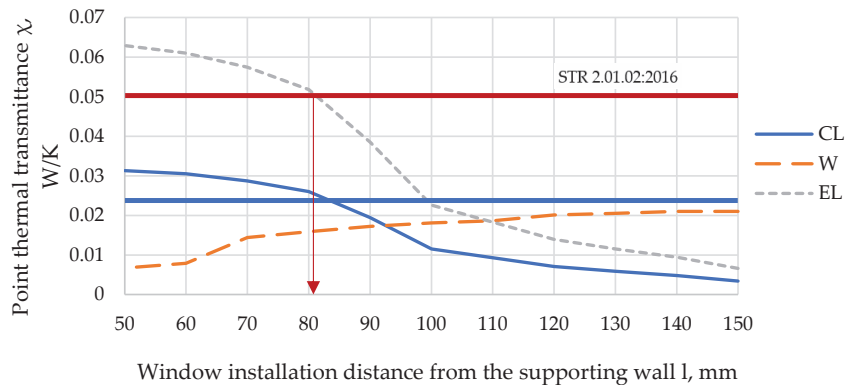


Figure 15. Compliance of the linear thermal transmittance of the investigated metal fasteners with the normative requirements.

This study focused on only one method of window installation using SWB. This preliminary study has given rise to a focus on ever-improving design solutions. This construction progress is influenced by energy policy, forcing us to rethink whether we are evaluating the energy efficiency of buildings or whether the standardized values for thermal bridges in the atlases are inappropriate. Therefore, from a prospective point of view, it would be possible to investigate other window installation types proposed in several atlases or in passive houses, thus providing solutions with extremely low thermal bridging effects.

5. Conclusions

This work is another small step towards improving the assessment of the energy performance of a building. Examining the method of installing a new high-performance window in a thermal insulation layer is important for highlighting the effect of installing a window on the wall of a building. Given that windows are the most thermally conductive elements in a building, this paper guides both the scientific community and practitioners on trends in thermal bridges that are completely changing using different assessment methods.

Comparing the values obtained by using 2-D and 3-D thermal bridge calculation methods, the values show a difference of 68%. The investigation showed that by insulating the window frame with SWB and not evaluating the metal fasteners, we can reduce the value of the thermal bridge at the junction of the wall and the window frame by 80%. However, the evaluation of metal fasteners reduces the thermal bridge value by up to 37% compared to the standard option without insulation.

Furthermore, comparing the results of 2-D and 3-D calculation methodologies, the arrangement of the thermal bridge values according to the length l from the load-bearing layer took the opposite trend. Therefore, it is risky to evaluate thermal bridges only with the 2-D methodology when designing energy-efficient buildings.

Author Contributions: Conceptualization, J.Š., J.R., D.A.K., E.K. and P.A.F.; methodology, J.Š., J.R., D.A.K. and P.A.F.; software, J.Š., J.R., D.A.K. and P.A.F.; validation, J.Š., J.R., D.A.K., E.K. and P.A.F.; formal analysis, J.Š., J.R., D.A.K., E.K. and P.A.F.; investigation, J.Š., J.R., D.A.K. and P.A.F.; resources, J.Š., J.R., D.A.K., E.K. and P.A.F.; data curation, J.Š., J.R., D.A.K., E.K. and P.A.F.; writing—original draft preparation, J.Š., J.R., D.A.K.; writing—review and editing, J.Š., J.R., D.A.K., E.K. and P.A.F.; visualization, J.Š., J.R., D.A.K. and E.K.; supervision, J.Š., J.R., D.A.K. and P.A.F.; funding acquisition, D.A.K. All authors have read and agreed to the published version of the manuscript.

Funding: This research was funded by Poland Ministry of Science and Higher Education, grant number WZ/WB-IIŚ/7/2022.

Acknowledgments: This research was supported by the Basic Science Research Program through the Kaunas Technology University (KTU) and it was carried out as part of a Bialystok University of Technology grant and financed by a research subsidy provided by the minister responsible for science WZ/WB-IIŚ/7/2022. It is a part of Memorandum of Understanding for scientific cooperation between Bialystok University of Technology and Kaunas University of Technology for the years 2021–2026.

Conflicts of Interest: The authors declare no conflict of interest.

References

1. National Energy and Climate Plans (NECPs). European Commission. Available online: https://ec.europa.eu/energy/topics/energy-strategy/national-energy-climate-plans_en (accessed on 27 July 2021).
2. Building Performance Institute Europe (BPIE). *Renovation Strategies of Selected EU Countries. A Status Report on Compliance with Article 4 of the Energy Efficiency Directive*; BPIE: Brussels, Belgium, 2014. Available online: [Renovation-Strategies-EU-BPIE-2014.pdf](#) (accessed on 1 March 2022).
3. EN. Directive (EU) 2018/844 of the European Parliament and of the Council of 30 May 2018 amending Directive 2010/31/EU on the energy performance of buildings and Directive 2012/27/EU on energy efficiency; the European Parliament and the Council of the European Union. *Off. J. Eur. Union* **2018**, *35*, L156–L175.
4. Building Performance Institute Europe (BPIE). *Future-Proof Buildings for All Europeans*; BPIE: Brussels, Belgium, 2019. Available online: <https://globalabc.org/resources/publications/bpie-future-proof-buildings-all-europeans> (accessed on 1 March 2022).

5. COM/2020/562 Final. Investing in a Climate-Neutral Future for the Benefit of Our People. Communication from the Commission to the European Parliament, the Council, the European Economic and Social Committee and the Committee of the Regions. Stepping up Europe's 2030 Climate Ambition Brussels. Available online: <https://eur-lex.europa.eu/legal-content/EN/TXT/?uri=CELEX%3A52020DC0562> (accessed on 1 March 2022).
6. Renovation Wave | Energy. Available online: https://ec.europa.eu/energy/topics/energy-efficiency/energy-efficient-buildings/renovation-wave_en (accessed on 1 March 2022).
7. Bergero, S.; Cavalletti, P.; Chiari, A. Energy refurbishment in existing buildings: Thermal bridge correction according to DM 26/06/2015 limit values. *Energy Procedia* **2017**, *140*, 127–140. [[CrossRef](#)]
8. O'Grady, M.; Lechowska, A.A.; Harte, A.M. Application of infrared thermography technique to the thermal assessment of multiple thermal bridges and windows. *Energy Build.* **2018**, *168*, 347–362. [[CrossRef](#)]
9. ISO. *EN ISO 10211:2017*; Thermal Bridges in Building Construction—Heat Flows and Surface Temperatures—Detailed Calculations. CEN Committee ISO/TC 163/SC; International Organization for Standardization: Geneva, Switzerland, 2017.
10. Theodosiou, T.; Tsikaloudaki, K.; Bikas, D.; Aravantinos, D.; Kontoleon, K.N. Assessing the use of simplified and analytical methods for approaching thermal bridges with regard to their impact on the thermal performance of the building envelope. In Proceedings of the World SB 14 Conference on the Sustainable Building: Result, Barcelona, Spain, 28–30 October 2014. Available online: http://wsb14barcelona.org/programme/pdf_poster/P-059.pdf (accessed on 1 March 2022).
11. Theodosiou, T.G.; Papadopoulos, A.M. The impact of thermal bridges on the energy demand of buildings with double brick wall constructions. *Energy Build.* **2008**, *40*, 2083–2089. [[CrossRef](#)]
12. Citterio, M.; Cocco, M.; Erhorn-Klutting, H. Thermal bridges in the EPBD context: Overview on MS approaches in regulations. In *ASIEPI Information Paper*. 2008. Available online: https://www.buildup.eu/sites/default/files/P064_EN_ASIEPI_WP4_IP1_p3073.pdf (accessed on 1 March 2022).
13. Evola, G.; Margani, G.; Marletta, L. Energy and cost evaluation of thermal bridge correction in Mediterranean climate. *Energy Build.* **2011**, *43*, 2385–2393. [[CrossRef](#)]
14. Martin, K.; Escudero, C.; Erkoreka, A.; Flores, I.; Sala, J.M. Equivalent wall method for dynamic characterization of thermal bridges. *Energy Build.* **2012**, *55*, 704–714. [[CrossRef](#)]
15. Gao, Y.; Roux, J.J.; Zhao, L.H.; Jiang, Y. Dynamical building simulation: A low order model for thermal bridges losses. *Energy Build.* **2008**, *40*, 2236–2243. [[CrossRef](#)]
16. Tadeu, A.; Simoes, I.; Simoes, N.; Prata, J. Simulation of dynamic liner thermal bridges using a boundary element method model in the frequency domain. *Energy Build.* **2011**, *43*, 3685–3695. [[CrossRef](#)]
17. Berggren, B.; Wall, M. Calculation of thermal bridges in (Nordic) building envelopes—Risk of performance failure due to inconsistent use of methodology. *Energy Build.* **2013**, *65*, 331–339. [[CrossRef](#)]
18. Ascione, F.; Bianco, N.; de Rossi, F.; Turni, G.; Vanoli, G.P. Different methods for the modeling of thermal bridges into energy simulation programs: Comparisons of accuracy for flat heterogeneous roofs in Italian climates. *Appl. Energy* **2012**, *97*, 405–418. [[CrossRef](#)]
19. Capozzoli, A.; Gorrino, A.; Corrado, V. A building thermal bridges sensitivity analysis. *Appl. Energy* **2013**, *107*, 229–243. [[CrossRef](#)]
20. Construction Technical Regulation STR 2.01.02: 2016; *Design and Certification of Energy Performance of Buildings*; Ministry of Environment: Vilnius, Lithuania, 2020.
21. Cerneckiene, J.; Zdankus, T.; Valancius, R.; Fokaides, P.A. Numerical Investigation of the impact of longitudinal thermal bridging on energy efficient buildings under humid continental climate conditions: The Case of Lithuania. In *IOP Conference Series: Earth and Environmental Science*; IOP Publishing: Bristol, UK, 2020; Volume 410, p. 012105.
22. Fokaides, P.A.; Apanaviciene, R.; Cerneckiene, J.; Jurelionis, A.; Klumbyte, E.; Kriauciunaite-Neklejonoviene, V.; Pupeikis, D.; Rekus, D.; Sadauskiene, J.; Seduikyte, L.; et al. Research Challenges and Advancements in the field of Sustainable Energy Technologies in the Built Environment. *Sustainability* **2020**, *12*, 8417. [[CrossRef](#)]
23. De Angelis, E.; Serra, E. Light steel-frame walls: Thermal insulation performances and thermal bridges. *Energy Procedia* **2014**, *45*, 362–371. [[CrossRef](#)]
24. Grudzińska, M.; Brzyski, P. The Occurrence of Thermal Bridges in Hemp-lime Construction Junctions. *Period. Polytech. Civ. Eng.* **2019**, *63*, 377–387. [[CrossRef](#)]
25. Udrea, I.; Popa, R.T.; Mladin, E.C.; Georgescu, M.S.; Ochinciu, C.V. Thermal bridges evaluation for a Passive House building in Romanian Southern climate. In Proceedings of the 2017 8th International Conference on Energy and Environment (CIEM), Bucharest, Romania, 19–20 October 2017; Proceedings Paper: International Conference on Energy and Environment. pp. 456–459.
26. Sadauskiene, J.; Ramanauskas, J.; Seduikyte, L.; Dauksys, M.; Vasylius, A. A simplified methodology for evaluating the impact of point thermal bridges on the high-energy performance of a passive house. *Sustainability* **2015**, *7*, 16687–16702. [[CrossRef](#)]
27. Rruumala. Available online: <https://www.ruumala.com/lt/metaliniai-ankeriai/ploksti-kronsteinai/> (accessed on 1 March 2022).
28. Lithuanian Passive House. Available online: <https://www.pasyvusnamas.lt/langu-montavimas-siltinimo-sluoksnyje/langu-dezes> (accessed on 1 March 2022).
29. Hallik, J.; Kalamees, T. A new method to estimate point thermal transmittance based on combined two-dimensional heat flow calculation. In Proceedings of the 12th Nordic Symposium on Building Physics (nsb 2020), E3SWeb of Conferences, Tallinn, Estonia, 6–9 September 2020; Volume 172, p. 08005. [[CrossRef](#)]

30. Tsukamoto, Y.; Tomikawa, Y.; Sakagami, K.; Okuzono, T.; Maikawa, H.; Komoto, Y. Experimental assessment of sound insulation performance of a double window with porous absorbent materials its cavity perimeter. *Appl. Acoust.* **2020**, *165*, 107317. [CrossRef]
31. Tang, S.K. A review on natural ventilation-enabling façade noise control devices for congested high-rise cities. *Appl. Sci.* **2017**, *7*, 175. [CrossRef]
32. Huang, H.; Qiu, X.; Kang, J. Active noise attenuation in ventilation windows. *J. Acoust. Soc. Am.* **2011**, *130*, 176–188. [CrossRef]
33. Rockwool. Available online: <https://docplayer.me/3412936-Redair-tm-link-monteringsanvisning.html> (accessed on 1 March 2022).
34. ISO. *EN ISO 14683:2017*; Thermal Bridges in Building Construction—Linear Thermal Transmittance—Simplified Methods and Default Values. International Organization for Standardization: Geneva, Switzerland, 2017.
35. Terentjevas, J.; Šadauskaitė, M.; Šadauskienė, J.; Ramanauskas, J.; Buska, A.; Fokaides, P.A. Numerical investigation of buildings point thermal bridges observed on window-thermal insulation interface. *Case Stud. Constr. Mater.* **2021**, *15*, e00768. [CrossRef]
36. Lawrence Berkeley National Laboratory (LBNL). THERM—Two-Dimensional Building Heat-Transfer Modeling. 2021. Available online: <https://windows.lbl.gov/software/therm> (accessed on 1 March 2022).
37. Blocon, A.B. HEAT3—Heat Transfer in Three Dimensions. 2021. Available online: <https://buildingphysics.com/heat3--3/> (accessed on 1 March 2022).
38. Claesson, J. Dynamic thermal networks: A methodology to account for time-dependent heat conduction. In Proceedings of the 2nd International Conference on Research in Building Physics, Leuven, Belgium, 14–18 September 2003; pp. 407–415.
39. Krawczyk, D.A. Optimization of Energy Consumption while Maintaining Recommended Indoor Air Quality in a Lecture Hall- A case study. In Proceedings of the 16th International Conference on the Sustainable Energy Technologies, Bolonia, Italy, 17–20 July 2017.
40. Nait, N.; Bourbia, F.; Bauchahn, Y. Effect of thermal insulation on energy efficiency of the building envelope-semi dry climates. In Proceedings of the Advances on Sustainable Cities and Building Development, Sb-Lab 2017, Porto, Portugal, 15–17 November 2017.
41. Misiopceki, C.; Bouquin, M.; Gustavsen, A.; Jelle, B.P. Thermal Modeling and Investigation of the Most Energy-Efficient Window Position. *Energy Build.* **2018**, *158*, 1079–1086. [CrossRef]
42. Ascione, F.; Bianco, N.; De Masi, R.F.; Mauro, G.M.; Musto, M.; Vanoli, G.P. Experimental validation of a numerical code by thin film heat flux sensors for the resolution of thermal bridges in dynamic conditions. *Appl. Energy* **2014**, *124*, 213–222. [CrossRef]
43. Šadauskiene, J.; Ramanauskas, J.; Vasylius, A. Impact of point thermal bridges on thermal properties of building envelopes. *Therm. Sci.* **2020**, *24*, 2181–2188. [CrossRef]
44. Ilomets, S.; Kuusk, K.; Paap, L.; Arumagi, E.; Kalamees, T. Impact of linear thermal bridges on thermal transmittance of renovated apartment buildings. *J. Civ. Eng. Manag.* **2016**, *23*, 96–104. [CrossRef]

Article

Energy Consumption of Apartment Conversion into Passive Houses in Hot-Summer and Cold-Winter Regions of China

Yonghan Li ^{1,2}, Wei Yin ^{1,2,3,*}, Yawen Zhong ^{1,2}, Mingqiao Zhu ^{1,2}, Xiaoli Hao ^{1,2}, Yongcun Li ^{1,2}, Yuwen Ouyang ^{1,2} and Jie Han ⁴

¹ School of Civil Engineering, Hunan University of Science and Technology, Xiangtan 411201, China

² Hunan Engineering Research Center for Intelligently Prefabricated Passive House, Xiangtan 411201, China

³ College of Architecture, Hunan University, Changsha 410012, China

⁴ School of Architecture and Transportation Engineering, Guilin University of Electronic Technology, Guilin 541004, China

* Correspondence: yinwei@hnust.edu.cn

Abstract: Passive houses have strong thermal insulation and airtightness of doors and windows, and they are generally used in cold climates. This case study aims to evaluate the energy-saving potential of this technology in the hot-summer and cold-winter areas (Cf in Köppen climate classification) of China. The results show that after enhancing the thermal insulation and airtightness, the energy consumption in winter significantly decreased by 62% overall. However, the energy consumption of cooling in the transition season and summer increased, which is caused by overheating. Hybrid ventilative cooling and shading can solve this problem. In particular, when the indoor temperature range is set to the adaptive thermal comfort of natural ventilation, the energy consumption from air conditioner cooling can be greatly reduced by 81% overall. Passive houses combined with ventilative cooling has significant application value in this climate zone.

Keywords: building energy efficiency; passive house; apartment; ventilative cooling; sunshade

Citation: Li, Y.; Yin, W.; Zhong, Y.; Zhu, M.; Hao, X.; Li, Y.; Ouyang, Y.; Han, J. Energy Consumption of Apartment Conversion into Passive Houses in Hot-Summer and Cold-Winter Regions of China. *Buildings* **2023**, *13*, 168. <https://doi.org/10.3390/buildings13010168>

Academic Editor: Cristina Carpino

Received: 29 November 2022

Revised: 28 December 2022

Accepted: 4 January 2023

Published: 9 January 2023



Copyright: © 2023 by the authors. Licensee MDPI, Basel, Switzerland. This article is an open access article distributed under the terms and conditions of the Creative Commons Attribution (CC BY) license (<https://creativecommons.org/licenses/by/4.0/>).

1. Introduction

Global warming has become an issue for all humankind, and thus, efforts should be directed toward reducing the consumption of non-renewable energy. Among them, building energy efficiency is an important means to reduce carbon emissions [1]. The passive house concept started in Germany in 1988, which aims to reduce the energy consumption for heating and cooling and CO₂ emissions and provide a more comfortable indoor environment compared to the usual old building [2]. Technologies to achieve passive houses include enhancing the thermal insulation of the envelope, improving the airtightness of doors and windows, and recovering heat from ventilation to improve energy efficiency.

1.1. Energy Efficiency of Passive Houses

Jürgen et al. [3] compared the energy-saving effect of using passive house technology in Yekaterinburg, Tokyo, Shanghai, Las Vegas, Abu Dhabi and Singapore through a simulation method. The results show that passive houses have energy-saving potential in all climate zones throughout the world, using 75% to 95% less energy than conventional buildings. Fei et al. [4] conducted a three-year performance monitoring and evaluation of a passive house public building located in Qingdao, China (a seaside city in a cold region), and found that the annual energy efficiency was improved by approximately 69% compared to the current standard. Yang et al. [5] monitored the energy system of a new passive house school building in southern Germany for three years. The results show a two-thirds reduction in CO₂ emissions. Egon et al. [6] evaluated three buildings in southern Brazil, and their energy consumption decreased by 83.5%, 56.3% and 55.1%, while their thermal comfort satisfaction increased significantly.

1.2. Overheating

However, the overly high thermal insulation and airtightness of passive houses may produce overheating in the summer and transitional seasons. For example, Ridley et al. [7] carried out detailed monitoring of UK homes certified to passive house standards, which experienced overheating problems in the summer, especially in living rooms. The main reasons are higher internal gain, low sunshade and summer ventilation rate than expected. Rohdin et al. [8] presented the experience of newly built passive houses in Sweden and compared nine passive houses with traditional buildings in terms of the thermal environment and energy. It was also shown that there is a higher number of complaints related to high temperatures during summer in the passive houses. Its main concern is the lack of ventilation, and the indoor temperature is severely affected by internal gains from cooking and showering. Paris et al. [9] measured passive house performance in Cyprus, and there were some overheating problems in all zones during the summer period.

1.3. Ventilative Cooling and the Mixed-Mode Method

One of the methods for reducing overheating in passive houses is to use ventilation cooling, including natural ventilation or night ventilation [8,10]. Therefore, the switch between outdoor air cooling and air-conditioning cooling becomes a method named the mixed-mode.

The mixed-mode combines a ventilative system with an air-conditioning system to use as much outside air as possible to cool the building when the outside conditions are suitable for indoor air. When outdoor air cannot meet cooling needs, machinery should be used to lower indoor temperatures to maintain thermal comfort. Now there are a number of classification schemes that describe the mixed-mode. Usually based on whether they exist in the same space, or run at the same time, can be divided into three operation modes such as Concurrent (Same space, same time), Change-over (Same space, different times) and Zoned (Differed spaces, same time) [11]. Change-over operation mode is used in this paper.

Regarding the thermal comfort of the mixed-mode, Max et al. [12] pointed out that the traditional PMV-PPD theoretical model (the predicted mean vote and the predicted percentage of dissatisfied) cannot well describe the thermal comfort of the occupants in the mixed-mode building. Luo et al. [13] conducted a field investigation in mixed-mode building in subtropical climate. The results show that the adaptive model is more suitable for mixed-mode buildings than the steady-state comfort model (PMV), especially when natural ventilation was being utilized. Ricardo et al. [14] concluded that a wider range than PMV can be used during air conditioning operation in Brazilian temperate and humid climate, and that the adaptive model can be used in mixed-mode buildings when air conditioning is not operating. Many studies in different countries or climate zones have proposed different mixed-mode control methods and comfort models, which show good thermal comfort and energy saving effects. For example, Massimo et al. [15] (New South Wales, Australia), development of a new comfort-oriented control strategy for a mixed-mode building. The comfort-oriented controller was proved to be superior to the baseline controller in terms of maintaining comfort, as well as a reduction in building energy consumption. Elena et al. [16] (Southwest Spain) proposed an adaptive model for hybrid buildings, and the results show that it has energy saving potential without sacrificing the comfort of the occupants. Sherif et al. [17] (arid climates in four countries) evaluated the potential of a range of mixed-mode cooling systems and ventilation strategies. The results show that the mixed-mode of office buildings has great potential for energy saving, and should be able to provide a satisfactory indoor environment. Ricardo et al. [18] (southern Brazil) conducted field studies on thermal comfort and this was conducted in three mixed-mode office buildings, and adaptive thermal comfort models were developed for the natural ventilation and air conditioning mode of mixed-mode buildings. Daniel et al. [19] (south-west of Spain) applied the adaptive comfort algorithms to mixed-mode buildings.

The results show that energy demand is reduced by 74.6% and energy consumption is reduced by 59.7%.

For the control strategy of the mixed-mode, the opening and closing of windows and air conditioning are controlled according to indoor and outdoor air parameters, such as indoor and outdoor temperature, humidity, wind speed (Gwynne et al. [20]), outdoor pollutants (Chen et al. [21]), and indoor CO₂ (Katarina et al. [10]). Laia et al. [22], Hu and Karava [23], Peter et al. [24], and Zhao et al. [25] all demonstrated that model predictive control (MPC) based on future weather data and indoor factors is a more advanced control strategy.

1.4. Shading for Cooling

Another approach to building cooling is shading, which is influenced by equipment (e.g., Hussain et al. [26], Kim et al. [27]), user behaviour (e.g., Kevin [28], William et al. [29]), and control strategies (e.g., Line et al. [30], Amir et al. [31], Yun et al. [32]).

1.5. Goals and Framework of the Paper

In general, passive houses are suitable for cold climates due to the longer winter periods. In northern China, passive houses are suitable for cold climate regions and extremely cold climate regions. In central-south China, there is a climate region named the hot-summer and cold-winter area, in which the suitability of passive house technology is still unknown. Therefore, this paper first investigated the indoor environment of apartments in that area and then predicted its energy efficiency when transformed into a passive house. Finally, solutions to the existing problems are proposed.

2. Investigation in Apartments

2.1. Local Weather

As one of five China's architectural climate zones, the hot-summer and cold-winter region is located from latitude 25° to 35° north and longitude 103° to 123° east, fully or partially including 16 provinces with a population of approximately 500 million, as shown in Figure 1. In this zone, the average dry bulb temperature of the coldest month ranges from 0 to 10 °C, the average temperature of the hottest month is 25 to 30 °C, the number of days with average daily temperature ≤5 °C is 0 to 90 days, the number of days with average daily temperature ≥25 °C is 49 to 110 days, and the average relative humidity is 30% to 80% year-round. This region belongs to Cf in Köppen climate classification.

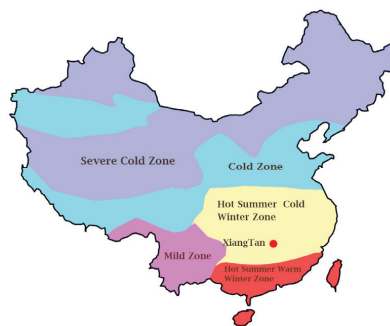


Figure 1. The location of the hot-summer and cold-winter climate zone and Xiangtan, from Bing Maps.

The location of the building is Xiangtan, which is located in the middle of the hot-summer and cold-winter area. It is located at latitude 27.83 and longitude 112.94, as shown by the red dot in Figure 1. Figure 2 shows the local dry-bulb temperature monthly in a typical meteorological year. The shaded boxes represent 25–75% of the temperature distribution, and the data are from the China Meteorological Database [33]. The horizontal

line is the median, and the small squares represent the monthly mean temperature. The average monthly outdoor temperature in winter (December to February) is approximately 5–7 °C, and the monthly average temperature in summer (June to September) is 20–28 °C. This results in the demand for heating in winter and cooling in summer.

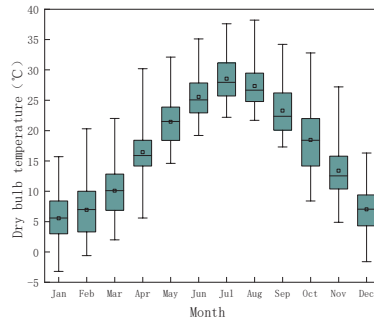
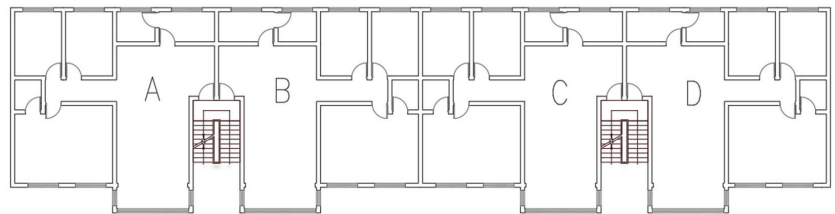


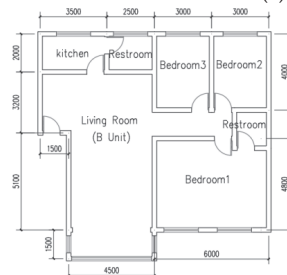
Figure 2. The monthly dry bulb temperature in Xiangtan.

2.2. Building Information

This building is an apartment built in 2005. Before the publication of the new code in 2010, about 60% apartment buildings in China have adopted a similar envelope structure and apartment type. It has a total of six floors, each floor has four households with two ladders, and the floor height is 3.1 m, as shown in Figure 3. Figure 3a shows the floor plan of each floor, where the four households (A–D) are exactly the same, each with an area of 138 m². Figure 3b shows the details of the building of household B, in which the south-facing windows of the living room balcony are 2.1 m high and 4.2 m wide, and the east–west windows are 1.5 m high and 0.9 m wide. Bedroom 1 has two windows, and bedrooms 2 and 3 have one window individually, each 1.5 m high and 1.8 m wide. A photo of the south façade is shown in Figure 3c.



(a) Floor plan of the apartment



(b) Details of household B



(c) Photo of the south façade

Figure 3. An apartment building in a hot-summer and cold-winter climate zone in China, households of A, B, C, and D from left to right.

2.3. Occupancy and Heating Equipment

The measurement is carried out in households B and C together. The thermal insulation of their envelope structures is exactly the same, in line with the “Energy-saving Design Standards for Residential Buildings in Hot-summer and Cold-winter Areas” JGJ134-2001 [34]. The specific parameters are similar to those shown in the left column of Table 1. There is no central heating or cooling system for the whole building. Occupants are allowed to use the system as they like. Some owners use electric heaters and others use gas-fired wall mounted boilers for heating. In summer, all users use split air conditioners for cooling. Household B heats the entire house by a gas wall-hung boiler, the maximum heating capacity of the gas boiler is 28 kW, and the temperature of the hot water provided by the boiler shall not be lower than 60 °C, as shown in Figure 4a, and radiators, as shown in Figure 4b. Household C has only three low-power electric ovens covered by quilts for heating, as shown in Figure 4c, each with a power of 50 to 100 W. The total heating capacity of the electric ovens is from 150 to 300 W. This heating method is widely used in hot-summer and cold-winter areas in China. There were four people in each family, including two adults and two children. Due to privacy reasons, this study did not measure the exact house occupancy rate, but since the adults were all teachers and during the winter vacation, it was assumed that the house occupancy rate was similar.

2.4. Measurement Instruments

The environmental parameters recorded in the indoor environment were the indoor temperature and humidity by an Onset HOBO thermometer (± 0.21 °C and $\pm 2\%$ RH) placed on a 1.2 m table, as shown in Figure 5a. The CO₂ concentration was recorded by a BoHu Indoor Air Quality Monitor (± 50 PPM), as shown in Figure 5b, whose time interval was 10 min. Energy consumption was counted through smart sockets for the statistics of electrical appliances, as shown in Figure 5c. A gas meter was used to record gas consumption. Outdoor parameters such as solar radiation, outside temperature, humidity, wind speed and direction were obtained from local weather stations.

Table 1. Thermal parameters of existing buildings and passive houses.

	Existing Building (Old Standard, JGJ134-2001)		Passive House (New Standard, DBJ43/T017-2021)		
	Main Envelope Material	W/(m ² ·K)	The Added Envelope	The Standard Limit W/(m ² ·k)	W/(m ² ·K)
Roof	20 mm mixed mortar 120 mm reinforced concrete 30 mm slag concrete 20 mm cement mortar 30 mmXPS board 40 mm waterproof layer	0.81	+160 mmEPS board	0.15–0.35	0.16
Exterior walls	20 mm mixed mortar 240 mm reinforced concrete 20 mm cement mortar 35 mm thermal insulation mortar 10 mm anti-crack mortar	1.08	+140 mmEPS board	0.15–0.40	0.19
Interior wall	20 mm mixed mortar 200 mm shale hollow brick 20 mm mixed mortar	1.85	+two sides 6 mmEPS board	1.0–2.0	1.09
Floor	30 mm cement mortar 120 mm reinforced concrete 20 mm expanded glass bead insulation mortar	1.90	+10 mmEPS board	1.0–2.0	1.19
Windows		4.7	Low-E vacuum glass	≤ 2.0	1
Doors		3	thermal insulation door	1.0–1.4	1
Number of air infiltration, h ⁻¹					
Rooms	1			0.1	



(a) Gas boiler in household B



(b) Radiator in household B



(c) The oven covered with a quilt, in household C

Figure 4. Equipment for heating.

(a) Thermometer



(b) Air quality monitor



(c) Electricity-statistics plugs

Figure 5. Instruments for measurement.

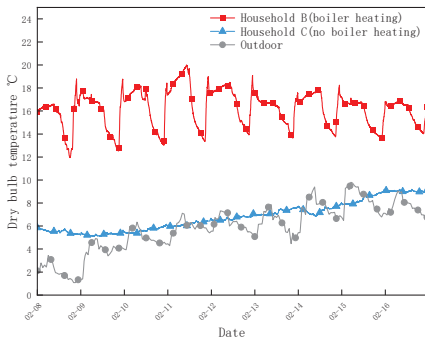
2.5. Survey Results and Analysis

(1) Bedroom 1

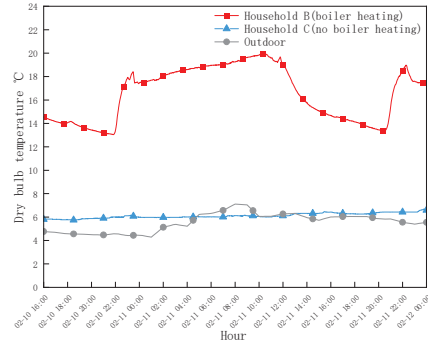
The investigation lasted a total of eight days from 8 to 16 February 2022. As shown in Figure 6a, the heating time of household B is relatively regular. The gas boiler is turned on at about 21:00 to 22:00, and the temperature begins to rise significantly, and the indoor temperature reaches the peak in the early morning. The gas boiler was shut down approximately the next day between 10:00 and 12:00, after which the temperature began to drop.

The indoor temperature of household C is between 6 and 8 °C when there is no boiler heating, and the average value is only 6.8 °C. This average temperature is only 0.3 °C higher than the average outdoor temperature of 6.5 °C, indicating that it is very cold indoors. Therefore, the residents generally sit around the stove and obtain thermal comfort by covering themselves with quilts, as shown in Figure 4c. Figure 6a also shows that the trend of indoor temperature rises slightly with increasing outdoor temperature, which indicates that the thermal insulation and airtightness of the building are relatively poor. However, the average indoor temperature of household B increased to 16.2 °C when there was boiler heating. However, the changing trend of the indoor temperature was not affected by the outdoor conditions.

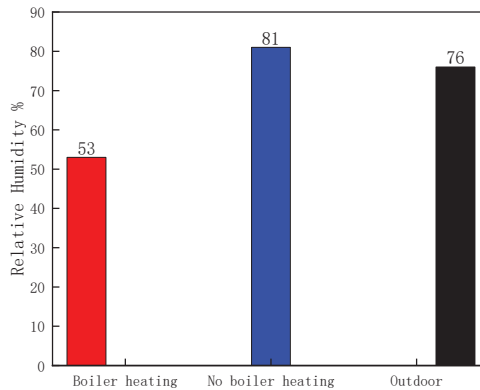
Regarding the temperature change during the day, Figure 6b shows the situation on February 11. It is clear that bedroom 1 is only above 16 °C for part of the day, from 22:00 the previous day to 12:00 the next day. When the heating was stopped, the temperature in room one quickly dropped below 16 °C. While this average temperature met the minimum requirements of the Chinese heating standard “Code for Design of Heating, Ventilation and Air Conditioning in Civil Buildings” GB 50736-2012 [35] in hot-summer and cold-winter regions, occupants complained that the room was cold.



(a) Indoor temperature over 8 days



(b) Indoor temperature on 11 February



(c) Average relative humidity on 11 February

Figure 6. Thermal environment in bedroom 1.

Further observation in Figure 6b shows that there was someone in the bedroom from 20:00 the night before to 12:00 the next day, and the temperature continued to rise. The heating was turned off after 12:00, and thus the temperature dropped continuously. Heating was started at 20:00 in the evening again.

As shown in Figure 6c, the humidity of household C without boiler heating is higher than that outdoors, which is caused by humidity sources such as the human body and cooking. However, when the temperature of household B with boiler heating increases, the relative humidity decreases.

The concentration of CO₂ in the two bedrooms is shown in Figure 7. The CO₂ concentration of the room with heating is significantly higher than that of the room without heating. This is because the users of household B added sealing strips to the windows to increase the airtightness of the room. Apartment C does not have added sealing strips. According to the attenuation of CO₂ concentration to estimate, the air exchange rate of apartment B with sealing strips is from one to three times per hour, and that of apartment C without sealing strips is from 3 to 10 times per hour. This also explains why the temperature of household C in Figure 6 is very low.

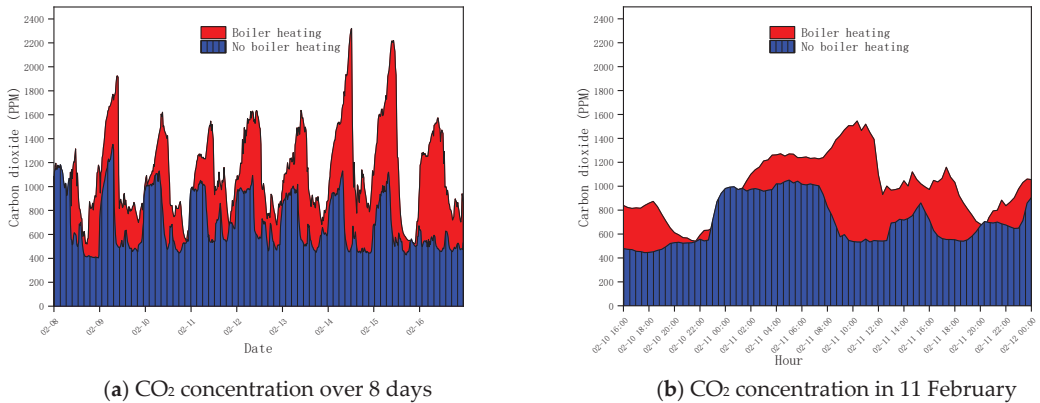


Figure 7. CO₂ concentration in bedroom 1.

Figure 7a shows that the CO₂ concentration of heated bedroom 1 continues to rise from 0:00 a.m. to 8:00 a.m. every day. The CO₂ concentration in the bedroom dropped significantly when the person left the bedroom during the day. The average concentration in heated rooms was 1085 ppm, which exceeded the limit of 1000 ppm required in China's norm "Indoor Air Quality Standard" GB/T18883-2022 [36]. The unheated room had an average concentration of 686 ppm.

The variation of CO₂ concentration during the day, Figure 7b shows the situation on February 11.

CO₂ concentrations continued to rise from 22:00 the night before to 12:00 the next day. After 12:00, CO₂ concentration began to decrease with human activity. The CO₂ concentration of household C did not change significantly.

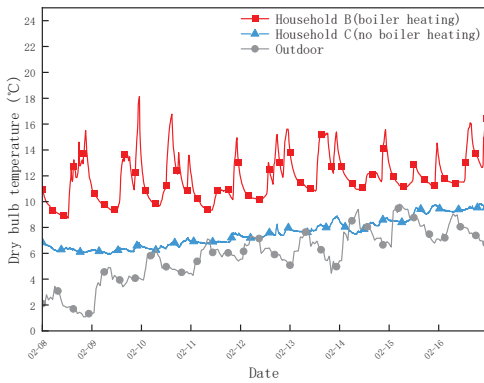
The situation in bedroom 2 is very similar to that in bedroom 1, and thus it is omitted.

(2) Living room

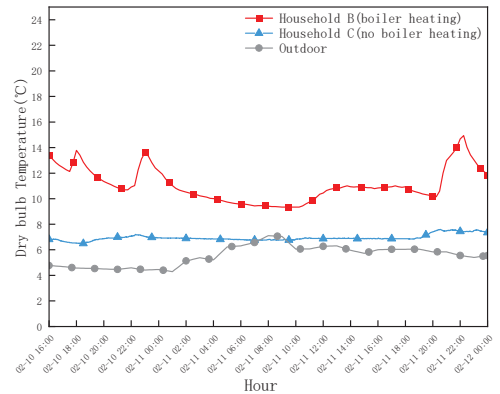
As shown in Figure 8a, compared with the bedroom 1 of household B, the heating control strategy of household B's living room is relatively complex. Generally, when the gas boiler is turned on for heating at around 12:00, the temperature begins to rise significantly. Then, around 23:00 when the gas boiler heating was turned off, the temperature started to drop noticeably. However, during this period, the temperature rose and fell significantly, because people went out and other behaviours to turn off the heating of the gas boiler.

The indoor temperature of the living room of household C was between 6 and 9 °C when there was no heating, with an average value of 7.6 °C. It is 0.8 °C higher than the temperature of bedroom 1 because, during the winter vacation, people spent a lot of time in the living room. Another reason may be that the living room is adjacent to the kitchen, and its cooking and other behaviours increase the indoor temperature. The temperature of the living room of household B with heating is 11.8 °C, which is significantly lower than that of the bedroom. This is because the living room has a large area, many windows and more infiltrated air.

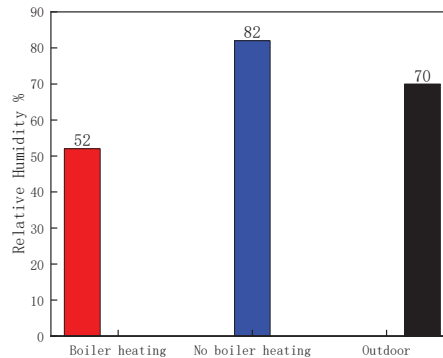
As shown in Figure 8b, the living room temperature of household B began to rise after 12:00. The reason is that the resident just got up, went to the living room, and turned on some heat. Starting at 20:00 at night, the heating power reaches the maximum, and thus the maximum indoor temperature is reached at 23:00. For the unheated living room of household C, the indoor air temperature is 6.9 °C, which is only 1 °C higher than the outdoor temperature of 5.9 °C.



(a) Indoor temperature in 8 days



(b) Indoor temperature on 11 February



(c) Relative humidity on 11 February

Figure 8. Thermal environment in the living room.

For the relative humidity, as shown in Figure 8c, the unheated room is close to the indoor humidity. The humidity of household B with heating is significantly lower than that of household C without heating, which is still due to the increase in temperature.

Figure 9a shows that the CO₂ concentration of household B (with boiler heating) is higher than that of household C (without boiler heating), which is due to the addition of sealing strips to the windows of household B's living room, which enhances the airtightness. However, compared to bedroom 1 (Figure 7), the time with a concentration over 1000 ppm is much less because the living room has more windows and more infiltrated air.

As shown in Figure 9b, the CO₂ concentration of household b increased significantly from 12:00 to 18:00, and its average value obviously exceeded 1000 ppm. CO₂ levels start to fall after 6:00 but start to rise again at 9:00.

(3) Energy consumption

In household C (no boiler heating), the power consumption of the electric oven covered with a quilt (Figure 5c) is counted through the power socket (Figure 3c). The energy consumption of household B (boiler heating) is calculated by gas meter, excluding domestic hot water and cooking gas. For comparison, the gas consumption is converted into electricity consumption (the conversion factor is 0.342) according to the Source Energy Conversion Factors in EnergyPlus, and the results are shown in Figure 10. The energy

consumption of household B in a week was 725 kWh, while household C only used 28 kWh of electricity, and the ratio of the two was about 19:1.

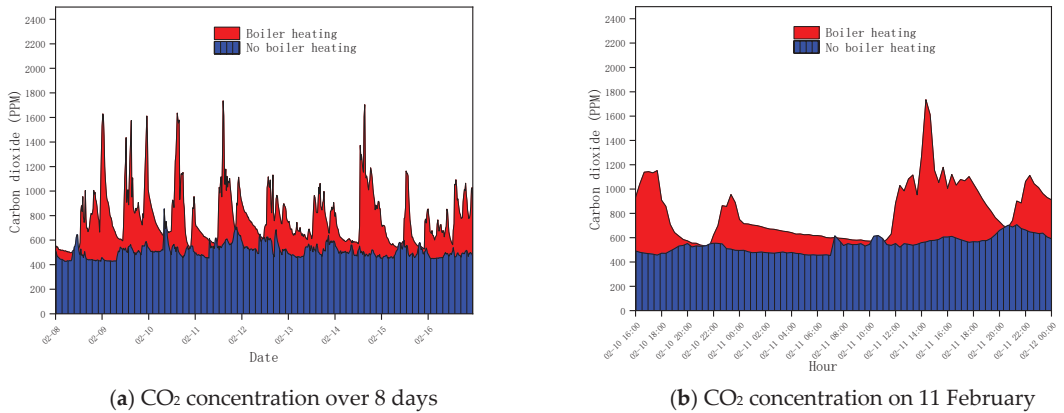


Figure 9. CO₂ concentration in the living room.

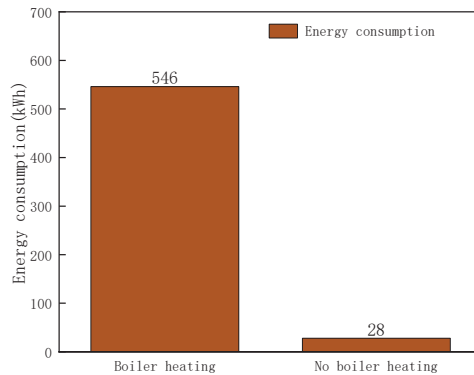


Figure 10. Energy consumption.

3. Building Models

3.1. Building Geometry and Envelope

The model of this apartment is modeled by SketchUp, with a total of six floors and four households on each floor, as shown in Figure 11. Then, the envelope parameters are set by OpenStudio, as shown in Table 1. The parameters in the left column of Table 1 are from the architectural drawings. The building was designed to composite “Design Standard for Energy-saving Residential Buildings in Hot Summer and Cold Winter Areas” JGJ134-2001. If it is converted into a passive house, its thermal parameters come from the “Hunan Province Passive Ultra-low Energy Residential Building Energy Saving Design Standard” DBJ43/T017-2021 [37] and the “Design Standard for Energy Efficiency of Residential Buildings in Hot-summer and Cold-winter Zone” JGJ134-2010 [38], as shown in the right column of Table 1. Obviously, the indicators of thermal insulation and airtightness in the new standard are significantly enhanced. Finally, the model was exported from OpenStudio V2.9.1 to EnergyPlus V9.2 software for the setting of ventilation and shading control strategies.

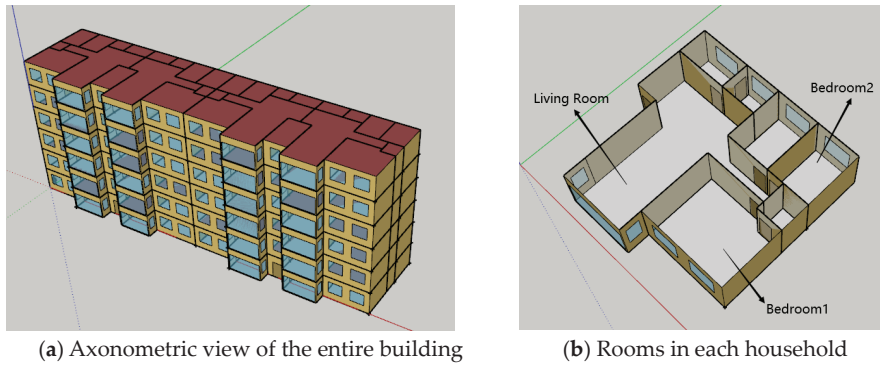


Figure 11. The apartment model in SketchUp.

The occupations of the two surveyed families are teachers, and they are on winter vacation. According to the weekend situation in the new standard DBJ43/T017-2021, settings such as the occupancy rate, utilization rate of electrical equipment, and lighting turn-on time are shown in Figure 12. Among them, the personnel density is $32 \text{ m}^2/\text{person}$, the electrical equipment power density is $8 \text{ W}/\text{m}^2$, the lighting power density is $5 \text{ W}/\text{m}^2$, and the per capita fresh air volume is $30 \text{ m}^3/(\text{h}\cdot\text{p})$.

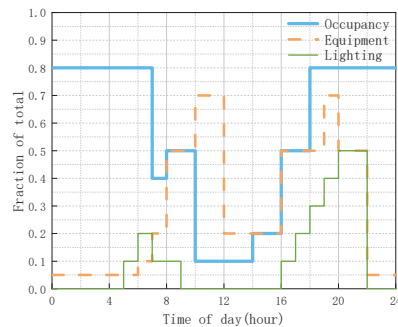


Figure 12. Occupancy rate and equipment power.

3.2. Model Calibration

The temperatures of bedroom 1 in household B from simulation and measurement are shown in Figure 13. There is a difference between the two in the details, which is due to the difference between the occupancy rate in the simulation and the actual situation. Nonetheless, the trends of the two are very similar, and the averages are almost the same. The simulated temperatures of other rooms are also very close to the measured temperatures. Coefficient of Variation of the Root-Mean-Square Error (CV[RMSE]) is 22.2%. Normalized Mean Bias Error (NMBE) is 10.6%.

3.3. Control Strategies for Ventilation and Shading

Natural ventilation is calculated using the airflow network model in EnergyPlus [39]. The infiltration ventilation is mainly carried out through the windows on the outer wall, the air mass flow exponent is set to 0.667, and the air mass flow coefficient is set to $0.001 \text{ kg}/\text{s}$. The module for the air-conditioning system was the ideal loads air system, which is used for prediction for building performance but does not require full modelling. The ideal load air system is usually the only air conditioning component, and the user does not need to specify the air loop, water loop, etc. [39].

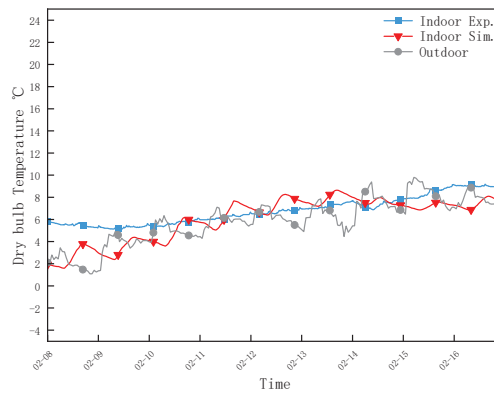


Figure 13. Simulated and measured temperatures of bedroom 1 in household C.

This study proposes four control strategies:

Control strategy 1, air-conditioning + infiltration wind. The ideal air conditioning system is chosen for 24-h continuous control of the room. The indoor temperature is maintained at 20–26 °C, and the windows are closed at all times. When the indoor temperature is >26 °C, the air conditioner is used for cooling. Heating is started when the indoor temperature is lower than 20 °C, and the per capita fresh air volume is 30 m³/(h.p).

Control strategy 2, hybrid ventilation + infiltration wind. It is based on control strategy 1, which increases natural ventilation. Natural ventilation is performed when the indoor temperature met the following three conditions: 20 °C < indoor temperature < 26 °C, indoor temperature > outdoor temperature, and 15 °C < outdoor temperature < 30 °C.

Control strategy 3, hybrid ventilation with adaptive thermal comfort model in ASHRAE55. Richard et al. [40] proposed that the acceptable mean outdoor temperature is between 10 °C and 33.5 °C under natural ventilation. Based on the suggestion from Chen et al. [41], the acceptable indoor operative temperature for 90% of the month was set in Table 2 by the hybrid ventilation availability manager in EnergyPlus. It can be seen that the local period from March to November is suitable for hybrid ventilation. When the indoor operative temperature is within the range in Table 2, natural ventilation is performed. Otherwise, the window is closed and heating or cooling is performed.

Table 2. Indoor operative temperature for adaptive thermal comfort under natural ventilation, °C.

Month	Monthly Mean Outdoor Temperature	90% Acceptance	
		Lower Temperature Limit	Upper Temperature Limit
1	5.5		
2	6.9		
3	10.1	18.4	23.4
4	16.4	20.4	25.4
5	21.5	22.0	27.0
6	25.6	23.2	28.2
7	28.5	24.1	29.1
8	27.3	23.8	28.8
9	23.3	22.5	27.5
10	23.3	22.5	27.5
11	13.4	19.4	24.4
12	7.0		

Control strategy 4, automatic sunshade. Based on control strategy 1, the automatic sunshade of the outer roller blind is added, which is opened when the indoor temperature is higher than 22 °C from 9:00 a.m. to 5:00 p.m. It has no natural ventilation, but the infiltration air volume is 0.1 h⁻¹, which is the same as that of control strategy 1.

3.4. Cases for Simulation

Based on the existing buildings and the four control strategies above, as shown in Table 3, the following five scenarios are summarized for the energy simulation in the next chapter.

Table 3. Description of cases for simulation.

Scenarios	Description	Insulation of Envelope	Control Strategy, Infiltration and Sunshade
Case 1	Existing apartment +air-conditioning	Old standards, JGJ134-2001	Control strategy 1 Infiltration, 1 h^{-1} No shading
Case 2	Passive apartment +air-conditioning	New standards, DBJ43/T017-2021	Control strategy 1 Infiltration, 0.1 h^{-1} No shading
Case 3	Passive apartment +hybrid ventilation	New standards, DBJ43/T017-2021	Control strategy 2 Infiltration, 0.1 h^{-1} No shading
Case 4	Passive apartment +hybrid ventilation with adaptive thermal comfort	New standards, DBJ43/T017-2021	Control strategy 3 Infiltration, 0.1 h^{-1} No shading
Case 5	Passive apartment +automatic sunshade	New standards, DBJ43/T017-2021	Control strategy 4 Infiltration, 0.1 h^{-1} Automatic shading

4. Simulation Results and Analysis

4.1. Effect of a Passive House

As shown in Figure 14, Case 1 represents an existing building, which is similar to the apartment investigated above. Case 2 represents a passive house, which is equivalent to adding thermal insulation and airtightness to Case 1. The heating energy consumption of Case 1 is 14 times that of Case 2, but the cooling energy consumption of the former is 4% lower than that of the latter. Obviously, the enhancement of thermal insulation and airtightness is very significant for the reduction of heating energy consumption, but it has the effect of increasing the cooling energy consumption.

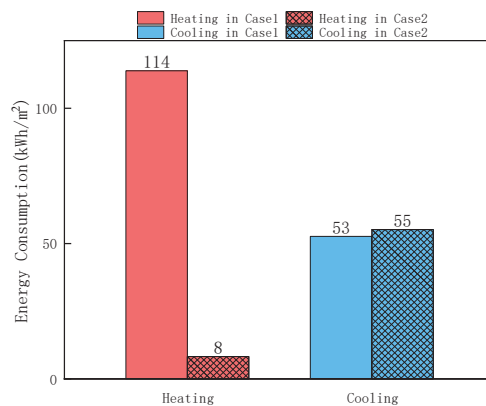
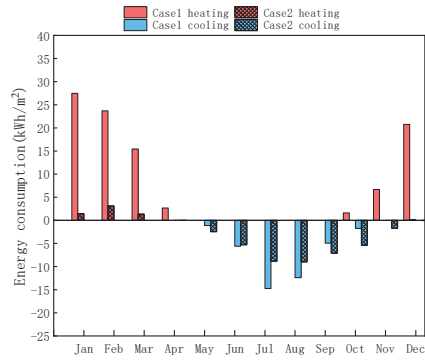


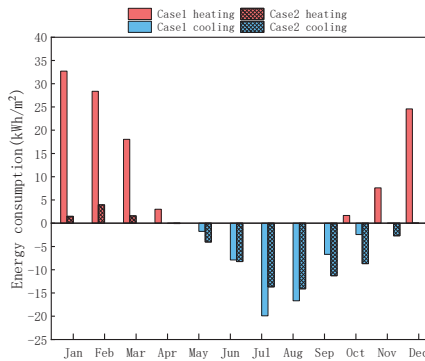
Figure 14. The impact of a passive house on energy consumption, Case 2 (passive apartment +air-conditioning) vs. Case 1 (existing apartment +air-conditioning).

To further analyse the composition of energy consumption, Figure 15 shows the monthly average energy consumption of the living room, bedroom 1 and bedroom 2. The heating energy consumption of the living room dropped significantly in January, February, March, November and December, with an average drop of 92%. Among them, the heating energy consumption in April was reduced to 0, which means that the indoor comfortable

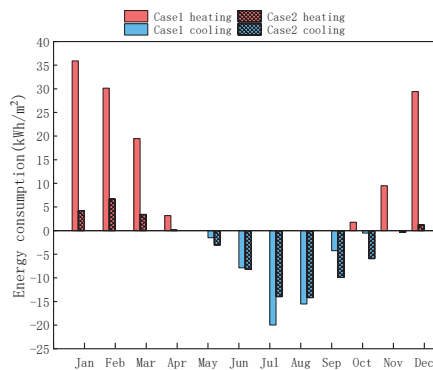
temperature can be maintained completely relying on the thermal insulation of the building envelope. October's fall weather temperatures drop significantly, and thus there is a small amount of heating demand.



(a) Bedroom 1



(b) Living room 1



(c) Bedroom 2

Figure 15. Monthly energy consumption, Case 1 (existing apartment + air-conditioning) vs. Case 2 (passive apartment + air-conditioning).

May, June, September, and October are typical transition seasons in the region, and their cooling energy consumption rose by 67%. This shows that the building is overheated due to the enhancement of thermal insulation and airtightness. Even during the hotter days of November, there was a need for cooling. July and August are the summer months in the region, and cooling energy consumption dropped by 29%.

The changing trends and proportions of the living room and bedroom 2 are similar, as shown in Figure 15b,c, respectively.

Therefore, passive house renovation has a significant reduction effect on heating energy consumption. The cooling energy consumption in summer is slightly lower, but the overheating in the transition season causes the air conditioning energy consumption to increase. The combined effect of the two is a slight increase in cooling energy consumption. Therefore, to solve the problem of the overheating of passive houses, the cooling effect of hybrid ventilation and automatic shading will be discussed below.

4.2. Hybrid Ventilation

It can be seen from Section 4.1 that, after the enhancement of thermal insulation and airtightness, the building has overheated, and thus Section 4.2 discusses the energy-saving effect of adding automatic window ventilation, namely, Case 3. Among them, the apartment limits the indoor temperature between 20 °C and 26 °C by opening windows for natural ventilation. Since the trends and proportions of energy consumption changes in the three rooms are similar, the next analysis is only for the data of bedroom 1, as shown in Figure 16.

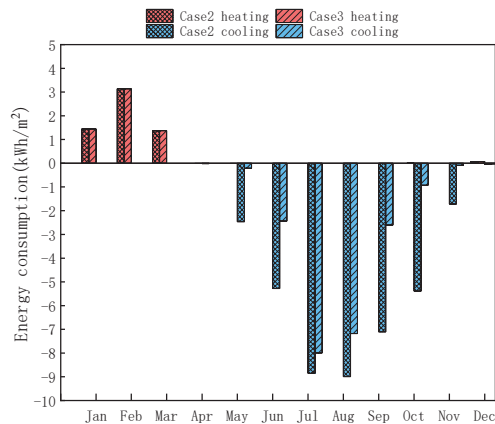


Figure 16. Monthly energy consumption, Bedroom 1, Case 3 (passive apartment + hybrid ventilation) vs. Case 2 (passive apartment + air-conditioning).

As seen from Figure 16, compared to Case 2 (passive apartment + air-conditioning), in Case 3 (passive apartment + hybrid ventilation) in the transition season (May, June, September, October, and a few days in November), the average energy consumption for cooling decreased by an average of 72%. Furthermore, in summer (July and August), the cooling energy consumption decreased by an average of 15%. However, the energy consumption for heating hardly changed.

To determine the reasons for the cooling energy consumption in the transition season and summer, we chose two typical months, July (transition season) and September (summer), and gave the curves of indoor and outdoor temperature changes. As shown in Figure 17a, the local outdoor temperature in July was much higher than 26 °C, and the temperature was lower than 26 °C on only a few days. Therefore, the indoor temperature of the two cases is higher than 26 °C most of the time, and the natural ventilation cooling potential is very small.

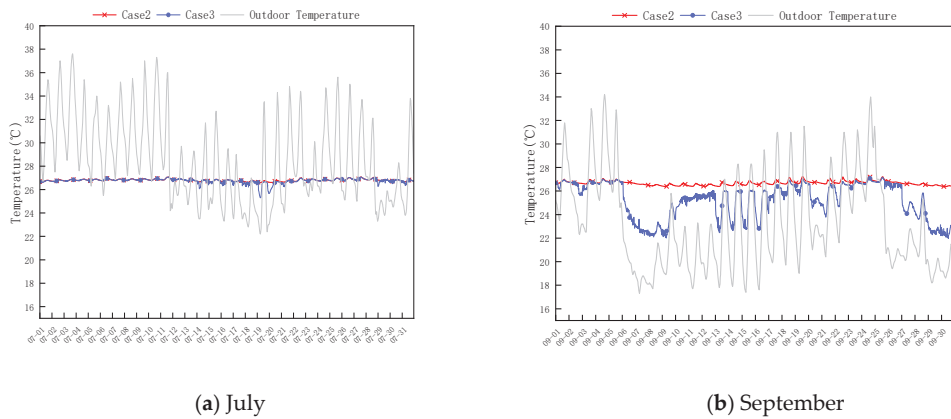


Figure 17. Hourly temperature, Bedroom 1, Case 2 (passive apartment + air-conditioning) vs. Case 3 (passive apartment + hybrid ventilation).

As shown in Figure 17b, the outdoor temperature was lower than 26°C more than 50% of the time in September, and thus the ventilation cooling potential was obvious. The average temperature of Case 3 is 1.5°C lower than that of Case 2 after using hybrid ventilation.

According to statistics, the annual cooling energy consumption of the entire house is reduced by 43% on average. The Section 4.3 advances the discussion of larger temperature ranges when considering adaptive thermal comfort.

4.3. Hybrid Ventilation with Adaptive Thermal Comfort

According to the statistics of Richard et al. [39], the thermal comfort range of the human body under natural ventilation is significantly larger than that in an air-conditioned environment or heating environment. Case 4 uses the temperature range for adaptive thermal comfort in ASHRAE55. As shown in Figure 18, the average energy consumption for cooling during the transition season (May, June, September, October, and a few days in November) decreased by an average of 90%. Furthermore, in summer (July and August), the cooling energy consumption dropped by an average of 76%. Even in winter, heating energy consumption dropped by 24%. Obviously, this is due to the broadening of the temperature range.

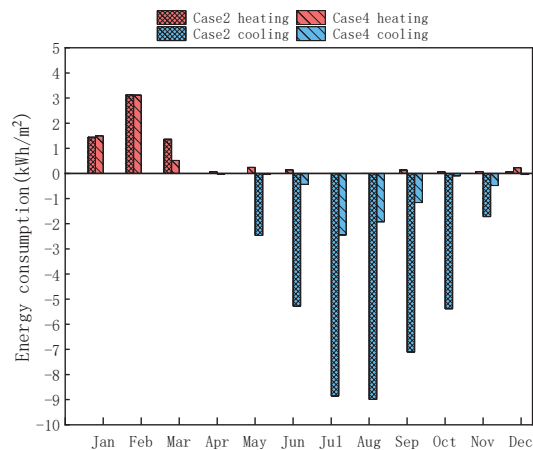


Figure 18. Monthly energy consumption, Bedroom 1, Case 4 (passive apartment + hybrid ventilation with adaptive thermal comfort) vs. Case 2 (passive apartment + air-conditioning).

Figure 19 shows the indoor and outdoor dry bulb temperatures for bedroom 1 in summer (July) and in the transition season (September). Figure 19a shows that in July, the indoor temperature of Case 4 was higher than 26 °C but less than 30 °C. The average temperature of Case 4 was 1.9 °C higher than that of Case 2.

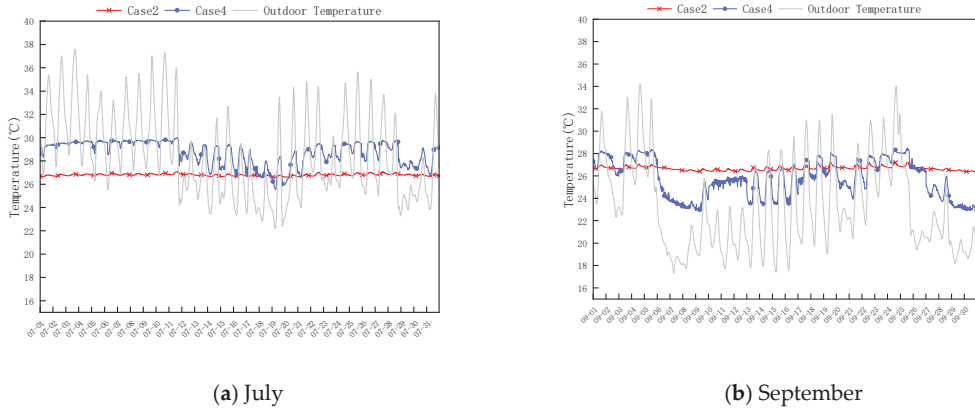


Figure 19. Hourly temperature, Bedroom 1, Case 4 (passive apartment + hybrid ventilation with adaptive thermal comfort) vs. Case 2 (passive apartment + air-conditioning).

As shown in Figure 19b, in September, the cooling effect of Case 4 was more obvious, which was 1.5 °C lower than that of Case 2. Compared to Case 3, Case 4 makes full use of natural ventilation for cooling.

In summary, the annual cooling energy consumption drops even more when the temperature range is the natural ventilation thermal comfort temperature range.

4.4. Automatic Sunshade

In addition to ventilation, shading is another means of eliminating overheating in a building. On the basis of Case 2, Case 5 adds an automatic sunshade. As shown in Figure 20, in bedroom 1, the energy consumption of Case 5 is reduced compared to that of Case 2 in the transition season and summer, and the reduction is 22.7%.

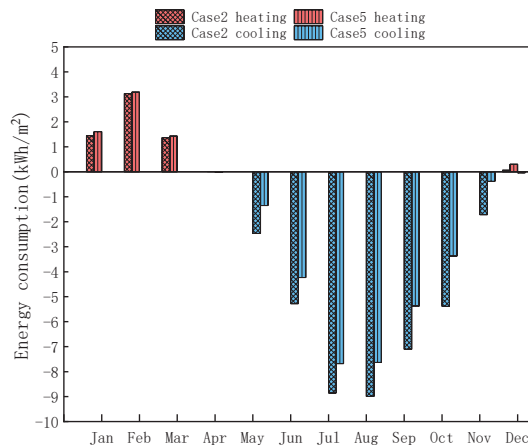


Figure 20. Monthly energy consumption, Bedroom 1, Case 5 (passive apartment + automatic sunshade) vs. Case 2 (passive apartment + air-conditioning).

As shown in Figure 21, the average temperature drops of Case 5 under shading control in summer (July) and the transitional season (September) were 0.05 °C and 0.07 °C, respectively, compared to Case 2.

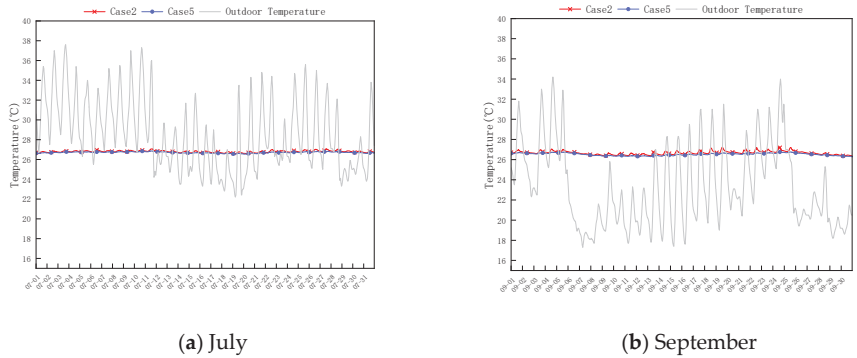


Figure 21. Hourly temperature, Case 5 (passive apartment + automatic sunshade) vs. Case 2 (passive apartment + air-conditioning).

After calculation, the annual cooling energy consumption of the entire apartment has been reduced by 17%. Thus, shade-controlled automatic shades have some cooling potential but are not as good as hybrid ventilation locally.

4.5. Airflow Rate

As shown in Figure 22, the monthly ventilation volumes of Case 1, Case 2, Case 3, and Case 4 are drawn on a graph, as shown in 22. Compared to the existing building (Case 1), the ventilation volume of the passive house (Case 2) is reduced by one tenth. After the use of hybrid ventilation (Case 3), the ventilation volume increased significantly in the transition season and summer. When considering the adaptive thermal comfort of natural ventilation (Case 4), the fresh air volume is further increased. However, ventilation is still low during the four winter months.

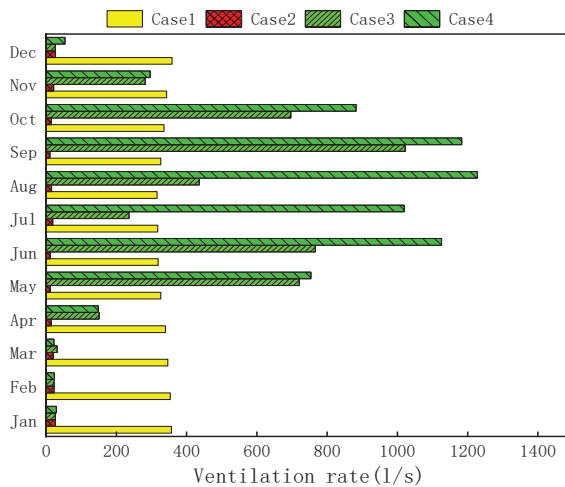


Figure 22. Monthly airflow rate, Bedroom1, Case 1 vs. Case 2 vs. Case 3 vs. Case 4.

5. Discussion

This paper first investigates the indoor thermal environment of two existing apartment buildings in winter. Two typical heating models in the existing building were investigated. One is high energy consumption and not warm enough, and another is low energy consuming but cold. The survey data show that the average indoor temperature is only 6.8 °C in the apartment without boiler heating. When there is boiler heating, the average temperature can only reach 16.2 °C. This shows that the thermal insulation and airtightness of the existing buildings are very poor.

Based on the survey data, this study established a similar model (Case 1) in Energy-Plus and enhanced the thermal insulation and airtightness of the envelope (Case 2). The predicted results show that when the thermal insulation and airtightness of the envelope structure are enhanced, the heating energy consumption in winter is reduced by 93%. However, the energy consumption of cooling in the summer and transitional seasons increased by 4%. This shows that the building has overheating problems, which came from the side effect of strengthening the thermal insulation and airtightness.

The overall energy consumption is reduced by 62%, which is similar to the results obtained in the Qingdao passive house located in a cold region of China (with an annual energy efficiency improvement of about 69% compared to current standards) [4]. In the concept of optimized passive house located in Brazil, the energy demand can be reduced by 55% to 83% [6]. If the passive house model in this study is optimized, further energy saving potential can be achieved.

As for the problem of overheating, we have adopted hybrid ventilation measures to solve it. When the indoor temperature range is set to 18–26 °C (Case 3), the cooling energy consumption can be reduced by approximately 40% compared to Case 2. When the temperature range is set in the thermal adaptation range (Case 4, approximately 10–33 °C), the cooling energy consumption can be reduced by 81% compared to Case 2.

Proof in reality is that the occupants need to turn on the air conditioner to cool down the house during the transition season in another apartment that has been converted into a passive house. In fact, according to our living experience in these areas of China named hot-summer and cold-winter, people are very accustomed to natural ventilation by opening windows. The reason for overheating was that the openable area on the windows was too small, which caused complaints from residents, as shown in Figure 23. These overheating phenomena and complaints are similar to findings in the literature [7–9].



Figure 23. The openable area of the window is very small in a local passive house for experiments.

In addition, the case of an automatic sunshade (Case 5) is also discussed. The results show a reduction in cooling energy consumption of approximately 17% relative to Case 2. Shading has a certain cooling effect, but it is not as good as natural ventilation by 76%.

In summary, the energy-saving effect of passive house technology in China's hot-summer and cold-winter regions is mainly reflected in winter. In the summer and transitional seasons, natural ventilation and shading are required for cooling; otherwise, the building will overheat.

Limitations of this study: The heat transfer coefficient and airtightness settings of the envelope are too simplified, and only two types of hybrid ventilation strategies and one shading control strategy are simulated. The effect of heat recovery is not discussed in this paper, and more field measurements are needed to validate the predictions. This article is a case study, the parameters are also approximate, and the results may have certain errors. Nonetheless, the simulated energy efficiency rate of change is similar to the real situation. The results provide a basic direction for local passive house reconstruction and provide a reference for the construction of passive houses in similar climate regions throughout the world. As a preliminary study, we have only made a short-term simulation forecast, and the conversion of apartments to passive houses is in progress. Due to the difficulty in adding too thick of an insulation structure in old buildings and the difficulty in ensuring air tightness during construction, the renovation of passive houses may not reach the level predicted by simulation. In the next step, we will study the renovated passive houses. Additionally, we try to simulate and predict the optimal envelope structure in the region through sensitivity analysis to reduce energy consumption.

6. Conclusions

In China's hot-summer and cold-winter areas, there is a large number of old apartments. Upon converting them into passive houses, the energy saving potential is still unknown. This study investigated the existing apartment building and then simulated the energy saving potential of the building with enhanced thermal insulation and airtightness through EnergyPlus. The results show the following:

1. The thermal insulation and airtightness of the existing local apartments are very poor. Enhancing the thermal insulation and airtightness of doors and windows can significantly reduce the energy consumption in winter by 62% overall. However, overheating will occur in transitional seasons and summer, which will increase the energy consumption for cooling.
2. Hybrid ventilation can solve the problem of overheating well, especially considering the adaptive comfort range for natural ventilation. The energy consumption will reduce by 81% overall.
3. Automatic shading has a certain cooling effect by 17% reducing of energy consumption of cooling, but it is lower than ventilation cooling by 76% reducing.

In future research, we will conduct measurements in an apartment which has just been refurbished as passive house to determine air quality, thermal comfort, and energy consumption in this area, and study the optimum level of the thermal insulation for the retrofit building.

Author Contributions: Writing—original draft preparation; investigation, Y.Z. and Y.L. (Yonghan Li); writing—review and editing, W.Y., M.Z. and X.H.; supervision, Y.L. (Yongcun Li), Y.O. and J.H. All authors have read and agreed to the published version of the manuscript.

Funding: This study was funded by the National Natural Science Foundation of China (No. 51308206), International Science and Technology Cooperation Program of China (No. 2014DFA72190), National Natural Science Foundation of Hunan Province of China (No. 2021JJ30269, 2021JJQNJJ0546, 2020JJ6028), Natural Science Foundation of Guangxi (No. 2018GXNSFAA281212).

Acknowledgments: The original idea for the study came from the collaboration with IEA- EBC-Annex62 Ventilative Cooling and IEA-EBC-Annex 80 Resilient Cooling.

Conflicts of Interest: The authors declare no conflict of interest.

References

1. Research Center of Tsinghua University for Building Energy Efficiency. *2020 Annual Report on China Building Energy Efficiency*; China Construction Industry Press: Beijing, China, 2021. (In Chinese)
2. Ionescu, C.; Baracu, T.; Vlad, G.-E.; Necula, H.; Badea, A. The Historical Evolution of the Energy Efficient Buildings. *Renew. Sustain. Energy Rev.* **2015**, *49*, 243–253. [[CrossRef](#)]
3. Schnieders, J.; Feist, W.; Rongen, L. Passive Houses for Different Climate Zones. *Energy Build.* **2015**, *105*, 71–87. [[CrossRef](#)]
4. Han, F.; Liu, B.; Wang, Y.; Dermentzis, G.; Cao, X.; Zhao, L.; Pfluger, R.; Feist, W. Verifying of the Feasibility and Energy Efficiency of the Largest Certified Passive House Office Building in China: A Three-Year Performance Monitoring Study. *J. Build. Eng.* **2022**, *46*, 103703. [[CrossRef](#)]
5. Wang, Y.; Du, J.; Kuckelkorn, J.M.; Kirschbaum, A.; Gu, X.; Li, D. Identifying the Feasibility of Establishing a Passive House School in Central Europe: An Energy Performance and Carbon Emissions Monitoring Study in Germany. *Renew. Sustain. Energy Rev.* **2019**, *113*, 109256. [[CrossRef](#)]
6. Vettorazzi, E.; Figueiredo, A.; Rebelo, F.; Vicente, R.; Grala da Cunha, E. Optimization of the Passive House Concept for Residential Buildings in the South-Brazilian Region. *Energy Build.* **2021**, *240*, 110871. [[CrossRef](#)]
7. Ridley, I.; Clarke, A.; Bere, J.; Altamirano, H.; Lewis, S.; Durdev, M.; Farr, A. The Monitored Performance of the First New London Dwelling Certified to the Passive House Standard. *Energy Build.* **2013**, *63*, 67–78. [[CrossRef](#)]
8. Rohdin, P.; Molin, A.; Moshfegh, B. Experiences from Nine Passive Houses in Sweden—Indoor Thermal Environment and Energy Use. *Build. Environ.* **2014**, *71*, 176–185. [[CrossRef](#)]
9. Fokaides, P.A.; Christoforou, E.; Ilic, M.; Papadopoulos, A. Performance of a Passive House under Subtropical Climatic Conditions. *Energy Build.* **2016**, *133*, 14–31. [[CrossRef](#)]
10. Cakyova, K.; Figueiredo, A.; Oliveira, R.; Rebelo, F.; Vicente, R.; Fokaides, P. Simulation of Passive Ventilation Strategies towards Indoor CO₂ Concentration Reduction for Passive Houses. *J. Build. Eng.* **2021**, *43*, 103108. [[CrossRef](#)]
11. About Mixed-Mode. Available online: <https://cbe.berkeley.edu/mixedmode/aboutmm.html> (accessed on 28 December 2022).
12. Deuble, M.P.; de Dear, R.J. Mixed-Mode Buildings: A Double Standard in Occupants' Comfort Expectations. *Build. Environ.* **2012**, *54*, 53–60. [[CrossRef](#)]
13. Luo, M.; Cao, B.; Damiens, J.; Lin, B.; Zhu, Y. Evaluating Thermal Comfort in Mixed-Mode Buildings: A Field Study in a Subtropical Climate. *Build. Environ.* **2015**, *88*, 46–54. [[CrossRef](#)]
14. Forgiarini Rupp, R.; Ghisi, E. Predicting Thermal Comfort in Office Buildings in a Brazilian Temperate and Humid Climate. *Energy Build.* **2017**, *144*, 152–166. [[CrossRef](#)]
15. Fiorentini, M.; Serale, G.; Kokogiannakis, G.; Capozzoli, A.; Cooper, P. Development and Evaluation of a Comfort-Oriented Control Strategy for Thermal Management of Mixed-Mode Ventilated Buildings. *Energy Build.* **2019**, *202*, 109347. [[CrossRef](#)]
16. Barbadilla-Martín, E.; Salmerón Lissén, J.M.; Guadix Martín, J.; Aparicio-Ruiz, P.; Brotas, L. Field Study on Adaptive Thermal Comfort in Mixed Mode Office Buildings in Southwestern Area of Spain. *Build. Environ.* **2017**, *123*, 163–175. [[CrossRef](#)]
17. Ezzeldin, S.; Rees, S.J. The Potential for Office Buildings with Mixed-Mode Ventilation and Low Energy Cooling Systems in Arid Climates. *Energy Build.* **2013**, *65*, 368–381. [[CrossRef](#)]
18. Rupp, R.F.; de Dear, R.; Ghisi, E. Field Study of Mixed-Mode Office Buildings in Southern Brazil Using an Adaptive Thermal Comfort Framework. *Energy Build.* **2018**, *158*, 1475–1486. [[CrossRef](#)]
19. Sánchez-García, D.; Rubio-Bellido, C.; del Río, J.J.M.; Pérez-Fargallo, A. Towards the Quantification of Energy Demand and Consumption through the Adaptive Comfort Approach in Mixed Mode Office Buildings Considering Climate Change. *Energy Build.* **2019**, *187*, 173–185. [[CrossRef](#)]
20. Mhuireach, G.Á.; Brown, G.Z.; Kline, J.; Manandhar, D.; Moriyama, M.; Northcutt, D.; Rivera, I.; Van Den Wymelenberg, K. Lessons Learned from Implementing Night Ventilation of Mass in a Next-Generation Smart Building. *Energy Build.* **2020**, *207*, 109547. [[CrossRef](#)]
21. Chen, J.; Brager, G.S.; Augenbroe, G.; Song, X. Impact of Outdoor Air Quality on the Natural Ventilation Usage of Commercial Buildings in the US. *Appl. Energy* **2019**, *235*, 673–684. [[CrossRef](#)]
22. Ledo Gomis, L.; Fiorentini, M.; Daly, D. Potential and Practical Management of Hybrid Ventilation in Buildings. *Energy Build.* **2021**, *231*, 110597. [[CrossRef](#)]
23. Hu, J.; Karava, P. Model Predictive Control Strategies for Buildings with Mixed-Mode Cooling. *Build. Environ.* **2014**, *71*, 233–244. [[CrossRef](#)]
24. May-Ostendorp, P.; Henze, G.P.; Corbin, C.D.; Rajagopalan, B.; Felsmann, C. Model-Predictive Control of Mixed-Mode Buildings with Rule Extraction. *Build. Environ.* **2011**, *46*, 428–437. [[CrossRef](#)]
25. Zhao, J.; Lam, K.P.; Ydstie, B.E.; Loftness, V. Occupant-Oriented Mixed-Mode EnergyPlus Predictive Control Simulation. *Energy Build.* **2016**, *117*, 362–371. [[CrossRef](#)]
26. Alzoubi, H.H.; Al-Zoubi, A.H. Assessment of Building Façade Performance in Terms of Daylighting and the Associated Energy Consumption in Architectural Spaces: Vertical and Horizontal Shading Devices for Southern Exposure Facades. *Energy Convers. Manag.* **2010**, *51*, 1592–1599. [[CrossRef](#)]

27. Kim, G.; Lim, H.S.; Lim, T.S.; Schaefer, L.; Kim, J.T. Comparative Advantage of an Exterior Shading Device in Thermal Performance for Residential Buildings. *Energy Build.* **2012**, *46*, 105–111. [[CrossRef](#)]
28. Van Den Wymelenberg, K. Patterns of Occupant Interaction with Window Blinds: A Literature Review. *Energy Build.* **2012**, *51*, 165–176. [[CrossRef](#)]
29. O'Brien, W.; Kapsis, K.; Athienitis, A.K. Manually-Operated Window Shade Patterns in Office Buildings: A Critical Review. *Build. Environ.* **2013**, *60*, 319–338. [[CrossRef](#)]
30. Karlsen, L.; Heiselberg, P.; Bryn, I.; Johra, H. Solar Shading Control Strategy for Office Buildings in Cold Climate. *Energy Build.* **2016**, *118*, 316–328. [[CrossRef](#)]
31. Tabadkani, A.; Roetzel, A.; Li, H.X.; Tsangrassoulis, A. A Review of Automatic Control Strategies Based on Simulations for Adaptive Facades. *Build. Environ.* **2020**, *175*, 106801. [[CrossRef](#)]
32. Yun, G.; Yoon, K.C.; Kim, K.S. The Influence of Shading Control Strategies on the Visual Comfort and Energy Demand of Office Buildings. *Energy Build.* **2014**, *84*, 70–85. [[CrossRef](#)]
33. Meteorological Information Center of China Meteorological Administration; Department of Building Technology and Science, Tsinghua University. *Meteorological Data Set for Building Thermal Environment Analysis in China*; China Architecture & Building Press: Beijing, China, 2005. (In Chinese)
34. Ministry of Housing and Urban-Rural Development of the People's Republic of China. *JGJ134-2001*; Design Standard for Energy Efficiency of Residential Buildings in Hot-Summer and Cold-Winter Zone. China Architecture & Building Press: Beijing, China, 2001. (In Chinese)
35. Ministry of Housing and Urban-Rural Development of the People's Republic of China. *GB 50736-2012*; Design Code for Heating Ventilation and Air Conditioning in Civil Buildings of China. China Architecture & Building Press: Beijing, China, 2012. (In Chinese)
36. General Administration of Quality Supervision, Inspection and Quarantine of the People's Republic of China. *GBT18883-2002*; Indoor Air Quality Standard. General Administration of Quality Supervision, Inspection and Quarantine of the People's Republic of China: Beijing, China, 2002. (In Chinese)
37. Ministry of Housing and Urban-Rural Development of Hunan Province in China. *DBJ43/T017-2021*; Design Standard for Energy Efficiency of Passive Ultra-Low Energy Residential Buildings in Hunan. China Architecture & Building Press: Beijing, China, 2021. (In Chinese)
38. Ministry of Housing and Urban-Rural Development of the People's Republic of China. *JGJ134-2010*; Design Standard for Energy Efficiency of Residential Buildings in Hot-Summer and Cold-Winter Zone. China Architecture & Building Press: Beijing, China, 2010. (In Chinese)
39. U.S. Department of Energy. *EnergyPlus Documentation*; U.S. Department of Energy: Washington, DC, USA, 2021.
40. de Dear, R.J.; Brager, G.S. Thermal Comfort in Naturally Ventilated Buildings: Revisions to ASHRAE Standard 55. *Energy Build.* **2002**, *34*, 549–561. [[CrossRef](#)]
41. Chen, X.; Yang, H.; Zhang, W. Simulation-Based Approach to Optimize Passively Designed Buildings: A Case Study on a Typical Architectural Form in Hot and Humid Climates. *Renew. Sustain. Energy Rev.* **2018**, *82*, 1712–1725. [[CrossRef](#)]

Disclaimer/Publisher's Note: The statements, opinions and data contained in all publications are solely those of the individual author(s) and contributor(s) and not of MDPI and/or the editor(s). MDPI and/or the editor(s) disclaim responsibility for any injury to people or property resulting from any ideas, methods, instructions or products referred to in the content.

Energy-Saving Design and Energy Consumption Analysis of a New Vacuum Refrigerator

Nuonan Zhang ^{1,†}, Yun Guo ^{1,*,†}, Weijian Yuan ¹ and Yaolin Lin ²

¹ School of Mechanical and Automotive Engineering, Shanghai University of Engineering Science, Shanghai 201620, China; m010119608@sues.edu.cn (N.Z.); 011717228@sues.edu.cn (W.Y.)

² School of Environment and Architecture, University of Shanghai for Science and Technology, Shanghai 200093, China; ylin@usst.edu.cn

* Correspondence: graceguo1980@126.com

† First two authors contributed equally to this paper and should be considered co-first authors.

Abstract: With the goal of carbon peak and carbon neutrality, fossil energy is becoming increasingly exhausted. Optimizing energy structure and saving energy and reducing consumption are the top priority. With the rapid development of modern science and technology, vacuum refrigerator has been greatly applied and popularized in various fields, such as food production, medicine and biology. However, in the actual operation process, the energy consumption of vacuum refrigerator is high, which does not meet the concept of energy conservation and environmental protection. The inner and outer push-pull structure of the sealing door makes it occupy too much space when opening the door, which is very inconvenient. In this paper, a vacuum refrigeration energy-saving device and the TRNSYS 16 software are used to simulate the energy-saving device. The results show that the device can reduce the number of vacuum refrigeration pumps and greatly reduce the loss of energy consumption. In addition, the new sealing door structure can also reduce the space occupied during its expansion and improve the utilization of space.

Keywords: carbon peak; carbon neutrality; energy consumption; vacuum refrigerator; sealing door; TRNSYS 16

Citation: Zhang, N.; Guo, Y.; Yuan, W.; Lin, Y. Energy-Saving Design and Energy Consumption Analysis of a New Vacuum Refrigerator. *Buildings* **2022**, *12*, 203. <https://doi.org/10.3390/buildings12020203>

Academic Editor: Umberto Berardi

Received: 18 November 2021

Accepted: 3 February 2022

Published: 11 February 2022

Publisher's Note: MDPI stays neutral with regard to jurisdictional claims in published maps and institutional affiliations.



Copyright: © 2022 by the authors. Licensee MDPI, Basel, Switzerland. This article is an open access article distributed under the terms and conditions of the Creative Commons Attribution (CC BY) license (<https://creativecommons.org/licenses/by/4.0/>).

1. Introduction

In January 2021, at the dialogue meeting of “Davos agenda” of the world economic forum, China proposed to accelerate the adjustment and optimization of industrial structure and energy structure, advocate a green and low-carbon way of production and life, and strive to reach the peak of carbon dioxide emission by 2030 and achieve carbon neutrality by 2060 [1]. At present, China is still the largest energy consumer in the world, and energy consumption is the main carbon dioxide emission source in China [2], accounting for about 88% of all carbon dioxide emissions [3]. With the massive consumption of energy, the energy problem has become one of the common concerns of people. Energy resources are an important material basis for people’s survival and development in society [4]. The utilization and development of energy is related to the development of the whole national economy and the production and life of human beings [5]. Therefore, how to effectively use energy and save energy is the focus of attention now.

Vacuum refrigerators are widely used in vacuum coating, surface treatment, optoelectronics, aerospace, Shi Ying crystals, solar collector tubes, scientific research institutes, biopharmaceuticals, food production, electronic industry, metal processing and other industries [6,7]. A vacuum refrigerator is a piece of refrigeration equipment equipped for vacuum system, which can provide cold source. It has the following characteristic: fast adsorption of water, oil and steam, which can shorten the extraction time by 60–90% and increase the production capacity of the existing vacuum system by 20% to 100%, etc. Roughly

speaking, vacuum means that the air pressure in a region is much less than the atmospheric pressure. The energy consumption of processing is the main problem of vacuum freeze-drying technology at present, so it also increases the production cost. Zhou et al. [8] of Shanghai University of Engineering Science put forward that a freeze-dryer system using solar absorption refrigeration in combination with buildings can effectively reduce energy consumption. Through the solar absorption refrigeration system, the cold energy is supplied to the freeze-dryer and buildings at the same time, so that the cold energy can be used step by step. Zhang et al. [9] of Zhejiang University think that the traditional freeze dryer has high running cost and high energy consumption, which limits the wide application of freeze-drying technology. They put forward a freeze dryer based on a closed regeneration loop of hygroscopic solution, made thermodynamic analysis and concluded that the new freeze dryer has high energy saving potential in a wide operating range. Liu et al. [10] of Xi'an Jiaotong University established a mathematical model for exergy analysis of freeze-drying process. The model considered five operations: freezing, primary drying, secondary drying, steam condensation and vacuum pumping, among which the energy consumption loss under freezing and vacuum operation was low. Luo et al. [11] of Shandong Jianzhu University analyzed the energy saving of food freeze-drying, which provided a theoretical basis for how to carry out pretreatment and pre-freezing in the process of freeze-drying and how to control temperature and pressure to shorten the drying time. Rahman et al. [12] of University of Sharjah developed a new air freeze-drying system, evaluated its parameters and compared the drying characteristics and physical quality between vacuum freezing and traditional AFD. The results showed that the system was a suitable and feasible alternative without affecting the quality. Through the vacuum cooling experiment, Han Houde [13] of Shanghai Maritime University obtained that the power consumption of compressor, vacuum pump and other equipment accounted for 68%, 18% and 14% of the total energy consumption respectively and pointed out that about 10 min after the flash, if the compressor was unloaded by 25%, the total energy consumption of the unit could be reduced by about 8%. Several small capacity vacuum pumps are selected for the vacuum device, which are all put into operation before flash, accelerate the vacuum pumping rate, shorten the no-load operation time of the compressor, save the total energy consumption of the compressor, reduce the number of vacuum pumps put into operation after flash and reduce the total energy consumption of the vacuum pump.

However, in the existing studies, there is little research on vacuum freeze-drying driven by a single vacuum refrigeration pump. In the prior art, each vacuum freezer has a separate refrigeration system [14], and when multiple vacuum freezers need to be used at the same time, multiple refrigeration systems need to be equipped at the same time, which leads to higher energy consumption [15]. The market application of vacuum freeze dryer has been seriously hindered by the production projects with high energy consumption in the world, and many environmental problems have followed, which do not conform to the concept of energy conservation and environmental protection. Therefore, it is necessary for us to analyze the energy consumption of vacuum freezers to reduce the energy consumption as much as possible [16]. In addition, the sealing doors of general vacuum refrigerators are of push-pull structure inside and outside, which easily occupies a large space when opening the door. Especially in places where the installation space of vacuum refrigerators is limited, the push-pull design of sealing doors [17] inside and outside is very inconvenient to use. Therefore, the research focus of this paper is to study and analyze the energy consumption optimization of a vacuum refrigerator energy-saving device which only needs a single vacuum refrigeration pump to realize the refrigeration of multiple vacuum refrigerators at the same time. This energy-saving device can reduce the use of vacuum refrigeration pumps [18], optimize the system configuration, effectively reduce its energy consumption and achieve the environmental protection concept of energy saving and emission reduction.

The general idea of this paper is: according to the analysis of the total energy consumption of the vacuum refrigerator, the energy-saving transformation of the general vacuum

refrigerator with high energy consumption in the actual operation process is carried out, and a new energy-saving device which can use a single vacuum refrigeration pump to drive multiple vacuum refrigerators through the air-conditioning transmission box is designed. Furthermore, the simulation connection diagrams of four schemes are simulated and designed by TRNSYS 16 software for comparison, setting the simulation parameters and the simulation running time to 8760 h (i.e., one year) for energy consumption analysis and comparison and finally obtaining the results. At the same time, the sealing door structure of the vacuum refrigerator device is creatively designed. The flexible movement of the sealing door is realized through the design of the box door locking mechanism and the box locking mechanism, which can effectively reduce the occupied space and improve the space utilization rate.

2. Energy Consumption of Refrigeration System of Vacuum Refrigerator

The vacuum freezer is the key piece of equipment for the production of freeze-dried preparations, and the refrigeration system is one of the key systems of the vacuum freezer [19]. The refrigeration system mainly provides the low temperature required by freeze drying for the vacuum refrigerator in normal production. The physical state of the refrigerant changes through the action of the compressor, so as to absorb the external heat or release its own heat and achieve the effect of low temperature control.

The measurement of energy consumption of refrigeration system is mainly carried out from the following two aspects [20]: one is the measurement of refrigeration capacity, that is, the measurement of refrigeration capacity produced by refrigerator; the second is the measurement of energy consumption, that is, the energy consumed by the refrigerator to produce these cold quantities. Through the test results of refrigerating capacity and energy consumption, the working condition of the refrigerator is analyzed, and the factors leading to higher energy consumption of the refrigerator in operation are found. The refrigeration system is diagnosed and measures are taken to make the refrigerator run with energy saving and high efficiency.

The measuring method of refrigerating capacity of refrigeration unit is to measure the flow rate of cold water and the temperature of inlet and outlet and calculate the refrigerating capacity by the following Formula (1) [21]:

$$Q_0 = cm(t_{in} - t_{out}) \quad (1)$$

Q_0 —refrigeration capacity produced by refrigerator, (kW);

c —specific heat capacity of cold water, (kJ/(kg·°C));

m —cold water flow, (kg/s);

t_{in} —cold water inlet temperature of refrigerator, (°C);

t_{out} —cold water outlet temperature of refrigerator, (°C).

The energy consumption of the refrigerator is calculated according to the following Formula (2) by measuring or reading the current, voltage and power factor of the refrigerating unit:

$$P = UI\cos\varphi \quad (2)$$

P —power consumption of refrigerator, (kW);

U —ac voltage value, (V);

I —ac current value, (A);

$\cos\varphi$ —power factor.

Among them, ac voltage is measured by voltmeter on distribution cabinet; ac current is measured by ammeter on distribution cabinet; and power factor is measured by power factor meter.

In the proportion of total energy consumption of vacuum refrigerator, the power consumption of compressor, vacuum pump and other equipment accounts for about 68%, 18% and 14% of the total energy consumption respectively [13]. From the above analysis, it can be seen that the compressor and vacuum refrigeration pump are the main energy

consumption parts. Therefore, the current main energy-saving measures are mainly aimed at the compressor and vacuum refrigeration pump. The adjustment of cooling capacity and energy consumption of vacuum refrigeration pump can be achieved by controlling the pumping speed of vacuum refrigeration pump or the number of vacuum refrigeration pumps. Therefore, the following will introduce a new energy-saving device of vacuum refrigerator to explore the impact of the number of vacuum refrigeration pumps on the total energy consumption of vacuum refrigerator.

3. A Novel Energy-Saving Device of Vacuum Refrigerator

In this paper, an energy-saving device of vacuum freezer is introduced, which can realize refrigeration of multiple vacuum freezers at the same time with only one vacuum refrigeration pump. The energy-saving device has applied for Chinese patent (national application number: CN202110091271.2), and its structure diagram is shown in Figure 1.

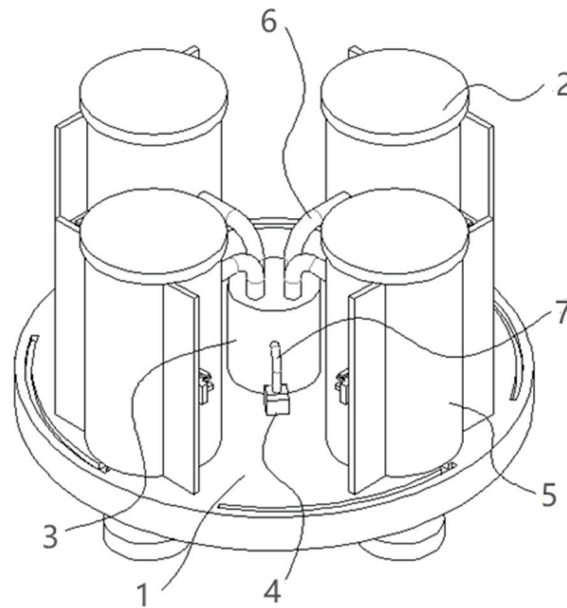


Figure 1. Energy saving device of vacuum refrigerator. 1—base, 2—vacuum freezing storage tank, 3—cold air conveying box, 4—vacuum refrigeration pump, 5—sealing door, 6—conveying pipe, 7—air duct.

3.1. Composition of Energy-Saving Device

The energy-saving device of vacuum refrigerator is shown in Figure 1. The energy-saving device consists of a base, a cold air delivery box, a vacuum refrigeration pump, a delivery pipe and an air duct and a number of vacuum refrigeration storage tanks, etc.

The device comprises a base. The upper surface of the base is fixedly connected with a vacuum freezing storage tank in a circumferential direction. The center of the upper surface of the base is fixedly connected with a cold air conveying box. A conveying pipe is arranged at the top of the cold air conveying box. One end of the conveying pipe penetrates through the inner wall of the vacuum freezing storage tank. A vacuum pump is fixedly arranged on the upper surface of the base. The output end of that vacuum pump is fixedly connected with an air duct. A first mounting plate is symmetrically fixed on the outer wall of the vacuum freezing storage tank. One side of that first mount plate is provided with a mounting groove. A sealing door is clamped inside the installation groove.

3.2. Connection Mode of Energy-Saving Device Components

The connection mode of each component is as follows: a cold air delivery box is arranged at the center of the base. A vacuum refrigeration pump is arranged on the base and connected with the cold air delivery box through an air duct. A number of vacuum freezing storage tanks are circumferentially distributed on the base around the outside of the cold air conveying tank, and each vacuum freezing storage tank is connected with the cold air conveying tank through a conveying pipe.

3.3. Specific Embodiments of Energy-Saving Devices

In this embodiment, it is preferred that the base is in the shape of a disc, the cold air conveying box is arranged at the center of the disc, one end of the air duct is connected with the top of the cold air conveying box and the other end is connected with the vacuum freezing storage tank. The cold air in the cold air conveying box can be transmitted to each vacuum freezing storage tank to realize the low temperature control inside the vacuum freezing storage tank. As shown in Figure 1, there are four vacuum freezing tanks, which are evenly distributed near the edge of the disc. The vacuum refrigeration pump is installed on the upper surface of the base and communicates with the cold air delivery box through an air duct. In this embodiment, it is further preferred that both the cold air delivery box and the vacuum freezing storage tank are provided with insulation layers.

As shown in Figure 2, in which Figure 2a is a schematic side view of the energy-saving device of the vacuum freezer with the sealing door closed, we can see the base located below, and the sealing door is arranged on the outward side of the vacuum freezer tank. Figure 2b is a partially enlarged schematic diagram of the area A in Figure 2a, which is a part of the box locking mechanism. The area A is arranged on the vacuum freezing storage tank and includes a positioning plate, a first mounting plate perpendicular to the positioning plate, a second mounting plate parallel to the positioning plate and a limit clip passing through the mounting plate.

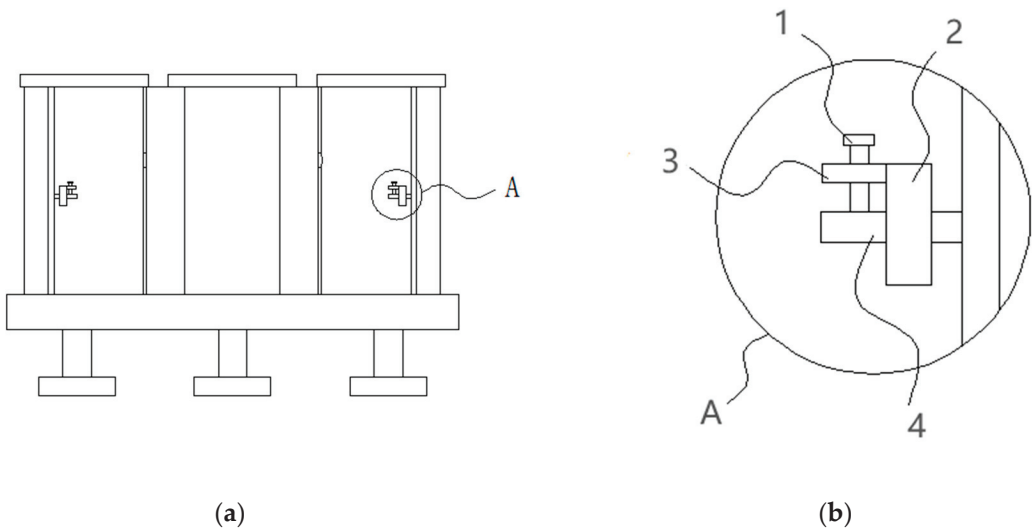


Figure 2. Schematic side view of energy saving device of vacuum refrigerator. (a) schematic side view of energy-saving device of vacuum freezer with closed sealing door; (b) partial enlarged schematic diagram of area A. 1—limit clip, 2—first mounting plate, 3—second mounting plate, 4—positioning plate.

As shown in Figure 3, in which Figure 3a is a structural schematic diagram of the energy-saving device of the vacuum freezer without the sealing door, we can clearly see the situation inside the vacuum freezer. It can be seen that the chute is composed of an annular chute (a section of arc chute) which is arranged outside the vacuum freezing storage tank and runs along the circumferential direction of the cold air delivery tank, and a radial chute which is arranged between the outward side of the vacuum freezing storage tank and the annular chute. Furthermore, preferably, one end of the circumferential chute is located in front of the outward side of the vacuum freezing tank, and the radial chute is connected with the end of the circumferential chute. Figure 3b is a partially enlarged schematic diagram of area B in Figure 3a, which is also a part of the box locking mechanism. The area B is arranged on the vacuum freezing storage tank and includes a first mounting plate perpendicular to the positioning plate and a second mounting plate parallel to the positioning plate. The first mounting plate is provided with a mounting slot for the positioning plate to pass through, and the second mounting plate is provided with a second limiting hole.

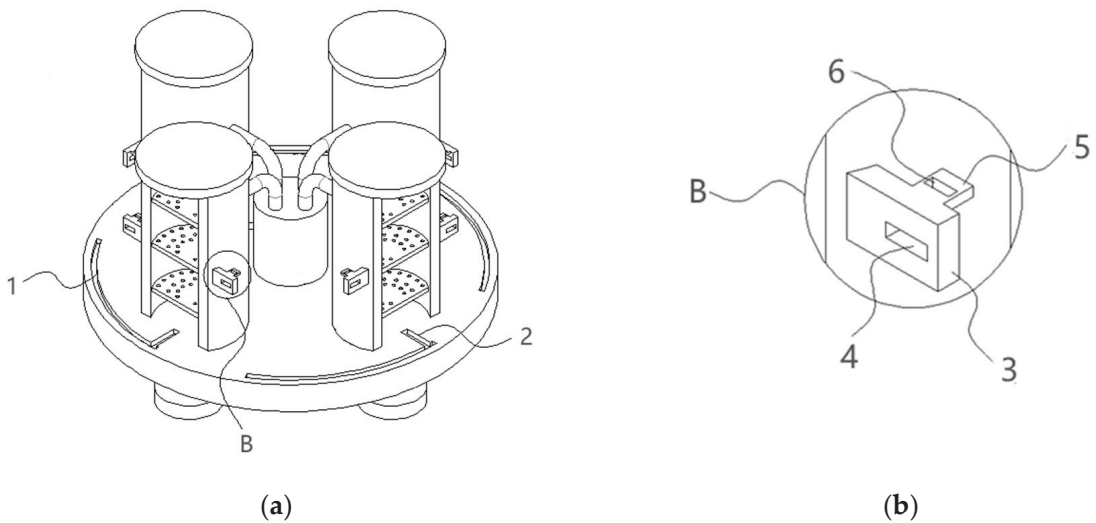


Figure 3. Schematic diagram of the structure of the energy-saving device of the vacuum refrigerator (the sealing door is not shown). (a) Structural schematic diagram of the energy-saving device of the vacuum freezer without the sealing door; (b) partial enlarged schematic diagram of area B. 1—circumferential chute, 2—radial chute, 3—first mounting plate, 4—mounting groove, 5—second mounting plate, 6—second limiting hole.

As shown in Figure 4, in which Figure 4a is a schematic diagram of the front structure of the sealing door, it is preferred that the sealing door is composed of a sealing door body for sealing with the vacuum freezing storage tank and support plates symmetrically arranged on both sides of the sealing door body. This constitutes a door locking mechanism, which includes a positioning plate and a first limiting hole provided on the positioning plate. Figure 4b is a left structural diagram of the sealing door, which is also a part of the locking mechanism of the box body. Preferably, the chute assembly consists of a chute arranged on the base and a limit slider arranged at the bottom of the sealing door and slidably connected with the chute. Further, it is preferable that the sealing door body is filled with an insulating layer, as shown in Figure 4c,d.

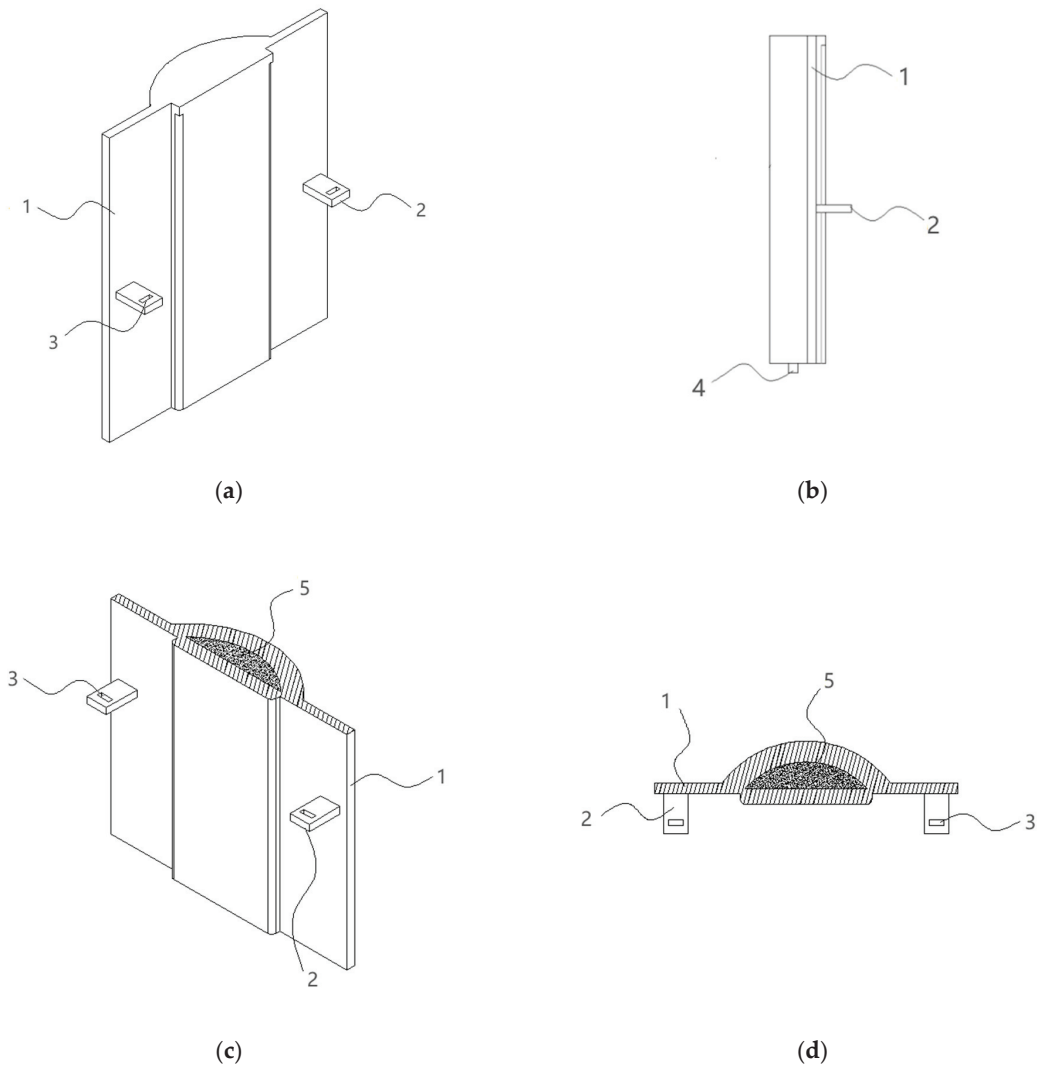


Figure 4. Schematic diagram of related structure of sealing door. (a) Front view; (b) side view; (c) interior view; (d) top view. 1—support plate, 2— positioning plate, 3—first limit hole, 4—limit slider, 5—insulation layer.

From the above Figures 1–4, it can be seen that the sealing door is arranged on the outward side of the vacuum freezing storage tank, and the sealing door can move in the circumferential direction relative to the cold air delivery tank on the base through the chute assembly to realize opening and closing and can be locked with the vacuum freezing storage tank in the closed state through the locking assembly. Preferably, the locking assembly comprises door locking mechanisms arranged on two supporting plates and box locking mechanisms symmetrically arranged on both sides of the vacuum freezing storage tank and matched with the door locking mechanisms. The locking assembly also includes a limiting clip penetrating through the first limiting hole and the second limiting hole (from top to bottom), which is used for realizing the stable attachment between the sealing door and the vacuum freezing storage tank.

As shown in Figure 5, the blue road map is the refrigerant water road map, the red road map is the cooling water circulation road map and the rest of the dotted lines are the data output routes.

In order to reflect the energy-saving characteristics of this device, a simulation connection diagram of the control device is constructed according to the same principle. This is the second scheme, which has a set of absorption refrigeration and four vacuum refrigeration pumps, and its simulation connection diagram is shown in Figure 6.

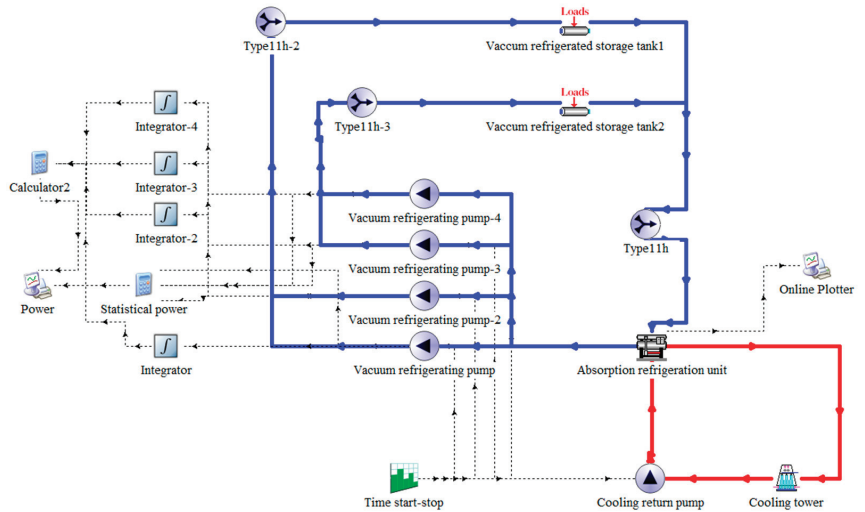


Figure 6. Scheme 2: simulation connection diagram of control device.

Then, the simulation connection diagram of Scheme 3 and Scheme 4 is constructed. Scheme 3 has two groups of absorption refrigeration units and a single vacuum refrigeration pump, and its simulation connection diagram is shown in Figure 7 below. Scheme 4 has a set of absorption refrigeration units and two vacuum refrigeration pumps, and its simulation connection diagram is shown in Figure 8 below.

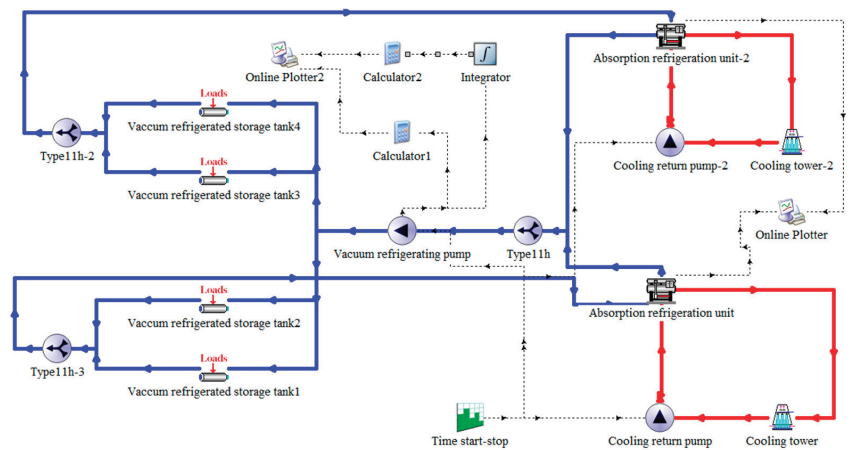


Figure 7. Scheme 3: simulation connection diagram of a single vacuum refrigeration pump.

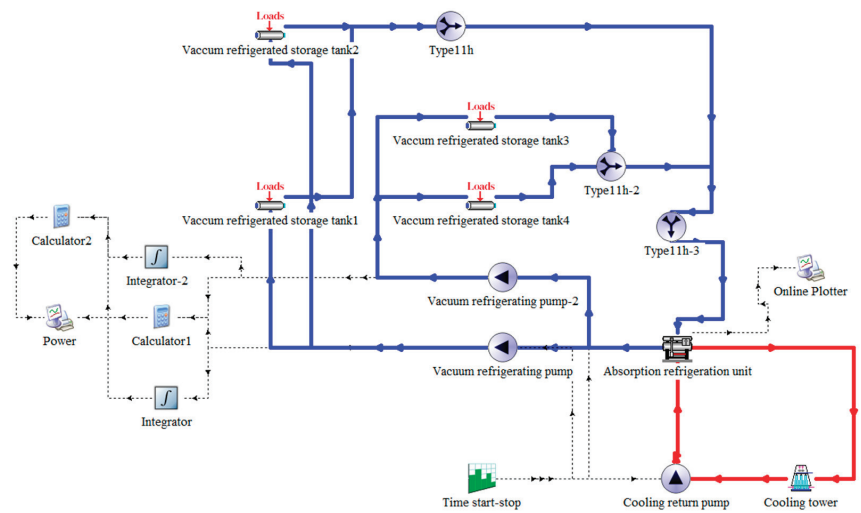


Figure 8. Scheme 4: simulation connection diagram of two vacuum refrigeration pumps.

4.2. Simulation Parameter Setting

The absorption refrigeration unit used in this paper is lithium bromide water absorption refrigeration unit. Because the selection of lithium bromide absorption refrigeration unit should consider the refrigerant itself and the cooling capacity loss of water system, it should generally be 10–15% larger than the calculated cooling load of air conditioning. To simulate the energy-saving effect of vacuum refrigeration pump, through the online survey data and referring to the model parameters of units on the market, this paper takes xz-30 refrigeration unit as the cooling supply of the simulation system. In the simulation connection diagrams shown in Figures 5–8 above, the refrigerating capacity of the absorption refrigeration unit is 348.8 kW, and the evaporation consumption is less than 900 kg/h. So the rated COP value is set to 2.58, and the inlet temperature of cooling water is 32 °C; the flow rate of refrigerant water and cooling water is set at 90,000 kg/h. Each absorption refrigeration unit is equipped with one cooling tower, the maximum flow rate is 324,000 m³/h and the maximum power of fans is 7.5 kW. The rated power of each vacuum refrigeration pump is set to 15 kW, and the rated power of the cooling water return pump is also set to 15 kW. The time start/stop device controls the start/stop state of the vacuum refrigeration pump and the cooling water return pump and is set to work from 10:00 a.m. to 10:00 p.m. every day.

4.3. Selection of Simulation Module

In this paper, the absorption refrigeration unit adopts type-107, the vacuum refrigeration pump and cooling circulating water pump adopt type-114, the vacuum refrigeration storage tank adopts type-682, the time starter and stop adopts type-14 h, the real-time display and power adopt type-65c, the cooling tower adopts type-51b and the type-11 h is the combined three-way valve, which is used to transfer the chilled water in the absorption refrigeration unit. Furthermore, the shunt flows through the vacuum freezing storage tank and then recombines together to achieve the purpose of chilled water circulation.

4.4. Simulation Running Results

The running time of the simulation connection diagram of this energy-saving device is set to 8760 h (i.e., one year), and the daily working time is from 10:00 a.m. to 10:00 p.m. TRNSYS 16 software can generate the following simulation data diagram by clicking the run button through the simulation module adopted by the user and the set parameter values.

1. According to the simulation Scheme 1 of TRNSYS 16 software, when the rated power of a vacuum refrigeration pump is 15 kW, it can be concluded that the annual cumulative energy consumption of a group of absorption refrigeration units corresponding to a single vacuum refrigeration pump is 54,750 kWh, as shown in Figure 9. At the same time, it can be concluded that the annual refrigerating capacity of a single vacuum refrigeration pump is 32,400 kW, as shown in Figure 10.

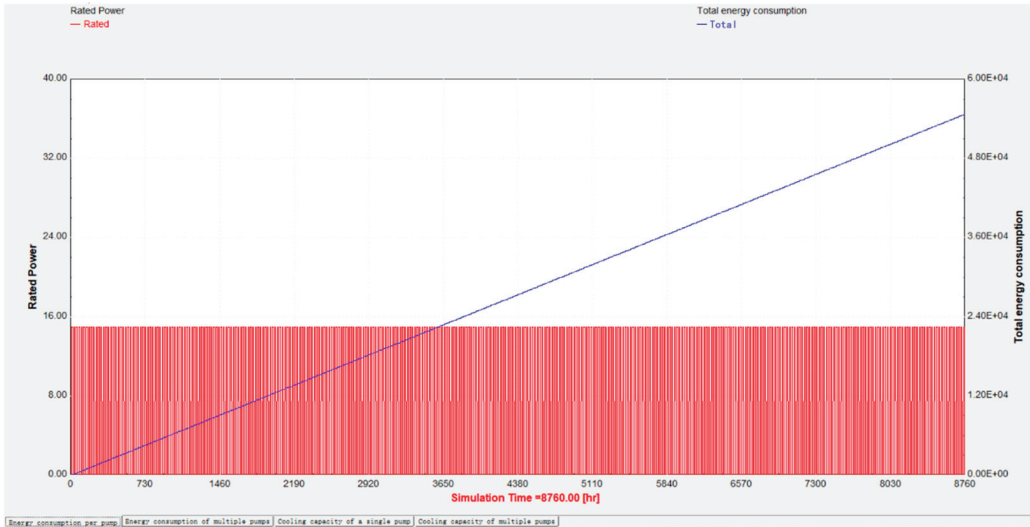


Figure 9. Scheme 1: annual cumulative energy consumption of a single vacuum refrigeration pump (unit: kWh).

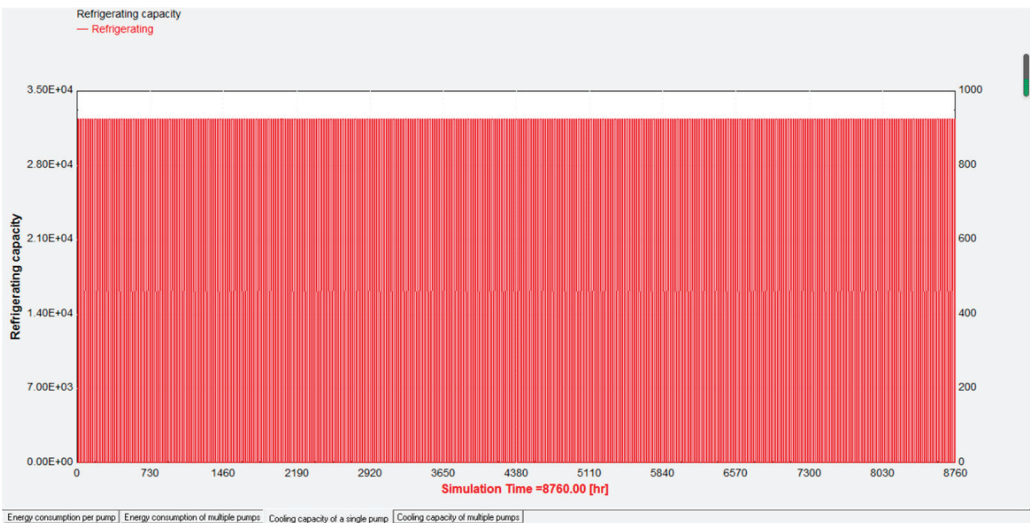


Figure 10. Scheme 1: annual cooling capacity of a single vacuum refrigeration pump (unit: kW).

2. According to the simulation Scheme 2 of TRNSYS 16 software, when the rated power of one vacuum refrigeration pump is 15 kW, that is, the total power of the four vacuum refrigeration pumps is 60 kW, it can be concluded that the annual cumulative energy consumption of a group of absorption refrigeration units corresponding to the four

vacuum refrigeration pumps is 219,000 kWh, as shown in Figure 11. At the same time, it can be concluded that the annual refrigerating capacity of several vacuum refrigeration pumps is 64,800 kW, as shown in Figure 12.



Figure 11. Scheme 2: annual cumulative energy consumption of several vacuum refrigeration pumps (unit: kWh).

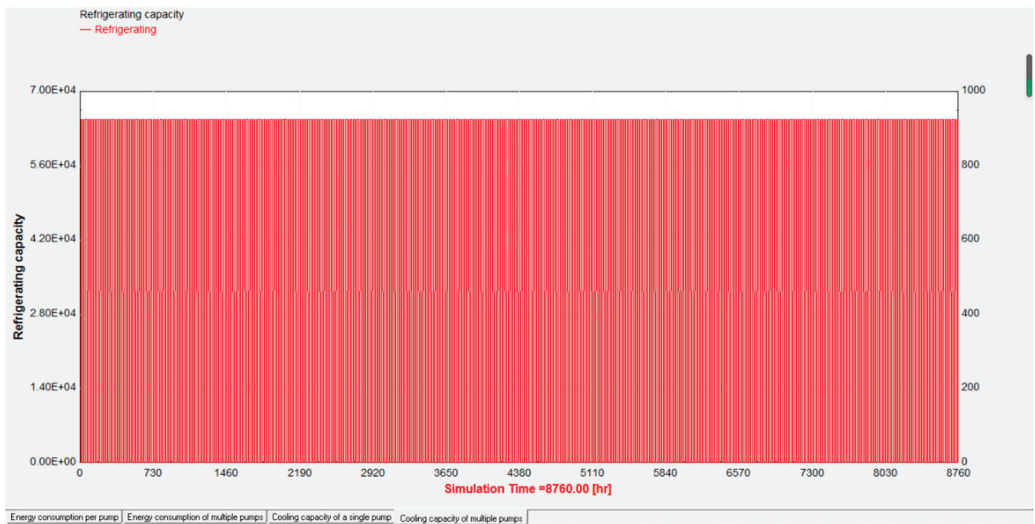


Figure 12. Scheme 2: annual cooling capacity of several vacuum refrigeration pumps (unit: kW).

3. According to the simulation Scheme 3 of TRNSYS 16 software, when the rated power of a vacuum refrigeration pump is 15 kW, it can be concluded that the annual cumulative energy consumption of two groups of absorption refrigeration units corresponding to a single vacuum refrigeration pump is 54,750 kWh, as shown in Figure 13. At the same time, it can also be concluded that the annual refrigeration capacity of a

single vacuum refrigeration pump is 64,800 kW, and its refrigeration capacity is the sum of refrigeration capacity 1 and refrigeration capacity 2, as shown in Figure 14.

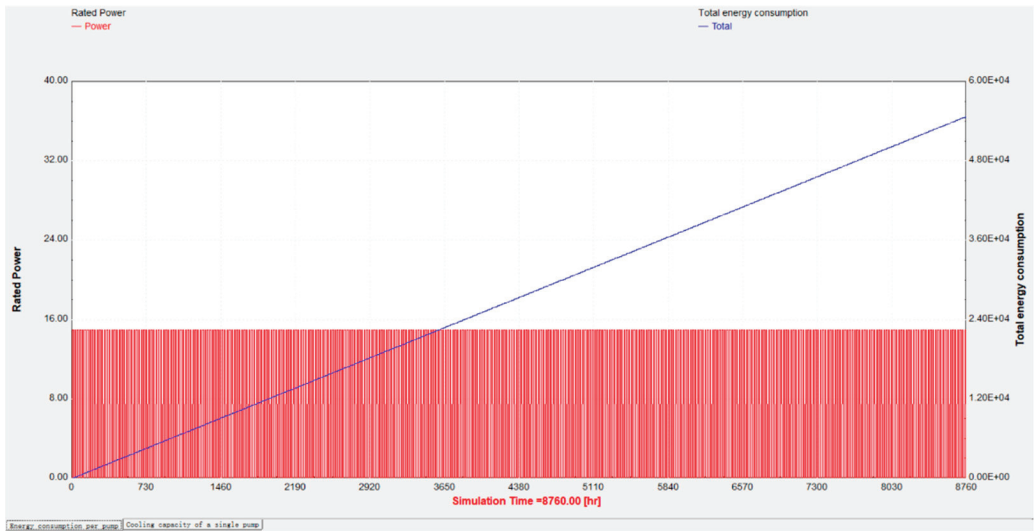


Figure 13. Scheme 3: annual cumulative energy consumption of a single vacuum refrigeration pump (unit: kWh).

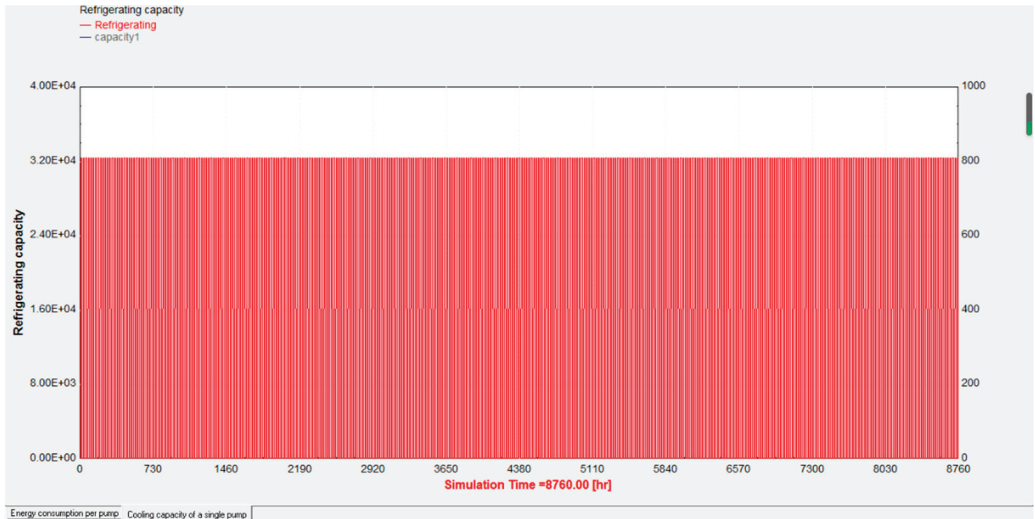


Figure 14. Scheme 3: annual cooling capacity of a single vacuum refrigeration pump (unit: kW).

- According to the simulation Scheme 4 of TRNSYS 16 software, when the rated power of one vacuum refrigeration pump is 15 kW, that is, when the total power of the two vacuum refrigeration pumps is 30 kW, it can be concluded that the annual cumulative energy consumption of a group of absorption refrigeration units corresponding to the two vacuum refrigeration pumps is 109,500 kWh, as shown in Figure 15. At the same time, it can be concluded that the annual refrigerating capacity of several vacuum refrigeration pumps is 64,800 kW, as shown in Figure 16.

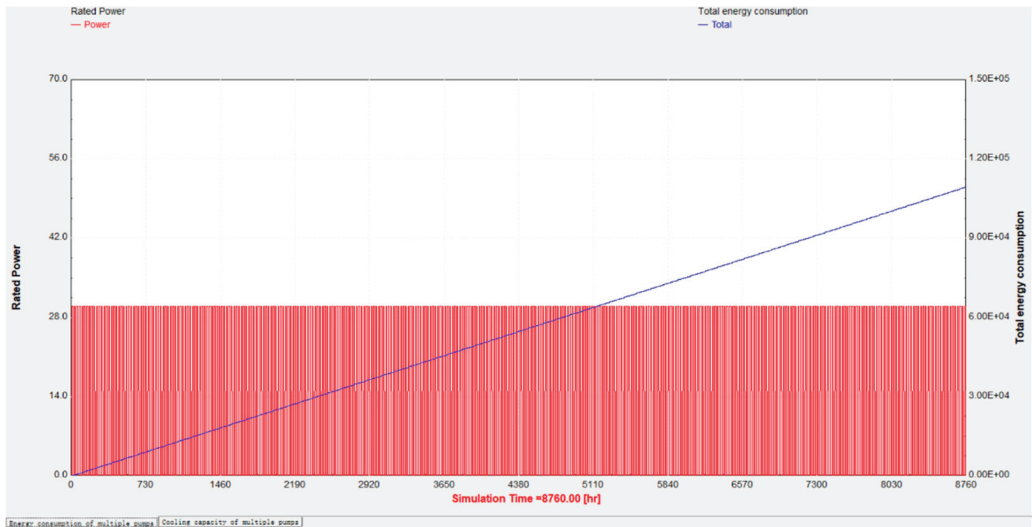


Figure 15. Scheme 4: annual cumulative energy consumption of two vacuum refrigeration pumps (unit: kWh).

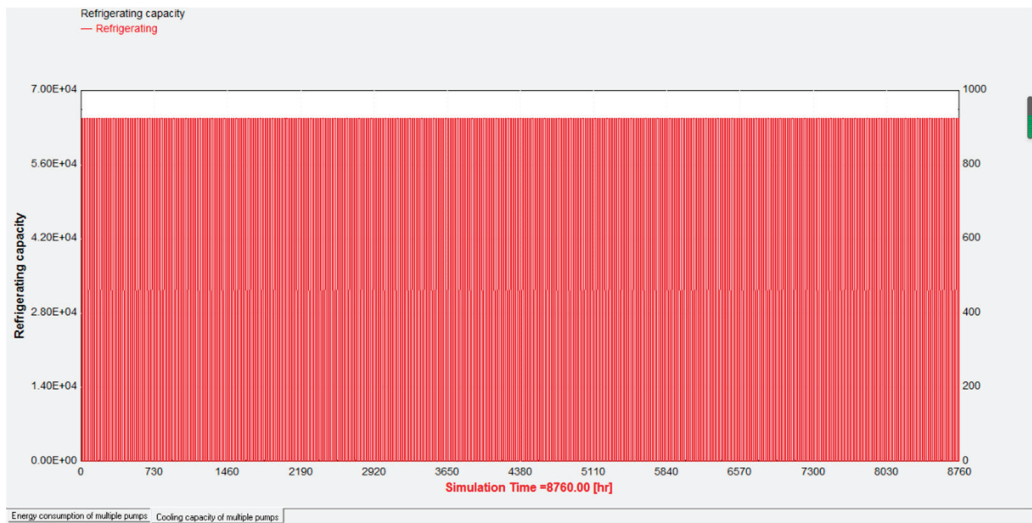


Figure 16. Scheme 4: annual cooling capacity of two vacuum refrigeration pumps (unit: kW).

4.5. Analogue Data Analysis

According to the above Figures 9–16, in Scheme 1, when a single vacuum refrigeration pump works all year round at rated power of 15 kW, the accumulated energy consumption is 54,750 kWh, and the refrigerating capacity provided by a single vacuum refrigeration pump is 32,400 kW. In Scheme 2, it can be seen from the data diagram that several vacuum refrigeration pumps work all year round at rated power of 15 kW, that is, when the total power is 60 kW and the accumulated energy consumption is 219,000 kWh. On average, the accumulated energy consumption of many vacuum refrigeration pumps is the same as that of a single vacuum refrigeration pump, but the refrigerating capacity of many vacuum refrigeration pumps is 64,800 kW, and the average refrigerating capacity of each vacuum refrigeration pump is 16,200 kW, which is 50% less than that provided by a single

vacuum refrigeration pump when working. Scheme 3 also works in the whole year with the rated power of 15 kW, and the accumulated energy consumption is 54,750 kWh, but in this scheme, when two absorption refrigeration units correspond to a single vacuum refrigeration pump, the refrigeration capacity provided by them is 64,800 kW. In Scheme 4, two vacuum refrigeration pumps work at rated power all year round, and the accumulated energy consumption is 109,500 kWh. Compared with Scheme 2, the refrigeration capacity provided is also 64,800 kW. The difference is that Scheme 4 can provide refrigeration for four vacuum refrigeration tanks.

Therefore, under the same energy consumption, the same load conditions and the same power and energy consumption, when a number of refrigeration pumps operate, the refrigeration capacity provided by a single refrigeration pump is worse than that provided by a single refrigeration pump. This causes some of the refrigeration pumps to be in a working state of wasting energy consumption, resulting in excessive energy consumption, unnecessary consumption and increased operation cost. Therefore, under the same circumstances, using a single vacuum refrigeration pump can reduce the use of vacuum refrigeration pumps, thus reducing the number of vacuum refrigeration pumps put into operation, reducing the energy consumption of vacuum refrigeration pumps, effectively reducing the total energy consumption loss of the energy-saving device and finally achieving the effect of energy saving and emission reduction.

5. Discussions

1. According to the simulation of the whole-year operation of the energy-saving device of the vacuum refrigerator by TRNSYS 16 software, it can be seen from the simulated data that compared with the original existing technology, when the rated power is 15 kW, the energy consumption accumulated by a single vacuum refrigeration pump in the whole year is the same as that accumulated by each vacuum refrigeration pump averaged by a number of vacuum refrigeration pumps, which is 54,750 kWh. However, the refrigerating capacity of a single vacuum refrigeration pump is 50% higher than the average refrigerating capacity of each vacuum refrigeration pump, which is 32,400 kW. Therefore, the vacuum freezer avoids the waste of energy taste and can achieve the effect of saving energy and reducing consumption.
2. Comparing the third scheme with the first scheme, it can be seen that when a single vacuum refrigeration pump corresponds to two refrigeration units, the refrigeration capacity provided is 64,800 kW, and cold air is provided for four vacuum refrigeration tanks. For comparison, Scheme 1 of two groups need two vacuum refrigeration pumps to supply cold air to four vacuum refrigeration tanks. It can be seen from the comparison between Scheme 1 and Scheme 3 that only one vacuum refrigeration pump is needed in Scheme 3 to supply refrigeration to four vacuum refrigeration storage tanks, which effectively reduces the use of vacuum refrigeration pumps and greatly reduces the energy consumption in operation.
3. Comparing Scheme 4 with Scheme 2, in Scheme 4, only two vacuum refrigeration pumps are needed, which can provide refrigeration for four vacuum refrigeration storage tanks under the condition of reaching the same refrigeration capacity of 64,800 kW. So it can be seen that in Scheme 2, two of the four vacuum refrigeration pumps operating all year round are in a no-load state, which undoubtedly increases the operation energy consumption and working cost. However, there is also a problem in Scheme 4 that the average distribution of refrigeration capacity of each vacuum freezing storage tank is not as much as that in Scheme 2, which may result in the technological requirements of frozen materials not being able to be met. Therefore, the relationship between advantages and disadvantages in Scheme 4 still needs to be judged separately.
4. In today's technology, each vacuum refrigerator, i.e., vacuum refrigeration storage tank, has a separate refrigeration system. However, when multiple vacuum refrigeration storage tanks are required for production at the same time, multiple refrigeration

systems need to be independently connected with multiple vacuum refrigeration pumps to transport chilled water to achieve the purpose of refrigeration. In this way, increasing the use of multiple refrigeration pumps will lead to high energy consumption. The refrigeration capacity of the system is provided by the chilled water of the absorption refrigeration unit, and the vacuum refrigeration pump is used to transport the chilled water to the vacuum refrigeration storage tank. Compared with Scheme 1 and Scheme 3, although Scheme 3 can meet the premise of reducing energy consumption with one vacuum refrigeration pump, the refrigeration capacity provided is twice that of Scheme 1. However, there is the question as to whether increasing the use of pumps will really affect the cooling capacity. According to Schemes 1, 2, and 4, it is not that increasing the number of vacuum refrigeration pumps can affect the rate of conveying chilled water and improve the refrigeration capacity. On the contrary, it may make the transportation speed of chilled water too fast and affect the heat exchange with the materials in the vacuum refrigeration storage tank. The contact time is too short, resulting in poor refrigeration effect, futile increase in the number of refrigeration pumps and increased energy consumption.

6. Conclusions

1. Compared with the prior art, the energy-saving device can realize the refrigeration of a number of vacuum freezers at the same time with only one vacuum refrigeration pump, thereby greatly reducing the use of the vacuum refrigeration pump, greatly reducing the energy consumption and meeting the environmental protection concept of energy conservation and emission reduction.
2. According to the device, the sealing door can slide along the circumferential chute and the radial chute through the design of the circumferential chute, the radial chute, the sealing door, the second limiting hole, the first limiting hole and the limiting clamping strip, so that the flexible movement of the sealing door on the base is realized, the occupied space of the sealing door is greatly reduced and the utilization rate of space is greatly improved.
3. Compared with conventional devices, the energy-saving device has remarkable energy-saving effect and can save energy and reduce consumption and refrigeration operation cost by reducing the use of vacuum refrigeration pumps put into operation.
4. The limitation of this work is that it is currently in the stage of simulation theory experiment. At present, there are few relevant studies on reducing energy consumption by driving multiple vacuum refrigeration storage tanks by a single vacuum refrigeration pump. The simulation content of this paper may have some deviation in the actual situation, and the results need to be verified through further research, analysis and practice.

Author Contributions: Conceptualization, N.Z. and Y.G.; methodology, N.Z.; software, W.Y.; validation, N.Z., Y.G. and Y.L.; formal analysis, N.Z.; investigation, N.Z.; resources, Y.G.; data curation, N.Z. and W.Y.; writing—original draft preparation, N.Z.; writing—review and editing, N.Z.; visualization, N.Z.; supervision, Y.G. and Y.L.; project administration, Y.G.; funding acquisition, Y.G. All authors have read and agreed to the published version of the manuscript.

Funding: This paper is supported by National Natural Science Foundation of China (Grant No. 51606116) and Major Scientific and Technological Research Projects of Shanghai Science and Technology Commission (Grant No. 19195810800).

Institutional Review Board Statement: Not applicable.

Informed Consent Statement: Not applicable.

Data Availability Statement: The data presented in this study are available on request from the corresponding author.

Conflicts of Interest: The authors declare no conflict of interest.

References

1. Xi Jinping's Special Speech at the World Economic Forum's Davos Agenda Dialogue. Available online: <https://baijiahao.baidu.com/s?id=1689862031132475454&wfr=spider&for=pc> (accessed on 25 January 2021).
2. Huang, J.; Jiao, F. Research on the coupling relationship between energy consumption and carbon emission in view of high-quality development of economy. *Ecol. Econ.* **2021**, *37*, 22–27+34.
3. *BP Statistical Review of World Energy*; BP: London, UK, 2020.
4. Hu, X. *Energy Management*; Aerospace Press: Beijing, China, 1993; pp. 6–8.
5. Wu, Y. Energy-the motive force of human society's production and life. *Econ. Geogr.* **1983**, *1*, 72–76.
6. Du, M.; Chen, J. Validation method of vacuum freeze dryer. *Metro. Meas. Technol.* **2018**, *45*, 51–53.
7. Ren, H. Vacuum freeze drying technology and its application in the field of traditional Chinese medicine. *Mech. Electr. Inf.* **2016**, *4*, 12–21.
8. Zhou, Z.; Guo, Y.; Lin, Y. Energy-saving evaluation of a solar integrated vacuum freeze-dryer and building air conditioning system. *Energy Explor. Exploit.* **2021**, *39*, 608–619. [[CrossRef](#)]
9. Zhang, S.; Luo, J.; Chen, G.; Wang, Q. Thermodynamic analysis of a freeze-dryer utilizing hygroscopic solution. *Dry. Technol.* **2018**, *36*, 697–708.
10. Liu, Y.; Zhao, Y.; Feng, X. Exergy analysis for a freeze-drying process. *Appl. Therm. Eng.* **2007**, *28*, 675–690. [[CrossRef](#)]
11. Luo, N.; Shu, H. Analysis of Energy Saving during Food Freeze Drying. *Procedia Eng.* **2017**, *205*, 3763–3768. [[CrossRef](#)]
12. Rahman, S.M.A.; Saidur, R. A novel atmospheric freeze dryer using simultaneous application of subzero and hot air streams using a vortex chiller. *Dry. Technol.* **2016**, *34*, 1406–1413. [[CrossRef](#)]
13. Han, H. Energy Consumption Analysis and Energy Saving Technology Research of Vacuum Refrigeration Equipment. *Chin. J. Refrig. Technol.* **1994**, *4*, 16–21.
14. Yan, G.; Liu, Y.; Qian, S.; Yu, J. Theoretical study on a vapor compression refrigeration system with cold storage for freezer applications. *Appl. Therm. Eng.* **2019**, *160*, 114091. [[CrossRef](#)]
15. Ana, G.R.G.; Pieter, J.V.B.; Steven, D.M.; Thomas, D.B.; Jos, C.; Jo, D. Analysis of a pharmaceutical batch freeze dryer: Resource consumption, hotspots, and factors for potential improvement. *Dry. Technol.* **2019**, *37*, 1563–1582.
16. Wang, J.; Wang, W.; Ren, X.; Jia, Y. Exergy analysis of the vapor compression refrigeration. *J. Hebei Univ. Eng. Nat. Sci. Ed.* **2008**, *4*, 71–73+80.
17. Ma, L. Design and structural optimization of sealing trolley in liquid batching line. *Wuhan Polytech. Univ.* **2018**.
18. Yuan, Y. Study on energy saving of vacuum cooling device. *Mech. Electr. Equip.* **2008**, *4*, 23–26+31.
19. He, T.; Chen, P. Analysis and treatment of common faults in refrigeration system of freeze dryer. *Mech. Electr. Inf.* **2021**, *9*, 20–21.
20. Wang, J. Analysis of common problems in refrigeration system of freeze dryer. *Sci. Techno. Vis.* **2014**, *4*, 91.
21. Bai, X.; Sun, C.; Guo, L.; Wang, H. Tests and analysis on energy consumption of heating ventilating and air-conditioning systems in commercial buildings. *J. Chongqing Univ.* **2008**, *6*, 637–641.
22. Xie, Z.; Gong, Y.; Ye, C.; Yao, Y.; Liu, Y. Numerical Analysis and Optimization of Solar-Assited Heat Pump Drying System with Waste Heat Recovery Based on TRNSYS. *Processes* **2021**, *9*, 1118. [[CrossRef](#)]

Article

Psychological Drivers of Hotel Guests' Energy-Saving Behaviours—Empirical Research Based on the Extended Theory of Planned Behaviour

Qian-Cheng Wang ¹, Ke-Xin Xie ², Xuan Liu ³, Geoffrey Qi Ping Shen ², Hsi-Hsien Wei ^{2,*} and Tian-Yi Liu ⁴¹ Department of Land Economy, University of Cambridge, Cambridge CB3 9EP, UK; qw250@cam.ac.uk² Department of Building and Real Estate, The Hong Kong Polytechnic University, Hong Kong 999077, China; zoexk.xie@connect.polyu.hk (K.-X.X.); geoffrey.shen@polyu.edu.hk (G.Q.P.S.)³ Department of Built Environment, Eindhoven University of Technology, 5600 MB Eindhoven, The Netherlands; x.liu1@tue.nl⁴ Department of Engineering, University of Cambridge, Cambridge CB2 1AG, UK; tl499@cam.ac.uk

* Correspondence: hsi-hsien.wei@polyu.edu.hk

Abstract: The hospitality industry is an important energy consumer and carbon emitter. Behaviour-driven energy conservation is a strategy with great promise to strengthen the energy efficiency of hotel buildings. The aim of this study is to explore the driving psychological factors of hotel guests' energy-saving intentions and behaviours. This paper constructs two extensions of the theory of planned behaviour (TPB) with personal norms, past behaviours, and self-determined motivation to explain the guests' energy-saving behaviour in hotel buildings. This research compares the explanatory power of the original TPB and two extensions with structural equation modelling. The analysis is based on 530 valid, self-reported data from 827 surveyed hotel guests in Shanghai. The analysis suggests that the extended model gains greater explanatory power in predicting the behaviour patterns by employing the above three additional factors. In addition, self-determined motivation presents a more significant impact than other more developed TPB predictors, such as intention and perceived behaviour control. Aside from that, past behaviour replaces attitude as the most critical predictor of hotel energy-saving intention in the extended models. In addition to the existing interventions in office and residential buildings, the research highlights the role of self-determination in hotel energy conservation and further emphasises the long-term benefit of encouraging pro-environmental behaviours in hotel guests. The findings expand the existing research on pro-environmental behaviours and will contribute to energy-saving behaviour intervention in hotel buildings and policy formulations for sustainable hotel operation and maintenance.

Citation: Wang, Q.-C.; Xie, K.-X.; Liu, X.; Shen, G.Q.P.; Wei, H.-H.; Liu, T.-Y. Psychological Drivers of Hotel Guests' Energy-Saving Behaviours—Empirical Research Based on the Extended Theory of Planned Behaviour. *Buildings* **2021**, *11*, 401. <https://doi.org/10.3390/buildings11090401>

Academic Editors: Yaolin Lin and Wei Yang

Received: 1 August 2021

Accepted: 6 September 2021

Published: 8 September 2021

Keywords: hotel energy conservation; TPB; personal norms; past behaviour; self-determination; guest behaviour; pro-environmental behaviour

Publisher's Note: MDPI stays neutral with regard to jurisdictional claims in published maps and institutional affiliations.



Copyright: © 2021 by the authors. Licensee MDPI, Basel, Switzerland. This article is an open access article distributed under the terms and conditions of the Creative Commons Attribution (CC BY) license (<https://creativecommons.org/licenses/by/4.0/>).

1. Introduction

The hospitality industry has been recognised as an important energy consumer [1]. Upadhyay and Vadam [2] reported that 60% of carbon emissions from the hospitality industry come from energy consumption, which increased by 25–30% over the last few decades. The excessive energy use burdens hotel operators with operating costs of an additional 3–6% [2]. Governments have promoted policies to reduce the energy use and environmental impacts of the hospitality industry [3]. However, the existing policies aimed at improving hotels' energy efficiency tend to operate by punishing their owners rather than by modifying end users' resource consumption, contributing to 75% of hotels' environmental impacts [4]. Such approaches to regulation have increased the burden on hotel operators but achieved little in energy conservation [4,5].

There are also some other strategies to support sustainable hotel building operation. In addition to promoting eco-friendly energy systems and design (e.g., [6,7]), various em-

pirical studies have examined behaviour-driven energy conservation in family (e.g., [8,9]), office [10], and campus buildings [11] and reported that interventions, such as normative setting and energy-saving tips, can reduce building energy demand by 10–25% [12,13]. As guests tend to consume even more energy in hotels than at home [14], promoting conservation behaviours among hotel guests could be another promising energy-saving and carbon-reduction strategy in the hospitality industry. According to Liu et al. [8] and Lopes et al. [15], behaviour-driven energy conservation strategies presented remarkable feasibility in the previous studies. Particularly, these energy-saving strategies show two obvious advantages for the hospitality industry: (1) they require less capital investment, and (2) they can achieve energy-saving goals relatively quickly. However, there is a critical lack of a systematic understanding of the behavioural factors as energy efficiency promoters [16] and the potential leverage of policies [15].

Some previous studies have looked at hotel guests' waste reduction and water conservation behaviours [17–19]. For example, Han et al. (2020) explored the influence of normative, affective, and habitual factors on guests' water conservation and towel reuse intentions, and another study revealed the impact of environmental awareness on young vacationers' recycling and conservation intentions [19]. These studies have significant contributions to both promoting sustainable behaviour (e.g., [20]) and building and urban energy performance modelling (e.g., [21,22]). However, the psychological mechanisms behind hotel guests' energy conservation behaviour remain underexplored. An in-depth understanding of guests' energy conservation behavioural processes could therefore boost the development of effective interventions.

To bridge these gaps, this study aims to explain hotel guests' energy conservation behaviours from a psychological perspective. The researchers surveyed 827 hotel guests in Shanghai and invited the respondents to report their psychological information and four typical hotel energy conservation behaviours during their stays. The study first reviews the existing literature on the green hotel visiting and pro-environmental behaviours of hotel guests. Next, this research employs the theory of planned behaviour (TPB) and two extended models as the theoretical frameworks and conducts structural equation modelling analysis to gauge how psychological factors impacted energy conservation intentions and behaviours. The Section 3 then discusses the data collection and analysis method. The Section 4 presents the data analysis results in detail. This study is expected to shed new light on understanding the critical psychological factors of hotel guests on their energy-saving behaviours and inform the design of psychological interventions for hotel guests for sustainable hospitality sector development.

2. Literature Review

2.1. Green Hotels and Guest Behaviours

Over the past decade, the hotel industry has paid increasing attention to environmental responsibility and sustainability. In addition to promoting eco-friendly construction and high-efficiency building services, some studies have advanced the concept of green hotels and sustainable hotels [23]. As well as attaching great importance to environmental responsibility in a general sense [24], green hotel operation strategies encourage hotels to reduce unnecessary services through more environmentally friendly room and catering management [25]. This operating mode can also potentially boost profits, not only by reducing operating costs, but also by attracting guests who value environmental protection.

Some scholars have explored the behavioural dimensions of visiting green and sustainable hotels. For example, an empirical study employing self-reported data from the United States sought to explain sustainable hotel visiting intention using the theory of reasoned action (TRA) and TPB (for details, see Section 2.2) [26]. Similarly, Rahman and Reynolds (2019) investigated the effect of environmental value on sustainable hotel visiting intention and guests' willingness to make sacrifices when staying in such hotels. In addition, some studies have analysed the characteristics of guests visiting green hotels. For example, empirical evidence found that business and leisure travellers held different attitudes towards

green hotel visiting [27], and a few studies have proposed and implemented behavioural interventions to promote green hotel visiting [28]. However, the operation of green hotels also faces challenges. Barber [29] examined individual preferences about hotel offerings of products and services and found that less than a quarter of green hotel guests were willing to accept reduced services.

Some researchers argued that hotels should encourage guests to actively reduce their wasteful behaviour rather than passively endure reduced levels of service [18,19,30]. Based on the above research, the conservation behaviours of hotel guests can be usefully subdivided into energy conservation, water conservation, and the reduction of unnecessary hotel services, and some studies have provided psychological explanations of the latter two behavioural categories. Untaru et al. [17], for instance, developed an extended TRA to explain hotel guests' water conservation behaviour, while Han et al. [18] highlighted the contributions of environmental value, concerns, and awareness to two hotel guests' pro-environmental behaviours. Additionally, a few studies have developed psychological interventions to promote towel reuse behaviour. Reese et al. [31] observed that social normative information significantly enhanced towel reuse during 132 visits to 2 hotels, and Gössling et al.'s large field experiment in Spain established that normative messages increased towel reuse by 6.8% and bed linen reuse by 1.2% [32].

Behaviour-based hotel energy conservation shows strong potential in the hospitality industry. Ayoub et al. [33] analysed a hotel case in Qatar and found that the energy consumption could be cut down by 2.74–15.80% through energy-saving behaviour promotion, while the energy-saving potential of envelope redesign was only 7.50%. An empirical study in China also reported that by adjusting guests' usage of air conditioning, hotels in the Yangtze River region in China could save up to 20% on energy consumption [34]. The above studies divided the hotel energy-saving behaviours into four categories: (1) sustainable use of air conditioning; (2) sustainable use of other hotel appliances; (3) hot water conservation; and (4) persuading others to save energy. Although the above studies thoroughly discussed sustainable behaviours in hotels, there is a critical lack of a systematic understanding of energy-saving behaviours of the guests in hotels. As a result, industry and research community interest in behaviour-driven hotel energy-saving approaches has thus far been minimal.

2.2. Theory of Planned Behaviour and Its Extension

Over the past half-century, several psychological models for explaining individual behaviours have been proposed. In the case of voluntary behaviours, Ajzen and Fishbein [35] developed and elaborated the TRA, which assumes that people's decision-making processes are based on rationality and can yield reasonable choices, but a variety of factors may affect behaviour indirectly via behavioural intentions [36]. Ajzen subsequently proposed the TPB [37], an extension of the TRA aimed at a more extensive explanation and better prediction of both voluntary and involuntary behaviours. The TPB employs three psychological variables to explain behavioural intentions: attitude, subjective norms, and perceived behavioural control (PBC). According to Ajzen [38], attitude describes a person's general evaluation of a specific behaviour; subjective norms reflect his or her perceptions of the feelings of others about that behaviour, which often have a major influence on individual decision making; and PBC is the individual's perception of how easy or hard it would be to engage in the behaviour. In addition to intention, PBC is another factor potentially related to behaviour and decision.

According to Han and Yoon [39,40], the TPB remains one of the most influential behaviour frameworks in the field of environmental psychology. Previous studies have employed it to explain common green behaviours, including but not limited to recycling (e.g., [41,42]), using public transportation (e.g., [43]), consumption of organic food (e.g., [44]), sustainable consumption and investment (e.g., [45]), and household energy conservation (e.g., [8,46]). Some scholars have used the TPB for predicting pro-environmental behaviours in the specific sphere of hotel management, whether for employees (e.g., [47]) or

guests (e.g., [18,48,49]). Others (e.g., [50,51]) have used the TPB to predict consumers' green hotel visiting intentions. Some studies, however, found that the TPB's variables do not contribute significantly to certain pro-environmental behaviours, such as Hameed et al. [52], who found a non-significant correlation between the attitude towards green products and eco-conscious behaviour. Similarly, Ateş [53] reported that subjective norms could not predict pro-sustainability behaviour, and Liu et al. [8] discovered that the relevance between subjective norms and household energy-saving behaviour was non-significant. After considering the above literature comprehensively, this study puts forward the following four hypotheses in the first theoretical model:

Hypothesis 1 (H1). *Attitude is positively correlated with hotel energy-saving intention.*

Hypothesis 2 (H2). *Subjective norms are positively correlated with hotel energy-saving intention.*

Hypothesis 3 (H3). *Perceived behavioural control is positively correlated with hotel energy-saving intention.*

Hypothesis 4 (H4). *Perceived behavioural control is positively correlated with hotel energy-saving behaviours.*

Hypothesis 5 (H5). *Intention is positively correlated with hotel energy-saving behaviours.*

The TPB can be extended or otherwise modified for use in various contexts [54]. Particularly, many studies have added moral-normative factors to it as a means of boosting its explanatory power (e.g., [50,55]). Klöckner [56] provides a widely accepted definition of moral norms: "The reflection of a personal value system in a given situation (p. 1030)." Unlike subjective norms, moral norms (also called personal norms) emphasise the behavioural effects of personal, internalised emotions. The evidence thus far suggests that moral norms can significantly influence people's intentions to engage in green behaviours. For example, Gao et al. [57] found that the strength of their participants' ethics was positively and significantly correlated with their household energy conservation intentions. Through case studies in Taiwan and India, Chen and Tung [50] and Verma and Chandra [51] all demonstrated the critical role of moral norms in decision making for patronizing green hotels.

Past behaviour is another critical factor potentially contributing to the socio-psychological theoretical framework [58,59]. Past behaviour refers to the "studied behaviour that the participants had performed in the past" [60]. There are several studies that posited and empirically tested the vital role of past behaviour in individuals' pro-environmental decision formation (e.g., [61–63]). In the hospitality industry, Han et al. ([26,58]) provided empirical evidence showing the significant correlation between past behaviour and green hotel visiting intention and bicycle touring. Aside from that, Hu et al. [64] also evidenced the significant impact of past behaviour on zero-litter initiatives in tourism areas. The meta-analysis results of Kunssen et al. [65] suggest that integrating the factor of past behaviour can greatly improve the capability and effectiveness of models predicting and explaining decision making or behavioural processes.

Therefore, the discussion above then leads to two more hypotheses in extended model I (see Figure 1):

Hypothesis 6 (H6). *Personal norms are positively correlated with hotel energy-saving intention.*

Hypothesis 7 (H7). *Past behaviour is positively correlated with hotel energy-saving intention.*

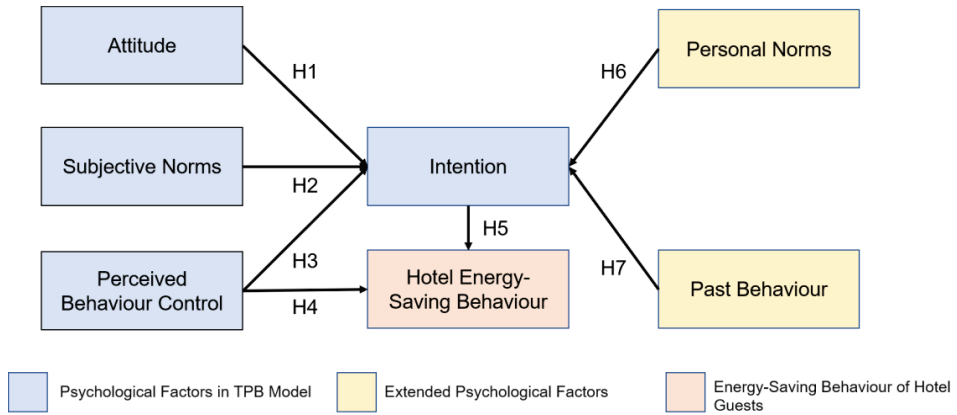


Figure 1. The employed theoretical model and hypotheses in extended model I.

In addition to moral norms and past behaviour, much empirical research suggested self-determined motivation as another potential predictor (e.g., [14,66,67]). Self-determined motivation is an item from the self-determination theory (SDT) and the model of goal-directed behaviour [68]. This item covers these internal driving sources of motivation, such as a need to gain skill, knowledge, and independence [69]. Some recent works have observed the significant roles of self-determined motivation in pro-environmental behaviours (e.g., [70,71]). Several studies that connect the self-determined motivation factor to the conventional TPB model (or extended models) have advocated the synthesis of self-determination (e.g., [67,72,73]), which is also supported by Hagger et al.’s review connecting the TPB and SDT [74]. Aside from that, further substantial evidence supporting that self-determination can influence both intentions (e.g., [67,75]) and choices or behaviours (e.g., [76]). Miao et al. [14] especially examined the impact of self-determination motivation on several pro-environmental behaviours of hotel guests. Considering the above evidence, this research puts forward two more hypotheses in extended model II (see Figure 2):

Hypothesis 8 (H8). *Self-determined motivation is positively correlated with hotel energy-saving intention.*

Hypothesis 9 (H9). *Self-determined motivation is positively correlated with the energy-saving behaviours of hotel guests.*

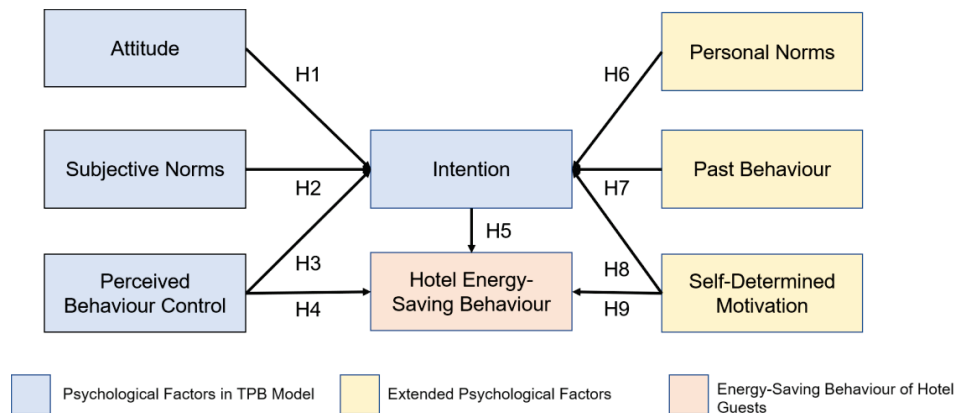


Figure 2. The employed theoretical model and hypotheses in extended model II.

3. Methodology

3.1. The Procedure and the Measures

This research employed a questionnaire-based survey to collect self-reported data from hotel guests. The questionnaire is one of most commonly used methods in pro-environmental behaviour research (e.g., [46,57,77]), which makes it more efficient and more clearly tailored to understanding the characteristics of the target groups than other approaches, such as focus group interviews and government statistics. The researchers convened a three-round pilot study with purposely selected participants. The researchers invited the pilot study participants to provide their feedback via face-to-face discussion, and the researchers then revised the wording, level of detail, and order of some questionnaire items based on those participants' suggestions. Before distributing the questionnaire on a large scale, the researchers conducted a second and third pilot with sample sizes of 30 and 63 guests, respectively, and made further small adjustments to the instrument based on the additional feedback they received. After three rounds of a pilot study, the researchers conducted the questionnaire survey in Shanghai, a representative of the rapidly developing mega cities of Mainland China. In the end, the researchers received 827 completed and partially completed questionnaires, including 530 deemed to have valid data.

The questionnaire had three sections on the respondents' psychological characteristics, energy-saving behaviour evaluation, as well as sociodemographic information. The Section 1 comprised 21 items adapted from previous studies, including [18,26,46,78], covering the psychological variables of the extended TPB in 6 dimensions: attitude, subjective norms, PBC, moral norms, past behaviour, and intention. The Section 2 evaluated the self-reported performance of guests' four typical energy-saving behaviours in hotels. In both of these sections, all the items were responded to with the same 5-point Likert scale, ranging from 1 (completely disagree) to 5 (completely agree). Lastly, the Section 4 of the questionnaire focused on demographic information, including gender, age, education, and income. The items in Sections 1 and 2 are presented in Table 1.

Table 1. Questionnaire design of Sections 1 and 2.

Construct	Code	Item
Attitude	ATT-1	I think that conserving energy when staying in hotels is useful for protecting the environment
	ATT-2	I think energy conservation behaviours in hotels are wise.
	ATT-3	I think energy conservation behaviours in hotels are valuable for alleviating energy shortages.
Subjective Norms	SJN-1	I think my family members want me to save energy in hotels.
	SJN-2	I think my boss and colleagues want me to save energy in hotels.
	SJN-3	I think that people who are important to me want me to save energy in hotels
Perceived Behaviour Control	PBC-1	It is difficult for me to engage in energy conservation behaviours in hotels.
	PBC-2	Whether to engage in energy conservation behaviours in hotels is entirely up to me.
Personal Moral Norms	PMN-1	Saving energy when in hotels is a moral imperative for me.
	PMN-2	Guilty feeling will appear if I did not save energy when in hotels.
	PMN-3	My ethics do not allow me to waste energy when in hotels.
Past Behaviour	PBH-1	I did energy saving behaviours when I visited hotels in the last year.
	PBH-2	I made efforts to save energy when I visited hotels in the last year.
	PBH-3	My efforts to save energy in hotels has increased in the last year.
Intention	INT-1	I am willing to save energy in hotels.
	INT-2	I am willing to make efforts to save energy in hotels.
	INT-3	I am willing to abide by the energy-saving guidelines of the hotels that I am staying in.

Table 1. Cont.

Construct	Code	Item
Self-Determined Motivation	SDM-1	I will feel pleased if I can contribute to the environment.
	SDM-2	I will gain recognition from others by performing energy-saving behaviours in hotels.
	SDM-3	Doing energy-saving behaviour in hotels is an integrate part of my life.
	SDM-4	I will feel guilty if I do not do energy-saving behaviour in hotels.
	SDM-5	I fulfil energy-saving behaviour to avoid be criticised by the public.
Behaviour	HEB-1	I performed well in sustainable A/C use behaviour during this hotel stay.
	HEB-2	I performed well in sustainable appliance and lighting use during this hotel stay.
	HEB-3	I performed well in hot water conservation during this hotel stay.
	HEB-4	I performed well in persuading and encouraging others' energy conservation during this hotel stay.

In practice, participants completed an online survey for a small financial incentive (in the form of a hotel breakfast or voucher). The survey had a time limit of 30 min, and the screen displayed only one question on the screen at a time. The introduction of each section presented a sentence "There is no preferred answer, only your opinion matters" to reduce the potential social desirability bias. Before the start of the survey, the system presented an explanation of the research aim with an e-letter at the beginning of the questionnaire and confirmed their confidential and voluntary participation.

3.2. Data Analysis

This research employed structural equation modelling (SEM) to exam the path coefficient between the factors. SEM has been widely employed in pro-environmental behaviour research, such as that on household energy conservation [46], smartphone recycling [77], sustainable tourism [79], and green hotel visiting [26]. In this study, we employed partial least squares SEM (PLS-SEM) instead of co-variance-based SEM (CB-SEM). In this study, the researchers adopted PLS-SEM for its suitability in explorative research and the targets' prediction and significant flexibility in handling a relatively small sample size in questionnaire-based surveys [80]. This study followed the instructions of Anderson and Gerbing [81] to conduct a two-step analytical procedure (i.e., measurement modelling and structural modelling). SmartPLS 3.0 was employed as the tool in this process.

4. Results

This section reports the respondent profile and the SEM analysis results. The presentation of the SEM analysis results took place in two stages: (1) measurement modelling and (2) structural modelling.

4.1. Respondent Profile

This research collected 530 valid responses, and Figure 3a,b illustrates the sociodemographic information of the respondents who provided valid responses.

Figure 3 presents the demographic characteristics of the 530 questionnaire respondents. The gender ratio of the respondents was basically in line with the local demographic characteristics; female and male respondents accounted for 42.26% and 57.74% of the total, respectively. Aside from that, the age distribution of the respondents also followed the characteristics of the local hotel guests, where customers under the age of 40 made up the majority. It is worth noting that most of the respondents had received a college degree, diploma training, or more, which was higher than the local demographic statistics. In addition, 31.51% of the respondents' income levels ranged from RMB 100,000 (approximately USD 14,285) to RMB 150,000 (approximately USD 21,428), and 25.09% were below RMB 100,000.

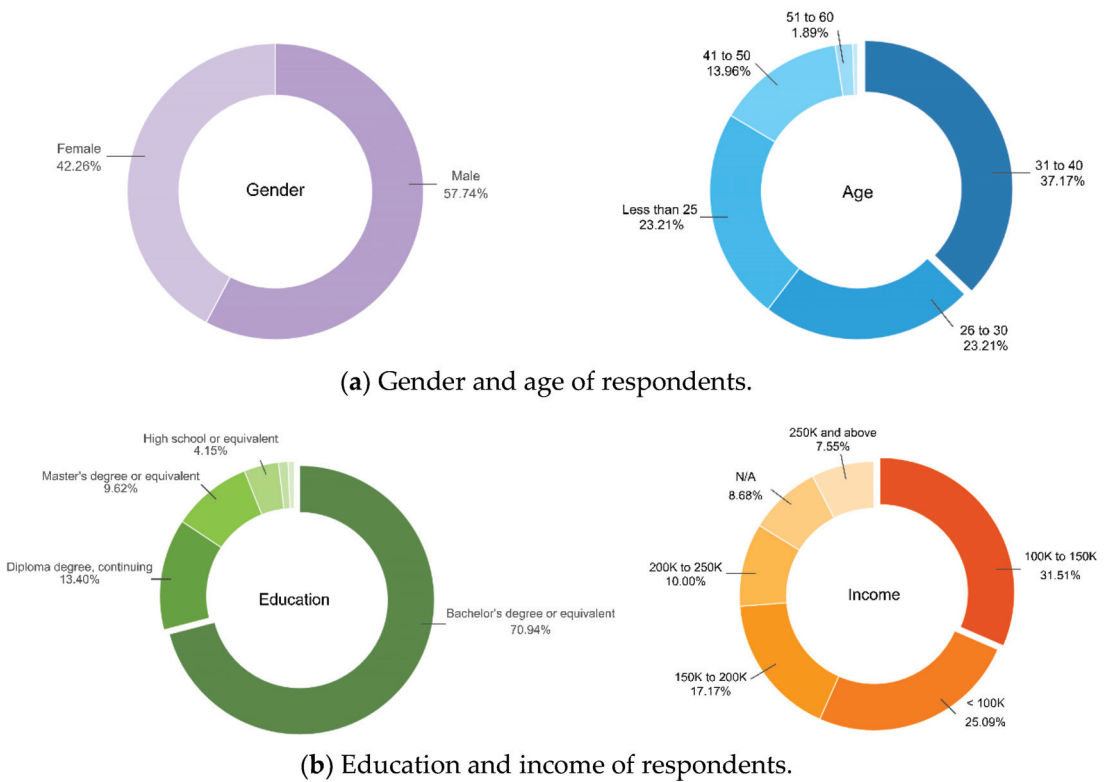


Figure 3. The respondent profiles.

4.2. Measurement Modelling Evaluation

This research conducted analysis by employing SmartPLS 3.0. Measurement modelling was conducted to determine whether the measurement items and structures satisfied the degree of reliability and validity. This study's measurement modelling was divided into the following procedures: (1) a convergent validity (CV) test and (2) a discriminant validity (DV) test. The PLS algorithm method was used to evaluate the internal reliability and consistency of the test items. It had four common criteria: (1) that the factor loading of each item should be greater than 0.5; (2) that the Cronbach's alpha coefficients of each construct should be reported to be 0.5 or above [82]; (3) that the composite reliability of each construct should be larger than 0.7; and (4) that the average variance extracted (AVE) of each construct should be larger than 0.5. Table 2 presents the CV test results and demonstrates that all the constructs in the questionnaire satisfied the CV standard of statistics.

The Heterotrait-Monotrait (HTMT) ratio for DV assessment is also examined in Table 3. The HTMT criterion should be below 0.9 to achieve discriminant validity. The HTMT ratio results in the table suggest that the measurements satisfied the statistical requirements.

Table 2. Convergent validity results of the three models.

Construct	No. of Items	TPB Model			Extended Model I			Extended Model II					
		Loading Range	Cronbach's Alpha	CR	AVE	Loading Range	Cronbach's Alpha	CR	AVE	Loading Range	Cronbach's Alpha	CR	AVE
ATT	3	0.774–0.803	0.694	0.830	0.620	0.774–0.803	0.694	0.830	0.620	0.774–0.803	0.694	0.830	0.620
SJN	3	0.769–0.865	0.763	0.861	0.674	0.769–0.865	0.763	0.861	0.674	0.769–0.865	0.763	0.861	0.674
PBC	2	0.748–0.821	0.739	0.762	0.616	0.748–0.821	0.739	0.762	0.616	0.645–0.823	0.739	0.762	0.616
PMN	3					0.693–0.827	0.627	0.801	0.574	0.693–0.827	0.627	0.801	0.574
PBH	3					0.636–0.799	0.566	0.776	0.538	0.636–0.799	0.566	0.776	0.538
SDM	5									0.567–0.758	0.705	0.803	0.542
INT	3	0.735–0.845	0.733	0.848	0.652	0.743–0.840	0.733	0.849	0.652	0.743–0.839	0.733	0.849	0.652
HEB	4	0.524–0.722	0.526	0.732	0.509	0.524–0.722	0.526	0.732	0.509	0.557–0.675	0.526	0.736	0.512

Table 3. Discriminant validity results.

	ATT	SJN	PBC	PMN	INT	PBH	HEB	SDM
ATT								
SJN	0.652							
PBC	0.838	0.490						
PMN	0.609	0.835	0.592					
INT	0.752	0.507	0.532	0.701				
PBH	0.557	0.310	0.442	0.451	0.882			
HEB	0.619	0.745	0.787	0.823	0.694	0.476		
SDM	0.554	0.704	0.606	0.806	0.645	0.583	0.688	

Note: *SJN* refers to subjective norms, *PBC* refers to perceived behaviour control, *PMN* refers to personal moral norms, *PBH* refers to past behaviour, *HEB* refers to hotel energy-saving behaviour, and *SDM* refers to self-determined motivation.

4.3. Hypotheses Testing and Structural Modelling

The structural model was assessed for its collinearity issues, coefficient of determination (R^2), predictive relevance (Q^2), effect value (f^2), and whether the relationship of the indicators was significant to the structural model. The Variance Inflation Factor (VIF) was employed to evaluate the collinearity statistics, with values suggested to be above 0.20 and 5 [83]. The R^2 value was used to explain the predictive accuracy of the variables, and a value above 0.2 was considered highly accurate [84]. The construct cross-validated redundancy measured the predictive relevance of the variables, and a Q^2 value above 0 indicated acceptable relevance [85]. The effect of a latent predictor was suggested to use the included and excluded R^2 values of the structural model and adopt the formula $f^2 = (R^2_{incl} - R^2_{excl}) / (1 - R^2_{incl})$ for calculation [86]. The small, medium, and large effect sizes used the values of 0.02, 0.15, and 0.35 as bounds, respectively [86].

Table 4 shows the results of the collinearity assessment. The VIF value of the constructs of the model was between 1.058 and 1.653, which indicates that the structure had no collinearity issues.

The results of the coefficient of determination (R^2) and predictive relevance (Q^2) of the three models and f^2 of the two extended models are presented in Table 5. The results indicate that all the R^2 and Q^2 values met the accuracy requirement, and the R^2 increased from 0.419 to 0.545 and 0.553 from the TPB model to the other two extended models, respectively. The value of Q^2 remained at 0.221 for the TPB model and extended model I and grew to 0.263 for extended model II. Thus, the explanation of the three models showed an upward trend from the TPB model to extended model II. The effect value (f^2) for the path to hotel energy-efficient intention and behaviour in extended model I were 0.277 and

0.000, respectively, which indicated a medium and lack of effect, respectively. The value of the effect (f^2) of the hotel energy-efficient intention and behaviour in extended model II rose to 0.300 and 0.057, respectively, which revealed a medium-to-large effect and a small effect, respectively, after adding additional paths. Table 5 presents the coefficient of determination (R^2) and predictive relevance (Q^2) of the three models and the effect value (f^2) of the extended models.

Table 4. Collinearity assessment for the model.

Constructs	VIF								
ATT-1	1.332	PMN-1	1.159	SDM-1	1.339	INT-1	1.543	HEB-1	1.126
ATT-2	1.349	PMN-2	1.370	SDM-2	1.247	INT-2	1.593	HEB-2	1.094
ATT-3	1.372	PMN-3	1.290	SDM-3	1.222	INT-3	1.321	HEB-3	1.126
SJN-1	1.515	PBH-1	1.201	SDM-4	1.468			HEB-4	1.125
SJN-2	1.653	PBH-2	1.272	SDM-5	1.336				
SJN-3	1.511	PBH-3	1.113						
PBC-1	1.058								
PBC-2	1.058								

Note: *ATT* refers to attitude, *SJN* refers to subjective norms, *PBC* refers to perceived behaviour control, *PMN* refers to personal moral norms, *PBH* refers to past behaviour, *SDM* refers to self-determined motivation, *INT* refers to intention, and *HEB* refers to hotel energy-saving behaviour.

Table 5. The results of the coefficient of determination (R^2), predictive relevance (Q^2), and effect value (f^2).

Latent Variables	TPB Model		Extended Model I			Extended Model II		
	R Square	Q^2	R Square	Q^2	f^2	R Square	Q^2	f^2
Intention	0.419	0.267	0.545	0.347	0.277	0.553	0.353	0.300
Behavior	0.221	0.083	0.221	0.083	0.000	0.263	0.101	0.057

After reliability and validity testing, this study employed the bootstrapping method with 5000 resamples to test the significance for structural modelling. The structural modelling results of the three models are summarised in Table 6 and illustrated in Figures 4–6.

Table 6. Structural modelling analysis results.

Path Coefficients	TPB Model			Extended Model I			Extended Model II		
	β	T Values	Sig.	β	T Values	Sig.	β	T Values	Sig.
ATT -> Intention	0.326	6.662	***	0.229	5.179	***	0.220	5.198	***
SJN -> Intention	0.135	2.928	0.003 **	0.036	0.872	0.383	0.007	0.158	0.874
PBC -> Intention	0.356	9.074	***	0.213	5.137	***	0.204	5.101	***
PBC -> Behaviour	0.183	4.074	***	0.184	4.135	***	0.144	3.330	0.001 **
Intention -> Behaviour	0.346	7.650	***	0.346	7.661	***	0.230	4.438	***
PBH -> Intention				0.334	8.808	***	0.308	8.064	***
PMN -> Intention				0.215	5.625	***	0.181	4.622	***
SDM -> Intention							0.120	3.038	0.002 **
SDM -> Behaviour							0.259	5.444	***

Note: (1) *ATT* refers to attitude, *SJN* refers to subjective norms, *PBC* refers to perceived behaviour control, *PMN* refers to personal moral norms, *PBH* refers to past behaviour, *SDM* refers to self-determined motivation, *INT* refers to intention, and *HEB* refers to hotel energy-saving behaviour. (2) *** $p < 0.001$; ** $p < 0.001$.

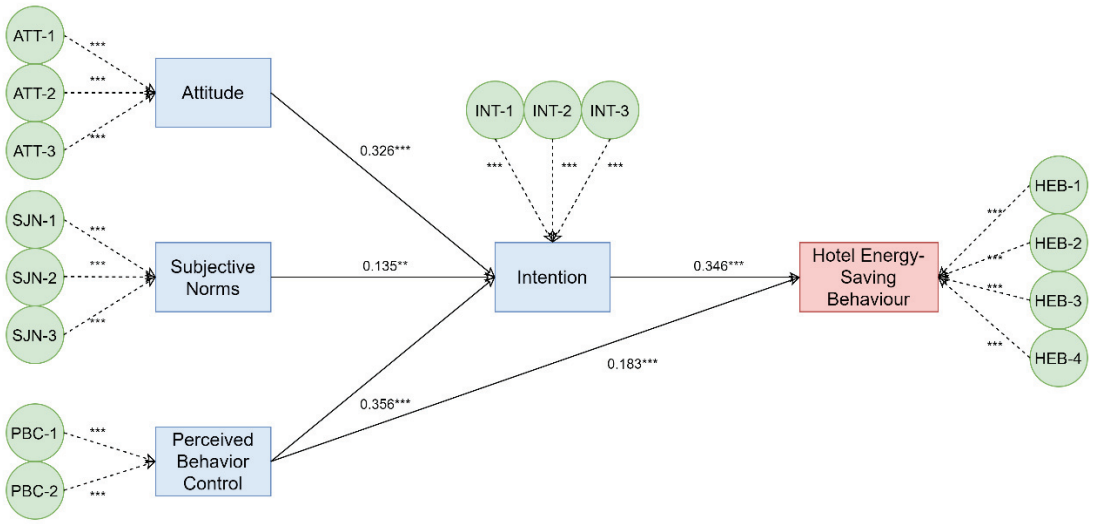


Figure 4. Structural modelling results of the TPB model. Note: *** $p < 0.001$; ** $p < 0.001$.

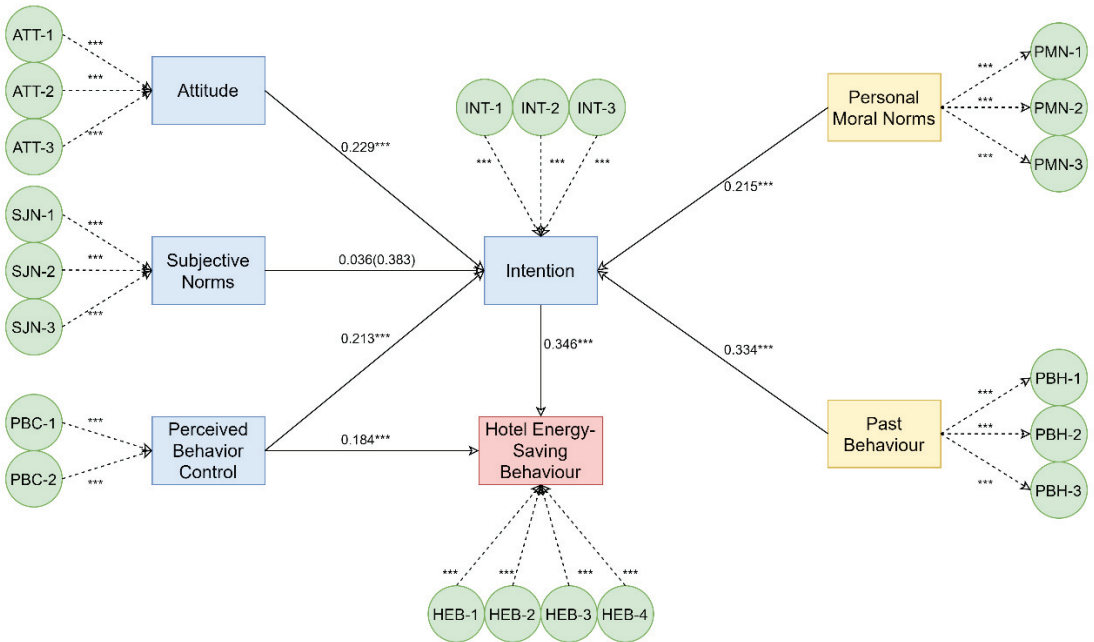


Figure 5. Structural modelling results of extended model I. Note: *** $p < 0.001$.

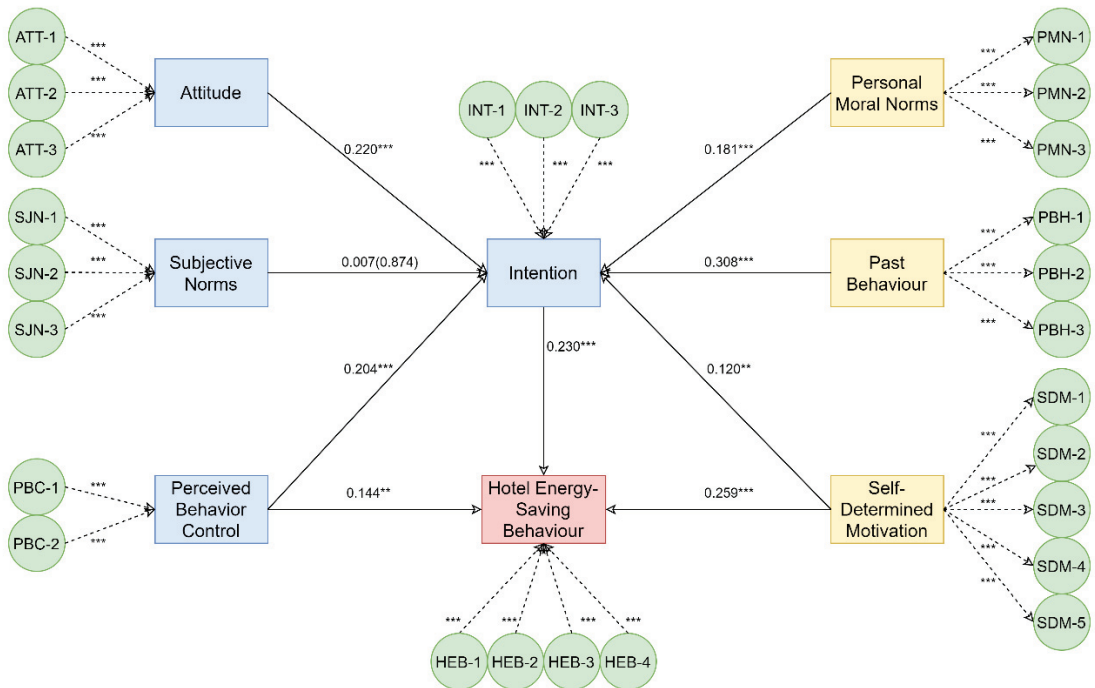


Figure 6. Structural modelling results of extended model II. Note: *** $p < 0.001$; ** $p < 0.001$.

The TPB model (Figure 4) included three attributes of the original TPB model. The coefficient of determination explained 41.9% of the variance in intention to perform hotel energy-conservation behaviour and 22.1% of the employed hotel energy-saving behaviour. In Figure 4, the results of the analysis present that all TPB attributes influenced the hotel energy conservation intention. Among the three TPB attributes, PBC ($\beta = 0.356, p < 0.001$) had the greatest effect on hotel energy conservation intention. Additionally, attitude ($\beta = 0.326, p < 0.001$) was the second-greatest influence on customers' energy conservation intention. However, the relationship between subjective norms ($\beta = 0.135, p = 0.003$) and intention was very small. The results suggest that intention ($\beta = 0.346, p < 0.001$) had a high positive correlation with hotel energy-saving behaviours. At the same time, a smaller correlation between PBC ($\beta = 0.183, p < 0.001$) and hotel energy-conservation behaviour was presented.

Extended model I (Figure 5) included two additional attributes: personal moral norms and past behaviour. The explanation of the intention increased to 54.5%, and the explanation of behaviour remained the same at 22.1%. The analysis results reported that past behaviour ($\beta = 0.334, p < 0.001$) had the strongest impact on hotel energy conservation intention. As a second influencing factor, attitude ($\beta = 0.229, p < 0.001$) positively influenced customers' energy conservation intention. Figure 5 shows that personal moral norms ($\beta = 0.215, p < 0.001$) and PBC ($\beta = 0.213, p < 0.001$) had a strong influence on hotel energy conservation intention. On the contrary, subjective norms ($\beta = 0.036, p = 0.396$) were not statistically significant to hotel energy conservation intention. The relationship between PBC ($\beta = 0.184, p < 0.001$) and hotel energy-saving behaviour was similar to that of the conventional TPB model ($\beta = 0.346, p < 0.001$).

Extended model II further considered self-determined motivation as an attribute. The SEM analysis results of extended model II are illustrated in Figure 6. The extended model explained 55.3% of the variance in intention, and the explanation of hotel energy-conservation behaviour rose from 22.1% to 26.3%. Table 6 reveals that past behaviour

($\beta = 0.308, p < 0.001$) produced the greatest effect on hotel energy conservation intention. In extended model II, attitude ($\beta = 0.220, p < 0.001$), PBC ($\beta = 0.204, p < 0.001$), personal moral norms ($\beta = 0.181, p < 0.001$), and self-determined motivation ($\beta = 0.120, p = 0.002$) significantly and positively related to respondents' hotel energy-efficient intentions. Self-determined motivation ($\beta = 0.259, p < 0.001$) had a greater impact on hotel energy-saving behaviour than intention ($\beta = 0.230, p < 0.001$) and PBC ($\beta = 0.144, p = 0.001$).

5. Discussion

This research employed the TPB and two extended models to explain the energy-saving behaviours of hotel guests. The analysis suggests that the conventional TPB model could explain hotel energy-saving behavioural patterns well. All three TPB factors showed significant influence on the energy-saving intentions of hotel guests. However, extended model I illustrated an enhanced explanatory power of hotel energy-saving intention by employing two additional psychological variables (i.e., moral norms and past behaviour). Extended model II further improved the explanatory powers of both hotel energy-saving intention and behaviour by considering self-determined motivation.

It is worth noting that the statistical correlations between the subjective norms and hotel energy-saving intention became significant in both extended models. There are two potential explanations. First, hotels provide a more private environment than a home or office. In hotels, guests are less disturbed by families or colleagues. Therefore, guests' attitudes and behaviour controls, instead of pressure from families, friends, or the public, play a more important role in their energy-saving intentions. Previous studies have found similar effects in homes (e.g., [87]), offices (e.g., [57]), and campuses (e.g., [88]). The temporary nature of the hotel stay may further reduce the impact of subjective norms. Second, the socio-economic backgrounds of the respondents may provide another possible explanation. The average age of the respondents was younger than (and their average education and income levels were higher than) the local demographic characteristics. This means that they were more exposed to environmental knowledge in compulsory education and internet propaganda. At the same time, previous research suggests that more educated and younger people are more likely to rely on rational thinking when making decisions [57,89], which might have caused the insignificant impact of subjective norms on the guests' willingness to save energy in hotels.

Consistent with previous studies on pro-environmental behaviour (e.g., [26,64]), our analysis also shows the important role played by past behaviour in hotel energy-saving behaviour. The individual's previous actions and experiences often have an impact on subsequent choices and behaviours. Some past behaviours have the potential to be transformed into habits and also produce emotional traces that affect individual choices [60]. This finding has important policy significance; the significant impact of past behaviour should be considered to promote hotel energy conservation. Therefore, hotels or the government may consider encouraging energy-saving behaviours by providing subsidies to guests who engage in energy-saving behaviours at an early stage. The changes in energy consumption behavioural patterns may have a long-term positive impact on the sustainable development of the hotel industry.

Extended model II evidenced that both the energy-efficient intentions and behaviours of hotel guests were significantly associated with self-determined motivation. These findings are consistent with previous behavioural research (e.g., [67,72]), which suggests the meeting of individuals' basic psychological needs for autonomy and their motivation. It is worth noting that the influence of self-determined motivation on hotel energy-saving behaviour transcends that of intention and PBC, which further highlights the role of self-motivation and self-efficacy in hotel energy conservation. Therefore, the hotel industry and the government might explore hotel energy-saving strategies based on autonomous motives by paying attention to the social structural environmental factors and the characteristics of hotel consumers.

In line with most of the existing pro-environment studies (e.g., [90,91]), this research also observed the important roles of attitude, behaviour control, and personal moral norms in hotel energy-saving behavioural patterns. Among them, behaviour control presented a stronger impact on the energy-saving intention of hotel guests. The hospitality industry can promote hotel energy conservation by increasing energy-saving convenience and reducing the perceived behavioural difficulty. For example, some commonly used low-cost interventions in home and office energy-saving schemes (e.g., energy labels [92] and energy-saving tips [93]) can also be applied in hotel energy conservation as well. However, there might be obstacles to applying some special energy-saving interventions in hotel buildings. First, hotel stays are generally much shorter in their time periods than in situations with homes and offices. This unique nature makes it difficult to enhance guests' environmental attitudes and personal norms through environmental education. Second, compared with household residents and employees, hotel guests are less manageable and tend to provide less personal information. Therefore, there is still some difficulty in determining the energy consumption baseline of each guest and providing customised energy-saving interventions in hotel operations.

The authors acknowledge that this study has a few limitations. First, the energy-saving behavioural performance of hotel guests came from self-reported data rather than objective observations. There were many factors potentially affecting the subjective evaluation process of their behaviours, and social desirability bias may have existed. Therefore, further studies would benefit from real-time energy-saving behaviour records and objective evaluations. The rapid development of sensors, smart meters, and the internet of things (IoT) make it possible to record hotel guests' electricity and energy consumption behaviour. However, it is worth noting that hotel guests' privacy and data security must be considered more carefully in the collection of actual behaviours. Second, only surveying hotels in the urban area of Shanghai limited the generality of the findings. Although Shanghai shares common characteristics with many cities and regions, there are also differences in cultural and demographic characteristics among the cities and areas. Therefore, the results of this study may only be valid in certain situations and not applicable to other situations. In future studies, researchers can consider obtaining data from multiple regions and countries.

6. Conclusions

This study employed the TPB and two extended models to examine the driving factors of the energy-efficient intentions and behaviours of hotel guests. This research extended the TPB model by adding personal norms, past behaviour, and self-determined motivation. We first found that all three TPB factors could predict hotel energy efficiency intentions. However, the statistical link between subjective norms and intention became weak and insignificant in the extended models. The researchers observed a significant enhanced explanatory power after employing the three additional variables. Significantly, the analysis suggests that past behaviour replaces attitude to be the most critical predictor of hotel energy-saving intention, and self-determined motivation also presents a stronger correlation to hotel energy-saving behaviour than behaviour control and intention. The analysis suggests that some widely used interventions in family and office energy-saving schemes (e.g., energy-saving tips, a normative setting, and energy saving bonds) can be employed in hotel buildings as well. This study further emphasises the long-term benefit of encouraging hotel guests' pro-environmental behaviours and highlights the role of self-determination in hotels' sustainable operation and energy conservation. The findings would contribute to understanding the driving factors and psychological patterns of hotel energy-saving intentions and behaviours. These works are critical to the formulation of energy-saving policies and interventions, as well as occupant typology studies for hotel building energy simulation and modelling.

Author Contributions: Conceptualisation, Q.-C.W. and X.L.; methodology, Q.-C.W.; software, X.L.; validation, Q.-C.W., K.-X.X. and T.-Y.L.; formal analysis, Q.-C.W. and K.-X.X.; investigation, K.-X.X.; resources, H.-H.W.; data curation, K.-X.X. and T.-Y.L.; writing—original draft preparation, Q.-C.W. and X.L.; writing—review and editing, K.-X.X. and G.Q.P.S.; visualisation, X.L.; supervision, H.-H.W.; project administration, H.-H.W. and G.Q.P.S. All authors have read and agreed to the published version of the manuscript.

Funding: The research was financially supported by both China Scholarship Council and the Cambridge Commonwealth, European & International Trust via scholarships.

Institutional Review Board Statement: The study was conducted according to the guidelines of the Declaration of Helsinki.

Informed Consent Statement: Informed consent was obtained from all subjects involved in the study.

Data Availability Statement: Not Applicable.

Acknowledgments: The authors would like to acknowledge Yi-Xuan Wang of The Hong Kong Polytechnic University for the data source. The authors would like to express their kindest gratitude to survey respondents and the anonymous reviewers.

Conflicts of Interest: The authors declare no conflict of interest.

References

- Jones, P.; Hillier, D.; Comfort, D. Sustainability in the global hotel industry. *Int. J. Contemp. Hosp. Manag.* **2014**, *26*, 5–17. [\[CrossRef\]](#)
- Upadhyay, A.; Vadam, C. The role of energy consumption in Hotel Operations. In Proceedings of the 22nd International Annual EurOMA Conference, Neuchatel, Switzerland, 28 June–1 July 2015; pp. 1–10.
- Xu, P.; Chan, E.H.W.; Qian, Q.K. Success factors of energy performance contracting (EPC) for sustainable building energy efficiency retrofit (BEER) of hotel buildings in China. *Energy Policy* **2011**, *39*, 7389. [\[CrossRef\]](#)
- Cingoski, V.; Petrevska, B. Making hotels more energy efficient: The managerial perception. *Econ. Res. Istraživanja* **2018**, *31*, 87–101. [\[CrossRef\]](#)
- Liu, S.; Wei, S.; Zhang, K.; Kong, X.; Wu, W. Investigation and analysis on the energy consumption of starred hotel buildings in Hainan Province, the tropical region of China. *Energy Convers. Manag.* **2013**, *75*, 570–580. [\[CrossRef\]](#)
- Yu, C.-R.; Guo, H.-S.; Wang, Q.-C.; Chang, R.-D. Revealing the Impacts of Passive Cooling Techniques on Building Energy Performance: A Residential Case in Hong Kong. *Appl. Sci.* **2020**, *10*, 4188. [\[CrossRef\]](#)
- Mak, B.L.; Chan, W.; Li, D.; Liu, L.; Wong, K.F. Power consumption modeling and energy saving practices of hotel chillers. *Int. J. Hosp. Manag.* **2013**, *33*, 1–5. [\[CrossRef\]](#)
- Liu, X.; Wang, Q.; Wei, H.-H.; Chi, H.-L.; Ma, Y.; Jian, I.Y. Psychological and Demographic Factors Affecting Household Energy-Saving Intentions: A TPB-Based Study in Northwest China. *Sustainability* **2020**, *12*, 836. [\[CrossRef\]](#)
- Liu, X.; Wang, Q.-C.; Jian, I.Y.; Chi, H.-L.; Yang, D.; Chan, E.H.-W. Are you an energy saver at home? The personality insights of household energy conservation behaviors based on theory of planned behavior. *Resour. Conserv. Recycl.* **2021**, *174*, 105823. [\[CrossRef\]](#)
- Zhang, Y.; Wang, Z.; Zhou, G. Determinants of employee electricity saving: The role of social benefits, personal benefits and organizational electricity saving climate. *J. Clean. Prod.* **2014**, *66*, 280–287. [\[CrossRef\]](#)
- Faghihi, V.; Hessami, A.R.; Ford, D.N. Sustainable campus improvement program design using energy efficiency and conservation. *J. Clean. Prod.* **2015**, *107*, 400–409. [\[CrossRef\]](#)
- Abrahamse, W.; Steg, L.; Vlek, C.; Rothengatter, T. A review of intervention studies aimed at household energy conservation. *J. Environ. Psychol.* **2005**, *25*, 273–291. [\[CrossRef\]](#)
- Bhushan, N.; Steg, L.; Albers, C. Studying the effects of intervention programmes on household energy saving behaviours using graphical causal models. *Energy Res. Soc. Sci.* **2018**, *45*, 75–80. [\[CrossRef\]](#)
- Miao, L.; Wei, W. Consumers' pro-environmental behavior and the underlying motivations: A comparison between household and hotel settings. *Int. J. Hosp. Manag.* **2013**, *32*, 102–112. [\[CrossRef\]](#)
- Lopes, M.; Antunes, C.H.; Martins, N. Energy behaviours as promoters of energy efficiency: A 21st century review. *Renew. Sustain. Energy Rev.* **2012**, *16*, 4095–4104. [\[CrossRef\]](#)
- Iweka, O.; Liu, S.; Shukla, A.; Yan, D. Energy and behaviour at home: A review of intervention methods and practices. *Energy Res. Soc. Sci.* **2019**, *57*, 101238. [\[CrossRef\]](#)
- Untaru, E.-N.; Ispas, A.; Candrea, A.N.; Luca, M.; Epuran, G. Predictors of individuals' intention to conserve water in a lodging context: The application of an extended Theory of Reasoned Action. *Int. J. Hosp. Manag.* **2016**, *59*, 50–59. [\[CrossRef\]](#)
- Han, H.; Chua, B.-L.; Hyun, S.S. Eliciting customers' waste reduction and water saving behaviors at a hotel. *Int. J. Hosp. Manag.* **2019**, *87*, 102386. [\[CrossRef\]](#)
- Han, H.; Kiatkawsin, K.; Ryu, H.B.; Jung, H.; Kim, W. Determinants of young vacationers' recycling and conservation behavior when traveling. *Soc. Behav. Pers. Int. J.* **2019**, *47*, 1–11. [\[CrossRef\]](#)

20. Burns, S.B.; Savan, B. The Post-Intervention Persistence of Energy Conservation Behaviors: An Evaluation of the ‘Start Green’ Program. *Sustainability* **2018**, *10*, 809. [\[CrossRef\]](#)
21. Uddin, M.; Wang, Q.; Wei, H.H.; Chi, H.L.; Ni, M. Building information modeling (BIM), System dynamics (SD), and Agent-based modeling (ABM): Towards an integrated approach. *Ain Shams Eng. J.* **2021**. [\[CrossRef\]](#)
22. Happle, G.; Fonseca, J.A.; Schlueter, A. A review on occupant behavior in urban building energy models. *Energy Build.* **2018**, *174*, 276–292. [\[CrossRef\]](#)
23. Butler, J. The compelling ‘hard case’ for ‘green’ hotel development. *Cornell Hosp. Q.* **2008**, *49*, 234–244. [\[CrossRef\]](#)
24. Chan, E. Gap analysis of green hotel marketing. *Int. J. Contemp. Hosp. Manag.* **2013**, *25*, 1017–1048. [\[CrossRef\]](#)
25. Ilin, E.L.; Miloradov, K.A.; Kovaltchuk, A.P. ‘Green Hotel’: Concepts and Implementation. *J. Environ. Manag. Tour.* **2019**, *10*, 300–306.
26. Han, H.; Hsu, L.-T.; Sheu, C. Application of the Theory of Planned Behavior to green hotel choice: Testing the effect of environmental friendly activities. *Tour. Manag.* **2010**, *31*, 325–334. [\[CrossRef\]](#)
27. Millar, M.; Mayer, K.J.; Baloglu, S. Importance of Green Hotel Attributes to Business and Leisure Travelers. *J. Hosp. Mark. Manag.* **2012**, *21*, 395–413. [\[CrossRef\]](#)
28. Nimri, R.; Patiar, A.; Kensbock, S. A green step forward: Eliciting consumers’ purchasing decisions regarding green hotel accommodation in Australia. *J. Hosp. Tour. Manag.* **2017**, *33*, 43–50. [\[CrossRef\]](#)
29. Barber, N.A. Profiling the potential ‘green’ hotel guest: Who are they and what do they want? *J. Hosp. Tour. Res.* **2014**, *38*, 361–387. [\[CrossRef\]](#)
30. Scheibehenne, B.; Jamil, T.; Wagenmakers, E.-J. Bayesian evidence synthesis can reconcile seemingly inconsistent results: The case of hotel towel reuse. *Psychol. Sci.* **2016**, *27*, 1043–1046. [\[CrossRef\]](#)
31. Reese, G.; Loew, K.; Steffgen, G. A Towel Less: Social Norms Enhance Pro-Environmental Behavior in Hotels. *J. Soc. Psychol.* **2014**, *154*, 97–100. [\[CrossRef\]](#)
32. Gössling, S.; Araña, J.E.; Aguiar-Quintana, J.T. Towel reuse in hotels: Importance of normative appeal designs. *Tour. Manag.* **2018**, *70*, 273–283. [\[CrossRef\]](#)
33. Ayoub, N.; Musharavati, F.; Pokharel, S.; Gabbar, H.A. Energy consumption and conservation practices in Qatar—A case study of a hotel building. *Energy Build.* **2014**, *84*, 55–69. [\[CrossRef\]](#)
34. Wang, Y.; Xu, Z.; Wang, Z.; Li, H. Analysis of thermal energy saving potentials through adjusting user behavior in hotel buildings of the Yangtze River region. *Sustain. Cities Soc.* **2019**, *51*, 101724. [\[CrossRef\]](#)
35. Ajzen, I.; Fishbein, M. The prediction of behavior from attitudinal and normative variables. *J. Exp. Soc. Psychol.* **1970**, *6*, 466–487. [\[CrossRef\]](#)
36. Hill, R.J.; Fishbein, M.; Ajzen, I. Belief, Attitude, Intention and Behavior: An Introduction to Theory and Research. *Contemp. Sociol.* **1977**, *6*, 244. [\[CrossRef\]](#)
37. Ajzen, I. The theory of planned behavior. *Organ. Behav. Hum. Decis. Process.* **1991**, *50*, 179–211. [\[CrossRef\]](#)
38. Ajzen, I. From Intentions to Actions: A Theory of Planned Behavior. In *Action Control*; Springer: Berlin/Heidelberg, Germany, 1985; pp. 11–39. [\[CrossRef\]](#)
39. Han, H.; Yoon, H.J. Hotel customers’ environmentally responsible behavioral intention: Impact of key constructs on decision in green consumerism. *Int. J. Hosp. Manag.* **2015**, *45*, 22–33. [\[CrossRef\]](#)
40. Verma, V.K.; Kumar, S.; Chandra, B. Big Five personality traits and tourist’s intention to visit green hotels. *Indian J. Sci. Res.* **2017**, *15*, 79–87.
41. Largo-Wight, E.; Bian, H.; Lange, L. An Empirical Test of an Expanded Version of the Theory of Planned Behavior in Predicting Recycling Behavior on Campus. *Am. J. Health Educ.* **2012**, *43*, 66–73. [\[CrossRef\]](#)
42. Tonglet, M.; Phillips, P.S.; Read, A.D. Using the Theory of Planned Behaviour to investigate the determinants of recycling behaviour: A case study from Brixworth, UK. *Resour. Conserv. Recycl.* **2004**, *41*, 191–214. [\[CrossRef\]](#)
43. Ambak, K.; Kasvar, K.K.; Daniel, B.D.; Prasetyo, J.; Ghani, A.R.A. Behavioral Intention to Use Public Transport Based on Theory of Planned Behavior. *MATEC Web Conf.* **2016**, *47*, 3008. [\[CrossRef\]](#)
44. Scalco, A.; Noventa, S.; Sartori, R.; Ceschi, A. Predicting organic food consumption: A meta-analytic structural equation model based on the theory of planned behavior. *Appetite* **2017**, *112*, 235–248. [\[CrossRef\]](#)
45. He, P.; Veronesi, M. Personality traits and renewable energy technology adoption: A policy case study from China. *Energy Policy* **2017**, *107*, 472–479. [\[CrossRef\]](#)
46. Wang, Q.-C.; Chang, R.; Xu, Q.; Liu, X.; Jian, I.Y.; Ma, Y.-T.; Wang, Y.-X. The impact of personality traits on household energy conservation behavioral intentions—An empirical study based on theory of planned behavior in Xi’an. *Sustain. Energy Technol. Assess.* **2020**, *43*, 100949. [\[CrossRef\]](#)
47. Chan, E.S.W.; Hon, A.H.Y.; Chan, W.; Okumus, F. What drives employees’ intentions to implement green practices in hotels? The role of knowledge, awareness, concern and ecological behavior. *Int. J. Hosp. Manag.* **2014**, *40*, 20–28. [\[CrossRef\]](#)
48. Budovska, V.; Delgado, A.T.; Øgaard, T. Pro-environmental behaviour of hotel guests: Application of the Theory of Planned Behaviour and social norms to towel reuse. *Tour. Hosp. Res.* **2020**, *20*, 105–116. [\[CrossRef\]](#)
49. Georgescu, M.-A.; Herman, E. Are Young People Ready to Have a Pro-Environmental Sustainable Behaviour as Tourists? An Investigation of Towel Reuse Intention. *Sustainability* **2020**, *12*, 9469. [\[CrossRef\]](#)

50. Chen, M.-F.; Tung, P.-J. Developing an extended Theory of Planned Behavior model to predict consumers' intention to visit green hotels. *Int. J. Hosp. Manag.* **2014**, *36*, 221–230. [[CrossRef](#)]
51. Verma, V.; Chandra, B. An application of theory of planned behavior to predict young Indian consumers' green hotel visit intention. *J. Clean. Prod.* **2018**, *172*, 1152–1162. [[CrossRef](#)]
52. Hameed, I.; Waris, I.; Haq, M.A.U. Predicting eco-conscious consumer behavior using theory of planned behavior in Pakistan. *Environ. Sci. Pollut. Res.* **2019**, *26*, 15535–15547. [[CrossRef](#)] [[PubMed](#)]
53. Ateş, H. Merging Theory of Planned Behavior and Value Identity Personal norm model to explain pro-environmental behaviors. *Sustain. Prod. Consum.* **2020**, *24*, 169–180. [[CrossRef](#)]
54. Ajzen, I. The theory of planned behavior: Frequently asked questions. *Hum. Behav. Emerg. Technol.* **2020**, *2*, 314–324. [[CrossRef](#)]
55. Kaiser, F. A moral extension of the theory of planned behavior: Norms and anticipated feelings of regret in conservationism. *Pers. Individ. Differ.* **2006**, *41*, 71–81. [[CrossRef](#)]
56. Klöckner, C.A. A comprehensive model of the psychology of environmental behaviour—A meta-analysis. *Glob. Environ. Chang.* **2013**, *23*, 1028–1038. [[CrossRef](#)]
57. Gao, L.; Wang, S.; Li, J.; Li, H. Application of the extended theory of planned behavior to understand individual's energy saving behavior in workplaces. *Resour. Conserv. Recycl.* **2017**, *127*, 107–113. [[CrossRef](#)]
58. Han, H.; Meng, B.; Kim, W. Emerging bicycle tourism and the theory of planned behavior. *J. Sustain. Tour.* **2016**, *25*, 292–309. [[CrossRef](#)]
59. Chorlton, K.; Conner, M.; Jamson, S. Identifying the psychological determinants of risky riding: An application of an extended Theory of Planned Behaviour. *Accid. Anal. Prev.* **2012**, *49*, 142–153. [[CrossRef](#)]
60. Yuriev, A.; Dahmen, M.; Paillé, P.; Boiral, O.; Guillaumie, L. Pro-environmental behaviors through the lens of the theory of planned behavior: A scoping review. *Resour. Conserv. Recycl.* **2020**, *155*, 104660. [[CrossRef](#)]
61. Oztekin, C.; Teksöz, G.; Pamuk, S.; Sahin, E.; Kilic, D.S. Gender perspective on the factors predicting recycling behavior: Implications from the theory of planned behavior. *Waste Manag.* **2017**, *62*, 290–302. [[CrossRef](#)] [[PubMed](#)]
62. Knussen, C.; Yule, F. 'I'm Not in the Habit of Recycling' The Role of Habitual Behavior in the Disposal of Household Waste. *Environ. Behav.* **2008**, *40*, 683–702. [[CrossRef](#)]
63. Moon, S.-J. Investigating beliefs, attitudes, and intentions regarding green restaurant patronage: An application of the extended theory of planned behavior with moderating effects of gender and age. *Int. J. Hosp. Manag.* **2020**, *92*, 102727. [[CrossRef](#)]
64. Hu, H.; Zhang, J.; Wang, C.; Yu, P.; Chu, G. What influences tourists' intention to participate in the Zero Litter Initiative in mountainous tourism areas: A case study of Huangshan National Park, China. *Sci. Total Environ.* **2018**, *657*, 1127–1137. [[CrossRef](#)]
65. Knussen, C.; Yule, F.; MacKenzie, J.; Wells, M. An analysis of intentions to recycle household waste: The roles of past behaviour, perceived habit, and perceived lack of facilities. *J. Environ. Psychol.* **2004**, *24*, 237–246. [[CrossRef](#)]
66. Wittenberg, I.; Blöbaum, A.; Matthies, E. Environmental motivations for energy use in PV households: Proposal of a modified norm activation model for the specific context of PV households. *J. Environ. Psychol.* **2018**, *55*, 110–120. [[CrossRef](#)]
67. Webb, D.; Soutar, G.; Mazzarol, T.; Saldaris, P. Self-determination theory and consumer behavioural change: Evidence from a household energy-saving behaviour study. *J. Environ. Psychol.* **2013**, *35*, 59–66. [[CrossRef](#)]
68. Perugini, M.; Bagozzi, R.P. The role of desires and anticipated emotions in goal-directed behaviours: Broadening and deepening the theory of planned behaviour. *Br. J. Soc. Psychol.* **2001**, *40*, 79–98. [[CrossRef](#)]
69. Howard, J.L.; Gagné, M.; Bureau, J.S. Testing a continuum structure of self-determined motivation: A meta-analysis. *Psychol. Bull.* **2017**, *143*, 1346. [[CrossRef](#)]
70. Masson, T.; Otto, S. Explaining the difference between the predictive power of value orientations and self-determined motivation for proenvironmental behavior. *J. Environ. Psychol.* **2021**, *73*, 101555. [[CrossRef](#)]
71. Tagkaloglou, S.; Kasser, T. Increasing collaborative, pro-environmental activism: The roles of Motivational Interviewing, self-determined motivation, and self-efficacy. *J. Environ. Psychol.* **2018**, *58*, 86–92. [[CrossRef](#)]
72. Hagger, M.S.; Chatzisarantis, N.L.D.; Harris, J. The Process by Which Relative Autonomous Motivation Affects Intentional Behavior: Comparing Effects Across Dieting and Exercise Behaviors. *Motiv. Emot.* **2006**, *30*, 306–320. [[CrossRef](#)]
73. Hagger, M.S.; Chatzisarantis, N.; Harris, J. From Psychological Need Satisfaction to Intentional Behavior: Testing a Motivational Sequence in Two Behavioral Contexts. *Pers. Soc. Psychol. Bull.* **2006**, *32*, 131–148. [[CrossRef](#)]
74. Hagger, M.S.; Chatzisarantis, N. Integrating the theory of planned behaviour and self-determination theory in health behaviour: A meta-analysis. *Br. J. Health Psychol.* **2009**, *14*, 275–302. [[CrossRef](#)]
75. Hagger, M.; Chatzisarantis, N.; Hein, V.; Soós, I.; Karsai, I.; Lintunen, T.; Leemans, S. Teacher, peer and parent autonomy support in physical education and leisure-time physical activity: A trans-contextual model of motivation in four nations. *Psychol. Health* **2009**, *24*, 689–711. [[CrossRef](#)] [[PubMed](#)]
76. Lavergne, K.J.; Sharp, E.C.; Pelletier, L.G.; Holtby, A. The role of perceived government style in the facilitation of self-determined and non self-determined motivation for pro-environmental behavior. *J. Environ. Psychol.* **2010**, *30*, 169–177. [[CrossRef](#)]
77. Zhang, Y.; Wu, S.; Rasheed, M.I. Conscientiousness and smartphone recycling intention: The moderating effect of risk perception. *Waste Manag.* **2019**, *101*, 116–125. [[CrossRef](#)] [[PubMed](#)]
78. Pelletier, L.G.; Tuson, K.M.; Green-Demers, I.; Noels, K.; Beaton, A.M. Why Are You Doing Things for the Environment? The Motivation Toward the Environment Scale (MTES)1. *J. Appl. Soc. Psychol.* **1998**, *28*, 437–468. [[CrossRef](#)]
79. Pye, S.; Daly, H. Modelling sustainable urban travel in a whole systems energy model. *Appl. Energy* **2015**, *159*, 97–107. [[CrossRef](#)]

80. Hair, J.F., Jr.; Matthews, L.M.; Matthews, R.L.; Sarstedt, M. PLS-SEM or CB-SEM: Updated guidelines on which method to use. *Int. J. Multivar. Data Anal.* **2017**, *1*, 107–123. [[CrossRef](#)]
81. Anderson, J.C.; Gerbing, D.W. Structural equation modeling in practice: A review and recommended two-step approach. *Psychol. Bull.* **1988**, *103*, 411. [[CrossRef](#)]
82. Hatcher, L.; Stepanski, E.J. *A Step-By-Step Approach to Using the SAS System for Univariate and Multivariate Statistics*; SAS Institute: Cary, NC, USA, 1994.
83. Hair, J.F.; Ringle, C.M.; Sarstedt, M. PLS-SEM: Indeed a Silver Bullet. *J. Mark. Theory Pract.* **2011**, *19*, 139–152. [[CrossRef](#)]
84. Wee, S.-C.; Choong, W.-W. Gamification: Predicting the effectiveness of variety game design elements to intrinsically motivate users' energy conservation behaviour. *J. Environ. Manag.* **2018**, *233*, 97–106. [[CrossRef](#)] [[PubMed](#)]
85. Chin, W.W. The partial least squares approach to structural equation modeling. *Mod. Methods Bus. Res.* **1998**, *295*, 295–336.
86. Cohen, J. *Statistical Power Analysis for the Behavioral Sciences*; Academic Press: Cambridge, MA, USA, 2013.
87. Ru, X.; Wang, S.; Yan, S. Exploring the effects of normative factors and perceived behavioral control on individual's energy-saving intention: An empirical study in eastern China. *Resour. Conserv. Recycl.* **2018**, *134*, 91–99. [[CrossRef](#)]
88. Du, J.; Pan, W. Examining energy saving behaviors in student dormitories using an expanded theory of planned behavior. *Habitat Int.* **2020**, *107*, 102308. [[CrossRef](#)]
89. Prud'Homme, B.; Raymond, L. Sustainable development practices in the hospitality industry: An empirical study of their impact on customer satisfaction and intentions. *Int. J. Hosp. Manag.* **2013**, *34*, 116–126. [[CrossRef](#)]
90. Chen, M.-F. Extending the theory of planned behavior model to explain people's energy savings and carbon reduction behavioral intentions to mitigate climate change in Taiwan—moral obligation matters. *J. Clean. Prod.* **2016**, *112*, 1746–1753. [[CrossRef](#)]
91. Shalender, K.; Sharma, N. Using extended theory of planned behaviour (TPB) to predict adoption intention of electric vehicles in India. *Environ. Dev. Sustain.* **2020**, *23*, 665–681. [[CrossRef](#)]
92. Gram-Hanssen, K.; Bartiaux, F.; Jensen, O.M.; Cantaert, M. Do homeowners use energy labels? A comparison between Denmark and Belgium. *Energy Policy* **2007**, *35*, 2879–2888. [[CrossRef](#)]
93. Ueno, T.; Sano, F.; Saeki, O.; Tsuji, K. Effectiveness of an energy-consumption information system on energy savings in residential houses based on monitored data. *Appl. Energy* **2006**, *83*, 166–183. [[CrossRef](#)]

Review

A Review on the Research and Development of Solar-Assisted Heat Pump for Buildings in China

Yaolin Lin ^{1,*}, Zhenyan Bu ¹, Wei Yang ^{2,*}, Haisong Zhang ³, Valerie Francis ² and Chun-Qing Li ⁴

¹ School of Environment and Architecture, University of Shanghai for Science and Technology, Shanghai 200093, China

² Faculty of Architecture, Building and Planning, The University of Melbourne, Melbourne 3010, Australia

³ Evergrande Property Services, Evergrande Group, Guangzhou 511458, China

⁴ School of Engineering, RMIT University, Melbourne 3000, Australia

* Correspondence: ylin@usst.edu.cn (Y.L.); wei.yang@unimelb.edu.au (W.Y.)

Abstract: The building sector accounts for over 40% of global energy consumption. The utilization of renewable energy systems such as the solar-assisted heat pump (SAHP) in buildings has been shown to improve building energy efficiency and achieve carbon neutrality. This paper presents a review of the research and development of solar-assisted heat pumps for buildings in China. It firstly introduces the different stages of solar-assisted heat pump research. Secondly, the research on different types of heat pumps, the core components of heat pumps, the computer software used, and the economic feasibility evaluation of solar-assisted heat pumps are presented. Thirdly, the application of SAHPs in practical projects is examined and relevant regulations, standards, and policies for solar-assisted heat pump development in China are highlighted. Finally, recommendations for the future development of solar-assisted heat pumps in China are suggested.

Keywords: solar-assisted heat pump (SAHP); energy efficiency; research and development; China

Citation: Lin, Y.; Bu, Z.; Yang, W.; Zhang, H.; Francis, V.; Li, C.-Q. A Review on the Research and Development of Solar-Assisted Heat Pump for Buildings in China.

Buildings **2022**, *12*, 1435. <https://doi.org/10.3390/buildings12091435>

Academic Editor: Christopher Yu-Hang Chao

Received: 5 August 2022

Accepted: 7 September 2022

Published: 13 September 2022

Publisher's Note: MDPI stays neutral with regard to jurisdictional claims in published maps and institutional affiliations.



Copyright: © 2022 by the authors. Licensee MDPI, Basel, Switzerland. This article is an open access article distributed under the terms and conditions of the Creative Commons Attribution (CC BY) license (<https://creativecommons.org/licenses/by/4.0/>).

1. Introduction

Since the energy shortage and oil crisis in the 1970s, it has been evident that any development at the expense of environmental deterioration is not sustainable [1]. The increase in building energy consumption is one of the most important factors that contribute to energy shortages, as buildings consume up to 45% of the primary energy globally [2]. With rapid urbanization, the total energy consumption in China continued to grow since 2005 and surpassed the United States in 2009 [3]. According to the statistics from the China Building Energy Conservation Association, the total building energy consumption reached 2.233 billion tons of standard coal in China in 2019, accounting for 46% of the total national primary energy consumption [4]. In addition, carbon emissions in the building sector were 50% of the national carbon emissions [4]. To reduce carbon emissions from fossil fuels, China has increased its investment in renewable energy, such as solar energy. It has been at the forefront of the utilization of renewable energy for sustainable development. Since 2013, China surpassed Europe as the investment leader in the renewable energy industry. In 2017, China's total installed solar power generation capacity reached 53 GW, accounting for half of the global total solar power generation [5]. In addition, China's total investment in renewable energy reached $\$8.34 \times 10^{10}$, far exceeding the $\$5.55 \times 10^{10}$ investment in the USA, ranking China first in the world [5]. According to the World Energy Statistics yearbook, the world's solar power generation capacity has increased by 127 GW in the past 20 years [6]. China is the largest contributor to the growth of renewable energy (1.0 EJ/year), followed by Europe (0.7 EJ/year) and the United States (0.4 EJ/year). Figure 1 presents the comparison of solar power generation in China, the United States, Europe, and Japan. It can be seen that, since 2017, China has become the largest solar power-generating country in the world, with an installation capacity reaching 253.8 GW in 2020.

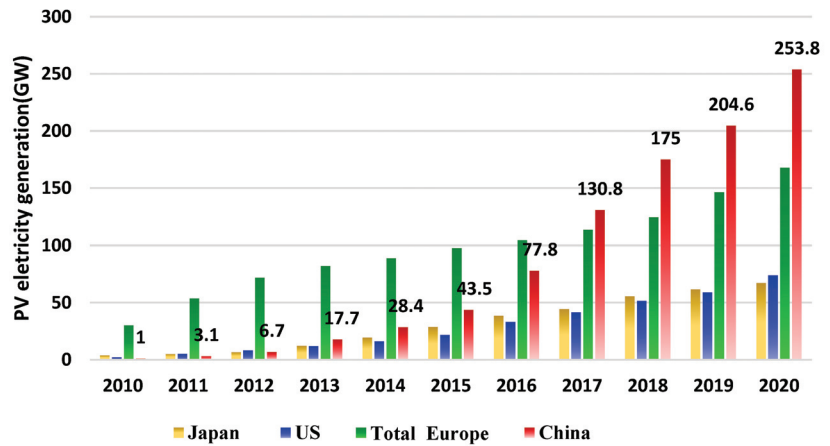


Figure 1. Solar photovoltaic power generation from 2010 to 2020 in various countries [6].

Since the issue of the “Green Building Evaluation Standard” in 2006, building energy efficiency has received wide attention in China [7]. In particular, renewable energy application in buildings is regarded as one of the focuses in the future [8]. Professor Jiang proposed the transition to a low-carbon energy system based on renewable energy in 2017 [9]. China has set a target to reach the peak of carbon dioxide emissions by 2030 and carbon neutrality by 2060 [10]. Therefore, it is critical to adopt clean energy sources in the building sector to reduce carbon emissions. Of many sources of carbon emission, the heating, ventilation, and air-conditioning (HVAC) system accounts for 50%–70% of building energy consumption [11]. Therefore, it is an important area to be considered in building energy reduction. Since many emerging energy resources come from solar energy, the rational development and utilization of solar energy resources are essential to solving future energy shortage problems [12]. The application of the solar-assisted heat pump in buildings can reduce building energy consumption by utilizing solar energy to power the HVAC system/improve the HVAC system’s efficiency.

The solar heat pump technology was developed with the breakthrough in monocrystalline silicon cells and selective solar absorptive coatings in the 1950s using solar energy as the heat source [13]. Since then, the concept of the direct expansion solar-assisted heat pump (DX-SAHP) and other types of solar-assisted heat pump systems (SAHP) with single or multiple heat sources including solar energy have been proposed [14,15]. Typically, a SAHP system is an integration of a traditional heat pump and solar thermal panels, which function as a low-temperature heat source. The heat produced is used to feed the evaporator. Due to a higher evaporator temperature, their coefficients of performance (COPs) are much higher than those of traditional heat pumps. In addition, with multiple heat sources, SAHPs can work stably under different climatic conditions [16]. A large number of experimental and theoretical studies and system optimizations have subsequently been conducted in developed countries [17–19]. By comparison, China’s research on SAHPs started later in the 1980s [20]. At the beginning of the 21st century, Ji and Pei et al. [15] conducted comprehensive research on photovoltaic electric/thermal heat pumps. Since then, many universities and research institutes have carried out studies on SAHPs leading to great progress theoretically and practically [21].

China has a vast territory with rich solar energy resources [22]. There are five climatic regions in China: the severe cold region, cold region, hot summer and cold winter region, mild region, and hot summer and warm winter region [23]. The total annual solar irradiations vary in the range of 3340 MJ/m²–8400 MJ/m² across the countries, with a median value of 5852 MJ/m². High solar irradiations are distributed across different climatic regions including Qinghai (severe cold region), Xinjiang (severe cold region and cold region),

southern Ningxia (cold region), Gansu (cold region), southern Inner Mongolia (severe cold and cold region), northern Shanxi (cold region), Liaoning (severe cold region), south-eastern Hebei (cold region), southeastern Shandong (cold region), southeastern Henan (cold region), western Jilin (severe cold region), central and southwestern Yunnan (mild region), southeastern Guangdong (hot summer and warm winter region), southeastern Fujian Guangdong (hot summer and warm winter region), eastern and western Hainan Island (hot summer and warm winter region), and Qinghai-Tibet Plateau (severe cold region and cold region). Although they have abundant solar energy resources, in most areas their economy is less developed. In the more developed regions of China, the advantages of solar energy resources are not obvious, and SAHP development is driven by the local heating energy demand and financial support for clean energy systems from governments [24].

The research and development of SAHP and its application in buildings in China are quite different from that of other countries due to China's complex climatic conditions and economic situation. Therefore, it is important to carry out a comprehensive and systematic review of the research and development of SAHP in China. Firstly, this paper introduces the different stages in the research and development of SAHP for buildings in China. Secondly, the research on different types of heat pumps, the core components of heat pumps, the computer software used, and the economic feasibility evaluation of solar-assisted heat pumps is presented. Thirdly, the application of SAHP in practical projects is examined and the relevant regulations, standards, and policies for solar-assisted heat pump development in China are highlighted. Finally, recommendations for the future developments of solar-assisted heat pumps in China are suggested.

2. Stages of SAHP Research in China

Developed countries such as the United States, Japan, and Denmark have conducted a large number of studies on SAHP since it was first proposed in 1955. The research on SAHP started late in China, and the renewable energy applications in China are still in a rapid development stage [25]. The following section summarizes the publication trend for SAHP research in China in recent decades and divides it into four stages according to the research topics and timelines.

2.1. Research Publication Trend from 1981 to 2021

This review searched the literature published in databases including CNKI, Web of Science, Baidu, and Google Scholar and focused on SAHP research in China from 1986 to 2021. A total number of 1224 publications were found (Figure 2), and after careful selection within the areas of the building environment, energy consumption, numerical simulation, experimental and theoretical analysis, policy and system optimization, based on the quality and authority, e.g., from core collections of the Chinese literature database, government official websites, and the Science Citation Index (SCI) database, 153 representative papers and electronic documents were selected. It should be noted that the primary purpose of this review is to focus on the research and development of SAHPs in the building sector, and therefore theoretical analyses of the application of heat pumps in other areas such as drying and dehumidification were excluded.

From Figure 2, it can be observed that fewer than ten papers were published annually before 2000, meaning renewable energy resources did not receive much attention during that time period. In 2005, the enactment of the Law of Renewable Energy of the People's Republic of China greatly supported the large-scale application of solar, thermal, and photovoltaic electric power in China [26]. This appears to have stimulated research on SAHP with relatively steady growth in publications. With the implementation of the National Tenth Five-Year Plan, the development of clean energy represented by solar, thermal, and photovoltaic power generation was formulated as an important national energy development strategy. With governmental support, more and more studies were devoted to SAHPs [27]. The rapid rise of the solar industry in China was attributed to the favorable world economic environment and government policies. However, during the period from

2008 to 2014, the emergence of the global financial crisis had a significant impact on the new energy industry. Meanwhile, due to a lack of innovations and core technologies, the overall quality and technological level were low, compared with developed countries, leading to overproduction in solar-related industries in China [28]. In 2013, photovoltaic product demand was less than 60% of its output, and the polysilicon industry supply exceeded 67% of market demand by the end of the year [29]. The bankruptcy of the largest photovoltaic company in China was indicative of the overproduction of PV industries reaching their peak level. This fluctuation appears to be reflected in the number of publications during this same period. With the promulgation of relevant subsidy policies for the solar energy industry by the central government after 2014, research on SAHPs again became more prominent and the number of publications has been on the rise since 2015.

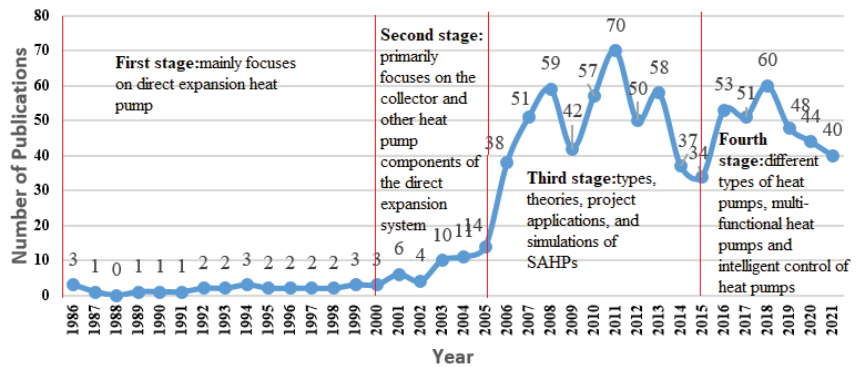


Figure 2. Publication trends from 2010 to 2021.

2.2. Research Topics in Different Periods

From the literature survey, it was found that Chinese scholars began to carry out experimental studies on the SAHP manufactured by Hitachi in 1985 and then gradually conducted some theoretical research on SAHP [30]. According to the research topics and timelines, the SAHP research can be divided into four stages.

The first stage of the study lasted from 1985 to 2000. The main research topics and timelines are shown in Figure 3. At this stage, the research mainly focuses on direct expansion heat pumps. Although few research outcomes were presented during this period, they did provide important references for future theoretical and experimental research. The representative research results of the first stage are the performance outcomes of the DX-SAHP system. The technical difficulty of this research stage is that, in conventional SAHPs, the solar collector and heat pump are used to operate as two separate units with high energy losses.

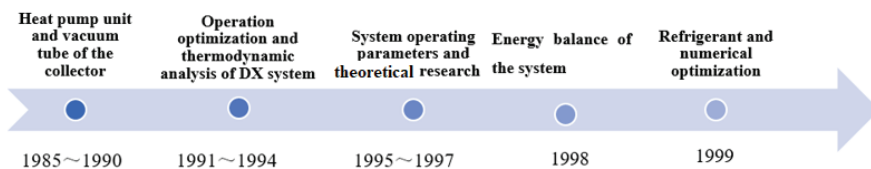


Figure 3. Timeline of SAHP research between 1985 and 2000.

The second stage was from 2001 to 2005 when the research on the SAHP system expanded considerably. Figure 4 categorizes the areas of research during this period. It can be seen from Figure 4 that the research primarily focuses on the collector and other heat pump components of the direct expansion system [31]. At the same time, preliminary

research was carried out on different types of SAHPs, such as multiple heat sources and non-direct expansion heat pumps, which lays good foundations for subsequent studies [32]. The representative research results of the second stage are the optimization of the heat exchanger and solar heat collector. The technical difficulties of this research stage are the lack of more environmentally friendly refrigerants, standard system application specifications, and fixed heat sources, which make it impossible to greatly improve the thermal efficiency of the system.

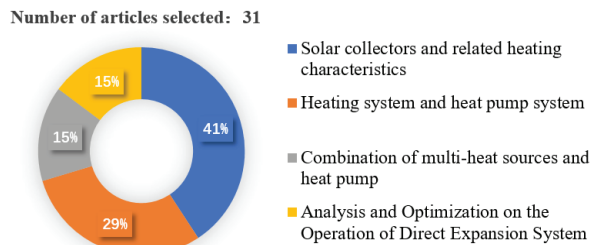


Figure 4. Categories and contribution proportions of SAHP research between 2001 and 2005.

The third stage is from 2006 to 2015, which is a period of development with some fluctuation. During this period, fruitful theoretical achievements were made in the types, theories, project applications, and simulations of SAHPs. The main research categories and corresponding contributions are presented in Figure 5. It can be observed that a large proportion of the studies still focus on direct expansion systems and a small proportion of them concentrates on experimental research on non-direct expansion systems. In addition, multi-functional SAHPs such as the photovoltaic thermal (PV/T) system, the photovoltaic solar energy system, ground source auxiliary, and other new types of SAHPs have become the focus of research in this period due to their high efficiency and ability to meet different operating conditions [33,34]. The representative research results of the third stage are the design of multiple heat source systems, e.g., solar-assisted ground source heat pumps (SGHP), and the emergence of various high-efficiency heat and electricity cogeneration systems. The technical difficulties of this research stage are the low system thermal efficiency and low system application rate due to cost factors such as material prices, inadequate information to gather collectors' lifespans and performances under high temperature operating conditions, and the experimental verification of numerical models.

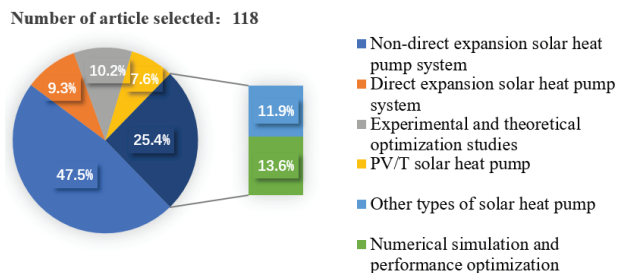


Figure 5. Categories and contribution proportions of SAHP research between 2006 and 2015.

The fourth stage is from 2016 to now, which is again a period of rapid development. Figure 6 presents the research categories and contribution proportion during this time. It can be observed that the research focuses switched to different types of heat pumps, multi-functional heat pumps, and the intelligent control of heat pumps. Based on the direct-expansion system, new systems with different connections on the main components of the heat pumps and combinations with various heat sources have been explored, such as

the PV/T system, the sewage source heat pump system, the air and solar energy heat pump compound machine, etc. [35–37]. In addition, during this period, significant achievements have been made in the application of refrigerants, and many practical projects on SAHPs were carried out. Furthermore, the optimal control of SAHPs has gradually become the research focus. The representative research results of the fourth stage are on the enhancement of the efficiency of the photovoltaic/thermal (PV/T) collector, e.g., micro-channel heat pipes and concentrating heat collectors, as well as automated and intelligent control of the SAHP system. The technical difficulties of this research stage are the integration of wind and geothermal heat sources into SAHP systems and optimization of the system configuration, the integration of terminal units and the SAHP system, and a lack of specific guidelines for SAHP application in the residential sector.

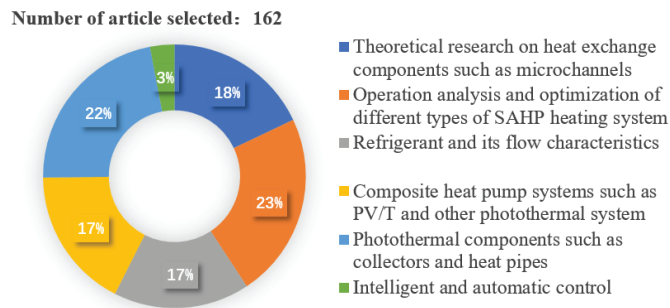


Figure 6. Categories and contribution proportions of SAHP research between 2016 and 2021.

The research progress on SAHP systems in China can be summarized in Figure 7. It can be concluded that SAHP research in China has undergone significant advancements in heat source selection, theoretical optimization, numerical simulation, etc. New types of systems such as PV/T-SAHP and geothermal auxiliary SAHP systems were developed based on direct expansion and non-direct expansion SAHP systems. Excellent achievements were made after 2015 when the Chinese government proposed a continuous transformation of energy structures and high-quality development with the “Paris Agreement” being signed in December 2015 [38].

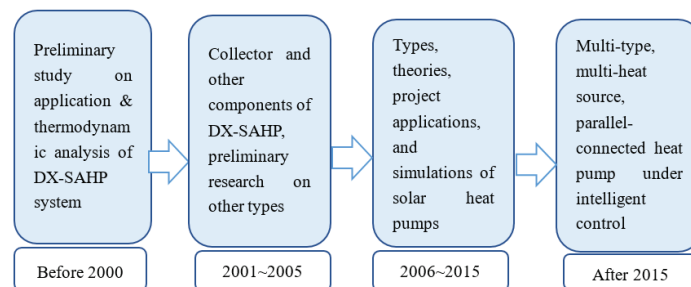


Figure 7. Research progress on SAHP in China.

More research publications and diverse topics on SAHP can be expected in the next decade as the Chinese government has proposed its goals of achieving carbon peak and carbon neutrality at the United Nations Climate Conference in 2020. Meeting the carbon neutrality targets will bring significant investment in new renewable energy research and projects, which will stimulate Chinese researchers to carry out more in-depth research on SAHP.

3. Research on SAHP

3.1. Research on the Types of Heat Pumps

SAHP technology is an effective combination of solar collectors and traditional heat pumps. The SAHP is based on the transformation of the heat exchanger of the traditional heat pump by utilizing solar energy as the heat source, or combined with other energy sources, to improve the coefficient of performance of the heat pump. From the ways of solar energy utilization, SAHP systems can be divided into photovoltaic-solar-assisted heat pumps (PV-SAHP), photothermal-solar-assisted heat pumps (PT-SAHP), and photovoltaic/thermal-solar-assisted heat pumps (PV/T-SAHP).

The PV-SAHP systems can be divided into direct solar-assisted heat pumps (DX-SAHP), indirect solar-assisted heat pumps (IX-SAHP), and PV/T-SAHP systems, according to the different connection methods and heat collection media. In the DX-SAHP system, the refrigerant flows into the solar collector directly and is heated. The collector is the heat source for evaporation. In the IX-SAHP system, the solar collector and the heat pump evaporator operate independently, and heat is absorbed through a heat exchanger. According to the differences in the connection between the solar heat collection cycle and the heat pump cycle, they can be classified as series, parallel, and dual heat source heat pumps [39,40]. The PV/T-SAHP system simultaneously utilizes solar energy, electric energy, and other forms of ambient energy. PV/T modules are used as a heat collection evaporator combined with an SAHP cycle to realize the comprehensive utilization of solar energy, photoelectricity, and heat, and improve the overall efficiency of the heat pump system [41]. The PV/T system will be one of the focuses of future research.

Table 1 lists the main components for the different types of SAHP systems.

Table 1. Classification and system components of SAHP systems.

Classification	System Components	Ref.
PV-SAHP	PV evaporator (photovoltaic and heat pump evaporation), photovoltaic conversion device (inverter), auxiliary evaporator, heat pump system (evaporator, condenser, compressor, expansion valve), public grid, building heating, and domestic hot water system.	[39]
DX-SAHP	Solar collector, heat exchanger, pump, heat pump system (evaporator, condenser, compressor, expansion valve), domestic hot water system, and hot water storage tank (optional).	[40]
IX-SAHP (Series)	Flat plate collector, compressor, condenser, evaporator, expansion valve, pump, and domestic hot water system.	[42]
IX-SAHP (Parallel)	Flat plate collector, compressor, condenser, expansion valve, water pump, hot water inlet, hot water outlet, evaporator, and hot water tank.	[42]
IX-SAHP (Hybrid)	Flat plate collector, compressor, condenser, evaporator, expansion valve, water pump, hot water inlet, and hot water outlet.	[42]
PV/T-SAHP	Solar air collector (photovoltaic module, heat absorption plate, airflow channel, edge and back insulation layer, metal frame), compressor, hot water storage tank with a built-in condensing coil, and expansion valve.	[41]

The SAHP system combines solar energy utilization and building energy supply through the heat pump cycle. In the DX-SAHP system, the refrigerant flows directly through the collector/evaporator and then passes through various components such as the compressor to complete a cycle [39]. For IX-SAHP, the solar collector absorbs heat and transfers it to the system evaporator through the heat exchanger. The refrigerant absorbs heat in the evaporator, evaporates, and then passes through the compressor, condenser, and throttle valve to complete a cycle [42]. Compared with IX-SAHP, the application of the collector in the DX-SAHP system makes the system structure more simplified and compact for the following reasons: (1) the refrigerant in the solar collector directly absorbs heat and vaporizes, leading to higher thermal performance; (2) at the same time, the working fluid in the collector is refrigerant instead of water, which can prevent the freezing problem of

solar collectors on cold nights [39]; (3) for the collector, the refrigerant absorbs heat and evaporates in the collector, which can maintain a low collector temperature and effectively improve the efficiency of the collector. The disadvantage of DX-SAHP is that the thermal performance of the system is closely related to the change in solar radiation intensity. As the daily solar radiation intensity can vary from 0 W/m^2 to 800 W/m^2 , the thermal performance of the system fluctuates greatly [43]. Figure 8a–d display the system diagrams for DX-SAHP and IX-SAHP in series, parallel, and hybrid connections. In a series system, the solar collector and the heat pump evaporator are connected in series and exchange heat through an intermediate medium. In the parallel system, the solar heat collection system and the heat pump system are connected in parallel, and both can produce hot water [43]. Figure 8e presents the system diagram of a PV/T-SAHP system. Compared with normal photovoltaic-assisted solar heat pumps, the PV/T systems address both the cooling need of photovoltaic modules and the heat absorption need of the evaporator. The solar energy utilization efficiency is significantly improved when the photoelectric and photothermal conversions are carried out at the same time. In addition, the working temperature of the photovoltaic cell is decreased, and the photoelectric efficiency is increased. As the heat source of the heat pump, the PV/T heat collection module increases the evaporation temperature and evaporation pressure of the working fluid of the evaporator so that the coefficient of performance of the heat pump can be improved [44].

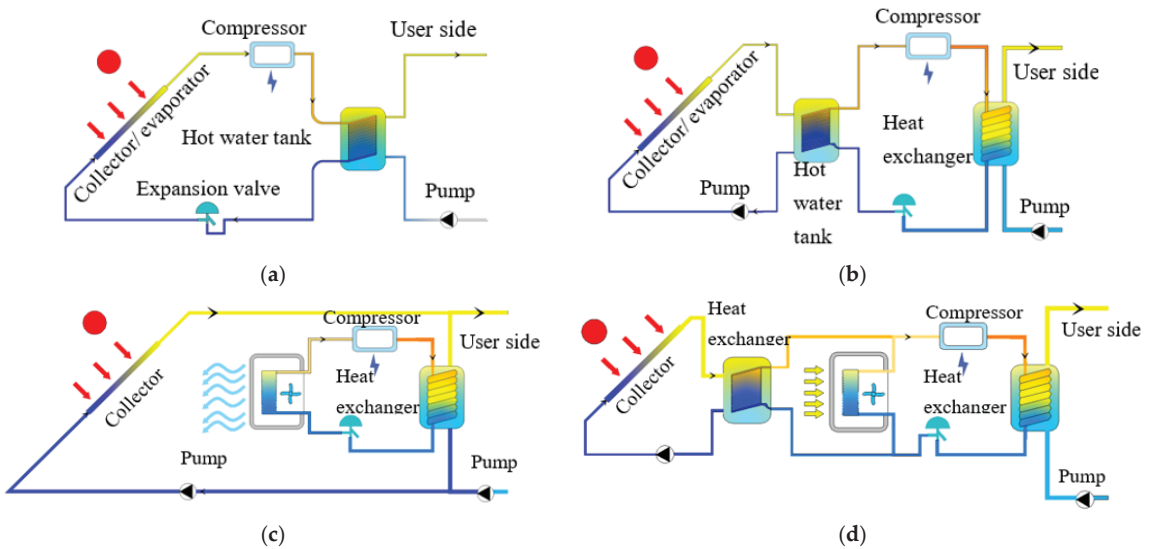


Figure 8. Cont.

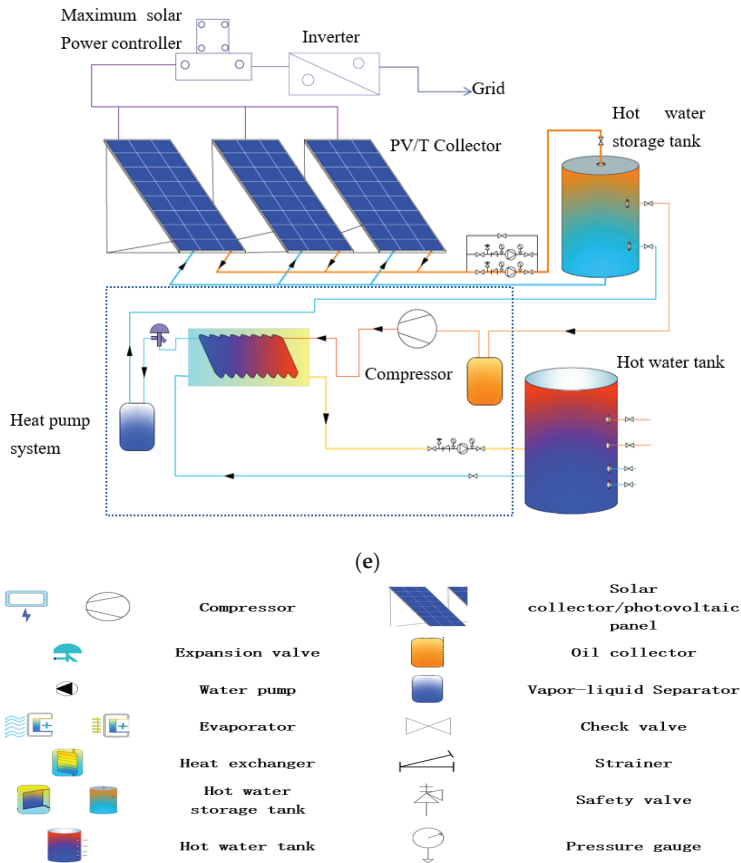


Figure 8. Different types of SAHPs. (a) Schematic diagram of DX-SAHP; (b) Series connection of IX-SAHP; (c) Parallel connection of IX-SAHP; (d) Hybrid connection of IX-SAHP; (e) PV/T-SAHP [43].

3.2. Research on the Core Components of Heat Pumps

The SAHP system follows the basic reversed Carnot cycle, assuming that the refrigerant gas compression is adiabatic and reversible, so that there is no pressure loss outside the compressor and throttling device, and there is no heat exchange with the ambient environment except with the evaporator and condenser. The theoretical cycle of DX-SAHP can be described as two isobaric heat transfer processes of isentropic compression and adiabatic throttling [42]. In practice, due to the complexity of the system and environmental factors, overheating, subcooling, and pressure drops exist during the refrigerant cycle; therefore, it is much more complicated than the reversed Carnot cycle [40]. The solar collector/evaporator, compressor, and piping system are the core parts of the SAHP. Their performance directly affects the operating efficiency of the entire system. Therefore, they will be separately discussed in the following sections. Meanwhile, the research on heat exchangers and refrigerant flow characteristics will be presented.

3.2.1. Solar-Collector/Evaporator

Current PV/T collector/evaporator research focuses on the heat exchanger where the bare-plate structure is common for most evaporators [45–51]. As the finned tube structure has the advantages of material saving, lightweight, and high heat exchange efficiency, the tube-fin structure heat collecting evaporator receives wide attention [43]. Figure 9 provides a schematic diagram of a solar collector module. Figure 10 is the cross-sectional view of

a heat pipe of a PV collector/evaporator, with Table 2 summarizing the investigations on evaporator-related components by Chinese scholars. Based on the comparison of the systems' COP, a significant improvement in the system performance can be found after the optimization of the materials and structural configurations of the evaporator.

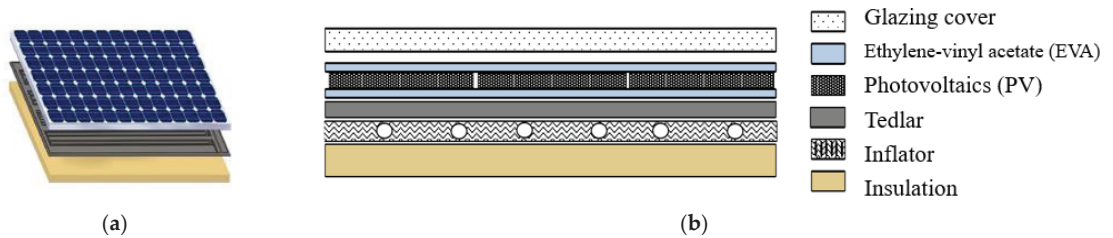


Figure 9. Structure layered diagram of PV/T collector/evaporator [40]. (a) Structure diagram; (b) Sectional view.

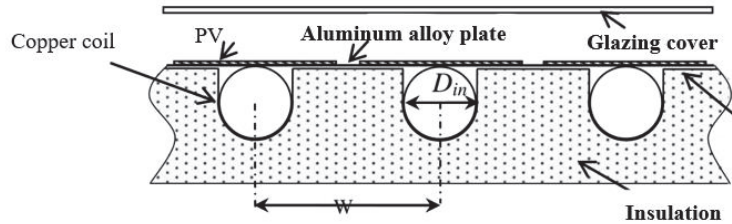


Figure 10. Cross-sectional view of the heat pipe of the PV collector/evaporator [41].

The collector/evaporator is responsible for heat collection. At the same time, the working fluid evaporates in the collector/evaporator and absorbs heat from solar thermal conversion and ambient air which increases the evaporator temperature and improves the system COP. Therefore, they are the key components to exploit solar radiation to improve the system's efficiency. The technical difficulties in the research on collector/evaporators lie in how to improve the absorptivity of the collector/evaporator and their heat transfer performance. The corresponding solutions are to use finned tube structures with high heat exchange efficiency and selective absorption coating for the collector/evaporator.

The above literature survey shows that the improvement of the collector/evaporator and the load matching between the evaporator/condenser and the compressor have always been the focus of the research. Many studies have been carried out on the structural arrangement of vertical copper–aluminum finned tube collector evaporators and fins. Moreover, investigations have been conducted on the arrangement between the heat-absorbing plate and the evaporator, refrigerant selection, and structural optimization of the collector/evaporator. The evaporator structure and material selection have a great influence on the operation of the whole DX-SAHP system.

Table 2. Investigations on evaporator components of the SAHP system.

Author	Year	System Type	Note	Average COP	Ref.
Ji et al.	2009	PV/T DX SAHP	The system can produce electricity and heat at the same time. The performance of the heat pump was tested, and the numerical model was validated. The photovoltaic efficiency (instantaneous rate of conversion from solar energy to electricity) of the system was >12% during the period of measurement (from 8:00 a.m. to 16:00 a.m.), which was higher than other types of photovoltaic/thermoelectric systems.	3.5	[45]
Song	2020	DX SAHP with Novel Fresnel Photovoltaic + Triethylene Glycol (TEG) Hybrid Evaporator	Experimental investigation was conducted, and it was shown that under the irradiation of 800 W/m ² , the maximum photovoltaic power generation can be increased by 43.77 W, and the electrical efficiency can be increased by 1.40%. Meanwhile, the COP of the hybrid system can reach 7.89.	7.89	[44]
Xu et al.	2006	Dual-source DX-SAHP	Simulation was performed for a system with a tube-fin structure evaporator, and it was shown that the overall energy efficiency for hot water heating was improved, and the system worked properly even during rainy days and produced hot water at 55 °C under all weather conditions.	4.6–5	[46]
Qin et al.	2018	New Direct Expansion Variable Frequency Fin-tube Solar/Air Assisted Heat Pump Water Heater	System performance was tested with a solar simulator in the enthalpy difference laboratory, and the results show that the energy consumption of the compressor was almost not affected by ambient temperature, solar irradiation, and operating mode. Energy consumption of the evaporator and COP increases with the increase in ambient temperature and solar irradiation. It was recommended to operate the compressor at 60 Hz under ambient temperatures of 20 °C to 30 °C and average solar irradiation of 900 W/m ² .	<4.15	[47]
Long et al.	2019	New Water Refrigerant SAHP System	The system is configured with a tube-fin evaporator. It can obtain heat from low-temperature water easier than the traditional water refrigerant evaporator and, therefore, has better performance in utilizing air sources and solar energy through heat pumps in cold seasons.	3.87–4.45	[48]
Cai et al.	2019	Series DX-SAHP system	The system is configured with a tube-fin structure evaporator and a bare plate structure collector in series. The average COP increases from 2.78 to 3.31 with the ambient temperature rising from 5 °C to 30 °C and from 2.71 to 3.22 with solar radiation increasing from 100 W/m ² to 300 W/m ² .	2.71 *	[49]
Ji et al.	2020	DX-SAHP system with tube-fin structure heat-collecting evaporator	The influence of environmental parameters on the operation of the system is compared with that of the bare plate structure system. It was found that the COP of the bare-plate type system and the finned-tube type DX-SAHP increased by 6.6% and 16.2%, respectively, with the ambient temperature rising from 5.0 °C to 15.0 °C. Under frost conditions, the COP of the finned-tube type system decreases from 1.72 to 1.54 with relative humidity rising from 50% to 90%, while the COP of the bare-plate type system increases by 16.3%, with the relative humidity rising from 70% to 90%.	2.56–2.58	[50]
Wang and Quan	2015	Dual-source heat pump (DSHP) system	The whole system is equipped with two evaporators, and the heat of the evaporators can be provided by an air source or solar energy. It was found that COPs of the dual-heat-source operating mode and single-heat-source operating mode varied in the range of 1.70 to 3.27 and 1.45 to 3.18, with mean values of 2.49 and 2.24, respectively.	4.08	[51]

* At an ambient temperature of 10 °C and solar irradiation of 100 W/m².

3.2.2. Operation and Thermal Characteristics of the Compressor

The operating frequency, solar irradiation intensity, and ambient air temperature are the three most important factors that affect the performance of the SAHP. In particular, the performance of the compressor plays a key role in the system's performance [52]. The matching between different components is very important, especially the matching between the area of the collector/evaporator and the compressor capacity [53]. Table 3 lists the theoretical investigations on the characteristics of the compressor by Chinese scholars. It can be found that the system COP can be improved by adjusting the compressor speed under different working conditions.

Table 3. Theoretical investigations on the characteristics of the compressor.

Scholar	Year	System Type	Note	Average COP	Ref.
Cai and Li	2019	New air source hybrid SAHP	Experiment was conducted on a new type of air-source hybrid SAHP and results from the experiment show that the compressor has the largest exergy loss in the heat pump system.	5.02	[49,54]
Kong et al.	2020	DX-SAHP hot water heater system	Under steady state and actual working conditions, the influence of different compressor speed adjustment methods on system performance is analyzed, and it is shown that the compressor speed has little effect on the heating power demand of the system, and a reasonable compressor speed adjustment method will help improve the energy efficiency and stability of DX-SAHP systems.	4.6	[55]
Pei and Ji	2007	Photovoltaic SAHP	High-frequency mode helps improve the condensing capacity and photovoltaic and thermal efficiency. Low-frequency mode results in a reduction in compressor power consumption and the compression ratio. Therefore, the compressor frequency should increase with the increase of solar radiation intensity to improve the thermal efficiency of the system.	3.8–4.2	[56]
Li and Huang	2021	SAHP	The effect of compressor speed on the performance of the SAHP system under different operating conditions was studied experimentally, and it was shown that when the solar radiation intensity was low, increasing the compressor speed could significantly improve the heating capacity of the system. When the ambient temperature is low, increasing the compressor speed will slightly reduce the system's COP, but it can help improve the system's heating capacity.	7.7	[57]
He	2019	PV-SAHP test bench	The effect of compressor frequency on system heating performance and system power generation under different weather conditions was verified. The results show that the average value of solar irradiation intensity and ambient air temperature does not have an obvious impact on the compressor operation frequency and average COP.	4.4–4.7	[58]
Dong	2015	DX-SAHP water heater test bench	System performance was obtained via a data acquisition and monitoring system in Qingdao. It is concluded that the COP of the SAHP system can be above 6.0 in summer, and the COP in cold winter can be above 4.0.	4.0–4.38 in winter mode	[59]
Dong et al.	2013	DX-SAHP	Variation of the compressor capacity with solar radiation intensity was simulated, and the authors concluded that the adjustment of the compressor frequency can greatly improve the system performance of the SAHP.	>3.0	[60]
Qin et al.	2017	DX-SAHP test bench	The effect of compressor frequency on system performance and frost formation under different modes was tested. It was shown that when the compressor frequency is 60 Hz, the system COP under the air energy mode are greater than that in the dual-source mode and vice versa when the compressor frequency is 45 Hz or 30 Hz.	Up to 3.54, 45 Hz, dual-source mode.	[53]
Li et al.	2007	New DX-SAHP hot water system	Simulation and validation of the system performance under various operating conditions were carried out in Shanghai. The results show that, due to the use of the capacity adjustment method of the inverter compressor, the COP of the system can reach 5.29 ~6.93 on sunny days in autumn, and the COP of the system can reach 3.11 on a rainy night with an ambient temperature of 17.1 °C.	Up to 5.29~6.93 in autumn	[61]

The compressor is a fundamental component of the SAHP system, as it is responsible for circulating the refrigerant throughout the system. The choice of the compressor may deeply affect the system's performance and reliability. The technical difficulties of the research on compressors are how to match the compressor with solar heat gain under different climatic conditions while improving the system performance and also avoiding short-cycling under low load conditions. The solutions are to use variable frequency compressors and using dynamic frequency control.

The above literature survey demonstrates that lots of work has been carried out on the variation of working conditions of the SAHP under ambient environments. It can be summarized that (1) the dynamic matching of the compressor, collector/evaporator, and other components affects the overall performance of the SAHP system, and it is crucial for the improvement of the system COP; (2) the dynamic frequency adjustment strategy on the performance of the compressor is highly sensitive to regional environmental and weather factors. Simply adjusting the operating frequency of the compressor does not lead to a significant improvement in the thermal performance of the system. Further research can be carried out to obtain the optimal variable capacity control strategy by considering multiple influencing factors. In addition, more in-depth experimental tests are needed to optimize the operation modes of multi-functional composite heat pumps such as PV and PV/T heat pumps.

3.2.3. Refrigerant and Its Flow Characteristics

Chlorofluorocarbons (CFCs) are widely used in refrigeration cycles due to their excellent thermodynamic and chemical properties. Considering the ozone depletion potential and the impact of chlorofluorocarbon-containing refrigerants, including CFCs, Hydrochlorofluorocarbons (HCFCs), and Hydrofluorocarbons (HFCs), on the atmospheric environment, the search for suitable environment-friendly and high energy performance refrigerants has been one area of the research focus [62]. Many studies have been conducted on the characteristics of refrigerants in DX-SAHP systems. In China, the production of R11 and R12 has been prohibited, and the production of R22 is based on a quota and will be prohibited in 2030 [63]. Potential alternative refrigerants for R12 include R134A, R152A, R142B, etc., among which R134A is widely used in heat pump air conditioners [64]. Studies have shown that SAHP systems using R-12 and R-22 have the highest COP, and R-134A has the best performance among all the alternative refrigerants. Compared with R-134A, the COPs of all mixed azeotropic refrigerants can be lower by up to 20% [65]. An important research direction in China is to study the use of environmentally friendly refrigerants and their flow characteristics in the heat pump system. Among them, the refrigerant mass flow rate adjustment is of great importance for the efficient operation of the heat pump system [65]. Table 4 shows the recent investigations on the refrigerant of SAHP by Chinese scholars. It can be found that most of the studies focus on R134a, R290a, and R410a. The systems with R134a have the highest COPs under different working conditions. Therefore, it can be considered the best refrigerant and will be widely used in SAHPs.

Table 4. Recent investigations on the refrigerant of SAHP by Chinese scholars.

Author	Year	System Type	Note	Average COP	Ref.
Zhao et al.	2000	DX-SAHP	Simulation was performed for the system with R134a and R12 as refrigerants, and the results show that the COP of the R134a system could reach 4.0–6.5 with a discharge temperature of the compressor lower than that of the R12 system.	4.0–6.5	[66]
Kong et al.	2018	DX-SAHP	The control strategy of the DX-SAHP system with R134a as the refrigerant was developed by adjusting the degree of superheating and the control method of the DX-SAHP system with variable frequency compressor was also developed.	3.9–5.22	[67]

Table 4. Cont.

Author	Year	System Type	Note	Average COP	Ref.
Kong et al.	2020	DX-SAHP	Experimental investigation was carried out on two DX-SAHP systems with R134a and R290 as the refrigerants, respectively. The results show that the average COP of the system using the R290 refrigerant is higher than that of the R134a system under winter conditions.	2.72	[68]
Wang et al.	2018	SAHP	Theoretical analysis was performed on the system performance of the SAHP using R1234yf and R134a as the refrigerants. The results show that the COP of the dual-source heat pump system using R134a is about 2% to 3.4% higher than that of the R1234yf system. R1234yf as an alternative refrigerant of R134a has broad application prospects.	5.61 (R1234yf) 6.68 (R134a)	[69]
Yang et al.	2020	DX-SAHP	An experimental study was carried out for a DX-SAHP using R290 as refrigerant under actual weather conditions for a whole year. The annual average heating power was found to be 1358.6 W. The maximum, minimum, and annual average system COP were found to be 5.99, 2.04, and 3.88, respectively.	3.88	[70]
Ouyang	2012	Dual-source CO ₂ heat pump	A theoretical analysis and optimization study of a dual heat source solar-assisted transcritical CO ₂ heat pump system suitable for winter conditions in north China was performed.	4.97	[71]
Kong et al.	2010	DX-SAHP	A DX-SAHP experimental system using propane as the refrigerant was developed.	4.2	[72]
Li et al.	2020	new solar-assisted heat pump multifunctional composite machine (SAHPMCM)	The working principle of the new solar-assisted heat pump multifunctional composite machine (SAHPMCM) is introduced. The PID control method on the expansion valve, system setting, and experimental results on the corresponding COP were given.	4.5	[36]
Zhang	2014	DX-SAHP	A study was carried out on the effects of refrigerant charge and system design parameters on the performance of the heat pump. It was found that when the area of the solar collector is 6.0 m ² , the length of the condenser tube is 70 m, and the inner diameter of the condenser tube is 9 mm, 70–80% of the refrigerant is distributed in the evaporator and condenser, and the most suitable refrigerant charge is 1.65–1.75 kg.	3.5–5.5	[73]
Kong et al.	2017	DX-SAHP	A simulation program of the DX-SAHP water heater system using R410a was developed, and the influence of five parameters, including the refrigerant charge on the thermal performance of the system, was analyzed under fixed superheat at the collector/evaporator outlet.	4.1–6	[74]
Zhang et al.	2013	DX-SAHP	A mathematical model of the refrigerant charge was developed, and the simulation results show that most of the refrigerant exists in the heat exchanger, of which over 50% remains in the condenser. In order to avoid refrigerant leakage, a refrigerant charge of 1.65–1.75 kg was recommended.	3.8	[73]
Qi et al.	2014	Solar-air energy dual-source integrated heat pump system	A Tandon cavitation coefficient calculation model was developed under a Maple environment and the R134a refrigerant charge was obtained which was close to the actual optimum refrigerant charge.	3.7–4.5	[75]
Kong et al.	2021	DX-SAHP	A neural network model was developed to predict the mass flow rate of the R290 refrigerant. It was found that the increase of solar radiation intensity leads to an overall increase in the mass flow rate of R290; however, with the increase in ambient temperature, the influence of solar radiation intensity on the mass flow rate of refrigerant decreased.	4.38–5.69	[76]
Wang	2021	DX-SAHP	A new subcooling control system was proposed, and the influence of the subcooling degree on the new system was studied. The results show that, with the increase in subcooling degree, the heat supply per unit of refrigerant mass flow will increase, and the heating coefficient will increase first and then decrease. When the subcooling degree is 4 K, the heating COP is the highest. When the subcooling degree is controlled within the range of 2 K~ 5 K, the heating COP is maintained at the high-level range.	4.0–6.5	[77]

The refrigerant is the working fluid in the refrigeration cycle and, as such, is highly important. The technical problem of the research is to find refrigerants with a low environmental impact that leads to high system COP. Environmentally friendly refrigerants are the potential solutions to solve these problems.

Based on the above literature survey, it can be seen that due to the environmental problems caused by HCFCs refrigerants such as R22 and R12, searching for new green and environmentally friendly refrigerants to replace traditional refrigerants has become the focus of the research. Alternative refrigerants including R134a, R152a, R142b, R410a, etc., have been proposed as replacement refrigerants. Among these, it is worthwhile to mention that many studies focused on the application of the R134a refrigerant in the DX-SHAP, especially its influence on energy consumption and system COP. In addition, theoretical and experimental studies on the application of new refrigeration cycles such as transcritical CO₂ to SAHP systems, as well as research on the flow characteristics of new environmentally friendly refrigerants in PV/T-SAHP systems, are relatively few in China. As the physical properties, charging capacity, and type of refrigerant are important factors affecting the COP and energy consumption of the system, more investigation on its operating performance and system optimization are needed.

3.2.4. Performance of the Dual-Source Heat Pump

The heat exchange performance of the heat pump system is very important to improve the operation performance of the heat pump and antifog in cold winter. Chinese scholars have carried out experimental and theoretical studies on the heat exchange performance for different types of SAHPs, including solar-assisted air source heat pumps, solar-assisted soil-source heat pumps, solar-assisted water source heat pumps, etc. [78,79]. Table 5 lists the relevant studies on the performance of the dual-source SAHPs by Chinese scholars.

Table 5. Relevant studies on the heat exchange performance of SAHPs by Chinese scholars.

Author	Year	System Type	Note	Ref.
Huang et al.	2017	Solar-assisted air source heat pump	The mathematical model of the solar collector was developed. The study shows that the energy efficiency ratio of the system can be improved by 1~2 with solar radiation.	[78]
Cai	2019	Air source solar-assisted heat pump (AS-SAHP)	Through theoretical analysis and experimental validation, it was concluded that with the increase in solar radiation intensity on the collector/evaporator side, the system COP can be significantly increased with a relatively small increase in power consumption.	[49]
Wan et al.	2020	Solar and air dual heat source two-stage compression CO ₂ heat pump water heater system	The component model and the thermal physical property parameter model of the refrigerant were developed. Simulation results show that when the flow rate of solar hot water is 0.6 m ³ /h and the outdoor environment is 15 °C, the system COP increase by 11.6%, compared with the air source heat pump.	[80]
Hou	2008	SAHP	Economic analysis was performed for SAHPs with air source and three conventional energy sources as auxiliary heat sources. The results show that in Lanzhou, the air source heat pump water heating system has economic advantages over other systems.	[81]
Yang et al.	2008	Solar-assisted soil-source heat pump	The heat storage characteristics of soil for the U-shaped buried tube heat exchanger were carried out through simulation and experimental validation. It was shown that the intermittent heat storage method is beneficial to the recovery of soil temperature and further improves the heat storage efficiency of soil.	[82]

Table 5. Cont.

Author	Year	System Type	Note	Ref.
Wanget al.	2008	Solar-ground coupled heat pump system (SGCHPS)	Through experiment and computer simulations, it was concluded that the underground heat storage performance of SGCHPS strongly depends on the intensity of solar radiation and the ratio between the volume of the water tank and the area of the solar collector. It is suggested that the reasonable ratio of the volume of the water tank to the area of the solar collector should be within the range of 20~40 L/m ² .	[83]
Han et al.	2008	SGCHPS	A computer program on the SGCHPS was developed, and the simulation results show that the annual average heating performance coefficient of the system under combined solar and soil source energy operation mode was 2.674.	[84]
Xu et al.	2015	SGCHPS	The computer model was developed under the TRNSYS environment, and the heating mode operation was validated with an experiment. It was concluded that under the combined heating mode, the soil temperature at different buried depths mainly depends on the solar radiation intensity, and a high soil temperature can ensure high system energy performance.	[85]
Gao et al.	2020	SGCHPS	The imbalance efficiencies of ground source heat pumps (SGHP) were analyzed, and Beijing, Harbin, and Zhengzhou were selected as representative cities from cold regions, severe cold regions, and hot summer and cold winter region analysis. The results show that the operating time for SGCHPS was shorter than SGHP, with more energy reduction, and it can keep the unbalance rate at 1% after system optimization.	[86]
Yi	2009	Solar-assisted water source heat pump	The experimental study shows that under the testing conditions, the COP of the system in the heating and cold storage mode was in the range of 5.8~6.2.	[87]
Qu	2015	Solar-assisted water source heat pump	A computer model was developed to simulate the application of the system in a villa in Beijing under the TRNSYS environment. The results show that when the temperature difference between the supply and return water of the collector was at 7 °C, the COP of the system can reach 2.47.	[88]
Li	2011	Solar-assisted underground water source heat pump	An economic analysis for the application of a solar-assisted underground water source heat pump system in a residential building in Shenyang was performed. Compared with oil-fired boilers and electric boilers, the proposed system is more energy efficient. However, it is less economical than coal-fired boilers but with minimal environmental pollution.	[89]
Ma	2020	Solar-air-wastewater multi-energy complementary heat pump system	Through computer simulation and experimental validation, it was shown that the system is applicable in hot summer and cold winter regions. When there is not enough space for a solar collector or the heating capacity of the system is not enough to meet the demand of the building, it can be considered to add a sewage water source as auxiliary energy.	[90]

Based on the above survey of the literature, it can be concluded that the coupling of solar energy and other heat sources needs to take advantage of the abundance of energy sources in the specific region. This is because multi-energy-source heat pumps usually have higher COPs than that of single-source heat pumps. Few papers have focused on the intelligent control of the SAHPs; although, it is very important to match the dynamic user demand and achieve energy saving in practice. More studies are needed to optimize the capacity matching among all the components of the heat pump to achieve high system energy efficiency.

3.3. Research on the Performance of SAHP

Different commercially available software and programming language have been used by scholars to conduct simulations of the performance of the SAHP system, among which TRNSYS was most favored by the researchers due to its ability to dynamically simulate the annual building thermal load, heating/air conditioning system operation, solar energy system, ground source, hybrid connection SAHP performance, etc. Table 6 lists representative numerical studies on SAHP systems and the programs used by the researchers.

Table 6. Numerical studies on the SAHP system by Chinese scholars.

Author	Year	System	Program and Results	Ref.
Cai	2015	PV/T-assisted heat pump water heating system (PV/TA + HPWH)	A computer model was developed under the MATLAB environment using the Simulink platform. It was validated with experimental data in June 2013 and showed sufficient confidence under fluctuating solar radiation conditions.	[91]
Dai et al.	2017	Hybrid photovoltaic solar-assisted loop heat pipe/heat pump system (PV-SALHP/HP)	A computer program was written to simulate the performance of the PV-SALHP/HP system. The results show that, on typical sunny days in spring and autumn, the operation under the hybrid LHP/HP mode leads to 40.6% energy saving compared with the operation under the HP mode. Note: Software platform not specified.	[92]
Zhou et al.	2020	Micro-channel PV/T modules based direct-expansion SAHP system	A unified calculation computer program was written in C language to simulate the annual performance of a novel DX-SHAP system with microchannel PV modules for space heating. The results of the simulation were validated with daily experimental data with a maximum error of 7.2%.	[93]
Luo et al.	2020	Non-direct expansion solar-assisted air source heat pump	A computer program was written under the TRNSYS environment to simulate the performance of the system installed in residential houses in Shangri-La. The relationship between the heat pump capacity and the heating area was obtained.	[94]
Wang	2020	SAHP hot water system	A computer program was written under the TRNSYS environment to evaluate the energy and economic performance of the system with an energy-efficient conservation operation strategy.	[95]
Shen	2015	Parallel SAHP system	A computer model was developed under the TRNSYS environment for the parallel SAHP system, and the annual operation performance of the system was simulated.	[96]
Yin	2013	SGCHPS	Mathematical models for each component of the system were developed, and a computer program was written under the TRNSYS environment. The performance of different system connection methods was analyzed, and it was recommended to set the location of the solar energy supplement hot spot between the outlet of the heat pump unit and the inlet of the buried pipe.	[97]
Li	2017	Solar-assisted air source heat pump integrated domestic hot water system (SASIHDPHW)	A computer program was written under the TRNSYS environment to simulate the performance of the SASIHDPHW system, and it was validated with experimental results with a difference of less than 10%. The annual average COP of the system was found to be 4.12, which is 11.7% higher than that of an air-source heat pump.	[98]
Wei et al.	2019	SAHP	A computer program was written under the MATLAB environment using the Simulink platform, and the impact of solar radiation intensity, area of the collector/evaporator, etc. were analyzed.	[99]
Guan et al.	2009	Solar-storage and ground source heat pump hot water supply system	A computer model was developed under the TRNSYS environment to optimize the solar water heating system of a demonstration project in Tianjin. The results show that solar energy and renewable energy (solar energy + ground source energy) accounted for 62.8% and 86.5% of the total heat supply, respectively.	[100]

Figure 11 lists the simulation platforms/programming languages adopted by the researchers. It can be found that a large proportion of the computer models were developed under the TRNSYS/MATLAB environment. TRNSYS is most favored by researchers for whole system performance analysis, while MATLAB is welcome for analyzing the operating characteristics of a certain component in the SAHP system and the dynamic energy

performance under different environmental conditions. The CFD software, such as ANSYS and Fluent, is used to perform analysis of indoor thermal and humidity environments.

From the literature survey, it can be concluded that current studies focus on whole system operation performance or component level simulation, or indoor environmental condition analysis. Few studies have been conducted to investigate the optimal control strategies and their impact on indoor thermal and humidity, which could be the future direction of research.

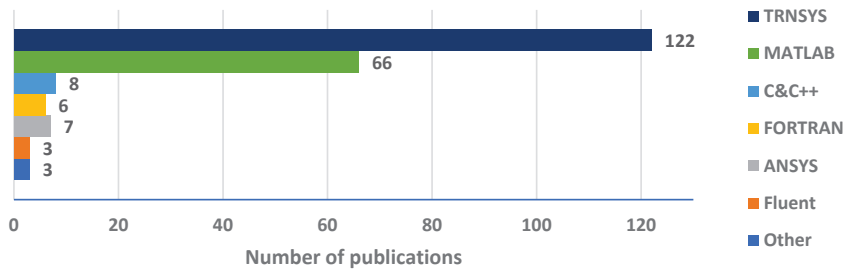


Figure 11. Simulation platforms/programming languages adopted by the researchers.

3.4. Economic and Feasibility Evaluation

The economic and feasibility evaluation of the SAHP system is also an important area of research. Although the SAHP systems utilize renewable energy, the installation of such systems requires extra costs [100,101]. In addition, the SAHP system might not be able to provide enough cooling and heating when solar radiation is low. In this case, an auxiliary heating/cooling system would be needed, which would result in additional investment costs. Therefore, the economic and feasibility evaluation of the SAHP system is critical. Table 7 lists the relevant studies of SAHP from Chinese scholars.

Table 7. Economic and feasibility evaluation of SAHP.

Author	Year	Focus	Conclusion	Ref.
Yu	2007	Environmental benefits of SAHP	It was found that after the introduction of the environmental protection tax, the price of coal power will rise significantly, the economy of SAHP will become worse due to the need of electricity for auxiliary heating, and the environmental benefits of SAHPs are worse than natural gas boilers.	[102]
Feng	2012	Economic and Environmental Benefit Evaluation of PV-SAHP Water Heaters (PV-SAHPWH)	PV-SAHPWH has the highest initial cost and lowest operating cost in the Nanjing area compared with other hot water systems, leading to the lowest lifecycle cost and highest environmental benefits.	[103]
Luo et al.	2009	Thermal performance evaluation and economic analysis of air source heat pump-assisted heating solar hot water system	Through reasonable component size matching, the COP of the air source heat pump unit can still reach 2.5 to 3.3 in the coldest month. The use of the system can lead to great energy saving potential compared with other cold/heat sources and is economically feasible.	[104]
Jing	2015	Energy saving potential, economical, and environmental analysis of the air source heat pump-assisted solar water heating system	Compared with oil-fired and gas-fired hot water boiler systems, the energy consumption and dynamic annual cost of this system are both the lowest.	[105]

Table 7. Cont.

Author	Year	Focus	Conclusion	Ref.
Liu	2011	Economic and environmental benefits of air source heat pump-assisted solar water heating system	Compared with other conventional hot water systems, the air source heat pump-assisted solar water heating system led to the lowest annual operating energy consumption and the best economic and environmental benefits in Chongqing.	[106]
Peng	2010	Economic and environmental benefits of air source heat pump-assisted solar water heating system	Compared with other conventional water heating systems applied in the Yangze River and the Huai River region, the solar energy guarantee rate is 46%, and the energy consumption is the lowest. The environmental benefits of the system are comparable to the gas-fired boiler system.	[107]
Hou et al.	2008	Economic impact factors of heat pump-assisted solar centralized hot water system	Compared with the other three alternative conventional solar energy auxiliary heat source systems, while considering the impact of the increase in energy price, the use of air source heat pumps as auxiliary heat sources has strong economic competitive advantages, as well as social and environmental benefits in large-scale application in the cold regions in northwest China.	[81]

From Table 7, it can be found that most of the investigations were on the energy saving potential and economical and environmental analysis of the system, especially the air source heat pump-assisted solar water heating system as it is common and easy to be implemented. Analysis of other types of systems is relatively rare and very little research could be found on exergy analyses of the system, which could be the future research direction.

4. Application of SAHP

The application of SAHP in a certain region is related to the solar power generation capacity in that region. Figure 12 presents the solar power generation by region in China in 2019. It can be observed that solar power generation concentrates in the northwest, east coast, and north China regions. The solar power generation in the northern region of China (north of Qinling and Huaihe River) is much higher than that in the southern region, which could be due to the better local solar energy resources and more supportive government policies in northern regions. As a result, more SAHP projects were developed in northern regions. Table 8 lists the representative SAHP projects in China since 2001 that have been implemented and put into operation. The projects were selected from the national and local government official websites. Those local renewable demonstration projects have been completed and put into operation with proven energy-saving data and benefits. These projects demonstrate innovation and economic and environmental protection benefits compared with traditional projects.

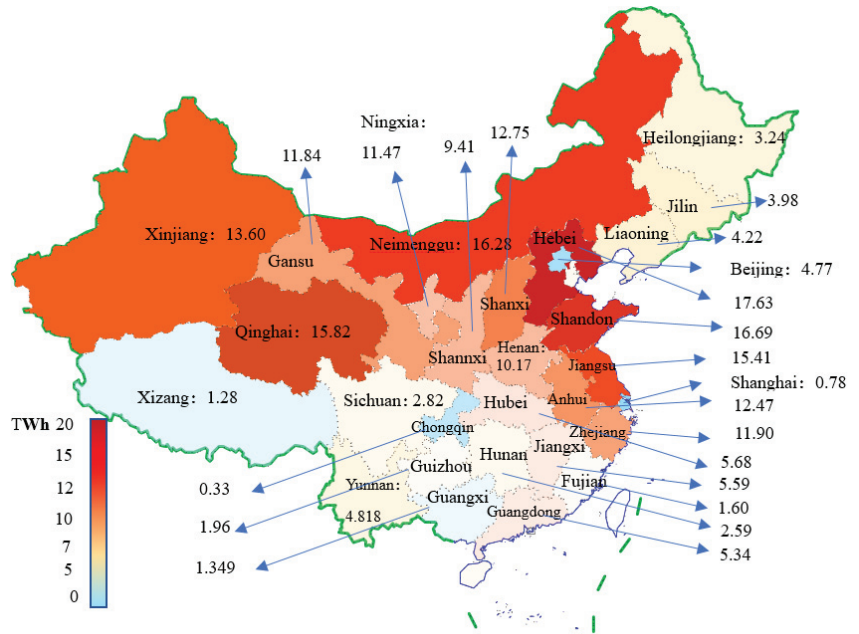


Figure 12. Solar power generation by region in China in 2019 (TWh) [3].

Table 8. List of representative SAHP projects in China.

Year	Project Name	Location	Project Information	Operation Benefits	Comparison with Traditional System	Ref.
2004	Olympic Village SAHP Hot Water System	Chaoyang District, Beijing	The system was designed to supply hot water to the Olympic Village prepared for the 2008 Beijing Olympic Games. Hot water heating was mainly through solar energy and assisted by a heat pump.	An automatic intelligent controller was adopted with real-time performance detection. Automation control was realized.	Compared with the oil-fired boiler heating system, the energy-saving ratio is more than 60%, and, compared with the electric heating system, the energy-saving ratio is 90%.	[101]
2004	Solar air conditioner heat pump system in Beijing Tianpu Group Industrial Park	Chuanyue Road, Lucheng Industrial Zone, Daxing District, Beijing	An absorption lithium bromide solar air conditioning system was adopted. It was the largest solar air-conditioning system among the new energy demonstration buildings in China at that time, and it is also one of the buildings with the largest percentage of renewable energy usage in the total energy consumption of China.	The air conditioning and heating requirements of the new energy demonstration building are satisfied, and the heat collection efficiency in winter and summer reaches 0.2 and 0.4, respectively.	Compared with the traditional gas boiler, 1600 m ³ of natural gas can be saved every year.	[108]
2006	Solar system of a holiday hotel in Pudong New Area, Shanghai	Pudong New Area, Shanghai	The system adopts a solar collector and supplementary heating equipment, an intelligent control system, an SAHP water heater, hot water tank, etc., with a design power for hot water of 1745 kW.	As dual heat sources (solar and air energies) are used, even when solar irradiation intensities are low, the energy consumed by the system is only 50% of that of the solar hot water system.	A total of 2,076,390 m ³ of natural gas is saved during the 15-year life span with a CO ₂ emissions reduction of 6,175,183 kg.	[109]
2011	Asian Games City Solar Water Source Heat Pump Project	Panyu, Guangzhou	The system is designed to supply domestic hot water for residential buildings (1.14 million m ²) by solar heating in the Asian Games City and provide cooling by river water source (from the Lijiang River) heat pump for some single buildings (250,000 m ²). It is listed as a national renewable energy building application demonstration project.	The water source heat pump is used as an auxiliary heat source for solar energy. The highest daily water consumption during the competition could still be met when there was no solar heat collection.	Compared with gas heating, 5723 m ³ of natural gas with 260 kg of CO ₂ emission was reduced during the operation period.	[110]

Table 8. Cont.

Year	Project Name	Location	Project Information	Operation Benefits	Comparison with Traditional System	Ref.
2015	Shijiazhuang City Ground Source Heat Pump + Solar + Energy Storage System Project	No. 88, South Second Ring East Road, Shijiazhuang City	Solar energy and ground source heat pump systems combined with energy storage technology are used to provide heating, cooling, and domestic hot water for industrial and government buildings.	Cooling demand was satisfied by the ground source heat pump, and domestic hot water demand was satisfied by the solar energy system with an auxiliary electric heater.	Energy savings were equal to 79 t of standard coal every year, CO ₂ and other carbon oxide emissions were reduced by more than 188 t, NO _x emissions were reduced by 0.7 t, and SO _x and other sulfur oxide emissions were reduced by 1.32 t.	[111]
2015	Combined cooling, heating, and power demonstration project using ground source heat pump coupled solar energy in Ruzhou City, Henan Province	Ruzhou City, Henan Province	The system was designed to provide cooling, heating, and power to the Ruzhou No. 2 High School, and the project was awarded first place in the Henan Province Construction Science and Technology Progress Award.	The cooling and heating energy consumption of the building was significantly reduced by using geothermal and solar energy. The overall system COP was in the range of 3.8–4.4 all year-round. Meanwhile, the soil thermal imbalance problem was solved.	Compared with the coal-fired boiler + electric heating system before retrofit, the yearly operation cost was reduced by CNY 664,700 (135 t of standard coal). Compared with the coal-fired boiler system, the investment cost was reduced by CNY 410,000.	[112]
2016	Beijing Daxing Village Household Solar Energy + Air Source Heat Pump Heating Retrofit Project	Daxing, Songzhuang Town, Tongzhou District, Beijing	The system was designed to provide heating and domestic hot water for the working farmer with a heating area of 60 m ² and hot water demand of 250 L/d. The system was able to operate under ultra-low temperatures.	The system COP was able to reach 2.2 under low-temperature conditions in winter.	The energy savings on the daily electricity consumption was about 25 kWh (CNY 1500 of electricity in heating season).	[113]
2019	Solar + Water Source Heat Pump Heating Project of Caina Township Government, Qushui County, Lhasa, Tibet	Caina Township, Lhasa, Tibet	The system was designed to provide heating needs of government office buildings and dormitory buildings in a heating area of 5830 m ² with a design heating temperature of 18°C in winter, and the number of heating days was 150.	The heating COP of the water source heat pump was 2.0. The overall system heating COP was 3.85. The leaving water temperature from the collector reached 73.6 °C, which can satisfy the heating and hot water needs in winter.	During the test in a heating season, energy savings of equal to 128 t of standard coal and CO ₂ emission reduction of 448.9 t were achieved. CNY 7.16 × 10 ⁶ cost savings can be achieved compared with electric heating in a 20-year life span.	[114]
2020	Multi-energy source cooling and heating system retrofit project of Liaoning Building	Liaoning Building, Shenyang City, Liaoning Province	A retrofit project was designed for the cooling and heating system of the Liaoning Building. A water source heat pump was used for cooling and heating the air-conditioning system. An electric heat storage boiler was used to supply hot water to the radiator for heating. A solar heating system was used to provide domestic hot water. At the same time, natural gas was used as the steam heat source for the kitchen and washing machine.	The water source heat pump system was preferred for heating using the electric heat storage boiler as an auxiliary system during the valley's electricity demand period. The solar energy system was preferred for producing domestic hot water. The maximum system heating COP reached 4.1 and the average heating COP of the water source heat pump was 3.6.	Compared with the coal boiler system, annual energy savings equal to 1977 t of standard coal, and cost savings of CNY 3.4 × 10 ⁶ were achieved.	[115]

Figures 13 and 14 provide an overview of the Beijing Daxing Village Household Solar Energy + Air Source Heat Pump Heating Retrofit Project and the Solar + Water Source Heat Pump Heating Project of Caina Township Government, respectively.

The above projects point out that in regions with sufficient radiation during the heating season, DX-SAHP is suggested for seasonal heating. In regions with sufficient annual irradiation throughout the year, it is advisable to use solar heating assisted with a dual-source heat pump for heating. In cold regions that required heating most of the time in the year and with insufficient radiation, a combination of a non-direct expansion heat pump system with thermal storage technology as an auxiliary heat source is recommended. Furthermore, most projects are implemented in coastal areas in the east and inland areas with moderate solar energy resources and developed economies. Although solar energy resources are abundant in the northwest regions, southwest regions, and Tibetan regions, very few SAHP projects could be found in these regions. Therefore, to help reach carbon peak and carbon neutrality, it is recommended to promote SAHP projects in these regions.



Figure 13. Overview of the Beijing Daxing Village Household Solar Energy + Air Source Heat Pump Heating Retrofit Project [113].



Figure 14. Overview of the Solar + Water Source Heat Pump Heating Project of Caina Township Government [114].

5. Regulations, Standards, and Policies Related to SAHP

The solar energy industry is part of both the renewable energy industry and the energy-saving industry. Currently, the regulations, standards, and policies for SAHP mainly focus on solar thermal utilization and water heaters. Compared with large-scale solar heat collection projects, the standards and technical regulations of different types of SAHPs and hot water systems still need improvement. It is also important to increase the formulation and implementation of economic policies for SAHPs [116].

5.1. Regulations and Standards for SAHP in China

Table 9 lists the relevant regulations for SAHP in China. It can be seen that early regulations mostly focused on solar energy hot water systems due to their easy installation. “Technical specification for solar photovoltaic and thermal heat pump system (T/CECS 830-2021)” [117] is the first relatively complete technical regulation on the utilization of SAHP in the past ten years. In addition, the mandatory policies of relevant laws and regulations on SAHPs mainly focus on solar thermal utilization.

With the proposal of new national strategies for reaching carbon peak and carbon neutrality, a complete technical specification and design standard is needed for solar thermal utilization and SAHP application to support and promote the extensive application of SAHPs in China. In addition, there are very few mandatory policies for solar energy and heat pump engineering technology. Therefore, in the future development of SAHPs, the government still needs to formulate and improve relevant laws and regulations and develop practical guidelines for implementation accordingly.

Table 9. Relevant regulations and standards in China.

Implementation Date	Regulation	Status	Note	Ref.
2009.6.1	Specifications of air source heat pump-assisted domestic solar water heating system (GB/T 23889-2009)	Current	This specifies the terms and definitions, classification and nomenclature, technical requirements, measurement and test methods, inspection rules and documentation, marking and packaging of air source heat pump assisted domestic solar water heating systems.	[118]
2011.9.29	Test methods for the solar-plus-supplementary water heating system (tank capacity more than 0.6 m ³) (GB/T 26973-2011)	Current	The performance test method for solar water heating systems with auxiliary energy (the volume of the water storage tank is greater than 0.6 m ³) is specified. It does not apply to solar water heating systems with auxiliary heating by heat pumps.	[119]
2012	Technical code for solar air conditioning system of civil buildings (GB 50787-2012)	Current	Mandatory specification for design calculations of solar collector systems.	[120]
2018	Technical standard for solar water heating system of civil buildings (GB 50364-2018)	Current	Mandatory specifications for solar collector systems, hot water supply systems, and auxiliary heat source systems.	[121]
2019.6.4	Test method for domestic direct-expansion solar heat pump water heating system NB/T 10155-2019	Current	It specifies the test methods for DX-SAHP hot water systems for household and similar purposes and specifies the classification and coding, technical requirements, test methods, and inspection rules.	[122]
2019	Technical standard for solar heating system (GB50495-2019)	Current	Mandatory specification for solar heating design.	[123]
2021.8.1	Technical specification for solar photovoltaic and thermal heat pump system T/CECS 830-2021	Current	This standardized the design, installation, commissioning, acceptance, operation, and maintenance of the solar photovoltaic heat pump system and gave a detailed system description for each component of the solar photovoltaic heat pump system as well as the design, installation, and system selection.	[117]
2021	Notice of the Ministry of Housing and Urban-Rural Development on Printing and Distributing the Atlas of Passive Solar Heating in Rural Areas (Trial) and the Technical Guidelines for the Application of Household Air Source Heat Pump Heating (Trial)	Current	Guide the project development of solar energy and heat pump systems in northern rural areas through "Atlas of Passive Solar Heating in Rural Areas (Trial)" and "Technical Guidelines for Application of Household Air Source Heat Pump Heating (Trial)"	[124]

5.2. Government Financial Subsidy Policy for Solar Industry

The solar photovoltaic industry in China has great development potential with policy-based financial support and market-based financial support. However, due to the high investment risk and uncertain yield in the renewable energy market, market-based financial support is not yet mature enough. Therefore, setting up economic policies that can provide guidance and incentives to the solar energy industry is very important at the early stage [125]. For example, the average photovoltaic power generation cost is about six times that of thermal power. However, among all primary energy sources, the proportion of solar power generation energy has steadily increased. By 2020, the annual solar energy utilization nationwide reached over 1.140×10^8 tons of equivalent standard coal [126].

From 2012 to 2021, the proportion of solar power generation increased from 0.07% to 4% of the total national power generation [127].

The SAHP industry belongs to the new energy industry and renewable energy industry, and the government has been providing special subsidies to solar photovoltaic cells and modules [128]. Article 25 of the “Renewable Energy Law of the People’s Republic of China”, revised in 2009, states that the renewable energy development and utilization projects listed in the National Renewable Energy Industry Development Guidance Catalog are eligible for loan application and can receive financial assistance with discounted loans from financial institutions [26].

Table 10 lists the financial subsidy policies for the photovoltaic solar energy industry from the central government. Financial subsidies for the solar energy industry mainly include subsidies for initial investment, on-grid tariffs, and financial subsidies for technology research and development and personnel training in the photovoltaic industry. The subsidy policies come from many different ministries, such as the National Development and Reform Commission, Energy Administration, and China Development Bank, and the subsidies are not unified [129].

Table 10. Financial subsidy policies for the photovoltaic solar energy industry from the central government.

Time	Solar Subsidy Policy	Policy on Subsidy	Ref.
2009	“Golden Sun” Demonstration Project	This stipulates two subsidy methods for centralized photovoltaic power generation and distributed photovoltaic power generation. The subsidies for centralized photovoltaic power generation and distributed photovoltaic power generation are in the range of CNY 0.75 to 1 CNY/kWh, and 0.35 CNY/kWh, respectively.	[130]
2016	Notice on the adjustment of the benchmark on-grid tariff of photovoltaic power generation and onshore wind power generation	The benchmark on-grid electricity price (tax included) for new photovoltaic power plants in 2017 for Class I, II, III, and Tibet Autonomous Region areas would be lowered to 0.65 CNY/kWh, 0.75 CNY/kWh, 0.85/kWh, and 1.05 CNY/kWh, respectively.	[131]
2020	Notice of the National Development and Reform Commission on Matters Concerning the 2020 On-grid Electricity Price Policy for Photovoltaic Power Generation	For industrial and commercial distributed photovoltaic power, it included financial subsidies in 2020 based on the power generation scale, and for household distributed photovoltaic power, the subsidy is 0.08 CNY/kWh.	[128]

In addition to the central government’s subsidies, local governments have also introduced a large number of relevant subsidy policies to encourage the development of the solar industry, which are added to the national subsidies. The subsidies offered by the local governments can be mainly divided into power demand/consumption subsidies and one-time investment subsidies. With the support from the subsidies, the Return On Investment (ROI) of distributed photovoltaic power generation projects can be significantly improved [125]. Table 11 lists the representative subsidies from local governments.

Table 11. Subsidies from different local governments.

Location	Policy on Subsidies	Ref.
Wuxi, Jiangsu	A one-time subsidy of 200,000 CNY/MW for distributed photovoltaic power stations.	[132]
Beijing	The subsidy standard is 0.4 CNY/kWh (tax included) for building integrated photovoltaic (BIPV) projects. For photovoltaic power generation projects in general industrial, commercial, and agricultural residential buildings, the subsidy standard is 0.3 CNY/kWh (tax included).	[133]
Shanghai	A subsidy of 0.4 CNY/kWh for a home-owner, and a subsidy of 0.25 CNY/kWh for an enterprise, for a period of 5 years. In 2014, the total newly added distributed photovoltaic power generation in Shanghai receiving subsidies is 200 MW.	[134]
Jiangsu	During the period from 2012 to 2015, if the photovoltaic power generation projects newly put into operation in the province did not receive national financial subsidies, they would be given subsidies of 1.2 CNY/kWh in 2014 and 1.15 CNY/kWh in 2015 from the provincial government.	[135]
Luoyang, Henan	For distributed photovoltaic grid-connected power generation projects completed before the end of 2015, and preferentially using components produced by enterprises in Luoyang City, a reward of 0.1 CNY/W will be given according to their installed capacity, and the reward will continue for 3 years.	[136]
Shangluo, Shaanxi	A 5% tax refund to some photovoltaic and ancillary product manufacturers registered locally. A 5% refund of labor service tax to enterprises that install photovoltaic generators of no less than 50 MW.	[137]
Hangzhou, Zhejiang	A subsidy of 0.05 CNY/kWh will be given to the photovoltaic grid-connected ground power stations that are constructed on schedule from 2016 to 2018, and the subsidy will be continued for 5 years (60 months). The annual subsidy for a single project does not exceed 5×10^6 RMB, and the annual subsidy for the same enterprise does not exceed 1.0×10^7 RMB.	[138]

According to the analysis of fiscal policies in Tables 10 and 11, the number of subsidies from the state and local governments provided to the solar energy industry, especially the photovoltaic industry, is steadily increasing. At the same time, with the national macro policy, the supporting photovoltaic policies in local regions are more active. However, due to poor project supervision and the low entry barrier of this industry, there have been problems such as fraudulent subsidies and fake projects that disrupt the market order, which discourage the enthusiasm of the enterprise [139]. Therefore, financial subsidies for the solar energy industry should move reasonably towards investment subsidies, electricity price subsidies, and consumption subsidies in order to stimulate and develop the clean energy consumption markets [132].

5.3. Fiscal, Tax, and Financial Policies for the Photovoltaic Industry

In terms of income tax, the National Development and Reform Commission has added solar photovoltaic products to the “National Environmental Protection Industry Equipment Product Catalog” which was released in 2010. With this, relevant enterprises can enjoy tax reductions and exemptions in terms of investment credits and accelerated depreciation for equipment [116]. For Value-Added Tax (VAT), when the scale of distributed photovoltaic power plants is small and the monthly online sales revenue is less than CNY 20,000, VAT is exempt. When the annual sales revenue exceeds CNY 500,000, VAT must be paid. According to the notice of the PV power VAT policy issued by the Ministry of Finance and the State Taxation Administration, taxpayers can enjoy a 50% refund of VAT immediately after collection, and enterprises can be exempt from a certain percentage of income tax within a certain period of time [129].

In recent years, the China Development Bank has provided various support for distributed photovoltaic project implementation [125]. The financing methods for solar photovoltaic enterprises mainly include equity financing, debt financing, policy financing, financial leasing, internet crowdfunding, internet wealth management and third-party

financing [140], among which bank loans are the primary financing method. In terms of policy financing, the China Development Bank is the leading provider for the new energy industry [141]. As of August 2013, the China Development Bank has provided loans of CNY 4.105×10^{11} to photovoltaic solar energy, and the Bank of China offered CNY 3.01×10^{12} green finance in 2014, mainly to support wind power and solar photovoltaic industry [142]. As of March 2017, a total of 60 banks across the country have launched “photovoltaic loans” to support the development of the photovoltaic industry, mainly from Zhejiang, Jiangsu, Jiangxi, Shandong, Shanxi Province, etc. [143].

Multiple guidelines and policies have been issued for the use of clean energy in building design and renovation in a number of domestic provinces and cities. For example, the economic policies issued in Hubei, Shandong, and other provinces and cities provide guidance on projects related to solar energy + “multi-energy complementary heat utilization”, cooling, heating, electricity trigeneration, solar/air source energy, ground source, and other clean energy sources.

6. Recommendations for Future Improvement

The vigorous development of the SAHP industry requires the formulation of government policies, the R&D and innovation vitality of enterprises, the fairness and improvement of the market, and the improvement of relevant laws and regulations. Therefore, a good development environment will help the SAHP industry in China step into a more promising future. Some recommendations for future improvement are elaborated as follows.

6.1. Expansion of Research Directions on SAHP

In addition to the traditional research directions on SAHPs, the following areas can be explored in the future: (1) SAHPs + intelligent control and remote monitoring systems, (2) multi-source heat pumps, (3) advanced heat storage and exchange unit (HSEU) technology, (4) advanced machine learning and multi-objective evolutionary optimization models that can be used for performance prediction and optimization of SAHP technology, (5) energy-efficient and low-carbon operation of heat pumps [144]. In addition, in-depth R&D on solar panel arrays, heat pumps with heat recovery, thermal storage and thermal storage technologies, and specific technology case studies can help identify potential ways for promoting the development of SAHPs to meet the requirements of a carbon-neutrality target. For example, the combination of soil source and solar energy heat pump technology, which has dual heat sources, can make the system more flexible and reliable and reduce the power consumption of the compressor [145]. Therefore, the combination of digitalization and intelligence technology for sustainable development may become a future research direction for SAHP.

6.2. Strengthen Industrial Chain Development and Increase the Output of Fundamental R&D

The development of any industry is inseparable from innovation and scientific research outputs. The proportion of transformation of theoretical achievements into practical application projects is relatively low in China, showing a large gap compared with developed countries such as the United States and Europe. Therefore, the experiences from developed countries need to be used. For example, Japan has put great emphasis on the development and protection of core technologies during the development of the solar energy industry with staged support from the state and local governments. During the early development stage, the government subsidizes enterprises to promote technology research and development. After the technology is mature, solar energy products can be introduced into the market, which will effectively reduce the cost of industrial promotion [118]. The Chinese government should increase investment in fundamental research and development of solar energy utilization technology in order to lead breakthroughs in key technologies such as solar cell materials as soon as possible [146].

6.3. Establish Positive Interaction between Local Government and Enterprises and Optimize Industrial Structure

To promote the development of the solar energy industry, it is crucial to building a benign interaction between local governments, the market, and enterprises. The local governments should create a healthy market environment, formulate rules for fair marketing, and replace traditional planning methods with more market economic methods [118]. They also must actively fill the loopholes and fix shortcomings in the market industry chain. It is necessary to supervise the solar energy industrial chain and utilize the advantages of local resources to increase resource utilization efficiency [147]. More policies should be introduced to improve the effectiveness of the role of the local government in SAHP industry development.

To optimize and upgrade the industrial structure, the process of production factors such as capital, labor, land, and technology should flow from the production sectors with low value-added, poor efficiency, and high consumption to those with high value-added, high efficiency, and low consumption. Large solar energy companies with a low production cost and high efficiency can be encouraged to merge with small companies with a high production cost and low efficiency to create a more competitive and vigorous market [148]. More specifically, more support should be provided to the development of the equipment manufacturing industry, parts production enterprises, and technical research and development institutions [149].

6.4. Develop Specific Fiscal and Financial Subsidy Policy for SAHP Industry

So far, no specific fiscal and financial subsidy policies have been developed for the SAHP industry in China. Most of the existing subsidy policies were developed for the solar photovoltaic industry. However, there are some macro policies for the promotion of solar water heaters and solar heating [150,151]. Therefore, the government should develop more flexible and specific subsidy policies for the SAHP industry to promote the application of SAHP in buildings.

The subsidy policies can be made concerning the following aspects: (1) Product subsidy: the government compensates for some of the SAHP products in order to reduce their expenses while increasing their output. As a result, production and consumption grow, but the price remains the same; (2) consumer subsidy: the government subsidizes the consumers to incentivize them to use more SAHP products; (3) employment subsidy: the government gives this incentive to SAHP companies and organizations in order to enable them to provide more job opportunities. The above subsidy policies should be provided based on market needs to avoid overproduction.

7. Conclusions

This paper provides a systematic review of the research, application, regulations, standards, and financial policies related to solar-assisted air heat pumps for buildings in China. Recommendations for the future development of the solar energy industry in China are also provided. The following conclusions can be made based on the literature review:

- (1) Current research focuses on the theoretical and experimental investigation of the performance of the main components of the solar air heat pump system, in particular the collector/evaporator, compressor, and heat exchanger, and the characteristics of the refrigerant. More attention should be paid to the intelligent control and optimal operation of the system and integration with buildings to achieve maximum energy savings. In addition, more comprehensive economic and feasibility evaluation studies should be carried out for different types of SAHP systems;
- (2) Due to the uneven distribution of solar energy resources and economic growth, the development of SAHP should take advantage of regional resources and complement solar energy with other clean energy resources. The selection of the appropriate type of SAHP in a particular region should consider the climate conditions of that region. It is also important to strengthen the cooperation between enterprises and

local governments to increase resource utilization efficiency for the development of SAHP projects.

- (3) There is a lack of specific fiscal and financial subsidy policies for SAHP. To promote the application of SAHP in buildings, the government should develop relevant subsidy policies according to the market needs. The subsidy should cover product subsidies, consumer subsidies, and employment subsidies.

Author Contributions: Y.L. and W.Y. contributed to the conception of the study and the development of the methodology. Y.L., Z.B., W.Y., V.F., H.Z. and C.-Q.L. wrote the manuscript. All authors have read and agreed to the published version of the manuscript.

Funding: This work was funded by the Natural Science Foundation of Hubei Province, grant number 2017CFB602.

Institutional Review Board Statement: Not applicable.

Informed Consent Statement: Not applicable.

Data Availability Statement: Not applicable.

Acknowledgments: The authors acknowledge the support from the R&D center of the transportation industry of health and epidemic prevention technology, the Ministry of Transportation of the People's Republic of China.

Conflicts of Interest: The authors declare no conflict of interest.

Abbreviations

AS-SAHP	air source solar-assisted heat pump
CFC	Chlorofluorocarbon
COP	coefficients of performance
DSHP	Dual-source heat pump
DX-SAHP	direct expansion solar-assisted heat pump
EVA	Ethylene-vinyl acetate
HCFC	Hydrochlorofluorocarbon
HFC	Hydrofluorocarbon
HVAC	heating, ventilation, and air-conditioning
IX-SAHP	indirect solar-assisted heat pump
PT-SAHP	photothermal-solar-assisted heat pump
PV	Photovoltaics
PV/T	photovoltaic thermal
PV/TA + HPWH	PV/T-assisted heat pump water heating system ()
PV/T-SAHP	photovoltaic/thermal-solar-assisted heat pump
PV-SAHP	photovoltaic-solar-assisted heat pump
PV-SAHPWH	PV-SAHP water heaters
PV-SALHP/HP	photovoltaic solar-assisted loop heat pipe/heat pump system
SAHP	solar-assisted heat pump system
SAHPMCM	solar-assisted heat pump multifunctional composite machine
SASHPDHW	solar-assisted air source heat pump integrated domestic hot water system
SGCHPS	solar-ground coupled heat pump system
TEG	Triethylene Glycol

References

1. Castleton, H.F.; Stovin, V.; Beck, S.B.M. Green roofs, building energy savings and the potential for retrofit. *Energy Build.* **2010**, *42*, 161–179. [CrossRef]
2. Wei, X. Literature Review on Building Energy efficiency. *Cap. Constr. Manag. Optim.* **2019**, *31*, 13–16.
3. National Bureau of Statistics. China Energy Statistics; Yearbook Appendix 2–10: Total end-use energy consumption. China Statistics Press: Beijing, China, 2021.
4. China Building Energy Efficiency Association, Building Energy Consumption and Carbon Emission Data Professional Committee. Available online: <https://www.cabee.org/site/content/24237.html> (accessed on 4 April 2022).

5. FS-UNEP Collaborating Centre. Available online: https://www.fs-unep-centre.org/wp-content/uploads/2020/06/GTR_2020.pdf (accessed on 21 April 2022).
6. British Petroleum (BP). Available online: <https://www.bp.com/content/dam/bp/business-sites/en/global/corporate/pdfs/energy-economics/statistical-review/bp-stats-review-2021-full-report.pdf> (accessed on 5 August 2022).
7. Yao, R.; Li, B.; Ding, Y.; Liu, M. Overview of green building development. *HVAC* **2006**, *36*, 27–31.
8. Zhang, X. Study on the Application of Renewable Energy in Architectural Design. *Des. Case* **2020**, *3*, 1–7.
9. Jiang, Y. China Urban Energy 2050. *New Energy Econ. Trade Watch.* **2017**, *12*, 26–27.
10. Xi, J. Speech at the general debate of the 75th session of the United Nations General Assembly. *Bull. State Counc. People's Repub. China* **2020**, *28*, 5–7.
11. Chua, K.J.; Chou, S.K.; Yang, W.M.; Yan, J. Achieving better energy-efficient air conditioning—A review of technologies and strategies. *Apply Energy* **2013**, *104*, 87–104. [[CrossRef](#)]
12. Xu, T. Parameter Matching and Scheduling Optimization of Solar Heat Pump Hot Water System. Master's Thesis, Hangzhou University of Electronic Science and Technology, Hangzhou, China, 2021.
13. Zhao, Y. Overview of the development of solar energy utilization and future trends. *China Electr. Power* **2003**, *36*, 63–70.
14. Sporn, P.; Ambrose, E.R. The heat pump and solar energy. In Proceedings of the World Symposium on Applied Solar Energy, Phoenix, AZ, USA, 1–5 November 1955.
15. Pei, G. Comprehensive Performance Study of Photovoltaic a Solar Heat Pump System and Multifunctional Heat Pump System. Ph.D. Thesis, University of Science and Technology of China, Anhui, China, 2006.
16. Badieli, A.; Golizadeh Akhlaghi, Y.; Zhao, X.; Shittu, S.; Xiao, X.; Li, J.; Fan, Y.; Li, G. A chronological review of advances in solar assisted heat pump technology in 21st century. *Renew. Sustain. Energy Rev.* **2020**, *132*, 110–132. [[CrossRef](#)]
17. Kara, O.; Ulgen, K.; Hepbasli, A. Exergetic assessment of direct-expansion solar-assisted heat pump systems: Review and modeling. *Renew. Sustain. Energy Rev.* **2008**, *12*, 1383–1401. [[CrossRef](#)]
18. Omojaro, P.; Breitkopf, C. Direct expansion solar assisted heat pumps: A review of applications and recent research. *Renew. Sustain. Energy Rev.* **2013**, *22*, 33–45. [[CrossRef](#)]
19. Zu, W.; Li, Q. Solar heat pump development status and application analysis at home and abroad. Proceeding of the 17th Academic Exchange Conference of the Building Thermal Power Branch of the Architectural Society of China, Taiyuan, China, 8 October 2011.
20. Zhang, Q.; Tetsu, F. Exergy analysis for heat pump and exergy efficiency of solar heat pump. *Acta Energ. Sol. Sin.* **1985**, *6*, 333–340.
21. Liu, P.; Guan, X.; Mu, Z.J.; Ma, H. Research and development of solar heat pump technology in China. *Adv. Chem. Eng.* **2009**, *28*, 328–333.
22. Luo, Y.; He, X.; Wang, C. *Solar Energy Utilization Technology*, 9th ed.; Chemical Industry Press: Beijing, China, 2013.
23. Ministry of Housing and Urban-Rural Development of the People's Republic of China. *Uniform Standard for Design of Civil Buildings (GB 50352-2019)*; China Construction Industry Press: Beijing, China, 2019.
24. Xu, Z. Adaptability Research and Optimization of Solar Heat Pump Hot Water System in Different Climate Regions. Master's Thesis, Taiyuan University of Technology, Taiyuan, China, 2021.
25. Bu, Z.; Sun, D.; Lin, B.; Lin, W.; Yang, J. Practice and innovation: A review of green building development in China. *HVAC* **2012**, *42*, 1–8.
26. National Energy Administration. Available online: http://www.nea.gov.cn/2017-11/02/c_136722869.htm (accessed on 4 April 2022).
27. Wang, Y.; Xu, X.; Li, C.; Li, D.; Wang, J. Study on the amount and replacement ratio of conventional energy for renewable energy building applications. *Build. Sci.* **2020**, *36*, 100–106.
28. Zhang, C. Opportunities and challenges of China's solar industry under the financial crisis. *Mark. Res.* **2008**, *9*, 7–13.
29. Xiao, X. Ways, obstacles and policy suggestions for the transformation and upgrading of the photovoltaic industry—An investigation based on Wuxi Hairun. *China Econ. Trade Her.* **2014**, *16*, 49–52.
30. Liu, M.S. Solar heat pump type air conditioner. *Refrigeration* **1986**, *1*, 89.
31. Hou, X. Study of Solar-Soil Source Heat Pump System in the Middle and Lower Reaches of Yangtze River in Winter. Master's Thesis, Huazhong University of Science and Technology, Wuhan, China, 2005.
32. Kuang, Y.; Li, Y.; Wang, R.; Zhang, X. Experimental study on direct expansion solar heat pump air conditioning and hot water system. In Proceedings of the Third Symposium on New Technologies for Refrigeration and Air Conditioning, Hangzhou, China, 20–23 April 2005.
33. Pei, G.; Ji, J.; He, W.; Sun, W. Performance study of PV/T solar heat pump system. *Strateg. Study CAE* **2006**, *9*, 49–56.
34. Pei, G.; Ji, J.; Liu, K.L.; He, H.F.; Lu, J.P. Characteristics of photovoltaic-solar heat pumps at different condensing water temperatures. *J. Univ. Sci. Technol. China* **2006**, *36*, 1044–1050.
35. Wang, Y. Experimental Study of A Solar-Wastewater Source Composite Heat Pump System. Master's Thesis, Harbin Institute of Technology, Harbin, China, 2021.
36. Li, G.; Yu, H.; Zhang, Y.; Yan, H.; Zhang, H.; Jiang, P. PID simulation implementation and experimental analysis of a new solar heat pump compound machine (SAHPM). *Acta Energ. Sol. Sin.* **2020**, *41*, 22–26.
37. Li, H.; Sun, Y.; Fu, X.S. New solar photovoltaic-loop heat pipe/heat pump hot water system. *Acta Energ. Sol. Sin.* **2020**, *41*, 22–26.
38. Peng, X. Clean nuclear energy, green development. *South. Energy Constr.* **2015**, *4*, 1.
39. Huang, W. Theoretical and Experimental Study of Direct Expansion Solar Heat Pump System. Ph.D. Thesis, University of Science and Technology of China, Hefei, China, 2017.

40. Liu, Y. Research on the Performance of Solar One-Air Composite Heat Source Heat Pump System. Ph.D. Thesis, Xi'an University of Architecture and Technology, Xi'an, China, 2010.
41. Li, G. Research on the Performance of Solar Heat Pump Water Heater Based on Photovoltaic/Photovoltaic Collector Evaporator. Master's Thesis, Shanghai Jiaotong University, Shanghai, China, 2018.
42. Tie, Y. Study on the Thermal Performance and Operational Characteristics of A New Air Source Heat Pump Assisted Heating Solar Water Heating System. Master's Thesis, Kunming University of Science and Technology, Kunming, China, 2010.
43. Che, J. Research on Thermal Performance of Direct Expansion Solar Heat Pump Hot Water System. Master's Thesis, Xi'an University of Architecture and Technology, Xi'an, China, 2019.
44. Pei, G.; Ji, J.; Liu, K.; He, H.; Lu, J.; Han, C.; He, W. Performance of PV-SAHP under different condensing water temperatures. *J. Univ. Sci. Technol.* **2006**, *36*, 1044–1050.
45. Ji, J.; He, H.; Chow, T.; Pei, G.; He, W.; Liu, K. Distributed dynamic modeling and experimental study of PV evaporator in a PV/T solar-assisted heat pump. *Int. J. Heat Mass Transf.* **2009**, *52*, 1365–1373. [[CrossRef](#)]
46. Xu, G.; Zhang, X.; Deng, S. A simulation study on the operating performance of a solar–air source heat pump water heater. *Appl. Therm. Eng.* **2006**, *26*, 1257–1265. [[CrossRef](#)]
47. Qin, J.; Ji, J.; Huang, W.; Qin, H.; Modjinou, M.; Li, G. Experimental Study of a Novel Direct-Expansion Variable Frequency Finned Solar/Air-Assisted Heat Pump Water Heater. *Int. J. Photoenergy* **2018**, *2018*, 5986463. [[CrossRef](#)]
48. Long, J.; Zhang, R.; Lu, J.; Xu, F. Heat transfer performance of an integrated solar-air source heat pump evaporator. *Energy Convers. Manag.* **2019**, *184*, 626–635. [[CrossRef](#)]
49. Cai, J.; Li, Z.; Ji, J.; Zhou, F. Performance analysis of a novel air source hybrid solar assisted heat pump. *Renew. Energy* **2019**, *139*, 1133–1145. [[CrossRef](#)]
50. Ji, W.; Cai, J.; Ji, J.; Huang, W. Experimental study of a direct expansion solar-assisted heat pump (DX-SAHP) with finned evaporator and comparison with conventional DX-SAHP. *Energy Build.* **2020**, *207*, 109632. [[CrossRef](#)]
51. Wang, G.; Quan, Z.; Zhao, Y.; Sun, C.; Deng, Y.; Tong, J. Experimental study on a novel PV/T air dual-heat-source composite heat pump hot water system. *Energy Build.* **2015**, *108*, 175–184. [[CrossRef](#)]
52. Kong, X.Q.; Zhang, D.; Li, Y.; Yang, Q.M. Thermal performance analysis of a direct-expansion solar-assisted heat pump water heater. *Energy* **2011**, *36*, 6830–6838. [[CrossRef](#)]
53. Qin, J. Experimental Study on the Performance and Frosting of Solar/Air Direct Expansion Inverter Fin Heat Pump Water Heaters. Master's Thesis, University of Science and Technology of China, Hefei, China, 2017.
54. Li, Y.W.; Wang, R.Z.; Wu, J.Y.; Xu, Y.X. Experimental performance analysis on a direct-expansion solar-assisted heat pump water heater. *Appl. Therm. Eng.* **2006**, *27*, 2858–2868. [[CrossRef](#)]
55. Kong, X.; Wang, B.; Shang, Y.; Li, J.; Li, Y. Influence of different regulation modes of compressor speed on the performance of direct-expansion solar-assisted heat pump water heater. *Appl. Therm. Eng.* **2020**, *169*, 115007. [[CrossRef](#)]
56. Pei, G.; Ji, J.; Han, C.; Fan, W. Performance of solar assisted heat pump using PV evaporator under different compressor frequency. In Proceedings of the ISES Solar World Congress 2007: Solar Energy and Human Settlement, Beijing, China, 18–21 September 2007; Volume II.
57. Li, Z.; Huang, X. Simulation analysis of the influence of compressor speed on a solar-assisted heat pump hot water system. *Earth Environ. Sci.* **2021**, *23*, 012102. [[CrossRef](#)]
58. Li, Y.; Wang, R.; Wang, T.; Wu, J.; Xu, Y. Thermal performance analysis and optimal design of direct expansion solar heat pump water heaters. *J. Sol. Energy* **2007**, *28*, 465–470.
59. Dong, S. Operation Control and Energy Management of Variable Capacity Direct Expansion Solar Heat Pump Water Heater. Master's Thesis, Shandong University of Science and Technology, Qingdao, China, 2015.
60. Dong, Y.; Yang, Y. Simulation study on variable capacity control of direct expansion solar heat pump. *Friends Sci.* **2013**, *12*, 7–9.
61. Li, Y. Optimization Analysis and Variable Capacity Operation of Direct Expansion Solar Heat Pump Hot Water Plant. Ph.D. Thesis, Shanghai Jiao Tong University, Shanghai, China, 2007.
62. Harby, K. Hydrocarbons and their mixtures as alternatives to environmental unfriendly halogenated refrigerants: An updated overview. *Renew. Sustain. Energy Rev.* **2017**, *73*, 1247–1264. [[CrossRef](#)]
63. HVACR. Available online: https://bao.hvacr.cn/202106_2091978.html (accessed on 18 April 2022).
64. Liu, N. Research on the Performance of R134a Heat Pump System. Master's Thesis, Tangshan North China University of Technology, Tangshan, China, 2020.
65. Xu, X.; Pan, Y.; Deng, S.; Xia, L.; Chan, M. Experimental study of a novel capacity control algorithm for a multi-evaporator air conditioning system. *Appl. Therm. Eng.* **2013**, *50*, 975–984.
66. Zhao, J.; Liu, L.; Li, L.; Zhu, Q.; Tu, F. R134a for direct expansion solar heat pump systems. *J. Tianjin Univ.* **2000**, *33*, 303–305.
67. Kong, X.; Jiang, K.; Dong, S.; Li, Y.; Li, J. Control strategy and experimental analysis of a direct-expansion solar-assisted heat pump water heater with R134a. *Energy* **2018**, *145*, 17–24. [[CrossRef](#)]
68. Kong, X.; Zhang, M.; Yang, Y.; Li, Y.; Wang, D. Comparative experimental analysis of direct-expansion solar-assisted heat pump water heaters using R134a and R290. *Sol. Energy* **2020**, *203*, 187–196. [[CrossRef](#)]
69. Wang, H.; Zhang, S.; Han, D. Performance comparison of solar-air source composite heat pumps based on R1234yf and R134a refrigerants. *Energy Conserv.* **2018**, *37*, 54–60. [[CrossRef](#)]

70. Yang, Y. Experimental Study on the Heat Production Performance of R290 Direct Expansion Solar Heat Pump System. Master's Thesis, Handong University of Science and Technology, Qingdao, China, 2020.
71. Ouyang, J. Theoretical Analysis and Optimization Study of Solar-Assisted Transcritical CO₂ Heat Pump System. Master's Thesis, North China Electric Power University, Beijing, China, 2012.
72. Kong, X.; Dong, S.; Jiang, K.; Li, Y. Experimental system design of propane for direct expansion solar heat pump. *Exp. Sci. Technol.* **2019**, *17*, 6–12.
73. Zhang, D.; Wu, Q.B.; Li, J.P.; Kong, X.Q. Effects of refrigerant charge and structural parameters on the performance of a direct-expansion solar-assisted heat pump system. *Appl. Therm. Eng.* **2014**, *73*, 522–528. [[CrossRef](#)]
74. Kong, X.Q.; Li, Y.; Lin, L.; Yang, Y.G. Modeling evaluation of a direct-expansion solar-assisted heat pump water heater using R410A. *Int. J. Refrig.* **2017**, *76*, 136–146. [[CrossRef](#)]
75. Jin, X.; Qin, H.; Liu, C. Study on the refrigerant charge of solar/air energy dual source integrated heat pump. *Refriger. Air Cond.* **2014**, *27*, 101–106.
76. Kong, X.; Ma, S.; Ma, T.; Li, Y.; Cong, X. Mass flow rate prediction of direct-expansion solar-assisted heat pump using R290 based on ANN model. *Sol. Energy* **2021**, *215*, 375–387. [[CrossRef](#)]
77. Wang, B.; Kong, X.; Yan, X.; Shang, Y.; Li, Y. Influence of subcooling on performance of direct-expansion solar-assisted heat pump. *Int. J. Refrig.* **2021**, *122*, 201–209. [[CrossRef](#)]
78. Huang, Z. *Research on the Characteristics of Solar and Air Source Composite Heat Pump System*; Southeast University: Nanjing, China, 2017.
79. Wei, Z.; Xu, B. Research on solar–water source heat pump technology. *Enterp. Technol. Dev.* **2015**, *34*, 17–20.
80. Fang, L. Research on the Characteristics of Solar and Air Composite Heat Source Two-Stage Compression CO₂ Heat Pump Water Heater System. Master's Thesis, Zhongyuan Institute of Technology, Zhengzhou, China, 2020.
81. Hou, J.; Gu, M.; Yang, Q.; Gao, M.; Zheng, M.; Ren, Y. Analysis of economic impact factors of heat pump assisted solar centralized hot water system. *J. Lanzhou Univ.* **2008**, *27*, 56–591.
82. Yang, W.; Shi, M.; Chen, Z. Numerical simulation and experimental validation of energy storage characteristics of solar-U-tube soil. *J. Southeast Univ. (Nat. Sci. Ed.)* **2008**, *38*, 651–656.
83. Wang, H.; Qi, C. Performance study of underground thermal storage in a solar-ground coupled heat pump system for residential buildings. *Energy Build.* **2008**, *40*, 1278–1286. [[CrossRef](#)]
84. Han, Z.; Zheng, M.; Kong, F. Simulation study of solar-soil heat storage heat pump heating system in severe cold regions. *Acta Energ. Sol. Sin.* **2008**, *29*, 574–580.
85. Xu, H. Research on the Characteristics of Combined Solar-Ground Source Heat Pump Heating for Residential Buildings. Master's Thesis, Shanghai University of Applied Engineering and Technology, Shanghai, China, 2015.
86. Gao, Y.; Sun, Z.; Lin, X.; Wang, C.; Sun, Z.; Chen, Y. Designing and Optimizing Heat Storage of a Solar-Assisted Ground Source Heat Pump System in China. *Int. J. Photoenergy* **2020**, *2020*, 4102350. [[CrossRef](#)]
87. Yi, Y. Study on Operational Characteristics of Solar Water Source Heat Pump Composite System. Master's Thesis, Hunan University, Changsha, China, 2009.
88. Qu, S.; Wang, D.; Dong, J.; Peng, L. Optimization study of solar water source heat pump system based on TRNSYS. *J. Nanjing Univ. Technol.* **2015**, *39*, 494–499.
89. Li, S. Research on Solar-Water Source Heat Pump Assisted Heating System. Master's Thesis, Shenyang University of Architecture, Shenyang, China, 2011.
90. Ma, C. Analysis of the Applicability of Solar-Air-Wastewater Multi-Energy Complementary System in Low-Energy Residential Building Retrofit. Master's Thesis, Harbin Institute of Technology, Harbin, China, 2020.
91. Tsai, H.L. Modeling and validation of refrigerant-based PVT-assisted heat pump water heating (PVTA-HPWH) system. *Sol. Energy* **2015**, *122*, 36–47. [[CrossRef](#)]
92. Dai, N.; Xu, X.; Li, S.; Zhang, Z. Simulation of hybrid photovoltaic solar assisted loop heat pipe/heat pump system. *Appl. Sci.* **2017**, *72*, 197. [[CrossRef](#)]
93. Zhou, J.; Ma, X.; Zhao, X.; Yuan, Y.; Yu, M.; Li, J. Numerical simulation and experimental validation of a micro-channel PV/T modules based direct-expansion solar heat pump system. *Renew. Energy* **2020**, *145*, 1992–2004. [[CrossRef](#)]
94. Xu, L.; Luo, X.; Li, M. Study on the matching of heat pump power and heating area of combined solar heat pump heating system in Shangri-La. *J. Yunnan Norm. Univ. (Nat. Sci. Ed.)* **2020**, *40*, 20–23.
95. Wang, X. Research and Application of Control Strategy for Solar-Thermal Pump Hot Water System. Master's Thesis, Hangzhou University of Electronic Science and Technology, Hangzhou, China, 2020.
96. Shen, Y. Numerical simulation study of solar/air source heat pump based on TRNSYS. *Cent. Air Cond. Mark.* **2015**, *1*, 80–83.
97. Yin, L. Simulation Study of Solar Coupled Soil Source Heat Pump System Based on TRNSYS. Master's Thesis, Taiyuan University of Technology, Taiyuan, China, 2013.
98. Li, Z. Performance Study of Solar Coupled Air Source Heat Pump Integrated Domestic Hot Water System. Master's Thesis, Taiyuan University of Technology, Taiyuan, China, 2017.
99. Wei, Y.; Deng, H.; Ma, L. Simulation and analysis of solar heat pump systems. *Lab. Res. Explor.* **2019**, *38*, 102–108.
100. Guan, Q. TRNSYS Simulation and Study of Solar-Storage and Ground Source Heat Pump Hot Water Supply System. Master's Thesis, Tianjin University, Tianjin, China, 2009.

101. Guangzhou Energy Research Institute Project Management Office, Comprehensive Planning Bureau, Chinese Academy of Sciences. Progress on the demonstration of solar heat pump central hot water system in the Olympic Village and Olympic venues. *Bull. Chin. Acad. Sci.* **2004**, *19*, 360–361+315.
102. Yu, G.; Zhang, X.; Meng, F. Technical and economic analysis of solar heat pump heating for single-family houses. *Build. Energy Effic.* **2007**, *35*, 55–57.
103. Feng, L. Simulation Study and Economic Analysis of Photovoltaic Solar Heat Pump System. Master's Thesis, Nanjing University of Technology, Nanjing, China, 2012.
104. Luo, H.; Tie, Y.; Li, M.; Zhong, H. Study on the thermal performance of air source heat pump assisted heating solar hot water system. *Build. Sci.* **2009**, *2*, 52–54.
105. Jing, Y. Performance Study of Air Source Heat Pump Assisted Solar Water Heating System. Master's Thesis, Huazhong University of Science and Technology, Wuhan, China, 2015.
106. Liu, Y. Simulation and Application of Air Source Heat Pump Assisted Solar Water Heating System in Hot Summer and Cold Winter Regions. Master's Thesis, Chongqing University, Chongqing, China, 2011.
107. Peng, J. Study on the Energy Saving and Environmental Benefits of Air Source Heat Pump Assisted Solar Water Heating System in Jianghuai Region. Master Thesis, Yangzhou University, Yangzhou, China, 2010.
108. Li, J.; Li, B. Demonstration application of large scale solar air conditioning/heat pump system. *Chin. J. Renew. Energy* **2004**, *4*, 26–27.
109. Jin, H.; Zhang, S.; Fan, S. Application of solar heat pump system in a hotel hot water system. *Build. Energy Effic. Green Build.* **2015**, *22*, 78–81.
110. Wang, Y.; Wang, Z.; Dong, L.; Zhao, S.; Liu, Z. Introduction to the design elements of solar water source heat pump project in Guangzhou Asian Games City. *Water Wastewater Eng.* **2011**, *37*, 76–79.
111. Li, R.; Chen, Y. Engineering application of ground source heat pump + solar energy + energy storage system. *Fly Ash Compr. Util.* **2015**, *4*, 45–47.
112. Kang, J.; Zhang, M. Ruzhou city soil source heat pump coupled with solar trigeneration demonstration project won the first prize of Henan province construction science and technology progress. *Constr. Wall Innov. Build. Energy-Sav.* **2015**, *8*, 71–72.
113. Yuan, W.; Li, P. Beijing Daxing village household solar + air source heat pump heating renovation project. *Constr. Sci. Technol.* **2016**, *22*, 90–91.
114. Chao, S.; Ding, H. Study on solar+water source heat pump heating project of Lhasa Cai Na Township Government. *Heat. Cool.* **2019**, *4*, 52–55.
115. Liu, Q.; Zhao, L. Operational study of multi-energy complementary cooling and heating system renovation project—Complementary application of ground source heat pump, solar energy and valley power storage system. *Constr. Budg.* **2020**, *11*, 76–79.
116. Xia, Y. Research on the Dilemma and Path of Solar Energy Industry Development in China. Master's Thesis, Shanghai University of Finance and Economics, Shanghai, China, 2020.
117. China Academy of Building Research Co., Ltd. *Technical Specification for Solar Photovoltaic and Thermal Heat Pump System T/CECS 830-2021*; China Planning Press: Beijing, China, 2021.
118. General Administration of Quality Supervision, Inspection and Quarantine of the People's Republic of China, National Standardization Administration of China. *Specifications of Air Source Heat Pump Assisted Domestic Solar Water Heating System: GB/T 23889-2009*; China Standard Press: Beijing, China, 2009.
119. General Administration of Quality Supervision, Inspection and Quarantine of the People's Republic of China, National Standardization Administration of China. *Technical Specification for Solar Water Heating Systems Assisted by Air Source Heat Pumps (Storage Tank Volume Greater than 0.6 m3): GB/T 26973-2011*; China Standard Press: Beijing, China, 2011.
120. Ministry of Housing and Urban-Rural Development of the People's Republic of China. *Technical Specification for Solar Air Conditioning Engineering in Civil Buildings: GB 50787-2012*; China Construction Industry Press: Beijing, China, 2012.
121. Ministry of Housing and Urban-Rural Development of the People's Republic of China. *Technical Standard for the Application of Solar Water Heating Systems in Residential Buildings (with Notes on Provisions): GB 50364-2018*; China Construction Industry Press: Beijing, China, 2018.
122. National Energy Administration. *Test Method for Domestic Direct Expansion Solar Heat Pump Water Heating Systems: NB/T 10155-2019*; China Construction Industry Press: Beijing, China, 2019.
123. Ministry of Housing and Urban-Rural Development of the People's Republic of China. *Solar Heat and Heating Engineering Standard (with Explanatory Notes): GB 50495-2019*; China Construction Industry Press: Beijing, China, 2019.
124. Central People's Government of the People's Republic of China. Available online: http://www.gov.cn/zhengce/zhengceku/2020-07/27/content_5530301.htm (accessed on 21 May 2022).
125. Geri, L. Research on Investment Benefits and Financial Support for Distributed Photovoltaic Power Generation. Master's Thesis, North China Electric Power University, Beijing, China, 2016.
126. Zhang, X. *Study on Energy Consumption Transition and its Social, Economic and Environmental Impacts*; China Social Science Press: Beijing, China, 2018; p. 80.

127. National Energy Administration; China Electricity Council; State Grid Corporation of China; China Southern Power Grid Co., Ltd.; China Huaneng Group Co., Ltd.; China Datang Group Co., Ltd.; China Huadian Group Co., Ltd.; National Energy Investment Group Co., Ltd.; State Power Corporation Investment Group Company; China Three Gorges Corporation Limited; et al. *China Electricity Yearbook 2021*; China Electricity Press: Beijing, China, 2022.
128. National Development and Reform Commission. Available online: https://www.ndrc.gov.cn/xxgk/zcfb/tz/202004/t20200402_1225031_ext.html (accessed on 27 April 2022).
129. Wu, S. Research on the Impact of Financial and Taxation Support Policies on Inefficient Investment in New Energy Industry. Master's Thesis, Xi'an Petroleum University, Xi'an, China, 2019.
130. Xie, B. Discussion on the investment efficiency of the Golden Sun demonstration project. *Renew. Energy* **2011**, *29*, 160–161.
131. National Development and Reform Commission. Available online: http://www.gov.cn/xinwen/2016-12/28/content_5153820.htm (accessed on 29 June 2022).
132. Ma, J. Research on Fiscal Policies to Promote the Development of Clean Energy in China. Ph.D. Thesis, China University of Geosciences, Beijing, China, 2014.
133. Beijing Development and Reform Commission. Available online: <http://fgw.beijing.gov.cn/so/s?tab=all&siteCode=1100000011> (accessed on 27 April 2022).
134. National Energy Administration. Available online: http://www.nea.gov.cn/2014-09/04/c_133620549.htm (accessed on 29 June 2022).
135. Shanghai Municipal Development and Reform Commission. Available online: http://service.shanghai.gov.cn/XingZhengWenDangKuJyh/XZGFDetails.aspx?docid=REPORT_NDOC_006422 (accessed on 27 April 2022).
136. National Energy Administration. Available online: http://www.nea.gov.cn/2014-09/04/c_133620485.htm (accessed on 27 April 2022).
137. Shaanxi Provincial People's Government. Shaanxi Provincial People's Government's implementation opinions on demonstrating and promoting distributed photovoltaic power generation. *Shaanxi Prov. People's Gov. Gaz.* **2015**, *2*, 35–37.
138. Hangzhou Municipal People's Government. Available online: http://www.hangzhou.gov.cn/art/2016/7/4/art_1209287_3815.html (accessed on 29 June 2022).
139. Wang, L. Simulation of Financial Incentive Policy Innovation and Effects in China's PV Industry. Master's Thesis, China University of Petroleum, Beijing, China, 2019.
140. Ma, Y. Research on the Financing Efficiency and Influencing Factors of Solar Photovoltaic Enterprises in China—Taking Listed Solar Photovoltaic Companies in China as an Example. Master's Thesis, Northwestern University, Xi'an, China, 2018.
141. Tang, X. Research on the Efficiency of Financing in China's New Energy Industry and the Factors Influencing It. Master's Thesis, Shanxi University of Finance and Economics, Taiyuan, China, 2019.
142. Yao, Y. Research on the Financing of New Energy Industry Development in China. Master's Thesis, Sichuan Academy of Social Sciences, Chengdu, China, 2016.
143. Wang, R. Research on Financial Support for the Development of New Energy Industry in China. Master's Thesis, Shanxi University of Finance and Economics, Taiyuan, China, 2018.
144. Fan, Y.; Zhao, X.; Han, Z.; Li, J.; Badiei, A.; Akhlaghi, Y.G.; Liu, Z. Scientific and technological progress and future perspectives of the solar assisted heat pump (SAHP) system. *Energy* **2021**, *229*, 120719. [[CrossRef](#)]
145. Wang, J.; Yao, H.; Zhao, S.; Zhang, W. Application and development of soil source and solar heat pump composite system. *Dist. Heat.* **2021**, *2*, 85–93.
146. Li, M.; Gao, L.; Wang, L.; Geng, Q.; Li, Y.; Cui, P.; Ji, J.; Huang, H. The development status and outlook of solar energy utilization technology in China under the goal of emission peak and carbon neutrality. *Sol. Energy* **2021**, *11*, 13–18.
147. Gao, X. A brief analysis of the prospects of solar energy in clean energy in China. *Low Carbon World* **2021**, *11*, 6–7.
148. Yun, G. Analysis of the Current Situation and Market Development Prospects of Commercial Utilization in the New Energy Industry. *China J. Commer.* **2015**, *14*, 121–123.
149. Yang, G. Research on the problems and countermeasures for the development of new energy industry in China. *China Strateg. Emerg. Ind.* **2018**, *44*, 1–2.
150. Shandong Economic and Information Commission Committee and Finance Department. Available online: http://innovation.jinan.gov.cn/art/2018/2/24/art_17708_974536.html (accessed on 4 July 2022).
151. Xianning Housing and Urban-Rural Development Bureau. Available online: http://zj.xianning.gov.cn/xxgk/xxgkml/tzgg/201803/t20180316_1280137.shtml (accessed on 4 July 2022).

Review

Aesthetically Appealing Building Integrated Photovoltaic Systems for Net-Zero Energy Buildings. Current Status, Challenges, and Future Developments—A Review

Mohammad Khairul Basher^{1,*}, Mohammad Nur-E-Alam^{1,2}, Md Momtazur Rahman¹, Kamal Alameh^{1,3} and Steven Hinckley¹

¹ School of Science, Edith Cowan University, Joondalup, WA 6027, Australia

² Institute of Sustainable Energy, Universiti Tenaga Nasional, Jalan IKRAM-UNITEN, Kajang 43000, Selangor, Malaysia

³ Alpha Solar Tech., Kewdale, WA 6105, Australia

* Correspondence: mkbasher@our.ecu.edu.au

Abstract: With the sharp increase in global energy demand, industrial and residential buildings are responsible for around 40% of the energy consumed with most of this energy portion being generated by non-renewable sources, which significantly contribute to global warming and environmental hazards. The net-zero energy building (NZEB) concept attempts to solve the global warming issue, whereby a building will produce, on-site, its required energy demand throughout the year from renewable energy sources. This can be achieved by integrating photovoltaic (PV) building materials, called building-integrated photovoltaic (BIPV) modules, throughout the building skin, which simultaneously act as construction materials and energy generators. Currently, architects and builders are inclined to design a building using BIPV modules due to the limited colors available, namely, black or blue, which result in a monotonous building appearance. Therefore, there is an increasing demand/need to develop modern, aesthetically pleasing BIPV green energy products for the use of architects and the construction industry. This review article presents the current stage and future goal of advanced building integrated photovoltaic systems, focusing on the aesthetically appealing BIPV systems, and their applications towards overcoming global challenges and stepping forward to achieve a sustainable green energy building environment. Additionally, we present the summary and outlook for the future development of aesthetically appealing building integrated photovoltaic systems.

Keywords: semitransparent PV; colored PV; BIPV; net-zero energy building; sustainable environment

Citation: Basher, M.K.; Nur-E-Alam, M.; Rahman, M.M.; Alameh, K.; Hinckley, S. Aesthetically Appealing Building Integrated Photovoltaic Systems for Net-Zero Energy Buildings. Current Status, Challenges, and Future Developments—A Review. *Buildings* **2023**, *13*, 863. <https://doi.org/10.3390/buildings13040863>

Academic Editors: Yaolin Lin and Wei Yang

Received: 20 February 2023

Revised: 14 March 2023

Accepted: 23 March 2023

Published: 25 March 2023



Copyright: © 2023 by the authors. Licensee MDPI, Basel, Switzerland. This article is an open access article distributed under the terms and conditions of the Creative Commons Attribution (CC BY) license (<https://creativecommons.org/licenses/by/4.0/>).

1. Introduction

Due to the industrial revolution and the growth in the global population over the past few decades, energy consumption has grown worldwide. By 2050, there will likely be close to 13 billion people on the planet. With such a sizable population and rising industrialization, more energy will be needed to sustain a typical and sustainable way of life. Global energy consumption is anticipated to surpass 0.74 billion Tera Joule (BTJ) by 2040 [1], and around 22.7 billion tons of fossil fuel, primarily anthracite coal, are needed to meet this energy requirement [2]. With increasing industrialization, today's modern infrastructure, including residential and commercial buildings, use substantially more energy than they did ten years ago. Whilst this increasing industrialization has offered social benefits and financial support to the world population, it has resulted in the migration of more and more people from rural to urban areas, and currently, 30–40% of global energy generated through different means is consumed by buildings and construction infrastructures [3–5]. As two-thirds of the world's population is expected to reside in urban areas by 2050, there will be a huge energy demand to ensure economic and social

growth [4]. Environmental risks and global warming brought on by non-renewable fossil fuel-based energy sources are forcing modern architects to consider climate change and on-site clean energy generation in their building designs [2]. In addition to climate change mitigation, employing sustainable renewable energy technology to prevent the use of non-renewable energy sources (oil, coal, and gas), which have been causing other horrendous environmental problems, such as the release of glasshouse gases, pollutants (such as trace metals, particulates, NO_x , and SO_2) into the atmosphere, tainted water from coal pollution, and unmanageable ash wastes [5]. Among the numerous technologies, photovoltaics (PV) is one of the most promising renewable energy technologies due to its two unique attributes, namely (i) simple and cost-effective, and (ii) low-maintenance operation. PV modules have no moving parts and convert solar energy into electrical energy in a very simplistic way compared to other conversion processes [6]. Figure 1 shows a glimpse of the key modern human civilization application areas where energy is one of the most important elements, besides other basic needs, to fulfill the demand of the world's large population.

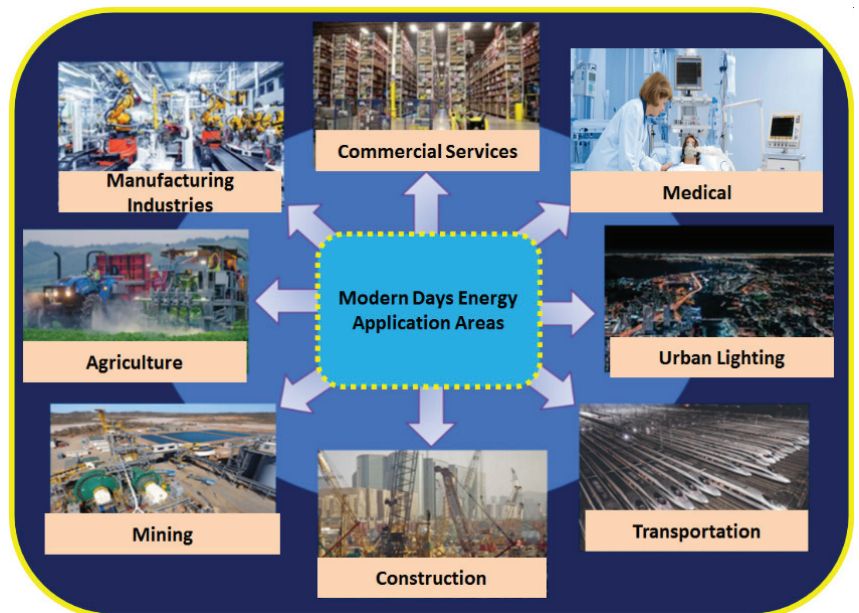


Figure 1. A glimpse of the key modern human civilization application areas where energy is one of the most important elements.

The application of PV panels in built environments has achieved more popularity due to their capacity to turn a house into a power generator [7]. This is accomplished by integrating PV modules into the building during or after construction. A building-integrated photovoltaic (BIPV) system supplies buildings with electricity, and can be designed to have thermal and sound insulation properties [8,9]. For example, double-glazed semitransparent solar glass panels used as facade elements (instead of plain glass elements) provide protective shielding from smoke, noise, heat, and other weather changes, while generating on-site energy. With the increase in electricity tariffs worldwide and the decrease in the price of PV panels, BIPV systems are becoming cost-effective building materials [10], particularly the semi-transparent BIPV glass panels, which help reduce the power consumption of the building by allowing only a portion (e.g., 40%) of sunlight to enter the building while converting the remaining sunlight to electricity. Commercially available window-glass-based BIPV systems comprise low-emissivity (low-E) thin films in addition to PV panels, which filter and control the spectral components of sunlight,

leading to high thermal insulation (less cooling/heating energy consumption), in addition to generating on-site energy [11,12].

BIPV systems have been widely adopted after the net-zero energy buildings (NZEB) concept was announced by the Directive of the European Parliament (2010/31/EU), stating that “all public buildings which are new must consume nearly zero-energy by 2018, and other new buildings by the end of 2020” [13]. The NZEB idea requires that buildings use as much energy as they produce on-site, using only renewable energy sources. The development of smart cities, where energy demand and supply are met by renewable energy sources and storage systems installed in the same city, offers the NZEB its greatest potential [3]. BIPV systems can therefore be used to meet the NZEB, aiming further to reach the goal of total zero-carbon built environment (ZCBE) [3,14–16]. According to the concise study found in Ref. [17], significant efforts have been made over the past 20 years to hasten the adoption of solar-electric systems by creating PV products that are completely integrated with building materials. The NZEB requirements have caused the worldwide BIPV industry to exceed yearly installations of 1 GW in the previous few years. The California Public Utilities Commission (CPUC) has established several NZEB targets, including requiring all new residential and commercial construction in the State to be net zero energy buildings by 2020 and 2030, respectively, and demanding retrofitting of 50 percent of existing buildings to meet NZEB targets by that same year [18,19].

Even though BIPV systems can generate power at a low cost when considering both the function of energy generators and the materials used in construction, the predicted BIPV adoption has been overstated. There are also obstacles and constraints, including specifications for design flexibility, aesthetics, durability, cost, performance, grid integration, standard compliance, and operation and maintenance [8,17]. On the other hand, due to the visual and aesthetic limitations of BIPV systems, which display black or dark blue colors depending on the photovoltaic technology employed, modern civilizations still have a negative attitude towards the application of BIPV technology [20–31]. To identify significant knowledge gaps in education, target audiences, and teaching objectives, Momir Tabakovic et al. have conducted a comprehensive study on the development of BIPV systems [23], with the issue of “aesthetics” being the topic of most importance, followed by BIPV software/tools, market maturity, and building envelope material attributes, as recommended by renowned BIPV experts and stakeholders. According to statistics, more than 85% of architects and building designers select BIPV products because of their aesthetic qualities rather than their high costs or low conversion efficiencies [32]. To increase public satisfaction and installation rates, BIPV products with apparent transparency, coloring, and adequate conversion efficiency are appealing [8,33–35]. However, to reach the NZEB goals and simultaneously protect the environment by lowering the energy demand (fossil fuels based), it is crucial to come across the issues related to the development of visually pleasing and high-performing BIPV products. Many studies have been conducted and reviewed the BIPV system in terms of products properties [36,37], technologies [38], economic analysis [39,40], energy performance evaluation [41], thermal performance [42], design tools [43,44], barriers, and facilitators [45,46]. However, it is quite tough to present state-of-the-art BIPVs in a single review study. According to our knowledge, no studies so far have been conducted to review the performance of aesthetics of the BIPV products, which is the most desired selection criterion for customers.

In this article, we utilize the required knowledge of BIPVs to identify the major issues related to the development of aesthetically attractive BIPV products for the future global PV market and stakeholders. We present the status and challenges of aesthetically pleasing BIPV technologies, products, and their applications, and possible future development techniques to improve simultaneously the physical appearance and electrical performance of BIPV products. We focus on the development of micro-patterned-based-semi-transparent thin-film PV panels (multicolored) using a direct printing process of colored (high-definition) images.

2. Current Status and Applications of Aesthetically Attractive BIPV Products

The integration of photovoltaic modules into buildings is possible on flat roofs, sloping roofs, facades, and solar shading systems. BIPV systems, on the other hand, replace the exterior skin of the structure, acting as both a temperature control system and a source of energy production. Therefore, in addition to saving money on electricity, BIPV may also result in material and labor savings [9]. Due to their broad categories, many distinct subcategories may be used to group BIPV products. According to a report on the most common applications of BIPV in Europe [23], two-thirds of BIPV applications are achieved in new construction, with one-third in retrofitted projects. Around 50% of the BIPV components are installed in roof facades, 25% on roofs, with the remaining components being a combined roof/facade product. Residential buildings account for 19% of BIPV installations. In contrast, historic structures, public infrastructure, showroom offices, universities, and schools account for 7%, 14%, 13%, and 9%, respectively. Hotels, sports facilities, and agricultural structures are among the other structures that have been using BIPV. Currently, more than 200 BIPV products are commercially available that address the major application areas of pitched roofs, facades, and flat and curved roofs [23,47,48]. Figure 2 presents examples of common BIPV products and their application types.



Figure 2. Example of BIPV products and their applications towards facing the green global challenges and achieving a sustainable green globe.

Visually appealing BIPV products have significant consumer demand despite having limited photo-conversion efficiency. Aesthetic attractiveness can be enhanced by transparent and colored BIPV products. The percentage of transparency and flexibility of color options defines the aesthetic of BIPV products. Therefore, a comprehensive review of the current trend and future developments of semitransparent and colored BIPV products can be helpful for the scientific community and the BIPV industry.

Many research groups have adopted different technologies for the development of transparent BIPV products, namely, windows, skylights, and curtain walls, driven by their high market demand. The overall market size of BIPV is presented in Figure 3. According to the report in Ref. [49], the price of BIPV products is now cost-effective compared to conventional building products and it will be even more cost-effective in the future. In

addition to the need for efficiency and lifetime improvement, the BIPV products should have merit in their unique aesthetics and design considerations, such as color, transparency, flexibility, different form-factors, and even being indistinguishable from conventional construction materials, such as architectural glass.

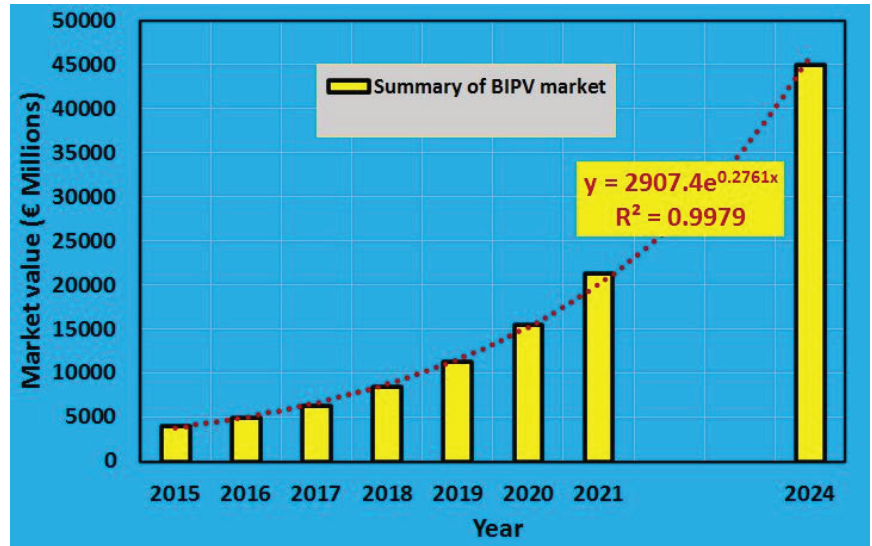


Figure 3. Summary of predicted BIPV technologies' market shares. This figure is reproduced by using the data up to 2021 that is presented in Ref. [50]. The data are digitally extracted and may have some variations from the original presentation. The BIPV technologies market share can be expected to reach above 45,000 (€ Millions) if the energy market grows without global disruption.

Very few thin film-based BIPV module types exhibit a semitransparent appearance due to the use of transparent conductive oxides as electrodes in place of grey-colored metals. Though it is quite tough to create a BIPV module that is completely transparent since the PV active layer must absorb part of the incident light to turn it into energy, but it is possible to create an acceptable BIPV product with the help of modern technologies and advanced knowledge. Another option is to change the distance between the PV-active zones, which would increase the BIPV module's transparency while simultaneously decreasing its area-specific efficiency. Typically, the BIPV system efficiency should be as high as possible, especially when the space on the roof and facade regions is limited [51].

2.1. Dye-Sensitized Solar Cells (DSSC) for BIPV Applications

In 2007, Seigo et al. [52] developed a highly transparent dye-sensitized solar cell (DSSC) through a screen printing process, where a Titanium dioxide (TiO₂) nanoparticles layer of 17 µm was printed on fluorine-doped tin oxide (FTO) coated glass. This screen-printed DSSC-PV device possessed around 60% transparency with 9.2% conversion efficiency. DSSC-based semi-transparent BIPV (orange-brown color) modules are installed as windows in the CSIRO Energy Institute, Australia [53,54]. Despite the simple fabrication process of screen-printed DSSC, the instability of liquid electrolytes at different temperatures makes it unfavorable for architects and building planners. Zhang et al., in 2015, fabricated TiO₂ nanotube-based DSSCs using the electrophoretic deposition (EPD) method [55]. Transparency of this type of solar cell was achieved by properly controlling the length, thickness, and inner diameter of the nanotubes. This type of DSSCs exhibited an average transparency of 55% along with 7.10% photon conversion efficiency (PCE); however, the complicated fabrication procedure for these DSSCs makes them suitable for

laboratory scales only [56]. Zhang et al. developed two transparent solar cell models based on quantum dots (QDs). In the first model, lead sulfide colloidal quantum dots (PbS CQDs) were used, which enable tuning the bandgap that matches the infrared spectral components of light. This PbS-based semi-transparent colloidal-quantum-dots-based solar cells (SCQDSCs), which were developed on transparent fluorine-doped tin oxide (FTO) glass, combining a Molybdenum trioxide (MoO_3) film as a hole transporting layer (HTL) and TiO_2 film as an electron transporting layer (ETL) that showed the AVT of around 22% and PCE of 3.88% only [50]. In the second solar cell model, Zhang et al. reduced the optical losses of the transparent Ag and Au electrodes by replacing them with a transparent nanolayered $\text{MoO}_3/\text{Au}/\text{MoO}_3$ (MAM) film structure that significantly increased the PCE to 5.4% and AVT to 24.1% [57]. These types of solar cells are still facing the problems of quantum dots loading and device stability, thus making them impractical commercially [58]. Figure 4 presents several examples of semitransparent and colored BIPV modules and their applications. A colored and semitransparent wall was developed by Konarka Technology, as indicated by the green line in Figure 4a, and a yellow-orange colored window based on DSSC technology developed by Daunia Solar Cell (Figure 4b) [54].



Figure 4. Semitransparent and colored BIPV modules and their applications. (a) DSSC-based red-orange colored wall installation [54], which is marked by the Green rectangular line; System provider: Konarka Technology (this company is out of market [59]), (b) DSSC-based yellow-orange colored window installation marked by the red line; system provider: Daunia solar cell (reproduced and modified from Ref. [53]), (c) OPV module; (image courtesy: Robert Coelius/Michigan Engineering)

(reproduced and modified from Refs. [60,61], and OPV based BIPV windows (photo courtesy. Dr. Renaud Demadrille (CEA Grenoble) and OPV modules are made by OPVIUS GmbH, Kitzingen, Germany. www.opvius.com, accessed on 20 November 2022 (reproduced and modified with permission from Ref. [62] (d) PVB polymer-based flooring products (reproduced and modified with permission from <https://www.onyx-solar.com>) [8], and (e) PVB polymer-based facade elements using thin-film technology (reproduced and modified with permission from www.soltechenergy.com) [8].

Dye-sensitized solar cells (DSSCs) exhibit great promise as a technology for generating electricity from sunlight due to their high efficiency and low cost. The efficiency of DSSCs can be optimized by increasing the fill factor, which is a metric that quantifies the cell's ability to convert generated current into usable power. The short-circuit current density and open-circuit voltage are crucial factors that affect the electrical output of the cell. Stability is a key factor that influences the long-term viability of DSSCs and can be enhanced by employing stable dyes and electrolytes. Additionally, the incident photon-to-current efficiency and spectral response of DSSCs are significant performance parameters that determine the cell's capability to convert various wavelengths of light into electrical energy. Through careful optimization of these performance parameters, DSSCs have the potential to emerge as a substantial source of renewable energy.

2.2. Organic Photovoltaic (OPV) Cells

Richard Lunt and his research group demonstrated a transparent organic photovoltaic (OPV) solar cell which absorbs near-infrared (NIR) wavelengths of light and transmits visible light only. This kind of OPV glass showed around 65% transparency with a small conversion efficiency of 1.3 (± 0.1) % only [63]. An organic solar cell having 10% efficiency together with 40% transparency has been developed for window applications by a research group at the University of Michigan, as can be seen in Figure 4c [61,62]. In addition, OPV manufacturing requires a very complex process of mixing multiple organic components, which typically have a limited lifetime, i.e., of a couple of years, which is much less than the 25-year lifetime of conventional inorganic solar panels. Neither OPV nor DSC has been able to increase their market share over a few years as was predicted. The product stability is poor and does not meet the standards of building materials (more than 20 years of functioning). However, vigorous DSC research efforts might create more potential BIPV devices over the next 10 years [54]. Chen et al., from the University of California, fabricated a transparent polymer solar cell (PSC) using solution processing technology, where a silver nanowire (AgNWs) coated organic conductor was used on the top of the front side electrode [64]. This PSC demonstrated an efficiency of around 4% and transparency of around 66% at 550 nm wavelength. The low efficiency and stability of such PSCs make them impractical for commercial applications. Onyx Solar, a solar panel manufacturer, has introduced PV-colored glasses that show different transparency levels with significant electrical, mechanical, optical, and thermal properties [8]. These colored products can be used in facades, skylights, flooring, canopies, and walkways as shown in Figure 4d. The Onyx technology involves laminating different polyvinyl butyral (PVB)-polymer colors with amorphous silicon solar cells. The colored polyvinyl butyral (PVB) encapsulants have also been developed SolTech Energy for building facades using CdTe-based thin-film solar panels (Figure 3e) [8]. However, in hot climates, the PVB interlayer typically softens when the PV module becomes warmer, at above 65 °C, which significantly affects the panels' performance [64].

2.3. Perovskite Solar Cells

A semi-transparent perovskite material-based solar cell was fabricated by the University of Antioquia, Spain [65] using an evaporation deposition technique. This single-junction perovskite solar cell contained a transparent methylammonium lead halide perovskite layer, which had lower bandgap energy than a photon leading to high near-infrared (NIR) absorption and visible light transmission, simultaneously. This semi-transparent per-

ovskite solar cell exhibited transparency of 30% and a power conversion efficiency (PCE) of 6.4%. Additionally, a research team from Stanford University developed a tandem solar cell configuration using opaque electrode perovskite (1.1 eV bandgap) on the bottom cell and semi-transparent perovskite (1.7–1.8 eV bandgap) on the top [66]. This tandem perovskite solar cell structure exhibited around 12.7% efficiency and a 77% peak transparency at about 800 nm. Yu et al. reported a semi-transparent perovskite solar cell development that exhibited 10% transparency and 16.75% PCE, which was the highest efficiency of its kind [67]. However, perovskite-based solar cells have limited stability and higher volatility [62]. Whilst Patel et al. developed the first-ever ultraviolet (UV) sensitive semi-transparent heterojunction solar cell utilizing the configuration of Ag/CuO_x/TiO₂/FTO, where the p-CuO_x/n-TiO₂ layer was made extremely narrow (150 nm) [68]. On the other hand, Kang et al. have demonstrated a color-neutral, flexible, and high-efficiency transparent solar cell utilizing the freestanding structure of n-type crystalline silicon microwires (SiMWs) [69]. For TSCs, a p-type polymer layer was developed on top of an n-type flat-tip SiMWs to form a heterojunction. This type of TSC utilized the visible wavelengths of light, exhibiting 8% PCE with average transparency (AVT) of around 10% and structural flexibility. Furthermore, Lee et al. have fabricated a transparent monocrystalline silicon solar cell by creating periodic microholes, which are invisible to the human eye, on the bare silicon wafer [70]. These micro holes act as transmission windows that allow the transfer of incident light resulting in the transparent substrate. The remaining opaque areas were dedicated to harnessing the incident light and converting it to electricity. This type of solar cell showed a PCE of around 12.2% with an AVT of 20%.

2.4. Luminescent Solar Concentrator (LSC) Based Transparent PV/BIPV Systems

A research team from Michigan State University has developed highly transparent, about 86% AVT, solar cells using a transparent luminescent solar concentrator (TLSC) based on organic salts [71]. In this TLSC, transparent NIR fluorescent dyes were utilized to harness NIR and UV light and transform them into visible light, then guide them to reach the edges of the glass where the opaque solar cells are mounted to convert the routed light to electricity. Figure 5a–c presents the working mechanism of LSC base PV modules, including custom build LSC-PV-based window panels, and practically installed as BIPV products. This TLSC demonstrated a PCE of about 0.4% only. Increased efficiency of around 2.35% for a concentrated type of transparent PV structure was later developed using phosphor pigments based on inorganic luminescent materials, coating-based transparent heat mirror (near-IR) reflector at the rear side, transparent diffractive materials, and thin-film based CuInSe₂ (CIS) PV modules at the edges [72]. The LSC-based semitransparent yellowish PV is shown in Figure 5b. In 2012, the Eni Research Center for Renewable Energy and the Environment in Novara successfully built an LSC-based BIPV shelter in Rome, Italy (shown in Figure 5c) to recharge electric bicycles and cars [73].

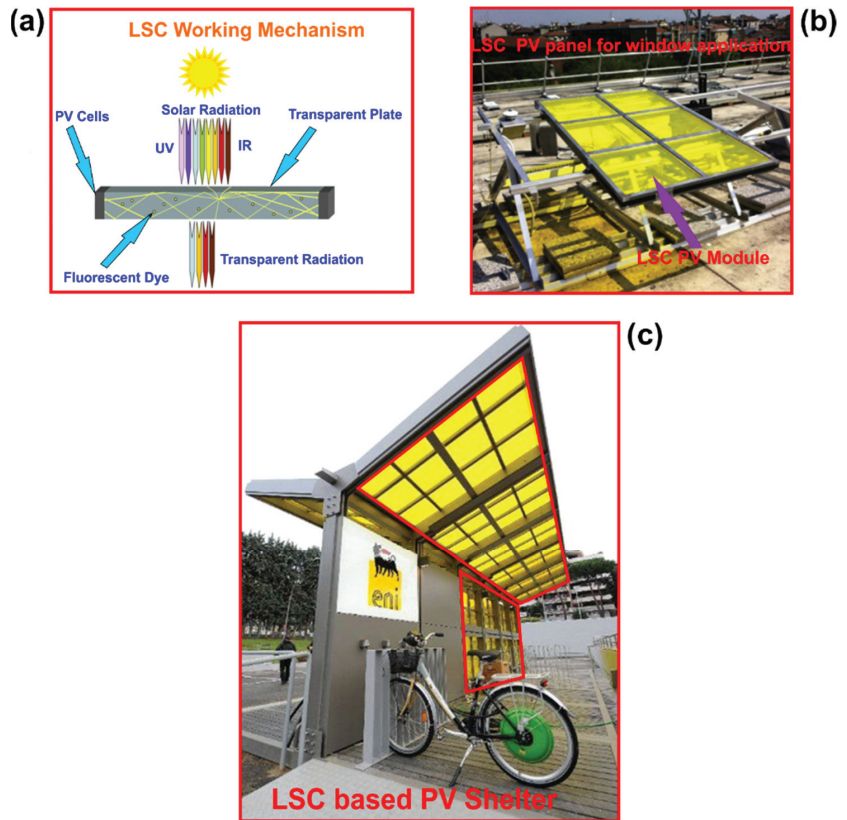


Figure 5. (a) The working mechanism of an LSC PV module (source: ENI Donegani Institute) (reproduced and modified with permission from Refs. [74,75]), (b) LSC-based window for BIPV (reproduced and modified with permission from Refs. [74,75]), and (c) LSC-based BIPV shelter in Rome, Italy (reproduced and modified from [61,73]).

2.5. Thin Film Based Semitransparent/Highly Transparent PV Systems

2.5.1. Silicon-Based Thin-Film BIPV Systems

Lim et al. fabricated a thin-film-based full-penetration (FP) semitransparent hydrogenated amorphous silicon (a-Si:H) solar cell, where they used 115 nm thickness of absorber layer with triple high band (HB) layers that significantly increase the carrier collection and decrease the shunt loss. This type of cell offers a PCE of 6.92% and average transmittance (AVT) of 23.6% [76]. Several colorful semi-transparent glass-to-glass (GTG) photovoltaic (PV) modules for BIPV applications were designed and fabricated (shown in Figure 6) by S. Y. Myong et al. in 2015, and are based on large-area hydrogenated amorphous silicon (a-Si:H). The combination of back contact transparency and laser patterning processes enabled several color choices. Although these colorful PV modules are aesthetically pleasing, they are not suited for commercial use due to their reduced transparency and photo conversion efficiency [77].

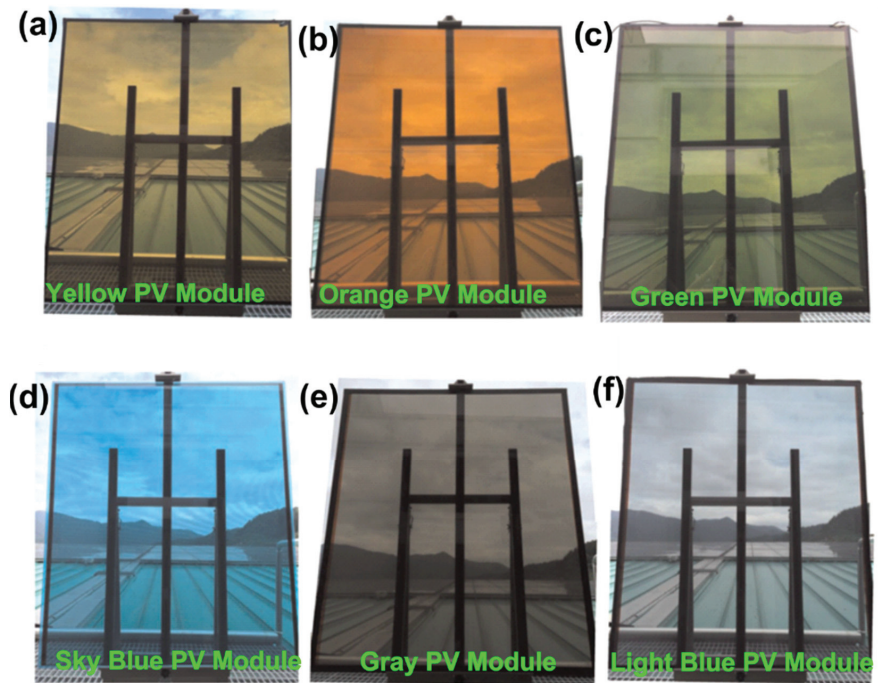


Figure 6. Front views of the fabricated a-Si:H semi-transparent glass-to-glass (GTG) PV module. (a) yellow PV module, (b) orange PV module, (c) green PV module, (d) sky blue PV module, (e) gray PV module, and (f) light blue PV module (reproduced and modified with permission from Ref. [77]).

Figure 7 presents a glimpse of a-Si-thin-film-based colored BIPV modules and their possible applications. IMT Neuchatel (Switzerland) designed and developed the first ever fully homogenous terracotta-like a-Si thin-film PV module (Archinsolar), shown in Figure 7a, using a textured anti-reflective front glass [54]. Recently, Xiamen Solar First Energy Technology Co., Ltd. has commercialized four different colored semitransparent PV modules, which are very attractive, as shown in Figure 7b [78]. Jong-Ho Yoon et al. investigated transparent thin-film amorphous silicon-based BIPV modules installed at the front glass part of the newly constructed R&D Institute building of Kolon Engineering and Construction, Co., Ltd., which is in Yongin city, Gyeonggi, in the central region of Korea. A front view of the structure is shown in Figure 7c, along with the BIPV module that has been set up in the lobby. Similar amorphous thin-film-based BIPV modules, made by KANEKA, Japan, have been deployed in Japan [79].

Solar Constructions [80] has designed and developed a silicon solar cell-based semi-transparent PV module by placing PV Cells on a panel of glass. The light transmission and, subsequently, the amount of shadowing supplied within the structure may be controlled by varying the spacing between Solar PV Cells. The transparency of such solar PV panels increases with the spacing between the cells; however, their PCE increases with the decrease of the space. Although these PV modules are mechanically stable and comparatively highly transparent and efficient, the inside views attained with a crystalline-Si semitransparent glass curtain wall look less appealing and very occluded by light and external view, hence causing visual fatigue, as shown in Figure 8 [80,81].

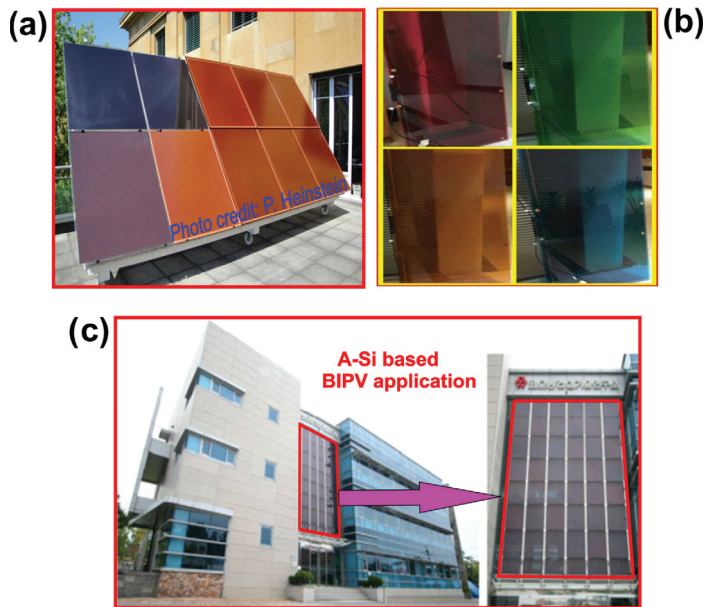


Figure 7. A-Si-based colored BIPV modules and their application. (a) First ever fully homogeneous colored BIPV products (reproduced and modified from [54]); (b) Four different colors commercialized PV modules (reproduced and modified from [78]); and (c) A-Si-based front surface building (reproduced and modified with permission from Ref. [79]).

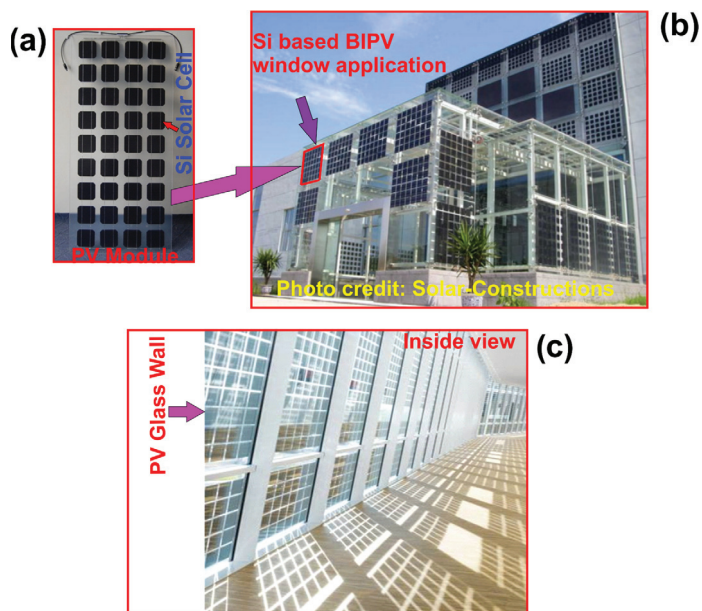


Figure 8. Crystalline silicon-based BIPV (a) Si module (reproduced and modified with permission from Ref. [80]); (b) application in building (reproduced and modified with permission from [80] [80]); (c) inside views attained with glass curtain wall (reproduced and modified from [81]).

2.5.2. Cadmium Telluride (CdTe) Based Thin-Film BIPV Systems

The most efficient semitransparent BIPV glass is that made by Advanced Solar Power (ASP)-China [82], which is based on thin-film cadmium telluride (CdTe) PV materials that are partially removed using laser micromachining to simultaneously achieve transparency and sunlight-to-electricity conversion. The ASP CdTe semitransparent PV glass shown in Figure 9a is currently the best BIPV option due to several reasons, namely: (i) relatively high efficiency (13% compared to 10% for the amorphous silicon counterpart and 3% for clear PV glass), (ii) most cost-effective (i.e., lowest \$/peak-watt), (iii) easy to manufacture (compared to crystalline silicon semitransparent glass), (vi) arbitrary transparency (10–90%, depending on how much of the PV material is removed by laser micromachining), and (v) less shadowing effect, as illustrated in Figure 9b,c, which offers beautiful appearance, uniform lighting, and light transmission, hence, a clear exterior view. The BIPV application of CdTe-based PV panels as façade and curtain wall is shown in Figure 9d,e, respectively. Note that the amount of CdTe material in the overall thin-film PV material is $\sim 0.1\%$ by weight, which is a minimal amount. In addition, because of (i) the small quantity, (ii) low solubility of CdTe, and (iii) module encapsulation, CdTe modules have been considered, at their end-of-life time, as non-hazardous waste according to the Toxicity Characteristic Leaching Procedure [83].

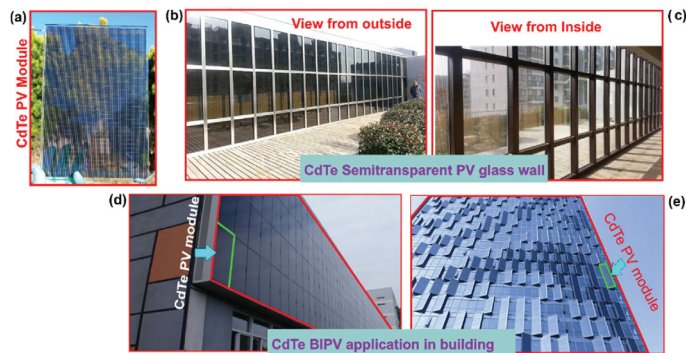


Figure 9. CdTe-based semitransparent BIPV (a) ASP CdTe semitransparent PV module, (b) Outside view (reproduced and modified from [84]), (c) inside view (reproduced and modified from [84,85]), (d) Application of CdTe Thin-Film based semi-transparent PV Glass as BIPV façade (reproduced and modified from [85]) and (e) Application of CdTe Thin-Film based semi-transparent PV Glass as BIPV curtain wall (reproduced and modified from [85]).

Note that the development of semitransparent PV glass faces several challenges, namely: (i) selection of PV materials [86], (ii) fabrication processes that enable arbitrary transparency and minimum vision distortion, (iii) high insulation properties and (iv) cost-effectiveness [56]. Different semitransparent PV glass technologies are currently being developed worldwide; however, around 80% of these technologies are still in the initial commercialization stages (under development and trials). The remaining 20% of semitransparent PV glass types available in the market or are close to commercialization suffer from various issues [87], including instability, volatility, low transparency, low PCE, high cost, and complexity [56]. To create a clear PV glass, the thickness of the PV strips required to be made small enough that the naked eye cannot visualize them; however, these typically act as diffraction gratings, thus leading to visual distortion. Nevertheless, the use of nonuniform spacing between the PV strips, i.e., quasi-crystal (aperiodic) structure, can resolve this problem to develop low-distortion commercially acceptable BIPV modules. Researchers summarize the overall key performance of different types of BIPV products and their techno-economic aspects [88–91].

3. Colored BIPV Systems, Status, and Challenges

On the other hand, the colorization of the BIPV products has significantly enhanced the aesthetics of the building because the color is the primary element that draws attention to how a panel appears [35]. Colored BIPV is a novel approach to integrating colored PV panels into current and historic building types. The main goal is to conceal the PV cells and make them invisible [75]. Researchers and manufacturers have followed different approaches to develop colored opaque PV panels, namely: (i) solar cells with anti-reflection coating; (ii) colored polymeric encapsulant films; (iii) layers or interlayers containing solar filters, colored or patterned coatings; (iv) semi-transparent and/or colored PV-active layers; and (v) printed, coated, or finished front glass [87]. Several studies reported that modification of antireflection (AR) coatings and dielectric materials made of silicon nitride (SiNx) can generate a variety of colors in crystalline silicon solar cells [35,92–94]. Additionally, by manipulating the thickness of AR film, different colors, namely, yellow, blue, green, pink, and orange, can be generated on top of the silicon solar cells [8]. Lof Solar was the first and world-leading inventor in the development of high-efficiency-colored solar cells since 2008 [95]. It has commercialized different colored polycrystalline Si solar cells produced by changing the thickness of the AR coating, as shown in Figure 10a [95]. Figure 10b shows the red-colored PV panels applied on the rooftop of the building [96]. The facade of the Kingsgate House, West London (Figure 10c) has been designed by Harden Cherry Lee Architects (HCL) [97] using a LOF Sparkling Gold PV module [98]. This aesthetically appealing building façade has installed 8000 LOF BIPV modules that can generate 29 kW of electricity [98]. LOF Solar technology created several attractive colored solar cells by modification of the AR-layer thickness that lowers the cell efficiency [99].

CSEM [100], a private, non-profit Swiss research and technology organization, has developed a patterned/colored interlayer that can be laminated inside the PV module as an extra encapsulant and act as an optical filter that diffuses and reflects the incoming visible solar spectrum, thus producing white appearance, as shown in Figure 11, and transmitting the infrared spectrum through, which is converted to electricity. This technique typically reduces the PCE to around 40%, compared to conventional uncolored solar modules [8].

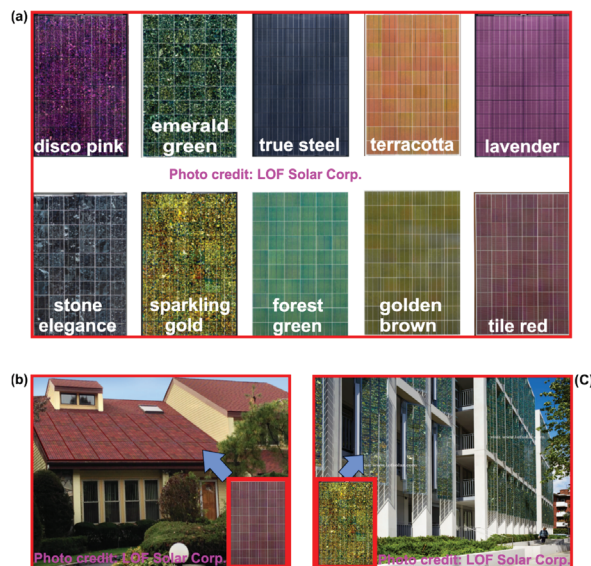


Figure 10. Crystalline Si-based opaque colored PV modules and their BIPV applications. (a) Various colored PV modules (reproduced and modified with permission from Ref. [95]), (b) red-colored BIPV rooftop application (reproduced and modified with permission from Ref. [101]), and (c) Sparkling gold BIPV façade application (reproduced and modified with permission from Ref. [102]).

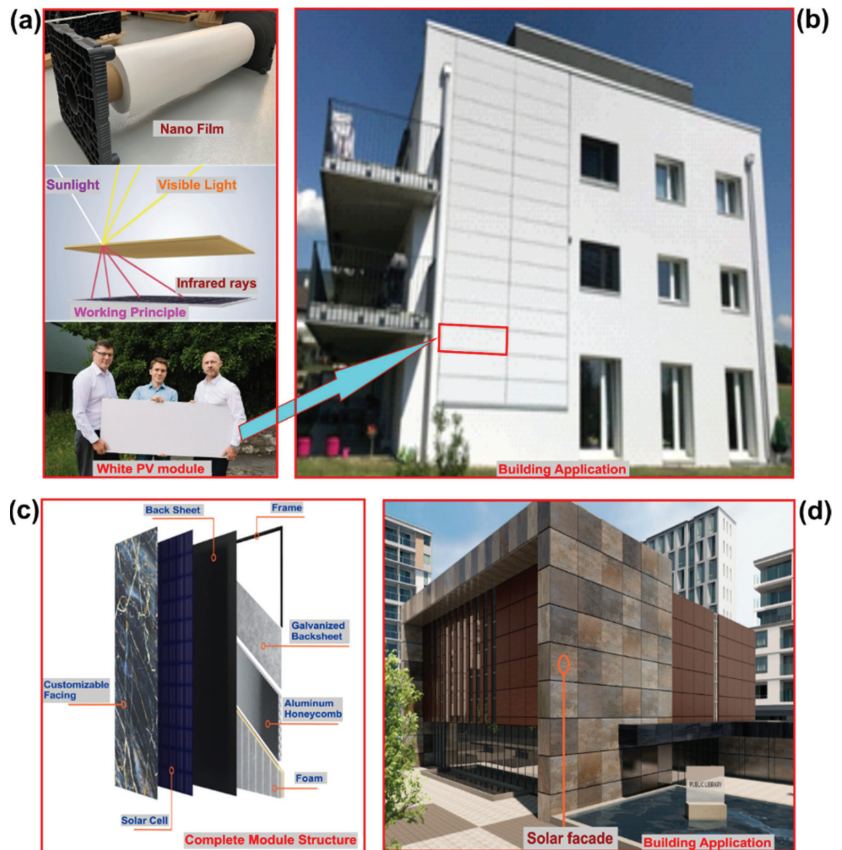


Figure 11. White appearance BIPV products based on using solar filtering. (a) white appearance nano film, working mechanism, and PV module of CSEM technology, (b) White BIPV product integrated into a building (reproduced and modified with permission from Refs. [103,104]), (c) Mitrex solar façade layers (reproduced and modified from [105]), and (d) Application of Mitrex solar façade in building (reproduced and modified with permission from Ref. [106]).

Many research groups and manufacturers have studied how to make PV panels more aesthetic and appealing by modifying the front glass cover of the solar panel. Kromatix™ technology by SwissINSO has developed a reflective coating having multiple nanolayers of TiO_2 and SiO_2 . To achieve high transmittance and colors that change depending on the viewing angle, this coating was put to the front glass of the PV module [107]. The use of highly effective and ecologically friendly nanotechnology surface treatments designed for solar energy is what Kromatix™ technology does to deliver color-treated glass for photovoltaic (PV) and thermal insulation properties (photovoltaic and thermal). This Kromatix™ technology has no paint, tint, screen printing, or digital printing; instead, they use atomic deposition methods to give the solar glass color. SwissINSO offers a variety of sizes and thicknesses of Kromatix™ glass and full-colored solar (PV or Thermal) panels. The BIPV application of Kromatix™, which is now offered in ten colors, including grey, dark grey, blue, green, blue-green, orange, bronze, and brass is depicted in Figure 12 [108]. The Swiss Federal Institute of Technology of Lausanne (EPFL) Campus, Lausanne, Switzerland retrofitted a building equipped with Kromatix™ blue PV modules, shown in Figure 12a, that covers a surface area of 1130 sq/ft where the installed capacity is 12 KWp [109]. Building integrated photovoltaics along with Kromatix™ blue-green to cre-

ate a magnificent solar wall were the sustainable retrofitting choices made by the Swedish Research Institute (RISE) in Bors, Sweden, shown in Figure 12b. SolarLAB has installed solar walls of 6000 square meters with a 720 kW_p capacity [109]. SolarLAB has installed another aesthetical BIPV facade at the Red River College Innovation Center, shown in Figure 12c, which is located in Winnipeg, Canada, using a Kromatix™ gold module. This façade uses varying sizes and shapes of custom panels that are up to 1400 by 2450 mm [110]. In a joint effort between Somiral [111,112] and Antec [113] a Kromatix™ grey solar wall with a capacity of about 55 kW is built for the school gymnasium (Figure 12d) in Leysin, Switzerland [114]. Swiss Architect bureau Kampfen Architects [101], in collaboration with Doma Solar [115], retrofitted the fifty-apartment residential building in Zurich, Switzerland, where Kromatix™ bronze colored PV modules were installed on the façade of a 180 sqm area [102]. Only renewable energy sources are used to meet the heating and hot water needs of the office and the production hall of Doma Solartechnik Headquarters located in Satteins, Austria. On the facades of 83 sqm, Kromatix™ blue, blue-green, grey, and brass are employed, shown in Figure 12f, which provides a stylish building-integrated thermal collector solution [116]. However, this technology is costly, time-consuming for color creation, and yields layers with poor transmittance [117,118] which is hard to be accepted by consumers.



Figure 12. Kromatix™ technology-based PV modules and their applications. (a) Retrofitted building of Swiss Federal Institute of Technology of Lausanne (EPFL) with blue modules (reproduced and modified with permission from Ref. [109]), (b) blue-green BIPV wall made by the Swedish Research Institute (RISE) in Bors, Sweden (reproduced and modified with permission from Ref. [109]), (c) BIPV façade by gold PV panels of the Red River College Innovation Center, at Winnipeg, Canada (use with the permission; copyright. SolarLab.dk and Garry Kopelow) [110], (d) grey BIPV of the school gymnasium in Leysin, Switzerland (reproduced and modified with permission from Ref. [114]), (e) bronze colored BIPV façade in a residential building in Zurich, Switzerland (reproduced and modified with permission from Ref. [102]), and (f) Doma Solartechnik Headquarters in Satteins, Austria (reproduced and modified with permission from Ref. [116]).

For demanding architectural solutions, Italian solar producer FuturaSun has created a red, building-integrated (BIPV) solar module of wattages around 230–245 W with an efficiency of 13.45% max. The 120 monocrystalline, multi-busbar, half-cut cells that make up the Silk Pro Red module may be created with a bespoke frame color. A brand-new line of colorful items comprises orange and silver modules. Wattages for the silver product vary from 280 W to 295 W, while those for the orange module range from 240 W to 255 W. The firm noted that these colored panels are ideal for conservative structures, repairs requiring installation on traditional roofs with tiles and brick tiles, or for usage surrounding historical architectures in town centers, where it is vital to guarantee overall harmony. These colored panels are perfect for use on pitched roofs and in creative facade compositions that take use of light and color [119–121]. Figure 13a–c shows the application of red-, orange-, and silver-colored PV modules in a building adaptive photovoltaic (BAPV). These colored PV modules can also be installed in a BIPV system, as shown in Figure 13d.

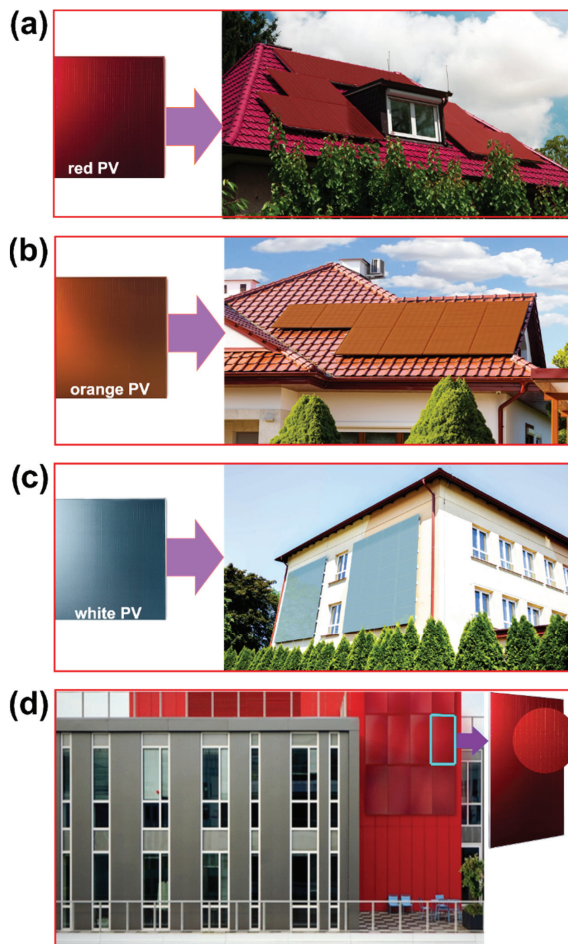


Figure 13. Colored PV modules of FuturaSun and their application (Photos by FuturaSun). (a) Red-colored BAPV (reproduced and modified with permission from Ref. [119]), (b) orange-colored BAPV (reproduced and modified with permission from [119]), (c) silver-colored BAPV (reproduced and modified with permission from Ref. [119]), and (d) red-colored BIPV (reproduced and modified from [120,121] with proper permission).

Lei-Ming Yu et al. have used a simple and efficient technique for developing polymer/Si heterojunction PVs with efficient color without the use of extra functional layers, all by adjusting the polymer layer's optical path [118], as shown in Figure 14. Constructive interference and reflectance were created by adjusting the optical refractive index and the thickness of the polymer layer at a certain wavelength. High color saturation and a wide color spectrum are seen in the resultant polymer/Si planar heterojunction PVs (e.g., pink, orange, yellow, green, blue, purple, etc.) in Figure 14a. Figure 14b shows the Bell tower of Yunnan University, China, which is decorated with vivid-colored polymer/Si-based Hybrid solar cells [122]. These multicolored heterojunction polymer/Si PVs exhibits good PCEs, with a peak value of 13.2% [122]. Another technique for developing aesthetic PV panels was reported, based on sandblasting, where sands are sprayed with higher velocities on the front surface of PV glass to create a milky white image [8]. ConstructPV [123] has designed and developed some BIPV glass sheets, as shown in Figure 14c, where attention was paid to the balance among power output, costs, and aesthetical appearance. However, the mechanical and optical properties of the PV glass are severely affected by this technique, making their lifetime short [124,125]. Hoffman [126] has proposed another technique for aesthetic coloration of a skylight facade system using ceramic digital printing. In this technology, an image is first printed on float PV glass by spraying ceramic ink pigments using multi-nozzle printer heads. With this technique, the most common printing pattern is typically seen as dots and commercially applied in a facade system. The limitation of the single-colored image of this method has been overcome by a research group at Lucerne University of Applied Sciences. They developed a printing method that produces multicolored images on the BIPV glass as illustrated in Figure 14d [112]. However, this printing approach severely attenuates solar irradiation by shading the PV cells, reducing the PV module's maximum output power [124].

The coloration processes of the front glass of the PV modules based on incorporating various types of impurities in glass is still ongoing research worldwide [127]. The most common impurity is iron oxide, which is responsible for the greenish color of the glass. This greenish color is a mixture of blue and yellow. The densities of coloring agents, such as iron oxide, could be tuned for different functions. For example, a low concentration of iron oxide is needed for glass panels employed as the front surface of the solar panel so that maximum light can be transmitted through to the solar cells to enhance the efficiency of the solar module [128]. Similarly, other metal oxide impurities can be used as coloring agents for the creation of a variety of color glass, as illustrated in Figure 14e [129,130]. Another route for the surface coloration of flat glass is based on the ion exchange process, whereby flat glasses are immersed into salt baths containing metallic ions, such as copper or silver, for red-brown or yellow-brown coloration, respectively [131,132]. Note that organic and inorganic color paints have been used to colorate PV panels. However, as discussed earlier, organic paints are not ideal due to their chemical instability. Inorganic paint colors are widely applied using screen printing, or using brushing or spraying [133,134]. All the colored PV glass panels suffered from the solar shading effect, leading to significantly reduced PCE [92]. Additionally, the conventional PV coloration technologies that maintain practical PEC levels have limited aesthetical colors.

The major issues of using existing BIPV products in buildings are: (i) limited colors and customers having no choice of any custom colors, or multiple colors in the same PV module; and (ii) low power conversion efficiency of commercially available colored BIPV modules. Although many industries have been commercializing several colored BIPV products, using, for example, intermediate encapsulant foil, multi-crystalline solar cell, EVA (ethyl vinyl acetate) encapsulated foil, multilayer interference optical filter, and digitally printed ceramic inks, these products are still suffered from: (i) dull appearance and no color flexibility, (ii) low conversion efficiency, or (iii) high production cost. Therefore, an innovative and cost-effective method is needed to ensure color flexibility (almost all colors) with high contrast and resolution and commercially viable PCE. As a result, the development of new superior, cost-effective high-definition colored Photovoltaic (PV) glass

technology and effective studies are very much needed to scale up the BIPV products and market as well.

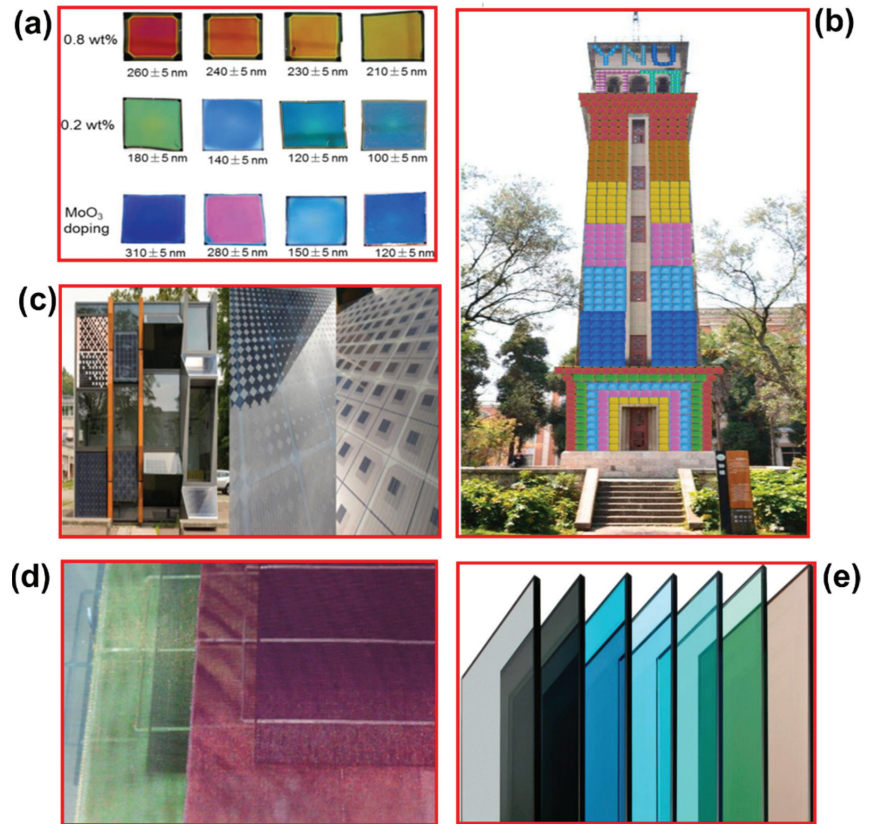


Figure 14. Realizing colored PVs using various technology. (a) Photographic images of different colorful polymer/Si-based Hybrid solar cells where polymer layers were doped with different MoO₃ doping concentrations (reproduced and modified with permission from Ref. [122]), (b) Bell tower of Yunnan University, China decorated with different colored polymer/Si-based Hybrid solar cells (reproduced and modified with permission from Ref. [122]), (c) BIPV glass modules realized using sandblast technique (reproduced and modified from Ref. [8], Source: SUPSI), (d) Ceramic digital printed PV cells (reproduced and modified from Ref. [135], Source: SmartFlex Solarfacades), and (e) AGC Glass Europe manufactured different colors of glasses used for the front cover of the PV module (reproduced and modified from AGC Glass Europe [136,137]).

4. Future Possible Research and Development in Aesthetics of the BIPV System

Currently, there is an urgent need for a high-definition colored PV technology that addresses the future zero-net-energy buildings goal through the development of viable and versatile BIPV solutions. Such a colored-imaging-based PV technology would enable the development of high-definition arbitrarily colored solar panels, which can be realized using a new micro-scale printing approach based on direct printing of high-resolution images onto the surfaces of flat or flexible PV panels. Several attempts have been made to print colored images onto PV panels in the printing laboratories at Edith Cowan University, Australia; however, printing thin layers of inks of different colors directly onto a dark solar panel typically yields dark images of very low contrast, making direct printing impractical. Additionally, placing a high-definition image in front of a PV panel typically

blocks most of the incident light, thus significantly reducing the panel's efficiency. To overcome this issue an optimal invisible micro-gap structure between the ink dots that maximize light penetration is one of the modern techniques to enhance output power while confirming an adequate image contrast, as reported by Basher et al. [138]. To the best of our knowledge, the current research on the development of colored PV modules is limited to only a few colors, and no studies have demonstrated micropatterned-based colored PV panels. Using the colored image-based PV technology, any image or painting can appear on the PV panels; however, an improved PCE is needed to be commercially acceptable. To enhance the efficiency, a high-resolution image (shown in Figure 15) can be converted to a micropatterned-based image by using Python, a high-level programming language, GIMP, image manipulation, and graphic design software. Figure 15 a–c presents the outcome of micropatterning of the randomly selected high-resolution multi-color image with a magnified view (Figure 15c) of the micropatterned image consisting of microdots and micro gaps. The micropattern acts as a mask for the image and only the microdots can print. A UV-flatbed printer can be used to print micropatterned images on off-the-shelf thin-film solar panels. Basher et al. theoretically calculated (Figure 15d) that about 75.5% of sunlight can be transmitted to the PV module through the micropatterned image. It is known that the more sunlight reaches the PV module, the higher efficiency will be achieved. The efficiency of the module can be further increased by carefully managing the black dots (Figure 15d) present in the micropatterned images. This is because the PV module underneath the micropatterned images is completely black. For example, if an image contains around 10% black microdots, 10% more light, which means a possibility of 85% sunlight incidence to the PV module, thus confirming the enhancement of photo-conversion efficiency.

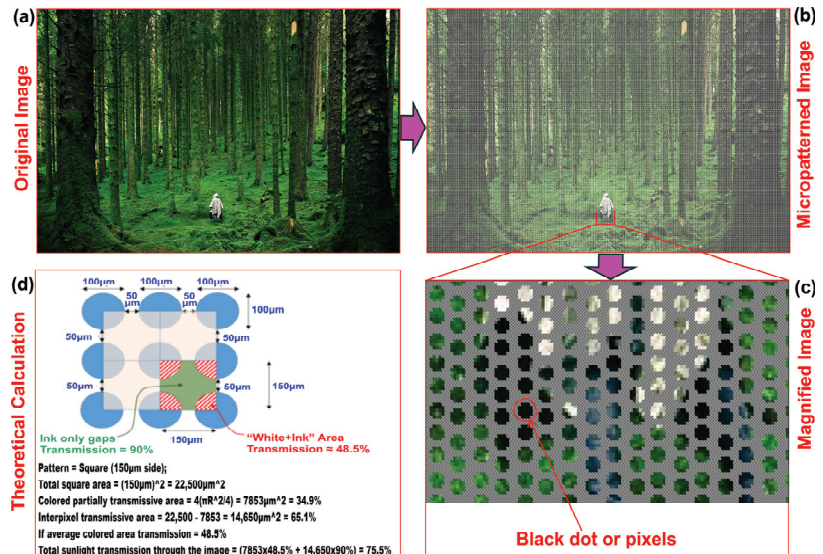


Figure 15. Formation of micropatterned image and light transmission calculation through it. (a) A randomly selected high-resolution nature image (reproduced and modified from [139]), (b) micropatterned image, (c) a magnified view of the micropatterned image, and (d) theoretical calculation of light transmission through a micropatterned image (reproduced and modified from [138]).

In addition, the image quality mostly depends on the number of dots per inch (DPI). It is clear from Figure 15b,c that increasing the DPI value increases the quality of the image. Additionally, the thickness of white ink and color ink dots significantly enhance image quality and conversion efficiency. However, the parameters, namely, the diameter of the dots, the gap between the dots, and the thickness of white ink and color ink, significantly

limit the PCE of the PV panel. In addition, a selective micropatterning approach (where some dark color microdots mean to be omitted) can be a potential research objective to enhance the PCE without compromising the visual aesthetic of the BIPV products. In the future, comprehensive research investigations can lead to achieving the goal of developing cost-effective, highly efficient, and aesthetically appealing BIPV modules with arbitrary color options. In addition to many advanced applications, such as building materials and energy generation, the prospective PV modules will provide an aesthetically appealing appearance, so that these can be suitable for various parts of buildings, namely, facades, curtain walls, roof tiles, etc. Therefore, architects will be able to design aesthetic green buildings featuring high energy generation capacities using the skin of buildings. Additionally, homeowners will have more options to choose aesthetically colorful multi-functional modern BIPV products that can be retrofitted and easily replaceable, thus contributing towards achieving the global net-zero energy buildings (NZEB) goal.

5. Conclusions

In this article, we have reviewed the existing literature on the realization, the current stage, market size, aesthetics, and challenges of BIPV products and materials required for future BIPV applications. In particular, we have reviewed the aesthetically attractive BIPV products and their applications and limitations. We have also discussed future approaches for solving the current issues of realizing aesthetic BIPV modules that open the way towards achieving net-zero energy buildings (NZEB). The advanced technical approach based on the development of high-definition colored PV modules with adequate image contrast and a power conversion efficiency (PCE) exceeding 85% of that of a bare PV panel will boost the use of BIPV products and expand their market values in near future. The performance of currently available BIPV products has so far obtained great improvement; however, some issues still should be considered in order to make a strong position in the energy niche market, such as the mechanism of improving the aesthetic of solar cells in conjunction with the carrier transport layer and interfaces. Furthermore, the application of image processing using nontoxic inks on PVs with high performance and stability should be explored. This is an ongoing research project; our group is actively working to establish an easy and cost-effective process to improve the efficiency of thin-film-based BIPV modules simultaneously with a highly acceptable visual appearance.

Author Contributions: Conceptualization, M.K.B. and K.A.; methodology, M.K.B., M.N.-E.-A. and K.A.; software, M.K.B.; validation, M.K.B., M.N.-E.-A. and K.A.; formal analysis, M.K.B., M.N.-E.-A., M.M.R., S.H. and K.A.; investigation, M.K.B., M.N.-E.-A., M.M.R., S.H. and K.A.; resources, S.H. and K.A.; data curation, M.K.B., S.H. and K.A.; writing—original draft preparation, M.K.B. and K.A.; writing—review and editing, M.K.B., M.N.-E.-A., M.M.R., S.H. and K.A.; visualization, M.K.B., M.N.-E.-A. and K.A.; supervision, K.A. and S.H.; project administration, M.K.B., K.A. and S.H.; funding acquisition, M.K.B., K.A. and S.H. All authors have read and agreed to the published version of the manuscript.

Funding: This research received no external funding.

Institutional Review Board Statement: Not applicable.

Informed Consent Statement: Not applicable.

Data Availability Statement: Not applicable.

Acknowledgments: The research was supported by the School of Science, Edith Cowan University, Australia.

Conflicts of Interest: The authors declare no conflict of interest.

Nomenclature

NZEB	Net-zero energy building
PV	Photovoltaic
BIPV	Building-integrated photovoltaic
BTJ	Billion Tera Joule
NO _x	nitrogen oxides
SO ₂	Sulfur dioxide
low-E	Low-emissivity
DEP	Directive of the European Parliament
ZCBE	Zero-carbon built environment
GW	gigawatt
CPUC	California Public Utilities Commission
DSSC	Dye-sensitized solar cell
TiO ₂	Titanium dioxide
μm	micrometer
FTO	Fluorine-doped tin oxide
CSIRO	Commonwealth Scientific and Industrial Research Organization
EPD	Electrophoretic deposition
PCE	Photon conversion efficiency
PbS CQDs	Lead sulfide colloidal quantum dots
SCQDSCs	Semi-transparent colloidal-quantum-dots-based solar cells
MoO ₃	Molybdenum trioxide
HTL	Hole transporting layer
ETL	Electron transporting layer
AVT	Average Visual Transmittance
OPV	Organic photovoltaic
NIR	Near-infrared
AgNWs	Silver nanowire
SiN _x	Silicon nitride
CuOx	Copper oxide
SiMWs	Silicon microwires
LSC	Luminescent solar concentrator
TLSC	Transparent luminescent solar concentrator
UV	Ultraviolet
IR	Infrared
CIS	CuInSe ₂
ENI	A research center in Novara, Italy
a-Si:H	Hydrogenated amorphous silicon
CdTe	Cadmium telluride
kW	Kilowatt
kWp	Kilowatt peak
EVA	Ethyl vinyl acetate
GIMP	Image Manipulation Program
DPI	Dots per inch

References

1. Tripathy, M.; Sadhu, P.K.; Panda, S.K. A Critical Review on Building Integrated Photovoltaic Products and Their Applications. *Renew. Sustain. Energy Rev.* **2016**, *61*, 451–465. [[CrossRef](#)]
2. Vasiliev, M.; Nur-E-Alam, M.; Alameh, K. Recent Developments in Solar Energy-Harvesting Technologies for Building Integration and Distributed Energy Generation. *Energies* **2019**, *12*, 1080. [[CrossRef](#)]
3. Attia, S. *Net Zero Energy Buildings (NZEB): Concepts, Frameworks and Roadmap for Project Analysis and Implementation*; Elsevier: Amsterdam, The Netherlands, 2018; ISBN 9780128124628.
4. Owusu, P.A.; Asumadu-Sarkodie, S. A Review of Renewable Energy Sources, Sustainability Issues and Climate Change Mitigation. *Cogent Eng.* **2016**, *3*, 1167990. [[CrossRef](#)]
5. Asumadu-Sarkodie, S.; Owusu, P.A. Feasibility of Biomass Heating System in Middle East Technical University, Northern Cyprus Campus. *Cogent Eng.* **2016**, *3*, 1134304. [[CrossRef](#)]

6. Kumar, N.M.; Sudhakar, K.; Samykano, M. Performance Comparison of BAPV and BIPV Systems with C-Si, CIS and CdTe Photovoltaic Technologies under Tropical Weather Conditions. *Case Stud. Therm. Eng.* **2019**, *13*, 100374. [\[CrossRef\]](#)
7. Snow, M.; Prasad, D. *A Source Book for Building Integrated Photovoltaics (BiPV)*; Routledge: London, UK, 2005; pp. 1–128.
8. Eder, G.; Peharz, G.; Trattinig, R.; Bonomo, P.; Saretta, E.; Frontini, F.; Polo López, C.S.; Rose Wilson, H.; Eisenlohr, J.; Martin Chivelet, N.; et al. *Coloured BIPV Market, Research and Development IEA PVPS Task 15, Subtask E Report T 15-07: 2019*; Report IEA-PVPS T15-07: 2019; International Energy Agency: Paris, French, 2019; p. 60.
9. Jelle, B. Building Integrated Photovoltaics: A Concise Description of the Current State of the Art and Possible Research Pathways. *Energies* **2015**, *9*, 21. [\[CrossRef\]](#)
10. Gholami, H.; Røstvik, H.N. Economic Analysis of BIPV Systems as a Building Envelope Material for Building Skins in Europe. *Energy* **2020**, *204*, 117931. [\[CrossRef\]](#)
11. Ng, P.K.; Mithraratne, N.; Kua, H.W. Energy Analysis of Semi-Transparent BIPV in Singapore Buildings. *Energy Build.* **2013**, *66*, 274–281. [\[CrossRef\]](#)
12. Leite Didoné, E.; Wagner, A. Semi-Transparent PV Windows: A Study for Office Buildings in Brazil. *Energy Build.* **2013**, *67*, 136–142. [\[CrossRef\]](#)
13. EUR-Lex-02010L0031-20181224-EN-EUR-Lex. Available online: <https://eur-lex.europa.eu/eli/dir/2010/31/2018-12-24> (accessed on 13 April 2020).
14. Wong, P.W.; Shimoda, Y.; Nonaka, M.; Inoue, M.; Mizuno, M. Semi-Transparent PV: Thermal Performance, Power Generation, Daylight Modelling and Energy Saving Potential in a Residential Application. *Renew. Energy* **2008**, *33*, 1024–1036. [\[CrossRef\]](#)
15. Peng, J.; Curcija, D.C.; Lu, L.; Selkowitz, S.E.; Yang, H.; Zhang, W. Numerical Investigation of the Energy Saving Potential of a Semi-Transparent Photovoltaic Double-Skin Façade in a Cool-Summer Mediterranean Climate. *Appl. Energy* **2016**, *165*, 345–356. [\[CrossRef\]](#)
16. Bayoumi, M. Impacts of Window Opening Grade on Improving the Energy Efficiency of a Façade in Hot Climates. *Build. Environ.* **2017**, *119*, 31–43. [\[CrossRef\]](#)
17. Ballif, C.; Perret-Aebi, L.E.; Lufkin, S.; Rey, E. Integrated Thinking for Photovoltaics in Buildings. *Nat. Energy* **2018**, *3*, 438–442. [\[CrossRef\]](#)
18. California [USA]-NZE. Available online: <https://nzebnew.pivotaldesign.biz/definitions-policies/international-roadmaps/california-usa/> (accessed on 15 November 2022).
19. Zero Net Energy. Available online: <https://www.cpsc.ca.gov/industries-and-topics/electrical-energy/demand-side-management/energy-efficiency/zero-net-energy> (accessed on 15 November 2022).
20. Cohen, J.J.; Reichl, J.; Schmidthaler, M. Re-Focussing Research Efforts on the Public Acceptance of Energy Infrastructure: A Critical Review. *Energy* **2014**, *76*, 4–9. [\[CrossRef\]](#)
21. Mittag, M.; Kutter, C.; Ebert, M.; Wilson, H. Power Loss Through Decorative Elements in the Front Glazing of BIPV Modules, In Proceedings of the 33rd European Photovoltaic Solar Energy Conference and Exhibition, Amsterdam, The Netherlands, 26 September 2017.
22. Munari Probst, M.C.; Roecker, C. Criteria for Architectural Integration of Active Solar Systems IEA Task 41, Subtask A. *Energy Procedia* **2012**, *30*, 1195–1204. [\[CrossRef\]](#)
23. Tabakovic, M.; Fechner, H.; Van Sark, W.; Louwen, A.; Georghiou, G.; Makrides, G.; Loucaidou, E.; Ioannidou, M.; Weiss, I.; Arancon, S.; et al. Status and Outlook for Building Integrated Photovoltaics (BIPV) in Relation to Educational Needs in the BIPV Sector. *Energy Procedia* **2017**, *111*, 993–999. [\[CrossRef\]](#)
24. Goh, K.C.; Goh, H.H.; Yap, A.B.K.; Masrom, M.A.N.; Mohamed, S. Barriers and Drivers of Malaysian BIPV Application: Perspective of Developers. *Energy Procedia* **2017**, *180*, 1585–1595. [\[CrossRef\]](#)
25. Yang, R.J.; Zou, P.X.W. Building Integrated Photovoltaics (BIPV): Costs, Benefits, Risks, Barriers and Improvement Strategy. *Int. J. Constr. Manag.* **2016**, *16*, 39–53. [\[CrossRef\]](#)
26. Karakaya, E.; Sriwannawit, P. Barriers to the Adoption of Photovoltaic Systems: The State of the Art. *Renew. Sustain. Energy Rev.* **2015**, *49*, 60–66. [\[CrossRef\]](#)
27. Yang, R.J. Overcoming Technical Barriers and Risks in the Application of Building Integrated Photovoltaics (BIPV): Hardware and Software Strategies. *Autom. Constr.* **2015**, *51*, 92–102. [\[CrossRef\]](#)
28. Azadian, F.; Radzi, M.A.M. A General Approach toward Building Integrated Photovoltaic Systems and Its Implementation Barriers: A Review. *Renew. Sustain. Energy Rev.* **2013**, *22*, 527–538. [\[CrossRef\]](#)
29. Taleb, H.M.; Pitts, A.C. The Potential to Exploit Use of Building-Integrated Photovoltaics in Countries of the Gulf Cooperation Council. *Renew. Energy* **2009**, *34*, 1092–1099. [\[CrossRef\]](#)
30. Prieto, A.; Knaack, U.; Auer, T.; Klein, T. Solar Façades—Main Barriers for Widespread Façade Integration of Solar Technologies. *J. Façade Des. Eng.* **2017**, *5*, 51–62. [\[CrossRef\]](#)
31. Scognamiglio, A.; Privato, C. Starting Points for a New Cultural Vision of Bipv. In Proceedings of the 23rd European Photovoltaic Solar Energy Conference and Exhibition, Valencia, Spain, 1–5 September 2008.
32. Lee, K.T.; Lee, J.Y.; Seo, S.; Guo, L.J. Colored Ultrathin Hybrid Photovoltaics with High Quantum Efficiency. *Light. Sci. Appl.* **2014**, *3*, e215. [\[CrossRef\]](#)
33. Lien, S.-Y. Artist Photovoltaic Modules. *Energies* **2016**, *9*, 551. [\[CrossRef\]](#)

34. Attoey, D.E.; Aoul, K.A.T.; Hassan, A. A Review on Building Integrated Photovoltaic Façade Customization Potentials. *Sustainability* **2017**, *9*, 2287. [[CrossRef](#)]
35. Peharz, G.; Berger, K.; Kubicek, B.; Aichinger, M.; Grobbauer, M.; Gratzner, J.; Nemitz, W.; Großschädl, B.; Auer, C.; Prietl, C.; et al. Application of Plasmonic Coloring for Making Building Integrated PV Modules Comprising of Green Solar Cells. *Renew. Energy* **2017**, *109*, 542–550. [[CrossRef](#)]
36. Shukla, A.K.; Sudhakar, K.; Baredar, P. Recent Advancement in BIPV Product Technologies: A Review. *Energy Build.* **2017**, *140*, 188–195. [[CrossRef](#)]
37. Jelle, B.P.; Breivik, C.; Drolsum Røkenes, H. Building Integrated Photovoltaic Products: A State-of-the-Art Review and Future Research Opportunities. *Sol. Energy Mater. Sol. Cells* **2012**, *100*, 69–96. [[CrossRef](#)]
38. Parida, B.; Iniyar, S.; Goic, R. A Review of Solar Photovoltaic Technologies. *Renew. Able Sustain. Energy Rev.* **2011**, *15*, 1625–1636. [[CrossRef](#)]
39. Gholami, H.; Røstvik, H.N.; Müller-Eie, D. Holistic Economic Analysis of Building Integrated Photovoltaics (BIPV) System: Case Studies Evaluation. *Energy Build.* **2019**, *203*, 109461. [[CrossRef](#)]
40. Branker, K.; Pathak, M.J.M.; Pearce, J.M. A Review of Solar Photovoltaic Levelized Cost of Electricity. *Renew. Able Sustain. Energy Rev.* **2011**, *15*, 4470–4482. [[CrossRef](#)]
41. Martellotta, F.; Cannavale, A.; Ayr, U. Comparing Energy Performance of Different Semi-Transparent, Building-Integrated Photovoltaic Cells Applied to “Reference” Buildings. *Energy Procedia* **2017**, *126*, 219–226. [[CrossRef](#)]
42. Luo, Y.; Zhang, L.; Wang, X.; Xie, L.; Liu, Z.; Wu, J.; Zhang, Y.; He, X. A Comparative Study on Thermal Performance Evaluation of a New Double Skin Façade System Integrated with Photovoltaic Blinds. *Appl. Energy* **2017**, *199*, 281–293. [[CrossRef](#)]
43. Shukla, A.K.; Sudhakar, K.; Baredar, P. A Comprehensive Review on Design of Building Integrated Photovoltaic System. *Energy Build.* **2016**, *128*, 99–110. [[CrossRef](#)]
44. Jakica, N. State-of-the-Art Review of Solar Design Tools and Methods for Assessing Daylighting and Solar Potential for Building-Integrated Photovoltaics. *Renew. Able Sustain. Energy Rev.* **2018**, *81*, 1296–1328. [[CrossRef](#)]
45. Curtius, H.C. The Adoption of Building-Integrated Photovoltaics: Barriers and Facilitators. *Renew. Energy* **2018**, *126*, 783–790. [[CrossRef](#)]
46. Carlander, J.; Thollander, P. Barriers to Implementation of Energy-Efficient Technologies in Building Construction Projects—Results from a Swedish Case Study. *Resour. Environ. Sustain.* **2022**, *11*, 100097. [[CrossRef](#)]
47. Frontini, F.; Bonomo, P.; Chatzipanagi, A.; Verberne, G.; van den Donker, M.N.; Folkerts, W. BIPV Product Overview for Solar Facades and Roofs 2015. Available online: <https://repository.tno.nl//islandora/object/uuid:001d6c37-b26c-40e5-af19-8f39cc9989a5> (accessed on 22 November 2022).
48. Delponte, E.; Marchi, F.; Frontini, F.; López, C.S.P.; Fath, K.; Batey, M. BIPV in EU28, from Niche to Mass Market: An Assessment of Current Projects and the Potential for Growth through Product Innovation. In Proceedings of the 31st European Photovoltaic Solar Energy Conference and Exhibition (EU PVSEC 2015), Hamburg, Germany, 14–18 September 2015; pp. 3046–3050. [[CrossRef](#)]
49. Project Reports. Available online: <https://www.pvsites.eu/downloads/category/project-results?page=3> (accessed on 22 November 2022).
50. Zhang, X.; Eperon, G.E.; Liu, J.; Johansson, E.M.J. Semitransparent Quantum Dot Solar Cell. *Nano Energy* **2016**, *22*, 70–78. [[CrossRef](#)]
51. Zhang, W.; Lu, L.; Peng, J.; Song, A. Comparison of the Overall Energy Performance of Semi-Transparent Photovoltaic Windows and Common Energy-Efficient Windows in Hong Kong. *Energy Build.* **2016**, *128*, 511–518. [[CrossRef](#)]
52. Ito, S.; Chen, P.; Comte, P.; Nazeeruddin, M.K.; Liska, P.; Péchy, P.; Grätzel, M. Fabrication of Screen-Printing Pastes from TiO₂ Powders for Dye-Sensitized Solar Cells. *Prog. Photovolt. Res. Appl.* **2007**, *15*, 603–612. [[CrossRef](#)]
53. Acciari, G.; Adamo, G.; Ala, G.; Busacca, A.; Caruso, M.; Giglia, G.; Imburgia, A.; Liveri, P.; Miceli, R.; Parisi, A.; et al. Experimental Investigation on the Performances of Innovative PV Vertical Structures. *Photonics* **2019**, *6*, 86. [[CrossRef](#)]
54. Heinstein, P.; Ballif, C.; Perret-Aebi, L.-E. Building Integrated Photovoltaics (BIPV): Review, Potentials, Barriers and Myths. *Green* **2013**, *3*, 125–156. [[CrossRef](#)]
55. Zhang, J.; Li, S.; Yang, P.; Que, W.; Liu, W. Deposition of Transparent TiO₂ Nanotubes-Films via Electrophoretic Technique for Photovoltaic Applications. *Sci. China Mater.* **2015**, *58*, 785–790. [[CrossRef](#)]
56. Husain, A.A.F.; Hasan, W.Z.W.; Shafie, S.; Hamidon, M.N.; Pandey, S.S. A Review of Transparent Solar Photovoltaic Technologies. *Renew. Able Sustain. Energy Rev.* **2018**, *94*, 779–791. [[CrossRef](#)]
57. Zhang, X.; Hägglund, C.; Johansson, M.B.; Sveinbjörnsson, K.; Johansson, E.M.J. Fine Tuned Nanolayered Metal/Metal Oxide Electrode for Semitransparent Colloidal Quantum Dot Solar Cells. *Adv. Funct. Mater.* **2016**, *26*, 1921–1929. [[CrossRef](#)]
58. Mora-Seró, I. Current Challenges in the Development of Quantum Dot Sensitized Solar Cells. *Adv. Energy Mater.* **2020**, *10*, 2001774. [[CrossRef](#)]
59. Konarka Technologies—Wikipedia. Available online: https://en.wikipedia.org/wiki/Konarka_Technologies (accessed on 9 January 2023).
60. Solar Cells with 30-Year Lifetimes for Power-Generating Windows. Available online: <https://ece.engin.umich.edu/stories/solar-cells-with-30-year-lifetimes-for-power-generating-windows> (accessed on 10 January 2023).
61. Semi-Transparent Organic Solar Cell for Window Applications—Pv Magazine International. Available online: <https://www.pv-magazine.com/2021/09/16/semi-transparent-organic-solar-cell-for-window-applications/> (accessed on 18 July 2022).

62. Brus, V.V.; Lee, J.; Luginbuhl, B.R.; Ko, S.J.; Bazan, G.C.; Nguyen, T.Q. Solution-Processed Semitransparent Organic Photovoltaics: From Molecular Design to Device Performance. *Adv. Mater.* **2019**, *31*, 1900904. [CrossRef]
63. Lunt, R.R.; Bulovic, V. Transparent, near-Infrared Organic Photovoltaic Solar Cells for Window and Energy-Scavenging Applications. *Appl. Phys. Lett.* **2011**, *98*, 113305. [CrossRef]
64. Chen, C.-C.; Dou, L.; Zhu, R.; Chung, C.-H.; Song, T.-B.; Zheng, Y.B.; Hawks, S.; Li, G.; Weiss, P.S.; Yang, Y. Visibly Transparent Polymer Solar Cells Produced by Solution Processing. *ACS Nano* **2012**, *6*, 7185–7190. [CrossRef]
65. Roldán-Carmona, C.; Malinkiewicz, O.; Betancur, R.; Longo, G.; Momblona, C.; Jaramillo, F.; Camacho, L.; Bolink, H.J. High Efficiency Single-Junction Semitransparent Perovskite Solar Cells. *Energy Environ. Sci.* **2014**, *7*, 2968–2973. [CrossRef]
66. Bailie, C.D.; Christoforo, M.G.; Mailoa, J.P.; Bowring, A.R.; Unger, E.L.; Nguyen, W.H.; Burschka, J.; Pellet, N.; Lee, J.Z.; Grätzel, M.; et al. Semi-Transparent Perovskite Solar Cells for Tandems with Silicon and CIGS. *Energy Environ. Sci.* **2015**, *8*, 956–963. [CrossRef]
67. Yu, J.C.; Sun, J.; Chandrasekaran, N.; Dunn, C.J.; Chesman, A.S.R.; Jasieniak, J.J. Semi-Transparent Perovskite Solar Cells with a Cross-Linked Hole Transport Layer. *Nano Energy* **2020**, *71*, 104635. [CrossRef]
68. Patel, D.B.; Chauhan, K.R. 50% Transparent Solar Cells of CuO /TiO₂: Device Aspects. *J. Alloys Compd.* **2020**, *842*, 155594. [CrossRef]
69. Kang, S.B.; Kim, J.-H.; Jeong, M.H.; Sanger, A.; Kim, C.U.; Kim, C.-M.; Choi, K.J. Stretchable and Colorless Freestanding Microwire Arrays for Transparent Solar Cells with Flexibility. *Light. Sci. Appl.* **2019**, *8*, 121. [CrossRef]
70. Lee, K.; Kim, N.; Kim, K.; Um, H.-D.; Jin, W.; Choi, D.; Park, J.; Park, K.J.; Lee, S.; Seo, K. Neutral-Colored Transparent Crystalline Silicon Photovoltaics. *Joule* **2020**, *4*, 235–246. [CrossRef]
71. Zhao, Y.; Meek, G.A.; Levine, B.G.; Lunt, R.R. Near-Infrared Harvesting Transparent Luminescent Solar Concentrators. *Adv. Opt. Mater.* **2014**, *2*, 606–611. [CrossRef]
72. Vasiliev, M.; Alameh, K.; Badshah, M.; Kim, S.-M.; Nur-E-Alam, M. Semi-Transparent Energy-Harvesting Solar Concentrator Windows Employing Infrared Transmission-Enhanced Glass and Large-Area Microstructured Diffractive Elements. *Photonics* **2018**, *5*, 25. [CrossRef]
73. In Rome, Transparent Photovoltaic Shelters That Recharge Electric Bikes and Cars—GreenMe. Available online: <https://www.greenme.it/mobilita/trasporti/pensiline-fotovoltaico-trasparente-eni/> (accessed on 26 July 2022).
74. Aste, N.; Tagliabue, L.C.; Del Pero, C.; Testa, D.; Fusco, R. Performance Analysis of a Large-Area Luminescent Solar Concentrator Module. *Renew. Energy* **2015**, *76*, 330–337. [CrossRef]
75. Ghosh, A. Potential of Building Integrated and Attached/Applied Photovoltaic (BIPV/BAPV) for Adaptive Less Energy-Hungry Building's Skin: A Comprehensive Review. *J. Clean. Prod.* **2020**, *276*, 123343. [CrossRef]
76. Wook Lim, J.; Shin, M.; Lee, D.J.; Hyun Lee, S.; Jin Yun, S. Highly Transparent Amorphous Silicon Solar Cells Fabricated Using Thin Absorber and High-Bandgap-Energy n/i-Interface Layers. *Sol. Energy Mater. Sol. Cells* **2014**, *128*, 301–306. [CrossRef]
77. Yeop Myong, S.; Won Jeon, S. Design of Esthetic Color for Thin-Film Silicon Semi-Transparent Photovoltaic Modules. *Sol. Energy Mater. Sol. Cells* **2015**, *143*, 442–449. [CrossRef]
78. China Hot Sale High Efficiency 40W Transparent Thin Film Solar Panel—China Solar Panel, Transparent Solar Panel. Available online: <https://esolarfirst.en.made-in-china.com/product/eyxnjoxvrwvr/China-Hot-Sale-High-Efficiency-40W-Transparent-Thin-Film-Solar-Panel.html> (accessed on 10 August 2022).
79. Yoon, J.-H.; Song, J.; Lee, S.-J. Practical Application of Building Integrated Photovoltaic (BIPV) System Using Transparent Amorphous Silicon Thin-Film PV Module. *Sol. Energy* **2011**, *85*, 723–733. [CrossRef]
80. Transparent Solar Panels Semi Transparent Solar Panels. Available online: <http://www.solar-constructions.com/wordpress/transparent-solar-panels/> (accessed on 9 November 2022).
81. Solar BIPV/BIPV/Transparent Solar Panel—Energor Technology Co., Ltd.-Eclpaza.Net. Available online: https://www.eclpaza.net/products/solar-bipv-bipv-transparent-solar-panel_627393 (accessed on 1 August 2022).
82. Advanced Solar Power | ASP-LAM3 (164-218W) | Solar Panel Datasheet | ENF Panel Directory. Available online: https://www.enfsolar.com/pv/panel-datasheet/Thin-film/1024?utm_source=ENF&utm_medium=panel_profile&utm_campaign=enquiry_company_directory&utm_content=20020 (accessed on 9 November 2022).
83. Sinha, P.; Wade, A. Assessment of Leaching Tests for Evaluating Potential Environmental Impacts of PV Module Field Breakage. *IEEE J. Photovolt.* **2015**, *5*, 1710–1714. [CrossRef]
84. Photovoltaic Modules. Available online: <http://www.aldi.ru/page/view/16> (accessed on 1 August 2022).
85. Solstice Solar—BIPV Solution Provider. Available online: <https://solstice.id/products/cadmium-telluride-pv-glass/> (accessed on 1 August 2022).
86. Liao, W.; Xu, S. Energy Performance Comparison among See-through Amorphous-Silicon PV (Photovoltaic) Glazings and Traditional Glazings under Different Architectural Conditions in China. *Energy* **2015**, *83*, 267–275. [CrossRef]
87. Pelle, M.; Lucchi, E.; Maturi, L.; Astigarraga, A.; Causone, F. Coloured BIPV Technologies: Methodological and Experimental Assessment for Architecturally Sensitive Areas. *Energies* **2020**, *13*, 4506. [CrossRef]
88. Reddy, P.; Surendra Gupta, M.V.N.; Nundy, S.; Karthick, A.; Ghosh, A. Status of BIPV and BAPV System for Less Energy-Hungry Building in India—A Review. *Appl. Sci.* **2020**, *10*, 2337. [CrossRef]
89. Green, M.A.; Hishikawa, Y.; Dunlop, E.D.; Levi, D.H.; Hohl-Ebinger, J.; Yoshita, M.; Ho-Baillie, A.W.Y. Solar Cell Efficiency Tables (Version 53). *Prog. Photovolt. Res. Appl.* **2019**, *27*, 3–12. [CrossRef]

90. Solar Power 101: Complete Guide to Solar Energy | EnergySage. Available online: <https://www.energysage.com/solar/> (accessed on 10 March 2023).
91. Best Research-Cell Efficiency Chart | Photovoltaic Research | NREL. Available online: <https://www.nrel.gov/pv/cell-efficiency.html> (accessed on 10 March 2023).
92. Sehati, P.; Malmros, L.; Karlsson, S.; Kovacs, P. *Aesthetically Pleasing PV Modules for the Built Environment*; RISE Research Institutes of Sweden: Gothenburg, Sweden, 2019; ISBN 9789188907301.
93. Peharz, G.; Grosschädl, B.; Prietl, C.; Waldhauser, W.; Wenzl, F.P. Tuning the Colors of C-Si Solar Cells by Exploiting Plasmonic Effects. In *Next Generation Technologies for Solar Energy Conversion VII*; Sulima, O.V., Conibeer, G., Eds.; SPIE: Bellingham, WA, USA, 2016; Volume 9937, p. 99370P.
94. McIntosh, K.R.; Amara, M.; Mandorlo, F.; Abbott, M.D.; Sudbury, B.A. Advanced Simulation of a PV Module's Color. *AIP Conf. Proc.* **2018**, *1999*, 020017.
95. Solar Module Standard-PV-Module—Lof Solar—Color Solar Cell. Available online: <http://www.lofsolar.com/Standard-PV-Module#6> (accessed on 13 September 2022).
96. Red Solar Panel on the Roof-Lof Solar-Color Solar Cell. Available online: <http://www.lofsolar.com/LofsolarPerformance/redsolarpanelontheroof-172.html> (accessed on 13 September 2022).
97. Hcl Architects—Kingsgate House. Available online: <http://www.hcla.co.uk/projects/type/kingsgate-house> (accessed on 15 November 2022).
98. London Kingsgate House-Sustainable Homes Level 4-Lof Solar—Color Solar Cell. Available online: <http://www.lofsolar.com/LofsolarPerformance/londonkingsgatehouse-sustainablehomeslevel4-69.html> (accessed on 13 September 2022).
99. Aesthetically Pleasing PV Modules for the Built Environment. Available online: https://www.researchgate.net/publication/331036665_Aesthetically_pleasing_PV_modules_for_the_Built_Environment (accessed on 15 November 2022).
100. Perret-Aebi, L.-E.; Escarré, J.; Li, H.-Y.; Sansonnens, L.; Galliano, F.; Cattaneo, G.; Heinstejn, P.; Nicolay, S.; Bailat, J.; Eberhard, S.; et al. *When PV Modules Are Becoming Real Building Elements: White Solar Module, a Revolution for BIPV (Presentation Recording)*; Dhere, N.G., Wohlgemuth, J.H., Jones-Albertus, R., Eds.; SPIE: San Diego, CA, USA, 2015; p. 95630Q.
101. Home—Fight Zince + Partner Ag. Available online: <https://kaempfen.com/> (accessed on 15 November 2022).
102. SwissINSO—Stettbachstrasse. Available online: <https://www.swissinsoc.com/stettbachstrasse> (accessed on 25 October 2022).
103. Topic of the Week: BIPV (Part 3): A Solar Module as White as a Wall-Pv Europe—Solar Technology and Applications. Available online: <https://www.pveurope.eu/Products/Solar-Generator/Solar-modules/Topic-of-the-Week-BIPV-Part-3-A-solar-module-as-white-as-a-wall> (accessed on 27 April 2020).
104. BIPV Technology—Mitrex. Available online: <https://www.mitrex.com/technology/> (accessed on 24 September 2022).
105. Mitrex—Solar Façade. Available online: <https://www.mitrex.com/solar-facade/> (accessed on 20 October 2022).
106. Mitrex Green Building Projects. Available online: <https://www.mitrex.com/projects/> (accessed on 24 September 2022).
107. Folkerts, W. SEAC SUPSI Report 2015 BIPV Product Overview for Solar Facades and Roofs. Available online: <https://repository.tno.nl/islandora/object/uuid%3A001d6c37-b26c-40e5-af19-8f39cc9989a5> (accessed on 20 October 2022).
108. SwissINSO—Technology. Available online: <https://www.swissinsoc.com/technology> (accessed on 15 November 2022).
109. SwissINSO—EPFL. Available online: <https://www.swissinsoc.com/epfl> (accessed on 20 October 2022).
110. Red River College Innovation Center. Available online: <https://solarlab.dk/references-and-inspiration/rrc/> (accessed on 20 October 2022).
111. HOME | Somiral Energy. Available online: <https://www.somiral.com/> (accessed on 15 November 2022).
112. Mertin, S.; Hody-Le Caër, V.; Joly, M.; Scartezzini, J.-L.; Schüler, A. Coloured Coatings for Glazing of Active Solar Thermal Façades By Reactive Magnetron Sputtering. *Proc. CIBSAT 2011 CleanTech Sustain. Build.* **2011**, *1*, 31–36.
113. Available online: <https://www.antec-solar.de/kontakt/so-finden-sie-uns/> (accessed on 24 September 2022).
114. SwissINSO—Leysin School Gymnasium. Available online: <https://www.swissinsoc.com/leysin> (accessed on 20 October 2022).
115. Doma Vkw. Available online: <https://www.domavkw.at/> (accessed on 15 November 2022).
116. SwissINSO—DOMA. Available online: <https://www.swissinsoc.com/doma> (accessed on 25 October 2022).
117. Ahn, H.-S.; Gasonoo, A.; Lim, S.-M.; Lee, J.-H.; Choi, Y. Fabrication of Color Glass with High Light Transmittance by Pearlescent Pigments and Optical Adhesive. *Materials* **2022**, *15*, 2627. [CrossRef] [PubMed]
118. Gasonoo, A.; Ahn, H.-S.; Lim, S.; Lee, J.-H.; Choi, Y. Color Glass by Layered Nitride Films for Building Integrated Photovoltaic (BIPV) System. *Crystals* **2021**, *11*, 281. [CrossRef]
119. Coloured Solar Panels Silk®Pro Colour | Futurasun. Available online: <https://www.futurasun.com/en/products/photovoltaic-monocrystalline-coloured-panels/> (accessed on 13 September 2022).
120. Red BIPV Solar Module from Italy—Pv Magazine International. Available online: <https://www.pv-magazine.com/2021/09/30/red-bipv-solar-module-from-italy/> (accessed on 17 August 2022).
121. FuturaSun Launches SILK®Pro Coloured BIPV Panels. Available online: <https://solarbusinesshub.com/2021/10/08/futurasun-launches-silk-pro-coloured-bipv-panels/> (accessed on 17 August 2022).
122. Yu, L.-M.; Man, J.-X.; Chen, T.; Luo, D.; Wang, J.; Yang, H.; Zhao, Y.-B.; Wang, H.; Yang, Y.; Lu, Z.-H. Colorful Conducting Polymers for Vivid Solar Panels. *Nano Energy* **2021**, *85*, 105937. [CrossRef]

123. Constructing Buildings with Customizable Size Pv Modules Integrated in the Opaque Part of the Building Skin (Construct-Pv). Fp7-Energy-2011-2|Antonis Peppas|Research Project. Available online: <https://www.researchgate.net/project/Constructing-buildings-with-customizable-size-PV-modules-integrated-in-the-opaque-part-of-the-building-skin-Construct-PV-FP7-ENERGY-2011-2> (accessed on 1 May 2020).
124. Bousbaa, C.; Iferroudjene, N.; Bouzid, S.; Madjoubi, M.; Bouaouadja, N. Effects of Duration of Sand Blasting on the Properties of Window Glass. *Glass Technol.* **1998**, *39*, 24–26.
125. Bouaouadja, N.; Bouzid, S.; Hamidouche, M.; Bousbaa, C.; Madjoubi, M. Effects of Sandblasting on the Efficiencies of Solar Panels. *Appl. Energy* **2000**, *65*, 99–105. [[CrossRef](#)]
126. Hoffman, B. The Impact of Digital Printing with Ceramic Inks on Decorative and Functional Glass. *Glass Int.* **2013**, *36*, 38–40.
127. Bamford, C.R. Optical Properties of Flat Glass. *J. Non-Cryst. Solids* **1982**, *47*, 1–20. [[CrossRef](#)]
128. Ceglia, A.; Nuyts, G.; Meulebroeck, W.; Cagno, S.; Silvestri, A.; Zoleo, A.; Nys, K.; Janssens, K.; Thienpont, H.; Terryn, H. Iron Speciation in Soda-Lime-Silica Glass: A Comparison of XANES and UV-Vis-NIR Spectroscopy. *J. Anal. At. Spectrom.* **2015**, *30*, 1552–1561. [[CrossRef](#)]
129. Flygt, E.; Falk, T. *An Introduction to Glass: Craft, Technology and Art*; Glaflo: Vaxjo, Sweden, 2011; ISBN 9789170032950.
130. Karlsson, S.; Bäck, L.G.; Kidkhunthod, P.; Lundstedt, K.; Wondraczek, L. Effect of TiO₂ on Optical Properties of Glasses in the Soda-Lime-Silicate System. *Opt. Mater. Express* **2016**, *6*, 1198. [[CrossRef](#)]
131. Raszewski, F.C.; Murphy, K.A.; Shelby, J.E. Multilayer Colloid Formation in Soda Lime Silica Glass. *J. Non-Cryst. Solids* **2006**, *352*, 528–533. [[CrossRef](#)]
132. Bamford, C.; Cr, B. A Theoretical Analysis of the Optical Properties of Spectra Float Glass. *Phys. Chem. Glasses* **1976**, *17*, 209–213.
133. Slooff, L.H.; van Roosmalen, J.A.M.; Okel, L.A.G.; de Vries, T.; Minderhoud, T.; Gijzen, G.; Sepers, T.; Versluis, A.; Frumau, F.; Rietbergen, M.; et al. An Architectural Approach for Improving Aesthetics of PV. In Proceedings of the 33rd European Photovoltaic Solar Energy Conference and Exhibition, Amsterdam, The Netherlands, 25–29 September 2016; pp. 1–4. [[CrossRef](#)]
134. Tzikas, C.; Valckenborg, R.M.E.; Dörenkämper, M.; van den Donker, M.; Lozano, D.D.; Bognár, Á.; Loonen, R.; Hensen, J.; Folkerts, W. Outdoor Characterization of Colored and Textured Prototype PV Facade Elements. In Proceedings of the 35th European Photovoltaic Solar Energy Conference and Exhibition, Brussels, Belgium, 24–27 September 2018.
135. Solar Facades of Any Shape and Color-Industry News-Glass in China Com. Available online: <http://www.glassinchina.com/news/detail51036.html> (accessed on 11 November 2022).
136. Examples of AGC Planibel Coloured: Grey, Dark-Grey, Privablue, Dark. | Download Scientific Diagram. Available online: https://www.researchgate.net/figure/Examples-of-AGC-Planibel-Coloured-Grey-dark-grey-privablue-dark-blue-azur-green-and_fig27_337111523 (accessed on 29 September 2020).
137. Siriprom, W.; Teanchai, K.; Chamlek, O.; Sukphirom, S.; Ruangtaweep, Y.; Srisittipokakun, N.; Kaewkhao, J. Effects of Ni²⁺ Ions on Soda Lime Silicate Glasses. *Adv. Mater. Res.* **2013**, *770*, 307–310. [[CrossRef](#)]
138. Basher, M.K.; Nur-E-alam, M.; Rahman, M.M.; Hinckley, S.; Alameh, K. Design, Development, and Characterization of Highly Efficient Colored Photovoltaic Module for Sustainable Buildings Applications. *Sustainability* **2022**, *14*, 4278. [[CrossRef](#)]
139. Person Walking Between Green Forest Trees Free Stock Photo. Available online: <https://www.pexels.com/photo/person-walking-between-green-forest-trees-15286/> (accessed on 21 November 2022).

Disclaimer/Publisher’s Note: The statements, opinions and data contained in all publications are solely those of the individual author(s) and contributor(s) and not of MDPI and/or the editor(s). MDPI and/or the editor(s) disclaim responsibility for any injury to people or property resulting from any ideas, methods, instructions or products referred to in the content.

Article

Data-Driven Based Prediction of the Energy Consumption of Residential Buildings in Oshawa

Yaolin Lin ^{1,*}, Jingye Liu ¹, Kamiel Gabriel ^{2,*}, Wei Yang ³ and Chun-Qing Li ⁴

¹ School of Environment and Architecture, University of Shanghai for Science and Technology, Shanghai 200093, China

² Faculty of Engineering and Applied Science, Ontario Tech University, Oshawa, ON L1G 0C5, Canada

³ Faculty of Architecture, Building and Planning, The University of Melbourne, Melbourne 3010, Australia

⁴ School of Engineering, RMIT University, Melbourne 3000, Australia

* Correspondence: ylin@usst.edu.cn (Y.L.); kamiel.gabriel@ontariotechu.ca (K.G.)

Abstract: Buildings consume about 40% of the global energy. Building energy consumption is affected by multiple factors, including building physical properties, performance of the mechanical system, and occupants' activities. The prediction of building energy consumption is very complicated in actual practice. Accurate and fast prediction of the building energy consumption is very important in building design optimization and sustainable energy development. This paper evaluates 24 energy consumption models for 83 houses in Oshawa, Canada. The energy consumption, social and demographic information of the occupants, and the physical properties of the houses were collected through smart metering, a phone survey, and an energy audit. A total of 63 variables were determined, and based on the variable importance, three groups with different numbers of variables were selected, i.e., 26, 12, and 6 for electricity consumption; and 26, 13, and 6 for gas consumption. A total of eight data-driven algorithms, namely Multiple Linear Regression (MLR), Stepwise Regression (SR), Support Vector Machine (SVM), Backpropagation Neural Network (BPNN), Radial Basis Function Neural Network (RBFN), Classification and Regression Tree (CART), Chi-Square Automatic Interaction Detector (CHAID), and Exhaustive CHAID (ECHAID), were used to develop energy prediction models. The results show that the BPNN model has the best accuracies in predicting both the annual electricity consumption and gas consumption, with mean absolute percentage errors (MAPEs) of 0.94% and 0.94% for training and validation data for electricity consumption, and 2.63% and 0.16% for gas consumption, respectively.

Keywords: data-driven; electricity consumption; prediction model; gas consumption

Citation: Lin, Y.; Liu, J.; Gabriel, K.; Yang, W.; Li, C.-Q. Data-Driven Based Prediction of the Energy Consumption of Residential Buildings in Oshawa. *Buildings* **2022**, *12*, 2039. <https://doi.org/10.3390/buildings12112039>

Academic Editor: Francesco Asdrubali

Received: 13 October 2022

Accepted: 18 November 2022

Published: 21 November 2022

Publisher's Note: MDPI stays neutral with regard to jurisdictional claims in published maps and institutional affiliations.



Copyright: © 2022 by the authors. Licensee MDPI, Basel, Switzerland. This article is an open access article distributed under the terms and conditions of the Creative Commons Attribution (CC BY) license (<https://creativecommons.org/licenses/by/4.0/>).

1. Introduction

Globally, buildings consume about 30% of end energy usage and over 55% of electricity [1]. Building energy consumption is increasing with the growth of the global population. It is affected by a large number of physical and sociological factors. Accurate energy prediction can help quantify and compare the energy-saving potentials of different conservation measures, as well as assist design optimization [2,3].

There are two approaches to predict building energy consumption. One is based on a physical model, and the other is data driven. The physical modeling approach is also called the forward modeling approach. The forward modeling approach is usually conducted with commercial software, e.g., DOE-2, DesignBuilder, etc., with given inputs to estimate the building energy consumption through simulation. The differences of the outcomes among different software are typically small with the same/identical input values of the variables [4]. Fumo et al. [5] used EnergyPlus Benchmark Models to generate the determining factors based on the monthly electrical and fuel utility bills to estimate the hourly electricity consumption and fuel energy consumption for a hypothetical building in Atlanta, GA, and in Meridian, MS, with estimated errors within 10%. Amiri et al. [6]

developed a Stepwise Regression (SR) model, based on the simulation results from DOE-2, to predict the building energy consumption at the early design phase. The physical modeling approach requires detailed information about the building, mechanical systems, and occupants' activities to develop a mathematical model to estimate the building energy consumption, which might not be readily available. Meanwhile, the physical model could not take into account the sociological factors that potentially affect the energy-usage patterns of the occupants.

The data-driven approach uses data analysis through known data sets to overcome the limitations of physical models to predict the energy consumption. Typically, an energy-usage database is created through the simulation of building samples or data collection. Examples of data-driven approaches include Multiple Linear Regression (MLR), Classification and Regression Tree (CART), artificial neural network (ANN), etc.

MLR models have been developed to replace the outcomes from building simulation software. Chen et al. [7] developed a physical-based MLR model to predict the building cooling load based on the data set created through building energy simulation using EnergyPlus. It was demonstrated to have a stronger generalization ability than the BP-ANN and MLR models. By using this method, the space cooling load can be predicted based on the total cooling load. Ciulla et al. [8] used TRNSYS to run 1560 simulations of a non-residential building with different configurations across Italy to create an energy database and developed MLR models to estimate the building energy consumption with determination coefficients (R^2) higher than 0.9 and mean absolute error (MAE) lower than 10 kWh/m² year.

Stepwise Regression (SR) can help overcome the multicollinearity problem that could exist in the multiple regression problem and reduce the number of input variables. Tso and Yau [9] developed the SR analysis of the household electricity consumption in winter and summer in Hongkong. Zhao and Lin [10] proposed SR models to predict the energy consumption and visual discomfort of a passive house, compared with the simulated outcomes from DesignBuilder. R-squares of 0.9808 and 0.8487 were found, respectively, which demonstrate the potential of SR in predicting the building energy consumption.

The Support Vector Machine (SVM) helps to solve high-dimensional difficulty and local minima problems. Ma et al. [11] applied support vector regression (SVR) models to estimate the provincial building energy consumption in four provinces in Southern China. Seven parameters, including yearly mean outdoor dry-bulb air temperature, relative humidity, total solar radiation, urbanization ratio, gross domestic product, household consumption level, and total construction area of were used as inputs. Good agreements were found between the predicted and actual energy consumptions, with the mean square errors (MSEs) and correlation coefficients found to be less than 0.001 and greater than 0.99, respectively. Li et al. [12] developed a SVM model to estimate the office hourly cooling load with outdoor air temperature, relative humidity, and solar radiation intensity as the input variables. The SVM model outperforms the Backpropagation Neural Network (BPNN) model in terms of accuracy and generalization. Paudel et al. [13] developed a SVM model for a low-energy residential building in France, using a small representative day data set. The outdoor air temperature, horizontal solar radiation, solar gain transmitted through windows, solar energy absorbed by walls, occupancy profile, and time moving average of outdoor air temperature were used as input variables for the model. It was found that the model achieves higher prediction accuracy ($R^2 = 0.98$; RMSE = 3.4), compared to the one developed with all the data sets ($R^2 = 0.93$; RMSE = 7.1).

BPNN is the most widely used neural network. Ahmad et al. [14] developed feed-forward BPNN and random forest (RF) models to estimate the energy demand of the HVAC system in a commercial building in Madrid, Spain. The input variables include outdoor air temperature, dew point temperature, relative humidity, wind speed, duration time, number of guests on the day, and number of rooms booked. The results show that the RMSEs of the prediction results of the BPNN and RF models were 4.97 and 6.10, respectively. The BPNN model achieves a slightly better performance than the RF model in terms of accuracy.

Radial Basis Function Neural Networks (RBFNs) have been used to predict the energy consumption of university buildings. Han et al. [15] proposed an RBFN model to evaluate the energy performance of the buildings, using the University of California Irvine data sets. The predicted values agree well with the simulation outcome from Ecotech. Zhao et al. [16] developed an RBFN model to predict the energy consumption of colleague buildings in Fujian Province in China, with a maximum error of 13.3%.

Classification and Regression Tree (CART) is also one of the machine learning approaches favored by the researchers. Zekić-Sušac et al. [17] developed a CART model to predict the energy cost of public buildings in the Republic of Croatia. Capozzoli et al. [18] developed a CART model to predict the heating energy consumption in schools with an R-square of 0.86.

The Chi-Square Automatic Interaction Detector (CHAID) can be used to generate a multi-branched decision tree and determine the branch variables' values based on statistical significance. Yang and Wu [19] applied CHAID to find the energy-saving strategies for central air-conditioning system operation in Shenzhen, China. Kusiak et al. [20] developed a CHAID model to predict the building steam load with a mean absolute error (MAE) of 405 for training and 578 for testing.

Exhaustive CHAID (ECHAID) is another decision tree algorithm that ensures the same degree of freedom for all the inputs. Kusiak et al. [20] compared the outcomes from ECHAID model with the CHAID model in predicting the building steam load. The ECHAID achieved a mean absolute error (MAE) of 398 for training and 570 for testing. Yan et al. [21] developed an ECHAID model to predict the system coefficient of performance (COP) of a ground-source heat pump with an MAE of 0.098 for training and 0.105 for testing.

Researchers have also investigated other data-driven approaches; for example, Li et al. [22] developed a hybrid teaching–learning artificial neural network model (TL-ANN) to predict the hourly electrical energy consumption for two educational buildings located in USA and China, using weather conditions, calendar date, occupancy pattern, and historical energy usage data. Moayedi [23] compared the performances of three cooling load prediction models for a residential building. The elephant herding optimization (EHO), ant colony optimization (ACO), and Harris Hawks optimization (HHO), were combined with a multilayer perceptron neural network (MLP) model. The relative compactness of the building, surface area, wall area, roof area, overall height, orientation, glazing area, and glazing area distribution are used as inputs for the model. The results show that the EHO–MLP has the highest prediction accuracy, followed by HHO–MLP and ACO–MLP. Aruta et al. [24] developed an artificial neural networks (ANNs) model, using NARX (nonlinear autoregressive model with exogenous inputs) networks for training based on simulated heating load of a building in Rome from EnergyPlus. The outdoor air temperature and solar radiation were used as inputs and demonstrated satisfactory prediction performance. Ndiaye and Gabriel [25] used the latent root regression technique to reduce the number of input variables from 59 to 9, while achieving an R-square of 0.79 in predicting the housing unit electricity consumption in Oshawa. Still, they performed studies only on a few data-driven algorithms.

From the literature survey, it can be found that very few studies were conducted to predict the yearly residential building energy consumption based on actual energy consumption data. Many studies focus on monthly [26], daily [27–29], or hourly [13,27–30] energy consumption, based on the simulation outcomes from commercial software [26,31–35]. Short-term energy predictions are easily affected by seasonal variation and the outcomes from the simulation often deviate from actual energy consumption. In addition, the effects of occupants' behaviors on the energy usage are often neglected in the prediction model, and most of the parameters focus on weather data [26–29,31] or design parameters of the building envelope [26,31,33–35], thus causing deviations in energy consumption predictions for different households; social and demographic information are often neglected, as well. Moreover, many of the studies used fixed number of input variables and training/validation ratio, without seeking for the least number of inputs needed and

the models with the best performance. Therefore, it is important to develop a residential building energy prediction model based on the collected data from actual annual energy consumption, taking into account the social and demographic information and evaluate the impact of the number of input variables, as well as the training/validation ratio for the performance of the prediction model.

This paper attempts to develop yearly energy consumption prediction models for residential buildings in Oshawa. Data related to electricity consumption, gas consumption, physical information of the buildings, and social and demographic information of the residents were collected through smart metering, a phone survey, and energy auditing of a total of 83 households. A total of eight data-driven algorithms, namely Multiple Linear Regression (MLR), Stepwise Regression (SR), Support Vector Machine (SVM), Backpropagation Neural Network (BPNN), Radial Basis Function Neural Network (RBFN), Classification and Regression Tree (CART), Chi-Square Automatic Interaction Detector (CHAID), and Exhaustive CHAID (ECHAID), were used to develop energy prediction models to select the most suitable models for electricity consumption and gas consumption predictions. Different numbers of input variables and training/validation ratios were employed to find the models with the best prediction performance with the least number of inputs. The outcomes from this paper can provide references for residential-building energy prediction.

2. Method

The actual electricity and gas consumption data, physical properties, mechanical system information, and consumer information of 227 houses in Oshawa—which has a humid continental climate with large seasonal temperature variations, with warm summers and cold winters—were collected and analyzed. The energy consumption is for a full year. Firstly, smart meters were installed on 227 houses in Oshawa to obtain the electricity readings, and a phone survey on the social and demographic information of the occupants, as well as information on the electrical appliances, was conducted on the houses with installed smart meters. Energy audits were conducted according to the willingness of the house owner/renter. A total of 65 input and output parameters were identified after an analysis of the gathered information. During the data preprocessing, it was found that, due to the reluctance of some house owners/renters to disclose certain information, or that they were unclear about certain information, there were 144 samples with missing data for annual electricity consumption and 154 samples with missing data for gas consumption. Therefore, the predictions of electricity consumption and gas consumption are based on 83 and 73 residential buildings, respectively. Then three groups of input parameters are selected based on variable importance (VI) through statistical analysis. Finally, eight data-driven modeling approaches were used to develop electricity and gas consumption prediction models based on different groups of input parameters. The performances of different models were evaluated, and the best prediction models for electricity and gas consumption were identified. The IBM SPSS Statistics 26.0 and Clementine 12.0 were used to apply the algorithm [36]. A flowchart of the research strategy is presented in Figure 1.

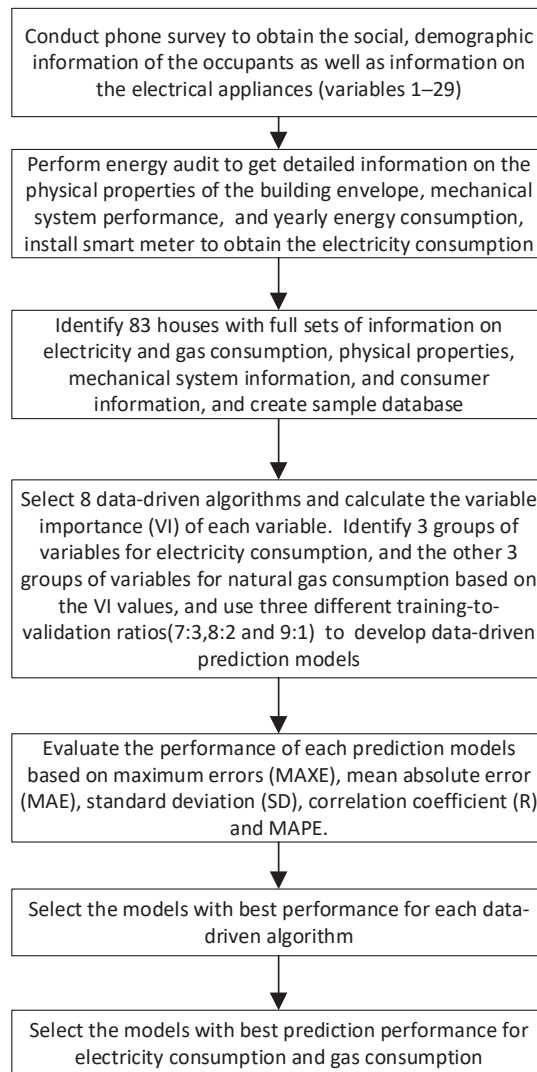


Figure 1. Flowchart of the research strategy.

2.1. Independent and Dependent Variables

Table 1 lists the variable names and their value ranges, where the independent variables 1–29 and 30–63 and dependent variables 64–65 were collected through a phone survey, energy audit, and smart metering. The range of values is formed based on the outcomes from the collected data.

Table 1. Variable names and value ranges.

No.	Information of the Variable	Variable Name	Collecting Method	Value Range
1	Number of halogen bulbs used outdoors	Halogen	Phone survey	0–5
2	Number of compact fluorescent lamp (CFL) bulbs used outdoors	CFL	Phone survey	0–4
3	Number of fluorescent bulbs used outdoors	Fluor	Phone survey	0–4
4	Number of incandescent lamps used outdoors	Incand	Phone survey	0–5
5	Awareness of the importance of reducing energy consumption	RedEnerg	Phone survey	1–5
6	Awareness of the importance of spending less on energy bill	SpenLess	Phone survey	1–5
7	Perceptions of government involvement in energy conservation	GvInvolv	Phone survey	1–5
8	Interested in learning more about ways to save energy indoors	LearnMor	Phone survey	1–5
9	Interest in using computer software to control indoor energy consumption	CompSoft	Phone survey	1–5
10	Number of occupants	NbOccup	Phone survey	1–6
11	Number of residents working full-time	FullTime	Phone survey	0–5
12	Number of residents working part-time	ParTime	Phone survey	0–1
13	Number of residents working in shifts	SiftWork	Phone survey	0–1
14	Number of people working or staying at home	FromHome	Phone survey	0–3
15	Housing situation	HomState	Phone survey	Owned (1), Rent (2)
16	Lights turned on when empty for a short period of time	LOnEmpty	Phone survey	1–3 Occurs more and more frequently
17	The moment when the outdoor lights in front of the house are turned on	TOnOutLt	Phone survey	1–3 Occurs more and more frequently
18	Feeling safe between neighbors	Safety	Phone survey	1–5 Increased sense of security
19	Worry about crime	Crime	Phone survey	1–5 Increased sense of security
20	Age of the homeowner	AgeRange	Phone survey	18–24 (1), 25–35 (2), 36–45 (3), 46–55 (4), 56–65 (5), over 65 (6)
21	Number of energy-saving electrical appliances purchased in the past 5 years	NbNewApp	Phone survey	0–7
22	Fuel type of the oven	OvenFuel	Phone survey	Natural gas (1), electricity (2)
23	Fuel type of the dryer	DryerFl	Phone survey	Natural gas (1), electricity (2)
24	Fuel type of the pool heaters	PHeatrFl	Phone survey	Unused (0), Solar (1), Natural Gas (2), Electricity (3)
25	Upgrade or renovation of the house in the past five to ten years	RecUpgd	Phone survey	Renovated (1), Not renovated (2)
26	Amount willing to spend on energy-efficient equipment (CAD)	WlgSpend	Phone survey	<\$100 (1), \$100–250 (2), \$250–500 (3), >\$1000 (4)
27	Highest level of education	LevelEdu	Phone survey	High School (1), College (2), University (3)
28	Gross household income before taxes (CAD/year)	HsIncome	Phone survey	<\$20,000 (1), \$20,000–\$39,999 (2), \$40,000–\$59,999 (3), \$60,000–\$79,999 (4), \$80,000–\$99,999 (5), >\$100,000 (6)
29	Born in Canada	BornCan	Phone survey	Yes (1), No (2)
30	Fuel type for heating system	HeatType	Energy audit	Electricity (1), Natural gas (2), Oil (3)

Table 1. Cont.

No.	Information of the Variable	Variable Name	Collecting Method	Value Range
31	House type	HsType	Energy audit	Single detached (1), Row end (2)
32	Number of floors	NbStoris	Energy audit	1–2
33	Heating system type	HSysType	Energy audit	Baseboard (1), medium-efficiency furnace (2), heat pump (3), high-efficiency boiler (4)
34	Fuel type for domestic water heaters	DHWFuel	Energy audit	Natural gas (1), Electricity (2)
35	Types of domestic hot water heater	DHWType	Energy audit	Condensing unit (1), Induced draft fan boiler (2), conventional tank heater (3)
36	Existing air-conditioning system	ACSyst	Energy audit	No (0), Yes (1)
37	Air-conditioning system type	ACType	Energy audit	central system (1), heat pump (2), Not applicable (3)
38	Year built	ConstYr	Energy audit	Pre 76 (1), 1976–1987 (2), 1988–2002 (3)
39	Heating system efficiency	HSysEffi	Energy audit	76–100%
40	Service length of the heating system (years)	HSysAge	Energy audit	0–35
41	Service length of the air-conditioning system (years)	ACAge	Energy audit	0–33
42	thermal resistance of the window ($m^2 \cdot K/W$)	TherReWind	Energy audit	0.99–2.64
43	thermal resistance of the external wall ($m^2 \cdot K/W$)	TherReWal	Energy audit	0.64–3.12
44	thermal resistance of the ceiling ($m^2 \cdot K/W$)	TherReCei	Energy audit	0.53–7.05
45	Area of the ceiling (m^2)	CeilArea	Energy audit	45.2–227.4
46	Area of the external wall (m^2)	TWlArea	Energy audit	52.8–317.6
47	Area of the window (m^2)	TWdArea	Energy audit	6.7–49.2
48	U-value of foundation wall ($W/(m^2 \cdot K)$)	FwUvalue	Energy audit	0.23–3.17
49	U-value of the basement ceiling ($W/(m^2 \cdot K)$)	BhUvalue	Energy audit	0.48–3.87
50	Air change rate per hour at 50 Pa	NbACH	Energy audit	1.49–14.88
51	Residential floor area (m^2)	ReFlArea	Energy audit	49–166
52	Building orientation	OriBuild	Energy audit	1 East 2 West 3 South 4 North 5 Northeast 6 Southeast 7 Northwest 8 Southwest
53	Building width (m)	WidBuild	Energy audit	5.18–16.46
54	Building depth (m)	DepBuild	Energy audit	7.01–16.46
55	Building perimeter (m)	PerBuild	Energy audit	28.65–52.43
56	Window type	TypWind	Energy audit	Single-layer (1), Double-layer (2), Double-layer Low-E (3)
57	Window frame type	TypWindFra	Energy audit	Wood (1), Vinyl (2), Metal (3)
58	Door type	TypDoor	Energy audit	Wood (1), Steel (2)
59	Door area (m^2)	AreDoor	Energy audit	0.94–6.8
60	Cooling system COP	COPRefSys	Energy audit	2–10
61	Ventilation system exhaust volume (m^3/h)	ExVolVenti	Energy audit	1–15
62	Floor area (m^2)	AreFloor	Energy audit	97.8–374.6
63	Total basement wall area (m^2)	AreBaseWal	Energy audit	43.4–117.5
64	Annual electricity consumption (kWh)	AnnPowConsu	Energy audit+smart metering	8944–50,415
65	Annual natural gas consumption (m^3)	AnnNaGEnConsu	Energy audit	0–5937

2.2. Prediction Model Development

The MLR, SR, SVM, BPNN, RBFN, CART, CHAID, and ECHAID were employed to develop electricity consumption and gas consumption prediction models.

2.2.1. Multiple Linear Regression

MLR has been widely used in building energy consumption prediction and can be used in the early design stage to improve the building performance [37] and hourly cooling load prediction [7]. In this paper, MLR is used to develop the relationship between the independent variables (variables 1–63), and dependent variables (variables 64 and 65). The MLR model can be presented as follows:

$$y = \beta_0 + \beta_1 x_1 + \beta_2 x_2 + \cdots + \beta_n x_p + \varepsilon \quad (1)$$

where β_0 denotes the regression constant; $\beta_1, \beta_2,$ and β_p denote the regression coefficients; x_i refers to the input variables; ε is the random error; and p denotes the number of independent variables involved in the regression.

The regression coefficients are determined based on the least square method, which minimizes the residual sum of squares (RSS). The RSS is calculated by the following equation:

$$\text{RSS} = \sum_{i=1}^n (y_i - \beta_0 - \beta_1 x_1 - \beta_2 x_2 - \cdots - \beta_p x_p)^2 \quad (2)$$

where n is the number of samples.

2.2.2. Stepwise Regression

The SR uses a step-by-step iterative approach to develop a regression model by selecting only the important independent variables. It is also widely used in building simulation [38]. In this paper, 63 independent variables were introduced into the regression model one-by-one and sorted according to their importance. Each dependent variable goes through an F-test and T-test and remains in the model if it is statistically significant.

2.2.3. Support Vector Machine

The SVM introduces the principle of structural risk minimization, which effectively solves the high-dimensional difficulty and local minima problem. Gao [39] developed an SVM model to predict building energy consumption based on historical data with good prediction performance. By studying the output/input variables relationship, the SVM predicts the output variable values of new samples with the same distribution as the training sample set. A loss function is introduced to correct the distance to the decision boundary, so as to determine the regression function. Thus, a prediction model is developed to predict the outputs for new samples with the same distribution [40].

2.2.4. Backpropagation Neural Network

The BPNN is the most widely used neural network. As a multilayer feed-forward neural network, it is trained according to an error backpropagation algorithm [41]. BPNN features arbitrarily complex pattern classification ability and demonstrates excellent multi-dimensional function mapping ability. It includes an input, a hidden, and an output layer. The least square error of the network is obtained by using the gradient descent method to for minimization.

2.2.5. Radial Basis Function Neural Network

RBFN utilizes radial basis functions (RBFs) as activation functions. The RBF network consists only of a single hidden layer that has its own way of computing the output. The input layer receives the input data and feeds them into the special hidden layer. The computations in the hidden layers are based on comparisons with prototype vectors from the training set. Each neuron computes the similarity between the input vector and its

prototype vector. RBFN has been proven to have a good prediction performance for the building cooling load [13].

2.2.6. CART

The CART is a classification algorithm that builds a decision tree based on Gini's impurity index [42]. It applies the binary segmentation method to recursively construct the binary decision tree process and uses the square error minimization criterion for feature selection for the regression tree. CART has been proven to achieve good performance in heating energy prediction [18].

2.2.7. CHAID

CHAID is based on adjusted significance testing, which was proposed by Kass et al. [43]. In this method, multi-branch decision trees can be generated. First, the F-test is carried out, and variables statistically similar to the target variable are combined; then p -values for the remaining variables are calculated, and the variable with the best predictor (lowest p -value) is selected as the first variable in the decision tree branches. The process repeats until the tree is fully grown. It has been successfully used to predict the steam load [20].

2.2.8. Exhaustive CHAID

As an improved algorithm based on CHAID, ECHAID is different from CHAID on the merging step [44]. The latter stops when all remaining categories are found to be statistically different. The former continues grouping, leaving only two super categories. In this way, all input variables are ensured to have the same degree of freedom. It has been successfully employed to predict the performance of heat pumps [21].

2.3. Choice of Input Variables

In order to eliminate the variables that are unimportant to the prediction of building energy consumption, the variable importance (VI) is employed to assist in the selection of the input variables to develop prediction models; detailed information in the calculation can be found in Ref. [45]. At the same time, the ratios of samples for training and validation are set as 7:3, 8:2, and 9:1, respectively. The data are split randomly.

2.4. Prediction Model Evaluation

The prediction model performance is evaluated through maximum errors (MAXEs), mean absolute error (MAE), standard deviation (SD), correlation coefficient (R), and MAPE. The MAE, SD, and R can be calculated as shown below:

$$\text{MAE} = \frac{1}{n} \sum_{i=1}^n (|\hat{y}_i - y_i|) \quad (3)$$

$$\text{SD} = \sqrt{\frac{\sum_{i=1}^n (|\hat{y}_i - y_i| - \text{MAE})^2}{n}} \quad (4)$$

$$\text{R} = \sqrt{1 - \frac{\sum_{i=1}^n (\hat{y}_i - y_i)^2}{\sum_{i=1}^n (\hat{y}_i - \bar{y})^2}} \quad (5)$$

$$\text{MAPE} = \frac{1}{n} \sum_{i=1}^n (|\hat{y}_i - y_i|) \times 100\% \quad (6)$$

where \hat{y}_i denotes the prediction value, y_i denotes the targeted value, \bar{y} denotes the average value of the targeted values, and n is the number of samples.

Evaluation on the validation of the performance of the prediction model based on MAXE, MAE, SD, R, and MAPE under different training-to-validation ratios (7:3, 8:2, and 9:1) to ensure the best performance and the least amount of data for training.

3. Results and Discussion

3.1. Results of Variable Selection

Depending on the variable importance (VI) of each variable, totals of 26, 12, and 6 variables were selected to develop the prediction models for electricity consumption (Table 2), and totals of 26, 13, and 6 variables were selected to develop the prediction models for natural gas consumption (Table 3).

Table 2. Variable selected for predicting electricity consumption.

Number of Variables	Variable Set
26 (importance of variable (IV) \geq 0.01)	HeatType, DHWFuel, AreFloor, HSEfficiency, HSAge, HSType, Halogen, NbOccup, TherReCeiling, FromHome, ACSyst, OriBuild, LONEmpty, TherReWall, SpenLess, Incand, NbACH, PHeatFl, AgeRange, LearnMor, ExVolVenti, FullTime, TWdArea, ConstYr, COPRefSys, CFL
12 (IV \geq 0.016)	HeatType, DHWFuel, AreFloor, HSEfficiency, HSAge, HSType, Halogen, NbOccup, TherReCeiling, FromHome, ACSyst, OriBuild
6 (IV \geq 0.05)	HeatType, DHWFuel, AreFloor, HSEfficiency, HSAge, HSType

Table 3. Variable selected for predicting natural gas consumption.

Number of Variables	Variable Set
26 (IV \geq 0.015)	HeatType, NbACH, HSEfficiency, TWIArea, Fluor, DHWFuel, Halogen, TherReWind, TherReWall, PerBuild, RedEnergy, NbOccup, PHeatFl, SpenLess, TypWindFra, CeilArea, OvenFuel, BhUvalue, DHWType, ReFlArea, TherReCeiling, WidBuild, HomState, FwUvalue, AreBaseWal, AreFloor
13 (IV \geq 0.022)	HeatType, NbACH, HSEfficiency, TWIArea, Fluor, DHWFuel, Halogen, TherReWind, TherReWall, PerBuild, RedEnergy, NbOccup, PHeatFl
6 (IV \geq 0.032)	HeatType, NbACH, HSEfficiency, TWIArea, Fluor, DHWFuel

3.2. Performance of Electricity Consumption Prediction Model

Analyses of the results of the prediction models for electricity consumption are presented in Tables A1–A8 in Appendix A. The regressions between predicted and simulated electricity consumption for the best models of each data-driven approach are presented in Figure 2a–h.

The outcomes of the MLR models on the prediction of electricity consumption are listed in Appendix A Table A1. It can be found that when the number of variables is 6 and the ratio of training sample vs. validation samples is 9:1, the MLR model has the best performance, with MAPEs of 15.05% for training and 11.71% for validation, respectively. Figure 2a presents the regression between predicted and simulated electricity consumption for the best MLR model. The model predicts pretty well when the electricity consumption is less than 35,000 kWh (93% of all the samples), and it underpredicts the electricity consumption when it exceeds 35,000 kWh.

The outcomes of the SR models on the prediction of electricity consumption are listed in Appendix A Table A2; they are similar to those of the MLR models. When the number of variables is 6 and the ratio of training sample vs. validation samples is 9:1, the SR model has the best performance with MAPEs of 14.79% for training and 14.18% for validation, respectively. Figure 2b presents the regression between predicted and simulated electricity consumption for the best SR model. The model also predicts pretty well when the electricity consumption is less than 35,000 kWh, and it underpredicts the electricity consumption when it exceeds 35,000 kWh.

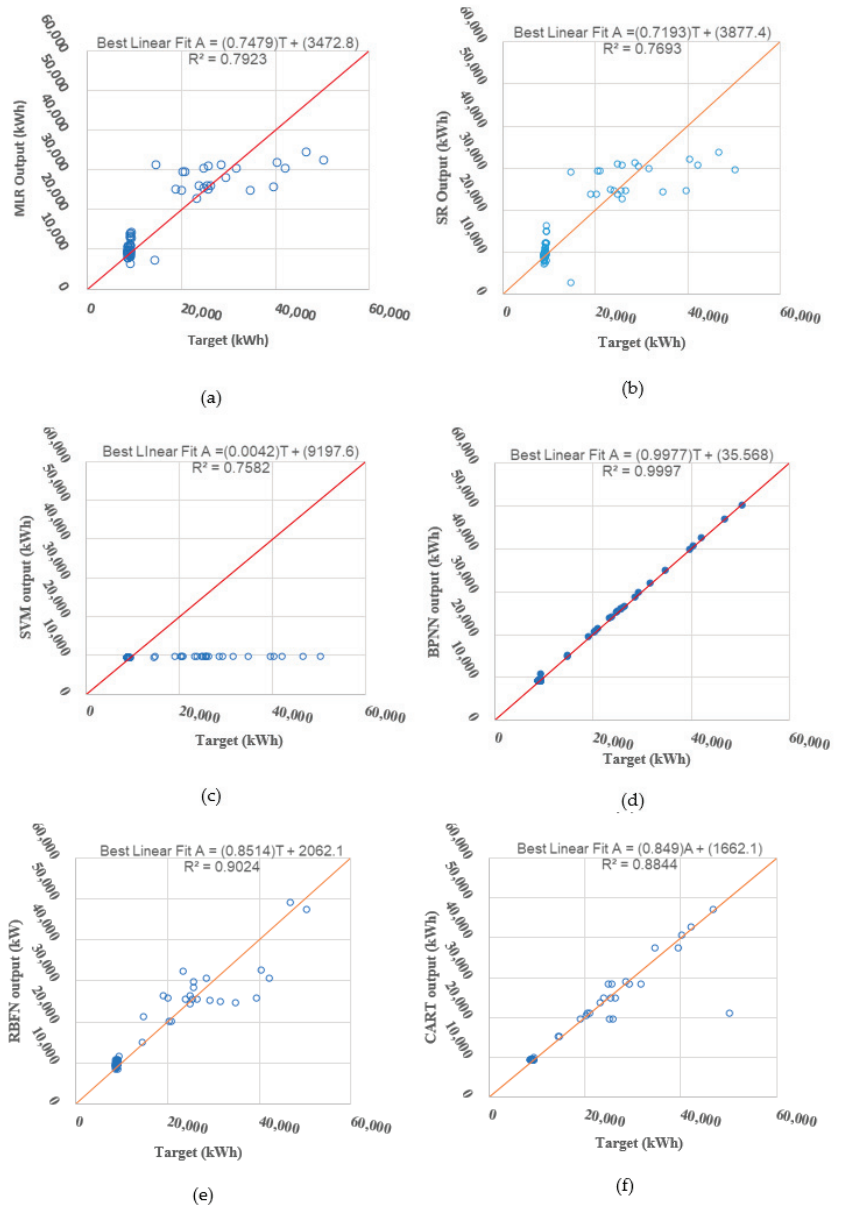


Figure 2. Cont.

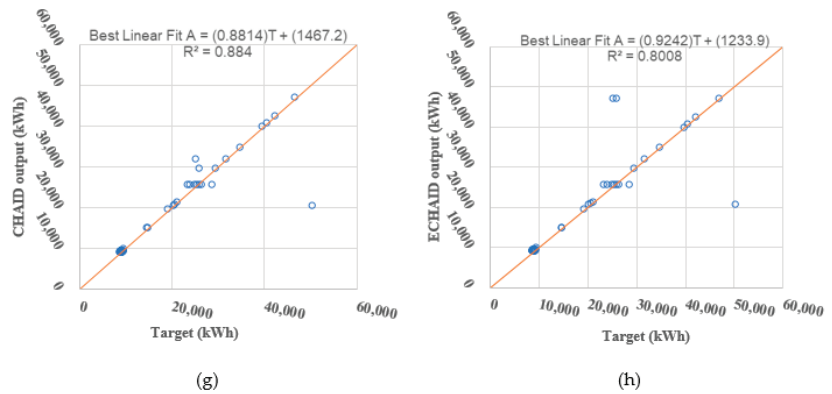


Figure 2. Regression between predicted and simulated electricity consumption: (a) MLR model vs. (b) BPNN model vs. (c) SVM vs. (d) BPNN model vs. (e) RNFN model vs. (f) CART model vs. (g) CHAID vs. (h) ECHAID model.

The outcomes of the SVM models on the prediction of electricity consumption are listed in Appendix A Table A3. It can be found that when the number of variables is 6 and ratio of training sample vs. validation samples is 7:3, the SVM model has the best performance, with MAPEs of 21.89% for training and 11.50% for validation, respectively. Figure 2c presents the regression between predicted and simulated electricity consumption for the best SVM model. The model predicts pretty well when the electricity consumption is around 10,000 kWh, and it underpredicts the electricity consumption when it exceeds 15,000 kWh.

The outcomes of the BPNN models on the prediction of electricity consumption are listed in Appendix A Table A4. It can be found that when the number of variables is 26 and the ratio of training sample vs. validation samples is 9:1, the BPNN model has the best performance, with MAPEs of 0.94% for training and 0.94% for validation, respectively. The number of inputs can be reduced to 12, with a correlation coefficient almost equal to 1.0 and MAPE less than 1.18%. Figure 2d presents the regression between predicted and simulated electricity consumption for the best BPNN model. Compared with the results from Ndiaye and Gabriel (2011), the R-square value is significantly improved from 0.79 to 0.997. The model predicts pretty well for all the samples.

The outcomes of the RBFN models on the prediction of electricity consumption are listed in Appendix A Table A5. It can be found that when the number of variables is 6 and the ratio of training sample vs. validation samples is 8:2, the RBFN model has the best performance, with MAPEs of 8.82% for training and 5.62% for validation, respectively. Figure 2e presents the regression between predicted and simulated electricity consumption for the best RBFN model. The model predicts pretty well when the electricity consumption is less than 35,000 kWh, and it tends to underpredict the electricity consumption when it is in the range of 35,000–40,000 kWh.

The outcomes of the CART models on the prediction of electricity consumption are listed in Appendix A Table A6. It can be found that when the number of variables is 6 and the ratio of training sample vs. validation samples is 7:3, the CART model has the best performance, with MAPEs of 1.41% for training and 5.50% for validation, respectively. Figure 2f presents the regression between predicted and simulated electricity consumption for the best CART model. The model predicts pretty well for almost all the samples, with the exception that it underpredicts one sample with actual consumption at around 50,000 kWh.

The outcomes of the CHAID models on the prediction of electricity consumption are listed in Appendix A Table A7. It can be found that when the number of variables is 26 and the ratio of training sample vs. validation samples is 7:3, the CHAID model has the best performance, with MAPEs of 0.87% for training and 5.03% for validation, respectively.

Figure 2g presents the regression between predicted and simulated electricity consumption for the best CHAID model. Similar to the CART model, it predicts pretty well for almost all the samples, with the exception that it underpredicts one sample with actual consumption at around 50,000 kWh.

The outcomes of the ECHAID models on the prediction of electricity consumption are listed in Appendix A Table A8. It can be found that when the number of variables is 26 and the ratio of training sample vs. validation samples is 7:3, the CHAID model has the best performance, with MAPEs of 0.92% for training and 9.89% for validation, respectively. Figure 2h presents the regression between predicted and simulated electricity consumption for the best ECHAID model. It predicts pretty well for almost all the samples, except that it overpredicts two samples with actual consumption at around 26,000 kWh and underpredicts one sample with actual consumption at around 50,000 kWh.

Table 4 presents the range of relative errors for the eight best prediction models for each data-driven approach. It can be found that the BPNN model has the best prediction performance, followed by the CHAID model, ECHAID model, CART model, and RBFN model. The performances of the SVM, SR, and MRL models are not as good as the other ones.

Table 4. Range of relative errors for the eight electricity consumption prediction models.

Method	≤5%	≤15%	≤25%	≤50%
MLR	38%	64%	79%	98%
SR	43%	68%	81%	94%
SVM	73%	73%	73%	75%
BPNN	99%	100%	100%	100%
RBFN	57%	85%	92%	100%
CART	89%	97%	98%	99%
CHAID	93%	98%	98%	99%
ECHAID	93%	97%	97%	97%

3.3. Performance of Natural Gas Consumption Prediction Model

The outcomes of the natural gas consumption prediction models are listed in Tables A9–A16 in Appendix A. The regressions between predicted and simulated natural gas consumption for the best models of each data-driven approach are presented in Figure 3a–h.

The outcomes of the MLR models on the prediction of natural gas consumption are listed in Appendix A Table A9. It can be found that when the number of variables is 13 and the ratio of training sample vs. validation samples is 7:3, the MLR model has the best performance, with MAPEs of 13.98% for training and 24.67% for validation, respectively. Figure 3a presents the regression between predicted and simulated natural gas consumption for the best MLR model. Good agreements are found between the predicted and actual energy consumption.

The outcomes of the SR models on the prediction of natural gas consumption are listed in Appendix A Table A10. Similar to the MLR model, when the number of variables is 13 and the ratio of training sample vs. validation samples is 7:3, the SR model has the best performance, with MAPEs of 14.03% for training and 24.89% for validation, respectively. Figure 3b presents the regression between predicted and simulated natural gas consumption for the best SR model. Good agreements are found between the predicted and actual energy consumption.

The outcomes of the SVM models on the prediction of natural gas consumption are listed in Appendix A Table A11. It can be found that when the number of variables is 26 and the ratio of training sample vs. validation samples is 7:3, the SVM model has the best performance, with MAPEs of 59.47% for training and 53.23% for validation, respectively. Figure 3c presents the regression between predicted and simulated natural gas consumption

for the best SVM model. Large deviations between the predicted value and actual energy consumption are found.

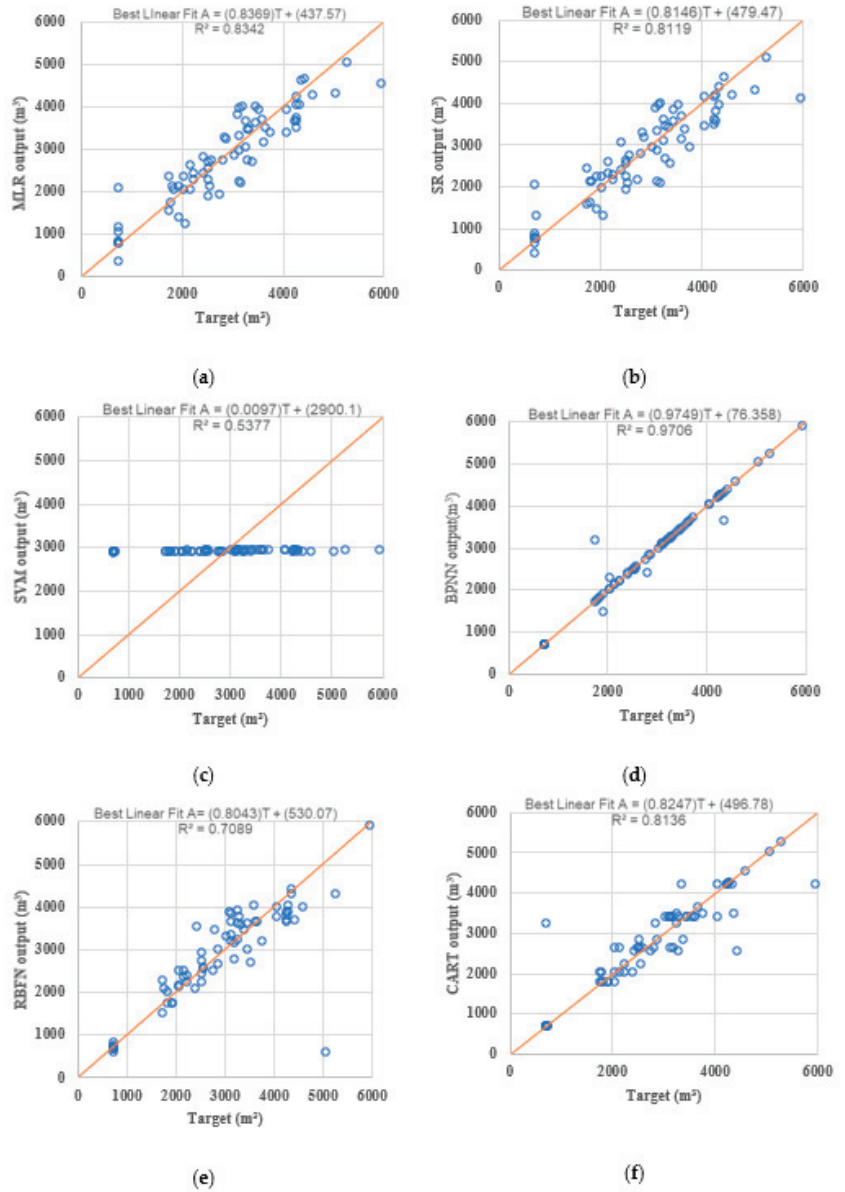


Figure 3. Cont.

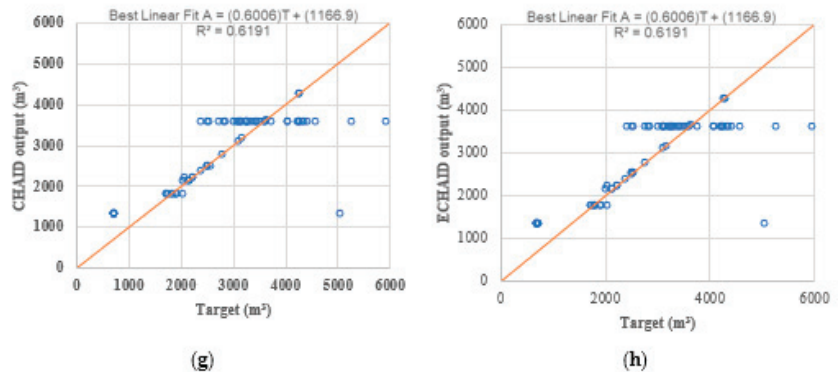


Figure 3. Regression between predicted and simulated natural gas consumption: (a) MLR model vs. (b) BPNN model vs. (c) SVM vs. (d) BPNN model vs. (e) RNFN model vs. (f) CART model vs. (g) CHAID vs. (h) ECHAID model.

The outcomes of the BPNN models on the prediction of natural gas consumption are listed in Appendix A Table A12. It can be found that when the number of variables is 26 and the ratio of training sample vs. validation samples is 9:1, the BPNN model has the best performance, with MAPEs of 2.63% for training and 0.16% for validation, respectively. The number of inputs can be reduced to 13, with a correlation coefficient higher than 0.979 and MAPEs less than 7.03%. When the number of inputs is reduced to 6, the correlation coefficient is still higher than 0.927, with MAPEs less than 11.63%. Figure 3d presents the regression between predicted and simulated natural gas consumption for the best BPNN model. The model predicts pretty well for almost all the samples.

The outcomes of the RBFN models on the prediction of natural gas consumption are listed in Appendix A Table A13. It can be found that when the number of variables is 6 and ratio of training sample vs. validation samples is 8:2, the RBFN model has the best performance, with MAPEs of 12.85% for training and 7.57% for validation, respectively. Figure 3e presents the regression between predicted and simulated natural gas consumption for the best RNFN model. The model predicts pretty well for all the samples, except under predicting one sample with natural gas consumption of 5049 m³.

The outcomes of the CART models on the prediction of natural consumption are listed in Appendix A Table A14. It can be found that when the number of variables is 13 and the ratio of training sample vs. validation samples is 7:3, the CART model has the best performance with MAPEs of 5.08% for training and 31.56% for validation, respectively. Figure 3f presents the regression between predicted and simulated natural gas consumption for the best CART model. The model predicts generally well for most of the samples, with big deviations for only a few samples.

The outcomes of the CHAID models on the prediction of natural consumption are listed in Appendix A Table A15. It can be found that when the number of variables is 6 and the ratio of training sample vs. validation samples is 7:3, the CHAID model has the best performance, with MAPEs of 18.74% for training and 24.72% for validation, respectively. Figure 3g presents the regression between predicted and simulated natural gas consumption for the best CHAID model. It can be observed that the model predicts generally well for some of the samples; however, for some of the samples, the natural gas consumption is predicted to be about 3600 m³ regardless of their actual consumption.

The outcomes of the ECHAID models on the prediction of natural consumption are listed in Appendix A Table A16. Similar to the CHAID model, when the number of variables is 6 and the ratio of training sample vs. validation samples is 7:3, the ECHAID model has the best performance, with MAPEs of 18.74% for training and 24.72% for validation, respectively. Figure 3h presents the regression between predicted and simulated natural gas consumption for the best ECHAID model, which is similar to the CHAID model.

Table 5 presents the ranges of relative errors for the eight best prediction models. It can be found that the BPNN model has the best prediction performance, followed by the CART model and RBFN model. The performance of other models is much poorer, with the SVM model being the worst case.

Table 5. Range of relative errors for the eight natural gas consumption prediction models.

Method	≤5%	≤15%	≤25%	≤50%
MLR	22%	62%	83%	98%
SR	25%	60%	82%	98%
SVM	6%	32%	48%	78%
BPNN	93%	96%	99%	99%
RBFN	30%	75%	93%	99%
CART	49%	83%	93%	99%
CHAID	38%	60%	76%	87%
ECHAID	38%	60%	76%	87%

4. Conclusions and Limitations

In this paper, eight data-driven methods were employed to develop energy prediction models for residential buildings in Oshawa with different numbers of input variables and training to validation ratios. The following conclusions can be made:

- (1) The performance of the prediction model can be improved through careful selections of variables based on VI and training to validation ratios. As only a small number of input variables are used, it can also help reduce the efforts of data collection.
- (2) With 26 input variables, the BPNN models have the best performance in predicting both the electricity consumption and gas consumption because their maximum error, mean absolute error, standard deviation, and MAPE are smaller than those of other models, and their correlation coefficient is larger than that of other models.
- (3) The MLR model has the worst performance in predicting the electricity consumption, and the SVM model has the worst performance in natural gas consumption prediction.
- (4) The number of inputs can be reduced to 12 in the BPNN model to predict the electricity consumption, with a correlation coefficient almost equal to 1.0 and MAPE ≤ 1.18%. By using the CART model, the number of inputs can be further reduced to 6, with a correlation coefficient ≥ 0.95 and MAPE ≤ 5.50%.
- (5) The number of inputs can be reduced to 13 in the BPNN model for natural gas consumption prediction with a correlation coefficient ≥ 0.979 and MAPE ≤ 7.03%. When it is further reduced to 6, the correlation coefficient of the BPNN model is still ≥ 0.927, with the MAPE ≤ 11.63%.
- (6) Based on the performance of the prediction models, when the human factor, e.g., SpenLess (awareness of the importance of spending less on energy bills), FromHome (number of people working or staying at home), and HomState (housing situation), are introduced, the performance of the prediction model can be improved. Those variables are often very difficult to introduce to develop physical models in traditional methods.

The limitations of the prediction models are as follows:

- (1) They can only be applied to residential buildings (houses) in Oshawa and cannot be applied to commercial buildings.
- (2) More data collection is needed, including weather data, to develop prediction models that are applicable throughout Canada.

Author Contributions: Y.L. and K.G. contributed to the conception of the study and the development of the methodology; Y.L., J.L., K.G., W.Y. and C.-Q.L. wrote the manuscript. All authors have read and agreed to the published version of the manuscript.

Funding: This work was funded by NATURAL SCIENCE FOUNDATION OF HUBEI PROVINCE, grant number 2017CFB602.

Data Availability Statement: The data presented in this study are available upon request from the corresponding author. The data are not publicly available due to their containing information that could compromise the privacy of the research participants.

Acknowledgments: The authors acknowledge the support from Natural Resources Canada, Oshawa Public Utility Corporation, Ontario Center for Excellence, and the Faculty of Engineering and Applied Science of University of Ontario Institute of Technology.

Conflicts of Interest: The authors declare no conflict of interest.

Appendix A

Table A1. Analysis of the results of the MLR model for electricity consumption.

Number of Variables	Training: Validation	Data Set	MAX Error	MAE	SD	R	MAPE
26	7:3	Training	9217	2759	3657	0.94	20.8%
		Validation	18,347	4300	5789	0.79	36.8%
	8:2	Training	10,174	2751	3691	0.93	20.5%
		Validation	17,416	3841	5310	0.85	32.1%
	9:1	Training	10,686	2568	3597	0.93	19.1%
		Validation	15,901	3571	5221	0.91	26.8%
12	7:3	Training	13,489	3040	4542	0.90	20.0%
		Validation	13,655	2242	3501	0.95	18.5%
	8:2	Training	13,496	2905	4428	0.90	19.2%
		Validation	13,830	2444	3733	0.95	19.8%
	9:1	Training	14,043	2712	4205	0.90	18.4%
		Validation	13,415	2748	4244	0.96	20.5%
6	7:3	Training	14,332	2864	4892	0.88	16.1%
		Validation	18,652	2207	4268	0.92	16.6%
	8:2	Training	14,339	2780	4795	0.88	15.8%
		Validation	19,260	2215	4560	0.93	15.5%
	9:1	Training	14,231	2584	4563	0.89	15.0%
		Validation	18,420	2179	4971	0.95	11.7%

Table A2. Analysis of the results of the SR model for electricity consumption.

Number of Variables	Training: Validation	Data Set	MAX Error	MAE	SD	R	MAPE
26	7:3	Training	12,178	3189	4520	0.90	21.9%
		Validation	17,646	2683	4364	0.91	21.9%
	8:2	Training	12,116	3080	4428	0.90	21.3%
		Validation	17,879	2728	4593	0.91	21.4%
	9:1	Training	12,450	2840	4209	0.90	19.8%
		Validation	17,765	3196	5387	0.92	22.9%
12	7:3	Training	13,208	3228	4722	0.89	21.2%
		Validation	17,633	2751	4371	0.91	22.5%
	8:2	Training	13,126	3109	4621	0.89	20.6%
		Validation	17,894	2811	4616	0.91	22.1%
	9:1	Training	13,636	2880	4402	0.89	19.2%
		Validation	17,612	3151	5314	0.94	22.3%
6	7:3	Training	15,664	2898	5033	0.87	16.4%
		Validation	21,563	2565	4918	0.90	18.2%
	8:2	Training	15,638	2814	4916	0.88	16.2%
		Validation	21,503	2681	5174	0.91	18.2%
	9:1	Training	15,443	2583	4694	0.88	14.8%
		Validation	21,016	2688	5740	0.95	14.2%

Table A3. Analysis of the results of the SVM model for electricity consumption.

Number of Variables	Training: Validation	Data Set	MAX Error	MAE	SD	R	MAPE
26	7:3	Training	37,611	6290	10,341	0.81	21.9%
		Validation	41,168	3595	9408	0.85	11.5%
	8:2	Training	37,611	5980	10,166	0.81	20.9%
		Validation	41,171	4051	9934	0.83	12.9%
	9:1	Training	37,612	5521	9791	0.82	19.5%
		Validation	41,171	5096	11,658	0.86	15.0%
12	7:3	Training	37,567	6278	10,325	0.84	21.9%
		Validation	41,129	3588	9396	0.86	11.5%
	8:2	Training	37,564	5969	10,150	0.84	20.9%
		Validation	41,127	4043	9920	0.86	12.9%
	9:1	Training	37,567	5511	9775	0.85	19.4%
		Validation	41,130	5086	11,643	0.89	14.9%
6	7:3	Training	37,514	6268	10,311	0.86	21.9%
		Validation	41,063	3582	9380	0.92	11.5%
	8:2	Training	37,519	5960	10,137	0.86	20.8%
		Validation	41,068	4036	9904	0.92	12.8%
	9:1	Training	37,515	5502	9761	0.87	19.4%
		Validation	41,064	5078	11,624	0.93	14.9%

Table A4. Analysis of the results of the BPNN model for electricity consumption.

Number of Variables	Training: Validation	Data Set	MAX Error	MAE	SD	R	MAPE
26	7:3	Training	16,131	2806	4381	0.91	16.5%
		Validation	13,618	2024	3386	0.95	14.4%
	8:2	Training	2554	422	833	1.00	1.9%
		Validation	156	237	411	1.00	1.5%
	9:1	Training	345	87	171	1.00	0.9%
		Validation	435	110	155	1.00	0.9%
12	7:3	Training	7112	376	1002	1.00	1.8%
		Validation	2735	300	549	1.00	1.9%
	8:2	Training	4586	743	1329	0.99	3.5%
		Validation	1803	427	566	1.00	2.7%
	9:1	Training	564	81	133	1.00	0.8%
		Validation	236	136	188	1.00	1.1%
6	7:3	Training	11,857	872	2110	0.98	3.9%
		Validation	2443	364	800	1.00	2.3%
	8:2	Training	13,089	1697	3586	0.94	7.7%
		Validation	3652	345	865	1.00	1.7%
	9:1	Training	17,032	2187	4537	0.89	10.3%
		Validation	20,134	1723	5297	0.94	6.5%

Table A5. Analysis of the results of the RBFN model for electricity consumption.

Number of Variables	Training: Validation	Data Set	MAX Error	MAE	SD	R	MAPE
26	7:3	Training	19,346	4214	5336	0.86	28.2%
		Validation	6519	2216	2641	0.96	20.1%
	8:2	Training	14,505	2846	4444	0.90	16.8%
		Validation	15,093	2274	4082	0.91	13.7%
	9:1	Training	13,076	2774	4252	0.90	19.1%
		Validation	8920	1942	2715	0.99	12.9%

Table A5. Cont.

Number of Variables	Training: Validation	Data Set	MAX Error	MAE	SD	R	MAPE
12	7:3	Training	15,797	2482	4227	0.91	14.3%
		Validation	3274	1135	1440	0.99	9.5%
	8:2	Training	17,058	3167	4966	0.87	19.5%
		Validation	7338	1788	2498	0.98	15.1%
	9:1	Training	15,795	2094	3855	0.92	12.2%
		Validation	2710	1154	1459	0.99	8.8%
6	7:3	Training	15,105	2100	3925	0.93	10.5%
		Validation	2989	902	1268	0.99	7.8%
	8:2	Training	14,315	1878	3708	0.93	8.8%
		Validation	3392	764	1095	1.00	5.6%
	9:1	Training	13,931	1428	2855	0.96	8.6%
		Validation	895	628	1142	1.00	6.0%

Table A6. Analysis of the results of the CART model for electricity consumption.

Number of Variables	Training: Validation	Data Set	MAX Error	MAE	SD	R	MAPE
26	7:3	Training	5224	460	1207	0.99	2.2%
		Validation	10,680	1420	3846	0.92	5.5%
	8:2	Training	5224	444	1176	0.99	2.1%
		Validation	10,680	1586	4097	0.92	5.9%
	9:1	Training	5224	618	2086	0.98	2.9%
		Validation	10,680	1408	3319	0.97	4.8%
12	7:3	Training	3850	275	717	1.00	1.2%
		Validation	18,575	1965	5466	0.83	7.0%
	8:2	Training	3850	268	700	1.00	1.2%
		Validation	18,575	2203	5825	0.83	7.7%
	9:1	Training	3850	462	1888	0.98	2.1%
		Validation	18,575	2354	6174	0.85	7.4%
6	7:3	Training	3745	338	881	1.00	1.4%
		Validation	29,551	1790	5937	0.87	5.5%
	8:2	Training	3745	327	859	1.00	1.4%
		Validation	29,551	2006	6298	0.87	6.1%
	9:1	Training	5915	387	1079	0.99	1.7%
		Validation	29,551	2629	7685	0.85	7.1%

Table A7. Analysis of the results of the CHAID model for electricity consumption.

Number of Variables	Training: Validation	Data Set	MAX Error	MAE	SD	R	MAPE
26	7:3	Training	3175	167	547	1.00	0.9%
		Validation	29,983	1684	6132	0.76	5.0%
	8:2	Training	3175	169	534	1.00	0.9%
		Validation	29,346	1846	6396	0.77	5.3%
	9:1	Training	10,496	833	2403	0.97	0.9%
		Validation	29,346	2831	8204	0.71	5.3%
12	7:3	Training	18,988	2538	5279	0.86	10.2%
		Validation	22,535	1191	4515	0.89	3.7%
	8:2	Training	18,988	2415	5143	0.86	9.8%
		Validation	22,535	1329	4807	0.89	3.9%
	9:1	Training	19,124	2166	4837	0.87	8.7%
		Validation	22,671	1798	5932	0.89	4.7%

Table A7. Cont.

Number of Variables	Training: Validation	Data Set	MAX Error	MAE	SD	R	MAPE
6	7:3	Training	18,988	2547	5279	0.86	10.3%
		Validation	22,535	1193	4515	0.89	3.7%
	8:2	Training	18,988	2420	5143	0.86	9.8%
		Validation	22,535	1332	4808	0.89	4.0%
	9:1	Training	19,124	2168	4837	0.87	8.8%
		Validation	22,671	1801	5932	0.89	4.76%

Table A8. Analysis of the results of the ECHAID model for electricity consumption.

Number of Variables	Training: Validation	Data Set	MAX Error	MAE	SD	R	MAPE
26	7:3	Training	3175	171	547	1.00	0.9%
		Validation	29,983	2928	8492	0.65	9.9%
	8:2	Training	3175	144	530	1.00	0.7%
		Validation	29,346	3272	8953	0.65	11.0%
	9:1	Training	18,441	1987	4555	0.89	7.5%
		Validation	21,988	1858	5803	0.89	5.2%
12	7:3	Training	18,259	2338	4962	0.88	9.0%
		Validation	21,806	1246	4432	0.89	3.9%
	8:2	Training	18,259	2216	4834	0.88	8.5%
		Validation	21,806	1382	4720	0.89	4.1%
	9:1	Training	18,441	2006	4555	0.89	7.7%
		Validation	21,988	1841	5808	0.89	5.0%
6	7:3	Training	18,259	2343	4962	0.88	9.1%
		Validation	21,806	1249	4432	0.89	3.9%
	8:2	Training	18,259	2221	4834	0.88	8.6%
		Validation	21,806	1377	4721	0.89	4.1%
	9:1	Training	18,441	2010	4555	0.89	7.8%
		Validation	21,988	1846	5808	0.89	5.0%

Table A9. Analysis of the results of the MLR model for natural gas consumption.

Number of Variables	Training: Validation	Data Set	MAX Error	MAE	SD	R	MAPE
26	7:3	Training	768	271	340	0.96	11.9%
		Validation	1452	603	835	0.77	32.6%
	8:2	Training	771	261	334	0.96	11.4%
		Validation	1460	662	876	0.76	35.8%
	9:1	Training	763	277	343	0.96	12.0%
		Validation	2172	734	1052	0.69	43.0%
13	7:3	Training	964	326	409	0.94	14.0%
		Validation	1381	526	649	0.86	24.7%
	8:2	Training	969	316	402	0.94	13.5%
		Validation	1394	577	684	0.86	27.1%
	9:1	Training	902	315	402	0.94	13.2%
		Validation	1831	666	855	0.82	33.5%
6	7:3	Training	2892	512	729	0.79	22.3%
		Validation	2494	469	757	0.81	21.0%
	8:2	Training	2882	506	720	0.78	21.9%
		Validation	2515	480	785	0.82	21.5%
	9:1	Training	2878	472	686	0.81	20.1%
		Validation	1523	458	714	0.88	26.2%

Table A10. Analysis of the results of the SR model for natural gas consumption.

Number of Variables	Training: Validation	Data Set	MAX Error	MAE	SD	R	MAPE
26	7:3	Training	1152	317	403	0.94	13.2%
		Validation	1723	625	806	0.78	30.7%
	8:2	Training	1153	305	395	0.94	12.7%
		Validation	1723	693	850	0.78	34.1%
	9:1	Training	989	327	415	0.93	13.5%
		Validation	1850	700	870	0.81	33.6%
13	7:3	Training	1091	331	426	0.93	14.0%
		Validation	1790	554	696	0.84	24.9%
	8:2	Training	1085	321	417	0.93	13.6%
		Validation	1797	608	733	0.83	27.4%
	9:1	Training	989	327	415	0.93	13.5%
		Validation	1850	700	870	0.81	33.6%
6	7:3	Training	2568	564	755	0.77	28.4%
		Validation	2482	585	866	0.73	28.0%
	8:2	Training	2559	559	744	0.77	27.9%
		Validation	2503	612	893	0.74	29.4%
	9:1	Training	2982	485	694	0.80	19.5%
		Validation	2493	533	908	0.79	27.2%

Table A11. Analysis of the results of the SVM model for natural gas consumption.

Number of Variables	Training: Validation	Data Set	MAX Error	MAE	SD	R	MAPE
26	7:3	Training	2313	940	1164	0.75	59.5%
		Validation	2991	958	1262	0.74	53.2%
	8:2	Training	2312	928	1148	0.75	58.3%
		Validation	2990	993	1311	0.78	56.0%
	9:1	Training	2192	926	1142	0.77	57.1%
		Validation	2872	1019	1427	0.74	73.4%
13	7:3	Training	2319	945	1168	0.80	59.9%
		Validation	2989	958	1265	0.78	53.4%
	8:2	Training	2317	933	1152	0.78	58.6%
		Validation	2986	993	1313	0.78	56.2%
	9:1	Training	2206	930	1146	0.77	57.3%
		Validation	2875	1019	1428	0.81	73.5%
6	7:3	Training	2325	947	1170	0.69	59.8%
		Validation	3000	959	1266	0.71	53.3%
	8:2	Training	2325	935	1154	0.69	58.6%
		Validation	3000	994	1314	0.74	56.1%
	9:1	Training	2215	933	1148	0.70	57.3%
		Validation	2887	1017	1430	0.83	73.3%

Table A12. Analysis of the results of the BPNN model for natural gas consumption.

Number of Variables	Training: Validation	Data Set	MAX Error	MAE	SD	R	MAPE
26	7:3	Training	1334	263	309	0.97	11.0%
		Validation	551	272	322	0.97	13.2%
	8:2	Training	1467	145	276	0.97	6.3%
		Validation	272	102	125	1.00	5.2%
	9:1	Training	663	55	226	0.98	2.6%
		Validation	13	2	5	1.00	0.2%

Table A12. Cont.

Number of Variables	Training: Validation	Data Set	MAX Error	MAE	SD	R	MAPE
13	7:3	Training	262	118	148	0.99	5.1%
		Validation	487	173	233	0.98	6.0%
	8:2	Training	809	191	259	0.98	8.2%
		Validation	186	138	168	0.99	6.3%
	9:1	Training	848	192	243	0.98	7.0%
		Validation	533	239	286	0.98	9.2%
6	7:3	Training	1463	374	460	0.92	11.9%
		Validation	1033	373	545	0.91	11.3%
	8:2	Training	2650	427	617	0.85	14.3%
		Validation	975	342	435	0.96	14.2%
	9:1	Training	913	338	435	0.93	11.6%
		Validation	512	282	376	0.97	10.3%

Table A13. Analysis of the results of RBFN model for natural gas consumption.

Number of Variables	Training: Validation	Data Set	MAX Error	MAE	SD	R	MAPE
26	7:3	Training	1320	470	607	0.86	18.7%
		Validation	973	458	587	0.89	23.2%
	8:2	Training	2848	525	717	0.79	21.2%
		Validation	1031	470	596	0.89	20.0%
	9:1	Training	2896	476	691	0.80	16.6%
		Validation	804	477	618	0.90	21.4%
13	7:3	Training	1171	381	469	0.92	16.5%
		Validation	789	319	407	0.95	15.6%
	8:2	Training	1424	441	539	0.89	18.2%
		Validation	706	346	420	0.95	17.0%
	9:1	Training	1816	447	562	0.87	17.4%
		Validation	666	419	496	0.94	20.4%
6	7:3	Training	2928	633	740	0.81	26.3%
		Validation	1008	500	712	0.84	27.7%
	8:2	Training	4432	394	744	0.79	12.9%
		Validation	695	230	324	0.97	7.6%
	9:1	Training	4555	395	731	0.79	13.2%
		Validation	461	222	246	0.99	9.3%

Table A14. Analysis of the results of the CART model for natural gas consumption.

Number of Variables	Training: Validation	Data Set	MAX Error	MAE	SD	R	MAPE
26	7:3	Training	634	133	209	0.98	5.0%
		Validation	1840	689	994	0.64	34.3%
	8:2	Training	660	164	247	0.98	5.7%
		Validation	2569	817	1155	0.55	39.2%
	9:1	Training	834	154	252	0.98	5.4%
		Validation	2440	723	1135	0.61	43.5%
13	7:3	Training	634	139	212	0.98	5.1%
		Validation	1840	605	924	0.69	31.6%
	8:2	Training	660	173	261	0.97	5.9%
		Validation	2569	705	1076	0.60	35.2%
	9:1	Training	834	162	264	0.97	5.6%
		Validation	2440	680	1124	0.63	41.5%

Table A14. Cont.

Number of Variables	Training: Validation	Data Set	MAX Error	MAE	SD	R	MAPE
6	7:3	Training	494	117	210	0.98	3.8%
		Validation	2569	806	1335	0.40	47.6%
	8:2	Training	660	143	222	0.98	4.5%
		Validation	2569	891	1406	0.34	51.9%
	9:1	Training	979	172	299	0.97	5.5%
		Validation	2569	998	1681	0.28	68.5%

Table A15. Analysis of the results of the CHAID model for natural gas consumption.

Number of Variables	Training: Validation	Data Set	MAX Error	MAE	SD	R	MAPE
26	7:3	Training	1366	271	438	0.93	7.7%
		Validation	2038	665	1012	0.64	37.4%
	8:2	Training	1411	280	442	0.93	8.1%
		Validation	2083	638	1015	0.65	37.0%
	9:1	Training	1589	242	441	0.92	6.6%
		Validation	2261	1007	1386	0.43	60.5%
13	7:3	Training	1246	254	421	0.93	7.9%
		Validation	672	708	988	0.66	41.4%
	8:2	Training	1915	430	647	0.83	14.5%
		Validation	2587	794	1184	0.46	43.5%
	9:1	Training	1390	230	407	0.94	6.1%
		Validation	2062	994	1392	0.40	57.4%
6	7:3	Training	3714	385	722	0.79	18.7%
		Validation	2339	612	799	0.78	24.7%
	8:2	Training	3714	377	709	0.79	18.2%
		Validation	2351	656	843	0.78	26.6%
	9:1	Training	1640	305	478	0.91	9.7%
		Validation	2312	861	1515	0.34	64.0%

Table A16. Analysis of the results of the ECHAID model for natural gas consumption.

Number of Variables	Training: Validation	Data Set	MAX Error	MAE	SD	R	MAPE
26	7:3	Training	1246	288	482	0.91	8.1%
		Validation	4164	920	1439	0.28	45.9%
	8:2	Training	1246	168	366	0.95	4.4%
		Validation	4164	1065	1551	0.19	51.4%
	9:1	Training	1589	242	441	0.92	6.6%
		Validation	2261	1007	1386	0.43	60.5%
13	7:3	Training	1913	397	643	0.84	13.1%
		Validation	2585	754	1136	0.47	40.6%
	8:2	Training	1915	382	631	0.84	12.6%
		Validation	2587	830	1201	0.45	44.8%
	9:1	Training	1150	243	427	0.93	6.9%
		Validation	1692	873	1294	0.52	58.2%
6	7:3	Training	3714	385	722	0.79	18.7%
		Validation	2339	612	799	0.78	24.7%
	8:2	Training	3714	377	709	0.79	18.2%
		Validation	2351	656	843	0.78	26.6%
	9:1	Training	1640	306	478	0.91	9.7%
		Validation	2312	861	1515	0.34	64.0%

References

1. International Energy Agency (IEA). Available online: <https://www.iea.org/reports/the-critical-role-of-buildings> (accessed on 19 September 2022).
2. Lin, Y.; Zhou, S.; Yang, W.; Li, C.-Q. Design optimization considering variable thermal mass, insulation, absorptance of solar radiation and glazing ratio using prediction model and Genetic Algorithm. *Sustainability* **2018**, *10*, 336. [CrossRef]
3. Lin, Y.; Yang, W. Application of Multi-objective Genetic Algorithm based Simulation for Cost-effective Building Energy Efficiency Design and Thermal Comfort Improvement. *Front. Energy Res.* **2018**, *6*, 25. [CrossRef]
4. Zhu, D.; Yan, D.; Wang, C.; Hong, T. Comparison of building energy consumption simulation software: DeST, EnergyPlus and DOE-2. *Build. Sci.* **2012**, *28*, 213–222.
5. Fumo, N.; Mago, P.; Luck, R. Methodology to estimate building energy consumption using EnergyPlus Benchmark Models. *Energy Build.* **2010**, *42*, 2331–2337. [CrossRef]
6. Amiri, S.S.; Mottahedi, M.; Asadi, S. Using multiple regression analysis to develop energy consumption indicators for commercial buildings in the U.S. *Energy Build.* **2015**, *109*, 209–216. [CrossRef]
7. Chen, S.; Zhou, X.; Zhou, G.; Fan, C.; Ding, P.; Chen, Q. An online physical-based multiple linear regression model for building's hourly cooling load prediction. *Energy Build.* **2022**, *254*, 11574. [CrossRef]
8. Ciulla, G.; D'Amico, A. Building energy performance forecasting: A multiple linear regression approach. *Appl. Energy* **2019**, *253*, 113500. [CrossRef]
9. Tso, G.K.F.; Yau, K.K.W. Predicting electricity energy consumption-A comparison of regression analysis, decision tree and networks. *Energy* **2007**, *32*, 1761–1768. [CrossRef]
10. Zhao, L.; Lin, Y.; Huang, X. Prediction Model for Energy Consumption and Visual Discomfort of Passive House Based on Stepwise Regression Analysis. *Build. Energy Effic.* **2021**, *49*, 50–55, 69.
11. Ma, Z.; Ye, C.; Ma, W. Support vector regression for predicting building energy consumption in southern China. *Energy Procedia* **2019**, *158*, 3433–3438. [CrossRef]
12. Li, Q.; Meng, Q.; Mochida, A. Applying support vector machine to predict hourly cooling load in the building. *Appl. Energy* **2009**, *86*, 2249–2256. [CrossRef]
13. Paudel, S.; Elmitri, M.; Le Corre, O. A relevant data selection method for energy consumption prediction of low energy building based on support vector machine. *Energy Build.* **2017**, *138*, 240–256. [CrossRef]
14. Ahmad, M.W.; Mourshed, M.; Rezgui, Y. Trees vs Neurons: Comparison between random forest and ANN for high-resolution prediction of building energy consumption. *Energy Build.* **2017**, *147*, 77–89. [CrossRef]
15. Han, Y.; Fan, C.; Yu, B. Energy efficient building envelope using novel RBF neural network integrated affinity propagation. *Energy* **2020**, *209*, 118414. [CrossRef]
16. Zhao, C.; Lin, S.; Xu, Q. Prediction of building energy consumption in college buildings based on GM-RBF neural network. *J. Nanjing Univ. Sci. Technol.* **2014**, *38*, 48–53.
17. Zekić-Sušac, M.; Has, A.; Knežević, M. Predicting energy cost of public buildings by artificial neural networks, CART, and random forest. *Neurocomputing* **2021**, *439*, 223–233. [CrossRef]
18. Capozzoli, A.; Grassi, D.; Causone, F. Estimation models of heating energy consumption in schools for local authorities planning. *Energy Build.* **2015**, *105*, 302–313. [CrossRef]
19. Yang, J.; Wu, J. Research on energy-saving optimization of commercial central air-conditioning based on data mining algorithm. *Energy Build.* **2022**, *272*, 112326. [CrossRef]
20. Kusiak, A.; Li, M.; Zhang, Z. A data-driven approach for steam load prediction in buildings. *Appl. Energy* **2010**, *87*, 925–933. [CrossRef]
21. Yan, L.; Hu, P.; Li, C.; Yao, Y.; Xing, L.; Lei, F.; Zhu, N. The performance prediction of ground source heat pump system based on monitoring data and data mining technology. *Energy Build.* **2016**, *127*, 1085–1095. [CrossRef]
22. Li, K.; Xie, X.; Yang, X. A hybrid teaching-learning artificial neural network for building electrical energy consumption prediction. *Energy Build.* **2018**, *174*, 323–334. [CrossRef]
23. Moayedi, H.; Mu'azu, M.A.; Foong, K.K. Novel swarm-based approach for predicting the cooling load of residential buildings based on social behavior of elephant herds. *Energy Build.* **2020**, *206*, 109579. [CrossRef]
24. Aruta, G.; Ascione, F.; Boettcher, O.; De Masi, R.F.; Mauro, G.M.; Vanoli, G.P. Machine learning to predict building energy performance in different climates. *IOP Conf. Ser. Earth Environ. Sci.* **2022**, *1078*, 012137. [CrossRef]
25. Ndiaye, D.; Gabriel, K. Principal component analysis of the electricity consumption in residential dwellings. *Energy Build.* **2011**, *43*, 446–453. [CrossRef]
26. Shen, M.; Sun, H.; Lu, Y. Household Electricity Consumption Prediction Under Multiple Behavioural Intervention Strategies Using Support Vector Regression. *Energy Procedia* **2017**, *142*, 2734–2739. [CrossRef]
27. Jain, R.K.; Smith, K.M.; Taylor, J.E. Forecasting energy consumption of multi-family residential buildings using support vector regression: Investigating the impact of temporal and spatial monitoring granularity on performance accuracy. *Appl. Energy* **2014**, *123*, 168–178. [CrossRef]
28. Rahman, A.; Srikumar, V.; Smith, A.D. Predicting electricity consumption for commercial and residential buildings using deep recurrent neural networks. *Appl. Energy* **2017**, *212*, 372–385. [CrossRef]

29. Wang, Z.; Liu, X.; Li, H. Energy performance prediction of vapor-injection air source heat pumps in residential buildings using a neural network model. *Energy Build.* **2020**, *228*, 110499. [[CrossRef](#)]
30. Kim, T.-Y.; Cho, S.-B. Predicting residential energy consumption using CNN-LSTM neural networks. *Energy* **2019**, *182*, 72–81. [[CrossRef](#)]
31. Bui, D.-K.; Nguyen, T.N.; Nguyen-Xuan, H. An artificial neural network (ANN) expert system enhanced with the electromagnetism-based firefly algorithm (EFA) for predicting the energy consumption in buildings. *Energy* **2020**, *190*, 116370. [[CrossRef](#)]
32. Farzana, S.; Liu, M.; Hossain, M.U. Multi-model prediction and simulation of residential building energy in urban areas of Chongqing, South West China. *Energy Build.* **2014**, *81*, 161–169. [[CrossRef](#)]
33. Guo, Z.; Moayedi, H.; Bahiraei, M. Optimal modification of heating, ventilation, and air conditioning system performances in residential buildings using the integration of metaheuristic optimization and neural computing. *Energy Build.* **2020**, *214*, 109866. [[CrossRef](#)]
34. Kerdan, I.G.; Gálvez, D.M. Artificial neural network structure optimisation for accurately prediction of exergy, comfort and life cycle cost performance of a low energy building. *Appl. Energy* **2020**, *280*, 115862. [[CrossRef](#)]
35. Chegari, B.; Tabaa, M.; Medromi, H. Multi-objective optimization of building energy performance and indoor thermal comfort by combining artificial neural networks and metaheuristic algorithms. *Energy Build.* **2021**, *239*, 110839. [[CrossRef](#)]
36. IBM. Available online: <https://www.ibm.com/spss> (accessed on 1 November 2022).
37. Asadi, S.; Amiri, S.S.; Mottahedi, M. On the development of multi-linear regression analysis to assess energy consumption in the early stages of building design. *Energy Build.* **2014**, *85*, 246–255. [[CrossRef](#)]
38. Wang, M.; Wright, J.; Brownlee, A.; Buswell, R. A comparison of approaches to stepwise regression on variables sensitivities in building simulation and analysis. *Energy Build.* **2016**, *127*, 313–326. [[CrossRef](#)]
39. Gao, Y. Research on Building Energy Consumption Prediction Method Based on machine Learning. PhD. Thesis, Beijing University of Civil Engineering and Architecture, Beijing, China, 2020.
40. Xue, W. *SPSS Modeler Data Mining Methods and Applications*, 3rd. ed.; Electronics Industry Press: Beijing, China, 2020.
41. Rumelhart, D.E.; Hinton, G.E.; Williams, R.J. Learning representations by back-propagating errors. *Nature* **1986**, *323*, 533–536. [[CrossRef](#)]
42. Breiman, L.; Friedman, J.H.; Olshen, R.A.; Stone, C.J. *Classification and Regression Trees*; Wadsworth Inc.: New York, NY, USA, 1984.
43. Kass, G.V. An exploratory technique for investigating large quantities of categorical data. *J. R. Stat. Soc.* **1980**, *29*, 119–127. [[CrossRef](#)]
44. Biggs, D.; de Ville, B.; Suen, E. A method of choosing multiway partitions for classification and decision trees. *J. Appl. Stat.* **1991**, *18*, 49–62. [[CrossRef](#)]
45. Zhang, X.; Wada, T.; Fujiwara, K.; Kano, M. Regression and independence based variable importance measure. *Comput. Chem. Eng.* **2020**, *135*, 106757. [[CrossRef](#)]

Article

Modelling Building Stock Energy Consumption at the Urban Level from an Empirical Study

Qunfeng Ji, Yangbo Bi, Mehdi Makvandi, Qinli Deng, Xilin Zhou and Chuancheng Li *

School of Civil Engineering and Architecture, Wuhan University of Technology, Wuhan 430070, China; jiq2flying@whut.edu.cn (Q.J.); byb@whut.edu.cn (Y.B.); mehdi_makvandi@whut.edu.cn (M.M.); deng4213@whut.edu.cn (Q.D.); zhou.xilin@whut.edu.cn (X.Z.)

* Correspondence: licc@whut.edu.cn

Abstract: Quantifying the energy consumption of buildings is a complex and multi-scale task, with the entire process dependent on input data and urban surroundings. However, most urban energy models do not account for the urban environment. This paper employs a physical-based, bottom-up method to predict urban building operating energy consumption, using imported topography to consider shading effects on buildings. This method has proven to be feasible and aligned well with the benchmark. Research also suggests that commercial and transport buildings have the highest energy use intensity, significantly more than residential and office buildings. Specifically, cooling demands far outweigh heating demands for these building types. Therefore, buildings in the commercial and transportation sectors would receive greater consideration for energy efficiency and improvements to the cooling system would be a priority. Additionally, the method developed for predicting building energy demand at an urban scale can also be replicated in practice.

Keywords: urban building energy modelling; physical-based bottom-up; building energy use; building types

Citation: Ji, Q.; Bi, Y.; Makvandi, M.; Deng, Q.; Zhou, X.; Li, C. Modelling Building Stock Energy Consumption at the Urban Level from an Empirical Study. *Buildings* **2022**, *12*, 385. <https://doi.org/10.3390/buildings12030385>

Academic Editor: Zhenjun Ma

Received: 25 February 2022

Accepted: 17 March 2022

Published: 21 March 2022

Publisher's Note: MDPI stays neutral with regard to jurisdictional claims in published maps and institutional affiliations.



Copyright: © 2022 by the authors. Licensee MDPI, Basel, Switzerland. This article is an open access article distributed under the terms and conditions of the Creative Commons Attribution (CC BY) license (<https://creativecommons.org/licenses/by/4.0/>).

1. Introduction

Cities emit 70% of CO₂ emissions and consume two-thirds of the energy produced in the world [1], while buildings consume more than one-third of the final energy consumption globally [2]; therefore, there are more opportunities to develop sustainably by increasing energy use efficiency in buildings. Such opportunities are particularly important for China, as a result of its exponential rate of urbanisation. The global data platform of Statista has shown that China has achieved a 64.72% population urbanisation rate at the end of 2021 [3]. This means that there will be a higher energy demand for buildings, resulting in higher carbon emissions. Therefore, it is significant to have a detailed knowledge of the dynamic energy consumption of the buildings in particular cities with compact urban environments. Figure 1 shows the amount of floor space, both under construction and to be completed, from 2015 and 2019, and the yearly increase is evident [4].

Quantifying urban-scale energy use in buildings is a complex, cross-sectoral, and multi-scale task, with the entire process highly dependent on the urban environment [5]. Hong et al. (2018) mention that the emergent of building energy modelling is one of the optimum supports available for energy efficiency, resilience, and sustainability [6], and the model extensively improves energy performance rating, energy-efficient design, code compliance, and optimised operations. Reinhart and Cerezo Davila (2016) explain that the urban building energy model could accommodate many spatial scale sizes from a block, district, and, ultimately, an entire city [7]. Ferrando et al. (2020) use a user-oriented overview to present the physics-based urban scale energy models' tools, balancing complexity, usability, accuracy, and computing requirements [8]. These scholars' generic modelling theory findings are relevant and significant for urban-scale energy modelling in its processes and applications. However, most urban building energy modelling has

mainly disregarded the impacts of the urban environment around buildings. For example, some have even wholly overlooked shading and the exchange of long-wave radiation of the environment and buildings.

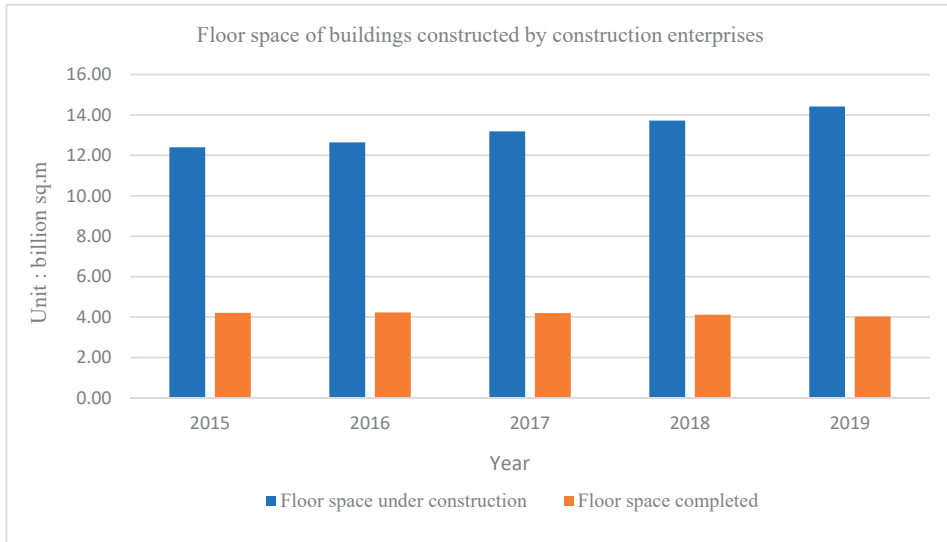


Figure 1. Floor space of buildings constructed by construction enterprises.

This paper reviews approaches to urban building energy models and then presents a simple method to predict building energy consumption from the diverse functions of building stock, as an example, by an archetypal physical-based, bottom-up approach. The urban building energy model in this study considers the impacts of the urban environment (e.g., overshadowing between buildings) on the simulation, which can fill the research gap in the previous study. Moreover, this study also presents all the processes that can be replicated, with minimal difficulties, to additional research references.

2. Literature Review of Urban Building Energy Modelling

Two approaches are fundamental to modelling urban building energy consumption: top-down or bottom-up. Prior scholars have used such approaches to modelling urban building energy for the study [1,5,9–11]. Top-down approaches treat a group of buildings as a single entity by estimating energy use at the sectoral building level, without considering differences between individual buildings. By contrast, based on bottom-up approaches, the energy consumption in individual buildings can be modelled, which can then be aggregated to the urban area. Figure 2 presents the approaches' outline of the urban building energy modelling.

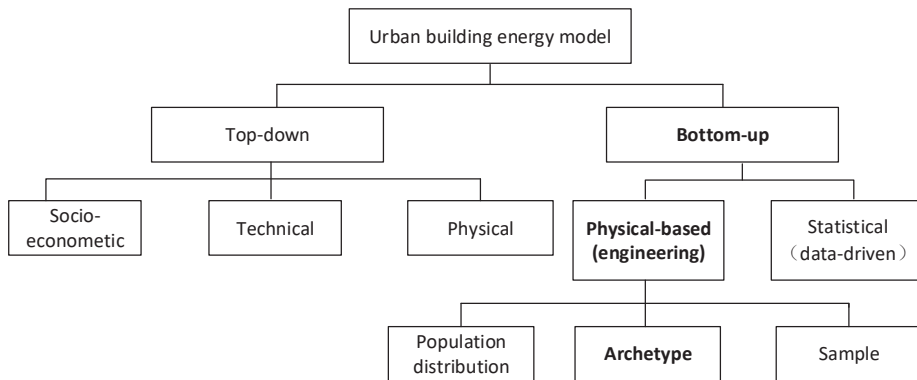


Figure 2. Approaches to modelling urban building energy.

2.1. Top-Down Model

The top-down model forecast of building consumption in urban areas is based on historical aggregate energy data; it also forecasts the long-term correlations between energy use within an urban area with different types of variables, such as the economy [12], overall climate conditions [13], and technical features, such as system or envelopes [14]. Such an approach is applicable on an aggregated level, divided into various physical, technological, and socio-econometric classifications. Therefore, top-down models do not provide details for current and future technological options, as they concentrate on macroeconomic trends, instead of individual physical factors that consume energy in the buildings.

2.2. Bottom-Up Model

Compared to the top-down model, bottom-up models focus on two types of disaggregated levels: physical-based and statistical models [15]. This necessitates a vast amount of empirical data to validate each component's description [16]. The statistical models utilise machine learning to determine energy demands from buildings; on the other hand, physics-based models use detailed modelling and simulation approaches that originated from building energy models [17].

Bottom-up models forecast energy demands within individual buildings, before scaling up to neighbourhoods or entire cities. Such models are robust in determining the optimum cost-effective measures to reduce carbon dioxide emissions, through the use of available technologies. Energy consumption from each building can be calculated using the models, up to an hourly basis, before scalability to the whole city is applied [18]. However, these models necessitate a vast amount of quantitative data, with limited accessibility, due to privacy and security. Table 1 summarises the advantages and disadvantages of top-down and bottom-up approaches.

The above table indicates that top-down models cannot distinguish energy consumption, due to individual end-uses. Commonly used variables include macroeconomic indicators, such as economy, price indices, and climatic conditions. Similarly, the reliance on historical data is a drawback, since top-down models cannot be used to model discontinuous technological advancements. In addition, the lack of detail of the energy consumption of individual end-uses makes it impossible to identify critical areas for improving energy efficiency. On the other hand, top-down models have the advantage of using only aggregate data, which is widely available, simplicity, and reliance on historical national energy values that provide “inertia” to the model.

Bottom-up models can determine how much energy is consumed by each end-use and identify areas where improvements can be made. This approach can determine total energy consumption, without using historical data to calculate energy consumption. The primary drawback of this approach is that the input data required is greater than that of

top-down models, and the bottom-up models are more complex, in terms of calculation or simulation techniques.

Table 1. Comparison of urban building energy modelling approaches [9,10,19].

Urban Building Energy Modelling Approaches	Top-Down	Bottom-Up	
		Physical-Based	Statistical-Based
Advantages	Can make a continuous long-term prediction.	Modelling with physically measurable data.	Modelling can take into account macroeconomic and socioeconomic impacts.
	Connections can be obtained between macroeconomics, social economics, and building energy consumption.	Energy consumption calculation, based on the heat balance equation of the building.	Include occupants' behaviour.
	Can predict building energy consumption under different energy policies and scenarios.	Total energy demand can be predicted as well as the different end-users can be given (e.g., heating, cooling, and lighting).	Simple to model and use.
	The input data is simple and does not require building construction details.	Can assess and quantify the impact of different technology combinations on energy consumption.	Can predict the proportion of energy consumption for typical different end uses.
Disadvantages	Highly depending on the data of historical energy consumption.	Occupant behaviour and many uncertainty factors relating to energy consumption should be assumed.	Data are limited to diversity and flexibility.
	Predict energy consumption, based on the past economic conditions.	A large amount of data should be investigated relating to buildings, and high computational volume.	Limited capacity to assess the impact of energy efficiency measures.
	Can not provide energy consumption of individual buildings, as well as the energy consumption of each component.	Ignore the impact of economic factors on energy consumption.	An extensive survey sample is required to represent the overall diversity.

2.3. Data Input and Output

These data are derived from various sources, including the geometry of the building, thermophysical characteristics of its components (e.g., walls, roofs, and glazing), use of equipment, weather data, and occupancy frequency. A simplified building prototype can be used to observe the overall effects from an individual building to a group of buildings [20].

Outputs from a simulation usually includes energy demands, efficiency, and the use of renewable energy in some cases [17]. These outputs could be presented both spatially or statistically. Data on individual buildings could be used to scale up, according to the requirements for statistical presentation.

However, the spatial distribution of energy demand in urban areas could not be represented within the statistical presentation, thus having less relevance in policies about urban planning. Conversely, geospatial techniques are used to determine large-scale energy demands in spatial presentation; thus, its main advantage is that it could precisely locate areas with high energy demand. Such information could assist in energy planning and conservation and guide policy-makers who may not be specialists in complex energy systems. Furthermore, the spatial presentation can include spatial variation, according to climate conditions.

2.4. Model Calibration

Recently, there has been much progress in calibrating energy models. Such progress includes pattern-based [21], Bayesian calibration [22], and optimisation-based methods [23,24]. There are mainly three approaches that have been widely used for calibration of energy models: manual calibration accompanied by a computer program or graphic representation, special testing and analytical approaches, and mathematical approaches [25].

Studies have demonstrated limitations for the calibration of urban building energy modelling, due to the vast number of simulations involving vast amounts of data, high levels of uncertainty, and interaction between buildings nearby. There is no consensus on conducting such a calibration, and previous studies have demonstrated these limitations. For example, Fonseca and Schlueter (2015) have conducted modelling around 1400 buildings, based on different archetypes, and the model error rate is at 1% to 19% by the energy service category at the neighbourhood scale [26]. Sokol et al. (2017) validated the method on a set of 2263 residential buildings, using monthly and annual measured energy data to calibrate [27]. However, the methods are only tested for residential buildings; they do not apply to other climate zones or building types.

3. Method

Figure 3 illustrates the process flow of the study, which can be broken down into three main steps. In step 1, data were collected, refined, and input. Buildings are also grouped based on their similar functions in this step. The second step involved urban building energy modelling by VirVil SketchUp plug-in and HTB2 calculation. The monthly calculation was used to calculate energy demand, and the results were output and compared with the benchmark level in step 3.

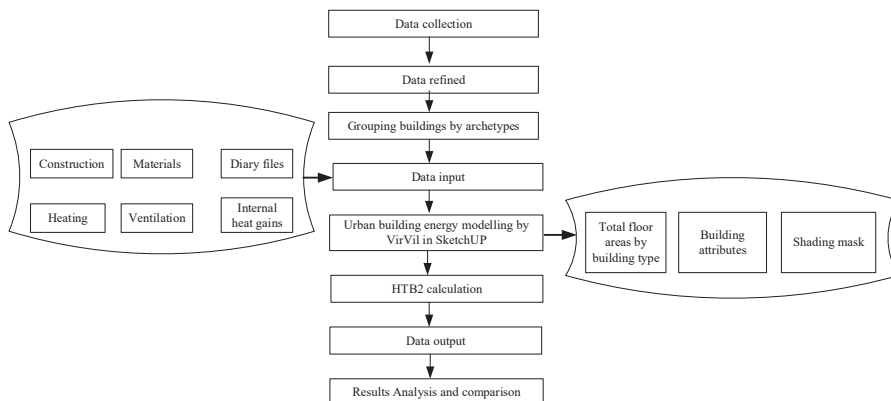


Figure 3. Research flow of this study.

3.1. Model Assumption and Principles

Data input and simulation were based on several assumptions. For example, each type of urban building energy model was viewed as a single function, regardless of its multifunctional. Although some of the buildings we investigated were mixed-use, they were still classified as single-use for simulation. A second problem was the lack of fabric construction data for residential buildings; therefore, we used local design standards (*The design standard for energy efficiency of residential buildings in hot summer and cold winter zone (2010)*; *the design standard for energy efficiency of public buildings (2015)*) for some parametric settings. Building energy modelling was based on two principles:

- (1) Topography, imported to consider its shading influence on the buildings, thus modelling urban building clusters in the actual urban geometry from Google Earth, which

can simulate how the urban environments influence urban building energy consumption.

- (2) Group buildings as archetypes, based on their functions for the simulation.

Categorising buildings into archetypes highly depends on the functions of buildings. VirVil plug-in developed by the Welsh School of Architecture, Cardiff University, is used to quantify energy consumption from building stock in this study [28]. It is based upon the calculation engineering of HTB2 (heat transfer in buildings) by modelling energy building stock [29]. This study only focuses on predicting operational energy consumption.

3.2. Data Description and Collection

This study used data collected, between 2015 and 2016, from the on-site survey, literature, local and national regulations, and websites. Table 2 illustrates the ways to collect these data. Data collected via on-site surveys are building information (their functions and floor areas), thermal properties (U values) (shown in Table 3), fabric constructions (materials, construction, and glazing type), internal gains, and diary files.

Table 2. Approaches to data collection.

Building Classification	Physical Buildings	Land Use	Diary File	Energy Supply
On-site survey	Website; local regulations	Local authority; website; on-site survey	Investigation; national standards	On-site survey
Residential, commercial, office and education, hotel, and transport	Location and climate zone; Characteristics and properties of buildings (construction, materials, etc.)	Proportions and built areas for each building type	Occupancy and operating schedule	Energy supply (electricity, gas, coal, renewables)

Table 3. Thermal insulation levels for residential and public buildings in this research.

Elements	U Values	U Values ($\text{w/m}^2/\text{°C}$)	
		Residential Buildings	Public Buildings
Wall		1.42	0.85
Ceiling		3.46	3.35
Ground		1.42	1.40
Roof		1.04	1.02
Window		5.4	5.32

3.3. Building Energy Modelling

3.3.1. The Software Used in This Research

The software adopted in this research includes HTB2 and VirVil SketchUp plug-in. Both of them are developed at the Welsh School of Architecture, Cardiff University.

HTB2 is a computer program designed for simulating the energy and environmental performance of buildings. It is also able to carry out dynamic thermal simulation and apply it to the field of low carbon design and energy efficiency of buildings. It has been developed for thirty years and extensively tested and validated [30].

The VirVil SketchUp plug-in is an extension development of HTB2 for urban scale modelling. By linking SketchUp with HTB2, it can effectively simulate the energy demand for multiple buildings on a community or urban scale, considering the shading effects from adjacent buildings.

3.3.2. Climatic Characteristics in Wuhan

Wuhan is in the hot summer and cold winter zones and experiences a severe climate in summer and winter periods. It is extremely hot in July and August and freezing during the cold winter period in January. Temperatures in the city average around 18 °C throughout the year. January is the coldest month, with an average temperature of minus 10 °C. Without the effect of direct solar radiation, the temperature can reach almost 40 °C in July and August, as shown in Figure 4.

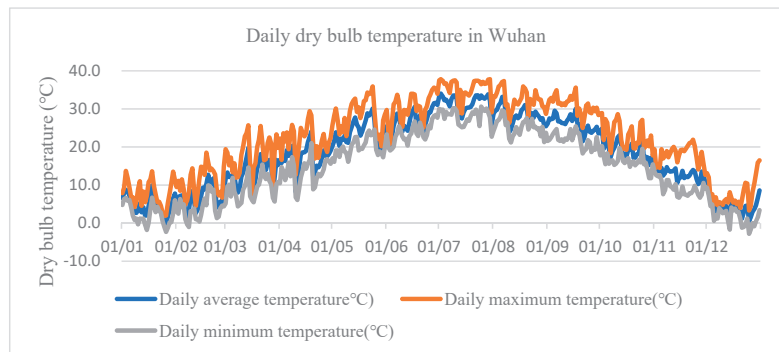


Figure 4. The statistics of daily dry bulb temperature in Wuhan [31].

In July, solar radiation peaks, with 650 MJ/m², as shown in Figure 5, for total monthly solar radiation.

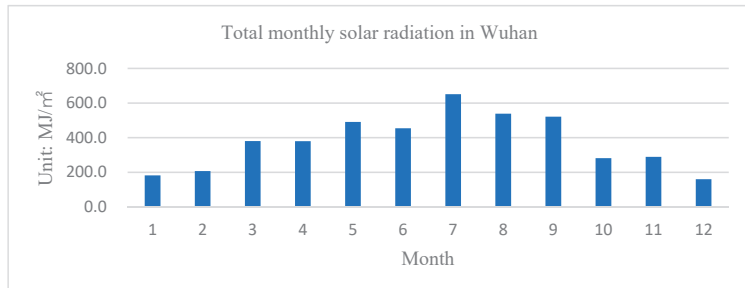


Figure 5. Total monthly solar radiation in Wuhan [31].

The meteorological parameters are derived from Wuhan city’s typical meteorological year (TMY) and used for energy simulations with HTB2. Meteorological data is available from the weather data of the EnergyPlus website (https://energyplus.net/weather-location/asia_wmo_region_2/CHN/CHN_Hubei.Wuhan.574940_CSWD (accessed on 16 March 2022)), which was extracted and converted from a “. epw” format into a “. met” format by using the HTB2 Weather File Software.

3.4. Simulation and Comparison

Simulation of the urban environment is complex, but the methodology simplifies it by using simple energy prediction tools and grouping similar buildings. Buildings are typically grouped according to their functions, such as residential, commercial, or office, which is reasonable for simple problems. The best way to group buildings in this study is based on their size and construction date. In order to achieve this, several building types are surveyed, and the results of these surveys are pooled together to produce groups of buildings with similar energy predictions. The time step for the calculation is set for 60 s, and the total run length is 365 days, as is the annual energy demand. After the simulation,

outcomes are compared with the benchmark levels of the literature to validate the accuracy of the simulation.

4. Case Study

4.1. General Introduction to the Study Area

The city of Wuhan is regarded as a city representative of hot summer and cold winter climatic zone in China. The urban building energy modelling consists of ten typical block zones near Wuchang railway station, at a radius of 1km, with an estimated area of 1.92 km², as displayed in Figure 6.

The majority of selected building blocks within the Wuchang district were built from the 1960 to the 2000s, with a wide range of building types, such as commercial, residential, hotels, and offices. Table 4 shows in-depth information for every block zone. As shown in Figure 7, 64%, 13%, and 12% of the buildings are residential, educational, offices, and commercial. Apart from the west square of the railway station, residential dwelling is the main building category in the eastern part of the station.



Figure 6. Ten-block zone for this study.

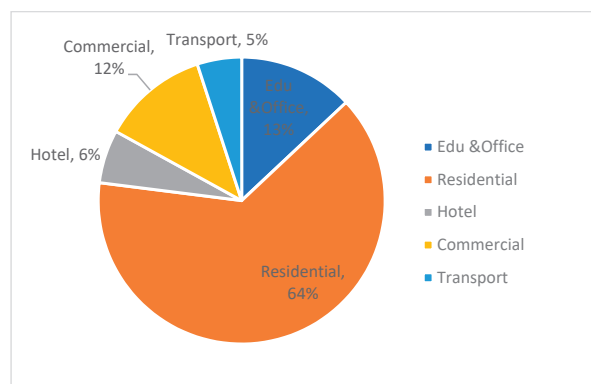


Figure 7. Proportion of building types in the areas for the study.

Table 4. Built-up area of individual block zone.

Land Zone	Areas (ha)	Building Type	Built-Up Area (m ²)
A	25.1	Office	22,645
		Commercial	27,307
		Residential	301,183
		Education	12,176
		Hotel	37,830
		Transport	3386
B1	5.6	Office	15,562
		Commercial	5696
		Hotels	58,966
		Residential	12,991
B2	1.7	Office	24,009
C	16.9	Transport	242,281
		Commercial	6872
D1	6.2	Office	71,747
		Commercial	44,964
		Residential	37,335
D2	0.8	Commercial	491
		Office	6667
E1	13.3	Office	22,225
		Commercial	14,866
		Residential	246,434
E2	12.8	Office	7640
		Commercial	15,957
		Education	4932
		Residential	246,705
F1	7.2	Office	16,971
		Commercial	9155
		Residential	108,627
F2	4.6	Office and medical	25,810
		Hotel	2158
		Education	7653
		Residential	67,210

4.2. Modelling Building Stock Energy Consumption

The most effective method of predicting the energy consumption of building blocks is modelling simulation. All the building archetypes will be modelled by SketchUp and calculated using the VirVil plug-in, which simulates the dynamic thermal performance of building stock. The plug-in was developed by Cardiff University and established a platform-linked calculation tool, HTB2, and a modelling tool, SketchUp.

The difference between VirVil with other simulation tools is that it could identify the interaction upon the buildings and their surroundings [32]. In addition, VirVil is a plug-in, which means it can be used conveniently with the SketchUp tool for modelling at the urban scale.

The buildings are designated into five categories for modelling purposes, as shown in Figure 8. They are education and office, commercial, residential, transport, and hotel. A few detailed building characteristics (e.g., building shape) were simplified as they pose little significance to energy consumption. The accuracy of this method was validated by comparing the simulation results with a benchmark level from the literature.

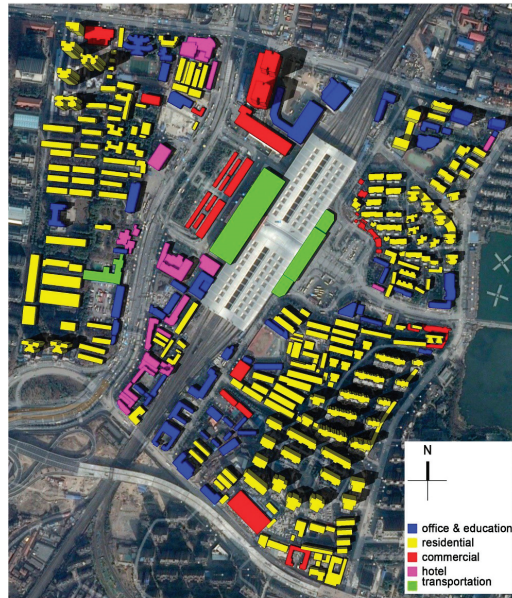


Figure 8. Modelling building stock with five building types in the study area.

4.3. Simulation Conditions

Data need to be input into the model to predict the energy demand of building stocks. Such data include fabric construction (ceiling, roof, walls, and floor), U value (thermal properties), climate conditions, the efficiency of space heating systems, and occupants. Simulations for heating and cooling demand are set under both local and national design standards with spatial data, such as building geometry, obtained through Google Earth. The details of the simulation setting, relating to building constructions, can be referenced from previous research [31]; data input and output are shown in Figure 9, and the operational schedule is set in Table 5.

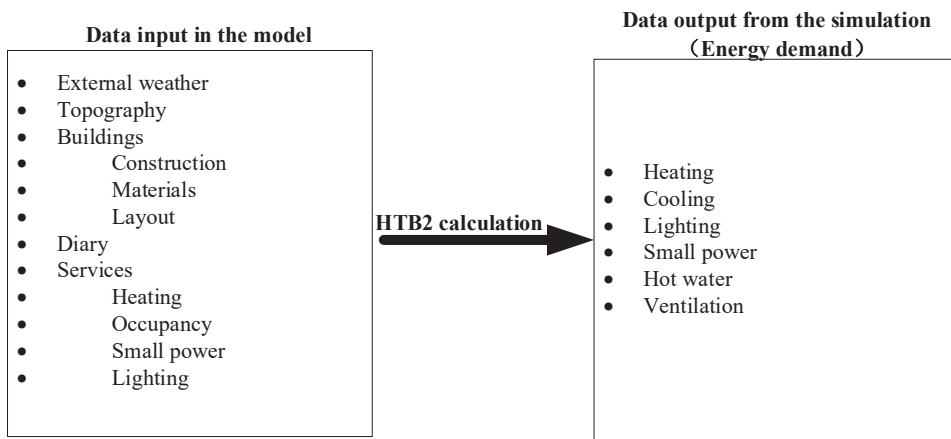


Figure 9. Data input to the data output of the model (HTB2 user manual 2.10).

Table 5. The parametric setting for urban building energy simulation (the design standard for energy efficiency of residential buildings in hot summer and cold winter zone (2010); the design standard for energy efficiency of public buildings (2015)).

Parametric Setting	Building Types				
	Residential Building	Hotel Building	Commercial Building	Office and Education Building	Transportation Building
Heating/cooling schedule	8 November–4 March; 6 May–8 September	8 November–4 March; 6 May–8 September	8 November–4 March; 6 May–8 September	8 November–4 March; 6 May–8 September	8 November–4 March; 6 May–8 September
	Mon–Fri 00:00–08:00 and 18:00–24:00 Sat–Sun 00:00–24:00	Mon–Sun 1:00–24:00	Mon–Sun 09:00–21:00	Mon–Fri 08:00–18:00	Mon–Sun 00:00–24:00
Setpoint (°C)	18/26	22/25	18/25	20/26	18/25
Internal heat gains (occupancy, lighting, and small power)	15 W/m ²	25 W/m ²	40 W/m ²	20 W/m ²	60 W/m ²
Air change per hour	1.0	2.0	2.5	2.0	2.5

5. Results Analysis and Validation

5.1. Results Analysis

Results of the simulation are operational energy demands from cooling and heating and other components, such as lighting, hot water, and small power, as depicted in Figure 10. Building types influence energy consumption, and electricity and natural gas are major contributors to carbon dioxide emissions.

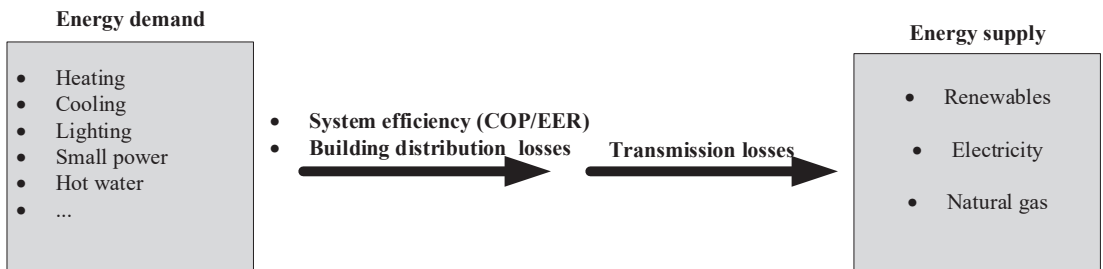


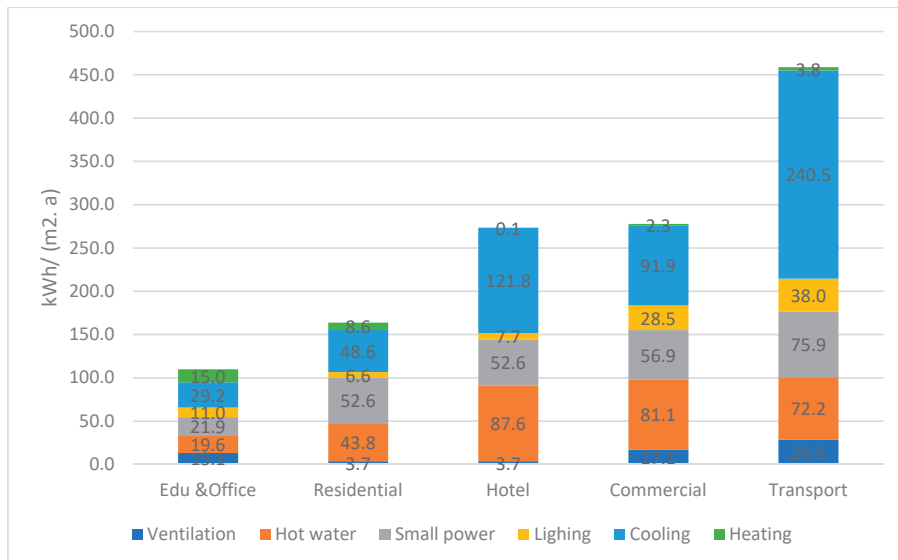
Figure 10. Energy demand to energy supply in buildings [31].

Table 6 shows the annual energy demand for heating and cooling among five building types. There is a noticeable difference between the energy demand for cooling and heating in the study area. In terms of cooling energy demand, residential buildings consume 45 GWh per year, followed by transport and commercial buildings. This may be because these types of buildings have the largest floor areas, therefore requiring the most cooling energy. While the areas occupied by transport buildings are not as large as other buildings, they consume more energy, as they are open 24 h a day, especially during extreme weather conditions.

Table 6. Output of annual heating and cooling demands, based on five building functions.

Building Type	Count	Building Floor Area (m ²)	Heating Demand (kWh/year)	Cooling Demand (kWh/year)	Heating Demand (kWh/m ² /year)	Cooling Demand (kWh/m ² /year)
Office and education	40	187,121	2,813,697	−5,471,758	15	−29
Residential	141	918,681	7,878,151	−44,640,650	9	−49
Hotel	15	88,825	7484	−10,816,210	0	−122
Commercial	20	174,181	39,160	−16,007,554	2	−92
Transport	3	71,188	270,576	−17,117,151	4	−240

Figure 11 depicts the energy demand of five types of buildings. These are cooling, hot water, SPW (small power), lighting, ventilation, and heating, with negligible proportions. Despite having the smallest floor area, transport buildings consume the most energy, followed by hotels and commercial buildings. Based on their functions and operational schedule, these features demonstrate high potential for energy savings in commercial and transportation buildings. Figure 11 also shows that the energy intensity (kWh/m²/a) from transport and commercial buildings is higher than that from residential and office buildings, clearly visible. It may be attributed to two factors: the longer time spent in daily operation in these two types of buildings and large number of people inside, which results in greater cooling demand in summer.

**Figure 11.** Energy demand by components of the five building types.

5.2. Results Validation

Table 7 compares the benchmark of energy use intensity, with the modelling prediction results for transport, commercial, hotels, office, and educational buildings; it clearly shows that the prediction results are in line with the benchmark, apart from residential buildings, which are more than the benchmark. There are several possible reasons for this. Firstly, the investigation does not provide data on the façade of residential buildings, so the simulation

is based on local building design standards. As such, this differs from actual situations, which would result in a discrepancy in energy demand for residential buildings.

Table 7. Benchmarks of energy demand (kWh/(m²·a) in Wuhan [33].

Building Type	Building Description	Mean Value	Standard Deviation	Prediction
Residential	Below 90 square metres	60.1	32.2	163.8
	Above 90 square metres area (excluding luxury residential)	43.9	32.2	
	Luxury residential	91.3	21.8	
Office	Standard office buildings (using a centralised air-conditioning system)	67.7	19.0	109.4
	Standard office buildings (using split air-conditioning)	58.1	36.2	
	Government office buildings with central air-conditioning system	90.4	27.4	
Educational	Kindergarten	29.7	14.0	
	Primary school	18.2	9.4	
Hotel	Three stars and above	233.1	114.6	273.3
	Below three stars	216.5	-	
Commercial	Large supermarket	263.8	92.1	277.8
	Large shopping malls	207.9	106.6	
	Medium and small supermarket	371.6	-	
	Middle and small shopping malls	207.6	-	
	Shops	43.2	-	
Transport	Bus terminal	55.0	-	458.8
	Railway station	469.6	-	

Moreover, since most residential buildings date back to the 1990s, while public buildings were constructed around 2005, the heating systems in most of them are inefficient and outdated. Additionally, central cooling systems were not used in Wuhan at that time, contributing to the high energy use intensity of the residential buildings. These factors

would significantly affect the difference between the predicted energy use intensity and benchmark level of residential buildings.

6. Discussion and Conclusions

This study employs physical-based, bottom-up models to predict urban building operational energy demand, and the modelling process involves data inputs, modelling, and validation. However, physical-based, bottom-up models are based on calculating every building's energy consumption, and they can deal with the interconnections between the buildings and the surrounding environment, e.g., shading effects. These models need a vast amount of data to characterise every building and require significant computational effort. Therefore, they are typically used for highly technical purposes, such as providing high-quality data for energy planning, large-scale community retrofitting, and optimisation.

For urban building energy model simulations, the largest uncertainty is associated with the definition and detailed description of archetypes that represent a building stock reliably. In most cases, it is impossible to estimate simulation uncertainty or calibrate an urban building energy model to reduce errors, because there is a tight restriction on access to measured building energy use and general lack of knowledge about the thermal properties of buildings.

The validation studies of urban building energy models for larger groups of buildings showed good agreement with measurements, but simulation errors were significantly higher for individual buildings [7,34].

This research made the building operational energy demand forecast based on hot summer and cold winter climatic zones, as an example, not considering other climate zones. However, energy demand from buildings is highly correlated with climate conditions particularly used for heating and cooling. Additionally, there were assumptions during the modelling of the building stock. For example, commercial buildings may have a mixed-function purpose. VirVil treats each type of building as a single function and the whole individual building as a thermal zone for calculation.

Furthermore, buildings consume energy from the whole life cycle. This research only focuses on operational energy consumption, while disregarding other processes, such as materials production and transport (embody energy).

This research successfully uses an archetype physical-based, bottom-up method to forecast the energy demand from building stock at the urban level. It concludes:

- An archetypal physics-based, bottom-up approach is feasible to predict urban energy consumption from building stock. Compared with the predicted outcome, the benchmark level proves that this is a feasible and reproducible approach.
- Findings indicate that transport and commercial buildings used the most energy, significantly more than office and residential buildings. Consequently, these two types of buildings would receive more attention for energy efficiency.
- The cooling demand far outweighs the heating demand across all building types in Wuhan. Hence, improving system cooling efficiency is a priority for energy savings.

Author Contributions: Methodology, Q.D.; conceptualisation, C.L.; formal analysis, Q.J., M.M. and Y.B.; investigation, M.M. and Y.B.; resources, Q.D. and C.L.; data curation, M.M. and Y.B.; writing—original draft, Q.J.; writing—review and editing, Q.J.; supervision, C.L.; project administration, X.Z.; funding acquisition, X.Z. All authors have read and agreed to the published version of the manuscript.

Funding: This study was funded by the Fundamental Research Funds for the Central Universities (WUT: 2021IVA006B; 2021IVA034) and Hubei Provincial Natural Science Foundation (grant no. 2021CFB005).

Informed Consent Statement: Not applicable.

Conflicts of Interest: The authors declare no conflict of interest.

References

- Hong, T.; Chen, Y.; Luo, X.; Luo, N.; Lee, S.H. Ten Questions on Urban Building Energy Modeling. *Build. Environ.* **2020**, *168*, 106508. [CrossRef]
- Ding, C.; Feng, W.; Li, X.; Zhou, N. Urban-Scale Building Energy Consumption Database: A Case Study for Wuhan, China. *Energy Procedia* **2019**, *158*, 6551–6556. [CrossRef]
- Statista China: Urbanisation. 2021. Available online: <https://www.statista.com/statistics/270162/urbanization-in-china/> (accessed on 20 February 2022).
- National Bureau of Statistics of China *China Statistical Yearbook*; China Statistics Press: Beijing, China, 2020.
- Wong, C.H.H.; Cai, M.; Ren, C.; Huang, Y.; Liao, C.; Yin, S. Modelling Building Energy Use at Urban Scale: A Review on Their Account for the Urban Environment. *Build. Environ.* **2021**, *205*, 108235. [CrossRef]
- Hong, T.; Langevin, J.; Sun, K. Building Simulation: Ten Challenges. *Build. Simul.* **2018**, *11*, 871–898. [CrossRef]
- Reinhart, C.F.; Cerezo Davila, C. Urban Building Energy Modeling—A Review of a Nascent Field. *Build. Environ.* **2016**, *97*, 196–202. [CrossRef]
- Ferrando, M.; Causone, F.; Hong, T.; Chen, Y. Urban Building Energy Modeling (UBEM) Tools: A State-of-the-Art Review of Bottom-up Physics-Based Approaches. *Sustain. Cities Soc.* **2020**, *62*, 102408. [CrossRef]
- Kavgic, M.; Mavrogianni, A.; Mumovic, D.; Summerfield, A.; Stevanovic, Z.; Djurovic-Petrovic, M. A Review of Bottom-up Building Stock Models for Energy Consumption in the Residential Sector. *Build. Environ.* **2010**, *45*, 1683–1697. [CrossRef]
- Swan, L.G.; Ugursal, V.I. Modeling of End-Use Energy Consumption in the Residential Sector: A Review of Modeling Techniques. *Renew. Sustain. Energy Rev.* **2009**, *13*, 1819–1835. [CrossRef]
- Zhao, H.; Magoulès, F. A Review on the Prediction of Building Energy Consumption. *Renew. Sustain. Energy Rev.* **2012**, *16*, 3586–3592. [CrossRef]
- Bentzen, J.; Engsted, T. A Revival of the Autoregressive Distributed Lag Model in Estimating Energy Demand Relationships. *Energy* **2001**, *26*, 45–55. [CrossRef]
- Ali, U.; Shamsi, M.H.; Hoare, C.; Mangina, E.; O'Donnell, J. Review of Urban Building Energy Modeling (UBEM) Approaches, Methods and Tools Using Qualitative and Quantitative Analysis. *Energy Build.* **2021**, *246*, 111073. [CrossRef]
- Huo, T.; Ren, H.; Cai, W. Estimating Urban Residential Building-Related Energy Consumption and Energy Intensity in China Based on Improved Building Stock Turnover Model. *Sci. Total Environ.* **2019**, *650*, 427–437. [CrossRef] [PubMed]
- Li, W.; Zhou, Y.; Cetin, K.; Eom, J.; Wang, Y.; Chen, G.; Zhang, X. Modeling Urban Building Energy Use: A Review of Modeling Approaches and Procedures. *Energy* **2017**, *141*, 2445–2457. [CrossRef]
- Shorrock, L.D.; Dunster, J.E. The Physically-Based Model BREHOMES and Its Use in Deriving Scenarios for the Energy Use and Carbon Dioxide Emissions of the U.K. Housing Stock. *Energy Policy* **1997**, *25*, 1027–1037. [CrossRef]
- Ferrando, M.; Causone, F. An Overview of Urban Building Energy Modelling (UBEM) Tools. *Build. Simul.* **2020**, *16*, 3452–3459.
- Heiple, S.; Sailor, D.J. Using Building Energy Simulation and Geospatial Modeling Techniques to Determine High Resolution Building Sector Energy Consumption Profiles. *Energy Build.* **2008**, *40*, 1426–1436. [CrossRef]
- Lim, H.; Zhai, Z.J. Review on Stochastic Modeling Methods for Building Stock Energy Prediction. *Build. Simul.* **2017**, *10*, 607–624. [CrossRef]
- Foliente, G.; Seo, S. Modelling Building Stock Energy Use and Carbon Emission Scenarios. *Smart Sustain. Built Environ.* **2012**, *1*, 118–138. [CrossRef]
- Sun, K.; Hong, T.; Taylor-Lange, S.C.; Piette, M.A. A Pattern-Based Automated Approach to Building Energy Model Calibration. *Appl. Energy* **2016**, *165*, 214–224. [CrossRef]
- Chong, A.; Lam, K.P.; Pozzi, M.; Yang, J. Bayesian Calibration of Building Energy Models with Large Datasets. *Energy Build.* **2017**, *154*, 343–355. [CrossRef]
- O'Neill, Z.; Eisenhower, B. Leveraging the Analysis of Parametric Uncertainty for Building Energy Model Calibration. *Build. Simul.* **2013**, *6*, 365–377. [CrossRef]
- Yang, T.; Pan, Y.; Mao, J.; Wang, Y.; Huang, Z. An Automated Optimisation Method for Calibrating Building Energy Simulation Models with Measured Data: Orientation and a Case Study. *Appl. Energy* **2016**, *179*, 1220–1231. [CrossRef]
- Monetti, V.; Davin, E.; Fabrizio, E.; André, P.; Filippi, M. Calibration of Building Energy Simulation Models Based on Optimisation: A Case Study. *Energy Procedia* **2015**, *78*, 2971–2976. [CrossRef]
- Fonseca, J.A.; Schlueter, A. Integrated Model for Characterisation of Spatiotemporal Building Energy Consumption Patterns in Neighborhoods and City Districts. *Appl. Energy* **2015**, *142*, 247–265. [CrossRef]
- Sokol, J.; Cerezo Davila, C.; Reinhart, C.F. Validation of a Bayesian-Based Method for Defining Residential Archetypes in Urban Building Energy Models. *Energy Build.* **2017**, *134*, 11–24. [CrossRef]
- Cardiff University VirVil SketchUp Extension. Available online: <http://u001.arch.cf.ac.uk/Plug-in/> (accessed on 16 January 2022).
- Jones, P.; Patterson, J.; Lannon, S. Modelling the Built Environment at an Urban Scale—Energy and Health Impacts in Relation to Housing. *Landsc. Urban Plan.* **2007**, *83*, 39–49. [CrossRef]
- Huang, J.; Jones, P.; Peng, R.; Li, X.; Hou, S. An Integrated Model for Urban Microclimate and Building Energy in High-Density Cities for Early Stage Design. In Proceedings of the 15th Conference of International Building Performance Simulation Association, San Francisco, CA, USA, 7–9 August 2017.

31. Ji, Q. Investigating Low Carbon Development of High-Density Building Clusters Located around Railway Passenger Transport Hubs in China. Ph.D. Thesis, Cardiff University, Cardiff, UK, 2018.
32. Bassett, T.; Lannon, S.C.; Waldron, D.; Jones, P.J. Calculating the Solar Potential of the Urban Fabric with SketchUp and HTB2. Presented at Solar Building Skins [Online]. Bressanone, Italy, 6–7 December 2012, Cardiff University, ORCA Website. Available online: <https://orca.cardiff.ac.uk/41395/> (accessed on 16 March 2022).
33. Yu, Y.; Li, Y.; Xiang, D.; Jiang, X. Study on energy consumption quota of civil buildings in Wuhan. *Build. Sci.* **2014**, *30*, 106–112. (In Chinese)
34. Dall'O', G.; Galante, A.; Torri, M. A Methodology for the Energy Performance Classification of Residential Building Stock on an Urban Scale. *Energy Build.* **2012**, *48*, 211–219. [[CrossRef](#)]

Article

A Design and Comparative Analysis of a Home Energy Disaggregation System Based on a Multi-Target Learning Framework

Bundit Buddhahai ¹, Suratsavadee Koonlaboon Korkua ^{2,*}, Pattana Rakkwamsuk ³ and Stephen Makonin ⁴¹ School of Informatics, Walailak University, Nakhon Si Thammarat 80161, Thailand² School of Engineering and Technology, Walailak University, Nakhon Si Thammarat 80161, Thailand³ School of Energy, Environment and Materials, King Mongkut's University of Technology Thonburi, Bangkok 10140, Thailand⁴ School of Engineering Science, Simon Fraser University, Burnaby, BC V5A 1S6, Canada

* Correspondence: ksuratsa@wu.ac.th

Abstract: Insightful information on energy use encourages home residents to conduct home energy conservation. This paper proposes an experimental design for an energy disaggregation system based on the low-computational-cost approaches of multi-target classification and multi-target regression, which are under the multi-target learning framework. The experiments are set up to determine the optimal learning algorithm and model parameters. In addition, the designated system can provide inference of the appliance power state and the estimated power consumption from both approaches. The kernel density estimation technique is utilized to formulate the appliance power state as a finite-state machine for the multi-target classification approach. Multi-target regression can directly provide the estimation of appliance power demand from the aggregate data, and this work unifies the system's design together with multi-target classification. The predictive performances obtained through the F-score (micro-averaged) and power estimation accuracy index for the power state inference and the estimated power demand, respectively, are shown to outperform a deep-learning-based denoising autoencoder network under the same data settings from both approaches. The results lead to a recommendation to apply the approach in home energy monitoring, which is mainly based on the characteristics of appliance power and the information that the residents wish to perceive.

Keywords: energy disaggregation; non-intrusive load monitoring; multi-target learning; home energy monitoring

Citation: Buddhahai, B.; Korkua, S.K.; Rakkwamsuk, P.; Makonin, S. A Design and Comparative Analysis of a Home Energy Disaggregation System Based on a Multi-Target Learning Framework. *Buildings* **2023**, *13*, 911. <https://doi.org/10.3390/buildings13040911>

Academic Editors: Yaolin Lin and Wei Yang

Received: 2 February 2023

Revised: 17 March 2023

Accepted: 21 March 2023

Published: 30 March 2023



Copyright: © 2023 by the authors. Licensee MDPI, Basel, Switzerland. This article is an open access article distributed under the terms and conditions of the Creative Commons Attribution (CC BY) license (<https://creativecommons.org/licenses/by/4.0/>).

1. Introduction

Energy disaggregation, or non-intrusive load monitoring (NILM), is a system of data analysis that aims to determine the operation status or energy consumption of individual appliances from the total energy consumption data of a building [1]. The benefit of perceiving the information on energy use at the appliance level was the motivation to reduce the use of some specific appliances or prevent energy wastage [2]. A study found that residential users could reduce energy costs by at least 12% when obtaining information on appliance-level energy use in a real-time scenario with a contrast of 4–8% when perceiving the traditional information on the whole energy usage on a weekly or monthly basis [3]. Another benefit to grid distributors was that the detailed information on energy use could help in shaping energy policy based on consumption behavior to balance the electricity demand and supply scheme [4].

Data learning and inference are important components for developing an efficient energy disaggregation system. The development of the system could be classified mainly into two categories: event-based and non-event-based systems [5]. The former category

dealt with detecting power switch events (power ON \leftrightarrow OFF), which had two sub-categories of detecting steady-state power consumption changes (ΔP and ΔQ) [1,6] and power-ON transient patterns [7,8]. Both features were different for each appliance, which could be utilized to learn if the target appliances were being turned on or off. The integration of both features for data learning could enhance the disaggregation performance since the latter would be unique for different appliance types [9]. The transient patterns, however, required dedicated and high-cost hardware to capture the high-frequency components and perform complex data processing. These challenges have inhibited the adoption of this approach to the current power meters, which usually perform data manipulation at low frequencies [10]. The non-event-based category, on the other hand, involved the operation of decomposing the appliance status from the aggregate data without relying on detecting switch events. Thus, it allowed the utilization of a low-frequency measurement system which could enable a lower cost of development. This category could mainly be classified into three sub-categories: pattern classification, hidden-Markov-model-based, and deep learning [5,11]. The first sub-category referred to mapping each sample of aggregate data to the operating status (ON/OFF) of appliances with the help of traditional classification algorithms, such as neural networks [12] and support vector machines [13]. This category treated each load label independently, which might not comply with a real scenario in which an appliance might be used together with other certain appliances (e.g., a DVD player and a television) [14]. The second sub-category involved applying a factorial hidden Markov model (FHMM) and its variant models to set up the model parameters using the probability density function. The model factorized the aggregate data into a sequence of operation states (as a finite-state machine model) for appliances that were hidden from the observer [15–17]. The major drawback of these approaches was the model's complexity, which increased exponentially when the number of appliances increased [5]. The third sub-category employed a deep neural network (DNN) framework which has been recently applied in many applications of data learning due to its capabilities of automatic feature processing and learning complex problems. Various network topologies were investigated to estimate the power demand for each appliance, for example, long short-term memory (LSTM) [18], convolutional neural networks (CNNs) [19,20], and autoencoder networks [21,22]. Another major drawback of these frameworks was the model's complexity, which involved a number of network parameters and configurations for model optimization.

From the previous studies, the major approaches could have the ability to provide one or two important pieces of information in the NILM application; (1) the identification of the appliance's operation state and (2) the estimation of the power demand for appliances. Some approaches could provide both pieces of information, but they have a high computational cost in the model's configuration. This paper proposes an NILM system design based on a low-computational-cost approach to the multi-target learning framework, which can formulate the problem in the multi-target data format well to identify multiple appliances. The framework is classified into two approaches: multi-target classification (MTC) and multi-target regression (MTR). The MTC approach formulates the appliance power state using kernel density estimation (KDE), the proposed method for power state modeling, as the finite-state machine. The MTR approach involved less data processing than the MTC, and each approach was previously proposed independently [23,24]. This work unifies the system design of both approaches under the multi-target learning framework. The experiments illustrate the process to obtain the optimal predictive performance of an appliance power state inference and the estimated power demand. In addition, a comparative analysis of the performance and characteristics of the approaches is delivered for a decision to apply in a home energy monitoring system. The key contributions of this work are summarized as follows:

- (1) An NILM system design based on multi-target classification and multi-target regression is proposed as a unified system of a multi-target learning framework. Both

approaches can provide the inference of an appliance power state and the estimated power demand, which are the key outputs of the system.

- (2) A power state modeling using KDE for the multi-target classification approach is proposed.
- (3) The comparative analysis of the predictive performance for the multi-target classification, multi-target regression, and a denoising autoencoder (DAE) approach is provided for the consideration of applying the approach in a field application.

2. Materials and Methods

This section describes the general concept of the multi-target learning framework, the experimental data, and the process that demonstrates how a home energy disaggregation using this framework could be implemented. Each topic is described as follows.

2.1. Multi-Target Learning

Multi-target learning is a subfield of supervised learning for multiple outputs tasks that learn data by simultaneously mapping a set of input features to a set of output labels [25]. The learning framework has been applied in many application areas such as image classification, text mining [26], and predicting the model parameters for plantation study [27]. The general learning framework has a task of determining a function $f: X \rightarrow Y$ from a training set of $\{(x_i, y_i) \mid 1 \leq i \leq n\}$, where n is the number of training samples, $x_i \in X$ is a vector of the input features, and $y_i \in Y$ is the associated output labels with x_i [25]. Then, the function acts as a learning model to provide predicted outputs to an unknown input sample. The common learning approach that can be applied to the NILM task is multi-target classification and multi-target regression [28,29]. This is because the purpose of the task is to determine the estimated power demand (numeric values) and/or the appliance operation states (nominal values) from the aggregate data.

Data manipulation for the multi-target learning framework can be classified into two approaches of problem transformation and algorithm adaptation [28,30]. The former approach uses a multi-target learner (classifier or regressor) to transform the multiple output labels into a set of individual or group of labels. It then uses a conventional single-output learning algorithm (as the based learner) to tackle the problem. The latter approach adapts the single-output learning algorithm to directly learn the multi-output data. The learning algorithms used in this work were under the problem transformation approach that is available by the experimentation tools, including:

- (1) Class relevance (CR) or single target (ST): treat and learns each output independently [26].
- (2) Classifier chain (CC) or regressor chain (RC): cascade each output label to the input features and build dependent classifiers/regressors for voting [31].
- (3) Random k-label sets with disjoint subsets (RAkELd): randomly partition the output labels into small groups of concatenated single-output problems [32].

A major advantage of data learning through the multi-target learning framework over the data learning through independent output labels (as the single-output data learning) is the characteristics of labels correlation among the outputs (as CC and RAkELd) which showed to provide outperform-predictive performances [31,32].

2.2. Experimental Data

The electricity consumption data used in this experiment were collected from a residence in Bangkok, Thailand and gathered as the Supplementary Material [33]. The data consist of an aggregate circuit and ten sub-circuits of appliance usage, with a one-minute interval for each sample and four months of data length. The electrical parameters for each circuit consist of the current (I), active power (P), reactive power (Q), and power factor (PF). In this work, six appliance labels (measurement circuits) that were frequently used and significantly contributed to total energy consumption were evaluated. The multi-target dataset was created using the four parameters of the aggregate circuit as the input (X) and the appliances' power state (for MTC data) or the appliances' power consumption (for

MTR data) as the outputs (Y). The load description for each appliance label was presented in Table 1.

Table 1. Load label under experiments.

Load Label	Power Range (kW)	Load Description
LTL	0.03–0.30	Living room lightings
LTB1	0.02–0.15	Bedroom 1 lightings
PGB1	0.06–1.60	Bedroom 1 plugging loads
PMP	0.09–1.60	Water pump
WTB1	0.01–3.20	Bedroom 1 water heater
ANB1	0.02–1.50	Bedroom 1 air-conditioner

2.3. Experimental Design

The data processing procedure is evaluated as an experimental design where the main objective is to determine the optimized learning model and predictive performance for both MTC and MTR approaches. For the MTC approach, KDE modeling converted the sub-circuits power data into the discrete power state of the appliances. The MTC dataset was constructed using the aggregate data as the input and the appliances' power state data as the outputs. The data learning was proceeded by selecting the optimized MTC algorithm and model parameters where the data inference process was to determine the predicted power state and relevant power consumption data of the appliances. For the MTR approach, the MTR dataset was constructed directly from the aggregate data and the sub-circuits power data. The data learning optimized the MTR algorithm and model parameters where the data inference provided the estimated power consumption and the relevant power state of the appliances. The evaluation procedure was summarized in the flowchart shown in Figure 1.

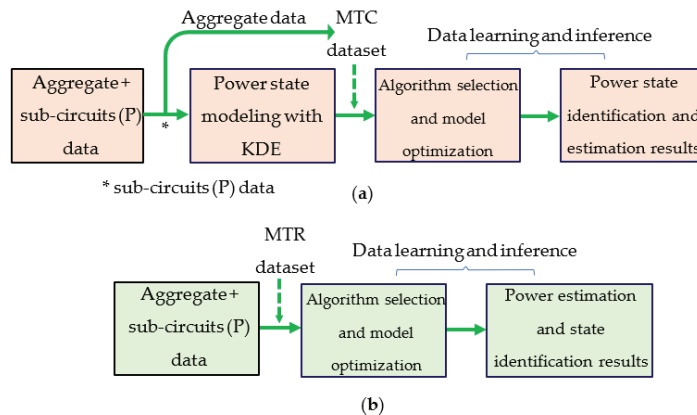


Figure 1. The procedure of experimental design for (a) multi-target classification (b) multi-target regression approach.

The KDE for MTC power state modeling is a statistical approach used for estimating the probability density function (PDF) of a random variable x with n samples (x_1, x_2, \dots, x_n) and a distribution function (f) [34]. The estimated shape or kernel estimator (\hat{f}) of the function can be described by Equation (1). K is the kernel function, in which the Gaussian distribution is chosen as an assumption of normal distribution for regular power data; h is the bandwidth of the kernel and acts as a smoothing parameter.

$$\hat{f}(x) = \frac{1}{nh} \sum_{i=1}^n K\left(\frac{x - x_i}{h}\right) \quad (1)$$

The main idea of using the technique for appliance power state modeling is the inherent power states which would exhibit a certain range of power demand data. The frequent data should be easily observed and extracted through a KDE plot. The parameter h was selected empirically to make the peaks obvious, and the positions of the peaks were determined through Python's `argrextrema` function which calculated the relative extrema within the list of data. Thus, the number and position of the peaks would represent the number of power states and the power representatives associated with that state, respectively.

The appliance power state of the MTC dataset was created by mapping the power data to the nearest element within the set of the power state representatives; the associated power state value could then be determined. For example, a three-state appliance label (the possible set of states was $\{0, 1, 2\}$) has the set of power representatives $\{0, 0.05, 0.25\}$ kW. If a data sample has the power data of 0.1 kW, it would be mapped to state '1' since it has the least distance among the associated power state representatives. For the MTR dataset, the power data were created using the actual power data from the individual appliance as the data for each output label.

To compare the predictive performance between the MTC and MTR, both classification and regression tasks from each approach were evaluated. The regression task from the MTC was obtained by mapping the result of the predicted state to its associated power representation values. The estimated appliance power data were then bound by the defined power states. The classification task from the MTR was obtained by defining the binary power state (on/off) for the actual and the estimated power data. This was achieved by having the power data below the operation state as described in Table 1 to be '0' (off), otherwise, '1' (on).

2.4. Evaluation Tools and Performance Index

This work used Python (ver. 3.7) with the Scikit-learn library (ver. 0.19.2) [35] and Meka (release 1.9.6) [36] for multi-target data learning and inference. The Python library provides the `sklearn.multioutput` method for both classification and regression tasks with a couple of learning algorithms from the problem transformation approach. The library, however, has partially supported the multi-target classification task, which would not be able to perform cross-validation tasks. Thus, Meka software, an application for learning multi-target classification algorithms, was used to perform this task instead. The performance indexes used in this work were based on determining the performance of power state identification as the classification task (Hamming score and F-score) and the performance of power consumption data estimation as the regression task (power estimation accuracy). Each index is described as follows.

- Hamming score: the compliment of Hamming loss (Hamming score = $1 - \text{Hamming loss}$), where Hamming loss [30] indicates the fraction of an incorrect classification through the entire set of output labels. Thus, the Hamming score can be expressed as Equation (2).

$$\text{Hamming score} = 1 - \frac{1}{n} \left(\sum_{i=1}^n \frac{1}{L} |\hat{y}_i \Delta y_i| \right) \quad (2)$$

where n and L are the number of samples and the number of output labels, respectively. Δ is the operator to determine the number of differences between the set of actual output labels (y) and the predicted labels (\hat{y}) for a sample. This index was used to evaluate performance for the whole output labels in the algorithm selection process by the Meka software.

- F-score: the harmonic mean between precision and recall was used for the classification task. This index was commonly employed to determine the appliance classification performance rather than the accuracy because the result would not be altered by data with high-imbalanced classes [16,37]. The micro-averaged value was used to make a fair comparison between the results of MTC (finite-state class: $\{0, 1, \dots, C\}$, C : number of classes) and MTR (binary class: $\{0, 1\}$). The key concept of micro-averaging was to average the calculation of tp , fp , and fn , respectively, across all samples first, which

was suitable for determining and comparing the output label with a different number of classes. The micro-averaged F-score was defined through the micro-averaged precision and micro-averaged recall, as presented in Equations (3)–(5).

$$\text{Precision (micro)} = \frac{\sum_{i=1}^L tp_i}{\sum_{i=1}^L tp_i + \sum_{i=1}^L fp_i} \quad (3)$$

$$\text{Recall (micro)} = \frac{\sum_{i=1}^L tp_i}{\sum_{i=1}^L tp_i + \sum_{i=1}^L fn_i} \quad (4)$$

$$F\text{-score (micro)} = \frac{2 \times \text{Precision(micro)} \times \text{Recall(micro)}}{\text{Precision(micro)} + \text{Recall(micro)}} \quad (5)$$

where tp_i , fp_i , and fn_i are the number of true positives, false positives, and false negatives, respectively, for the output label i . L is the number of output labels [30].

- The power estimation accuracy: the index determines how good the power estimation by the regression model [15,38] is by calculating the complement of the power estimation error ratio over the test samples. It is defined for the individual appliance label and the entire dataset by Equations (6) and (7), respectively.

$$\text{Power est. acc. (by label)} = 1 - \frac{\sum_{i=1}^n |\hat{y}_i - y_i|}{2(\sum_{i=1}^n y_i)} \quad (6)$$

$$\text{Power est. acc. (by dataset)} = 1 - \frac{\sum_{i=1}^n \sum_{l=1}^L |\hat{y}_i^l - y_i^l|}{2 \cdot \sum_{i=1}^n \sum_{l=1}^L y_i^l} \quad (7)$$

where y_i^l and \hat{y}_i^l are the actual and predicted output sample i of label l , respectively. n and L are the number of samples and the number of output labels, respectively.

3. Results and Discussion

This section provides the experimental results and analysis from the data learning process using the multi-target classification and multi-target regression approaches.

3.1. Multi-Target Classification Approach

3.1.1. Appliance Power States Modeling Using KDE

The number and representative data of power states for each appliance were analyzed using the KDE plot, as presented in Figure 2, which illustrated the distribution or density of appliance power data and inherent power states.

Appliance labels LTL and ANB1 had obvious peaks, which showed that they had distinguishable operation states (e.g., off/dim/full for lightings or off/on for an inverter-type air-conditioner) with a low variance in power data. On the other hand, the other appliance labels that consisted of multiple appliances (plugging appliances, PGB1) or continuous-variable appliances (water heater, WTB1) had a high variance of power data. These loads occurred along with inapparent peaks in the KDE plots, which were then averaged within the range to determine the representations. Each applicable peak and its position represented the power state and the power state representative value, which developed the number of power states, as the result shown in Table 2 outline.

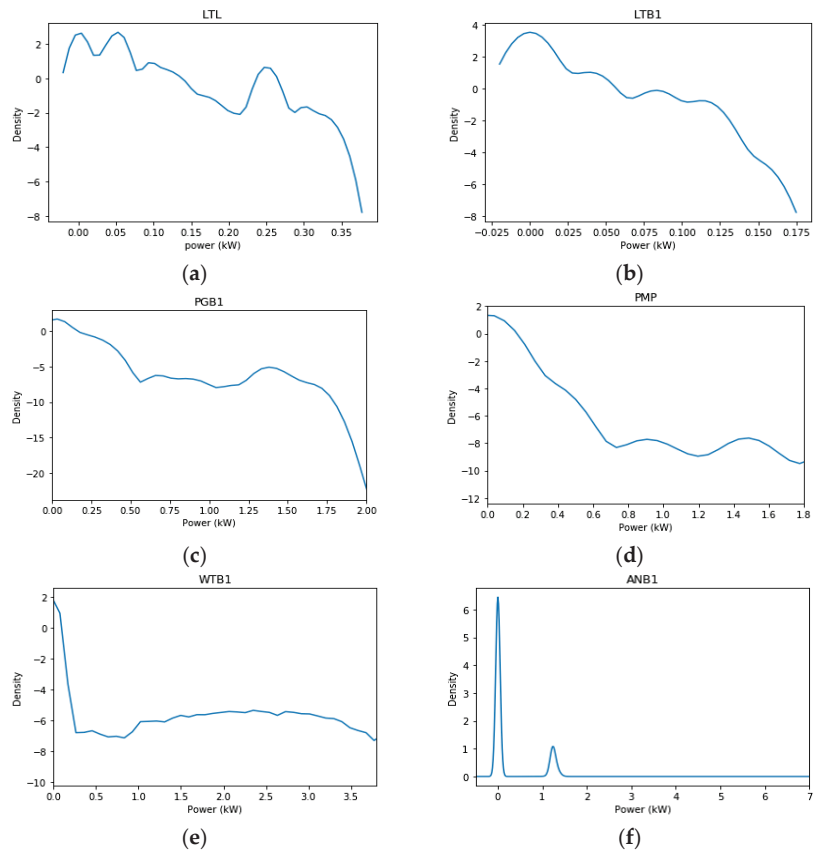


Figure 2. Power distribution through KDE plots for appliance label (a) LTL; (b) LTB1; (c) PGB1; (d) PMP; (e) WTB1; and (f) ANB1.

Table 2. Power state representation of appliance label using KDE plot.

Load Label	Power State Representatives (kW)	Number of States
LTL	{0, 0.05, 0.25}	3
LTB1	{0, 0.04, 0.11}	3
PGB1	{0.02, 0.40, 1.40}	3
PMP	{0, 0.33, 1.48}	3
WTB1	{0, 1.20, 2.35}	3
ANB1	{0, 1.24}	2

3.1.2. Algorithm Selection and Model Optimization

The experiment consisted of selecting the optimal classification algorithm by comparing the performance of some candidates. Then, the best candidate will be further evaluated to choose the best set of model parameters.

A performance evaluation of different learning algorithms was conducted through cross-validation ($K = 10$) to obtain a performance value over the whole dataset. Meka's Experimenter mode was used to perform the task where the experimentation was set for a comparative evaluation of multiple algorithms under the same environment setting. Table 3 presents the result of the comparison, where all the model parameters are set to default.

Table 3. Hamming score by different MTC algorithms.

Algorithm	Hamming Score
Class relevance (CR) + random forest	0.734 ± 0.002
Classifier chain (CC) + decision tree	0.734 ± 0.002
Classifier chain (CC) + random forest	0.734 ± 0.001
RAkELd + decision tree	0.735 ± 0.002
RAkELd + random forest	0.736 ± 0.001

The MTC algorithm RAkELd with random forest as the based classifier won the competition even though its result was not statistically significant in difference. This classifier was then tested for the best model parameters by using the MultiSearch function in Meka’s Explorer mode through the required parameters and test range. The function evaluated each combination of model parameters under the test range and returned the parameter setup that provided the best model performance.

For the RAkELd + random forest classifier, there were two parameters put into this test; ‘k’, which controlled the number of partitioned labels for the multi-target classifier (‘k’ was bounded by $1 \leq k < L/2$, where L was the number of output labels). The other parameter was numIterations, which controlled the number of trees in the random forest classifier. The results of the parameter selection and the optimal predictive performance are shown in Table 4.

Table 4. Model parameters selection and optimized performance for the MTC model.

Parameter	Evaluation Set	Optimized Parameter	Optimized Hamming Score
k (RAkELd)	{1, 2, 3, 4}	4	0.738
numIterations (random forest)	{30, 50, 80, 100}	80	

3.1.3. Testing Performance Evaluation

The optimized model setup was deployed for evaluating the predictive performance by individual labels using the Scikit-learn library. The dataset was split for the training set and test set by an 80:20 proportion. The model was created using the training set, and then we applied the model to predict the test set to obtain the F-score micro-averaged values, as the generalized model performance. The experiments of the power state classification performance and the power estimation accuracy were presented in the following subsections.

Power States Classification Accuracy

This evaluation described how well the model could correctly predict the power state of the appliances. The generalized classification performance of the MTC model is shown in Table 5.

Table 5. Power states identification performance by F-score based on the MTC model.

Load Label	F-Score
LTL	0.876
LTB1	0.896
PGB1	0.940
PMP	0.950
WTB1	0.982
ANB1	0.992

The result showed that the air-conditioner ANB1 obtained the highest F-score value since it was a high-power appliance label with a low fluctuation in terms of the power demand, and it had a lower number of power states (two-state model: OFF/ON). The

model could then distinguish the input data associated with the model more easily, with less confusion compared to other appliance labels with the three-state models.

Power Demand Estimation Accuracy

The predicted power state was mapped to the associated power state representative value, resulting in the estimated power demand predicted by the model. The power estimation accuracy, which compared the estimated power to the ground-truth data, was shown in Table 6.

Table 6. Power demand estimation accuracy associated with the MTC data.

Load Label	Power Estimation Accuracy
LTL	0.730
LTB1	0.520
PGB1	0.755
PMP	0.610
WTB1	0.710
ANB1	0.950

The ANB1 load label still obtained a high accuracy for power estimation since its power states prediction became accurate beforehand. Other load labels, however, were lower in accuracy; this was because their power data fluctuated quite dramatically, and that makes a significant difference between the ground truth and the power representatives as the estimated data.

Apart from the power estimation accuracy, the illustration of power plots could also represent how well the estimated power data could track the ground-truth data. Figure 3 showed a week of test data's power plots for each appliance label.

The lighting, plugging, and the water heater loads, which obtained relatively low power estimation accuracy values, had relevant results to the power plot profiles. For example, the plot showed several false positives for LTL and LTB1 labels, which made the performance value quite low, while PGB1 and WTB1 labels had a considerable gap between the ground truth and the estimated power data due to the fluctuation of the actual power data.

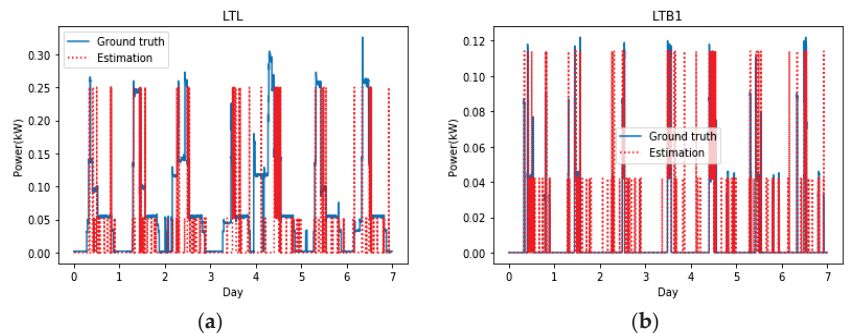


Figure 3. Cont.

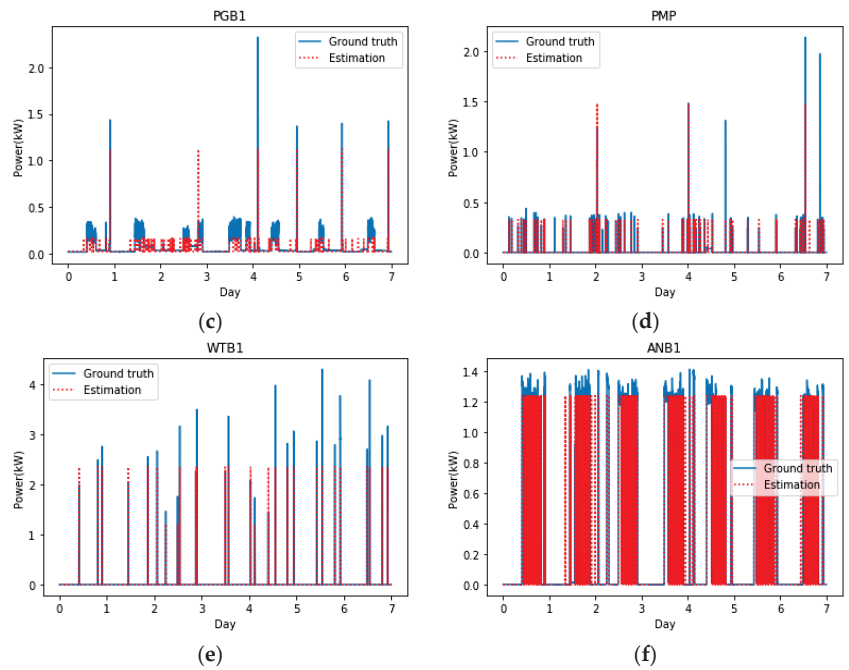


Figure 3. Power data plots of the ground truth and the estimation by the MTC model (a) LTL; (b) LTB1; (c) PGB1; (d) PMP; (e) WTB1; and (f) ANB1.

3.2. Multi-Target Regression Framework

The Python Scikit-learn library supports data learning and inference for the MTR dataset as in the following experiments.

3.2.1. Algorithm Selection and Model Optimization

The dataset was evaluated to pick an MTR algorithm with an optimal regression performance, and then the best candidate was further evaluated to obtain the optimal model parameters. The algorithm selection result through the power estimation accuracy by cross-validation ($K = 10$) was presented in Table 7.

Table 7. Power estimation accuracy by different MTR algorithms.

Algorithm	Power Estimation Accuracy
Single target (ST) + ridge regressor	0.590 ± 0.003
Single target (ST) + gradient boosting regressor	0.885 ± 0.001
Single target (ST) + random forest regressor	0.912 ± 0.001
Regressor chain (RC) + ridge regressor	0.590 ± 0.003
Regressor chain (RC) + random forest regressor	0.900 ± 0.001

The ST multi-target regressor with random forest as the based regressor provided the best result. The optimized regression model parameters were determined using the Python GridSearchCV function. This function evaluated the combination of two model parameters, `max_depth` (the maximum value of depth for the trees) and `n_estimators` (the number of trees in the forest), then it returned the set of parameters that provided the best predictive performance. Table 8 shows the results of this evaluation.

Table 8. Model parameters selection and optimized performance for the MTR model.

Parameter	Evaluation Set	Optimized Parameter	Optimized Power Estimation Accuracy
max_depth	{10, 20, 30, 40, 50}	20	0.915
n_estimators	{10, 20, 30, 50, 80}	80	

3.2.2. Testing Performance Evaluation

The optimized model setup was deployed for evaluating the power estimation performance using the same data split for the training set and test set as the MTC experiment. The experiments of the power estimation and power state prediction performance were presented in the following subsections.

Power Estimation Accuracy

This evaluation described how well the model could estimate the power demand for each appliance label. The generalized regression performance of the model that evaluated the test set was shown in Table 9.

Table 9. Power demand estimation accuracy associated with the MTR model.

Load Label	Power Estimation Accuracy
LTL	0.848
LTB1	0.545
PGB1	0.800
PMP	0.565
WTB1	0.930
ANB1	0.950

Power States Classification Accuracy

The estimated power data were mapped to a binary power state model (off/ on) using the appliance power on the threshold to discriminate between the two states. A multi-label dataset [14] was created and used the same data split as the MTCs experiments. The result of the F-score evaluation on the test set was presented in Table 10.

Table 10. Power states classification performance by F-score based on the MTR model.

Load Label	F-Score
LTL	0.943
LTB1	0.878
PGB1	0.900
PMP	0.980
WTB1	0.890
ANB1	0.990

The ANB1 load obtained a relatively high accuracy among both the power estimation and power state identification. This was due to high power with a low variant load profile, which would make the input data more distinguishable by the regression and classification models.

The illustration of power plots represents how well the estimated power data by the regression model could track the ground-truth data. Figure 4 shows a week of test data power plots for each appliance label. The estimated power data generated by the regression model was not unbound to the associated power state as the MTC approach was a benefit for the model improvement capability in data estimation. From the results, the lightings (LTL, LTB1), which were the low-power loads, obtained a fuzzy data estimation which was linked to the relatively low value of the power estimation accuracy. This was because the low power loads data contribute little change in the aggregate input data, making it hard for the model to accurately estimate the outputs.

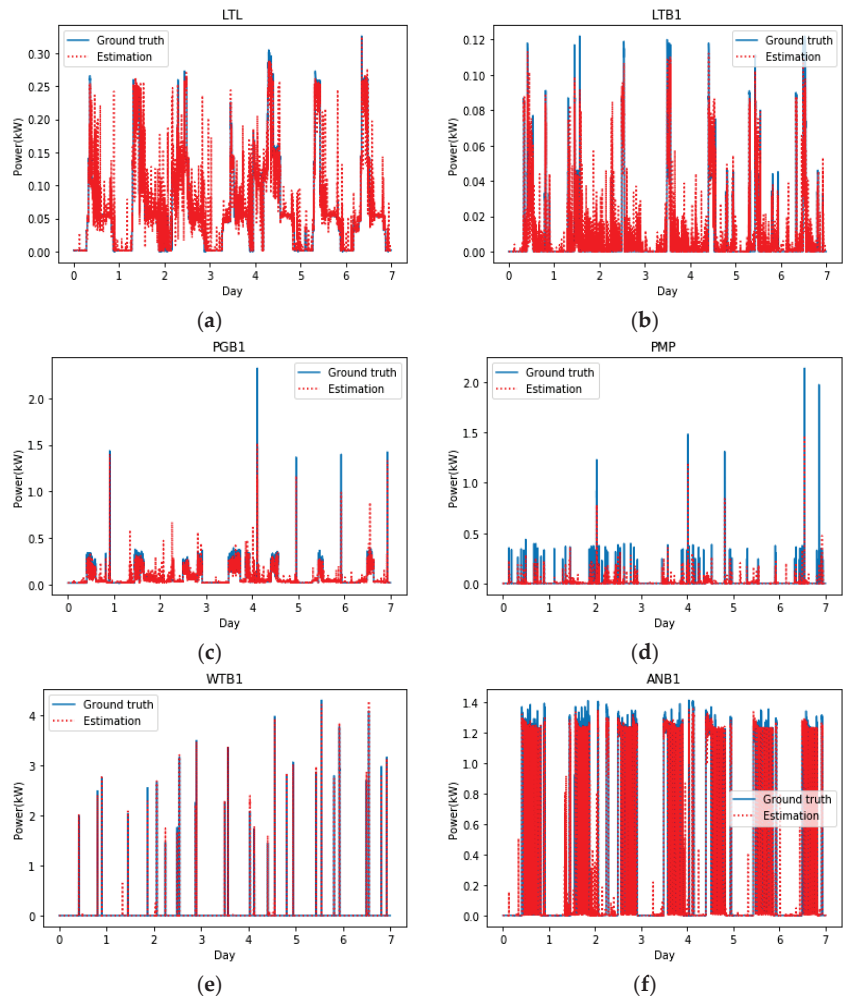


Figure 4. Power data plots of the ground truth and the estimation by the MTR model (a) LTL; (b) LTB1; (c) PGB1; (d) PMP; (e) WTB1; and (f) ANB1.

3.3. Performance Benchmarking

This experiment compared the predictive performance of the MTC and MTR approaches, and DAE, a state-of-the-art deep-learning-based approach, as the comparator. The DAE network was used since it provided a good performance among the other network topologies [39]. It aimed to recreate the clean signal or ground-truth power data from the aggregate power data, which acted as the noisy signal. The network architecture from the study was employed, which consisted of two 1D convolutional layers for the first and the last layer, with three dense layers in the middle. The network was implemented in Python using the neural-disaggregator library [40]. The results of the comparison were summarized using the F-score classification performance and the power estimation accuracy, as presented in Tables 11 and 12, respectively. Generally, the power output from each approach (to predict the power state for MTC and to estimate the power data for MTR) demonstrated a higher performance than its counterparts, which have an additional role in data processing. Thus, less data processing would provide less loss of information and demonstrate better accuracy results.

Table 11. F-score performance by the MTC and MTR approaches, and DAE network.

Load Label	MTC	MTR	DAE
LTL	0.876	0.943	0.724
LTB1	0.896	0.878	0.695
PGB1	0.940	0.900	0.665
PMP	0.950	0.980	0.780
WTB1	0.982	0.890	0.825
ANB1	0.992	0.990	0.950

Table 12. Power estimation accuracy performance by MTC, MTR, and DAE network.

Load Label	MTC	MTR	DAE
LTL	0.730	0.848	0.650
LTB1	0.520	0.545	0.505
PGB1	0.755	0.800	0.783
PMP	0.610	0.565	0.550
WTB1	0.710	0.930	0.805
ANB1	0.950	0.950	0.925

3.4. Discussion

The experiments were formulated to design an energy disaggregation system with MTC and MTR frameworks. These are low-computational-cost systems that are exemplified for the application of home energy monitoring.

The MTC framework formulated the appliance power state modeling with KDE as a finite-state machine, and the power state classification result obtained by the F-score was over 87% for each appliance. The effectiveness of the modeling technique would also be indicated through the relevant regression performance that obtained a power estimation accuracy for over 70% of appliances with a moderate- to high-power consumption. The experimental results, however, did not provide a good predictive performance value for appliances with continuous or highly fluctuated power consumption (e.g., water heater, pump). For this case, deploying a data pre-processing stage that filters out the anomalies before data learning would help obtain a better predictive performance.

The MTR approach provided a direct (no extra data pre-processing) power estimation for each appliance which, on average, presented a better regression performance than the MTC approach. The key result included the estimation accuracy of over 93% for high-power loads (water heater and A/C). The power state identification from the MTR approach would also present the performance value at a comparable level to the MTC, which was the direct classification approach. Using the F-score, the micro-averaged index could enhance the reliability of the performance benchmarking between models with a different number of class outputs (i.e., binary class and multi-class model).

The benchmarking DAE network provided an inferior predictive performance compared to the proposed MTC and MTR approaches due to the amount of sample data in the experiment. Generally, the DAE network would detect ranges of data that indicated power ON as the clean signal or features to be learned from each appliance. This made the model require a large number of training samples to obtain a good level of predictive performance using deep-learning-based approaches [39,41]. On the other hand, the proposed approach learned data on an individual sample basis, which could afford a satisfactory predictive performance with a moderate amount of data.

In the used case of the proposed approaches, if the appliances in the domain are mostly finite-state loads or users wish to gather insight into the appliance operation status for a predictive maintenance purpose, the MTC framework would be a recommended system. For example, if a certain power state (e.g., “Compressor on for A/C”) has taken an unusual period of operation compared to the other state (e.g., “Fan on”), then it would signify a malfunction or abnormal usage. If the users wish to focus on monitoring the

power demand of high-power appliances as a purpose of energy management, the MTR framework would be a recommended system because of the less data processing it requires.

A limitation of the MTC approach is the ability of the KDE method to catch and infer the appliance power state from continuous-power appliances (e.g., water heater, water pump). The power data from those appliances did not exhibit a frequent pattern in which the KDE could not properly identify the inherent power states and their associated power data. In case there are a large number of these appliances in the system, it is recommended to use the MTR approach to obtain a model with a decent predictive performance. For the MTR approach, the binary model of power state identification might not fit well for learning the operational state of multi-state appliances (e.g., fridge, washing machine). Thus, an additional step of data processing could be employed, such as power data mapping after the regression process to the prior knowledge of the power state assignment.

4. Conclusions

The proposed design of the home energy disaggregation system employs multi-target classification (MTC) and multi-target regression (MTR) approaches to predict the appliance power state identification and power demand estimation. The design is based on the optimization process of learning algorithm selection and model parameter selection. The power state modeling for MTC was designated using the KDE technique to determine the number of power states and the power representative data for each appliance. The MTR required no special data pre-processing before training the model, making the computational cost lower than the MTC approach. The MTC approach delivered the appliance power state identification through an F-score (micro-averaged) of 87–99% and a power estimation accuracy of 52–95% for the appliances under experiments. For the MTR approach, it delivered the appliance power estimation accuracy of 54–95% and the power state identification through an F-score (micro-averaged) of 87–99%. These performance results outperform the benchmarking deep neural network using DAE architecture under the same data settings. Deploying the proposed approach for a home monitoring system would rely on what data and type of appliances that users would wish to focus on because both approaches have strong and weak points in the process of data manipulation and the achieved predictive performance.

Future work could focus on improving the MTR model to obtain finite power state modeling instead of binary state modeling. This method helps the approach identify the power state more accurately when working with multi-state appliances. The result of the KDE method, that learns the inherent power states for the MTC approach, could be applied as the post-processing step. Another finite-state modeling technique could be using clustering methods such as DBSCAN [42] or hierarchical clustering [43]. These methods can learn to identify the number of clusters or power states from the power data without prior knowledge of the number of power states. Thus, a more refined power state model for the MTR approach would make the system more applicable to various types of appliances, leading to more efficient energy monitoring and management applications.

Supplementary Materials: The data used within the experiments can be downloaded from <https://data.mendeley.com/datasets/nmnk58bgtb/1> (accessed on 15 January 2023).

Author Contributions: Conceptualization, B.B. and S.K.K.; methodology, B.B. and S.K.K.; software, B.B.; validation, S.M. and P.R.; formal analysis, B.B. and S.K.K.; investigation, B.B., S.K.K., and S.M.; resources, B.B. and P.R.; data curation, B.B.; writing—original draft preparation, B.B. and S.K.K.; writing—review and editing, B.B.; visualization, B.B.; supervision, S.M. and P.R.; project administration, S.K.K.; funding acquisition, B.B. All authors have read and agreed to the published version of the manuscript.

Funding: This work was supported by the Research Grants from the Walailak University Research Fund under Contract WU66219.

Data Availability Statement: The data supporting the reported results will be available on request from the corresponding author.

Conflicts of Interest: The authors declare no conflict of interest.

References

- Hart, G.W. Nonintrusive appliance load monitoring. *Proc. IEEE* **1992**, *80*, 1870–1891. [\[CrossRef\]](#)
- Meguro, W.; Peppard, E.; Meder, S.; Maskrey, J.; Josephson, R. Going Beyond Code: Monitoring Disaggregated Energy and Modeling Detached Houses in Hawai‘i. *Buildings* **2020**, *10*, 120. [\[CrossRef\]](#)
- Armel, K.C.; Gupta, A.; Shrimali, G.; Albert, A. Is disaggregation the holy grail of energy efficiency? The case of electricity. *Energy Policy* **2013**, *52*, 213–234. [\[CrossRef\]](#)
- Zeifman, M.; Roth, K. Nonintrusive appliance load monitoring: Review and outlook. *IEEE Trans. Consum. Electron.* **2011**, *57*, 76–84. [\[CrossRef\]](#)
- Zoha, A.; Gluhak, A.; Imran, A.; Rajasegarar, S. Non-Intrusive Load Monitoring Approaches for Disaggregated Energy Sensing: A Survey. *Sensors* **2012**, *12*, 16838–16866. [\[CrossRef\]](#)
- Laughman, C.; Lee, K.; Cox, R.; Shaw, S.; Leeb, S.; Norford, L.; Armstrong, P. Power signature analysis. *IEEE Power Energy Mag.* **2003**, *99*, 56–63. [\[CrossRef\]](#)
- Leeb, S.B.; LeVan, M.S.; Kirtley, J.L.; Sweeney, J.P. Development and Validation of a Transient Event Detector. *AMP J. Technol.* **1993**, *3*, 69–74.
- Chang, H.H. Non-Intrusive Demand Monitoring and Load Identification for Energy Management Systems Based on Transient Feature Analyses. *Energies* **2012**, *5*, 4569–4589. [\[CrossRef\]](#)
- Norford, L.K.; Leeb, S.B. Non-intrusive electrical load monitoring in commercial buildings based on steady-state and transient load-detection algorithms. *Energy Build.* **1996**, *24*, 51–64. [\[CrossRef\]](#)
- Parson, O.; Ghosh, S.; Weal, M.; Rogers, A. An unsupervised training method for non-intrusive appliance load monitoring. *Artif. Intell.* **2014**, *217*, 1–19. [\[CrossRef\]](#)
- Huber, P.; Calatroni, A.; Rumsch, A.; Paice, A. Review on Deep Neural Networks Applied to Low-Frequency NILM. *Energies* **2021**, *14*, 2390. [\[CrossRef\]](#)
- Ruzzelli, A.G.; Nicolas, C.; Schoofs, A.; Hare, G.M. Real-Time Recognition and Profiling of Appliances through a Single Electricity Sensor. In Proceedings of the 2010 7th Annual Proceedings SECON, Boston, MA, USA, 21–25 June 2010. [\[CrossRef\]](#)
- Onoda, T.; Ratsch, G.; Muller, K.R. Applying Support Vector Machines and Boosting to a Non-Intrusive Monitoring system for Household Electric Appliances with Inverter. In Proceedings of the ICSC Symposium on Neural Computation, Berlin, Germany, 23–26 May 2000; pp. 1–7.
- Tsoumakas, G.; Katakis, I.; Vlahavas, I. Mining Multi-label Data. In *Data Mining and Knowledge Discovery Handbook*; Springer: Boston, MA, USA, 2010; pp. 667–685.
- Kolter, J.Z.; Johnson, M.J. REDD: A public data set for energy disaggregation research. In Proceedings of the Workshop on Data Mining Applications in Sustainability (SIGKDD), San Diego, CA, USA, 21 August 2011; pp. 59–62.
- Kim, H.; Marwah, M.; Arlitt, M.; Lyon, G.; Zhan, J. Unsupervised Disaggregation of Low Frequency Power Measurements. In Proceedings of the 2011 SIAM International Conference on Data Mining, Mesa, AZ, USA, 28–30 April 2011; pp. 747–758.
- Wu, Z.; Wang, C.; Peng, W.; Liu, W.; Zhang, H. Non-intrusive load monitoring using factorial hidden markov model based on adaptive density peak clustering. *Energy Build.* **2021**, *244*, 1–12. [\[CrossRef\]](#)
- Rafiq, H.; Zhang, H.; Li, H.; Ochani, M.K. Regularized LSTM Based Deep Learning Model: First Step towards Real-Time Non-Intrusive Load Monitoring. In Proceedings of the 2018 IEEE International Conference on Smart Energy Grid Engineering (SEGE), Oshawa, ON, Canada, 12–15 August 2018; pp. 234–239. [\[CrossRef\]](#)
- Zhou, A.; Li, S.; Liu, C.; Zhu, H.; Dong, N.; Xiao, T. Non-Intrusive Load Monitoring Using a CNN-LSTM-RF Model Considering Label Correlation and Class-Imbalance. *IEEE Access* **2021**, *9*, 84306–84315. [\[CrossRef\]](#)
- Jiang, J.; Kong, Q.; Plumbley, M.D.; Gilbert, N.; Hoogendoorn, M.; Roijers, D.M. Deep Learning-Based Energy Disaggregation and On/Off Detection of Household Appliances. *ACM Trans. Knowl. Discov. Data* **2021**, *15*, 1–21. [\[CrossRef\]](#)
- Bonfigli, B.; Felicetti, A.; Principi, E.; Fagiani, M.; Squartini, S.; Piazza, F. Denoising autoencoders for Non-Intrusive Load Monitoring: Improvements and comparative evaluation. *Energy Build.* **2018**, *158*, 1461–1474. [\[CrossRef\]](#)
- Langevin, A.; Carbonneau, M.A.; Cheriet, M.; Gagnon, G. Energy disaggregation using variational autoencoders. *Energy Build.* **2022**, *254*, 1–21. [\[CrossRef\]](#)
- Buddhahai, B.; Makonin, S. A Nonintrusive Load Monitoring Based on Multi-Target Regression Approach. *IEEE Access* **2021**, *9*, 163033–163042. [\[CrossRef\]](#)
- Buddhahai, B.; Wongseree, W.; Rakkwamsuk, P. An Energy Prediction Approach for a Nonintrusive Load Monitoring in Home Appliances. *IEEE Trans. Consum. Electron.* **2020**, *66*, 96–105. [\[CrossRef\]](#)
- Xu, D.; Shi, Y.; Tsang, I.W.; Ong, Y.S.; Gong, C.; Shen, X. Survey on Multi-Output Learning. *IEEE Trans. Neural Netw. Learn. Syst.* **2019**, *31*, 2409–2429. [\[CrossRef\]](#)
- Tsoumakas, G.; Katakis, I. Multi-Label Classification: An Overview. *Int. J. Data Warehous. Min.* **2017**, *3*, 1–17. [\[CrossRef\]](#)
- Kocev, D.; Dzeroski, S.; White, M.D.; Newell, G.R.; Griffioen, P. Using single- and multi-target regression trees and ensembles to model a compound index of vegetation condition. *Ecol. Model.* **2009**, *220*, 1159–1168. [\[CrossRef\]](#)
- Borchani, H.; Varando, G.; Bielza, C.; Larranaga, P. A survey on multi-output regression. *Wiley Interdiscip. Rev. Data Min. Knowl. Discov.* **2015**, *5*, 216–233. [\[CrossRef\]](#)

29. Basgalupp, M.; Cerri, R.; Schietgat, L.; Triguero, I.; Vens, A. Beyond global and local multi-target learning. *Inf. Sci.* **2021**, *579*, 508–524. [[CrossRef](#)]
30. Madjarov, G.; Kocev, D.; Gjorgjevikj, D.; Dzeroski, S. An extensive experimental comparison of methods for multi-label learning. *Pattern Recognit.* **2012**, *45*, 3084–3104. [[CrossRef](#)]
31. Read, J.; Pfahringer, B.; Holmes, G.; Frank, E. Classifier Chains for Multi-label Classification. In Proceedings of the European Conference on Machine Learning and Knowledge Discovery in Databases: Part II, Bled, Slovenia, 7–11 September 2009; pp. 1–16.
32. Tsoumakas, G.; Katakis, I.; Vlahavas, I. Random k-Labelsets for Multilabel Classification. *IEEE Trans. Knowl. Data Eng.* **2011**, *23*, 1079–1089. [[CrossRef](#)]
33. Buddhahai, B.; Wongseree, W.; Rakkwamsuk, P. Multi-Circuit Electric Consumption Data for Application of Energy Disaggregation. Available online: <https://data.mendeley.com/datasets/nmnk58bgtb/1> (accessed on 15 January 2023).
34. Parzen, E. On Estimation of a Probability Density Function and Mode. *Ann. Math. Stat.* **1962**, *33*, 1065–1076. [[CrossRef](#)]
35. Pedregosa, F. Scikit-learn: Machine Learning in Python. *J. Mach. Learn. Res.* **2011**, *12*, 2825–2830.
36. Read, J.; Reutemann, P.; Pfahringer, B.; Holmes, G. Meka: A multi-label/multi-target extension to weka. *J. Mach. Learn. Res.* **2016**, *17*, 667–671.
37. Batra, N.; Kelly, J.; Parson, O.; Dutta, H. NILMTK: An open source toolkit for non-intrusive load monitoring. In Proceedings of the 5th International Conference on Future Energy Systems, Cambridge, UK, 11–13 June 2014; pp. 265–276.
38. Makonin, S.; Popowich, F. Nonintrusive load monitoring (NILM) performance evaluation. *Energy Effic.* **2015**, *8*, 809–814. [[CrossRef](#)]
39. Kelly, J.; Knottenbelt, W. Neural NILM: Deep Neural Networks Applied to Energy Disaggregation. In Proceedings of the 2nd ACM International Conference on Embedded Systems for Energy-Efficient Built Environments, Seoul, Republic of Korea, 4–5 November 2015; pp. 55–64.
40. Krystalakos, O.; Nalmpantis, C.; Vrakas, D. Sliding Window Approach for Online Energy Disaggregation Using Artificial Neural Networks. In Proceedings of the 10th Hellenic Conference on Artificial Intelligence, Patras, Greece, 9–12 July 2018; pp. 1–6. [[CrossRef](#)]
41. Fang, Y.; Jiang, S.; Fang, S.; Gong, Z.; Xia, M.; Zhang, X. Non-Intrusive Load Disaggregation Based on a Feature Reused Long Short-Term Memory Multiple Output Network. *Building* **2022**, *12*, 1048. [[CrossRef](#)]
42. Schubert, E.; Sander, J.; Ester, M.; Kriegel, H.P.; Xu, X. DBSCAN Revisited, Revisited: Why and How You Should (Still) Use DBSCAN. *ACM Trans. Data. Syst.* **2017**, *42*, 1–21. [[CrossRef](#)]
43. Patel, S.; Sihmar, S.; Jatain, A. A study of hierarchical clustering algorithms. In Proceedings of the 2015 2nd International Conference on Computing for Sustainable Global Development, New Delhi, India, 11–13 March 2015; pp. 537–541.

Disclaimer/Publisher’s Note: The statements, opinions and data contained in all publications are solely those of the individual author(s) and contributor(s) and not of MDPI and/or the editor(s). MDPI and/or the editor(s) disclaim responsibility for any injury to people or property resulting from any ideas, methods, instructions or products referred to in the content.

Article

Influence of Building Density on Outdoor Thermal Environment of Residential Area in Cities with Different Climatic Zones in China—Taking Guangzhou, Wuhan, Beijing, and Harbin as Examples

Guang Yang ¹, Yingli Xuan ² and Zeng Zhou ^{3,*}¹ School of Civil Engineering, Liaoning Technical University, Fuxin 123008, China; yangguang_tm@lntu.edu.cn² Faculty of Engineering, Tokyo Polytechnic University, Tokyo 164-8678, Japan; y.xuan@arch.t-kougei.ac.jp³ School of Urban Design, Wuhan University, Wuhan 430072, China

* Correspondence: haomaoz@whu.edu.cn

Abstract: Outdoor wind and thermal environments in residential areas are greatly affected by the distance between buildings. A short distance is conducive to providing shade, and a long distance can enhance ventilation between buildings. In this study, four cities with different latitudes in China (Guangzhou, Wuhan, Beijing, and Harbin) were selected to research the relationship between the distance between buildings and thermal environments of residential areas. The results show that (1) when the distance between buildings is small, it is easier for wind paths to form. Wind paths can strengthen the wind velocity. When the distance between buildings exceeds 40–50 m, the building density is small, the building's resistance to the wind becomes smaller and smaller, and the wind speed will gradually increase. (2) When the distance is in the range of 20–50 m, the MRT (mean radiant temperature) rise rate of each city is similar. For every 10 m increase in the distance between buildings, the MRT increases by about 1.25 °C. (3) D = 50 m (D/H = 1.19) is an inflection point. When D is less than 50 m, within the range of 20–50 m, the smaller the D is, the lower the SET* (standard effective temperature) is, while when D is more than 50 m, the opposite trend is observed.

Keywords: MRT; SET*; surface temperature; latitudes; thermal environment

Citation: Yang, G.; Xuan, Y.; Zhou, Z. Influence of Building Density on Outdoor Thermal Environment of Residential Area in Cities with Different Climatic Zones in China—Taking Guangzhou, Wuhan, Beijing, and Harbin as Examples. *Buildings* **2022**, *12*, 370. <https://doi.org/10.3390/buildings12030370>

Academic Editors:
Mattheos Santamouris and
Radu Zmeureanu

Received: 24 January 2022
Accepted: 15 March 2022
Published: 17 March 2022

Publisher's Note: MDPI stays neutral with regard to jurisdictional claims in published maps and institutional affiliations.



Copyright: © 2022 by the authors. Licensee MDPI, Basel, Switzerland. This article is an open access article distributed under the terms and conditions of the Creative Commons Attribution (CC BY) license (<https://creativecommons.org/licenses/by/4.0/>).

1. Introduction

In recent years, with extremely hot weather becoming common, heat-related illnesses have become a serious problem threatening public health and safety [1–3]. In developing countries such as China, air temperatures hit high records year by year, and deaths caused by heat stroke have also been increasing [4,5]. During summer days people feel hotter; in order to achieve thermal comfort, people use air conditioning more frequently and for longer time, and the exhaust heat from external air conditioning causes deterioration of the outdoor thermal environment of urban areas [6,7]. With the gradual depletion of traditional energy sources and the increasingly serious effects of global warming, passive climate adaptable architectural designs can have low energy consumptions, zero energy consumption, and even negative energy consumption [8]—these have attracted increasing attention from researchers. Obtaining optimal building density is an important method for achieving passive climate adaptability in the outdoor thermal environment of residential areas. Many studies have focused on optimizing the outdoor thermal environment using methods such as greenery, water features, and pavement materials [9–15]; other studies have focused on optimizing buildings, through the layout, height, and density [16–23]. Once a residential area is built, the building density is difficult to change; therefore, through simulation calculations, studying the optimal building density is an important method for achieving passive climate adaptation in outdoor thermal environments.

Building density has great impact on outdoor thermal environments. Kubota et al. [18] researched the relationship between the building density and the average wind velocity (V) at pedestrian level in residential neighborhoods by using wind tunnel test, and found that residential areas with low density (shallow street canyon) can enhance ventilation. Zhou et al. [24] researched the relationship between the outdoor wind environment and building density (different piloti ratio) in Wuhan. There are many studies [25–27] that only focus on the outdoor wind environment, but for residential streets in the daytime in summer, the influence of temperature and radiation is very large, which must be considered. Bourbia et al. [28] researched the relationship between the geometry and the microclimate (shade area and temperature) of urban street canyons. Under low latitude conditions, solar access to streets can always be decreased by increasing H/W to larger values. Johansson [29] studied the impact of urban geometry on outdoor thermal comfort in dry and hot climate, and analyzed the environment through temperature, wind speed, MRT, and PET (physiological equivalent temperature). Xuan et al. [30] studied the outdoor thermal environment (V , MRT, SET^*) of residential communities with different building densities in Sendai, Japan, and Guangzhou, China, and obtained a series of quantitative simulation results. Taking Wuhan as an example, Zhou et al. [31] researched the outdoor thermal environment under different building densities (different piloti ratio), and gave the optimal range of the piloti ratio by considering various indicators, such as surface temperature, V , MRT, and SET^* . The MRT can reflect the joint action results of outdoor temperature, radiation, and wind speed. The SET^* takes human factors, such as human metabolic rate and clothing insulation, into account on the basis of MRT. The research on the relationship between urban building density and thermal environment in different latitudes in China is insufficient.

China has a vast territory with latitudinal values range from $3^{\circ}51' N$ to $53^{\circ}33.5' N$. As shown in Figure 1, five climatic zones are contained in China. From south to north, the outdoor thermal environment of the hot summer and warm winter zone, the hot summer and cold winter zone, the cold zone, and the severe cold zone have various problems. In order to clarify the influence of building density on outdoor thermal environment in cities with different climatic zones in China, four Chinese cities (Figure 1) from the hot summer and warm winter zone to the severe cold zone were taken into account: Guangzhou ($113^{\circ}33' E$, $23^{\circ}17' N$), Wuhan ($114^{\circ}13' E$, $30^{\circ}62' N$), Beijing ($116^{\circ}47' E$, $39^{\circ}80' N$), and Harbin ($126^{\circ}77' E$, $45^{\circ}75' N$).

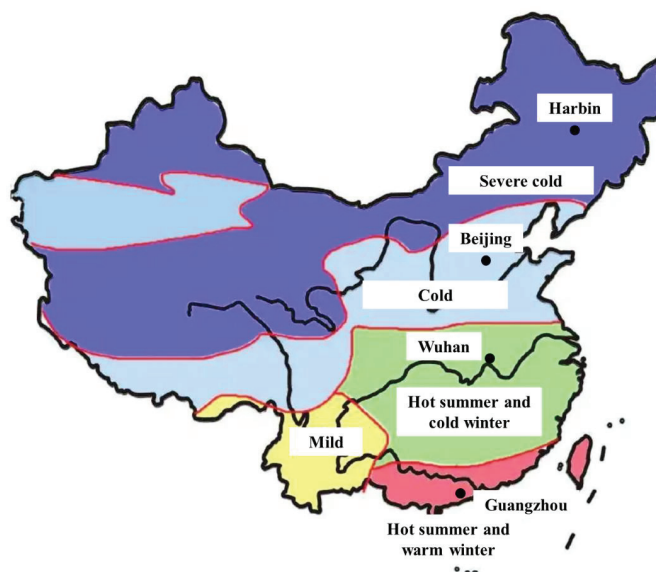


Figure 1. Layout of five climatic zones in China and the location of target cities.

Therefore, this study will comprehensively consider the thermal environmental factors (V, T, MRT, SET*), and carry out the simulation study of building density in several cities in different climatic regions and at different latitudes in China. This study aims to clarify the relationships between outdoor thermal environment factors and building density, and the appropriate ranges of building density will be proposed.

2. The Prediction Method

2.1. The Prediction Process

To predict outdoor thermal environment with high prediction accuracy, coupling analyses of convection, conduction, and radiation [32] were carried out with a numerical analysis system by integrating STAR-CD/RADX (CD adapco Group, Melville, NY, USA; Star-CD is a commercially available computational fluid dynamics software that uses fully unstructured mesh generation techniques and finite volume methods) with additional codes. A 3D, nonlinear k- ϵ turbulence model proposed by Craft et al. (1996) was adopted in CFD convection analyses [33]. Figure 2 shows the flowchart of the prediction method used in this study, and the prediction method has been used in many previous studies [30,31,34,35]. Our analysis was conducted in three steps. In step 1, 3D radiation and 1D conduction were carried out in order to obtain the surface temperatures of the ground and the buildings. In step 2, we conducted a non-isothermal CFD analysis using the surface temperature result gained in step 1. In step 3, MRT was calculated according to the results of wind speed and temperature obtained in step 2, and SET* was calculated in combination with human metabolic rate and clothing insulation.

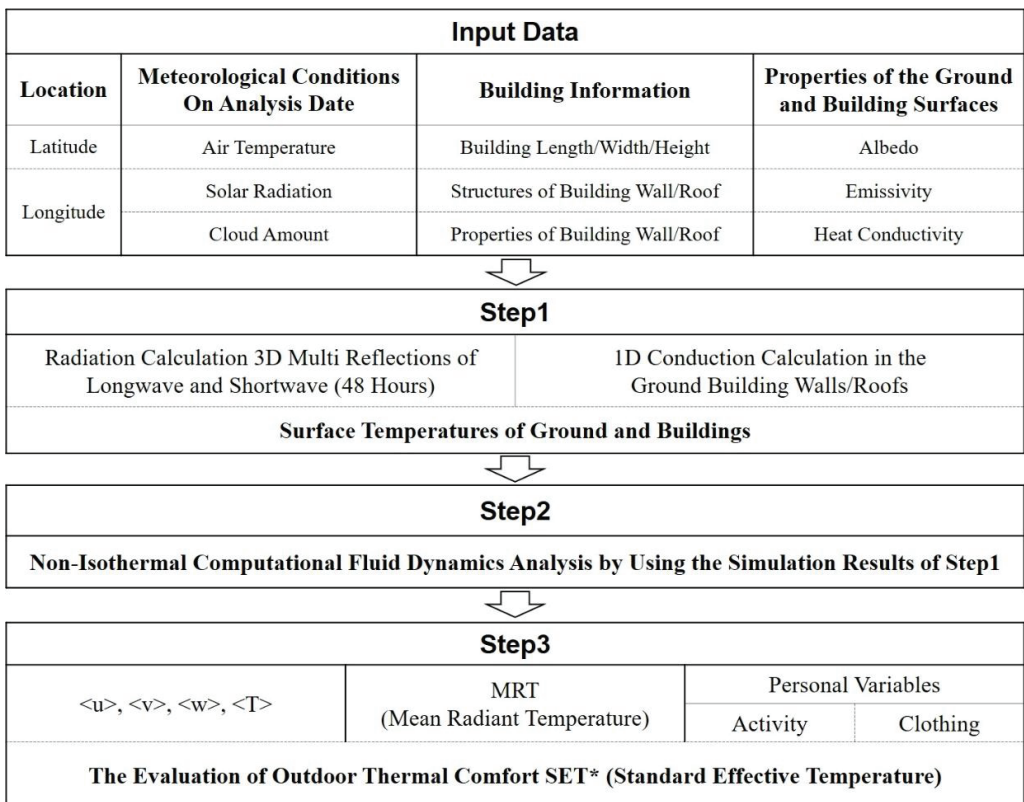


Figure 2. The flowchart of the prediction method for the outdoor thermal environment.

2.2. Accuracy and Validation

The predecessors of our research group have completed many comparisons and have verified the accuracy of this simulation method. Li et al. [35] simulated the outdoor wind environment using 15 turbulence models, and compared the simulation results with the wind tunnel test result provided by AIJ [36,37]. The results show that Suga cubic nonlinear $k-\epsilon$ model has high accuracy in solving the wind field.

All surfaces in the domain were divided into small surfaces to calculate the urban surface temperature. For each small surface, various factors were considered, including solar radiation, sky radiation, longwave radiation between the surface and other surfaces, convective heat transfer and latent heat transfer between the surface and ambient air, and conduction heat transfer through the surface. The shape factor was calculated by the Monte Carlo method [38,39] and the radiative heat transfer was calculated by Gebhart's absorption factor [40]. Due to the different absorptivity under shortwave and longwave radiation, the values of Gebhart's absorption factor were also different, so each surface was calculated separately. According to the former studies [34,41,42], and considering the above heat transfer, the urban surface temperature can be reproduced well.

Li et al. [43] carried out the actual measurement and numerical simulation in building blocks in Guangzhou in summer. Figure 3a shows the distribution of measuring points during actual measurement, and Figure 3b shows the analytical region in the simulation. Figure 4a shows velocity distribution and Figure 4b shows temperature distribution. Table 1 shows comparison between measurement and simulation values of velocities, and Table 2 lists the measurement and simulation values of temperatures in different points.

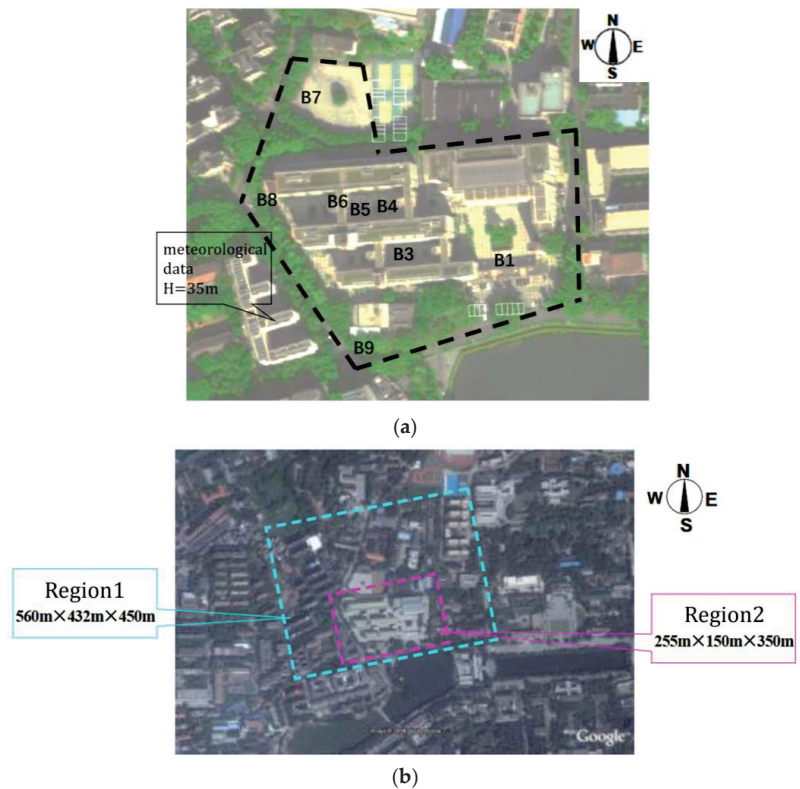


Figure 3. Measuring points and the analytical region. (a) The distribution of measuring points during the actual measurement. (b) The analytical region in the simulation.

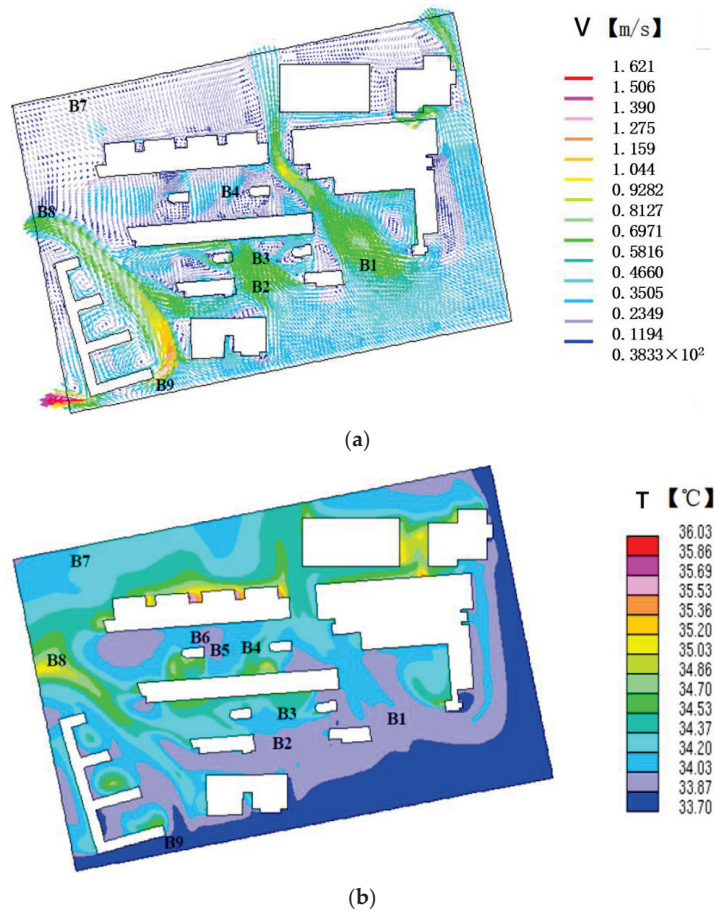


Figure 4. Simulation results at the height of 1.5 m above the ground (14:00, 15 August). (a) Velocity distribution. (b) Temperature distribution.

Table 1. Comparison between measurement and simulation values of velocities at 14:00, 15 August (m/s).

Measuring Point	B1	B2	B3	B4	B7	B8	B9
Measuring value	0.70	0.36	0.67	0.27	0.27	0.42	0.58
Simulation value	0.69	0.60	0.68	0.30	0.23	0.62	0.85
Difference	0.01	−0.24	−0.01	−0.03	0.04	−0.20	−0.27

Table 2. Comparison between measurement and simulation values of temperatures at 14:00, 15 August ($^{\circ}\text{C}$).

Measuring Point	B1	B2	B3	B4	B5	B6	B7	B8	B9
Measuring value	34.43	33.17	34.01	34.43	33.59	33.59	34.43	33.59	34.01
Simulation value	34.03	33.89	34.04	34.42	33.90	33.89	34.37	35.00	33.71
Difference	0.40	0.72	0.03	0.01	−0.31	−0.30	0.06	−1.41	0.30

As seen from the above, the wind speed simulation values of all measured points are basically in agreement with the measured values except B2, B8, and B9. The maximum

wind speed deviation is B9, and then B8 and B2, respectively. Measuring point 2 is located in the piloti space. Shrubs with a height of about 0.3 m are planted on the north and south sides of the piloti space to obstruct the air flow, but the grass did not sufficiently obstruct the air flow, so the wind velocity at B2 was greater than the measured value. B8 is located under tall trees with dense shade on the sidewalk, and B9 is located under the medium height trees with sparse shade at the intersection. The role of trees is neglected in the simulation, which leads to the simulation values of wind velocity at B8 and B9 being larger than the measured values. Except for B2 and B8, the simulated temperature values at all the measuring points were in good agreement with the measured values. The present simulation program is too simple to deal with the shrubs and trees, so the trees near B2 and above B8 and B9 cannot reflect the cooling effect of temperature well; as a result, the simulated temperature values at B2 and B8 are higher than the measured values. The simulated temperature at B9 is close to the measured value because the simulated wind speed is much higher than the measured wind speed. To sum up, the computer simulation method has good accuracy and can be used in case simulation calculation and research.

3. Simulation

3.1. Analyses Model and Cases

Figure 5 shows the typical residential areas in Guangzhou, Wuhan, Beijing, and Harbin. It can be seen that the typical modern residential areas in China are mainly in determinant, facing from north–south. Figure 6 shows the analysis model used in this study. In Figure 6a, the size of a monomer building and the analysis domain size are listed, and the mesh number and grid partition are also shown.

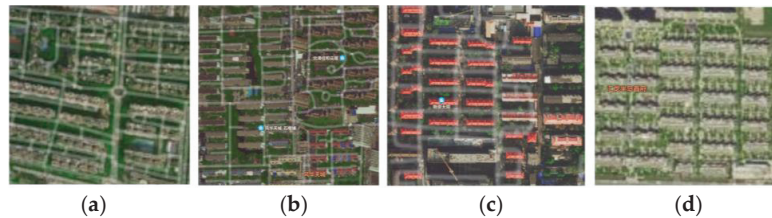


Figure 5. Residential area in cities of China. (a) Guangzhou, (b) Wuhan, (c) Beijing, (d) Harbin.

According to the “Guidebook for Practical Applications of CFD to Pedestrian Wind Environment around Buildings (AIJ Guideline)” [6], published by Architectural Institute of Japan, the analyses model shown in Figure 6a was created based on the typical Chinese residential area. In order to know the effects of building arrangement on outdoor thermal environment, 6 different north–south building distances (from 10 m to 60 m) in Guangzhou, Wuhan, Beijing, and Harbin, a total of 24 cases were taken into account. The 6 building arrangements in the target area are shown in Figure 6b, and all the analyzed cases are listed in Table 3.

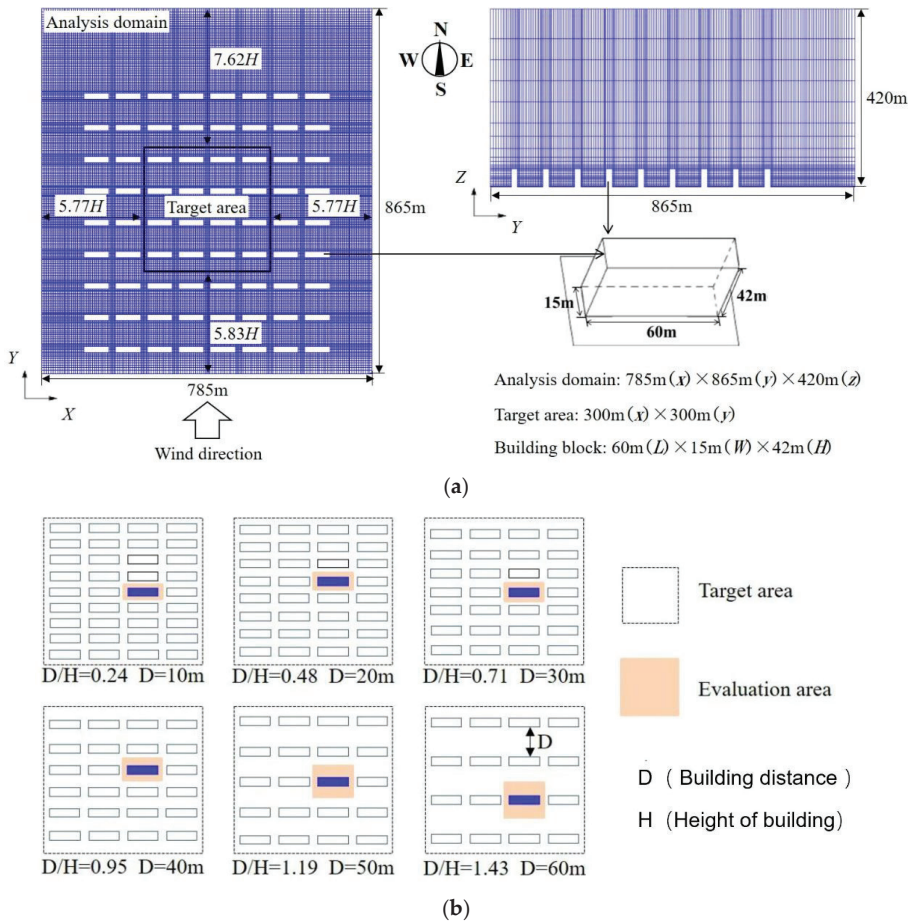


Figure 6. Analysis model used in this study. (a) Size and mesh of analysis model. (b) Different D/H and arrangement in the target area.

Table 3. Analysis cases.

Case Name	Analysis Date and Time	Air Temperature (°C)	Latitude (°)	The Distance between Buildings D (m)	Building Height H (m)	D/H
GZ-10	6/21	30.0 °C (Noon)	Guangzhou 23°17' N	10	42	0.24
GZ-20				20		0.48
GZ-30				30		0.71
GZ-40				40		0.95
GZ-50				50		1.19
GZ-60				60		1.43

Table 3. Cont.

Case Name	Analysis Date and Time	Air Temperature (°C)	Latitude (°)	The Distance between Buildings D (m)	Building Height H (m)	D/H
WH-10	6/21	32.2 °C (Noon)	Wuhan 30°62' N	10	42	0.24
WH-20				20		0.48
WH-30				30		0.71
WH-40				40		0.95
WH-50				50		1.19
WH-60				60		1.43
BJ-10	6/21	29.5 °C (Noon)	Beijing 39°80' N	10	42	0.24
BJ-20				20		0.48
BJ-30				30		0.71
BJ-40				40		0.95
BJ-50				50		1.19
BJ-60				60		1.43
HRB-10	6/21	28.0 °C (Noon)	Harbin 45°75' N	10	42	0.24
HRB-20				20		0.48
HRB-30				30		0.71
HRB-40				40		0.95
HRB-50				50		1.19
HRB-60				60		1.43

Note: GZ—Guangzhou; WH—Wuhan; BJ—Beijing; HRB—Harbin.

3.2. The Analysis Time

In our study, a weather database [44] in China was used. To compare the effect of distances between the north–south buildings on outdoor thermal environment in four different climatic cities in summer, 21 June, the summer solstice—when people in the northern hemisphere receive the most sunshine and daylight hours—was selected. Figure 7 was drawn according to the weather database, and the air temperatures on 21 June in cities of China were listed. Most people in China go to work from 8:00 to 17:00, and take a lunch break starting from 12:00. Among the three time points, Harbin, Beijing, and Wuhan have the highest temperature at 12:00, and Guangzhou has the highest temperature at 17:00. Guangzhou has low latitude, high solar radiation, and late sunset, so the temperature at 12:00 is not the highest. In order to facilitate comparison, 12:00 was selected as the analysis time.

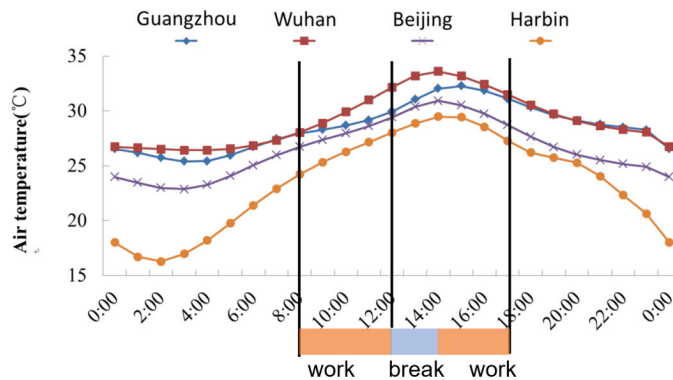


Figure 7. Air temperature on 21 June.

3.3. The Analysis Conditions

The air temperatures on typical summer day (shown in Figure 7) were used as the initial air temperature data in each city. In each case, a 48 h radiation simulation was carried out including a 24 h preliminary simulation. In radiation simulation step, direct irradiance and global irradiance were considered.

CFD analyses were carried out when the sun reaches its highest position during the whole year (12:00 local solar time) in each case. The inlet wind velocities were given as 2 m/s at 10 m height, which obeyed the logarithm law with a power index of 0.3 in all the four cities. The whole analyses consist of 3 steps as shown in Figure 2. Analysis conditions in step 1 were listed in Table 4. In step 2, non-isothermal CFD analyses were carried out with the surface temperature result gain in step 1, and the analysis conditions are shown in Table 5.

Table 4. Analysis conditions in step 1.

Analysis Date and Time	6/20, 00:00–6/21, 24:00
Domain Size	785 m (x) × 865 m (y) × 420 m (z)
Analysis Type	Three-dimensional analysis
Analysis State	Unsteady state
Turbulence Model	A cubic nonlinear k – ϵ model proposed by Craft et al. (1996)
Building Volume	60 m (x) × 15 m (y) × 42 m (z)
Temperature	Temperature conditions in Guangzhou, Wuhan, Beijing and Harbin (Figure 6)
Convective Heat Transfer Coefficient	Indoor: 5 W/m ² ·K Outdoor: 12 W/m ² ·K

In the final step, analyses were carried out based on the wind velocity and temperature results obtained in step 2. In this study, since the ground and building surfaces are covered with concrete, it is not necessary to solve the transfer equation of vapor. All the simulation area shares the same absolute humidity (0.024 kg/m³), and relative humidity was calculated based on the temperature results. MRT and human metabolic rate were carried out, and finally the SET* values in the target area were calculated.

Table 5. Analysis conditions in Step 2.

Analysis Date and Time	6/21, 12:00
Domain Size	785 m (x) × 865 m (y) × 420 m (z)
Analysis State	Steady state
Turbulence Model	Suga's cubic nonlinear k – ϵ model
Inflow	The wind direction: Southward Wind speed: 2 m/s (10 m) $\langle u \rangle: \langle u(z) \rangle = \langle u_s \rangle (z/z_s)^\alpha$ $\alpha = 0.3, z_s = 10 \text{ m}, u_s = 2 \text{ m/s}$ $k: k(z) = (I(z)u(z))^2$ $I(z) = 0.1(z/z_G)^{(-\alpha-0.05)}$ $z_G = 420 \text{ m}$ $\epsilon: \epsilon(z) = C_\mu^{1/2} k(z) \frac{u_s}{z_s} \alpha \left(\frac{z}{z_s} \right)^{(\alpha-1)}$ $C_\mu = 0.09$
Outflow	$\langle u \rangle, \langle v \rangle, w, k, \epsilon, T$: zero gradient
Lateral and Upper Surfaces	$\langle u \rangle, \langle v \rangle, k, \epsilon$: zero gradient, $\langle w \rangle = 0$
Ground and Building Surfaces	Velocity: Logarithmic law for smooth walls Temperature: 6/21 12:00 (True solar time) The result of step1
Advection Term Scheme	$\langle u \rangle, \langle v \rangle, \langle w \rangle, k, \epsilon, T$: MARS
Coupling Algorithm	SIMPLE

4. Results

4.1. Surface Temperature

Figure 8 shows the distribution of surface temperature when D is between 10 m and 60 m with 10 m intervals in Guangzhou, Wuhan, Beijing, and Harbin. At 12:00, because of the high solar elevation, there are few shadows between buildings, so the surface temperature is very high. In Wuhan, Beijing, and Harbin, the lower the urban latitude is, the higher the surface temperature is. The average ground temperatures in Wuhan from WH-10 to WH-60 were 44.2 °C, 46.5 °C, 49.8 °C, 53.1 °C, 54.4 °C, and 55.6 °C, respectively. Since the air temperature at 12:00 in Guangzhou is lower than that in Wuhan (Figure 7), the surface temperature in Guangzhou is lower than that in Wuhan too.

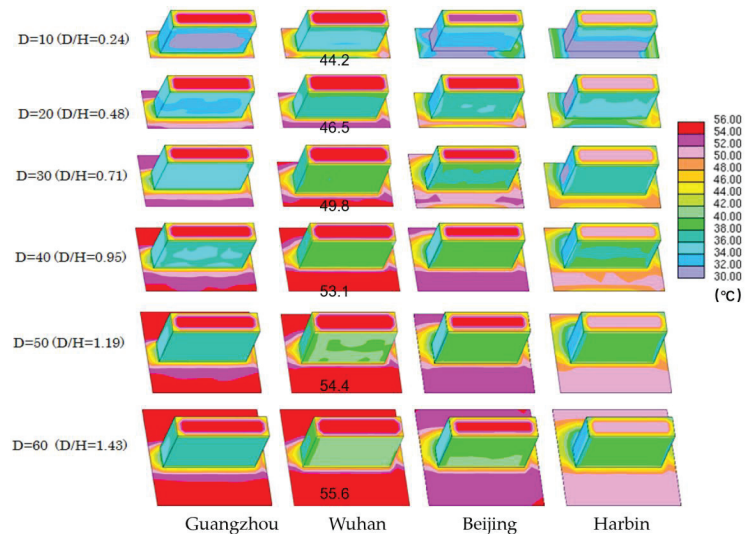


Figure 8. The distribution of outdoor surface temperature at 12:00.

4.2. Wind Velocity

Figure 9 shows the relationship between building distance and average wind velocity in four cities. With the distance between buildings becoming wider, the average wind velocities around the buildings in four cities decreases first and then increases. When D is small, it is easier to form wind paths. The wind path can strengthen the wind velocity. As the value of D gradually increases, the effect of the wind path decreases. When D exceeds 40–50 m, the building density is small, the building's resistance to the wind becomes smaller and smaller, and the wind speed will gradually increase.

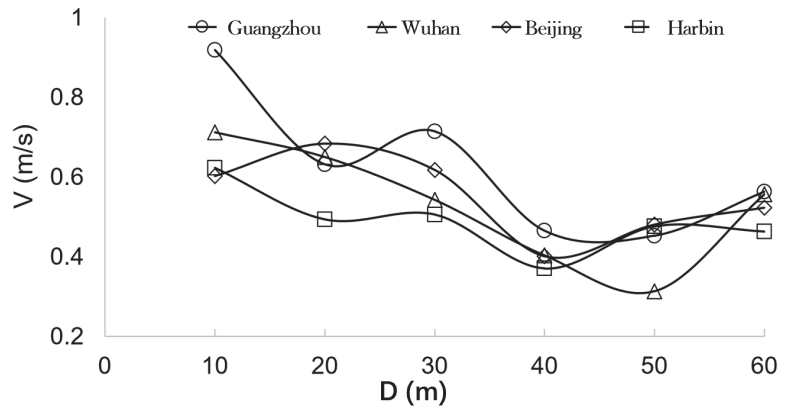


Figure 9. The relationship between building distance and average V in the four cities.

4.3. MRT

Figure 10a shows the distribution of MRT around the building at 1.5 m height when the sun is at its highest position. As the latitude getting lower, the average MRT at 1.5 m around the building increases. However, although the latitude of Guangzhou is lowest of the four cities, the results of average MRT in Guangzhou are lower than those cases in the other three cities. The reason is that Guangzhou city is located near the tropic of cancer, and when the sun at its highest position, the solar altitude is approximately close to 90° . When calculating the amount of radiation heat gain from the surrounding area for MRT, a smaller weight factor is assigned to the amount of radiation heat gain from upper direction than lateral direction.

Figure 10b shows the relationship between building distance and average MRT in four cities. The curve representing Wuhan is at the top and Harbin is at the bottom, which shows that from Wuhan to Harbin, with the increasing of latitude, the MRT value at 12:00 decreases. Among three key time points (8:00, 12:00, and 17:00), the temperature at 12:00 in Guangzhou is not the highest, so the MRT value is not the highest. The overall trend in Figure 10b is that MRT increases with the increasing of the distance between buildings. When the distance is in the range of 20–50 m, the MRT rise rate of each city is similar. For every 10 m increasing in the distance between buildings, the MRT increases by about 1.25°C .

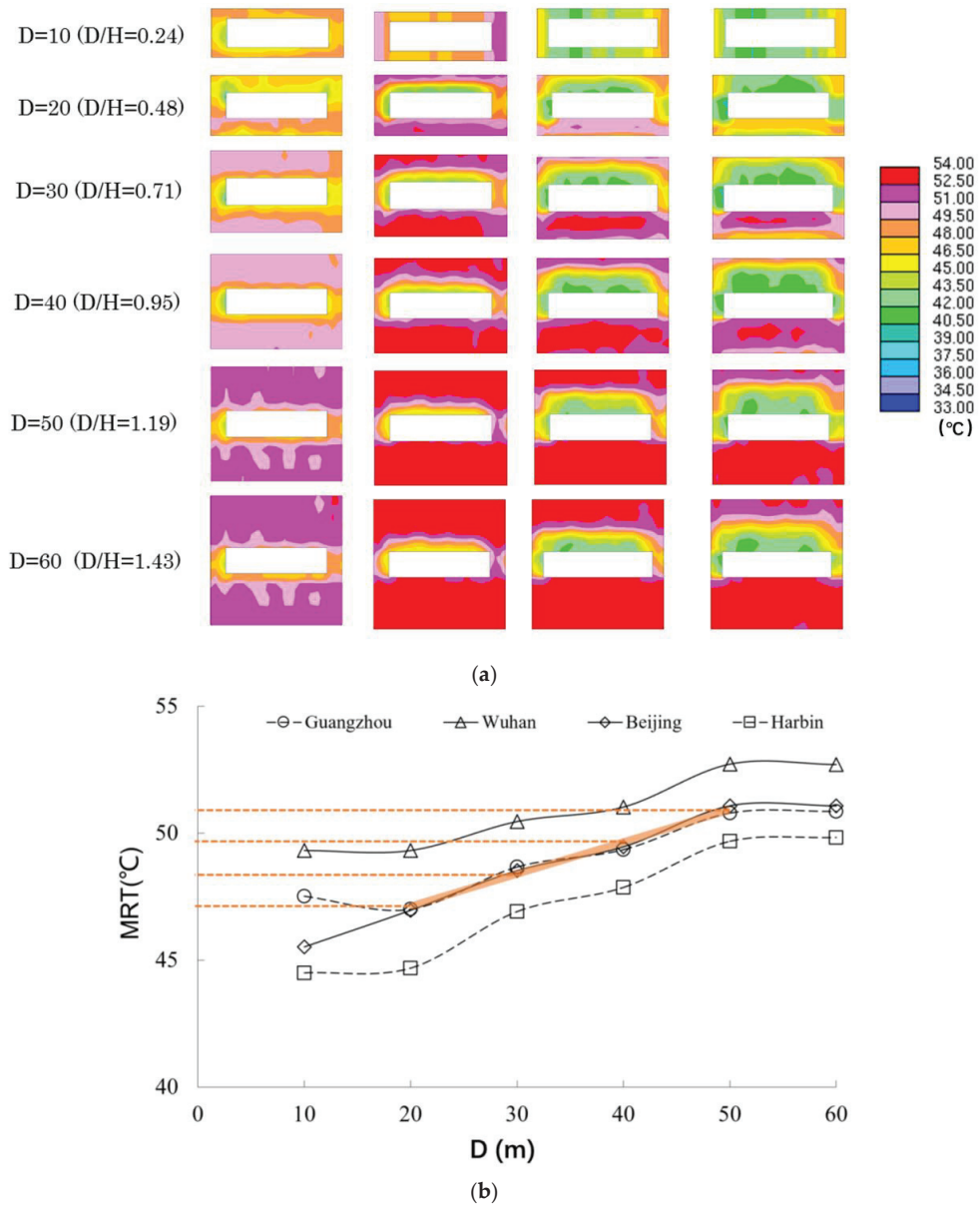


Figure 10. MRT results. (a) The distribution of MRT at 1.5 m, (b) The relationship between building distance and average MRT in four cities.

4.4. SET*

Figure 11a shows the result of SET* at 1.5 m around the building in 10 m, 30 m, and 60 m cases when the sun at 12:00 in the four selected cities. In Wuhan cases, the proportion of high SET* area is larger than the other three cities when the distance between buildings is the same. This is mainly because the Wuhan cases have higher MRT value as shown in Figure 10. In Wuhan, solar radiation reached the vertical surfaces are more than those in Guangzhou due to its relatively lower highest solar altitude, thus led to higher surface temperatures on vertical surfaces in Wuhan. On the other hand, as the latitude increases

from Wuhan to Harbin, the highest solar altitude of each city decreases. This caused the proportion of building shadows in Wuhan to be less than those in Beijing and Harbin when the distances between the buildings are the same.

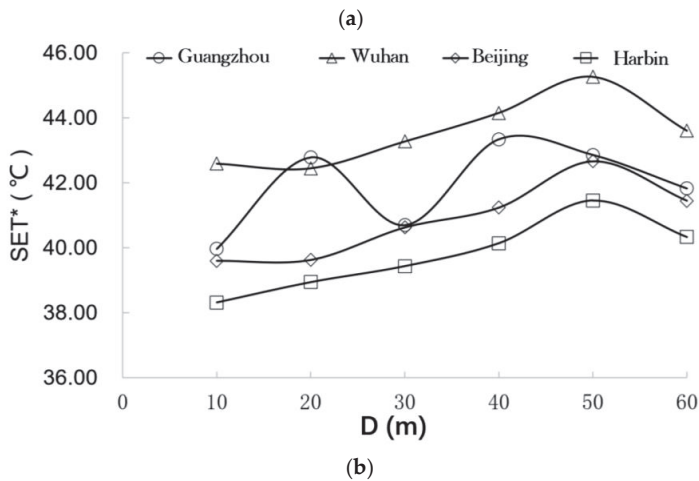
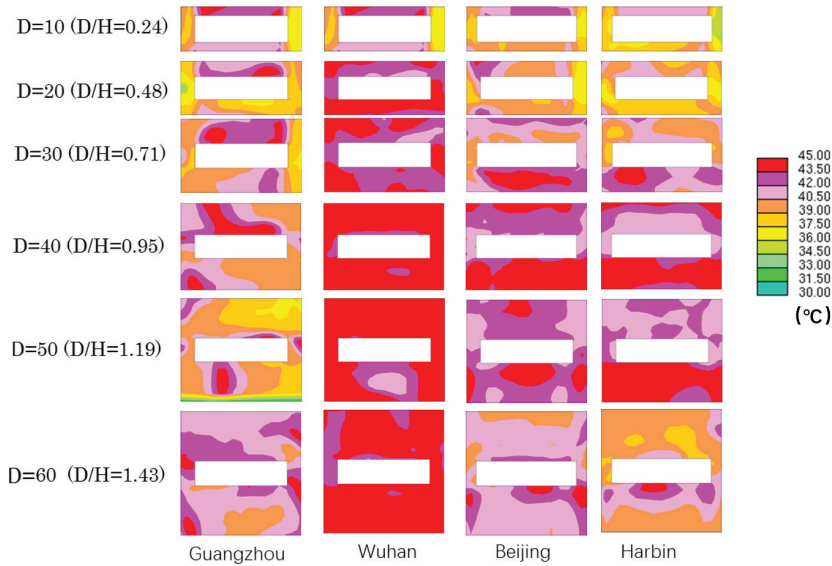


Figure 11. Results of SET*. (a) The distribution of SET* at 1.5 m. (b) Relationship between building distance and mean SET.

Figure 11b shows the relationship between building distance and mean SET* in four cities. As the distance between buildings decreases, a trend firstly increasing and then decreasing can be observed in the result of SET* around the building. For Wuhan, Beijing, and Harbin, D = 50 m (D/H = 1.19) is an inflection point. When D is less than 50 m, within the range of 20–50 m, the smaller the D is, the lower the SET* is, while D is more than 50 m, the opposite trend will be observed.

5. Discussion

The buildings in the simulation model of this study are simplified (Figure 6a), but the actual buildings have balconies, terraces, pitched rooves, and so on. In order to make the research results better applied to architectural design, it is necessary to conduct field survey on each typical residential area and compare the measured data with the simulated results so that the correction coefficient can be proposed.

On a typical meteorological day (21 June), the temperature at 12:00 in Wuhan, Beijing, and Harbin is the highest among the three key time points (8:00, 12:00, and 17:00), but the temperature in Guangzhou is the highest at 17:00. For comparison, 12:00 was selected as the analysis time. From the simulation results, the data of Guangzhou are quite different from those of the other three cities, and cannot form regular results with them. In future research, we can simulate the situation at 17:00 in Guangzhou to check whether it can achieve regularity with the simulation results of the other three cities.

6. Conclusions

Through simulation, we studied the relationships between thermal environment and building density in four different cities in China. The conclusions can be summarized as follows: for the outdoor wind environment of a residential area, when the distance between buildings is small, it is easier to form wind paths. The wind path can strengthen the wind velocity. As the value of the distance between buildings gradually increases, the effect of the wind path decreases. When the distance between buildings exceeds 40–50 m, the building density is low, the building's resistance to the wind becomes smaller and smaller, and the wind speed will gradually increase.

The overall trend of relationship between building density and MRT is that MRT increases with the increase in the distance between buildings. When the distance is in the range of 20–50 m, the MRT rise rate of each city is similar. For every 10 m increase in the distance between buildings, the MRT increases by about 1.25 °C.

As the distance between buildings decreases, a trend firstly increasing and then decreasing can be observed in the results; for Wuhan, Beijing, and Harbin, $D = 50$ m ($D/H = 1.19$) is an inflection point. When D is less than 50 m, within the range of 20–50 m, the smaller the D is, the lower the SET* is; meanwhile, when D is more than 50 m, the opposite trend will be observed.

Author Contributions: Conceptualization, G.Y. and Z.Z.; methodology, Y.X.; software, G.Y. and Z.Z.; validation, Y.X.; data curation, G.Y. and Z.Z.; writing—original draft preparation, G.Y. and Z.Z.; writing—review and editing, Z.Z.; funding acquisition, G.Y. and Z.Z.. All authors have read and agreed to the published version of the manuscript.

Funding: This project is funded by the science and technology funds from Liaoning Education Department (Grant No. LJ2019QL007) and the National Natural Science Foundation of China (Grant No. 51808410).

Institutional Review Board Statement: Not applicable.

Informed Consent Statement: Not applicable.

Conflicts of Interest: The authors declare no conflict of interest.

References

1. Medina-Ramón, M.; Zanobetti, A.; Cavanagh, D.P.; Schwartz, J. Extreme temperatures and mortality: Assessing effect modification by personal characteristics and specific cause of death in a multi-city case-only analysis. *Environ. Health Perspect.* **2006**, *114*, 1331–1336. [[CrossRef](#)]
2. Founda, D.; Giannakopoulos, C. The exceptionally hot summer of 2007 in Athens, Greece—A typical summer in the future climate? *Glob. Planet. Chang.* **2009**, *67*, 227–236. [[CrossRef](#)]
3. Harlan Sharon, L.; Ruddell Darren, M. Climate change and health in cities: Impacts of heat and air pollution and potential co-benefits from mitigation and adaptation. *Curr. Opin. Environ. Sustain.* **2011**, *3*, 126–134. [[CrossRef](#)]

4. Wu, W.; Xiao, Y.; Li, G.; Zeng, W.; Lin, H.; Rutherford, S.; Xu, Y.; Luo, Y.; Xu, X.; Chu, C.; et al. Temperature-mortality relationship in four subtropical Chinese cities: A time-series study using a distributed lag non-linear model. *Sci. Total Environ.* **2013**, *449*, 355–362. [\[CrossRef\]](#)
5. Liu, T.; Xu, Y.; Zhang, Y. Associations between risk perception, spontaneous adaptation behavior to heat waves and heatstroke in Guangdong province, China. *BMC Public Health* **2013**, *13*, 913. [\[CrossRef\]](#)
6. Watkins, R.; Palmer, J.; Kolokotroni, M.; Littlefair, P. The balance of the annual heating and cooling demand. within the London urban heat island. *Build. Serv. Eng.* **2002**, *23*, 207–213. [\[CrossRef\]](#)
7. Santamouris, M.; Papanikolaou, N.; Livada, I.; Koronakis, I.; Georgakis, C.; Argiriou, A.; Assimakopoulos, D.N. On the impact of urban climate on the energy consumption of buildings. *Sol. Energy* **2001**, *70*, 201–216. [\[CrossRef\]](#)
8. Song, Q.; Yang, L.; Yin, B. Building for the Climate Change: Passive Building. *Huazhong Arch.* **2014**, *4*, 11–15.
9. Hong, B.; Lin, B. Numerical studies of the outdoor wind environment and thermal comfort at pedestrian level in housing blocks with different building layout patterns and trees arrangement. *Renew. Energy* **2015**, *73*, 18–27. [\[CrossRef\]](#)
10. Hallaab, J.M. The potential of tree planting to climate-proof high density residential areas in Manchester, UK. *Landsc. Urban Plan.* **2012**, *104*, 410–417.
11. Pan, J.; Li, M. Impact of underlying surface structures of various urban blocks on the thermal environment by taking Lanzhou as a case study. *J. Saf. Environ.* **2012**, *6*, 140–145.
12. Whang, S.; Jeon, M.; Lee, S.; Kim, T.; Leigh, S. The effects of ground cover and shading on an outdoor thermal environment in an apartment complex. *Int. J. Sustain. Build. Technol. Urban Dev.* **2012**, *3*, 219–228. [\[CrossRef\]](#)
13. Weng, Q.; Lu, D.; Schubring, J. Estimation of land surface temperature-vegetation abundance relationship for urban heat island studies. *Remote Sens. Environ.* **2004**, *89*, 467–483. [\[CrossRef\]](#)
14. Arnfield, A.J. Two decades of urban climate research: A review of turbulence, exchanges of energy and water, and the urban heat island. *Int. J. Clim.* **2003**, *23*, 1–26. [\[CrossRef\]](#)
15. Santamouris, M. Cooling the cities—A review of reflective and green roof mitigation technologies to fight heat island and improve comfort in urban environments. *Sol. Energy* **2014**, *103*, 682–703. [\[CrossRef\]](#)
16. Ying, X.Y.; Zhu, W.; Hokao, K. Comparative Study of the Effect on Outdoor Wind Environment by High-rise Buildings Layout Types. *Sci. Geogr. Sin.* **2013**, *33*, 1097–1103.
17. Hsieh, C.M.; Chen, H.; Ooka, R.; Yoon, J.O.; Kato, S.; Miisho, K. Simulation analysis of site design and layout planning to mitigate thermal environment of riverside residential development. *Build. Simul.* **2010**, *3*, 51–61. [\[CrossRef\]](#)
18. Kubota, T.; Miura, M.; Tominaga, Y.; Mochida, A. Wind tunnel tests on the relationship between building density and pedestrian-level wind velocity: Development of guidelines for realizing acceptable wind environment in residential neighborhoods. *Build. Environ.* **2008**, *43*, 1699–1708. [\[CrossRef\]](#)
19. Ying, X.; Zhu, W.; Hokao, K.; Ge, J. Numerical research of layout effect on wind environment around high-rise buildings. *Arch. Sci. Rev.* **2013**, *56*, 272–278. [\[CrossRef\]](#)
20. Ali-Toudert, F.; Mayer, H. Numerical study on the effects of aspect ratio and orientation of an urban street canyon on outdoor thermal comfort in hot and dry climate. *Build. Environ.* **2006**, *41*, 94–108. [\[CrossRef\]](#)
21. Juan, A.A.; Karmelet, H. A comparison of thermal comfort conditions in four urban spaces by means of measurements and modelling techniques. *Build. Environ.* **2015**, *93*, 245–257.
22. Johansson, E.; Emmanuel, R. The influence of urban design on outdoor thermal comfort in the hot, humid city of Colombo, Sri Lanka. *Int. J. Biometeorol.* **2006**, *51*, 119–133. [\[CrossRef\]](#) [\[PubMed\]](#)
23. Hwang, R.L.; Lin, T.P.; Matzarakis, A. Seasonal effects of urban street shading on long-term outdoor thermal comfort. *Build. Environ.* **2011**, *46*, 863–870. [\[CrossRef\]](#)
24. Zhou, Z.; Deng, Q.; Mochida, A. Effect of Piloti on Wind Environment in Residential Area in a Hot and Humid City, Taking Residential Area in Wuhan as Study Case. In Proceedings of the 23rd Symposium on Wind Engineering, Tokyo, Japan, 12 December 2014; Volume 23, pp. 73–78.
25. Yang, F.; Qian, F.; Lau, S.S.Y. Urban form and density as indicators for summertime outdoor ventilation potential: A case study on high-rise housing in Shanghai. *Build. Environ.* **2013**, *70*, 122–137. [\[CrossRef\]](#)
26. Jin, H.; Liu, Z.; Jin, Y. The Effects of Residential Area Building Layout on Outdoor Wind Environment at the Pedestrian Level in Severe Cold Regions of China. *Sustainability* **2017**, *9*, 2310. [\[CrossRef\]](#)
27. Du, Y.; Mak, C. Improving pedestrian level low wind velocity environment in high-density cities: A general framework and case study. *Sustain. Cities Soc.* **2018**, *42*, 314–324. [\[CrossRef\]](#) [\[PubMed\]](#)
28. Bourbia, F.; Awbi, H.B. Building cluster and shading in urban canyon for hot dry climate: Part 2: Shading simulations. *Renew. Energy* **2004**, *29*, 291–301. [\[CrossRef\]](#)
29. Johansson, E. Influence of urban geometry on outdoor thermal comfort in a hot dry climate: A study in Fez, Morocco. *Build. Environ.* **2006**, *41*, 1326–1338. [\[CrossRef\]](#)
30. Xuan, Y.; Yang, G.; Li, Q.; Mochida, A. Outdoor thermal environment for different urban forms under summer conditions. *Build. Simul.* **2016**, *9*, 281–296. [\[CrossRef\]](#)
31. Zhou, Z.; Deng, Q.; Yang, G.; Lin, Y. Quantitative Study of Using Piloti for Passive Climate Adaptability in a Hot-Summer and Cold-Winter City in China. *Int. J. Environ. Res. Public Health* **2018**, *15*, 2202. [\[CrossRef\]](#) [\[PubMed\]](#)

32. Yoshida, S.; Murakami, S.; Ooka, R.; Mochida, A.; Tominaga, Y. CFD Prediction of Thermal Comfort in Microscale Wind Climate. In Proceedings of the 3rd International Symposium on Computational Wind Engineering, Tokyo, Japan, 14 January 2000; pp. 27–30.
33. Craft, T.J.; Launder, B.E.; Suga, K. Development and application of a cubic eddy-viscosity model of turbulence. *Int. J. Heat Fluid Flow* **1996**, *17*, 108–115. [[CrossRef](#)]
34. Chen, H.; Ooka, R.; Harayama, K.; Kato, S.; Li, X. Study on outdoor thermal environment of apartment block in Shenzhen, China with coupled simulation of convection, radiation and conduction. *Energy Build.* **2004**, *36*, 1247–1258. [[CrossRef](#)]
35. Li, Q.; Mochida, A.; Meng, Q.; Zhao, L. Comparison of Turbulence Models for Numerical Simulation of Outdoor Wind Environment around Building. *J. South China Univ. Technol.* **2011**, *39*, 121–127.
36. Yoshie, R.; Mochida, A.; Tominaga, Y.; Kataoka, H.; Harimoto, K.; Nozu, T.; Shirasawa, T. Cooperative project for CFD prediction of pedestrian wind environment in the Architectural Institute of Japan. *J. Wind. Eng. Ind. Aerodyn.* **2007**, *95*, 1551–1578. [[CrossRef](#)]
37. Yoshie, R.; Mochida, A.; Tominaga, Y.; Shirasawa, T.; Tanaka, H. AIJ Cooperative project for practical applications of CFD to air ventilation, pollutant and thermal diffusion in urban areas. In Proceedings of the Seventh International Conference on Urban Climate, Yokohama, Japan, 29 June–3 July 2009.
38. Howell, J.R.; Perlmutter, M. Monte Carlo Solution of Thermal Transfer through Radiant Media between Gray Walls. *J. Heat Transf.* **1964**, *86*, 116–122. [[CrossRef](#)]
39. Omori, T.; Yang, J.; Kato, S.; Murakami, S. Radiative Heat Transfer Analysis Method for Coupled Simulation of Convection and Radiation in Large-Scale and Complicated Enclosures: Part 1—Accurate Radiative Heat Transfer Analysis based on Monte Carlo Method. *Trans. Soc. Heat. Air-Cond. Sanit. Eng. Jpn.* **2003**, *28*, 103–113.
40. Gebhart, B. A New Method for Calculating Radiant Exchanges. *ASHRAE Trans.* **1959**, *65*, 321–332.
41. Schoonhoven, C.B.; Woolley, J.L. Urban thermal environment measurements and numerical simulation for an actual complex urban area covering a large district heating and cooling system in summer. *Atmos. Environ.* **2005**, *39*, 6362–6375.
42. Mochida, A.; Yoshino, H.; Miyauchi, S.; Mitamura, T. Total analysis of cooling effects of cross-ventilation affected by microclimate around a building. *Sol. Energy* **2006**, *80*, 371–382. [[CrossRef](#)]
43. Li, Q. *Effects of Building Clusters' Planning and Design on Outdoor Microclimate in Hot and Humid Zone*; South China University of Technology: Guangzhou, China, 2009.
44. Nation Meteorological Information Center. *China's Special Meteorological Data Set for Thermal Environment Analysis*; China Architecture & Building Press: Beijing, China, 2005.

Climate Change Performance of nZEB Buildings

Germán Ramos Ruiz ^{1,*} and Alba Olloqui del Olmo ²

¹ Department of Building Construction, Services and Structures, School of Architecture, Universidad de Navarra, 31009 Pamplona, Spain

² Marta González Arquitectos S.L., 28043 Madrid, Spain

* Correspondence: gramrui@unav.es

Abstract: Buildings are one of the key factors in working towards a low-carbon economy to help mitigate climate change. For this reason, many of the current regulations aim to reduce their consumption and increase their efficiency, as is the case in the European Union with the Energy Performance of Buildings Directive (EPBD). Terms such as nearly zero-energy buildings (nZEB) or zero-emission buildings (ZEB) are increasingly used. However, these terms and regulations focus on energy and emissions, ignoring user comfort. This research shows the performance of these buildings in the face of climate change, as their strengths are not limited to energy consumption or emissions, but also to improving user comfort. By examining the compliance of a real semi-detached house with the different Spanish energy regulations (NBE-CTE 79, CTE-DB HE 2013 and CTE-DB HE 2019), its performance in terms of energy and comfort in different future scenarios defined by the Intergovernmental Panel on Climate Change (IPCC) is evaluated. The results show that the building with nZEB criteria (CTE-DB-HE 2019) reduces its energy consumption by an average of 84.36% compared to the other two energy standards. In terms of comfort, measured according to the Fanger criteria (steady state model), the hours throughout the year in the “neutral” thermal sensation category are similar; however, the hours in the “slightly cool” category are reduced by 57%, improving by up to eight times the “slightly warm” category. The nZEB building proves to be more resilient to climate change by mitigating and homogenizing its response to climatic variations.

Citation: Ramos Ruiz, G.; Olloqui del Olmo, A. Climate Change Performance of nZEB Buildings. *Buildings* **2022**, *12*, 1755. <https://doi.org/10.3390/buildings12101755>

Academic Editors: Wei Yang and Yaolin Lin

Received: 23 September 2022

Accepted: 15 October 2022

Published: 20 October 2022

Publisher’s Note: MDPI stays neutral with regard to jurisdictional claims in published maps and institutional affiliations.



Copyright: © 2022 by the authors. Licensee MDPI, Basel, Switzerland. This article is an open access article distributed under the terms and conditions of the Creative Commons Attribution (CC BY) license (<https://creativecommons.org/licenses/by/4.0/>).

Keywords: nZEB buildings; energy codes; building energy models; Código Técnico de la Edificación; thermal waves; comfort

1. Introduction

High temperatures, drought and wildfires, availability of fresh water, floods, sea-level rise and coastal areas, etc. are some of the natural consequences of climate change [1]. Unfortunately, these are common words today, which is why there is global concern about climate change. Since the entry into force of the Paris Agreement, countries have pledged to take action to mitigate this situation. The goal is to reduce CO₂ emissions to hold “the increase in the global average temperature to well below 2 °C above preindustrial levels and pursuing efforts to limit the temperature increase to 1.5 °C above preindustrial levels” [2,3]. In the case of the European Union, the objective is to cut emissions by at least 55% by 2030 compared to 1990 levels, with an ultimate goal of reaching climate neutrality by 2050. This requires action in all sectors of the economy in a balanced and fair manner to preserve the EU’s competitiveness. For these reasons, the European Commission announced in December 2019 the European Green Deal as its roadmap to achieving EU climate neutrality by 2050 [4]. This document emphasizes the importance of buildings, since their construction, use and renovation require large amounts of energy and resources, being responsible for 40% of the energy consumed. In fact, in order to achieve these objectives, the European Commission estimates that existing buildings require an annual renovation rate twice as high as the current one (0.4–1.2%).

This roadmap includes among its documents the Energy Performance of Buildings Directive (EPBD). Its initial objectives (2002) [5] were the creation of a general framework for an energy calculation methodology for buildings, the application of minimum requirements for new buildings and for those undergoing major renovations, the implementation of energy performance certificates and the need for an inspection of HVAC systems in buildings older than 15 years. Subsequently, there was a recast (2010) [6], the “20/20/20” directive, the objective of which was to reduce energy consumption by 20%, increase the energy efficiency of HVAC systems by 20% and increase the use of renewable energies by 20% by 2020. In this version, the term nearly Zero Energy Building (nZEB) started to be used. Its initial definition was: “a building that has a very high energy performance, (. . .). The nearly zero or very low amount of energy required should be covered to a very significant extent by energy from renewable sources, including energy from renewable sources produced on-site or nearby”. Then, in 2018 [7], there was an amendment emphasizing the need for a progressive “transformation of existing buildings into nearly zero-energy buildings, in particular by an increase in deep renovations” and Member States were encouraged to provide guidelines and outline measures to achieve these goals on an equal basis for all citizens.

Currently, there is a proposed recast of the EPBD (2021) [8], which qualifies the definition of the term nearly Zero Energy Building, emphasizing that nZEB buildings require, to a significant extent, to be covered by renewable energy, rather than should be. As can be seen, the definition of the term nZEB is not so straightforward due to both economic and building design implications [9,10]. Many aspects remain to be defined, for example, the frequency with which the energy balance of the building should be calculated in order to take into account renewable energies. What is correct, an annual, monthly or hourly energy balance? [11,12]. In the case of dwellings with a Mediterranean climate, a zero annual energy balance may be easy to achieve due to the high energy generation that can be obtained in summer, but if the balance is considered on a monthly basis, it is difficult to achieve a zero energy balance in the winter months. This problem can be overcome if it is possible to share energy with other buildings throughout the year [13].

EU Member States should regularly monitor compliance with this Directive and are obliged to submit a report every four years to the Commission, but it is up to the Member States to define how to achieve these objectives. The best way is through the mandatory building regulations of each country, in particular those related to energy savings. In the case of Spain, the starting point is the energy code NBE-CT 79 of 1979 (“Norma Básica de la Edificación Condiciones Térmicas de los edificios”) [14], which was updated in 2006 with the technical building code CTE-DB-HE (“Código Técnico de la Edificación-Documento Básico-Ahorro de Energía”) [15]. This standard has been updated several times over the years as building requirements have increased. In 2017, this document defined a nearly zero energy consumption building—similar to nZEBs—as a building that meets the regulatory requirements established for new buildings in the CTE [16]. Fortunately, the requirements have been increasing in the following updates, the last one being CTE-DB HE 2019, which defines requirements close to the passive house, and approaches the definition of nZEB established by the EPBD directive [17].

There are several studies that analyze the savings potential of nZEB buildings based on the Spanish technical building code, such as the one by Cerezo-Narváez et al. that studied the impact of nZEB buildings in southern Spain, where energy savings of 69% to 127% are achieved, and a reduction in carbon dioxide emissions of 65% to 118% [18]; or the one conducted by García-Ballano et al. in which, using a geographic information system (GIS) with data of the transmittance of buildings, they delimit priority areas to increase the impact of European funds for the improvement of buildings [19].

In general, when we refer to an nZEB building, we are considering a building with an energy balance close to zero; however, there are other aspects to take into account in buildings, such as user response and their ability to create their own operating profiles and specify their comfort conditions [20]. This aspect, as Aste et al. point out [21], is one

of the factors responsible for the energy performance gap between energy models and reality. Buildings are designed according to energy regulations—based on reducing energy consumption—but when the building is used, users demand comfort and their changes in the use of the building alter its energy consumption.

The main objective of this research is to show the climate change performance of nZEB buildings, in particular of buildings considered nZEB by Spanish energy regulations. This behavior will be analyzed from two approaches: energy consumption and user comfort. The correlation of both aspects, taking into account climate change, allows us to know the advantages and disadvantages of this type of building so that they can be useful for designers, architects, engineers, etc., as well as for users and investors. There are quite a few studies that deal with nZEB buildings and their energy or comfort performance; some even deal with both topics at the same time, but none has been found that deals with both topics and focuses on the performance that this type of building has under climate change.

Regarding studies related to nZEB buildings and their energy consumption, there are examples that have studied from residential buildings [22] to university campuses [23]. D'Agostino et al. analyze the impact of the climate zone in which the building is located by studying eight different locations in the European Union [24]. Ascione et al. analyzed the resilience of nZEB buildings against climate change, highlighting that, in the future, the energy demand for heating or cooling is likely to increase due to thermal discomfort [25].

From research analyzing the comfort of nZEB buildings, all under real weather conditions, the main trend is the risk of overheating that occurs during free oscillation periods when the HVAC system is off [26,27]. Yang et al. highlight in their review of the implications of building energy consumption on user comfort [28] that the risk of the overheating of buildings whose cooling is based on natural ventilation is even greater in the context of climate change. In this regard, there is some resistance to include comfort limits in the definitions of nZEB buildings, as Attia et al. highlight: “Indoor environmental quality requirements regarding discomfort risk and mechanical ventilation are not well developed in most nZEB national plans”. The fact is that energy savings and comfort limits are opposing objectives, as Guillén-Lambea et al. explain: “setting the thermal comfort parameters for a nZEB is a big challenge because the parameters must provide adequate indoor thermal conditions while at the same time guaranteeing the sustainability of buildings”.

There are two main approaches to analyzing user comfort: the steady state model or heat balance and the adaptive comfort model. The first is based on the studies conducted by Fanger in the 1970s [29,30], in which he proposes two indices related to the perception of each user: the predicted mean vote index (PMV) and the predicted percentage of dissatisfied index (PPD); and classifies the indoor environment according to a scale that predicts the thermal sensation that users will have. It is the basis for UNE-EN ISO 7730:2006 [31] and ASHRAE 55-1992 [32]. The second model is based on the user's thermal sensation and their ability to adapt according to the ventilation and relative humidity of the spaces. It has indoor temperature ranges of 18–30 °C with relative humidities up to 80%. ASHRAE 55 standards from 2010 [33,34] and UNE-EN 16798-1:2020 [35], which replaces UNE-EN 15251:2008 [36], are based on this model.

In this research, the Fanger criterion (steady state model) has been chosen since the objective is to show the impact of climate change on the thermal sensation of nZEB buildings. This criterion allows to obtain a comfort category value in all indoor temperature ranges. In contrast, the adaptive criterion takes into account the outside temperature, and ranges within limits (18–30 °C) between which the user has the capacity to adapt its thermal comfort sensation with clothing, natural ventilation, etc. Outside these limits, no adaptive comfort values are obtained; however, with the Fanger criterion, the user's degree of discomfort is obtained on a thermal sensation scale.

The research is structured as follows. In Section 2, the process followed to obtain the results is described. The starting point is the creation of a building energy model (BEM) based on a real semi-detached house, to which different retrofits are carried out to comply with three updates of the Spanish energy regulation (Section 2.1). Then, the

process of obtaining the weather files with which each building will be simulated is explained (Section 2.2). The building energy models are simulated with a total of 38 weather files, from the normative one of the Spanish regulation to weathers created taking into account the scenarios of the Intergovernmental Panel on Climate Change (IPCC). Finally, Section 2.3 describes the simulation process to obtain the energy and comfort results for each combination. Section 3 shows the energy results obtained in terms of total, heating and cooling energy, and in relation to comfort, the hours of the year within each thermal sensation category (according to Fanger). Finally, Sections 4 and 5 show the discussion and conclusions of the research.

2. Analysis Method

Figure 1 shows the outline of the analysis method used to measure the performance of buildings with nZEB criteria to climate change, both in terms of energy consumption and comfort. It is divided into three sections: the development of the building energy model (BEM) in EnergyPlus, in this case according to the different Spanish technical energy codes; the preparation of the weather files with which the energy models will be simulated; and the results to be analyzed: energy consumption and user comfort.

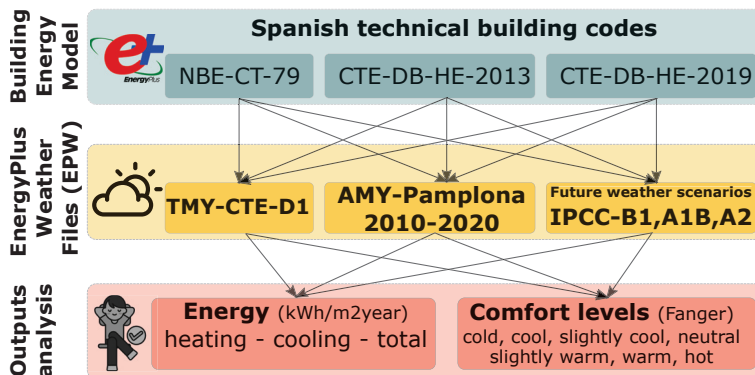


Figure 1. Scheme of the analysis method used.

2.1. Building Energy Model Used

The starting point is the creation of the building energy model in a simulation software, in this case EnergyPlus [37] as it is one of the most widely used softwares for performing energy simulations [38]. This software passed the BESTEST set by the ASHRAE 140 standard in 2004 [39,40], and has a very active community of developers who continue to make improvements to it to provide more capabilities while improving its accuracy. In May 2022, its buildings database was upgraded to the 2020 version of ASHRAE 140 standard [41].

This energy model is based on a semi-detached house built in 2005. Figure 2 shows, from left to right, an actual image of the building, together with the graphical representations of the model made in OpenStudio, one of the softwares that serve as the graphical interface for EnergyPlus [42,43]. It is a two-storey detached house with four bedrooms, two bathrooms and a toilet, living-dining room, kitchen and garage. It has a northeast-southwest orientation and has a series of verandas and overhangs that protect the building from solar radiation.

The use of this building has been considered appropriate because it was built before the first Spanish technical building code and, specifically, is based on the NBE-CT-79 standard. Based on this, two models were made to comply with the technical building codes of 2013 and 2019, since they are the ones that include significant changes focused on obtaining buildings with nZEB criteria. Table 1 shows some of the significant aspects that differentiate each of the energy codes.

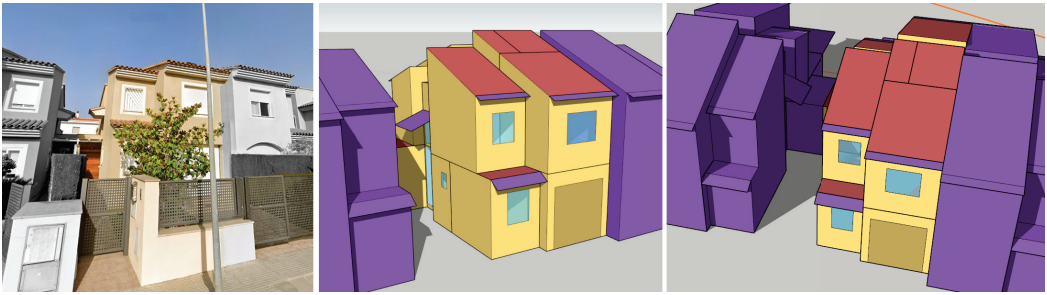


Figure 2. Semi-detached house under study. Real image and OpenStudio representation.

As a summary of the evolution of building regulations in Spain, the energy code (NBE-CT-79) was based on obtaining a value that expressed an overall transmittance coefficient, called the K-value, which is the weighted average of the thermal transmittance of each element of the thermal envelope as a function of its surface area. Some thermal envelope values were limited according to their climatic zone, so the K-value had to be below certain limits. In 2006, the technical building code was approved, eliminating this K-value and increasing the thermal transmittance requirements for each of the envelopes. Two new criteria have been added: limitation of primary energy consumption, both total and from non-renewable sources; and limitation of energy demand. In this case, Table 1 shows these parameters for the 2013 technical code instead of the 2006 version, as the latter is less demanding.

Finally, the current energy standard in force in Spain, the 2019 technical building code, implemented significant changes with respect to the previous ones. The limitation of energy consumption was eliminated, focusing on its control. The characteristics of the envelope were further limited and new aspects related to solar control in summer and the envelope air-tightness at 50 Pa were added. The K-value was also restored with limits depending on the compactness of the building, so that compact buildings with reduced overall transmittance are encouraged. The minimum contribution percentages of renewable energies to cover DHW demand were also increased. Although there is still room for improvement, the overall treatment of the different aspects of the building means that buildings designed to this standard can be considered nZEB buildings, as will be seen in their energy and comfort performance in Section 3.

The initial building energy model is based on the information about the real building as it was built. Thereafter, this model was modified to comply with the technical building codes CTE-DB-HE 2013 and CTE-DB-HE 2019, as if they were energy retrofittings of the real building. Since EnergyPlus does not have modules to certify that a given design complies with Spanish energy regulations, the process of creating the models involves the use of other software to provide us with the necessary information on the modifications to be made to these models to comply with the different Spanish energy regulations. This software is a plugin of Openstudio, the SG-Save [44]. The initial model takes into account the characteristics of the as-built building, which are modified and validated with SG-Save to comply with the two Spanish technical building codes, the CTE-DB HE 2013 and the CTE-DB HE 2019.

Table 1. Differences between the Spanish technical energy codes.

	NBE-CT-79 [14]	CTE-DB-HE 2013 [45]	CTE-DB-HE 2019 [17]	Unit
Limitation of primary energy consumption ⁽¹⁾				
-Non-renewable primary energy limit	-	90	38	kWh/m ² year
-Total primary energy limit	-	-	76	kWh/m ² year
Limitation and control of energy demand ⁽²⁾				
-Energy demand heating limit	-	47	-	kWh/m ² year
-Energy demand cooling limit	-	15–20	-	kWh/m ² year
Characteristics of the building envelopes (facades, roofs, etc.) ⁽³⁾				
-Walls and floors in contact with outside air	1.2–1.4	0.6	0.41	W/m ² K
-Ceilings in contact with outside air	0.9	0.4	0.35	W/m ² K
-Walls, floors and ceilings in contact with non-habitable spaces or with the ground	1.6	0.6	0.65	W/m ² K
-Dividing walls or interior partitions belonging to the thermal envelope	1.6	0.85–1.2	0.65	W/m ² K
-Openings (frame, glass and, if applicable, shutter box)	-	2.7	1.8	W/m ² K
-Doors with semi-transparent surface equal to or less than 50%	-	-	5.7	W/m ² K
-Horizontal interior partitions (same use)	1.4	1.2	1.2	W/m ² K
-Vertical interior partitions (same use)	1.8	1.2	1.2	W/m ² K
-Horizontal interior partitions (different use)	1.4	0.85	0.85	W/m ² K
-Vertical interior partitions (different use)	1.8	0.85	0.85	W/m ² K
-Air permeability of openings (100Pa overpressure)	-	27	9	m ³ /h · m ²
-K-value limit as a function of building shape (compactness)	0.84–1.47	-	0.48–0.67	W/m ² K
-Solar control of the thermal envelope ⁽⁴⁾	-	-	2	kWh/m ² month
-Limit value of the air change ratio at a pressure of 50 Pa ⁽⁵⁾	-	-	6–3	ACH
Building use profiles				
Schedules (setpoints, loads, ventilation, etc.)	-	(6)	(7)	
Contribution of renewable energies				
Minimum annual solar contribution for DHW	-	50	70	%

⁽¹⁾ Based on a 100 m² house. ⁽²⁾ The CTE-2013 is based on the limitation of energy demand and the CTE-2019 on its control. ⁽³⁾ All values are for the city of Pamplona (climate D1 according to the Spanish technical code). ⁽⁴⁾ Ability to block solar radiation and involves the full activation of the mobile shading devices. Month of calculation: July. ⁽⁵⁾ Depending on the compactness. More demanding the less compact. ⁽⁶⁾ All values are defined by the Spanish technical code. ⁽⁷⁾ Same schedules as in CTE-2013, except for the absence of 4 nighttime ACH in summer. This avoids the possibility of free cooling in summer.

Table 2 shows the general differences between the three models developed. As can be seen, the baseline energy model is very close to the CTE-DB-HE 2013 model. The year of construction, 2005, is very close to the creation of the first version of the Spanish technical building code (2006), so its construction characteristics are closer to that standard than to the NBE-CT 79. Its modifications are mainly based on the increase of insulation in façades, roofs and slabs-on-grade foundations; and on the replacement of window glazing beads, which slightly decreases their permeability, slightly reducing the overall infiltration of the building.

However, the CTE-DB-HE 2019 model does have significant changes with respect to the other two models, since the current regulation aims to obtain buildings that achieve the objectives set by the European Commission regarding the energy efficiency of buildings. In addition, if they follow the requirements of the CTE-DB-HE 2019 in terms of new buildings, they are considered nZEB buildings in Spain.

Table 2. General characteristics of the Building Energy Models according to the different Spanish technical building codes.

	NBE-CT-79	CTE-DB-HE 2013	CTE-DB-HE 2019
Building Envelope			
Façade: U value [W/m ² K]	0.325	0.229	0.127
Roof: U value [W/m ² K]	0.428	0.356	0.202
Slabs-on-grade foundations: U value [W/m ² K]	3.579	0.681	0.514
Windows: U-Factor [W/m ² K]	2.3	2.3	1.1
Frame and divider: Frame conductance [W/m ² K]	4	4	1.8
Windows permeability (m ³ /h·m ²)	50	27	9
Building systems			
HVAC systems-Heating: Performance [%]	0.85	0.85	0.98
DHW Boiler: Performance [%]	0.85	0.85	0.98
Exterior air changes [Ventilation and infiltrations]			
Natural ventilation [ach]	0.71	0.71	0.32
Mechanical ventilation with heat recovery (performance 0.76–0.8%) [ach]	0	0	0.63
Infiltrations [ach]	0.6	0.5	0.21
Renewable energies			
Solar collectors contribution [%]	-	-	76.7

Regarding the building envelope, not only was the thermal transmittance of the façades, roofs and slabs-on-grade foundations significantly decreased, but also the glazing and window frames were modified to reduce both the U-value of the glazing and the conductance of the window frames, reducing their permeability. As for the building's HVAC systems, the boiler was replaced with a more efficient one and solar thermal collectors were installed to reduce the energy demand for domestic heat water (DHW). No changes were made to the cooling system since the demand is not significant due to the weather of the site (Pamplona). Regarding air exchange between a building and the outside environment, there are two aspects to take into account: ventilation (natural or mechanical) and infiltrations. The NBE-CT 79 and CTE-DB-HE 2013 models have natural ventilation in their spaces, while the CTE-DB-HE 2019 model has a heat recovery unit that makes it possible to take advantage of the thermal energy of the air (heating or cooling), which means significant savings in its energy demand. All these actions contribute to reducing the overall infiltration of the building (air changes per hour-ACH), which reduces the energy demand to comply with the consumption limits established by the Spanish technical building code.

Finally, another key aspect of any nZEB building is the reduction of energy consumption due to the production of energy from renewable sources in or near the building itself. In the case of the CTE-DB HE 2019 model, it has solar thermal collectors that provide 76.7% of the annual DHW demand. However, as will be explained in Section 3, this contribution will not be taken into account in the results since the comparisons between the models are made only for heating and cooling, without taking into account DHW energy demand, since its energy demand is the same for the three models.

2.2. Weather File Creation

The second aspect of the analysis method is the creation of the weather files, with which we will perform the simulations. As shown in Figure 1, three types of weather files will be used: typical meteorological year (TMY), actual meteorological year (AMY) and future weather scenarios based on the Intergovernmental Panel on Climate Change (IPCC) [46,47]. As Bhandari et al. point out, each of these weather files should be selected based on the purpose, location, and engine used in the simulation [48].

Typical meteorological year files represent the weather at a location over a given period of time without taking into account extreme weather conditions. They are used to check

the performance of buildings under standard conditions, to obtain energy performance certificates, etc. In this case, the weather used is the one established by the Technical Building Code (CTE) for the place of the case study (Pamplona, Spain), which corresponds to D1 weather.

Actual meteorological year (AMY) files are specific to a given location and time period. They are produced using data from actual weather stations located in or around the building, and can even be obtained by interpolating data from other nearby weather stations. The latter option is often used by external data providers (third-party weather companies). This type of file takes into account what has happened at a particular place and time, so it includes information regarding unusual weather events that have occurred, such as heat and cold waves. They are used to calibrate building energy models, calculate utility costs and energy bills, study the actual performance of HVAC systems, etc. [49]. In this case study, the weather files are developed from the data of the weather stations of the Government of Navarra [50] and using the EnergyPlus auxiliary program, weatherconverter. Ten years have been chosen, from 2010 to 2020, which represent to some extent the onset of the climate change we are experiencing, as they include several hot and cold waves [51,52]. They also provide climate continuity with the IPCC future weathers (2020 to 2100).

Finally, future weather files that take into account the different climate change scenarios. Three tools are currently available to generate such files [53]: the CCWeatherGen tool, developed by Jentsch et al. in 2013 [54]; the WeatherShift tool, which is a collaborative project of Arup North America Ltd (Arup) and Argos Analytics LLC [55]; and the Meteororm software [56,57], which allows access to typical meteorological years and historical time series, as well as modifying weather files based on global climate models according to the IPCC Fourth Assessment Report (AR4-2007).

The CCWeatherGen tool, initially only valid for UK weather files, was later adapted to the whole world (CCWorldWeatherGen). Using a Microsoft Excel sheet, the weather file in *.epw format (EnergyPlus weather) was transformed into a future weather file through a morphing methodology that allowed us to obtain future weather files for the years 2020, 2050 and 2080 [54,58]. The *WeatherShift*TM tool is based on the representative concentration pathway emission scenarios (RCP4.5 and RCP8.5) of the IPCC fifth assessment report (AR5-2015). However, it generates weather files for cities near Madrid and Barcelona (in the case of Spain), quite far from Pamplona, the city under study. The Meteororm software allowed us to process weather files from 2020 to 2100 every 10 years for any location in the world. They are based on three future emissions scenarios—B1, A1B and A2—in order of weather severity. The B1 scenario is based on world population growth peaking mid-century, with rapid changes in economic structures towards a service and information economy; the A1B scenario assumes very rapid economic growth, a world population similar to B1 and rapid introduction of new, more efficient and balanced technologies using all energy sources; and the A2 scenario describes a very heterogeneous world with high population growth, slow economic development and slow technological change [59]. Due to its versatility and ease of use, it was the tool used for the generation of future weather scenarios in this study. Twenty-seven weather files are generated, nine for each climate change scenario (B1, A1B and A2 in order of climate severity), at 10-year intervals, from 2020 to 2100.

2.3. Simulation and Variables under Study

Once the building energy models and weather files to be used were defined, the next step of the methodology was the selection of the results to be analyzed. The results to be analyzed were energy (total, heating and cooling) and comfort levels; the former to analyze the impact on energy consumption of the requirements for a building to be considered nZEB according to the Spanish technical building code, and the latter to measure the performance of this type of buildings with regard to climate change. Whereas energy consumption is simple to measure (kWh/m² year), the measurement of user comfort can depend on many variables, as highlighted in the introduction (see Section 1).

As explained above, two main comfort models are available, the steady state model or heat balance and the adaptive comfort model. The Spanish technical building code does not consider the adaptive comfort model, but establishes, for example at residential level, limits for the temperature set-points at which users are supposed to be comfortable. The quantitative drawback of the adaptive model is that it does not provide information on the user's degree of comfort, but rather on his or her ability to adapt thanks to the outside environment. EnergyPlus has different modules for measuring user comfort (Fanger, Pierce Two-Node, Kansas State University Two-Node, ASHARE 55, etc.). Among them, the Fanger steady-state method was chosen because it allowed us to establish different comfort levels in the whole possible comfort–discomfort range. This facilitates the measurement of the degree of improvement or worsening of buildings with nZEB criteria in terms of comfort levels, where the “neutral” level is the desirable level as opposed to the extreme levels of “hot” and “cold”.

With all these data, it was possible to analyze the performance of buildings with nZEB criteria to climate change.

3. Results

Figure 3 shows the energy consumption results of the HVAC systems for the different models, taking into account all the weather scenarios described in Section 2.2. The DHW consumption of the models has not been taken into account in the plots since it is the same consumption for the three Spanish energy codes, although it is true that the CTE-DB HE 2019 model, in addition to having a higher efficiency boiler, has solar thermal collectors to reduce the DHW energy demand, specifically more than 75% of the energy required. It was decided not to add this consumption in order to highlight the differences that depend on the thermal envelope, since it is the envelope that is responsible for user comfort, which will be analyzed later in Figures 4–9.

The structure of Figure 3 is based on three bar charts, from top to bottom: total energy consumption, heating consumption and cooling consumption in kWh/m² year. As can be seen, the predominant consumption in Pamplona is heating, with cooling consumption being around 8.5% on average with respect to heating [for NBE-CT-79 and CTE-DB HE 2013 models]. Each color represents a model, with brown-sienna corresponding to the NBE-CT-79 model, gray to the CTE-DB HE 2013 model and dark green to the CTE-DB HE 2019 model. The weather scenarios are ordered from left to right as follows: the first one is the typical normative weather of the Spanish technical building code, in this case corresponding to climate zone D1 (similar to typical meteorological year-TMY); followed by ten real weather events of Pamplona from 2011 to 2020 (actual meteorological year-AMY), in which the background has been shaded to facilitate their analysis; and finally, the weather scenarios developed with the Meteornorm v7 software taking into account the IPCC considerations for climate change scenarios B1, A1B and A2 (in order of weather severity). They have been grouped by years, from 2020 to 2100.

As can be seen, the CTE D1 regulatory weather is similar to the real weather from 2011 to 2020, being one of the most demanding in terms of heating and therefore less severe in terms of cooling. However, what is really remarkable from the consumption graphs is the important difference between the NBE-CT-79 and CTE-DB HE 2013 models versus the CTE-DB HE 2019 model (an average of 84.36%). As explained in Section 2.1, this model complies with the requirements of the CTE-DB HE 2019 for new buildings, being considered by the Spanish regulations an nZEB building. The requirements of this standard make the building robust to the great weather variability of the years (2011 to 2020). The models of the previous technical building codes reproduce in their consumptions the weather changes with oscillations in their total consumptions of up to 30.9 kWh/m² year compared to 5 kWh/m² year of the CTE-DB HE 2019 model. This proves that nZEB buildings not only substantially reduce their consumption but are also prepared to deal with weather changes and are therefore robust.

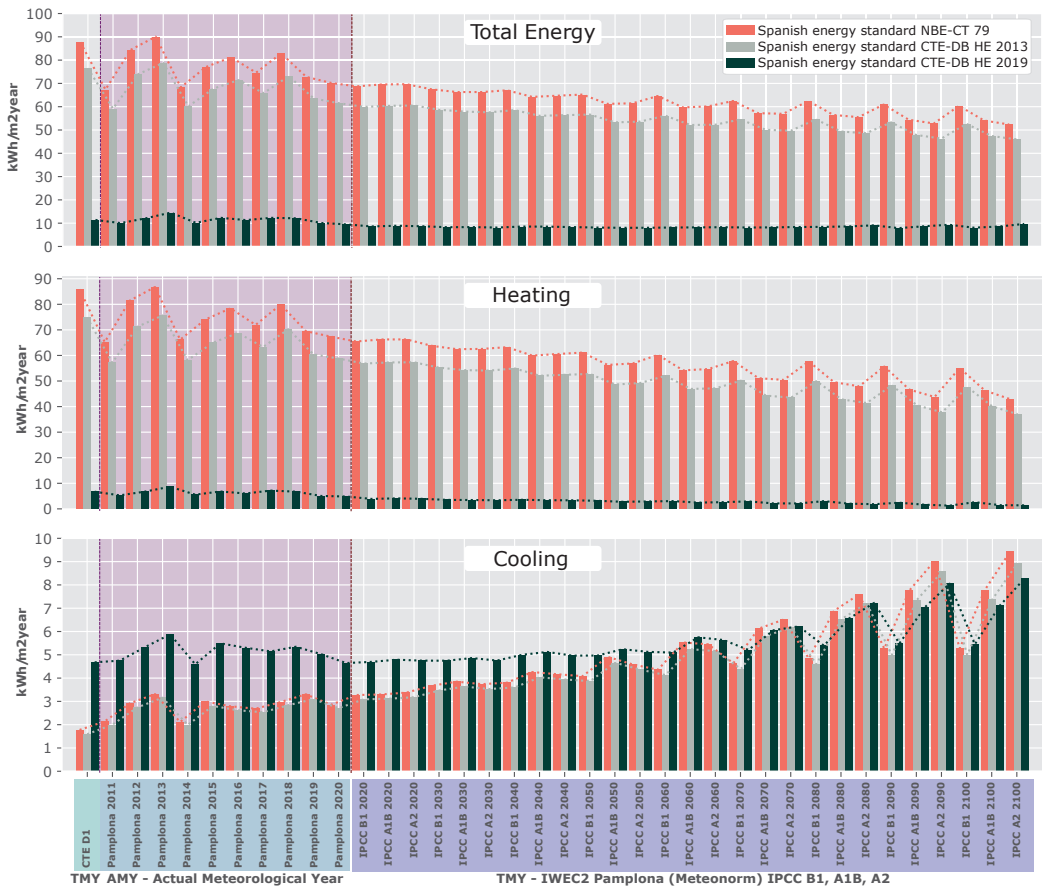


Figure 3. Energy consumption [Total, Heating, Cooling] taking into account, typical meteorological year, actual meteorological year and future weather scenarios (IPCC).

Regarding future weather scenarios, all graphs show a logical trend—global warming causes a decrease in heating consumption and an increase in cooling consumption. However, the change in total consumption is more noticeable in the NBE-CT-79 and CTE-DB HE 2013 models, with oscillations of up to $23.67 \text{ kWh/m}^2 \text{ year}$ compared to $1.79 \text{ kWh/m}^2 \text{ year}$ for the CTE-DB HE 2019 model. This variation appears to be larger for cooling consumption, but this is due to the scales of the graphs ($10 \text{ kWh/m}^2 \text{ year}$ versus $90 \text{ kWh/m}^2 \text{ year}$ for heating). In summary, it can be concluded that nZEB buildings are better prepared for climate change in terms of their energy consumption.

The next point to be analyzed is user comfort. Figures 4–9 show the comfort values of the different models both for the CTE D1 normative weather scenario and the real weathers from 2011 to 2020 (Figures 4–6) and for the future weathers taking into account the climate change scenarios defined in the IPCC, in this case those corresponding to scenario A2 (Figures 7–9). Appendix A shows these same comfort graphs, but with the remaining scenarios, A1B and B1.

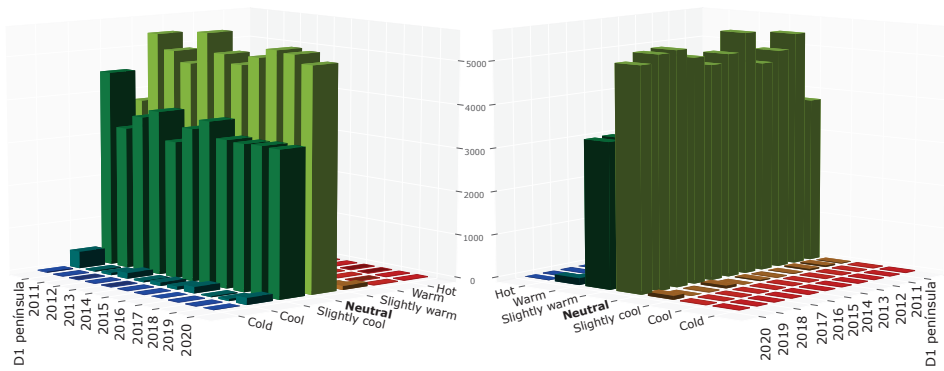


Figure 4. Comfort results taking into account the NBE CTE-79 standard and the Pamplona actual meteorological years (AMY).

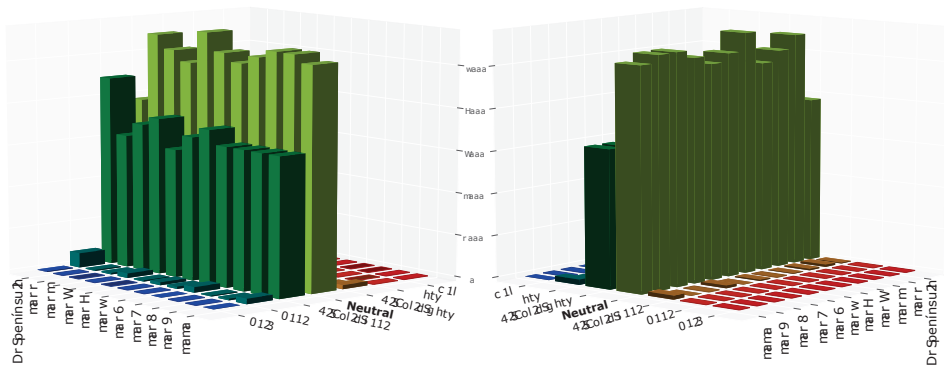


Figure 5. Comfort results taking into account the CTE-2013 standard and the Pamplona actual meteorological years (AMY).

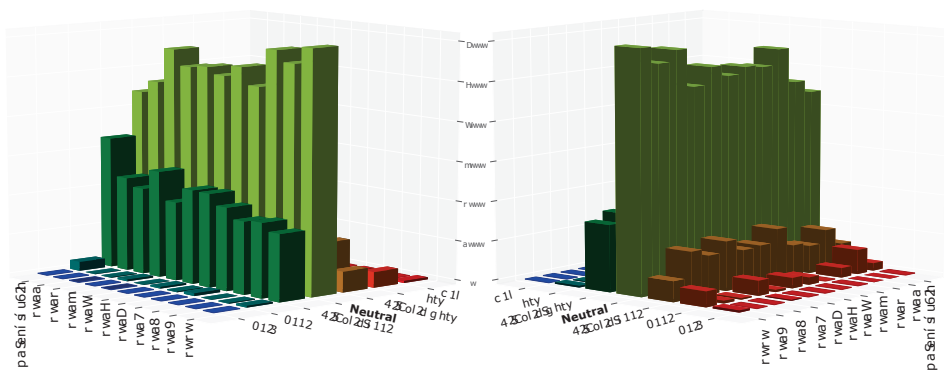


Figure 6. Comfort results taking into account the CTE-2019 standard and the Pamplona actual meteorological years (AMY).

Each of the figures is divided into three sections, from top to bottom, corresponding to the NBE-CT-79, the CTE-DB HE 2013 and the CTE-DB HE 2019 Spanish technical building codes. Each section has two views, since the bar diagram hides the results of the lower height bars. The height of each bar corresponds to the hours in which the living spaces

are in the same comfort category according to Fanger’s steady-state method [29,30]. Each year has a total of 8760 h, hours in which the spaces are configured with users undertaking a sedentary activity, with 1 “clo” of clothing and in which the temperature and relative humidity depend on the conditions of the envelope and the outside conditions (weather). Fanger established a temperature-based psychophysical scale to measure the degree of comfort or discomfort of users, with the following thermal sensations: “cold”, “cool”, “slightly cool”, “neutral”, “slightly warm”, “warm” and “hot”. What each bar shows is the annual sum of hours in each comfort category for a given model in a given weather. This facilitates the comparison of the comfort performance of the different models for the different weathers analyzed.

As can be seen in the graphs in Figures 4–6, the comfort level behavior of the NBE-CT-79 and CTE-DB HE 2013 models is similar, with a greater tendency towards “slightly cool” thermal sensations, with mean values of hours: “slightly cool” = 3502 h, “neutral” of 5132 h and “slightly warm” of 26 h. In contrast, the CTE-DB HE 2019 model not only has more hours of the year within the “neutral” range according to Fanger, with oscillations from 4432 to 6077 h, but its temperature distribution is more well-balanced with means of “slightly cool” of 2241 h and “slightly warm” of 926 h. It is true that there are hours when there may be a slight overheating of the spaces, which corresponds to what has been highlighted in Section 1; however, its overall thermal behavior is better in relation to the other models.

In the case of the graphs in Figures 7–9, those corresponding to weathers that take climate change into account, their behavior is similar. There is a greater range of hours in the “neutral” classification of the NBE-CT-79 and CTE-DB HE 2013 models (5611–6437 h) versus the CTE-DB HE 2019 model (5608–5991 h); however, the distribution of thermal sensations is more well-balanced in the CTE 2019 model, with averages of “slightly cold” hours of 1081 h and “slightly warm” of 1419 h, reducing the former by 57% and improving the latter by up to eight times. It is likely that nZEB buildings will have higher cooling consumptions in the future due to global warming; however, they will also have a more well-balanced thermal behavior than the rest of the buildings without nZEB criteria.

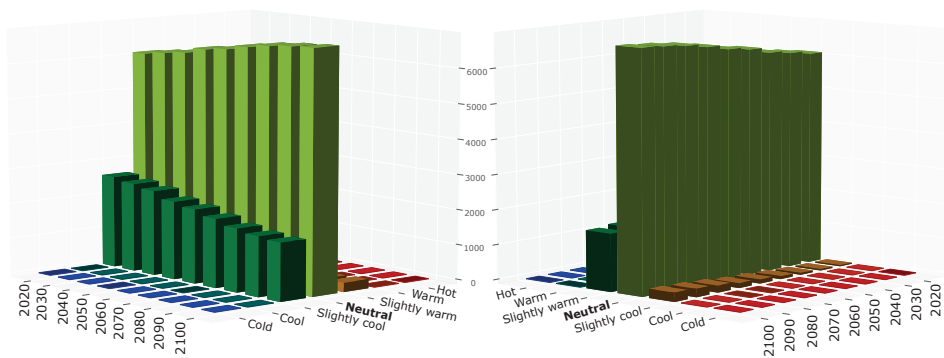


Figure 7. Comfort results taking into account the NBE CTE-79 standard and the Pamplona weather file generated with Meteornorm based on the IPCC scenario (A2).

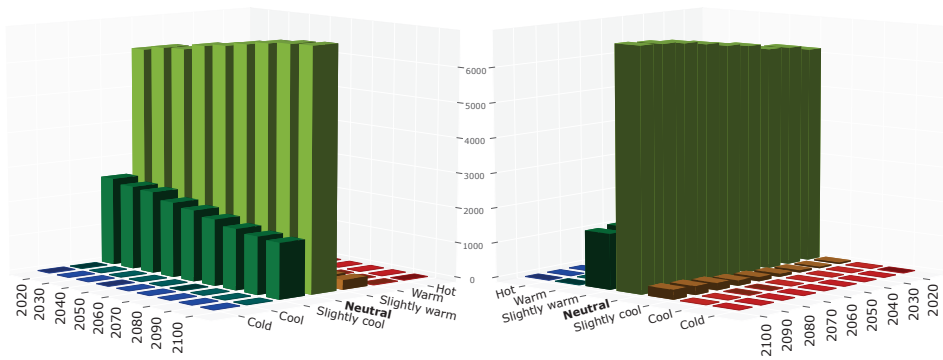


Figure 8. Comfort results taking into account the CTE-2013 standard and the Pamplona weather file generated with Meteorm based on the IPCC scenario (A2).

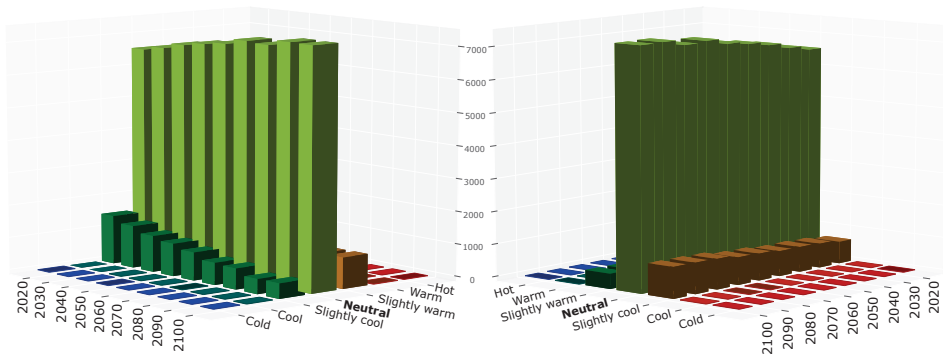


Figure 9. Comfort results taking into account the CTE-2019 standard and the Pamplona weather file generated with Meteorm based on the IPCC scenario (A2).

4. Discussion

One of the drawbacks of analyzing comfort in a building that follows the temperature setpoints of the energy standard is that these setpoints are defined in terms of user comfort ranges, so envelope retrofitting should only affect energy consumption and not comfort. In fact, for the residential case, the Spanish technical building code establishes minimum temperature ranges for winter of 17 °C from 23 h to 7 h and 20 °C from 7 h to 23 h; and in summer, maximum temperature ranges of 25 °C from 15 h to 23 h and 27 °C from 23 h to 7 h; which means that out of the 8760 h of the year, the residential building is only in free oscillation from 7 h to 15 h in summer. However, these values are lower (winter) and upper (summer) limits, which do not correspond to Fanger's "neutral" thermal sensation (the desirable one), so the distribution of thermal sensations based on this scale not only gives us information on which model has a greater number of hours in each comfort ranges, but also on how it is distributed throughout the year, both at times when it is within the setpoint temperature and when there are no limit values, the hours of free oscillation. As can be seen in the results, although the analyzed building is within the setpoint temperatures most of the year, its thermal behavior, directly related to the number of hours in each comfort range, varies significantly among the different Spanish technical building codes, with the CTE-DB HE 2019 being the one that achieves a building with a robust performance in the face of climate change.

The global energy crisis we are experiencing is forcing countries to consider different strategies to reduce their energy consumption and, therefore, reduce their energy dependence. In the case of Spain, on 1 August 2022, Royal Decree-Law 14/2022 was

approved, which temporarily modifies the temperature setpoints established in the energy regulations [60]. New minimum winter temperature limits of 19 °C and maximum summer temperature limits of 27 °C have been established. The Royal Decree-Law estimates that each degree of temperature increase or decrease represents an annual energy saving of 7%. However, user comfort does not understand this type of problem. As can be seen in Section 3, buildings with nZEB criteria make it possible to maintain an adequate degree of comfort for a longer period of time, with reduced energy consumption, being prepared for this type of decisions as well as for climate change variations.

5. Conclusions

Nearly Zero Energy Buildings are proving to be one of the measures with the greatest impact on the reduction of greenhouse gas emissions, as can be seen in the significant reduction of their consumption. For this reason, their introduction in the building sector is being promoted through mandatory regulations, as is the case of Spanish technical building code. There is a multitude of research that analyzes this type of building in terms of energy and even user comfort, although there are no studies that carry out both analyses simultaneously and, above all, that take into account the variations that climate change may entail in the future, as highlighted by Picard et al.: “Building performance and solar energy system simulations are clearly undertaken with standardized weather files, which do not generally take climate change into account.” [22].

This study analyzes all these aspects simultaneously in order to serve designers, architects, engineers, etc. as a useful tool to show users and investors that the benefits of this type of buildings are not only at the energy level but also at the comfort level, both if we take into account the current weather and the possible consequences of climate change. Often the interventions to be carried out to achieve this type of building have a long payback period if they are analyzed taking into account only energy savings, which sometimes prevents certain types of investments.

The main conclusions of the results obtained are described below:

- Energy savings of the different Spanish energy standards. There is a big difference between housing built according to Spanish standards NBE-CT-79 and CTE-HE 2013, versus the new construction criteria of the technical building code CTE-HE 2019 (an average of 84.36%), which considers these buildings nZEB buildings;
- Energy savings of nZEB buildings in relation to climate change. The study carried out with current (2011 to 2020) and future (2020 to 2100) weather series shows that these buildings are optimally adapted to both the meteorological oscillations of recent years and the severity of the climate change scenarios defined by the IPCC;
- Adjustment of Spanish regulations to the nZEB criteria. The reduction of the thermal transmittance of the envelopes, the increase in the performance of HVAC systems and the control of air exchange thanks to the reduction of infiltrations and the use of mechanical ventilation with heat recovery, have proven to be effective measures for obtaining nearly Zero-Energy Buildings (nZEB);
- Comfort performance of nZEB buildings in the face of climate change. It is also observed that this type of building is not only robust in energy terms, but when analyzing user comfort, its performance is significantly superior by homogenizing and balancing the distribution of thermal sensations in the spaces. This reduces the number of hours with thermal sensations according to Fanger of “slightly cool”, increasing the number of hours in both “slightly warm” and “neutral”. This is due to the greater insulation and airtightness of the spaces in this type of building, which makes the decrease or increase in temperatures when the air conditioning systems are turned off more homogeneous and well-balanced, thus increasing the comfort time of the users.

In summary, nZEB buildings are a safe bet to reduce greenhouse gas emissions while maintaining adequate comfort conditions and being able to adapt to climate oscillations, both current and those predicted in climate change scenarios.

6. Future Works

The comfort analysis used in this study is based on the steady state model or the heat balance, and does not take into account the adaptive comfort due to its dependence on the outside temperature. However, in a future study, both criteria will be analyzed simultaneously, since the adaptive model allows the identification of which times of the year are more critical, being able to subsequently measure comfort using the temperature-based psychophysical Fanger scale. The objective will be to evaluate whether the measures taken to obtain user comfort are cost-effective. Design decisions for the improvement of buildings to ensure adequate comfort conditions throughout the year often involve oversizing the facilities to respond to these critical moments. The quantification and evaluation of these periods in terms of comfort will make it possible to optimize the design and use of facilities subject to slight user discomfort.

Author Contributions: Conceptualization, methodology and validation, G.R.R. and A.O.d.O.; software, data curation, visualization and writing—original draft preparation, G.R.R.; writing—review and editing, G.R.R. and A.O.d.O. All authors have read and agreed to the published version of the manuscript.

Funding: This research received no external funding.

Institutional Review Board Statement: Not applicable.

Informed Consent Statement: Not applicable.

Conflicts of Interest: The authors declare no conflict of interest.

Appendix A. Comfort Analysis (IPCC Weathers)

Figures A1–A6 correspond to the user comfort results according to Fanger of the three models (NBE-CT-79, CTE-DB HE 2013 and CTE-DB HE 2019) under the different climate change scenarios established by the IPCC. Figures A1–A3 corresponds to scenario A1B and Figures A4–A6 to scenario B1. How to interpret each of these graphs is explained in the Section 3.

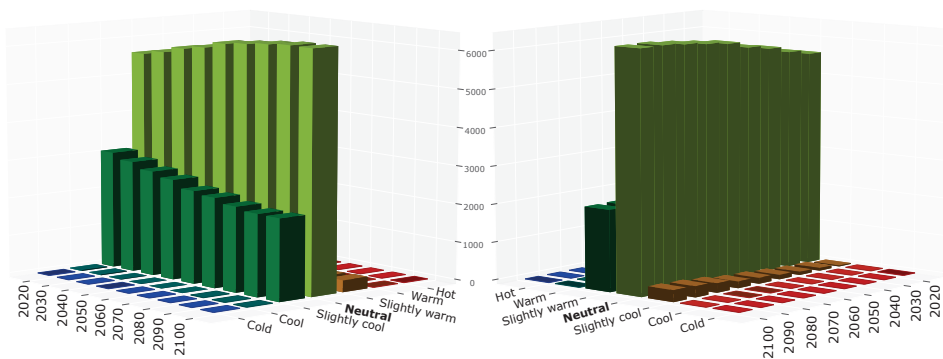


Figure A1. Comfort results taking into account the NBE CTE-79 standard and the Pamplona weather file generated with Meteonorm based on the IPCC scenario (1A1B).

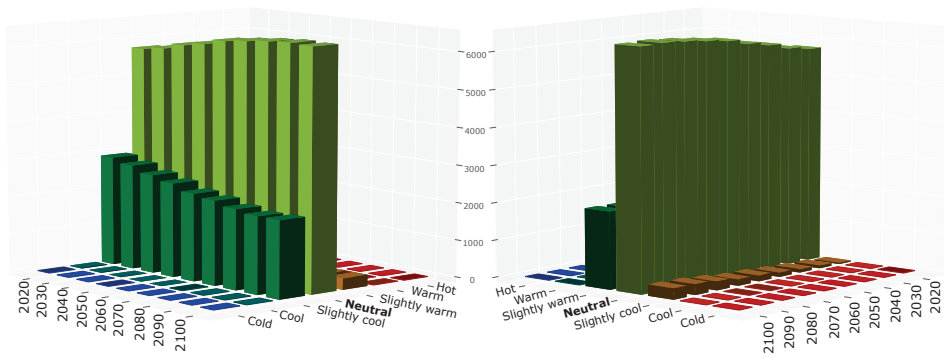


Figure A2. Comfort results taking into account the CTE-2013 standard and the Pamplona weather file generated with Meteornorm based on the IPCC scenario (1AB).

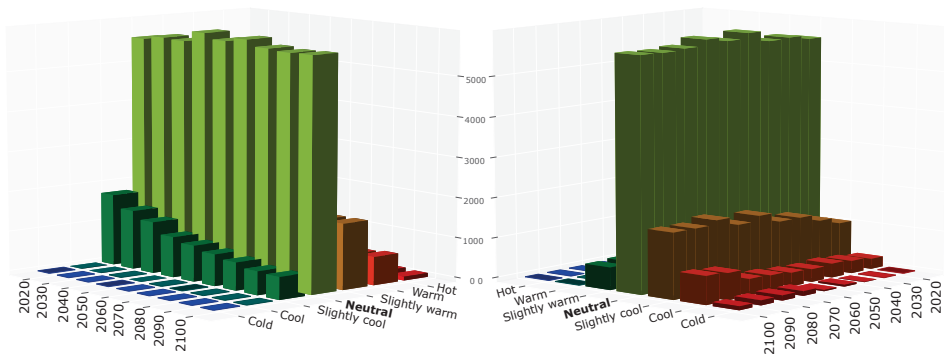


Figure A3. Comfort results taking into account the CTE-2019 standard and the Pamplona weather file generated with Meteornorm based on the IPCC scenario (1AB).

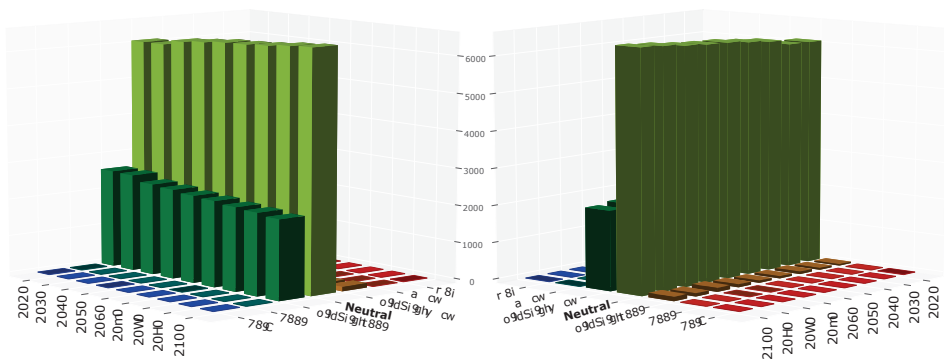


Figure A4. Comfort results taking into account the NBE CTE-79 standard and the Pamplona weather file generated with Meteornorm based on the IPCC scenario (B1).

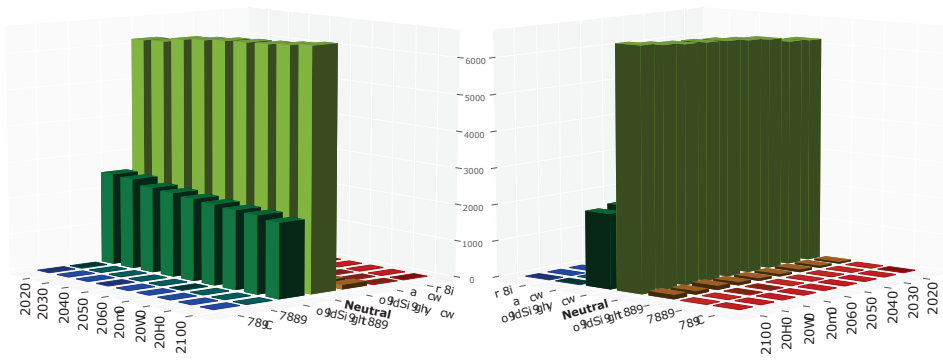


Figure A5. Comfort results taking into account the CTE-2013 standard and the Pamplona weather file generated with Meteorm based on the IPCC scenario (B1).

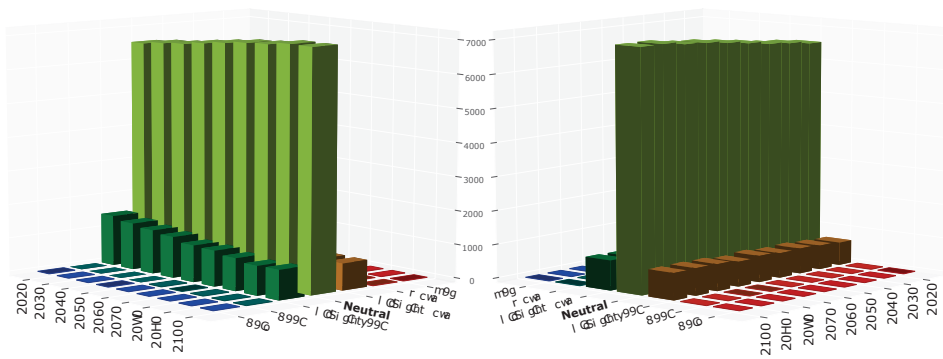


Figure A6. Comfort results taking into account the CTE-2019 standard and the Pamplona weather file generated with Meteorm based on the IPCC scenario (B1).

References

1. European Commission. Climate Action, Climate Change, Consequences. Available online: https://ec.europa.eu/clima/climate-change/consequences-climate-change_en (accessed on 26 July 2022).
2. Paris Agreement on Climate Change. Available online: <https://www.consilium.europa.eu/en/policies/climate-change/paris-agreement/> (accessed on 26 July 2022).
3. The United Nations Secretariat. United Nations Framework Convention on Climate Change. In Proceedings of the Conference of the Parties on Its Twenty-First Session, Paris, France, 30 November–13 December 2015.
4. A European Green Deal, Striving to be the First Climate-Neutral Continent. Available online: https://ec.europa.eu/info/strategy/priorities-2019-2024/european-green-deal_en#documents (accessed on 26 July 2022).
5. European Commission. Directive 2002/91/EC of the European Parliament and of the Council of 16 December 2002 on the energy performance of buildings. *Off. J. Eur. Union* **2002**, *1*, 65–71.
6. European Commission. Directive 2010/31/EU of the European Parliament and of the Council of 19 May 2010 on the energy performance of buildings (recast). *Off. J. Eur. Union* **2010**, *53*, 13–35.
7. European Commission. Directive 2018/844 of the European Parliament and of the Council of 30 May 2018 Amending Directive 2010/31/EU on the Energy Performance of Buildings and Directive 2012/27/EU on Energy Efficiency. Available online: https://eur-lex.europa.eu/legal-content/EN/TXT/?uri=uriserv%3A0J.L_2018.156.01.0075.01.ENG (accessed on 22 September 2022).
8. European Commission. Proposal for a Directive of the European Parliament and of the Council on the Energy Performance of Buildings (recast). Available online: <https://eur-lex.europa.eu/legal-content/EN/TXT/?uri=celex%3A52021PC0802> (accessed on 22 September 2022).
9. Erhorn-Kluttig, H.; Erhorn, H. National applications of the NZEB Definition—The Complete Overview. In *Concerted Action Energy Performance of Buildings*; Fraunhofer Institute for Building Physics: Stuttgart, Germany, 2018.
10. BPIE. *Nearly Zero Energy Buildings Definitions Across Europe*; BPIE: Brussels, Belgium, 2015.

11. Affordable Zero Energy Building-H2020 project. Definition of Indicators and Assessment Methods for Cost Effective nZEB and Energy+ Buildings. Available online: <https://ec.europa.eu/research/participants/documents/downloadPublic?documentId=080166e5c58728f7&appId=PPGMS> (accessed on 7 July 2022)
12. Hasan, A.; Mohamed, A.; Mohamed, H. Net-and nearly-zero energy buildings: A review of the definitions and case studies. In Proceedings of the Sixth International Conference on Heating, Cooling and Air Conditioning, Tehran, Iran, 26 May 2015.
13. Causone, F.; Tatti, A.; Pietrobon, M.; Zanghirella, F.; Pagliano, L. Yearly operational performance of a nZEB in the Mediterranean climate. *Energy Build.* **2019**, *198*, 243–260. [[CrossRef](#)]
14. De Gobierno, P. Real Decreto 2429/1979, de 6 de julio, por el que se aprueba la norma básica de edificación NBE-CT-79, sobre condiciones térmicas en los edificios. *Boletín Oficial del Estado* **1979**, *253*, 24524–24550.
15. CTE Código Técnico de la edificación. Código Técnico de la edificación. *Documento Básico de Ahorro de Energía; Spanish technical building code*; Government of Spain: Madrid, Spain, 2006.
16. CTE Código Técnico de la edificación. Código Técnico de la edificación. *Documento Básico de Ahorro de Energía; Spanish technical building code*; Government of Spain: Madrid, Spain, 2017.
17. CTE Código Técnico de la edificación. Código Técnico de la edificación. *Documento Básico de Ahorro de Energía; Spanish technical building code*; Government of Spain: Madrid, Spain, 2019.
18. Cerezo-Narváez, A.; Piñero-Vilela, J.M.; Ángel Rodríguez-Jara, E.; Otero-Mateo, M.; Pastor-Fernández, A.; Ballesteros-Pérez, P. Energy, emissions and economic impact of the new nZEB regulatory framework on residential buildings renovation: Case study in southern Spain. *J. Build. Eng.* **2021**, *42*, 103054. [[CrossRef](#)]
19. Javier García-Ballano, C.; Ruiz-Varona, A.; Monné Bailo, C.; Cabello Matud, C. Monitoring of housing blocks in Zaragoza (Spain) to validate the energy savings calculation method for the renovation of nZEB dwellings. *Energy Build.* **2022**, *256*, 111737. [[CrossRef](#)]
20. Al Dakheel, J.; Del Pero, C.; Aste, N.; Leonforte, F. Smart buildings features and key performance indicators: A review. *Sustain. Cities Soc.* **2020**, *61*, 102328. [[CrossRef](#)]
21. Aste, N.; Adhikari, R.; Buzzetti, M.; Del Pero, C.; Huerto-Cardenas, H.; Leonforte, F.; Miglioli, A. nZEB: Bridging the gap between design forecast and actual performance data. *Energy Built Environ.* **2022**, *3*, 16–29. [[CrossRef](#)]
22. Picard, T.; Hong, T.; Luo, N.; Lee, S.H.; Sun, K. Robustness of energy performance of Zero-Net-Energy (ZNE) homes. *Energy Build.* **2020**, *224*, 110251. [[CrossRef](#)]
23. Nik, V.M.; Coccolo, S.; Kämpf, J.; Scartezzini, J.L. Investigating the importance of future climate typology on estimating the energy performance of buildings in the EPFL campus. *Energy Procedia* **2017**, *122*, 1087–1092. [[CrossRef](#)]
24. D’Agostino, D.; Parker, D.; Epifani, I.; Crawley, D.; Lawrie, L. How will future climate impact the design and performance of nearly zero energy buildings (NZEBs)? *Energy* **2022**, *240*, 122479. [[CrossRef](#)]
25. Ascione, F.; De Masi, R.F.; Gigante, A.; Vanoli, G.P. Resilience to the climate change of nearly zero energy-building designed according to the EPBD recast: Monitoring, calibrated energy models and perspective simulations of a Mediterranean nZEB living lab. *Energy Build.* **2022**, *262*, 112004. [[CrossRef](#)]
26. Dartevelle, O.; van Moeseke, G.; Mlecnik, E.; Altomonte, S. Long-term evaluation of residential summer thermal comfort: Measured vs. perceived thermal conditions in nZEB houses in Wallonia. *Build. Environ.* **2021**, *190*, 107531. [[CrossRef](#)]
27. Attia, S.; Kurnitski, J.; Kosiński, P.; Borodinecs, A.; Deme Belafi, Z.; István, K.; Krstić, H.; Moldovan, M.; Visa, I.; Mihailov, N.; et al. Overview and future challenges of nearly zero-energy building (nZEB) design in Eastern Europe. *Energy Build.* **2022**, *267*, 112165. [[CrossRef](#)]
28. Yang, L.; Yan, H.; Lam, J.C. Thermal comfort and building energy consumption implications—A review. *Appl. Energy* **2014**, *115*, 164–173. [[CrossRef](#)]
29. Van Hoof, J. Forty years of Fanger’s model of thermal comfort: Comfort for all? *Indoor Air* **2008**, *18*, 182–201. [[CrossRef](#)] [[PubMed](#)]
30. Fanger, P.O. Assessment of man’s thermal comfort in practice. *Occup. Environ. Med.* **1973**, *30*, 313–324. [[CrossRef](#)] [[PubMed](#)]
31. UNE-EN ISO 7730: 2006; Ergonomics of the Thermal Environment—Analytical Determination and Interpretation of Thermal Comfort Using Calculation of the PMV and PPD Indices and Local Thermal Comfort Criteria. International Organization for Standardization: Geneva, Switzerland, 2006.
32. ASHRAE. ASHRAE 55: 1992 *Thermal Environmental Conditions for Human Occupancy*; ASHRAE Standard: Atlanta, GA, USA, 1992.
33. ASHRAE. ASHRAE 55: 2010 *Thermal Environmental Conditions for Human Occupancy*; ASHRAE Standard: Atlanta, GA, USA, 2010.
34. ASHRAE. ASHRAE 55: 2020 *Thermal Environmental Conditions for Human Occupancy*; ASHRAE Standard: Atlanta, GA, USA, 2020.
35. UNE-EN 16798-1:2020; Energy Performance of Buildings—Ventilation for Buildings—Part 1: Indoor Environmental Input Parameters for Design and Assessment of Energy Performance of Buildings Addressing Indoor Air Quality, Thermal Environment, Lighting and Acoustics—Module M1-6. International Organization for Standardization: Geneva, Switzerland, 2020.
36. UNE-EN 15251:2008; Indoor Environmental Input Parameters for Design and Assessment of Energy Performance of Buildings Addressing Indoor Air Quality, Thermal Environment, Lighting and Acoustics. International Organization for Standardization: Geneva, Switzerland, 2008.

37. Crawley, D.B.; Lawrie, L.K.; Winkelmann, F.C.; Buhl, W.; Huang, Y.; Pedersen, C.O.; Strand, R.K.; Liesen, R.J.; Fisher, D.E.; Witte, M.J.; et al. EnergyPlus: Creating a new-generation building energy simulation program. *Energy Build.* **2001**, *33*, 319–331. [CrossRef]
38. Nguyen, A.T.; Reiter, S.; Rigo, P. A review on simulation-based optimization methods applied to building performance analysis. *Appl. Energy* **2014**, *113*, 1043–1058. [CrossRef]
39. Henninger, R.H.; Witte, M.J. *EnergyPlus Testing with ANSI/ASHRAE Standard 140-2001 (BESTEST)*; US Department of Energy: Washington, DC, USA, 2004.
40. Henninger, R.H.; Witte, M.J.; Crawley, D.B. Analytical and comparative testing of EnergyPlus using IEA HVAC BESTEST E100–E200 test suite. *Energy Build.* **2004**, *36*, 855–863. [CrossRef]
41. Building Energy Simulation Test-Generation Simulation and Reporting (BESTEST-GSR). Available online: <https://github.com/NREL/BESTEST-GSR> (accessed on 22 September 2022).
42. OpenStudio Whole Building Energy Modeling using EnergyPlus and Advanced Daylight Analysis Using RADIANCE. Available online: <https://openstudio.net/> (accessed on 22 September 2022).
43. Guglielmetti, R.; Macumber, D.; Long, N. *OpenStudio: An Open Source Integrated Analysis Platform*; Technical Report; National Renewable Energy Lab.(NREL): Golden, CO, USA, 2011.
44. SG SAVE. Verificación del CTE-HE con EnergyPlus. Available online: <http://www.efinovatic.es/energyPlus/> (accessed on 7 October 2022).
45. CTE Código Técnico de la edificación. Documento Básico de Ahorro de Energía; Spanish technical building code; Government of Spain: Madrid, Spain, 2013.
46. IPCC, A. *The Intergovernmental Panel on Climate Change (IPCC)*; World Meteorological Organization, IPCC Secr. 2022. Available online: <https://www.ipcc.ch/> (accessed on 22 September 2022).
47. IPCC. *Summary for Policymakers: H.-O. Pörtner, D.C. Roberts, E.S. Poloczanska, K. Mintenbeck, M. Tignor, A. Alegría, M. Craig, S. Langsdorf, S. Lössche, V. Möller, A. Okem (Eds.); IPCC Sixth Assessment Report*; IPCC: Geneva, Switzerland, 2022.
48. Bhandari, M.; Shrestha, S.; New, J. Evaluation of weather datasets for building energy simulation. *Energy Build.* **2012**, *49*, 109–118. [CrossRef]
49. Henze, G.P.; Pfafferott, J.; Herkel, S.; Felmann, C. Impact of adaptive comfort criteria and heat waves on optimal building thermal mass control. *Energy Build.* **2007**, *39*, 221–235. [CrossRef]
50. Meteonavarra: Meteorology and Climatology of Navarra, Pamplona. Available online: <http://meteo.navarra.es/estaciones/estacion.cfm?IDestacion=455> (accessed on 7 October 2022).
51. AEMET Agencia Estatal de Meteorología. Listado de provincias afectadas por las Olas de calor registradas desde 1975. 2021. Available online: https://www.aemet.es/documentos/es/conocermas/recursos_en_linea/publicaciones_y_estudios/estudios/Olas_calor/RelacionProvincias2021.pdf (accessed on 22 September 2022)
52. AEMET Agencia Estatal de Meteorología. *Listado de Provincias Afectadas por las Olas de frío Registradas Desde 1975*; AEMET Agencia Estatal de Meteorología: Madrid, Spain, 2021.
53. Moazami, A.; Nik, V.M.; Carlucci, S.; Geving, S. Impacts of future weather data typology on building energy performance—Investigating long-term patterns of climate change and extreme weather conditions. *Appl. Energy* **2019**, *238*, 696–720. [CrossRef]
54. Jentsch, M.F.; Bahaj, A.S.; James, P.A. Climate change future proofing of buildings—Generation and assessment of building simulation weather files. *Energy Build.* **2008**, *40*, 2148–2168. [CrossRef]
55. Dickinson, R.; Brannon, B. Generating future weather files for resilience. In Proceedings of the International Conference on Passive and Low Energy Architecture, Los Angeles, CA, USA, 11–13 July 2016; pp. 11–13.
56. Remund, J.; Kunz, S. *Meteonorm*, Version 7. Meteotest. 2020. Available online: www.meteotest.com (accessed on 22 September 2022).
57. Remund, J.; Müller, S.; Schilter, C.; Rihm, B. The use of Meteonorm weather generator for climate change studies. In Proceedings of the 10th EMS Annual Meeting, Zürich, Switzerland, 13–17 September 2010; p. EMS2010-417.
58. Belcher, S.E.; Hacker, J.N.; Powell, D.S. Constructing design weather data for future climates. *Build. Serv. Eng. Res. Technol.* **2005**, *26*, 49–61. [CrossRef]
59. Pachauri, R.K.; Reisinger, A. *Climate Change 2007. Synthesis Report. Contribution of Working Groups I, II and III to the Fourth Assessment Report*; Intergovernmental Panel on Climate Change: Geneva Switzerland, 2008.
60. del Estado, J. *Real Decreto-ley 14/2022, de 1 de agosto, de medidas de sostenibilidad económica en el ámbito del transporte, en materia de becas y ayudas al estudio, así como de medidas de ahorro, eficiencia energética y de reducción de la dependencia energética del gas natural*; Government of Spain: Madrid, Spain, 2022.

Article

Design of Rural Human Settlement Unit with the Integration of Production-Living-Ecology of China Based on Dynamic Emergy Analysis

Yuan Chang ^{1,2}, Geng Geng ^{1,*}, Chongjie Wang ³, Yibing Xue ³ and Tian Mu ⁴¹ School of Architecture and Urban Planning, Shandong Jianzhu University, Jinan 250101, China² School of Art, Shandong Management University, Jinan 250357, China³ Shandong Co-Innovation Center of Green Building, Shandong Jianzhu University, Jinan 250101, China⁴ School of Art, Shandong Jianzhu University, Jinan 250101, China

* Correspondence: genggeng18@sdjzu.edu.cn

Abstract: It is of great theoretical and practical significance to optimize and improve the design of rural human settlement units through system ecology analysis based on emergy evaluation indices. From the perspective of system ecology, the rural living environment system is multivariate and complicated, with strong correlations and obscure boundaries between levels. Therefore, the definition of a rural human settlement unit in China is proposed in this research and can be divided into three scales: the microcosmic scale, mesoscale, and macroscopic scale. This research adopted a new method for the design of rural human settlement units by adopting emergy as a common dimension in order to solve the problem of dimensionality disunity between resource environment elements and society economy elements. Through the establishment of the static emergy analysis model and dynamic emergy prediction model, qualitative and quantitative analysis approaches of the rural human settlement unit were combined. According to the design orientations of industry-invigorative, environment-friendly, and ecology-balanced, corresponding with production-living-ecology integration, emergy evaluation indices including the emergy self-sufficiency ratio, emergy investment ratio, net emergy yield ratio, environmental load ratio, and emergy sustainable indices were calculated and predicted by means of system dynamics simulation. The dynamic emergy prediction results showed that the emergy self-sufficiency ratio and emergy sustainable indices basically presented a decreasing tendency, from 0.34 to 0.15 and from 0.76 to 0.57, respectively, with the passage of time; the values of the emergy investment ratio, net emergy yield ratio, and environmental load ratio basically presented an increasing tendency, from 2.13 to 2.78, from 1.66 to 2.12, and from 2.23 to 3.61, respectively, with the passage of time. In practice, the evaluation method based on the emergy analysis of the technical strategies and spatial arrangements of the rural human settlement unit can provide data support for designing standards, planning guidelines, and creating constructional instructions for the rural living environment of China.

Keywords: emergy; production-living-ecology; human settlement unit; system dynamic; emergy evaluation indices

Citation: Chang, Y.; Geng, G.; Wang, C.; Xue, Y.; Mu, T. Design of Rural Human Settlement Unit with the Integration of Production-Living-Ecology of China Based on Dynamic Emergy Analysis. *Buildings* **2023**, *13*, 618. <https://doi.org/10.3390/buildings13030618>

Academic Editors: Yaolin Lin and Wei Yang

Received: 6 February 2023

Revised: 20 February 2023

Accepted: 24 February 2023

Published: 26 February 2023



Copyright: © 2023 by the authors. Licensee MDPI, Basel, Switzerland. This article is an open access article distributed under the terms and conditions of the Creative Commons Attribution (CC BY) license (<https://creativecommons.org/licenses/by/4.0/>).

1. Introduction

Since the new socialist countryside construction policy was proposed in China, local governments have paid great attention to the construction of rural living environments and have advanced fruitful pilot demonstration projects [1,2]. Thus, significant progress has been made in terms of the urban development in rural areas and the construction of new rural communities [3,4]. Since the strong promotion of local government was the main approach to accelerate the pace of rural human settlement construction, we found few research or reports in the academic sector [5]. Most of the research focused on the relationship between human and land utilization [6]. The existing construction

pattern blindly imitates the pattern of urban human settlement construction, which has a lack of adequate scientific and specific guidance and leads to the relatively premature advance of the construction practice process and a series of ecological issues [7,8]. The grim situation of the rural ecological environment can be specifically summarized as the disequilibrium utilization of natural resources, serious rural environmental pollution, and the weak ecological awareness of rural construction.

In the human settlement research domain, urban human settlement as the research object has been more popular than rural human settlement, and policy making, as the research hotspot, has been seen as more interesting than construction design. Xue et al. [9] conducted an analysis of the temporal and spatial changes in the suitability and characteristics of urban human settlements in which the urban real human settlements index and pseudo-human settlements index was proposed. These research results can help decision-makers to identify the key factors influencing urban human settlements and make better decisions. Musakwa [10] presented data on the land and spatially integrated urban human settlements in strategic locations in South Africa. These data were used to facilitate decision-making on the land reform of human settlements as well as requirements for land-use management. Researchers of rural human settlements usually pay attention to three major areas: spatial utilization [11,12], agricultural production [13,14], and economic activities [15,16]. In conclusion, most social scientists have considered rural human settlement as a whole for qualitative results, other than hierarchic systems with explicit boundaries and detailed energy/mass circulation. Hence, the application of system ecology analysis and the conception of unitization for quantitative technical results should be considered in further studies.

The purpose of rural living environment optimization is to solve the practical problems facing human settlement quality and to provide reasonable territory design strategies and technological update methods in order to promote the “beautiful countryside” construction and the creation of a modern livable rural environment. “Promoting Beautiful Countryside” means integrating ecological construction by vigorously conducting afforestation activities, continuously improving the rural living environment, focusing on toilet upgrading and garbage treatment, accelerating the long-term mechanism for household sewage treatment, and building an ecological environment with a blue sky, green land, green mountains, and clean water [17]. The key measures for realizing rural revitalization are also in connection with the advanced and scientific design of rural human settlements, with strong maneuverability in protecting the natural pastoral style, continuing the rural regional culture, and elevating the quality of the rural living environment. Agricultural production, the living habitat, and the ecological environment are the three important components of the rural living environment system, among which there are mutualistic symbiotic relationships [18]. Present research on “production-living-ecological” are usually focused on the coupling coordination analysis of rural space [19–21]. Although the “production-living-ecological” concept contains research categories from different disciplines, it is necessary to combine the production, living, and ecological systems for interdisciplinary research to propose appropriate academic theories to guide the construction of rural human settlements and living environments. A framework of water consumption prediction and optimal allocation for “production-living-ecology” was put forward in the paper by Xu et al. [22]; taking the Zhangye Basin as an example, the water consumption for “production-living-ecology” was predicted and optimized in three scenarios: an economic development priority scenario, an environmentally sustainable development scenario, and a conventional development scenario. The work of Liao et al. [23] took the administrative village as the evaluation object, conducting an evaluation system from the angle of “production-living-ecology” optimization, and the ordered weighted average operator was introduced to weigh the functional potential of low-slope hills in a cultivated land protection ecological protection preference and urbanization development in Dali City. In another work, the value evaluation and classification model of land use function was established by Zou et al. [24] in rural land use planning and management in China based on the function of “production-living-ecology”. The disunity of the

evaluation system and the variableness of the evaluation criteria are common characteristics in existing studies. Introducing common indices for quantitative evaluation based on the system ecology theory for the “production-living-ecological” analysis of rural human settlement can effectively remedy the disunity and variableness issue.

To study the relationship between the natural environment and human society, scholars conducted quantitative research on the limited resources, considering energy as the common scale, which is confined to the same form of energy analysis [25,26]. Different types of energy are derived from different sources, where there is a fundamental difference between energy quality and value. Thus, incomparability between different forms of energy occurred in the quantitative research on the sustainable development of the resource environment and social economic system, defined as an organic community [27]. Energy analysis and evaluation is the core method of system ecology research [28]. Considering the fact that different types and sources of energy possess different energy qualities, which cannot be directly compared and calculated, Odum proposed the conception of “solar energy” as a metric to break through the barrier of different energy qualities in traditional energy analytical methods [29]. Energy creates a uniform dimension of energy flow, mass flow, and information flow, providing a new perspective for the quantification of essential data in the quantitative evaluation and understanding of the relevance of the resource environment system and social economy system [30].

Research findings related to the energy analysis of ecological systems recently concentrated on agricultural systems [31,32] and production, such as vegetable production [33], crop production [34], and green tea production [35]. As for the rural human settlement and living environment field, there are two research orientations: technical strategy and cultural feature. A diachronic energy method was proposed by Zhu et al. [36] to integrate the social development model, social-ecological factors, and energy assessment into the environmental history research framework. Some suggestions for the sustainable eco-tourism model, eco-agriculture technology, and social-ecological integrated governance were established. Methods for standardizing natural and economic inputs were developed by Falkowski et al. [37] to allow for a more comprehensive evaluation of the system. Energy values for the transfer of traditional ecological knowledge, maintenance, and creation were assessed at the individual and community levels. The findings highlighted the importance of protecting the sustainability of knowledge transfer systems that produce traditional ecological knowledge and developing a practical education system. Table 1 shows the existing methods for comprehensive sustainability assessments with evaluation indicators on rural human settlements.

Table 1. Existing methods for sustainability assessments with evaluation indicator comparisons.

Assessment Orientations	Assessment Methods	Assessment Goals
Agricultural production [38]	System dynamics [39]	Spatial planning and management [40]
Living habitat arrangement [41]	Energy analysis [42]	Energy source utilization [43]
Ecological environment [44]	Analytic hierarchy process [45]	Cultural revitalization [46]

From the perspective of system ecology, the rural living environment system is multivariate and complicated, with strong correlations and obscure boundaries between all levels of the system. Drawing lessons from the concept of a “unit”, with dual properties that are systematic and self-contained, the definition of a rural human settlement unit of China was proposed which can be divided into three scales: the microcosmic scale (courtyard unit), mesoscale (cluster unit), and macroscopic scale (village unit). Energetic flow diagrams were drawn and the total energy inputs/outputs of each scale were calculated through static energy analysis. According to the design orientations of industry-invigorative, environment-friendly, and ecology-balanced, corresponding with production-living-ecology integration for different spatial arrangements and technical strategies, respectively, energy evaluation indices including the energy self-sufficiency ratio (*ESR*), energy investment ratio (*EIR*), net energy yield Ratio (*EYR*), environmental

load ratio (*ELR*), and energy sustainable indices (*ESI*) were analyzed and predicted by means of a system dynamics simulation. The technical framework of this research is shown in Figure 1.

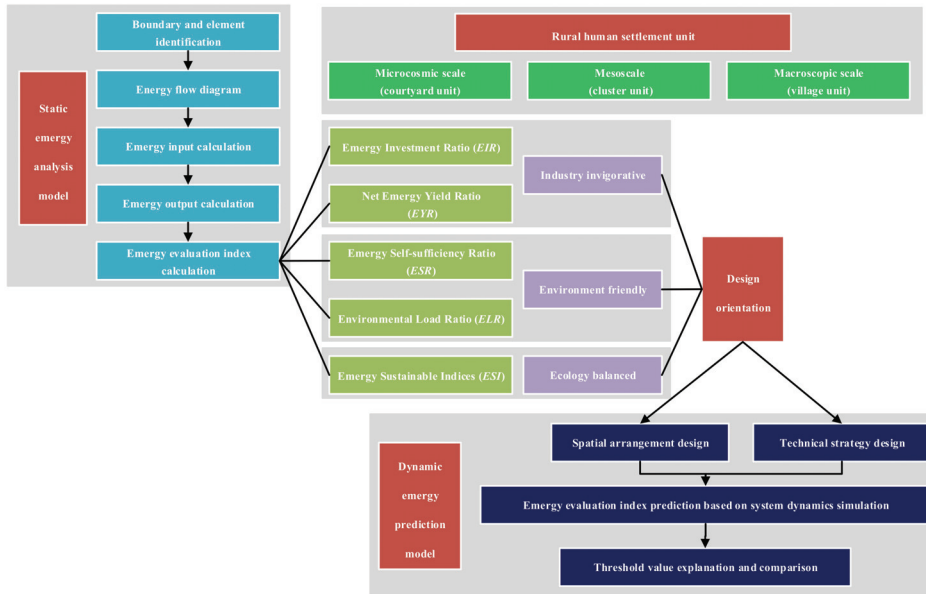


Figure 1. The technical framework of this research.

2. Methodology

2.1. Conception and Hierarchy Division of the Rural Human Settlement Unit

2.1.1. Rural Human Settlement Unit with the Integration of Production-Living-Ecology

It is necessary to establish a series of appropriate social organization patterns, metabolic technology systems, and spatial layout frameworks to support and coordinate with the sustainable development process of the rural human settlement. A “unit” is the result of the conceptualization of this appropriate scheme [47]. A unit is a self-contained system with clear boundaries, complete structure, proper scale, and specific function, which operates independently. Moreover, the element configuration is function-oriented, and the elements are mutually associated, interactive, and restrictive in a certain manner, forming an organic and orderly integrated unit. The most important feature of the unit is hierarchical, indicating that a smaller-scale unit is generally subordinate to a larger-scale unit, and the existence of a minimum unit that cannot be divided [48].

Due to the accelerating urbanization process in recent decades, the decline of the countryside has become an unavoidable objective reality, leaving dilapidated village houses and facilities as well as deserted farmland. Based on this, the government has been vigorously promoting the mergence and relocation of the villages, causing a great change in the rural human settlement form in China. In addition, capital injection has also led to unprecedented diversity in the form and substance of the countryside, such as the emergence of leisure and sightseeing agricultural parks and agricultural residences integrated with enterprises [49]. On the other hand, the inherent attribute that determines the potential scale hierarchy of the unit can be as small as a single courtyard or as large as a whole village. For this reason, unitary construction is the most appropriate analyzing approach for the classification, organization, and conceptualization of rural human settlements. Different from highly industrialized and globalized cities, rural areas are closely related to the local geography, climate, culture, and resource environment, which are so diversified that they

cannot be summarized by applying a standardized formula. The unitary construction of rural human settlements means that on the basis of universal research, strategies must be generated according to the actual conditions, which is the realistic pathway necessary to implement the sustainable development of rural human settlements and the living environment [50].

Unitization is the ecological strategy frame of the rural human settlement. Based on the role definition mentioned above, rural areas must adopt innovative production-living-ecology integration strategies to reduce their dependence and impact on the local environment. The most effective and direct mode is to establish each functional unit according to ecological principles and minimize or even eliminate the input of resources/energy and the output of waste through complementary symbiosis and integrated coordination among elements in the unit. In this interaction mechanism, the unit of the smallest scale (basic unit) with a relatively simple structure still needs external material transport and waste elimination. The main function of the smallest scale unit is to satisfy the requirement of people's activities in the unit. As the collection of the smallest scale units, the unit of intermediate scale with better functional characteristics needs to not only satisfy the requirement of people's activities but also improve the overall operational efficiency of the unit and reduce the input and output of external substances. The largest scale unit consists of intermediate scale units with various functional patterns and complementary relationships, which can reasonably achieve self-sufficiency to the maximum extent, completely handle self-generated waste, and realize independence.

According to the current investigations of the rural living environment, this research selected and trimmed statistical data from the 2017–2020 yearbook of China, including natural information (altitude, water resources, solar radiation, air temperature, precipitation, etc.), economy information (GNP, tourist income, investment, energy consumption, etc.), social information (demographic change, salary income, social goods and services consumption, etc.), and ecological information (construction land change, water and soil loss, waste emission and disposal, etc.), to establish the typical rural human settlement unit model of China. Considering the circulation mode of mass and energy among the agricultural production, living habitat, and ecological environment, with different emphasis, the rural human settlement unit can be divided into three scales on basis of the "unitization" conception (Figure 2). The hierarchy division of the rural human settlement unit is according to the ecological self-circulation radius; the radius of the macroscopic scale is 6.25 km, which is approximately the village scale, then the mesoscale scale and microcosmic scale are defined by the rural living habitat radius, respectively [51].

- Microcosmic scale (courtyard unit)
- Mesoscale (cluster unit)
- Macroscopic scale (village unit)

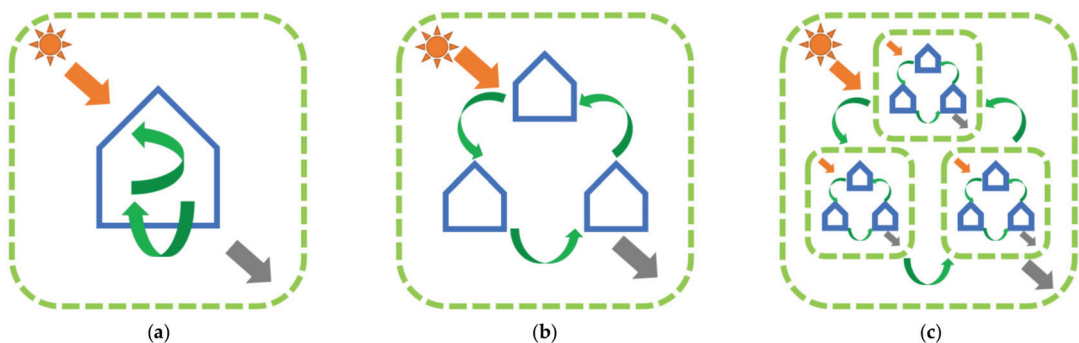


Figure 2. Schematic diagram of the hierarchical division of the rural human settlement unit. (a) Courtyard unit; (b) Cluster unit; and (c) Village unit.

2.1.2. The Hierarchy Division of the Rural Human Settlement Unit

(1) The element composition and system circulation of the microcosmic scale (courtyard unit)

The courtyard unit is the basic unit of life and production. Since the planting area is relatively small, fertilizer can be supplied from the biogas residue generated by the biogas digester. Scattered planting and breeding provide food for people, and agricultural waste such as the remaining stems and leaves can be utilized as fodder for poultry and livestock. The feces of poultry and livestock along with the organic refuse and fecal waste generated by people are the raw materials put into the biogas digester; water resources are mainly from external transportation and rainwater collection. The water resources from external transportation should experience a step utilization process, while the water resources from the rainwater collection can be used as domestic water in daily life and planting water. Eventually, the water resources will flow into the sewage purifier for filtration before gradually seeping into the underground. The energy demand includes electric energy and heat energy; electricity resources are mainly from external transportation and photovoltaic power generation. Through the fermentation of the household biogas digester and the continuous flow of nutrients, biogas can be continuously obtained for cooking and a solar water heater can provide hot water for daily washing. The energetic flow diagram according to the element composition and system circulation of the courtyard unit is shown in Figure 3.

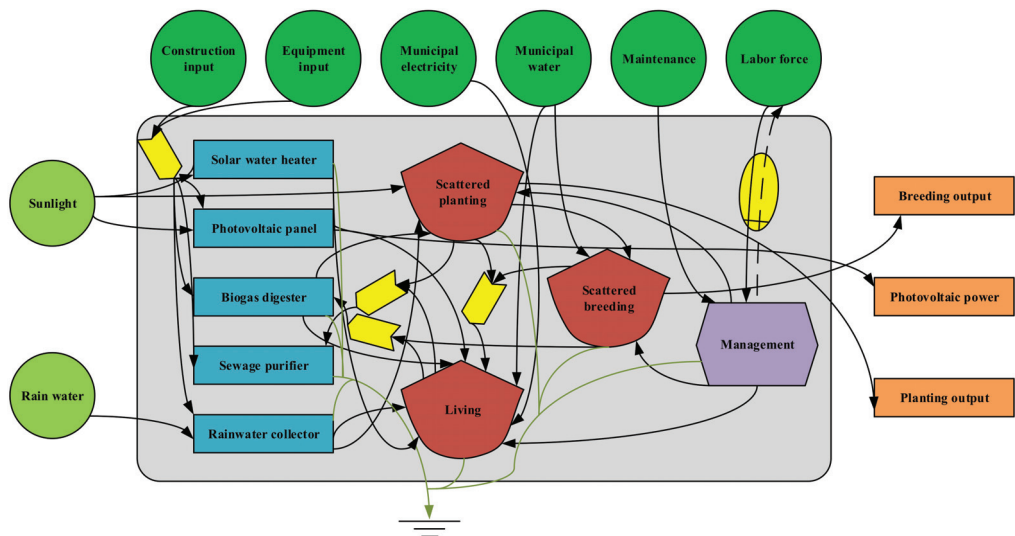


Figure 3. Energetic flow diagram of the courtyard unit.

(2) The element composition and system circulation of the mesoscale (cluster unit)

The cluster unit consists of several courtyard units. In addition, the cluster unit contains large areas of agricultural production space, road transportation infrastructure, and public space outside the living area. Centralized agricultural production activities such as crop planting and livestock breeding can be engaged in the agricultural production space. Feces from the centralized breeding along with the organic refuse and fecal waste generated by people are collected and discharged into the biogas field for biogas, biogas residue, and biogas slurry production through fermentation. Part of the biogas is directly supplied to the dwellers for cooking, and the other part is transferred to the biogas generator as raw material and converted into electricity. The biogas residue and biogas slurry are then returned to the farmland as fertilizer. The domestic sewage is discharged into the constructed wetland through a sewage network, which can not only purify the water source but also create a public leisure landscape in the unit. The impounding reservoir collects

and stores rainwater within a certain range in the cluster unit as water for agricultural planting and greening, which can save a large part of the water resources. The energetic flow diagram according to the element composition and system circulation of the cluster unit is shown in Figure 4.

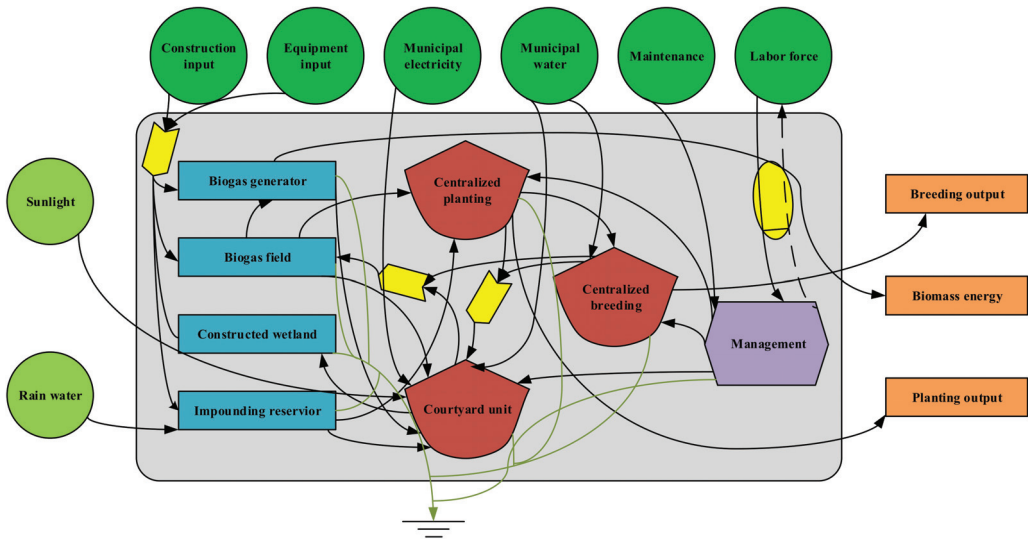


Figure 4. Energetic flow diagram of the cluster unit.

(3) The element composition and system circulation of the macroscopic scale (village unit)

Compared with the cluster units, the village unit is larger in scale, more diversified in production factors, and has great differences in spatial form. In this unit, the living community is formed by high-density residential areas in which the agricultural production space basically does not exist. The agricultural production space in the form of a modern agriculture park owns plenty of biomass resources, due to its main responsibility of large-scale planting and breeding along with its partial tourism and manufacturing function. Meanwhile, a medium-sized biogas field and biogas generator are not capable of meeting the requirements of human settlement, so a multifunctional biogas factory is selected for energy supplement. The circulation of the village unit consists of two systems: a living system in the high-density community and a production system in the modern agricultural park. The energetic flow diagram according to the element composition and system circulation of the village unit is shown in Figure 5.

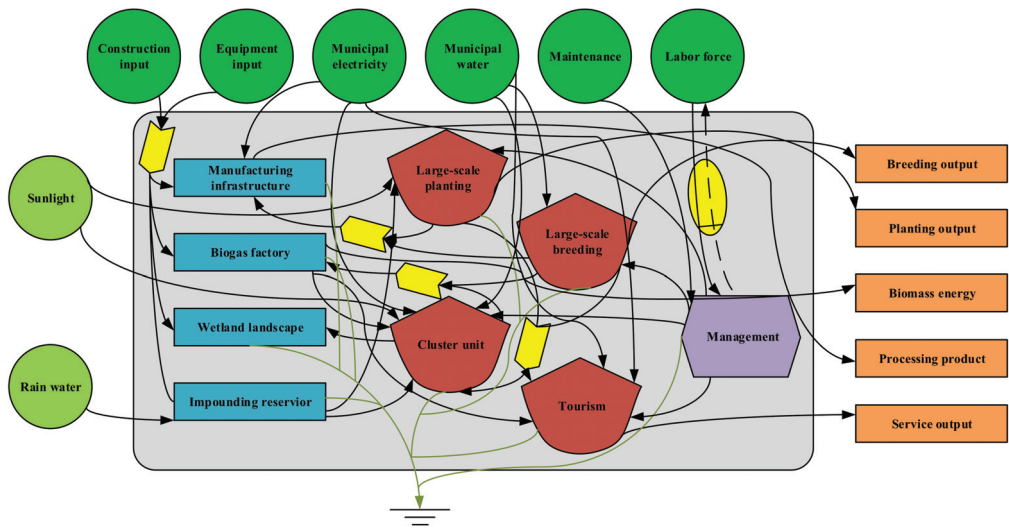


Figure 5. Energetic flow diagram of the village unit.

2.2. Analytical Procedures of the Ecological Energy Theory

Energy refers to the past available energy use to measure the flow of matter or energy into and out of a thermodynamic ecosystem account. It is the available solar energy or the energy contained in solar concrete energy used directly or indirectly to provide a service or product [29]. The unit of energy is emjoule, to distinguish it from joule, referring to the available energy of one kind consumed or produced in transformations. For example, sunlight, fuel, electricity, and human services can be put on a common basis by expressing them all as the emjoules of solar energy required to produce each one. Different forms of energy contain different energy qualities, and energy conversion work plays a dominant role in resolving the amount of energy. The following two terms of integration enable values that differ from other environmental accounting metrics: the “available” portion of energy volume and the contribution of memory “indirect” energy transfers. The thermodynamic basis of the energy theory has a particular emphasis on the availability of energy resources since availability determines the distance from the thermodynamic equilibrium of the ecosystem under observation and thus the ability of the target system to do work in relation to its surroundings.

2.2.1. Static Energy Analysis Model

The energy of a product or service can be calculated by the multiplication of an inefficiency factor (named transformity) and the quantity of available energy input or output. Hence, the total energy can be obtained by the summation of the energy value of each transformation process, which is expressed by Equation (1):

$$E_m = \sum_{i=1}^n (E_i \cdot Tr_i) \quad (1)$$

where E_m represents solar energy, E_i is the energy or mass input and output, and Tr_i is the transformity referring to the specific energy value of the input and output. Transformity measures the quality of energy, which is the intensive unit of energy. A higher transformity indicates a higher location in the energy hierarchy chain. The unit of transformity is sej/unit (J, kg, or g). The transformity value can be obtained from energy databases and previous research or it can also be derived from the global baseline. Thus, transformity becomes a matter of the ecosystem components and a sort of property of energy simultaneously [52].

The expression of the total energy input of natural resources is as follows (Equation (2)):

$$I = R + N \quad (2)$$

where R represents the energy input of renewable natural resources and N represents the energy input of non-renewable natural resources. The expression of the total energy input of auxiliary resources is as follows (Equation (3)):

$$U = P + O \quad (3)$$

where P represents the energy input of non-renewable purchased resources and O represents the energy input of organic resources. Then, the expression of total energy input is as follows (Equation (4)):

$$T = I + U \quad (4)$$

Researchers have conducted a large number of original studies to propose various energy evaluation indices for assessing the sustainability of the system or products according to the energy concept. Odum established the definition of energy evaluation indices, named the energy self-sufficiency ratio (ESR), energy investment ratio (EIR), net energy yield ratio (EYR), environmental load ratio (ELR), and energy sustainable indices (ESI) [53]. These energy evaluation indices are defined as follows (Equations (5)–(9)):

$$ESR = \frac{I}{T} \quad (5)$$

ESR is generally applied to analyze and evaluate the external exchange as well as the economic development level of the system. A higher value of ESR indicates more abundant internal resources, a stronger self-sufficiency capacity, and a weaker external exchange capacity of the system.

$$EIR = \frac{U}{I} \quad (6)$$

EIR is also known as the ratio of economic energy to environmental energy, which is applied to measure the economic development level and the environmental stress of the system. A higher value of EIR indicates a higher economic development level and less dependence on the natural environment of the system.

$$EYR = \frac{Y}{U} \quad (7)$$

where Y is the total energy output of the system.

EYR is adopted for measuring the ability of production processes to exploit internal resources. This indicator also shows the amount of gross energy required in order to maintain the production. The higher the EYR value, the greater the return obtained from the energy contributed to the system.

$$ELR = \frac{(U + N)}{R} \quad (8)$$

ELR reflects the pressure of production activities on the internal environment due to the excessive exploitation of internal non-renewable resources and/or investment from the external environment compared with renewable resources. The higher the ELR value, the more environmental pressure and negative impacts the system has.

$$ESI = \frac{EYR}{ELR} \quad (9)$$

ESI is the ratio of EYR to ELR , measuring the pressure on the internal environment, the ecological sustainability, and the net benefit to the society of the system. The system is

not sustainable with an *ESI* value of less than 1 and is moving toward a more sustainable direction with an *ESI* value between 1 and 10. The sustainability of the system is profound when the *ESI* value is greater than 10.

2.2.2. Dynamic Energy Prediction Model

The formulas of the system dynamics model are from the combination of mathematical expressions which accurately describe the relationship among the factors in a system. Figure 6 shows the system dynamics causal relationship diagram of the rural human settlement unit. According to the influencing factors that affect the energy evaluation indices, simplified as U (total energy input of auxiliary resources), R (energy input of renewable natural resources), and Y (total energy output), and the influencing logic (dynamics causal relationship), this study adopted system dynamics simulation software Vensim to edit the system dynamics formulas of the rural human settlement unit with different design orientations for the variation tendency prediction of the energy evaluation indices (2021–2035).

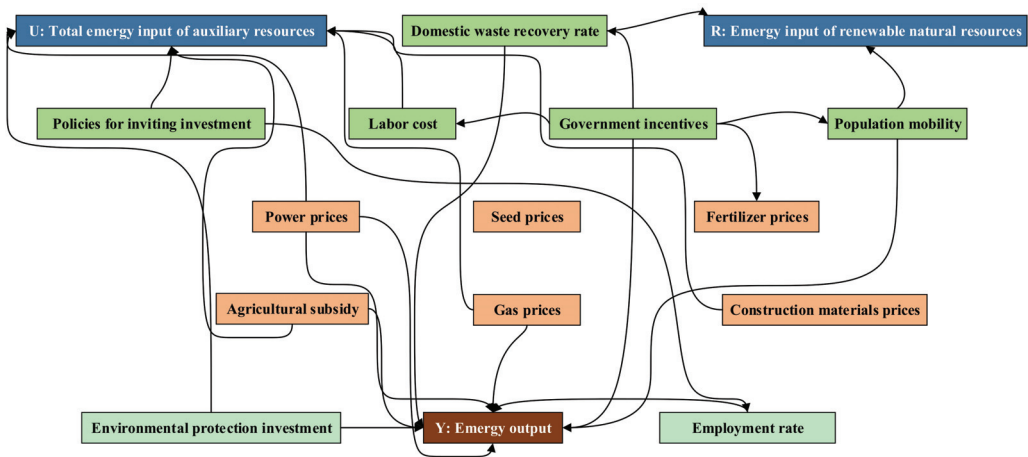


Figure 6. System dynamics causal relationship diagram of the rural human settlement unit.

The technical strategies and spatial arrangements of three design orientations, namely, ecology-balanced, industry invigorative, and environment-friendly, were set for the comparative analysis of the variation tendency prediction of the energy evaluation indices.

- Ecology-balanced design orientation

The principle of ecology-balanced design orientation is to achieve a highly adaptive, coordinated, and unified state through energy flow, material circulation, and information transfer between people and the environment within a certain period of time. When rural human settlement units attain equilibrium, the relationship among each composition inside of the system maintains a certain proportion. The input and output of energy and materials tend to be equal for a comparatively long time, and the structure and function are relatively stable. In addition, the system can return to the initial state through self-regulation when interfered with from the outside, according to the concept of sustainable development.

(1) Technical strategies

The technical strategies of ecology-balanced design orientation are identical to the technical strategies of the initial settings for static energy analysis. In the courtyard unit, technical strategies include a biogas digester, solar water heater, photovoltaic panel, sewage purifier, and rainwater collector; in the cluster unit, technical strategies include a medium-sized biogas field, small-sized biogas generator, constructed wetland with sewage concentrated disposal functions, and impounding reservoir for rainwater collection; and

in the village unit, technical strategies include a biogas factory, wetland landscape, and impounding reservoir.

(2) Spatial arrangements

The spatial arrangements of ecology-balanced design orientation are identical to the spatial arrangement of the initial settings for static emergy analysis. In the courtyard unit, spatial arrangements include roof planting, facade planting, courtyard planting, and courtyard breeding adjacent to the biogas digester; in the cluster unit, spatial arrangements include a centralized living area (courtyard units) surrounded by agricultural production space, a medium-sized biogas field combined with small-sized biogas generator adjacent to centralized breeding, and a public space consisting of constructed wetland and a leisure square; and in the village unit, spatial arrangements include a living area (cluster units) adjacent to a wetland landscape, away from large-scale breeding, combined with a biogas factory and modern agricultural park adjacent to the manufacturing infrastructure.

- Industry invigorative design orientation

The principle of industry invigorative design orientation is to maximumly exploit the potential of rural human settlement units regarding landscape design, crop planting, livestock breeding, energy manufacturing, tourism development, and the service industry, enhancing the efficiency and speed of the internal emergy flow. The main purpose of the design orientation is to realize the maximum emergy output. Of course, this design orientation will also lead to an increase in the utilization rate of non-renewable resources and the emission of pollutants.

(1) Technical strategies

The technical strategies of the industry invigorative design orientation are more suitable for agricultural-related production. Compared with the technical strategies of ecology-balanced design orientation, technical strategies are added that include automatic irrigation with more electric power consumption in the courtyard unit, a wind power generator for energy supply in the cluster unit, and geothermal energy utilization for leisure tourism and investment attraction in the village unit.

(2) Spatial arrangements

Compared with the spatial arrangements of ecology-balanced design orientation, roof planting, facade planting, and courtyard planting are replaced with greenhouse planting adjacent to buildings in the courtyard unit; the public space consisting of a constructed wetland and leisure square is replaced with distributed sewage disposal in the cluster unit; and the modern agricultural park adjacent to the manufacturing infrastructure is replaced with a modern agricultural park combined with a manufacturing infrastructure adjacent to leisure tourism in the village unit.

- Environment-friendly design orientation

The principle of environment-friendly design orientation is to establish a positive interactive relationship between people and the environment. The core objective of the design orientation is to regulate the production and consumption activities inside of the rural human settlement unit within the ecological carrying capacity and environmental capacity limitations, formulating critical feedback mechanisms of effective control of the production and consumption activities through the quality and state variation of the ecological environment elements. By analyzing the mechanism and pathway of the metabolic waste flow generation and discharge especially, this design orientation tends to effectively monitor the whole process of production and consumption activities. Multiple measurements are then adopted in order to reduce the amount of pollution production, ultimately realizing harmless pollution and lowering the adverse impact on the external ecological environment system.

(1) Technical strategies

The technical strategies of the environment-friendly design orientation are more suitable for environmental protection. Compared with the technical strategies of the ecology-balanced design orientation, the technical strategy sewage purifier is replaced with

geothermal heating in the courtyard unit; the small-sized biogas generator is replaced with solar power generation in the cluster unit; and the wetland landscape is eliminated in the village unit.

(2) Spatial arrangements

Compared with the spatial arrangements of ecology-balanced design orientation, roof planting and facade planting are eliminated in the courtyard unit; the leisure square is eliminated in the cluster unit; and the manufacturing infrastructure is eliminated in the village unit.

The dynamic variation tendency prediction of the emergy evaluation indices of the rural human settlement then can be applied in the following aspects: On the one hand, the dynamic emergy evaluation indices prediction can assist designers to analyze approaches to improve the energy efficiency levels by assessing the suitability under different design orientations, while on the other hand, the dynamic emergy evaluation indices prediction can assist administrators and developers to formulate a reasonable scheme for both economic and environmental benefits.

3. Results and Discussions

3.1. Static Emergy Analysis of the Rural Human Settlement Unit

3.1.1. Static Emergy Analysis of the Courtyard Unit

(1) Emergy input and output of the courtyard unit

Table 2 shows the emergy input and output of the courtyard unit in 2020. The emergy input consisted of renewable natural resources (*R*), non-renewable purchased resources (*P*), and organic resources (*O*). The total emergy input value was 4.30×10^{16} sej, in which the *R* input, *P* input, and *O* input accounted for 53.67%, 33.80%, and 12.53%, respectively. The emergy output consisted of planting, breeding, and photovoltaic power. The total emergy output value was 5.77×10^{16} sej, in which the planting output, breeding output, and photovoltaic power output accounted for 30.94%, 66.03%, and 3.03%, respectively.

Table 2. Emergy input and output of the courtyard unit.

	Item	Raw Data	Unit	Transformity (sej/Unit)	Solar Emergy (sej)
Renewable natural resources (<i>R</i>)	Sunlight	2.30×10^{16}	J	1	2.30×10^{16}
	Rain chemical	3.68×10^9	J	3.05×10^4	1.12×10^{14}
	Rain potential	4.77×10^7	J	4.70×10^4	2.24×10^{12}
	Total				2.31×10^{16}
Non-renewable purchased resources (<i>P</i>)	Construction	3.50×10^3	\$	3.40×10^{12}	1.19×10^{16}
	Maintenance	2.00×10^2	\$	3.40×10^{12}	6.80×10^{14}
	Equipment	5.80×10^2	\$	3.40×10^{12}	1.97×10^{15}
	Municipal electricity	60.40	\$	3.40×10^{12}	2.05×10^{13}
	Municipal water	16.30	\$	3.40×10^{12}	5.54×10^{12}
Total				1.46×10^{16}	
Organic resources (<i>O</i>)	Labor force	7.45×10^8	J	7.24×10^6	5.39×10^{15}
	Total input				4.30×10^{16}
Planting (<i>Y</i>)	Bean	5.49×10^9	J	6.90×10^5	3.79×10^{15}
	Vegetable	1.35×10^{11}	J	8.30×10^4	1.11×10^{16}
	Fruit	2.54×10^9	J	5.30×10^5	1.35×10^{15}
	Potato	1.96×10^{10}	J	8.30×10^4	1.63×10^{15}
	Total				1.79×10^{16}
Breeding (<i>Y</i>)	Pork	6.38×10^9	J	4.00×10^6	2.55×10^{16}
	Beef	1.73×10^9	J	4.00×10^6	6.92×10^{15}
	Poultry	2.12×10^9	J	1.70×10^6	3.60×10^{15}
	Dairy	4.12×10^8	J	2.00×10^6	8.24×10^{14}
	Egg	6.31×10^8	J	2.00×10^6	1.26×10^{15}
Total				3.81×10^{16}	
Others (<i>Y</i>)	Photovoltaic power	1.06×10^{10}	J	1.65×10^5	1.75×10^{15}
	Total output				5.77×10^{16}

(2) Emery evaluation index calculation of the courtyard unit

As can be seen from Table 3, the *EIR* value of the courtyard unit was 86.34%, indicating that the exploitation and utilization level of the natural resources of the unit at the microcosmic scale was comparatively low. The courtyard unit still depended on the construction and production facilities of urbanization and industry. Thus, the growth space of this evaluation index was relatively large in terms of ecological and self-sufficient development goals. The *EYR* value was 289.48%, which means that the emery output of the unit itself was capable of compensating for the purchase of emery and gaining emery profit. Few manpower resources with high emery value were invested in this unit except for the maintenance of buildings, equipment, and facilities, reflecting the acceptable production efficiency of the ecosystem. The *ELR* value was at an absolutely low level of 86.34%; the consumption of environmental resources and emission of wastes and pollutants were well regulated, and the environment loads lay in a secure range. The *ESR* value was 53.67%; on the one hand, the natural resources in this rural human settlement unit were relatively abundant, and the resource base and security level for economic development were comparatively high. On the other hand, this index also reflected the current situation of the insufficient emery purchasing power of the recycling system under the goal of self-sufficiency. The *ESI* value was 3.35, with powerful renewability and the promising prospect of sustainable development.

Table 3. Emery evaluation index calculation of the courtyard unit.

Item	Value
Emery input of renewable natural resources (<i>R</i>)	2.31×10^{16}
Emery input of non-renewable natural resources (<i>N</i>)	—
Total emery input of natural resources (<i>I</i>)	2.31×10^{16}
Emery of non-renewable purchased resources (<i>F</i>)	1.46×10^{16}
Emery input of organic resources (<i>O</i>)	5.39×10^{15}
Total emery input of auxiliary resources (<i>U</i>)	1.99×10^{16}
Total emery input (<i>T</i>)	4.30×10^{16}
Total emery output (<i>Y</i>)	5.77×10^{16}
Emery self-sufficiency ratio (<i>ESR</i>)	53.67%
Emery investment ratio (<i>EIR</i>)	86.34%
Net emery yield ratio (<i>EYR</i>)	289.48%
Environmental load ratio (<i>ELR</i>)	86.34%
Emery sustainable indices (<i>ESI</i>)	3.35

3.1.2. Static Emery Analysis of the Cluster Unit

(1) Emery input and output of the cluster unit

Table 4 shows the emery input and output of the cluster unit in 2020. The emery input consisted of renewable natural resources (*R*), non-renewable natural resources (*N*), non-renewable purchased resources (*P*), and organic resources (*O*). The total emery input value was 1.34×10^{19} sej, in which the *R* input, *N* input, *P* input, and *O* input accounted for 36.57%, 0.97%, 45.82%, and 16.64%, respectively. The emery output consisted of planting, breeding, and biogas energy. The total emery output value was 1.81×10^{19} sej, in which the planting output, breeding output, and biogas energy output accounted for 53.59%, 41.26%, and 5.15%, respectively.

Table 4. Emery input and output of the cluster unit.

	Item	Raw Data	Unit	Transformity (sej/Unit)	Solar Emery (sej)
Renewable natural resources (R)	Sunlight	4.84×10^{18}	J	1	4.84×10^{18}
	Rain chemical	2.01×10^{12}	J	3.05×10^4	6.13×10^{16}
	Rain potential	4.23×10^{10}	J	4.70×10^4	1.99×10^{15}
	Total				4.90×10^{18}
Non-renewable natural resources (N)	Net topsoil loss	7.56×10^{11}	J	1.7×10^5	1.29×10^{17}
	Construction	1.05×10^6	\$	3.40×10^{12}	3.58×10^{18}
Non-renewable purchased resources (P)	Maintenance	7.31×10^4	\$	3.40×10^{12}	2.49×10^{17}
	Equipment	6.80×10^5	\$	3.40×10^{12}	2.31×10^{18}
	Municipal electricity	9.74×10^2	\$	3.40×10^{12}	3.31×10^{14}
	Municipal water	5.82×10^2	\$	3.40×10^{12}	1.98×10^{14}
	Total				6.14×10^{18}
Organic resources (O)	Labor force	2.93×10^{11}	J	7.24×10^6	2.23×10^{18}
	Total input				1.34×10^{19}
Planting (Y)	Bean	4.78×10^{11}	J	6.90×10^5	3.30×10^{17}
	Vegetable	6.52×10^{11}	J	8.30×10^{19}	5.41×10^{16}
	Fruit	1.09×10^{11}	J	5.30×10^5	5.78×10^{16}
	Potato	1.96×10^{12}	J	8.30×10^4	1.63×10^{17}
	Corn	8.36×10^{12}	J	4.90×10^5	4.10×10^{18}
	Wheat	9.73×10^{12}	J	5.10×10^5	4.96×10^{18}
	Oil plant	5.14×10^{10}	J	6.90×10^5	3.55×10^{16}
	Total				9.70×10^{18}
Breeding (Y)	Pork	1.02×10^{12}	J	4.00×10^6	4.09×10^{18}
	Beef	5.68×10^{11}	J	4.00×10^6	2.27×10^{18}
	Poultry	4.35×10^{11}	J	1.70×10^6	7.40×10^{17}
	Dairy	8.26×10^9	J	2.00×10^6	1.65×10^{16}
	Egg	1.77×10^{11}	J	2.00×10^6	3.54×10^{17}
	Total				7.47×10^{18}
Others (Y)	Biogas energy	5.65×10^{12}	J	1.65×10^5	9.32×10^{17}
	Total output				1.81×10^{19}

(2) Emery evaluation index calculation of the cluster unit

As can be seen from Table 5, the *EIR* value of the cluster unit was 166.48%, indicating that the exploitation and utilization level of the natural resources of the unit at the mesoscale was distinctly higher than that of the unit at the microcosmic scale. Compared with the courtyard unit, the dependency and the quantity demanded of the external resources were lower. Generally speaking, the growth space of this evaluation index was still relatively large in terms of ecological and self-sufficient development goals. The *EYR* value was 215.76%, lower than that of the courtyard unit. More manpower resources with high emery value were invested in this unit, mainly for the construction of the impounding reservoir and the maintenance of the wetland. The *ELR* value was 170.84%, higher than that of the courtyard unit. The consumption of environmental resources and emission of wastes and pollutants were both strengthened, and the secure range of the environmental loads was extruded. The *ESR* value was 37.53%, lower than that of the courtyard unit. On the one hand, this was a reflection of the reduction in the natural resource utilization in this rural human settlement unit; on the other hand, this index also indicated that in order to realize the goal of self-sufficiency, the unit needed the supplement of external resources. The *ESI* value was 1.26, which means that the renewability is lower than that of the courtyard unit, therefore, internal resource utilization for the purpose of sustainable development should be promoted.

Table 5. Emergy evaluation index calculation of the cluster unit.

Item	Value
Emergy input of renewable natural resources (<i>R</i>)	4.90×10^{18}
Emergy input of non-renewable natural resources (<i>N</i>)	1.29×10^{17}
Total emergy input of natural resources (<i>I</i>)	5.03×10^{18}
Emergy of non-renewable purchased resources (<i>F</i>)	6.14×10^{18}
Emergy input of organic resources (<i>O</i>)	2.23×10^{18}
Total emergy input of auxiliary resources (<i>U</i>)	8.37×10^{18}
Total emergy input (<i>T</i>)	1.34×10^{19}
Total emergy output (<i>Y</i>)	1.81×10^{19}
Emergy self-sufficiency ratio (<i>ESR</i>)	37.53%
Emergy investment ratio (<i>EIR</i>)	166.48%
Net emergy yield ratio (<i>EYR</i>)	215.76%
Environmental load ratio (<i>ELR</i>)	170.84%
Emergy sustainable indices (<i>ESI</i>)	1.26

3.1.3. Static Emergy Analysis of the Village Unit

(1) Emergy input and output of the village unit

Table 6 shows the emergy input and output of the village unit in 2020. The emergy input consisted of renewable natural resources (*R*), non-renewable natural resources (*N*), non-renewable purchased resources (*P*), and organic resources (*O*). The total emergy input value was 2.02×10^{20} sej, in which the *R* input, *N* input, *P* input, and *O* input accounted for 31.99%, 0.87%, 49.27%, and 17.77%, respectively. The emergy output consisted of planting, breeding, biogas energy, processing product, and service. The total emergy output value was 2.37×10^{20} sej, in which the planting output, breeding output, biogas energy output, processing product output, and service output accounted for 31.14%, 46.20%, 2.66%, 7.51%, and 12.49%, respectively.

Table 6. Emergy input and output of the village unit.

	Item	Raw Data	Unit	Transformity (sej/Unit)	Solar Emergy (sej)
Renewable natural resources (<i>R</i>)	Sunlight	6.36×10^{19}	J	1	6.36×10^{19}
	Rain chemical	3.32×10^{13}	J	3.05×10^4	1.01×10^{18}
	Rain potential	4.64×10^{11}	J	4.70×10^4	2.18×10^{16}
	Total				6.46×10^{19}
Non-renewable natural resources (<i>N</i>)	Net topsoil loss	1.02×10^{13}	J	1.70×10^5	1.74×10^{18}
	Construction	1.42×10^7	\$	3.40×10^{12}	4.84×10^{19}
	Maintenance	8.95×10^5	\$	3.40×10^{12}	3.04×10^{18}
Non-renewable purchased resources (<i>P</i>)	Equipment	8.40×10^6	\$	3.40×10^{12}	2.85×10^{19}
	Municipal electricity	2.73×10^4	\$	3.40×10^{12}	9.28×10^{16}
	Municipal water	7.48×10^3	\$	3.40×10^{12}	2.54×10^{16}
	Total				9.95×10^{19}
Organic resources (<i>O</i>)	Labor force	4.96×10^{12}	J	7.24×10^6	3.59×10^{19}
	Total input				2.02×10^{20}
Planting (<i>Y</i>)	Bean	6.57×10^{12}	J	6.90×10^5	4.53×10^{18}
	Vegetable	8.05×10^{12}	J	8.30×10^4	6.68×10^{17}
	Fruit	2.13×10^{12}	J	5.30×10^5	1.13×10^{18}
	Potato	4.24×10^{13}	J	4.90×10^5	2.08×10^{19}
	Corn	5.10×10^{12}	J	1.48×10^5	7.55×10^{17}
	Wheat	8.67×10^{13}	J	5.10×10^5	4.42×10^{19}
	Oil plant	2.03×10^{13}	J	8.30×10^4	1.68×10^{18}
	Total				7.38×10^{19}
Breeding (<i>Y</i>)	Pork	1.71×10^{13}	J	4.00×10^6	6.85×10^{19}
	Beef	8.95×10^{12}	J	4.00×10^6	3.58×10^{19}
	Poultry	4.35×10^{11}	J	1.70×10^6	7.40×10^{17}
	Dairy	1.05×10^{11}	J	2.00×10^6	2.09×10^{17}
	Egg	2.12×10^{12}	J	2.00×10^6	4.24×10^{18}
	Total				1.09×10^{20}
Others (<i>Y</i>)	Biogas energy	3.83×10^{13}	J	1.65×10^5	6.32×10^{18}
	Processing product	5.24×10^6	\$	3.40×10^{12}	1.78×10^{19}
	Service	8.71×10^6	\$	3.40×10^{12}	2.96×10^{19}
	Total				5.37×10^{19}
	Total output				2.37×10^{20}

(2) Emergy evaluation index calculation of the village unit

As can be seen from Table 7, the *EIR* value of the village unit was 204.16%, indicating that the exploitation and utilization level of the natural resources of the unit at a macroscopic

scale continuously increased. Compared with the courtyard unit and cluster unit, the dependency and the quantity demanded of external resources continuously decreased. In other words, the growth space of this evaluation index was even larger in terms of ecological and self-sufficient development goals. The *EYR* value was 174.98%, lower than that of the courtyard unit and cluster unit. The proportion of manpower resources purchased continuously increased, mainly for the construction of manufacturing facilities and the management of tourism. The *ELR* value was 212.36%, higher than that of the courtyard unit and cluster unit. The environmental loads became heavier because of the increasing consumption of environmental resources and the emission of wastes and pollutants. The *ESR* value was 32.88%, lower than that of the courtyard unit and cluster unit, which indicates that it was impossible to realize the goal of self-sufficiency. Lastly, the *ESI* value was 0.82, which means the danger of unsustainability was emerging in this unit.

Table 7. Emery evaluation index calculation of the village unit.

Item	Value
Emery input of renewable natural resources (<i>R</i>)	6.46×10^{19}
Emery input of non-renewable natural resources (<i>N</i>)	1.74×10^{18}
Total emery input of natural resources (<i>I</i>)	6.63×10^{19}
Emery of non-renewable purchased resources (<i>F</i>)	9.95×10^{19}
Emery input of organic resources (<i>O</i>)	3.59×10^{19}
Total emery input of auxiliary resources (<i>U</i>)	1.35×10^{20}
Total emery input (<i>T</i>)	2.02×10^{20}
Total emery output (<i>Y</i>)	2.37×10^{20}
Emery self-sufficiency ratio (<i>ESR</i>)	32.88%
Emery investment ratio (<i>EIR</i>)	204.16%
Net emery yield ratio (<i>EYR</i>)	174.98%
Environmental load ratio (<i>ELR</i>)	212.36%
Emery sustainable indices (<i>ESI</i>)	0.82

3.2. Dynamic Emery Prediction of the Rural Human Settlement Unit

3.2.1. Dynamic Emery Prediction Model Verification

This research adopted a historical data verification method for the dynamic emery prediction model verification. The fractional error between the simulation value and the actual value was the validation criteria for whether the model passed the historical data verification. When the fractional error is smaller than 10%, the model can be considered as passing the verification. The fractional error is expressed as the following Equation (10):

$$\delta_{t,k} = \left| \frac{S_{t,k} - A_{t,k}}{A_{t,k}} \right| \quad (10)$$

where δ denotes the fraction error; t denotes the year of the simulation; and k denotes the variable attributes. When $k = 1$, the variable is *ESR*; $k = 2$, the variable is *EIR*; $k = 3$, the variable is *EYR*; $k = 4$, the variable is *ELR*; $k = 5$, the variable is *ESI*; S denotes the simulation value; and A denotes the actual value.

Considering the availability of the historical data, the *ESR*, *EIR*, *EYR*, *ELR*, and *ESI* of 2017–2020, calculated from the emery data, were selected as the historical data to be compared with the simulation data of the village unit for the verification of the prediction model (Table 8). The results showed that the maximum fractional error between the actual historical data and the simulation data of the village unit was 8.96%, which is within the acceptable range. In view of the scientific reliability of the prediction model certifiably passing the verification process, the dynamic emery evaluation indices prediction was proven to be capable of reflecting the development tendency of the rural human settlement unit.

Table 8. Dynamic energy prediction model verification.

Item	Year	Simulation Value	Actual Value	Fractional Error
ESR	2017	0.38	0.36	5.56%
	2018	0.36	0.34	5.88%
	2019	0.35	0.34	2.94%
	2020	0.33	0.33	0%
EIR	2017	1.97	1.92	2.60%
	2018	2.02	1.95	3.59%
	2019	2.05	2.01	1.99%
	2020	2.08	2.04	1.96%
EYR	2017	1.74	1.7	2.35%
	2018	1.75	1.72	1.74%
	2019	1.77	1.75	1.14%
	2020	1.78	1.75	1.69%
ELR	2017	1.99	1.86	6.99%
	2018	2.05	1.98	8.59%
	2019	2.14	2.07	3.38%
	2020	2.31	2.12	8.96%
ESI	2017	0.75	0.79	5.06%
	2018	0.76	0.79	3.80%
	2019	0.77	0.81	4.94%
	2020	0.8	0.8	2.44%

3.2.2. Dynamic Energy Evaluation Index Prediction

The dynamic energy evaluation indices prediction results of the rural human settlement are shown in Figure 7 (the village unit, for instance). The *ESR* values of the ecology-balanced design orientation of the rural human settlement unit were higher than those of the industry invigorative design orientation and lower than those of the environment-friendly design orientation. Because of the maximum avoidance of the external resource input from the manufacturing infrastructure, the initial *ESR* values of the environment-friendly design orientation were higher than those of the other two design orientations. The *ESR* values presented a decreasing tendency with the passage of time, indicating that the self-sufficiency abilities decreased with the gradual maturity of the development of tourism. In addition, the requirements for external resources and exchange activities with the external environment were also increasingly enhanced.

The *EIR* values of the environment-friendly design orientation of this unit were higher than those of the ecology-balanced design orientation and lower than those of the industry invigorative design orientation. The rural human settlement unit of the industry invigorative design orientation developed the internal resources for tourism and manufacturing infrastructure to the maximum so it was necessary to reinforce the monetary and manpower resource investment with regard to the investment attraction, publicity, and ancillary facility construction. According to the above reasons, the initial *EIR* values of the industry invigorative design orientation were higher than those of the other two design orientations. The *EIR* values basically presented an increasing tendency with the passage of time, indicating that with the increasingly enhanced energy output abilities, the proportions for infrastructure construction, maintenance, and operation investments were also heightened.

The *EYR* values of the ecology-balanced design orientation of this unit were higher than those of the environment-friendly design orientation and lower than those of the industry invigorative design orientation. The currency revenue of the tourism and agricultural processing industry was the main energy growth point, therefore the initial *EYR* values of the industry invigorative design orientation were higher than those of the other two design orientations. The *EYR* values basically presented an upward trend with the passage of time, indicating that with the development of society and the progress of technology, more efficient energy utilization modes and more reasonable spatial arrangements of the unit assisted the improvement of the capacity for energy output.

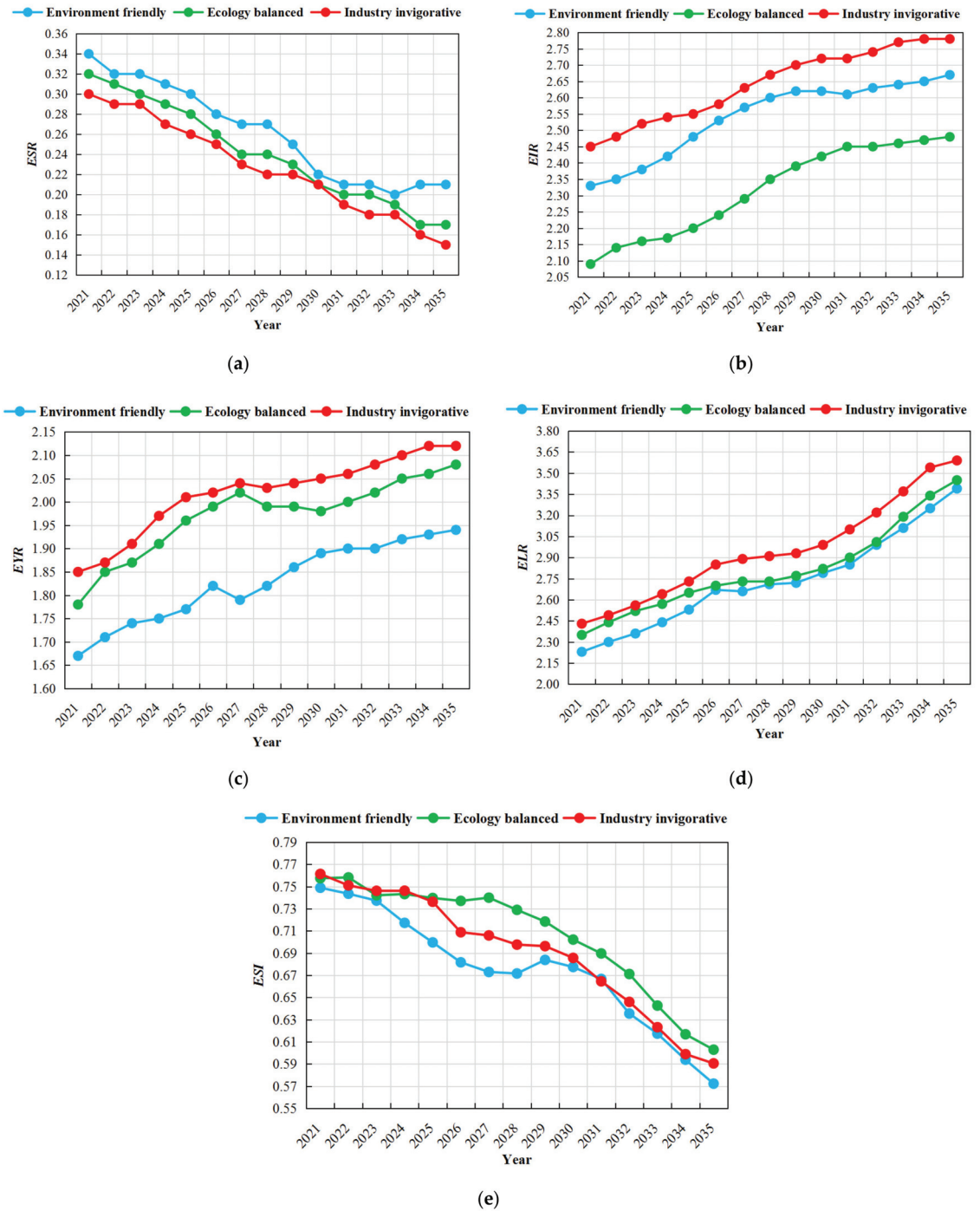


Figure 7. Dynamic energy evaluation indices prediction of the village unit. (a) ESR prediction; (b) EIR prediction; (c) EYR prediction; (d) ELR prediction; and (e) ESI prediction.

The *ELR* values of the ecology-balanced design orientation of this unit were higher than those of the environment-friendly design orientation and lower than those of the industry invigorative design orientation. The damage to the external environment of the rural human settlement unit of the industry invigorative design orientation was mainly from the investment attraction and ancillary facilities construction in the full life cycle, so the initial *ELR* values were higher than those of the other two design orientations. The *ELR* values basically presented an increasing tendency with the passage of time, indicating that the external resources input in the early stage of development was the direct cause, resulting in the increase in the energy emission to the external environment. The growth rates of the *ELR* values would decline from 2026 to 2031, which means that the construction pace in this period would have slowed down, releasing the external environmental pressure to a certain extent. The growth rates of the *ELR* values would then rise again after 2032, indicating that the production accumulation and external energy output in the early stage of development, coupled with possible population growth and the improvement of living standards, would lead to the increase in pollutant emissions in the next stage. With the expansion of the industrial scale, the negative impact of the rural human settlement unit on the external environment would be continuously strengthened in the forecastable future.

The *ESI* values of the industry invigorative design orientation of this unit were higher than those of the environment-friendly design orientation and lower than those of the ecology-balanced design orientation. The *ESI* values basically presented a downward trend with the passage of time, and the curve roughly corresponded to the curve of the *ELR*. The decline rates of the *ESI* values would decrease from 2026 to 2031 and rise again after 2032. At the macroscopic scale of the rural human settlement unit, both the initial and final values of the *ESI* with different design orientations in the prediction interval were lower than the critical value ($ESI = 1$) of sustainable development. However, decreasing *ESI* values do not represent decreasing sustainability. Due to the constant improvement of the unit in the early stage, the internal energy would accumulate continuously, which would become the intrinsic driving force for the sustainable development of the system. Although the *ESI* value would eventually approach zero in the forecastable future, the sustainable development capacity of the rural human settlement unit would not decrease, tending to dynamic equilibrium.

It is of great theoretical and practical significance to optimize and improve the design of rural human settlement units through system ecology analysis based on the energy evaluation indices. Theoretically, this research proposed a new method for the design of rural human settlement units by adopting energy as a common dimension in order to solve the problem of dimensionality disunity between environmental resource elements and society economy elements. Through the establishment of the static energy analysis model and dynamic energy prediction model, the qualitative and quantitative analysis approaches of the rural human settlement units were combined, expanding the application scope of system ecology and the energy theory. In practice, the results of this study have important application value for the formulation and implementation of the ecological and sustainable rural development strategy in China. The evaluation method based on the energy analysis of the technical strategies and spatial arrangements of the rural human settlement unit can provide data support for designing standards, planning guidelines, and creating constructional instructions for the rural living environment of China.

4. Conclusions

This study drew the following conclusions:

- (1) This research creatively proposed the concept of the rural human settlement unit of China, based on the ecological circulation characteristics of the rural living environment, which can be divided into three scales: the microcosmic scale (courtyard unit), mesoscale (cluster unit), and macroscopic scale (village unit). Three design orientations, namely, the industry invigorative, the environment-friendly, and the

- ecology-balanced, of the rural human settlement unit were provided, corresponding with the integration of production-living-ecology.
- (2) The results of the static emergy analysis indicated that the *ESR*, *EYR*, and *ESI* values of the rural human settlement units at a smaller scale were higher than those at a larger scale, while the *EIR* and *ELR* values of rural human settlement units at a smaller scale were lower than those at a larger scale.
 - (3) The results of the dynamic emergy prediction indicated that the *ESR* values of the environment-friendly rural human settlement unit > those of the ecology-balanced unit > those of the industry invigorative unit; the *EIR* values of the industry invigorative unit > those of the environment-friendly unit > those of the ecology-balanced unit; the *EYR* values of the industry invigorative unit > those of the ecology-balanced unit > those of the environment-friendly unit; the *ELR* values of the industry invigorative unit > those of the ecology-balanced unit > those of the environment-friendly unit; and the *ESI* values of the ecology-balanced unit > those of the industry invigorative unit > those of the environment-friendly unit. In addition, the *ESR* and *ESI* values basically presented a decreasing tendency from 0.34 to 0.15 and from 0.76 to 0.57, respectively, with the passage of time; the *EIR*, *EYR*, and *ELR* values basically presented an increasing tendency from 2.13 to 2.78, from 1.66 to 2.12, and from 2.23 to 3.61, respectively, with the passage of time.

Author Contributions: Conceptualization, Y.C. and C.W.; methodology, G.G.; software, G.G.; validation, G.G.; formal analysis, Y.C. and T.M.; investigation, Y.X.; resources, Y.X.; data curation, Y.C.; writing—original draft preparation, Y.C.; writing—review and editing, G.G. and T.M.; visualization, C.W.; supervision, C.W.; project administration, C.W.; funding acquisition, G.G. All authors have read and agreed to the published version of the manuscript.

Funding: This research was funded by the National Natural Science Foundation of China (NSFC Grant No. 52278024) and the Doctoral Research Foundation of Shandong Jianzhu University (No. X18098Z).

Data Availability Statement: No new data were created or analyzed in this study. Data sharing is not applicable to this article.

Acknowledgments: Special thanks to the School of Thermal Engineering, Shandong Jianzhu University for supporting technical consultation.

Conflicts of Interest: The authors declare no conflict of interest. The funders had no role in the design of the study; in the collection, analyses, or interpretation of data; in the writing of the manuscript; or in the decision to publish the results.

Abbreviations

Emergy input of renewable natural resources	<i>R</i>
Emergy input of non-renewable natural resources	<i>N</i>
Total emergy input of natural resources	<i>I</i>
Emergy of non-renewable purchased resources	<i>F</i>
Emergy input of organic resources	<i>O</i>
Total emergy input of auxiliary resources	<i>U</i>
Emergy self-sufficiency ratio	<i>ESR</i>
Emergy investment ratio	<i>EIR</i>
Net emergy yield ratio	<i>EYR</i>
Environmental load ratio	<i>ELR</i>
Emergy sustainable indices	<i>ESI</i>

References

- Zeng, X.; Zhao, Y.; Cheng, Z. Development and research of rural renewable energy management and ecological management information system under the background of beautiful rural revitalization strategy. *Sustain. Comput. Inform. Syst.* **2021**, *30*, 100553. [\[CrossRef\]](#)
- Wu, B.; Liu, L. Social capital for rural revitalization in China: A critical evaluation on the government's new countryside programme in Chengdu. *Land Use Policy* **2020**, *91*, 104268. [\[CrossRef\]](#)
- Gao, J.; Wu, B. Revitalizing traditional villages through rural tourism: A case study of Yuanjia Village, Shaanxi Province, China. *Tour. Manag.* **2017**, *63*, 223–233. [\[CrossRef\]](#)
- Li, B.; You, L.; Zheng, M.; Wang, Y.; Wang, Z. Energy consumption pattern and indoor thermal environment of residential building in rural China. *Energy Built Environ.* **2020**, *1*, 327–336. [\[CrossRef\]](#)
- Meng, X.; Liang, W.; Ding, P.; Wang, S.; Li, Y.; Long, E. Survey research on living environment and energy consumption in the west rural areas of China. *Procedia Eng.* **2015**, *121*, 1044–1050. [\[CrossRef\]](#)
- Wang, Y.Y.; Zhang, Y.P.; Yang, G.F.; Cheng, X.M.; Wang, J.; Xu, B. Knowledge mapping analysis of the study of rural landscape ecosystem services. *Buildings* **2022**, *12*, 1517. [\[CrossRef\]](#)
- Luo, X.; Yang, J.; Sun, W.; He, B. Suitability of human settlements in mountainous areas from the perspective of ventilation: A case study of the main urban area of Chongqing. *J. Clean. Prod.* **2021**, *310*, 127467. [\[CrossRef\]](#)
- Tang, L.; Ruth, M.; He, Q.; Mirzaee, S. Comprehensive evaluation of trends in human settlements quality changes and spatial differentiation characteristics of 35 Chinese major cities. *Habitat Int.* **2017**, *70*, 81–90. [\[CrossRef\]](#)
- Xue, Q.; Yang, X.; Wu, F. A two-stage system analysis of real and pseudo urban human settlements in China. *J. Clean. Prod.* **2021**, *293*, 126272. [\[CrossRef\]](#)
- Musakwa, W. Data on strategically located land and spatially integrated urban human settlements in South Africa. *Data Br.* **2017**, *15*, 805–808. [\[CrossRef\]](#)
- Yang, R.; Xu, Q.; Long, H. Spatial distribution characteristics and optimized reconstruction analysis of China's rural settlements during the process of rapid urbanization. *J. Rural Stud.* **2016**, *47*, 413–424. [\[CrossRef\]](#)
- Cao, Y.; Bai, Z.; Sun, Q.; Zhou, W. Rural settlement changes in compound land use areas: Characteristics and reasons of changes in a mixed mining-rural-settlement area in Shanxi Province, China. *Habitat Int.* **2017**, *61*, 9–21. [\[CrossRef\]](#)
- Cechin, A.; da Silva Araújo, V.; Amand, L. Exploring the synergy between Community Supported Agriculture and agroforestry: Institutional innovation from smallholders in a Brazilian rural settlement. *J. Rural Stud.* **2021**, *81*, 246–258. [\[CrossRef\]](#)
- Zhao, X.; Sun, H.; Chen, B.; Xia, X.; Li, P. China's rural human settlements: Qualitative evaluation, quantitative analysis and policy implications. *Ecol. Indic.* **2019**, *105*, 398–405. [\[CrossRef\]](#)
- Watts, J.D. Community living standards and rural household decision making. *J. Rural Stud.* **2020**, *80*, 23–33. [\[CrossRef\]](#)
- Wang, W.; Gong, H.; Yao, L.; Yu, L. Preference heterogeneity and payment willingness within rural households' participation in rural human settlement improvement. *J. Clean. Prod.* **2021**, *312*, 127529. [\[CrossRef\]](#)
- Li, G.; Jiang, C.; Zhang, Y.; Jiang, G. Whether land greening in different geomorphic units are beneficial to water yield in the Yellow River Basin? *Ecol. Indic.* **2021**, *120*, 106926. [\[CrossRef\]](#)
- Zhou, D.; Xu, J.; Lin, Z. Conflict or coordination? Assessing land use multi-functionalization using production-living-ecology analysis. *Sci. Total Environ.* **2017**, *577*, 136–147. [\[CrossRef\]](#)
- Tian, F.; Li, M.; Han, X.; Liu, H.; Mo, B. A production–living–ecological space model for land-use optimisation: A case study of the core Tumen River region in China. *Ecol. Model.* **2020**, *437*, 109310. [\[CrossRef\]](#)
- Wu, J.; Zhang, D.; Wang, H.; Li, X. What is the future for production-living-ecological spaces in the Greater Bay Area? A multi-scenario perspective based on DEE. *Ecol. Indic.* **2021**, *131*, 108171. [\[CrossRef\]](#)
- Yang, Y.; Bao, W.; Liu, Y. Coupling coordination analysis of rural production-living-ecological space in the Beijing-Tianjin-Hebei region. *Ecol. Indic.* **2020**, *117*, 106512. [\[CrossRef\]](#)
- Xu, Q.; Song, W.; Zhang, Y. Forecast and optimal allocation of production, living and ecology water consumption in Zhangye, China. *Phys. Chem. Earth.* **2016**, *96*, 16–25. [\[CrossRef\]](#)
- Liao, T.; Li, D.; Wan, Q. Tradeoff of Exploitation-protection and Suitability Evaluation of Low-slope hilly from the perspective of "production-living-ecological" optimization. *Phys. Chem. Earth.* **2020**, *120*, 102943. [\[CrossRef\]](#)
- Zou, L.; Liu, Y.; Yang, J.; Yang, S.; Wang, Y.; Cao, Z.; Hu, X. Quantitative identification and spatial analysis of land use ecological-production-living functions in rural areas on China's southeast coast. *Habitat Int.* **2020**, *100*, 102182. [\[CrossRef\]](#)
- Yi, H.; Braham, W.W. Uncertainty characterization of building emergy analysis (BEmA). *Build. Environ.* **2015**, *92*, 538–558. [\[CrossRef\]](#)
- Yi, H.; Srinivasan, R.S.; Braham, W.W.; Tilley, D.R. An ecological understanding of net-zero energy building: Evaluation of sustainability based on emergy theory. *J. Clean. Prod.* **2017**, *143*, 654–671. [\[CrossRef\]](#)
- Andrić, I.; Pina, A.; Ferrão, P.; Lacarrière, B.; Le Corre, O. The impact of renovation measures on building environmental performance: An emergy approach. *J. Clean. Prod.* **2017**, *162*, 776–790. [\[CrossRef\]](#)
- Tilley, D.R. Dynamic accounting of emergy cycling. *Ecol. Model.* **2011**, *222*, 3734–3742. [\[CrossRef\]](#)
- Zhang, J.; Srinivasan, R.S.; Peng, C. A systematic approach to calculate unit emergy values of cement manufacturing in china using consumption quota of dry and wet raw materials. *Buildings* **2020**, *10*, 128. [\[CrossRef\]](#)

30. Luo, Z.; Zhao, J.; Yao, R.; Shu, Z. Emergy-based sustainability assessment of different energy options for green buildings. *Energy Convers. Manag.* **2015**, *100*, 97–102. [[CrossRef](#)]
31. Artuzo, F.D.; Allegretti, G.; Santos, O.I.B.; da Silva, L.X.; Talamini, E. Emergy unsustainability index for agricultural systems assessment: A proposal based on the laws of thermodynamics. *Sci. Total Environ.* **2021**, *759*, 143524. [[CrossRef](#)] [[PubMed](#)]
32. Lewandowska-Czarnecka, A.; Buller, L.S.; Nienartowicz, A.; Piernik, A. Energy and emergy analysis for assessing changes in Polish agriculture since the accession to the European Union. *Ecol. Model.* **2019**, *412*, 108819. [[CrossRef](#)]
33. Cristiano, S. Organic vegetables from community-supported agriculture in Italy: Emergy assessment and potential for sustainable, just, and resilient urban-rural local food production. *J. Clean. Prod.* **2021**, *292*, 126015. [[CrossRef](#)]
34. Liu, Z.; Wang, S.; Xue, B.; Li, R.; Geng, Y.; Yang, T.; Li, Y.; Dong, H.; Luo, Z.; Tao, W.; et al. Emergy-based indicators of the environmental impacts and driving forces of non-point source pollution from crop production in China. *Ecol. Indic.* **2021**, *121*, 107023. [[CrossRef](#)]
35. Xu, Q.; Yang, Y.; Hu, K.; Chen, J.; Djomo, S.N.; Yang, X.; Knudsen, M.T. Economic, environmental, and emergy analysis of China's green tea production. *Sustain. Prod. Consum.* **2021**, *28*, 269–280. [[CrossRef](#)]
36. Zhu, J.; Yuan, X.; Yuan, X.; Liu, S.; Guan, B.; Sun, J.; Chen, H. Evaluating the sustainability of rural complex ecosystems during the development of traditional farming villages into tourism destinations: A diachronic emergy approach. *J. Rural Stud.* **2021**, *86*, 473–484. [[CrossRef](#)]
37. Falkowski, T.B.; Martinez-Bautista, I.; Diemont, S.A.W. How valuable could traditional ecological knowledge education be for a resource-limited future? An emergy evaluation in two Mexican villages. *Ecol. Model.* **2015**, *300*, 40–49. [[CrossRef](#)]
38. Qu, Y.; Zhan, L.; Jiang, G.; Ma, W.; Dong, X. How to Address “Population Decline and Land Expansion (PDLE)” of rural residential areas in the process of Urbanization: A comparative regional analysis of human-land interaction in Shandong Province. *Habitat. Int.* **2021**, *117*, 102441. [[CrossRef](#)]
39. Kong, X.; Liu, D.; Tian, Y.; Liu, Y. Multi-objective spatial reconstruction of rural settlements considering intervillage social connections. *Rural Stud.* **2021**, *84*, 254–264. [[CrossRef](#)]
40. Qu, Y.; Jiang, G.; Ma, W.; Li, Z. How does the rural settlement transition contribute to shaping sustainable rural development? Evidence from Shandong, China. *Rural Stud.* **2021**, *82*, 279–293. [[CrossRef](#)]
41. Gong, J.; Jian, Y.; Chen, W.; Liu, Y.; Hu, Y. Transitions in rural settlements and implications for rural revitalization in Guangdong Province. *Rural Stud.* **2022**, *93*, 359–366. [[CrossRef](#)]
42. Li, G.; Fang, C.; Qi, W. Different effects of human settlements changes on landscape fragmentation in China: Evidence from grid cell. *Ecol. Indic.* **2021**, *129*, 107927. [[CrossRef](#)]
43. Lu, Y.; Song, W.; Luy, Q. Assessing the effects of the new-type urbanization policy on rural settlement evolution using a multi-agent model. *Habitat. Int.* **2022**, *127*, 102622. [[CrossRef](#)]
44. Cyriac, S.; Firoz, C.M. Dichotomous classification and implications in spatial planning: A case of the Rural-Urban Continuum settlements of Kerala, India. *Land Use Policy* **2022**, *114*, 105992. [[CrossRef](#)]
45. Ji, Z.; Xu, Y.; Sun, M.; Liu, C.; Lu, L.; Huang, A.; Duan, Y.; Liu, L. Spatiotemporal characteristics and dynamic mechanism of rural settlements based on typical transects: A case study of Zhangjiakou City, China. *Habitat. Int.* **2022**, *123*, 102545. [[CrossRef](#)]
46. Shi, Z.; Ma, L.; Zhang, W.; Gong, M. Differentiation and correlation of spatial pattern and multifunction in rural settlements considering topographic gradients: Evidence from Loess Hilly Region, China. *J. Environ. Manag.* **2022**, *315*, 115127. [[CrossRef](#)]
47. Zhao, G.; Liang, R.; Li, K.; Wang, Y.; Pu, X. Study on the coupling model of urbanization and water environment with basin as a unit: A study on the Hanjiang Basin in China. *Ecol. Indic.* **2021**, *131*, 108130. [[CrossRef](#)]
48. Couto, A.; Martins, P.; Sano, E.; Martins, E.; Vieira, L.; Salemi, L.; Vasconcelos, V. Data for: Terrain units, land use/cover, and gross primary productivity of the largest fluvial basin in the Brazilian Amazonia/Cerrado ecotone: The Araguaia River Basin. *Data Br.* **2021**, *34*, 106636. [[CrossRef](#)]
49. Li, J.; Sun, W.; Li, M.; Linlin, M. Coupling coordination degree of production, living and ecological spaces and its influencing factors in the Yellow River Basin. *J. Clean. Prod.* **2021**, *298*, 126803. [[CrossRef](#)]
50. Van Niekerk, A. A comparison of land unit delineation techniques for land evaluation in the Western Cape, South Africa. *Land Use Policy* **2010**, *27*, 937–945. [[CrossRef](#)]
51. Hu, Q.; Wang, W. Quality evaluation and division of regional types of rural human settlements in China. *Habitat. Int.* **2020**, *105*, 102278. [[CrossRef](#)]
52. Zhang, J.; Srinivasan, R.S.; Peng, C. Ecological assessment of clay brick manufacturing in china using emergy analysis. *Buildings* **2020**, *10*, 190. [[CrossRef](#)]
53. Le Corre, O.; Truffet, L.; Lahlou, C. Odum-Tennenbaum-Brown calculus vs. emergy and co-emergy analysis. *Ecol. Model.* **2015**, *302*, 9–12. [[CrossRef](#)]

Disclaimer/Publisher’s Note: The statements, opinions and data contained in all publications are solely those of the individual author(s) and contributor(s) and not of MDPI and/or the editor(s). MDPI and/or the editor(s) disclaim responsibility for any injury to people or property resulting from any ideas, methods, instructions or products referred to in the content.

MDPI
St. Alban-Anlage 66
4052 Basel
Switzerland
www.mdpi.com

Buildings Editorial Office
E-mail: buildings@mdpi.com
www.mdpi.com/journal/buildings



Disclaimer/Publisher's Note: The statements, opinions and data contained in all publications are solely those of the individual author(s) and contributor(s) and not of MDPI and/or the editor(s). MDPI and/or the editor(s) disclaim responsibility for any injury to people or property resulting from any ideas, methods, instructions or products referred to in the content.



Academic Open
Access Publishing

[mdpi.com](https://www.mdpi.com)

ISBN 978-3-0365-9303-6